Forschungszentrum Jülich

Fusion Theory

Proceedings of the Seventh European Fusion Theory Conference

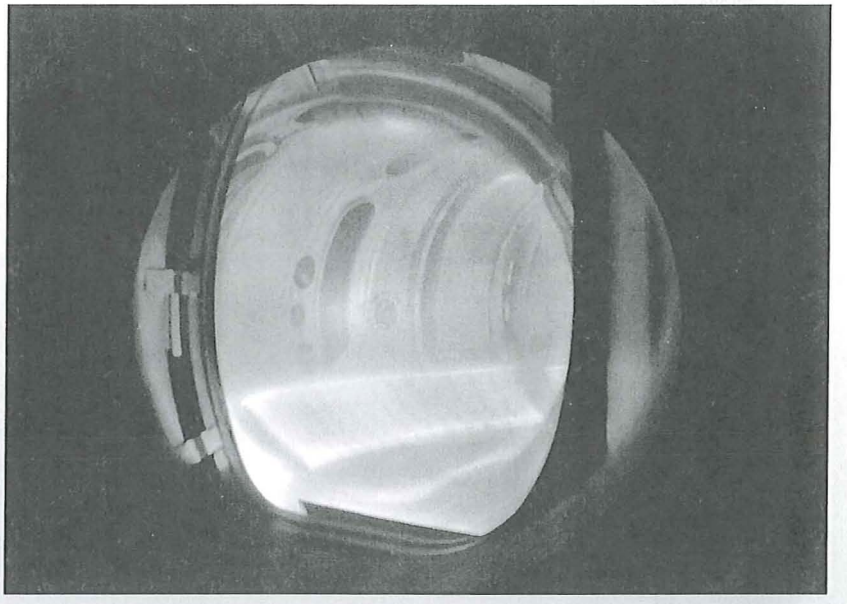

Edited by André Rogister

Energietechnik
Energy Technology

Schriften des Forschungszentrums Jülich
Energietechnik/Energy Technology Volume 1

Forschungszentrum Jülich GmbH
Institute for Plasma Physics

Fusion Theory

Edited by André Rogister

Proceedings of the Seventh European Fusion Theory Conference held in Jülich, Germany, 8–10 October 1997

Schriften des Forschungszentrums Jülich
Reihe Energietechnik/Energy Technology Volume 1

ISSN 1433-5522 ISBN 3-89336-219-3

Die Deutsche Bibliothek - CIP-Einheitsaufnahme

Fusion theory : proceedings of the Seventh European Fusion Theory Conference, held in Jülich, Germany, from 8 - 10 October 1997 / Forschungszentrum Jülich GmbH, Institute for Plasma Physics. Ed. by André Rogister. - Jülich : Forschungszentrum, Zentralbibliothek, 1998
(Schriften des Forschungszentrums Jülich : Reihe Energietechnik/Energy Technology ; Volume 1)
ISBN 3-89336-219-3

Publisher and Distributor:	Forschungszentrum Jülich GmbH Central Library D-52425 Jülich Germany Phone: +49 2461 61-5368 · Fax: +49 2461 61-6103 e-mail: zb-publikation@fz-juelich.de Internet: http://www.kfa-juelich.de/zb
Coverdesign:	Grafische Betriebe, Forschungszentrum Jülich GmbH
Printer:	Grafische Betriebe, Forschungszentrum Jülich GmbH

Printed on environmentally friendly paper.

Schriften des Forschungszentrums Jülich
Reihe Energietechnik/Energy Technology, Volume 1

ISSN 1433-5522
ISBN 3-89336-219-3

Preface

Controlled nuclear fusion research in magnetic confinement devices is being pursued world-wide with the long term aim of providing an inexhaustible, safe, environmentally benign energy source. Today's largest devices - JET (Joint European Torus), TFTR (Tokamak Fusion Test Reactor), JT-60 U - could already approach or reach scientific break-even with the optimum fusion fuel. One objective of the next step, ITER (International Tokamak Experimental Reactor), is to complete the demonstration of scientific feasibility of fusion by achieving controlled and sustained fusion burn for some 1000 seconds.

The role of theoretical research in this context is to provide a better understanding of the physical processes at work in the confined plasma supporting the fusion reactions; this should ultimately lead to better control of the most promising operation scenarios and possibly to improved concepts.

The main objective of the European Fusion Theory Conferences is to provide a forum for discussion of fusion oriented theoretical activities in Europe. The 7th EFTC was held in Jülich, Germany, from 08 — 10 October 1997. The meeting was attended by 85 delegates, most of them from Europe and a few from other continents. The papers presented at the conference were selected by the International Scientific Programme Committee on the basis of one page abstracts. Invited papers were selected to present overviews of major theoretical activities under way in European laboratories and universities.

The Scientific Programme Committee is comprised of the following members:

H. Wilhelmsson (Chair)	Chalmers University, Göteborg, Sweden
C. Alejaldre	Ciemat, Madrid, Spain
R. Balescu	ULB, Brussels, Belgium
D. Biskamp	MIPP, Garching, Germany
J.W. Connor	UKAEA, Abingdon, UK
D.W. Faulconer	ERM/KMS, Brussels, Belgium
W. Kerner	JET, Abingdon, UK (EU)
M. Lontano	ENEA-CNR, Milano, Italy

E.K. Maschke	CEA, Cadarache, France
P.K. Michelsen	National Laboratory, Risϕ, Denmark
A. Rogister	IPP/FZJ, Jülich, Germany
T.J. Schep	IPF/FOM, Nieuwegein, The Netherlands
F. Serra	IST, Lisboa, Portugal
K. Spatschek	Heinrich-Heine University, Düsseldorf, Germany
J. Vaclavick	CRPP, Lausanne, Switzerland
J. Weiland	Chalmers University, Göteborg, Sweden
F. Zonca	ENEA, Frascati, Italy

whose home laboratories or universities are affiliated with the **European Fusion Programme**, Directorate General XII, EU.

Previous European Fusion Theory Conferences were held at Utrecht (1995), Madrid (1993), Oxford (1991), Göteborg (1989), Varenna (1987) and Wépion (1985). The present proceedings are published at the occasion of the 7th Conference.

We would like to thank the board of directors of the Forschungszentrum Jülich, the Fusion Directorate-DG XII of the European Commission, the „Arbeitsgemeinschaft Plasmaphysik (APP)“ and the Graduierten Kolleg „Hochtemperatur-Plasmaphysik“ for sponsoring the conference. The extensive support of the Conference Service of the Forschungszentrum Jülich, and in particular of Dr. B. Krahl-Urban and Ms. A. Deußen, are gratefully acknowledged. We would like also to thank here Mrs. D. Petschner of the Institute for Plasmaphysics for her invaluable help.

André Rogister
Institut für Plasmaphysik
Association EURATOM-FZJ
Jülich

Karl-Heinz Spatschek
Heinrich-HeineUniversität Düsseldorf,
Düsseldorf

Contents

Invited Papers 1

M. R. O'Brien
Spherical tokamaks: challenges for theory in a new regime 3

T.J. Schep, V.P. Lakhin, E. Westerhof
Current-vortex filament model of nonlinear Alfvèn perturbations
of a finite-pressure plasma 11

J.J. Rasmussen
Transport and coherent structures 13

A. Zeiler, D. Biskamp, J.F. Drake, B.N. Rogers
Three-dimensional simulations of tokamak edge turbulence 21

M.Z. Tokar
Plasma states in tokamaks with strong impurity radiation 29

M. Zabiégo, T.A. Gianakon, S.E. Kruger, X. Garbet, G. Giruzzi,
E. Joffrin, C.C. Hegna, J.D. Callen
Finite-ß tearing-mode stability for tokamak discharges
with current-profile control 37

S. Brunner, M. Fivaz, J. Vaclavik
Gobal approach to the spectral problem of microinstabilities in
tokamak plasmas using a gyrokinetic model 45

A. Bondeson, M. Benda, M. Persson
Operational space of advanced tokamaks and constraints for
steady-state operation 53

E. Vanden Eijnden
Statistical description of plasma turbulence and anomalous transport 61

L. Garcia:
Rotation and enhanced confinement in tokamaks 63

Contributed Oral Papers 71

A.J.C. Beliën, B. van der Holst, J.P. Goedbloed, B.G. Hong, S.K. Kim
MHD stability analysis of negative central shear plasmas 73

G. Berge:
An Energy principle for stability of ideal magnetohydrodynamic systems
in stationary motion 75

W. Zwingmann, D.P. O`Brien, D. Bartlett
Equilibrium analysis of JET tokamak discharges 79

V. Naulin
Structures and transport in drift wave turbulence 83

H. Nordman, P. Strand, J. Weiland
Simulation of dimensionless scaling experiments on JET 87

J. Ongena, J. Boedo, G. Bonheure, R.V. Budny, C.E. Bush, P. Dumortier,
T. Evans, K. Hill, A. Hyatt, G. Jackson, A.M. Messiaen, D. Mueller,
A. Ramsey, G. Staebler, B. Unterberg, P.E. Vandenplas, M. Wade,
G. van Wassenhove, R.R. Weynants, TEXTOR-94, DIII-D, TFTR Teams
Overview of improved confinement in impurity seeded discharges in
TEXTOR-94, DIII-D and TFTR 91

S. Puri
Enhanced transport via Kirchhoff radiation 95

E. Lazzaro, R. Coelho, M. F. Nave
Aspects of driven reconnection of low order modes in tokamaks 99

M. Fivaz, O. Sauter, Kj. Appert, S. Brunner, T.M. Tran, J. Vaclavik
Study of second stability for ITG modes 103

A. Cardinali, S. Bernabei, F. Paoletti, W. Tighe, S. von Goeler
Theory of ion Bernstein and lower hybrid waves synergy 107

S.V. Kasilov
Modelling of quasi-linear RF heating effects in complex magnetic geometries 111

R. Nakach, Y. Gell
Multiple autoresonance accelerations generated from a chaotic base 115

S.E. Sharapov
Multiple Alfvèn eigenmodes in conventional and spherical tokamaks 117

D. Montgomery, J.W. Bates
Poloidal flows in resistive MHD equilibria 119

J.P. Goedbloed, A.E. Lifshitz
Critical issues in transonic magnetohydrodynamic flows 123

D.F. Escande, D. Bénisti
Dynamical interpretation of dynamo in the RFP 127

R. Balescu
A Map representing a stochastic magnetic field in a tokamak 131

A. Rogister
Enhanced rotation velocities and electric fields, sub-neoclassical
energy transport and density pinch from revisited neoclassical theory 133

Poster Contributions 137

L. Villard, M. Fivaz, J. Vaclavik
Simulations of ion-temperature-gradient modes in helical symmetry 139

P.K. Michelsen, J.J. Rasmussen, N. Chakrabati
Ion temperature gradient vortices in shear flow 143

V. Naulin
Numerical simulation of drift and flute modes in cylindrical gometry 147

M. Pozzo, M. Tessarotto, R. Zorat
Direct perturbative gyrokinetic approach for non hamiltonian systems 151

R. Zorat, M. Tessarotto
Improvements on nonlinear gyrokinetic particle simulations, based on δf-discretization scheme 155

T. Jessen, P.K. Michelsen, M. Saffman, W. Svendsen
Analysis of collective light scattering in terms of drift wave turbulence models 159

W.E. Han S. Barocio, A. Thyagaraja
Analysis of measured and simulated electromagnetic turbulence in COMPASS-D 163

M. Lontano, J. D'Avanzo, D. Ryutov
Long-range perturbations produced by a packet of ion-acoustic waves in a plasma 167

B. Weyssow, J.H. Misguich
Guiding centre trajectories in perturbed magnetic geometries 171

E. Vanden Eijnden:
A new renormalization scheme for turbulent transport 175

A. Kaleck, M. Tokar
Width of islands in a tokammak with a localized helical perturbation field 177

S.S. Abdullaev, K.H. Finken, A. Kaleck, K.H. Spatschek
Modelling of tokamak ergodic divertor by twist map 181

K.H. Finken, Th. Eich, A. Kaleck
Modelling efforts for the helical near field divertor of TEXTOR-94 185

H. Lasaar, M.Z. Tokar
Semi-analytical calculations of radiation losses from light impurities in a non-corona approximation 189

D. Reiser, D. Reiter, M. Tokar
Kinetic effects in the formation of a radiating layer 193

W. Kerner, O. Pogutse
The scaling of the edge temperature at the L-H transition based on the Alfvèn drift-wave instability 197

H.A. Claaßen, H. Gerhauser
The influence of impurities and heat flux gradients on the revised neoclassical transport in tokamaks 199

U. Daybelge, C. Yarim, M. Anguelova
Nonlinear plateau regime dynamics of the poloidal rotation in tokamaks 203

R. Sugaya
Fluctuation-induced transport and potential formation across a magnetic field 207

A.H. Nielsen, J.P. Lynov, J.J. Rasmussen
Particle transport across a circular shear layer with coherent structures 211

G. Cenacchi, A. Airoldi
Considerations on the IGNITOR performances 215

H. Gerhauser, H.A. Claaßen
Numerical study of the deformation of the ion distribution function
in the magnetic presheath 219

W.A. Cooper
Canonical and magnetic coordinates applied to relativistic guiding centre drifts 221

T.J. Schep, F. Pegaro, V.P. Lakhin
Plasma dynamics in extended MHD 225

B. van der Holst, R.J. Nijboer, J.P. Goedbloed
MHD cluster spectra of plasmas with flow 227

R. Zorat, J.L. Johnson, M. Tessarotto, R.B. White
Generalized MHD equilibria in the presence of shear flow 229

R.J. Nijboer, J.P. Goedbloed, A.E. Lifschitz
Stability of incompressible hyperbolic MHD flows 233

D. Grasso, E. Cafaro, F. Pegoraro, F. Porcelli, A. Saluzzi
Invariants and geometric structures in nonlinear hamiltonian
magnetic reconnection 237

E. Maschke, M. Berroukeche, B. Saramito
Numerical study of the nonlinear saturation of double tearing modes 241

R. Grauer, Ch. Marliani
Adaptive mesh refinement for singular current sheets in incompressible
magnetohydrodynamic flows 245

R. Storer
Resistive toroidal plasma spectra and power absorption from external fields 247

A. Ardelea, W.A. Cooper
Ideal MHD stability of plasmas with toroidal, helical and vertical field coils 251

O. Sauter, F. Hofmann, H. Reimerdes, I. Furno, R. Behn, M.J. Dutch,
Y. Martin, J.-M. Moret, C. Nieswand, Z.A. Pietrzyk, A. Pochelon
Comparison of high current disruption limit in elongated plasmas with
ideal and resistive MHD models 255

A. Rogister, D. Li
Operational limits in tokamaks 259

R. Paccagnella
Stability properties of the reversed field pinch with realistic boundary conditions 263

B. Dasgupta, P. Dasgupta, M. S. Janaki, T. Watanabe, T. Sato
Relaxed states of magnetized plasma with minimum dissipation 267

B.N. Kuvshinov, A.B. Mikhailovskii
A kinetic energy principle for a tokamak allowing for bounce and
transit resonances 271

E. Westerhof, V.P. Lakhin, T.J. Schep
Integrable motion of four current-vortex filaments 275

V. Tribaldos, J.A. Jiménez, J. Guasp, B.Ph. van Milligen
Future prospects of electron cyclotron heating and current drive in
TJ-II stellarator 279

D. Van Eester, R. Koch
Aspects of bounce-averaged Fokker-Planck modelling of radio
frequency heating in tokamaks 283

F. Louche
A solver for the non-linear Fokker-Planck equation 287

Y. Louis, P.U. Lamalle
Study of Landau interaction between electrons and radio frequency field,
incorporating phase decorrelation effects 291

D.W. Faulconer, R. Koch, V.I. Zasenko
Plasma dynamics in box of unshielded fast wave antenna 295

A. Jaun, K. Appert, T. Hellstsen, J. Vaclavik, L. Villard
On resonance absorption and continuum damping 299

Invited Papers

Spherical Tokamaks: Challenges for Theory in a new Regime

M R O'Brien

UKAEA, Fusion Culham, Abingdon, Oxon OX14 3DB, UK

(UKAEA/Euratom Fusion Association)

Abstract. There is increasing interest in spherical tokamaks with several new devices being constructed or planned. This is partly because of the success of experiments on START at Culham which have confirmed the compact, high β potential of the spherical tokamak. Spherical tokamaks pose new challenges for theory and modelling which often have built-in assumptions and orderings which are not valid for the low aspect ratio equilibria. In this paper, these challenges are outlined, covering the topics of plasma stability, heating and current drive, confinement, edge physics and steady-state operation.

I. Introduction

There are now low aspect ratio ($R/a < 2$) "spherical tokamaks" (STs) operating in the UK, the US and Japan, and several new devices under construction (e.g. MAST at Culham, NSTX at Princeton, GLOBUS-M in St. Petersburg, ETE in Brazil). The increasing interest is partly because of the success of experiments on START at Culham (aspect ratio $R/a \geq 1.25$ [1]). These experiments have confirmed the potential of the ST, with confinement and operating space at least as good as conventional tokamaks, and improved positional stability properties at high elongation. In particular, use of neutral beam heating equipment from Oak Ridge National Laboratory, has given record β for a tokamak (>30%, Figure 1, [1]). High β is possible because, as MHD calculations described below have confirmed, the ST β-limit has the Troyon scaling of plasma current divided by minor radius and toroidal field (I_P/aB_ϕ), and, for constant edge safety factor, I_P/aB_ϕ increases greatly as R/a reduces.

Spherical tokamak research is valuable for two reasons. Firstly, results from STs can be used to test models developed for conventional tokamaks ($R/a \geq 2.5$) in a new regime, and, if successful, this increases confidence in the use of these models for predicting the performance of larger devices (e.g. ITER). Secondly, the ST has the potential for compact, high β fusion devices (power plants and neutron sources). However, STs pose new challenges for theory and modelling which often have built-in assumptions and orderings which are incorrect for STs - these challenges are the subject of this paper. Thus many

theories and codes have to be revisited before being used for ST applications. The main change at low R/a is to the equilibrium, the main features of which are summarised in section II. Topics covered in subsequent sections are stability, confinement, edge physics, heating and current drive, and the possibility of steady-state operation utilising high-bootstrap-fraction regimes, akin to the "advanced tokamak" regime at conventional aspect ratio.

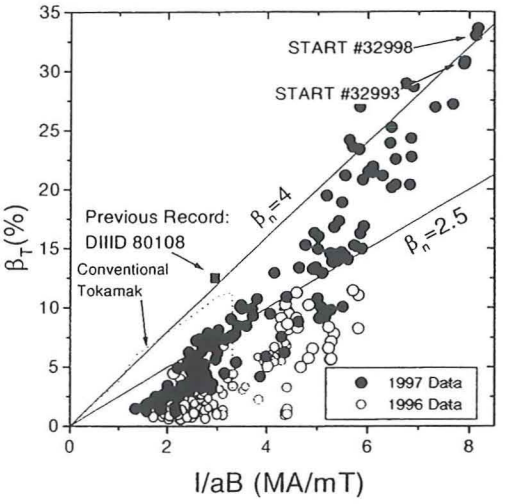

Figure 1 Plot showing record β values obtained on START by accessing much higher values of I_P/aB_ϕ than can be reached on conventional tokamaks.

II. Equilibria and Particle Orbits

The very high current-carrying (I_P/aB) potential arises because of the aspect ratio dependence of q_ψ at the plasma edge which varies as $(a^2B_\phi/RI_P)\ (1+\kappa^2)/2\ f(\varepsilon)$ with $f(\varepsilon)$ typically ~ $1/(1-\varepsilon)$ ($\varepsilon = a/R$). Therefore, for a given q_ψ, I_p rises rapidly as $\varepsilon = a/R$ rises. Also κ can be higher with the ST's improved vertical stability. This means high I_p/aB can be achieved, which is how the record β values on START were obtained (see Figure 1). A key, related parameter for the ST is I_p/I_{rod}, where I_p/I_{rod} is the current in the central rod which generates the toroidal field. As well as determining, for a given aspect ratio, the achievable β, in a power plant I_p/I_{rod} must be greater than ~ 1 for engineering reasons (recirculating power) - I_p/I_{rod} has reached 1.2 in START.

The low aspect ratio, high I_p/I_{rod}, and high β mean that ST equilibria can differ greatly from "usual" tokamak equilibria. A proper treatment of the equilibrium can be important when applying theory to STs. Properties of ST equilibria include:

- B_θ can exceed B_ϕ at the outboard side (large R) of the plasma. This means |B| can have a local minimum in the plasma, i.e. $\partial B/\partial R = 0$.
- The field line tilt at the outside edge of the plasma can be large (which affects, for example, coupling of waves to the plasma).
- At high I_p/I_{rod}, paramagnetism means B at the magnetic axis can be twice the vacuum field.
- Very high edge shear, dq/dr, near the plasma edge has a stabilising effects.
- The large field ratio between the inside and outside of flux surfaces can give a large trapped particle fraction (affecting neo-classical physics, current drive efficiencies, etc.). But this effect can be reduced or removed by "omnigeneity" - |B| almost constant on a flux surface- which arises from the interplay of the high B_θ and high paramagnetism, and can mean that some flux surfaces have local |B| minima.

These effects mean **fast ion orbits** can differ from those in conventional tokamaks. Because B_θ can exceed B_ϕ, the Larmor radius can be comparable with the guiding-centre banana width (see Figure 2). Omnigeneity means orbits can be wider near their bounce tips than in the equatorial plane, and there can be local particle trapping in the local |B| minimum. "Potato orbits" near the magnetic axis are more important than in conventional tokamaks, and might modify neo-classical effects [2]. Orbits of fast ions from neutral beam heating (e.g., in START, MAST, NSTX) need correct treatment for heating and current drive calculations [3]. Alpha-particle orbits also need correct treatment for ST fusion devices - calculations show confinement is generally good [4].

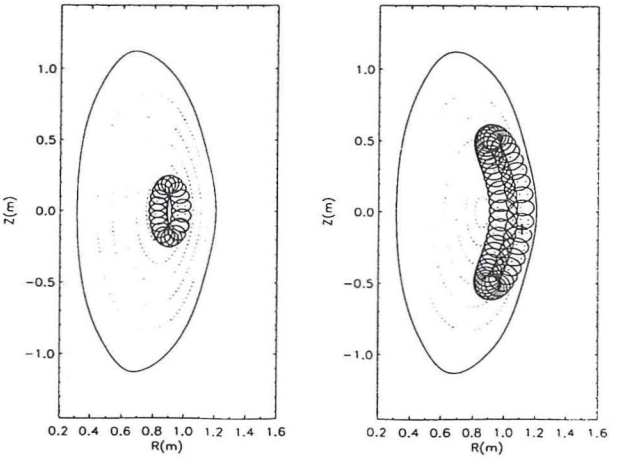

Figure 2 Typical fast ion orbits in MAST (from 80keV deuterium NBI, I_p = 1 MA, B_o = 0.42T).

III. Stability

The ERATO code has been used to study the aspect ratio dependence of first stability β-limits. Profiles were varied to be marginally stable to ballooning modes, and then kink stability was checked for these profiles. Results show a Troyon-type expression ($\beta(\%) = \beta_n I_p(MA)/a(m)B(T)$) holds good, for $\beta = \langle p \rangle / B^2$, with B the vacuum field at the geometric centre of the plasma: $\beta_n \geq 4$ is determined by ballooning stability for these profiles (Figure 3 and [5]), and has fairly slow variation with q_ψ and plasma shaping. ERATO calculations have shown that in the START record β discharges, the pressure profiles are close to marginal ballooning stability across the plasma. Spherical tokamaks also have the potential for second stability operation - see Section VI below.

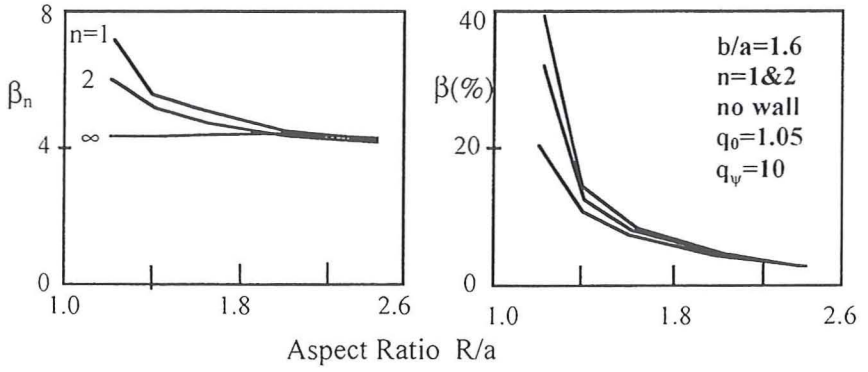

Figure 3 ERATO calculations show β_n is almost independent of R/a, and at low R/a is set by ballooning stability.

The high density, low field nature of the ST suggests modes driven by energetic particles (TAE-like modes) may be an issue ($v_{particle} > v_{Alfven}$), and evidence for "chirping"-like modes has been observed in beam-heated START plasmas [6]. An important issue for theory is therefore the evaluation of damping and driving mechanisms for ST equilibria [7].

IV. Heating and Current Drive

Since the tokamak density limit scales with I_p, the high current to field ratio in the ST implies high n_e/B, and therefore high ω_p/ω_c, meaning coupling and penetration of RF waves can be difficult. Neutral Beam Heating is therefore the most promising heating

method and has been very successful on START. However RF methods are possible, though challenging. Some of the issues for the various methods are now described.

Neutral Beam Heating & Current Drive: As noted above, orbit and trapping effects need to be treated correctly in heating and current drive calculations [2, 3].

Electron Cyclotron Heating & Current Drive: The high value of ω_{pe}/ω_{ce} in conceptual ST power plants restricts ECH to cyclotron harmonics $m \geq 3$, though $m = 2$ and $m = 3$ ECH will be options for low density operation in MAST. At high I_p and full field ($I_p/I_{rod} \sim 1$) the large distortion of the |B| contours away from R = const. lines means the m=2 resonance, and therefore the heating, can be central (Figure 4). In power plant equilibria ($I_p/I_{rod} > 1$), |B| has a local well on the outboard of the plasma. This can mean there is more than one resonant surface in the plasma so that waves launched from the outside mid-plane are absorbed near the plasma edge before they ever reach the more central resonance. Access of the waves to the plasma centre, e.g. for current drive, therefore requires launch from away from the equatorial plane avoiding the local well.

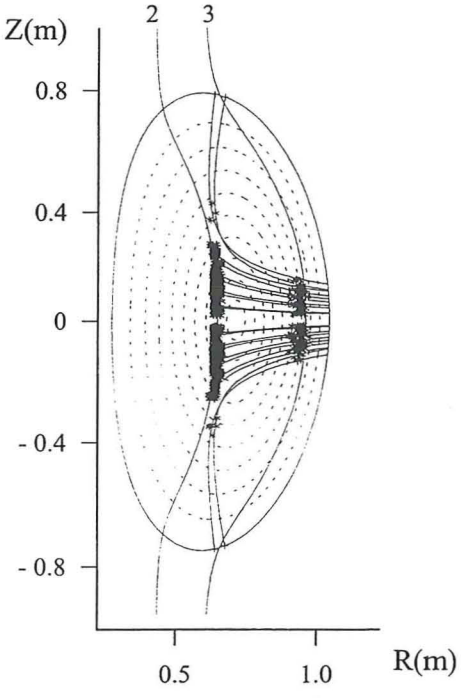

Figure 4 Absorption of 60 GHz ECRH X mode waves launched from the outboard side of MAST (I_P=2MA, B_{vac0}=0.7T, R=0.63m, a=0.43m, $n_{e0}=2\times10^{19}m^{-3}$, T_{e0} = 3 keV) at the second and third harmonic cyclotron resonances (which are the |B| contours marked 2 and 3). The large distortion of |B| contours away from R=const. lines is due to large paramagnetism in the toroidal field and the large poloidal field of the ST.

LHCD and ICRF: Wave accessibility is difficult, particularly for low $N_{||}$ waves desirable for current drive, but options have been identified which will be tested

experimentally. For LHCD, calculations show that accessibility may be possible for some launch conditions, with good current drive efficiency, and this will be tested on GLOBUS-M [8]. For ICRF, high harmonic fast waves look attractive for electron heating and current drive, and will be used on NSTX [9]. Coupling at high field line tilt is a key issue for both schemes - initial tests with high harmonic fast waves on CDX-U have been successful with heating demonstrated.

Current Drive: The effects of particle trapping in ST geometry need correct treatment for accurate calculation of current drive efficiencies. One outstanding issue is the effect of having local wells on a flux surface. This has similarities with current drive in stellarator and ripple fields, but differs because the variation is only in the poloidal and not the toroidal plane.

V. Confinement and Edge Physics

Spherical Tokamak experiments are valuable for testing scalings and theories for core and edge confinement in a new regime. For example, confinement analysis have been undertaken for START, as for conventional tokamaks, though this is particularly challenging as steady-state is generally not reached in START. Global analysis shows that ITER scaling laws give a reasonable fit to START data [10, 1], but in some plasmas they are exceeded by a factor ~2. Also, the degradation of confinement with beam power appears to be weaker than in conventional tokamaks. Preliminary 1D analysis using the ASTRA code implies the ion conductivity of beam-heated plasmas may be neo-classical. It is important to revisit physics-based scaling laws for STs, as these may require corrections for low aspect ratio (e.g. Lackner-Gottardi was modified to Connor-Lackner-Gottardi for application to START [11]).

A number of ST features are favourable for suppressing micro-instabilities, and therefore good confinement [12]. High β leads to high sheared diamagnetic flows, which help stabilise turbulence, and the high field at low major radius means particles spend a long time in the "good curvature" region of the tokamak. The presence of a magnetic well in $|B|$ can also improve stability. Figure 5, from preliminary calculations at Culham [13], shows that stability to ion temperature gradient modes is markedly improved at low aspect ratio.

Data from START are being compared with data from a conventional aspect ratio device (COMPASS-D) and used to test various scrape-off layer (SOL) models in a new regime, to help discriminate between these to improve predictions for ITER and MAST [14]. Results so far show some models perform much better than others for COMPASS-D (a

constant $\chi_\perp$ model, often used in edge codes, performs particularly badly), but all have difficulties reproducing START data. The SOL in START can be very narrow, particularly in high β, low q plasmas. These plasmas have some H-mode characteristics (sharp edge, flat density profile)) but others are missing (the temperature profile is peaked and clear ELMs have not yet been observed).

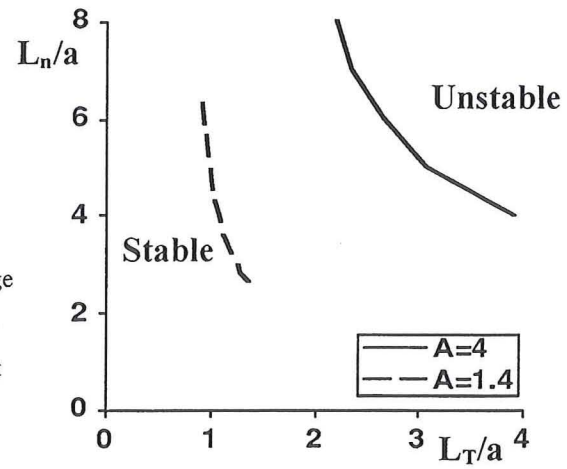

Figure 5 Plot showing that ITG modes are stable for a larger range of density and temperature scale-lengths at low aspect ratio than at conventional aspect ratio.

VI. Steady-state Regimes

Spherical tokamaks have the potential for steady-state regimes analogous to the "advanced tokamak" at conventional aspect ratio. These require almost all of the current to be driven by the pressure gradient (bootstrap, diamagnetic and Pfirsch-Schlüter currents), especially if trapped-particle reductions to the efficiency of the "seed" current drive are large. Theoretical studies are leading the way in identifying these regimes - experimental investigation awaits sustained plasmas with current drive on NSTX and MAST. Equilibria with R/a = 1.4 and a ratio of pressure-driven to total current ~ 99% have been calculated [15, 16] - these are intrinsically stable to ballooning modes but require a close conducting wall for stability to low n kink modes. These equilibria have current profiles which peak sharply in the high pressure gradient region close to the plasma edge - even so, the strong geometric shear at low aspect ratio means the safety factor q increases monotonically from the plasma centre to the plasma edge.

VII. Conclusions

Spherical tokamak physics offers new challenges to theories. It provides new opportunities to test calculations with data from experiments in a new regime - if successful,

this leads to models which can be applied with increased confidence to both STs and conventional tokamaks. Also, ST equilibria have novel features which often have to be included for accurate calculations of ST physics, which means that many theories and codes need to be revisited and adapted before they can be used for ST calculations. The ST is a promising option for compact fusion applications, but has some outstanding issues which require resolution - theory has a role to play here, particularly in identifying steady-state scenarios, optimum heating and current drive methods, and divertor solutions.

Acknowledgements

I would like to thank the many colleagues who have contributed material for this review. The ERATO code was used courtesy of CRPP, Lausanne, Switzerland. The work described was funded by the UK Department of Trade and Industry and by Euratom.

References

[1] A Sykes, et al., "High beta performance of the START Spherical Tokamak". Review paper at the 24th EPS Conf on Plasma Physics and Controlled Fusion, Berchtesgaden, 1997, to be published in Plasma Physics and Controlled Fusion, and references therein.
[2] Y R Lin-Liu and F L Hinton, to be published in Physics of Plasmas.
[3] D R Mikkelsen, et al., Physics of Plasmas **4** (1997) p3667.
[4] K G McClements and R O Dendy, "Alpha-particle Orbits in Spherical Tokamaks ...", to be published in proceedings of the 5th IAEA Technical Committee Meeting on Alpha-Particles in Fusion Research, JET, Sept. 1997.
[5] T C Hender, et al., Proceedings of 22nd EPS Conf on Plasma Physics and Controlled Fusion, Bournemouth, 1995, Part III, p233.
[6] K G McClements, et al., "Observations of MHD modes in the Alfven Frequency Range in Beam-Heated START Discharges", to be published in proceedings of the 5th IAEA Technical Committee Meeting on Alpha-Particles in Fusion Research, JET, Sept. 1997.
[7] Paper by S E Sharapov, these proceedings.
[8] V Gusev, Proc. International Workshop on Spherical Torus and US-Japan Workshop on Low Aspect Ratio Tokamaks, Culham, 1996, Vol I p550.
[9] S M Kaye, Proc. International Workshop on Spherical Torus and US-Japan Workshop on Low Aspect Ratio Tokamaks, Culham, 1996, Vol II p826.
[10] C M Roach, et al., Plasma Physics and Controlled Fusion **37** (1995) p679.
[11] A Sykes, et al., Proc. International Conference on Plasma Physics, Brazil 1994, American Institute of Physics Conference Proceedings 345, p110.
[12] G Rewoldt, et al., Physics of Plasmas **3** (1996) p1667.
[13] T J Martin, private communication.
[14] G F Counsell, et al., to be published in proceedings of 24th EPS Conference on Plasma Physics and Controlled Fusion, Berchtesgaden, 1997.
[15] R L Miller, et al., Physics of Plasmas **4** (1997) p1062.
[16] J Menard, et al., Nuclear Fusion **37** (1997) p595.

Current-Vortex Filament Model of Nonlinear Alfvén Perturbations in a Finite-Pressure Plasma

V.P.Lakhin *, T.J. Schep and E. Westerhof
FOM-Instituut voor Plasmafysica, "Rijnhuizen", Association Euratom-FOM,
P.O.Box 1207, 3430 BE Nieuwegein, The Netherlands

It is known that the MHD equations do not possess exact solutions that would be similar to point-vortices in two-dimensional hydrodynamics [1]. Unlike MHD, two-fluid equations of nonlinear dynamics of Alfvén perturbations in a homogeneous finite-pressure plasma, that take into account finite electron inertia and the Hall term, are shown to admit exact generalized solutions in the form of interacting angular current-vortex filaments. Three different types of filaments can exist. Each of these types is frozen into a different "velocity" field. Like the point-vortex model in hydrodynamics, the system of interacting curent-vortex filaments is Hamiltonian. Invariance of the Hamiltonian under translations and rotation entails the existence of three additional constants of the motion – two components of the linear momentum and the angular momentum. Generally speaking, only three constants of the motion (including the Hamiltonian) are in involution. Thus, the motion of two and of three filaments is integrable, and the motion of four filaments is nonintegrable (except in some special cases). Some particular solutions in the form of single and double filament chains will be given. It is found that the far field of a filament pair, consisting of two filaments with opposite intensities, reproduces the field outside the separatrix of the distributed dipole Alfvén vortex tube (see, e.g. [2]). This allows to simulate collisions of the distributed vortex tubes by the interaction between filament pairs. The emphasis will be put on integrable cases: the cases of vanishing linear momentum and of coaxial filament pairs. The reduction of the Hamiltonian by canonical transformations to one degree of freedom is found. On the basis of the corresponding phase diagram, a classification of the different collisional regimes is presented.

References

[1] V.I.Petviashvili, Plasma Phys.Rep., **19**, 256 (1993).

[2] A.B.Mikhailovskii, V.P.Lakhin, G.D.Aburdzhaniya et al., Plasma Phys.Contr.Fus., **29**, 1 (1987).

*Permanent address: Nuclear Fusion Institute, Russian Research Centre "Kurchatov Institute", 123182 Moscow, Russia

TRANSPORT AND COHERENT STRUCTURES

Jens Juul Rasmussen
Association EURATOM–Risø National Laboratory
Optics and Fluid Dynamics Department, OFD-129, Risø,
P.O. Box 49, DK-4000 Roskilde, Denmark
e-mail: jens.juul.rasmussen@risoe.dk

Abstract. The dynamics of vortical structures and their influence on turbulent transport is discussed for quasi-two-dimensional flows. The trapping and de-trapping of particles by individual vortical structures is illustrated and the diffusion in turbulent flows dominated by vortical structures will be described. The role of vortical structures in connection with the cross field plasma transport mediated by electrostatic fluctuations will be considered.

I. Introduction

Recent investigations have shown that the anomalous cross-field transport of particles and energy in magnetized plasmas can be ascribed to low frequency electrostatic fluctuations, in particular in the edge region (see e.g. [1, 2]). A striking similarity in the structure of the fluctuations and the associated transport has been found for different toroidal configurations like Tokamaks and Stellarators (see also [3]), and even for linear machines [4]. However, a detailed understanding of the underlying mechanism is still lacking.

Electrostatic fluctuations at low frequency are essentially propagating in a plane perpendicular to the magnetic field. They are dominated by the $\mathbf{E} \times \mathbf{B}$ drift and are driven unstable by, e.g., the pressure gradient. These fluctuations are well described by two-dimensional or quasi-two-dimensional models and they share many of the general features of turbulence in two-dimensional flows. It is well established that the emergence of coherent vortical structures is a characteristic feature of this kind of turbulent flows. These structures may evolve spontaneously by self-organization, they have long life-time and are of great importance for the large scale dynamics and in connection with the transport of mass and energy. They trap particles and convect them over large distances providing a transport mechanism, which is essentially different from diffusion-like transport. It is important to stress that vortical structures are strongly non-linear entities that are not wave-like, they often exist in regimes where linear waves cannot propagate, i.e., they may have propagation velocities outside the range of linear phase velocities. This has been invoked as a necessary requirement for the existence of steady vortex structures [5]. The vortices are then truly localized, they will not couple energy to linear waves and their life time is determined by dissipative effects. Strong quasi-steady vortices having propaga-

tion velocities coinciding with the linear phase velocity may still be sufficiently long lived to be of importance for dynamics of the flow and the associated transport. Here "long lived" designates a lifetime significantly longer than the characteristic time for dispersive spreading of a linear wave packet of the same size as the vortex.

II. Appearance of vortical structures

The existence of vortical structures is well established in fluid dynamics. The fundamental vortex structures are monopolar vortices, dipolar vortices (consisting of a pair of monopoles of opposite vorticity), and tripolar vortices (consisting of a central vortex and two satellites). It appears that higher order structures are not stable. Only the dipolar vortex is propagating in homogeneous flows. These structures are found to play a significant role in widely different areas as mixing in laboratory flows and large scale transport in geophysical flows in atmospheres and oceans. They have been subject of many investigations see, e.g., [5, 6, 7, 8] and references in these papers, where also the relationship between plasma turbulence and turbulence in "ordinary" fluids is discussed. The similarities between fluid models and models for electrostatic turbulence are restricted to the simplified models for plasma turbulence, like the so-called Hasegawa-Mima equation for drift-waves, which is similar to the so-called Charney equation for Rossby waves.

It has been argued that more complex ("realistic") models for electrostatic turbulence, where two or more fields are coupled, do not support vortex like solutions. However, these models are still essentially two-dimensional and the dominating non-linearity is of the convective type as in "simpler" models. As discussed in [5, 6, 8] stationary solutions in the form of vortical structures also exist for these complex models. In addition there are many numerical investigations that show clear evidence of vortical structures and their transport capacities for two-field models of drift-wave and flute type turbulence, see e.g. [6, 9, 10, 11, 12]. Also, in experiments vortex like structures have been identified in linear devices [4], toroidal devices without rotational transform [13] and in tokamaks [14].

The low frequency ion dynamics in the plane perpendicular to the magnetic field is governed by the ion vorticity equation for the conservation of the "potential" vorticity:

$$\frac{d\Pi}{dt} = \frac{d}{dt}\frac{\omega + \omega_{ci}}{n} = 0 \,, \tag{1}$$

where n is the density, $\omega = (\nabla \times \mathbf{v})\cdot\hat{z}$ is the vorticity, and ω_{ci} is the ion cyclotron frequency. Equation (1) is an exact relation, when the ion temperature gradient is negligible. In

the simplest case, where the convection velocity is the $\mathbf{E} \times \mathbf{B}$ drift velocity and the electrons are Boltzmann distributed, Eq. (1) reduces to the Hasegawa-Mima equation with: $\Pi = \nabla^2\phi - \phi + \kappa y$. ϕ is the electrostatic potential, taking the role of a streamfunction ($\mathbf{v} = -\nabla\phi \times \hat{z}$, $\omega = \nabla^2\phi$) and κ is proportional to the background density gradient in, say, the negative y–direction. Then with $\mathbf{B}_0 = B_0\hat{z}$ the linear drift waves are propagating in the negative x–direction with the maximum phase velocity given by κ. Equation (1) imposes strong restrictions on the dynamics of a fluid element, since if ω is not changing, this fluid element is bound to stay at the same y–position and can only move along the x–direction, i.e., perpendicular to the background gradients. Thus, in inhomogeneous systems the propagation of localized coherent structures will be strongly anisotropic, and no transport will take place along the gradients. If, on the other hand, the structure is decaying it will move down the density gradient to keep Π constant.

III. Vortex structures and particle trapping/detrapping

Vortex structures are characterized by the appearance of closed isolines in the vorticity. This causes the ability for trapping and long distance transport of particles. It is of key importance to know how particles are trapped and de-trapped in the vortical structures for understanding the vortex transport and its importance in fully developed turbulence. In Fig. 1 is shown an example of how particles can be de-trapped from a developing individual structure. We have considered the evolution of a monopolar vortex governed by the Hasegawa-Mima equation, which is solved numerically [15, 8]. Trajectories of selected particles initially released inside as well as outside the core of closed isolines in the vortex are plotted in the frame of reference moving with the vortex. The monopole is not a stationary solution, but is decaying by radiating linear waves. Sufficiently strong vortices can propagate over long distances mainly across the background density gradient, with a small velocity component along the gradient (as discussed in connection with Eq. (1)).

The loss rate of particles is estimated by calculating the time during which the particles are trapped as a function of their initial distance, r_0, from the vortex center, Fig. 1. Particles initially released outside the core, $r_c \approx 1.2$, are never effectively trapped. Particles initially released in the outer part of the core of closed isolines are lost at a nearly constant rate, whereas particles initially released deep inside the separatrix are effectively trapped and transported along with the vortex. Thus, the shrinking of vortex cores allows for gradual escape of transported particles induced by the non-stationary

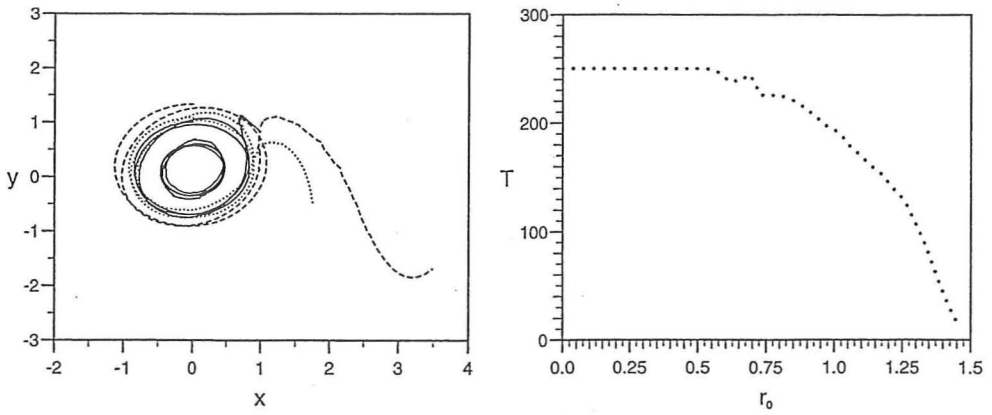

Figure 1: Selected particle trajectories in a monopolar vortex in the frame of refernce following the monopole. Dotted and dashed lines illustrate particles that are lost and full lines particles which are effectively trapped (left panel). Loss rate of particles initially released at a distance r_0 from the center of the vortex (right panel). T indicates the approximate time during which the particles are trapped. The figure is reproduced from [15]

propagation of a coherent structure. On the other hand, as the vortex cores are expanding particles will be trapped, as was demonstrated for a decaying dipole in a viscous homogeneous flow [16].

These observations support the general statement that there is almost no radial mixing inside the vortices. The vortex boundary appears impermeable for particles. This is observed even during strong vortex interactions such as merging of two equal signed vortices [7, 17]. Although for this process, which is important in developed two-dimensional turbulence, a significant amount of the particles originally trapped in the vortices is spread around the merged vortex structure.

From the observations described above it seems obvious that the presence of vortex structures in developed turbulence will have strong influence on the dispersion of particles. Although it is quite easy to identify at least strong vortices by visual inspection of the vorticity field (when this is available as in numerical simulations), it is important to have a quantitative method to distinguish vortices from the background field. For this purpose the so-called Weiss field [18], Q, has proven useful.

$$Q = \frac{1}{4}(\sigma^2 - \omega^2), \quad \text{where} \quad \sigma^2 = \left(\frac{\partial u}{\partial x} - \frac{\partial v}{\partial y}\right)^2 + \left(\frac{\partial u}{\partial y} + \frac{\partial v}{\partial x}\right)^2 \tag{2}$$

is the squared strain (deformation) and u and v are the x and y components of the velocity. Q can be used to separate the flow into regions where strain is dominating,

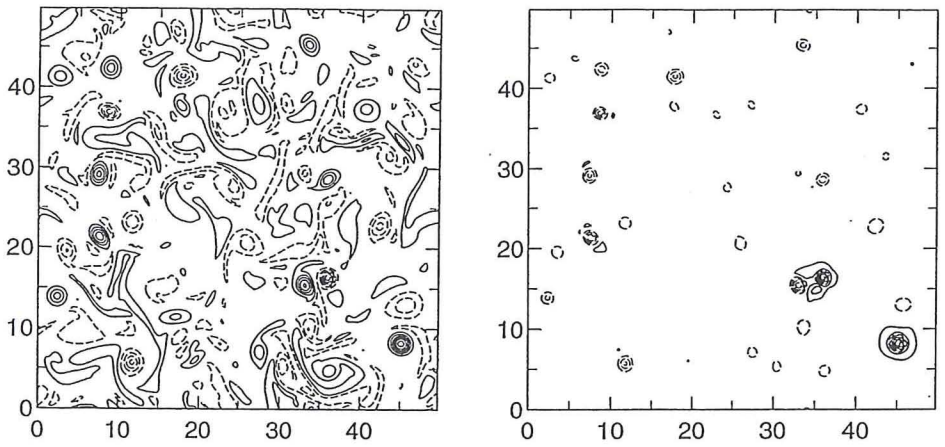

Figure 2: The vorticity field in the saturated state of the resistive drift wave turbulence (left panel). The corresponding Weiss field Q (right panel). The dashed contours indicate negative values, and solid indicate positive values. The figure is reproduced from Ref. [10]

$Q > 0$, and regions where vorticity is dominating, $Q < 0$. In the former regions the motion is hyperbolic, the passively advected vorticity will be strongly sheared and nearby fluid elements - or particles - separate exponentially, in the latter regions the motion is elliptic, the vorticity will be smoothly advected and nearby fluid elements stay together. Thus, the interior of vortices will be characterized by a negative Q.

In Fig. 2 we illustrate the significance of the Weiss field for characterizing the flow topology in developed drift wave turbulence [10]. The vorticity field is compared with the Weiss field. It is seen that $Q < 0$ in the vortices, while in general $Q > 0$ between the vortices. In the vicinity of the vortices Q takes its largest values; the dynamics here is strongly strain dominated. By considering the relative dispersion of pairs of particles initialized in different regions of the flow it was found that particles placed in the hyperbolic regimes separated much faster than particles in the elliptic regimes. For large positive values of Q the separation was found to be exponential, see Fig. 3.

For the case of single particle dispersion, defined as $A^2(t) = \langle(\mathbf{r}(t) - \mathbf{r}(t_0))^2\rangle$, in turbulent flows the classical results predicts that $A^2(t) = 2\langle v^2\rangle t^2$ for $t \ll T_L$ and $A^2(t) = 2Dt$ for $t \gg T_L$, where $T_L = \int_0^\infty C(\tau)d\tau$ is the Lagrangian integral time scale, $C(\tau)$ is the autocorrelation function, $\langle v^2\rangle$ is the mean square velocity fluctuation and D is the diffusion coefficient. In numerical simulations of forced and dissipative two dimensional turbulence, e.g., [19, 17], it was found that in addition to the two asymptotic regimes of

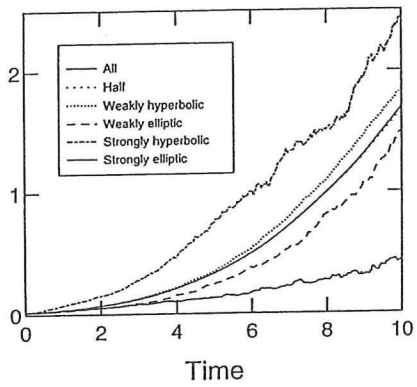

Figure 3: The relative dispersion in different regions of the flow field, parametrized by the Weiss field Q. "All" correspond to the average over all particles, "Half" is the average over half the particles chosen randomly, "Weakly hyperbolic" is average over particles in weakly hyperbolic regimes etc. The figure is reproduced from Ref. [10]

particle dispersion, there is an intermediate region of anomalous dispersion, characterized by $A^2(t) \propto t^\alpha$, typically with $\alpha = 5/4$. By conditional averaging over particles in hyperbolic regimes it was observed that their dispersion were also characterized by $\alpha \approx 5/4$, whereas particles in elliptic regimes have $\alpha \approx 5/3$. The reason that the exponent for the unconditional averages over all particles is close to the one found for the hyperbolic regimes is that the hyperbolic regimes covers the largest area of the field.

Although anomalous dispersion regimes have been commonly observed, e.g., [17], it seems not possible to find a unified value of α. Also different models that result in regimes of anomalous dispersion have been suggested, as for instance based on fractional Brownian motion, or a model for random walkers with two populations characterized by different de-correlation times [20]. But these models do not have the capacity of predicting a specific value of α, that is independent on the initial assumptions. Finally we note that the anomalous dispersion due to the presence of vortex structures in turbulent flows is related to the models for "*strange diffusion*" in disordered media with orderly structures [21].

From the discussion above it is evident that the transport of particles cannot be diffusion like in a turbulent flow which is dominated by - or just contains a significant number of - vortical structures, since the displacement of the particles is strongly dependent on their position.

The influence of vortical structures on the plasma transport have been investigated in simulations of drift-wave turbulence, see, e.g., the recent works [9, 11, 22] with results similar to the ones described above. It was clearly observed that the turbulent flux, defined as $\Gamma = \tilde{n}\tilde{v}_r$, where $\tilde{n}$ and $\tilde{v}_r$ are the fluctuating density and (radial) velocity component parallel to the density gradient, was locally enhanced in the vicinity of the vortical structures and, thus, strongly inhomogeneous in space. Particularly, it was observed that the dispersion of particles is strongly anisotropic, the dispersion is much stronger across the background density gradient than along the gradient. This is to be expected for a flow dominated by vortical structures, since they preferentially propagate perpendicular to the gradient (see the discussion in connection with Eq. (1)). Thus, the presence of vortical structures may in these cases limit the transport along the density gradient.

IV. Discussion - relation to cross field plasma transport

For low frequency electrostatic fluctuations the associated cross field plasma transport is described by the flux $\Gamma = \tilde{n}\tilde{v}_r$, where $\tilde{v}_r$ is obtained from $\tilde{\mathbf{E}} \times \mathbf{B_0}$, with $\tilde{\mathbf{E}}$ being the fluctuating azimuthal electric field. In particular, the time averaged value $\Gamma_0 = \langle\Gamma\rangle$ measures the net plasma transport caused by the fluctuations. The temporal evolution of Γ is usually found to be strongly intermittent, with an amplitude probability distribution function (PDF) far from a Gaussian [4, 23, 24]. The non-gaussian tail of the PDF, which is indicative of bursts in the flux, was found to be associated with the presence of vortical structures both in simulations of drift waves [12] and in experiments [4], although in general the PDF for Γ is non-Gaussian even if the distribution of $\tilde{\mathbf{E}}$ and $\tilde{n}$ both have gaussian PDF's [24].

We noted the similarity of the characteristics of the fluctuations and in particular the flux statistics in linear devices as Q-machines [4] and in the scrape off layer (SOL) of toroidal devices [3, 23]. Thus, we may speculate that coherent vortical structures also play a role in connection with the turbulent transport in the SOL [23]. The presence of the vortical structures will result in bursts of the turbulent flux. Thus, the transport is different from a diffusion-like process in agreement with the discussion in Sec. III and it is not meaningful to associate a diffusion coefficient with this transport process. Even if the bursts associated with the structures only contribute with a smaller part of the integrated flux, they could have serious consequences, which cannot be predicted from the averaged flux, Γ_0. A strong burst of hot plasma hitting the limiter or even the wall of the vessel can have lasting influence.

The influence of vortical structures will have serious consequences for modelling of the turbulence and the associated transport. A linear stability analysis cannot say much about the non-linear saturated state of the fluctuations and scaling arguments based on quasi-linear estimates of the transport coefficients will not be adequate. Thus, the modelling would require a full non-linear solution of complex models with several coupled equations. From such models one cannot expect to obtain a simple power law dependent scaling model for the transport coefficients.

References

[1] A.J. Wootton *et al.*, Plasma Physics and Controlled Fusion **34**, 2023 (1992).
[2] Wagner, F. and Stroth, U. 1993 Plasmas Phys. Control. Fusion **35**, 1321.
[3] M. Endler *et al.*, Physica Scripta **51**, 610 (1995);
[4] A.H. Nielsen *et al.*, Phys. Plasmas **3**, 1530 (1996). T. Huld *et al.*, Phys. Fluids B **3**, 1609 (1991).
[5] Nycander, J. *Chaos* **4**, 253,(1994).
[6] W. Horton and A. Hasegawa, Chaos **4**, 227 (1994).
[7] A.H. Nielsen *et al.*, Physica Scripta, **T63**, 49 (1997).
[8] J. Juul Rasmussen *et al.* Plasmas Phys. Control. Fusion, **36** B193 (1994).
[9] T. Dudok de Wit *et al.*, Phys. Rev. E **52** 6753 (1995).
[10] T.S. Pedersen *et al.* Phys. Plasmas **3**, 2939 (1996).
[11] V. Naulin and K. Spatschek, Phys. Rev. E **55** 5883 (1997).
[12] V. Naulin, These proceedings.
[13] F.J. Øynes *et al.*,, Phys. Rev. Let. **75**, 81 (1995).
[14] S. Benkadda *et al.*, Phys. Rev. Lett. **73**, 3403 (1994).
[15] G.G. Sutyrin *et al.* J. Fluid Mech. **268**, 103 (1994).
[16] A.H. Nielsen and J. Juul Rasmussen, Phys. Fluids **9**, 982 (1997).
[17] A. Provenzale *et al.*, in: *Mixing: Chaos and Turbulence*, Proc. NATO Advanced Study Institute, Cargese, Corsica, July 7-20, 1996.
[18] J. Weiss, Physica D **48**, 273 (1991).
[19] D. Elhmaidi *et al.* J. Fluid Mech. **257**, 533 (1993).
[20] G. Bofetta *et al.*, Phys. Lett. A **235**, 15 (1997).
[21] R. Balescu, Phys. Rev. E **55**, 2465 (1997).
[22] G. Manfredi and R.O. Dendy, Phys. Rev. Lett. **76** 4360 (1996); Phys. Plasmas **4**, 628 (1997).
[23] M. Endler *et al.*, Nucl. Fusion **35**, 1307 (1995).
[24] B.A. Carreras *et al.* Phys. Plasmas **3**, 2664 (1996).

Three-dimensional simulations of tokamak edge turbulence

A. Zeiler, D. Biskamp
Max-Planck-Institut für Plasmaphysik, EURATOM Association
85748 Garching, Germany

J. F. Drake, B. N. Rogers
Institute for Plasma Research, University of Maryland,
College Park, Maryland, 20742, USA

Abstract: The mechanisms of turbulent transport in the collisional tokamak edge plasma are investigated linearly and nonlinearly focusing specifically on the transition between resistive drive mechanisms and the turbulence driven by the collisionless toroidal η_i mode.

1. Introduction

The quantitative prediction of turbulent transport remains one of the most challenging problems in theoretical plasma physics as well as in the design of future toroidal confinement experiments. Whereas the ion energy confinement in the hot plasma core seems to be largely controlled by collisionless ion temperature gradient modes [1,2], resistive modes play a dominant role at the plasma edge [3,4,5]. In this regime the ion temperature dynamics is usually completely ignored. In simulations of η_i mode turbulence, on the other hand, the effects of the nonadiabatic electron response [1,2,6,7,8] are typically neglected. For a complete description of the plasma edge including such important topics as the formation of the H-mode transport barrier and the edge pedestal, both approximations are unjustified. It is therefore necessary to proceed to a more complete set of equations including both the nonadiabatic electron response and the complete ion temperature dynamics.

In this paper we discuss the complete set of electrostatic two fluid Braginskii equations based on linear eigenvalue calculations and nonlinear simulations.

2. Equations

Our investigations are based on the electrostatic drift-Braginskii equations [9,10] in a flux-tube domain using field-aligned coordinates [3,4], which we write here in dimensionless form:

$$\nabla_\perp \cdot \frac{d}{dt}\nabla_\perp(\phi + \tau\alpha_d p_i) + \hat{C}\frac{p_e + \tau p_i}{1+\tau} + \frac{\partial^2 h}{\partial z^2} = 0, \tag{1}$$

$$\frac{dn}{dt} + \frac{\partial \phi}{\partial y} - \left[\epsilon_n \hat{C}(\phi - \alpha_d p_e) - \epsilon_v \frac{\partial v_\parallel}{\partial z} - \alpha_d \epsilon_n (1+\tau)\frac{\partial^2 h}{\partial z^2}\right] = 0, \tag{2}$$

$$\frac{dT_e}{dt} + \eta_e \frac{\partial \phi}{\partial y} - \frac{2}{3}\left[\epsilon_n \hat{C}(\phi - \alpha_d p_e) - \epsilon_v \frac{\partial v_\parallel}{\partial z} - 1.71\alpha_d \epsilon_n (1+\tau)\frac{\partial^2 h}{\partial z^2} + \kappa_\parallel \frac{\partial^2 T_e}{\partial z^2}\right] = 0, \tag{3}$$

$$\frac{dT_i}{dt} + \eta_i \frac{\partial \phi}{\partial y} - \frac{2}{3}\left[\epsilon_n \hat{C}(\phi - \alpha_d p_e) - \epsilon_v \frac{\partial v_\parallel}{\partial z} - \alpha_d \epsilon_n (1+\tau)\frac{\partial^2 h}{\partial z^2}\right] = 0, \tag{4}$$

$$\frac{dv_\parallel}{dt} + \epsilon_v \frac{\partial}{\partial z}\frac{p_e + \tau p_i}{1+\tau} = 0, \tag{5}$$

with $p_e = n + T_e$, $p_i = n + T_i$, $h = \phi - \alpha_d(p_e + 0.71T_e)$, and the operators

$$\nabla_\perp^2 = \left[\frac{\partial}{\partial x} + 2\pi\hat{s}z\frac{\partial}{\partial y}\right]^2 + \frac{\partial^2}{\partial y^2}, \quad \frac{d}{dt} = \frac{\partial}{\partial t} - \left(\frac{\partial\phi}{\partial y}\frac{\partial}{\partial x} - \frac{\partial\phi}{\partial x}\frac{\partial}{\partial y}\right).$$

$$\hat{C} = [\cos(2\pi z) + 2\pi\hat{s}z\sin(2\pi z) - \epsilon]\frac{\partial}{\partial y} + \sin(2\pi z)\frac{\partial}{\partial x}.$$

The time and space units

$$t_0 = \left(\frac{RL_n}{2}\right)^{1/2}\frac{1}{c_s}, \quad L_\perp = 2\pi q_a\left(\frac{\nu_{ei}R\rho_s}{2\Omega_{ce}}\right)^{1/2}\left(\frac{2R}{L_n}\right)^{1/4}, \quad L_z = 2\pi q_a R, \tag{6}$$

are the natural choice for the resistive ballooning mode [3,11]. This normalization yields the dimensionless parameters

$$\alpha_d = \frac{\rho_s c_s t_0}{(1+\tau)L_n L_\perp}, \ \epsilon_n = \frac{2L_n}{R}, \ \epsilon_v = \frac{c_s t_0}{L_z}, \tag{7}$$

$$\tau = \frac{T_{i0}}{T_{e0}}, \ \kappa_\parallel = 1.6\alpha_d^2\epsilon_n(1+\tau), \ \eta_e = \frac{L_n}{L_{T_e}}, \ \eta_i = \frac{L_n}{L_{T_i}} \tag{8}$$

with $c_s^2 = (T_{e0} + T_{i0})/m_i$, $\rho_s = c_s/\Omega_{ci}$ and the profile e-folding lengths L_n, L_{T_e}, and L_{T_i}. $\hat{s}$ is the magnetic shear parameter and ϵ the inverse aspect-ratio.

In addition we summarize here expressions for several derived quantities. The ratio between the transverse scale lengths ρ_s and $L_\perp$ plays an important role in understanding the relation between resistive ballooning and η_i mode turbulence. In our dimensionless parameters this ratio is given by

$$\hat{\rho}_s \equiv \rho_s/L_\perp = (1+\tau)\alpha_d\epsilon_n^{1/2}. \tag{9}$$

The electron and ion diamagnetic frequencies, ω_*, the curvature frequency ω_c and the parallel diffusion rate $D_{\parallel e}$ are important for evaluating the linear properties of resistive ballooning and η_i modes. In dimensional units they are given by

$$\omega_{*e} = \frac{k_y cT_e}{eBL_n}(1+\eta_e), \ \ \omega_{*i} = \frac{k_y cT_i}{eBL_n}(1+\eta_i),$$

$$\omega_{ce} = \frac{2k_y cT_e}{eBR}[\cos(z/qR) + \hat{s}(z/qR)\sin(z/qR) - \epsilon], \ \ D_{\parallel e} = \frac{2T_e}{m_e\nu_{ei}},$$

and in our dimensionless units by

$$\hat{\omega}_{*e} = k_y\alpha_d(1+\eta_e), \ \hat{\omega}_{*i} = k_y\alpha_d\tau(1+\eta_i), \tag{10}$$

$$\hat{\omega}_{ce} = k_y\alpha_d\epsilon_n[\cos(2\pi z) + \hat{s}(2\pi z)\sin(2\pi z) - \epsilon], \ \hat{D}_{\parallel e} = (1+\tau)\epsilon_n\alpha_d^2. \tag{11}$$

3. Drive mechanisms

Two linear instabilities play an important role as a driver for the turbulence: the resistive ballooning mode and the toroidal η_i mode. We discuss the linear properties in some detail, in particular since our equations differ substantially from earlier treatments of the Braginskii equations due to the correct retention of the polarization drift in the ion

pressure equation [8,10]. The relationship between the two modes can be understood from a simplified set of linearized equations, where we drop the electron temperature dynamics, the parallel ion velocity and neglect the curvature terms in Eqs. (2) and (4)

$$-k_\perp^2 \hat{\rho}_{se}^2 \gamma(\hat{\phi} + \tau p_i) + i\hat{\omega}_{ce}(n + \tau p_i) + \hat{D}_{\|e}\frac{\partial^2}{\partial z^2}(\hat{\phi} - n) = 0, \tag{12}$$

$$\gamma n + i\hat{\omega}_{*e}\hat{\phi} + \hat{D}_{\|e}\frac{\partial^2}{\partial z^2}(\hat{\phi} - n) = 0, \tag{13}$$

$$\gamma\tau p_i + i\hat{\omega}_{*i}\hat{\phi} = \frac{5}{3}\tau(\gamma n + i\hat{\omega}_{*e}\hat{\phi}), \tag{14}$$

with $\hat{\phi} = \phi/\alpha_d$ and $\hat{\rho}_{se}^2 = \hat{\rho}_s^2/(1+\tau)$. For a given set of equilibrium parameters both the resistive ballooning mode and the η_i mode can exist simultaneously for the same value of $k_\perp$ but with different parallel localization. If the terms with $\hat{D}_{\|e}\partial^2/\partial z^2$ are small we obtain the dispersion relation for the local resistive ballooning mode

$$\gamma(\gamma - i\hat{\omega}_{*i}) = \frac{\hat{\omega}_{ce}(\hat{\omega}_{*e} + \hat{\omega}_{*i})}{k_\perp^2 \hat{\rho}_{se}^2}. \tag{15}$$

For a more complete treatment one has to take into account that the mode cannot be localized in the unfavorable curvature region at the outside of the torus unless the parallel wavelength is shorter than the connection length. This also limits the transverse wavelength and leads to the scaling defined in Eq. (6) (see Refs. [3,11] for details).

For $\partial/\partial z$ large the term with $\hat{D}_{\|e}$ dominates in Eq. (13) forcing the adiabatic relation $\hat{\phi} = n$. Combining Eqs. (12) and (13) we obtain

$$-k_\perp^2 \hat{\rho}_{se}^2 \gamma(n + \tau p_i) + i\hat{\omega}_{ce}(n + \tau p_i) - \gamma n - i\hat{\omega}_{*e} n = 0. \tag{16}$$

With Eq. (14) this leads to the dispersion relation for the toroidal η_i mode

$$\gamma^2\left[1 + k_\perp^2\hat{\rho}_{se}^2\left(1 + \frac{5}{3}\tau\right)\right] +$$

$$+ i\gamma\left[\hat{\omega}_{*e} - \hat{\omega}_{ce}\left(1 + \frac{5}{3}\tau\right) - k_\perp^2\hat{\rho}_{se}^2\hat{\omega}_{*e}\tau\left(\eta_i - \frac{2}{3}\right)\right] - \hat{\omega}_{ce}\hat{\omega}_{*e}\tau\left(\eta_i - \frac{2}{3}\right) = 0. \tag{17}$$

Unstable η_i modes can only exist if the last term in Eq. (17) is negative, *i.e.*, if $\eta_i > 2/3$. On the other hand this is also a sufficient condition for instability, since there is always a value of $k_\perp$ which makes the second term in the dispersion relation vanish. A second important threshold is the condition for the instability of long wavelength modes,

$$4\hat{\omega}_{ce}\hat{\omega}_{*e}\tau(\eta_i - 2/3) > [\hat{\omega}_{*e} - \hat{\omega}_{ce}(1 + 5\tau/3)]^2. \tag{18}$$

Since it is typically the longest wavelength component of the wave spectrum which dominates transport, transport from the η_i mode jumps sharply when this second threshold is exceeded.

The simple dispersion relations Eqs. (15) and (17) suffer from several significant shortcomings. It is not clear whether the η_i mode satisfies the adiabatic relation $\hat{\phi} = n$ sufficiently well at the plasma edge where the resistivity typically cannot be neglected. Furthermore the parallel sound wave has been neglected to obtain the local dispersion relation Eq. (17) and the sound wave can strongly impact stability, especially at long

wavelength. In the derivation of Eq. (15) on the other hand the ballooning structure of the resistive ballooning mode was completely ignored.

A more complete analysis is performed using numerical eigenvalue codes. As the only simplifications we still neglect the electron temperature dynamics and restrict the analysis to modes with $k_x = 0$. The calculations are performed in the range of typical plasma edge parameters $\alpha_d \sim 1$, $\epsilon_n \sim 0.05$, $\eta_i \sim 1$, $\hat{s} = 1$, and $\epsilon_v \sim 0.005$. Four main results are obtained [12]. First, the resistive ballooning and the toroidal η_i mode appear as distinct roots at comparable $k_\perp$ but with significantly different localization along the magnetic field. Second, the η_i mode has multiple roots whose growth rates are essentially independent of the plasma resistivity. Third, the ion pressure gradient enhances the resistive ballooning mode. Fourth, for parameters typical of the plasma edge, the long wavelength instability condition for the η_i mode is typically not satisfied and as a consequence resistive ballooning modes dominate the long wavelength component of the wave spectrum unless diamagnetic effects are sufficiently large to stabilize resistive ballooning modes ($\alpha_d > 0.8$). This last conclusion implies that ultimately resistive ballooning turbulence is typically the dominant driver of transport in the edge.

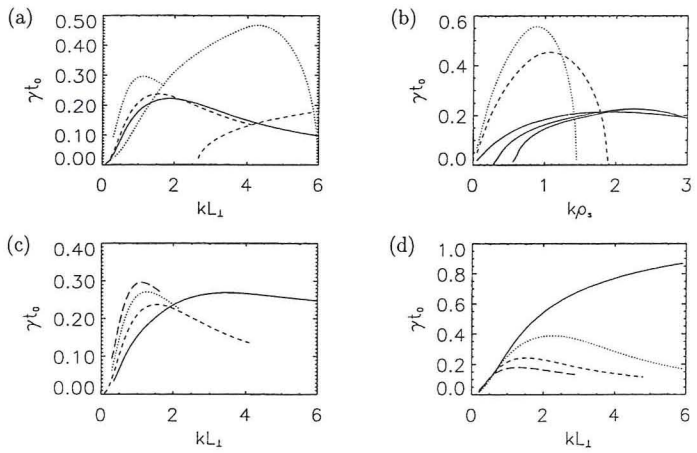

Figure 1: linear growth-rate γ versus k_y: *(a) two unstable roots*: $\alpha_d = 0.5$, $\epsilon_n = 0.05$, $\tau = 1$, $\eta_i = 0.5$ (solid line), $\eta_i = 1$ (dashed lines), $\eta_i = 3$ (dotted lines). *(b) η_i mode*: The three solid lines are obtained with the parameters $\alpha_d = 0.5$, $\tau = 1$, $\eta_i = 1$, and $\epsilon_n = 0.05/0.1/0.3$, the larger growth-rate at small k corresponding to the larger ϵ_n. The other lines correspond to $\epsilon_n = 0.3$ and $\eta_i = 3$ (dashed) and $\eta_i = 5$ (dotted). *(c) ion temperature gradient drive to the resistive ballooning mode*: $\alpha_d = 0.5$, $\epsilon_n = 0.05$, $\tau = 1$, $\eta_i = 0$ (solid), $\eta_i = 1$ (dashed), $\eta_i = 2$ (dotted), $\eta_i = 3$ (long dashes). *(d) resistive ballooning mode - diamagnetic stabilization*: $\epsilon_n = 0.04$, $\eta_i = 1$, $\tau = 1$, $\alpha_d = 0$ (solid), $\alpha_d = 0.25$ (dotted), $\alpha_d = 0.5$ (dashed), $\alpha_d = 0.75$ (long dashes).

The sound wave has essentially no affect on the stability of resistive ballooning modes. In the case of η_i modes in the edge the sound wave is weak and while it controls the poloidal structure and spatial localization of the unstable modes, the growth rates can typically be calculated relatively accurately by evaluating the local dispersion relation at the poloidal location corresponding to maximum growth. This simple rule of thumb breaks down at long wavelength where the sound wave causes significant poloidal delocalization of the mode. To clearly illustrate the relationship between resistive ballooning and η_i modes

we therefore present growth rates of the mode spectrum without sound wave dynamics but including the full nonadiabatic electron response. The detailed discussion of the role of the sound wave is presented in a separate paper [12] (see also Ref. [13]). In Figure 1 we show the growthrate γ versus k_y for various parameters. Whereas for $\eta_i = 0.5$ only one unstable root, the resistive ballooning mode, is observed (Fig. 1a), the η_i mode enters at steepened temperature gradient ($\eta_i = 1$) and is shifted to smaller k_y if η_i is increased further. According to the simple mixing length estimate $D \sim \gamma/k_y^2$ the η_i mode should not affect the transport if it destabilizes modes at significantly larger k than the resistive ballooning mode. The numerical results for the η_i mode agree surprisingly well with the adiabatic dispersion relation Eq. (17). We therefore conclude that the η_i mode is not strongly affected by the plasma resistivity and the nonadiabatic electron response. Hence we plot the η_i mode spectrum in Fig. 1b in terms of ρ_s rather than $L_\perp$. In this normalization resistivity enters only through the parameter α_d; consistently we observe no dependence on α_d. The variation of ϵ_n mainly affects the stability of long wavelength modes. At small ϵ_n typical for the plasma edge the small k_y part of the spectrum is stable. Increasing ϵ_n leads to destabilization of larger modes until the inequality Eq. (18) is satisfied and the mode is unstable at arbitrary long wavelength. Increasing η_i strongly enhances the growth-rate and shifts the spectrum towards smaller k_y (Fig. 1b). The influence of η_i on the resistive ballooning mode is demonstrated in Fig. 1c. Increasing η_i destabilizes the mode at small k_y and stabilizes it at large k_y. Note, however, that the driving effect of an increased η_i is weaker than for the η_i mode. Finally we recall the stabilizing influence of electron and ion diamagnetic effects proportional to α_d (Fig. 1d) (see also Ref. [11]).

Besides the two linear instabilities a third drive mechanism plays a dominant role over part of the parameter space: the nonlinear drift-wave instability [4,5,14,15,16]. Since the detailed mechanism is discussed elsewhere, we repeat here only the basic ideas. Dropping the curvature terms, the electron temperature dynamics and the parallel ion velocity and assuming the ions to be cold ($\tau = 0$), we obtain from Eqs. (1), (2)

$$\frac{d}{dt}\nabla_\perp^2\phi + \frac{\partial^2}{\partial z^2}(\phi - \alpha_d n) = 0, \tag{19}$$

$$\frac{dn}{dt} + \frac{\partial\phi}{\partial y} + \alpha_d\epsilon_n(1+\tau)\frac{\partial^2}{\partial z^2}(\phi - \alpha_d n) = 0. \tag{20}$$

It is well known that Eqs. (19) and (20) are linearly stable in sheared magnetic field [17]. Numerical simulations, however, show self sustained turbulence [15,16]. A key to the nonlinear mechanism is provided by the observation that the terms with $\partial^2/\partial z^2$ can be neglected for modes with long parallel wavelength. As a consequence, Eq. (19) for the vorticity is independent of n in this limit while Eq. (20) describes the passive convection of n and algebraic growth of the n spectrum. At finite amplitude the nonlinear interaction involves the full spectrum of modes, hence allowing for a coupling between n and ϕ at shorter parallel wavelength. Numerical simulations [16] and an analytic model [15] show, that this mechanism indeed leads to an amplification of the initial disturbance ϕ, which is responsible for the algebraic growth of the density disturbance.

The probably most important question is, which instability dominates the turbulent transport in a specific region of the parameter space. The scaling properties of the instability mechanisms and a large number of nonlinear simulations lead to the following picture which is plotted schematically in Fig. 2. Provided that $T_i \sim T_e$ and $\eta_i \sim 1$ the dominant parameters are α_d and ϵ_n. Due to the stabilizing influence of the diamagnetic

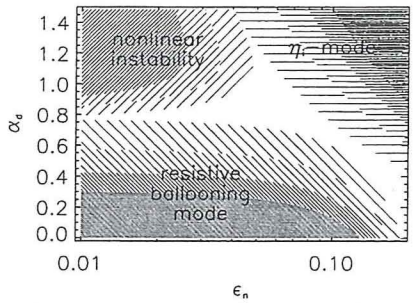

Figure 2: Schematic view of the α_d-ϵ_n parameter space, showing which instability dominates for a given set of parameters

		$\langle nv_r \rangle$		$\langle T_i v_r \rangle$		$\langle T_e v_r \rangle$	
ϵ_n	$\rho_s/L_\perp$	out	in	out	in	out	in
0.2	1.12	0.07	0	0.22	0	0.01	0
0.1	0.79	0.011	0.002	0.023	0.005	0.005	0.003
0.05	0.56	0.005	0.002	0.010	0.004	0.004	0.002
0.02	0.35	0.014	0.008	0.019	0.011	0.017	0.011
0.015	0.31	0.030	0.020	0.038	0.026	0.044	0.034
0.01	0.25	0.06	0.04	0.07	0.05	0.08	0.06

Table 1: Turbulent transport at $\alpha_d = 1.25$, $\tau = 1$, $\eta_i = 1$ and different values of ϵ_n. Other parameters are $\hat{s} = 1$, $\eta_e = 1$, $\kappa_\parallel = 0.05$, $\epsilon_v = 0$ and $\epsilon = 0.25$. The transport rates are time-averaged and taken at the torus outside ($z = 0, \pm 1$) and at the torus inside ($z = \pm 0.5$)

drifts the resistive ballooning instability is restricted to the low α_d regime. Since the ratio $\rho_s/L_\perp$according to Eq. (9) is small in this regime, the η_i mode drives modes at significantly shorter wavelength than the resistive ballooning mode (compare also Fig. 1a, dashed lines) and cannot compete with the ballooning mode as a driver for the transport. For increased α_d diamagnetic effects become stronger and the nonlinear drift-wave instability dominates at small ϵ_n [4,18]. If ϵ_n is also increased the ratio $\rho_s/L_\perp$ becomes larger and the η_i mode starts to dominate over the two resistive modes, which both scale approximately like $L_\perp$.

4. Results from nonlinear simulations

We now proceed to direct simulations of the complete set of nonlinear equations (1-5) and study the transition between the various instabilities. Unless stated otherwise the simulations are performed in a box of dimension $12L_\perp \times 12L_\perp \times 3L_z$. The numerical algorithm including the viscosities are described in detail in Refs. [4,18]. In the low-α ($\alpha \sim 0.5$) resistive ballooning regime the ratio $\rho_s/L_\perp$ is always small [compare Eq. (12)] for values of ϵ_n typical for the plasma edge. For larger values of ϵ_n, however, or when $\eta_i \gg 1$, long wavelength modes are unstable [see Eq. (18)] and the η_i mode can also be important. With the exception of these special cases the nonlinear simulations confirm that the resistive ballooning mode dominates the transport. The change compared to the cold ion limit [3,4,18] depends on the relative strength of two competing effects: the

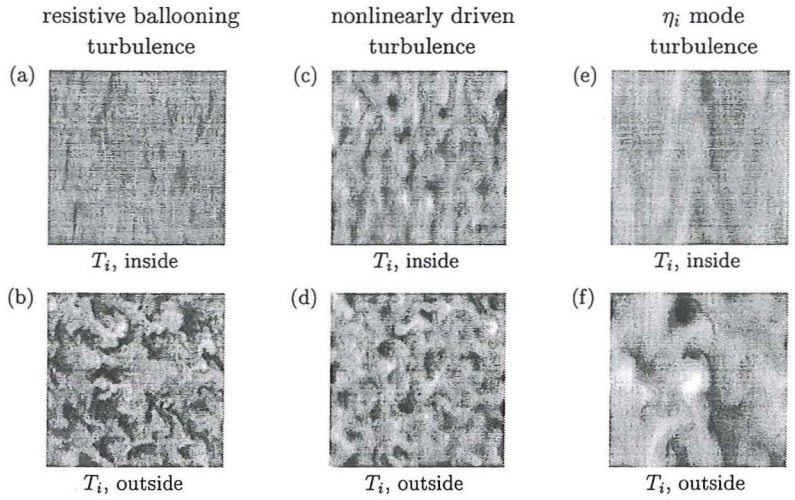

Figure 3: Structure of T_i at inside and outside midplane. The plots show poloidal cross-sections (x-y plane) at saturation, the poloidal angle increasing upwards and the profile gradients pointing to the left. White indicates high and black low temperature. The box size is $25\,L_\perp \times 25\,L_\perp \times 3\,L_z$ and $\eta_i = 1$. Plots (a) and (b) were obtained with $\alpha_d = 0.2$, $\epsilon_n = 0.05$, plots (c) and (d) with $\alpha_d = 1.25$, $\epsilon_n = 0.015$, and plots (e) and (f) with $\alpha_d = 1.25$, $\epsilon_n = 0.15$.

additional drive due to η_i versus the stabilization due to the ion diamagnetic drift.

In the high-α ($\alpha > 1$) regime, the η_i mode can become important for the small ϵ_n typical for the plasma edge. In this regime the resistive ballooning mode is stable and in the absence of ion thermal effects the turbulence is sustained by the nonlinear drift-wave instability which is strong when its characteristic scale length, which is typically comparable to $L_\perp$ [4], is greater than ρ_s, hence when $\rho_s/L_\perp = (1+\tau)\alpha_d\epsilon_n^{1/2}$ is small (compare Fig. 2). For finite ion temperature we show in Table 1 the transport rates for $\alpha = 1.25$, $\eta_i = 1$ and different values of ϵ_n corresponding to a variation of the ratio $\rho_s/L_\perp$. For $\epsilon_n = 0.2$ ($\rho_s \sim L_\perp$) the ion heat flux dominates, demonstrating the adiabatic nature of the underlying turbulence and the dominance of the η_i mode instability. The transport exhibits a large inside/outside asymmetry caused by the curvature driven mode. Reducing ϵ_n reduces the ion heat flux almost a factor of 10 and is a consequence of the stabilization of long wavelength modes (compare Fig. 1b, growth-rates for different ϵ_n). The transport rates decrease further for $\epsilon_n = 0.05$. At this point the transition to nonlinearly driven turbulence occurs, with the transport rates steadily increasing with further reductions in ϵ_n. The inside/outside asymmetry is now absent, a typical feature of the nonlinear instability, since it does not rely on toroidicity. The transport rates are of the same order, which is evidence for the nonadiabatic nature of the drive mechanism. In Fig. 2 we show plots of T_i in the plane perpendicular to the magnetic field at the low and high field sides of the torus. At low α_d the resistive ballooning mode dominates and the resulting turbulence is strongly peaked at the torus outside due to the localization of the driving instability. At high α_d the parameter ϵ_n controls whether the toroidal η_i mode dominates or the turbulence is driven by the nonlinear mechanism. Whereas at low ϵ_n (nonlinearly

driven regime) no difference is observed between inside and outside midplane, high ϵ_n (η_i driven regime) leads to a strong inside/outside asymmetry in the fluctuations.

5. Conclusions

In the low β limit being studied in this paper, there are three dominant instabilities which play an important role in the plasma edge region: the resistive ballooning mode, a nonlinear resistive drift-wave instability and the toroidal η_i instability. The region where each instability dominates depends on the parameters but the resistive ballooning mode typically dominates in lowest temperature region, the nonlinear instability dominates at intermediate temperatures and the η_i mode is important at higher temperatures. The turbulence is largely controlled by two parameters. The first parameter is the ratio $\rho_s/L_\perp$, where $L_\perp$ is the characteristic scale length for the two resistive modes and ρ_s is the collisionless scale length appropriate for the toroidal η_i mode. The parameter α_d measures the ratio of the two dominant time scales in the system: the ideal ballooning growthtime which is typical for the two curvature driven modes, and the diamagnetic frequency of modes with wavelength $L_\perp$. At small $\rho_s/L_\perp$ resistive instabilities dominate and the η_i mode is negligible. At low α_d the turbulence is driven by the resistive ballooning mode. If α_d is of order one diamagnetic effects become more important and the nonlinear drift-wave instability dominates. The η_i mode finally controls the turbulence if ρ_s and $L_\perp$ become comparable at higher temperature.

References

[1] R. E. Waltz, G. D. Kerbel and J. Milovich, Phys. Plasmas **1**, 2229 (1994).

[2] M. Kotschenreuther, W. Dorland, M. A. Beer, G. W. Hammett, Phys. Plasmas **2**, 2381 (1995).

[3] P. N. Guzdar, J. F. Drake, D. C. McCarthy, A. B. Hassam, C. S. Liu, Phys. Fluids B **5**, 3712 (1993).

[4] A. Zeiler, D. Biskamp, J. F. Drake, P. N. Guzdar, Phys. Plasmas **3**, 2951 (1996).

[5] B. Scott, Plasma Phys. Control. Fusion **39**, 471 (1997).

[6] R. E. Waltz, Phys. Fluids **31**, 1962 (1988).

[7] S. Hamaguchi, and W. Horton, Phys. Fluids B **2**, 1833 (1990).

[8] C. B. Kim, W. Horton, S. Hamaguchi, Phys. Fluids B **5**, 1516 (1993).

[9] S. I. Braginskii, in *Reviews of Plasma Physics*, edited by M. A. Leontovitch (Consultants Bureau, New York, 1965), Vol. I, p. 205.

[10] A. Zeiler, J. F. Drake, B. Rogers, Phys. Plasmas **4**, 2134 (1997).

[11] S. V. Novakovskii, P. N. Guzdar, J. F. Drake, C. S. Liu, Phys. Plasmas **2**, 781 (1995).

[12] A. Zeiler, D. Biskamp, J. F. Drake, B. N. Rogers, "Transition from resistive ballooning to η_i driven turbulence in tokamaks", submitted to Phys. Plasmas.

[13] F. Romanelli, Phys. Fluids B **1**, 1018 (1989).

[14] B. D. Scott, Phys. Rev. Lett. **65**, 3289 (1990).

[15] J. F. Drake, A. Zeiler, D. Biskamp, Phys. Rev. Lett. **75**, 4222 (1995).

[16] D. Biskamp, A. Zeiler, Phys. Rev. Lett. **74**, 706 (1995); A. Zeiler, D. Biskamp, J. F. Drake, Phys. Plasmas **3**, 3947 (1996).

[17] P. N. Guzdar, L. Chen, P. K. Kaw, and C. Oberman, Phys. Rev. Lett. **40**, 1566 (1978).

[18] A. Zeiler, J. F. Drake, D. Biskamp, Phys. Plasmas **4**, 991 (1997).

Plasma states in tokamaks with strong impurity radiation

M.Z.Tokar'

Institut für Plasmaphysik, Forschungszentrum Jülich GmbH, EURATOM Association,
Trilateral Euregio Cluster, D-52425 Jülich, Germany

I. Introduction

Throughout the whole history of fusion research physicists are confronted with the problem of plasma pollution by impurities. It was recognized already in early investigations that radiation from heavy metallic impurities from the plasma core can be a serious obstacle to reach thermonuclear temperatures. Utilization of light elements e.g. carbon, boron, beryllium, silicon as wall materials allows to reduce the central energy losses drastically. However, the radiation of these impurities from the edge can provoke contraction of the plasma column through development of a „detached plasma" or „Marfe". Optimal choice of seeded impurities (e.g. neon) and heating scenario allows to avoid this and the radiation cooling of the plasma edge can be used to reduce significantly the energy of charged particles which bombard the wall elements. Moreover, a remarkable improvement of the energy confinement can be achieved by these means.

II. Accumulation of high-Z impurities in plasma core

Due to low erosion level heavy metals like molybdenum and tungsten were often used in Tokamaks for fabrication of the wall elements. However, experiments have shown that this can lead to an uncontrolled accumulation of high-Z ions in the plasma core [1]. As a result very peaked profiles of radiation losses and flat or even hollow radial distributions of the plasma temperature arise which causes plasma disruptions. Understanding of physical mechanisms governing the accumulation of high-Z ions is one of the important components in the fusion program.

Numerous experiments on TEXTOR with test-limiters of molybdenum and tungsten and with puffing of xenon have revealed common characteristic for accumulation in ohmic plasmas [2]. When the mean electron density $\overline{n_e}$ exceeds a critical level of $2.5\text{-}3\cdot10^{13}\ cm^{-3}$ the radiation losses from the plasma core increase drastically and the temperature profile becomes flat in the center. Soon after beginning of these events sawteeth disappear and with a delay of some hundreds of milliseconds an internal disruption occurs. The latter leads to the plasma relaxation back to the state with a peaked temperature profile and a relatively small level of the central radiation. Such sequences of accumulation and disruption can repeat several times during a discharge.

In additionally heated discharges the tendency is opposite [2]: the central radiation decreases with increasing electron density. Moreover, it was demonstrated that after an accumulation in an ohmic phase of the discharge the plasma can be returned to a state with a low radiation from the core if an auxiliary heating is applied [3]. The situation changes again if neon is puffed to create a radiating peripheral layer in a plasma additionally heated by a neutral beam and bounded by a tungsten test-limiter [4]. In this case an accumulation of W ions happens if the mean electron density $\overline{n_e}$ is below than $3\text{-}3.5\cdot10^{13}\ cm^{-3}$.

Traditionally, the neoclassical transport of impurities is considered as to be the most plausible cause of the accumulation. According to the neoclassical theory [5] collisions of impurity particles of the charge Z with the background ions can lead to a profile of the impurity density n_I much more peaked than the density n of the plasma: $n_I \sim n^Z$. Recently

developed approach to transport analysis allowed to "extract" both the diffusivity and convection velocity of heavy impurities [4]. The results presented in Fig.1 confirm the neo-classical nature of transport processes leading to the accumulation. The agreement with the theoretical predictions suggests to explain the threshold of the accumulative instability also by the neo-classical transport behavior.

The radial flux of impurity ions, Γ_z, with the charge Z is given by the sum of diffusive and convective components:

$$\Gamma_z \equiv -D^z{}_\perp \, dn_z/dr + V^z{}_\perp n_z \qquad (1)$$

where $D_\perp{}^z$ is the anomalous diffusivity and the neo-classical convective velocity $V_\perp{}^z$ is governed by the gradients of the density n and temperature T of the background ions (here, deuterons):

$$V^z{}_\perp = D_{neo}\left(\eta\frac{d\ln n}{dr}+\theta\frac{d\ln T}{dr}\right) \qquad (2)$$

The parameters D_{neo}, η and θ are determined by n and T, the safety factor q, toroidal magnetic field B_ϕ, etc. In medium devices, like TEXTOR, heavy impurities have a relatively small path length between coulomb collisions with the background particles and belong to the Pfirsch-Schlüter regime [5]:

$$D_{neo}^{PS}=\frac{8\ln\Lambda}{3}\left(\frac{ceq}{B_t}\right)^2\sqrt{\frac{\pi m_i}{T}}n, \quad \eta=Z, \quad \theta=-\frac{1}{2}Z \qquad (3)$$

For conventional peaked profiles of the plasma parameters the components of the convection velocity due to dn/dr and dT/dr, respectively, are of different signs. The former is directed towards the plasma axis and can lead to peaking of the impurity density. The latter is of the opposite sign and prevents such a peaking i.e. it provides the so called *„temperature screening"*. In the case of "optimal" profiles with $n \propto \sqrt{T}$ being typical for ohmic discharges the net neo-classical flux of an impurity reduces to zero and the profile of the total impurity density $n_I = \sum_Z n_Z$ is flat.

The situation described above can become unstable [6]. Indeed, a spontaneous decrease of the central temperature leads to reduction of the temperature gradient and a weakening of the *"temperature screening"*. As a result the n_I profile peaks due to the part of $V_\perp$ proportional to the main ion density gradient, the central radiation increases and $T(0)$ drops further, i.e. an instability develops. The peaking of n_I generates a diffusive flux component directed toward the edge i.e. against the neo-classical convection. Besides that, the flattening of the temperature profile results in a reduction of conductive heat losses from the core. Thus, there is a competition between impurity diffusion and heat conduction as stabilising factors on the one hand and neo-classical convection and radiation as destabilising ones on the other hand. This competition determines the threshold of the instability and the condition of the onset of the accumulation of high-Z impurities.

In order to find a quantitative criterion of the instability, we have to consider the balance of impurity particles and energy in the plasma centre. Here the source of ions due to ionisation of neutrals coming from the wall, is negligible and the evolution of n_I is governed by the continuity equation in the following form:

$$\frac{\partial n_I}{\partial t}+\frac{1}{r}\frac{\partial(r\Gamma_I)}{\partial r}=0 \qquad (4)$$

where Γ_I is the sum of Γ_Z over all impurity charge states and is determined by equations (1), (2) and (3) with n_I and the averaged charge $Z_I = \sum_Z Zn_Z \Big/ n_I$ introduced instead of n_Z and Z.

In the equation for heat transfer:

$$3\frac{\partial\ nT}{\partial t} + \frac{1}{r}\frac{\partial}{\partial r}\left(-r\kappa_\perp \frac{\partial T}{\partial r}\right) = Q_{heat} - Q_{rad} \qquad (5)$$

$\kappa_\perp$ is the plasma heat conductivity, Q_{heat} and $Q_{rad}=nn_IL_I$ are the densities of the heating and radiated power; the impurity cooling rate L_I and averaged charge Z_I depend on the electron temperature but this dependence is weak under the conditions of the plasma core and is neglected in the qualitative analysis. The steady-state profiles are adopted as parabolic: $T/T(0) = 1-\left(r/a_T\right)^2$, $n/n(0) \propto \sqrt{T/T(0)}$ with a_T being a characteristic dimension for the temperature change.

Consider a small perturbation of stationary profiles: $\delta n_I, \delta T \propto exp\left(\gamma t - r^2/r_*^2\right)$. A dispersion relation following from linearization of equations (4) and (5) predicts that the increment γ has a maximum at a certain $r_* = r_{max}$. Thus, the threshold of the instability is determined by the condition $\gamma\left(r_{max}\right)=0$. This can be written as the following relation for the critical central plasma density in excess of which the instability sets in:

$$n_{cr} \equiv \frac{8D_\perp \kappa_\perp T(0)}{r_{max}^{\ 2} D_{neo}^{PS} Z_I n_I(0) L_I} \qquad (6)$$

Under conditions of ohmic discharges in TEXTOR (B_t=2.25T, $T(0)\approx 800eV$, $\kappa_\perp = 2\cdot 10^{17} cm^{-1}s^{-1}$), with a tungsten test-limiter ($C_I \equiv n_I(0)/n(0) \approx 2\cdot 10^{-5}$, $Z_I \approx 25$, $L_I \approx 6\cdot 10^{-25}$ W/cm^3) equation (6) leads to $n_{cr} \approx 5\cdot 10^{13} cm^{-3}$ in agreement with observations [7].

Seeding of light impurities enhances the frequency of coulomb collisions of high-Z ions and their neoclassical flow. This can also trigger an accumulation as it was observed in TEXTOR when neon was puffed to produce edge cooling [4]. Quantitatively the influence of light impurities can be taken into account if instead of n one introduces the value $N = n + n_I Z_I \sqrt{m_I/m_i}$, with n_I, Z_I and m_I being the density, charge and mass of light impurities. For "optimal" plasma profiles the neon ion density is more peaked in the core than n, the components of the convective velocity of high-Z ions do not compensate each other and there is a net convective flow of them toward the plasma axis due to dn_I/dr. This flow is proportional to the Pfirsch-Schlüter diffusivity i.e. inversely proportional to the square root of the temperature (see equation (3)). This opens a new channel for an instability: a diminution of $T(0)$ causes an increment of the flow of high-Z ions toward the axis through the increase of D_{neo}^{PS}, $n_I(0)$ and central radiation grow and the temperature diminishes further. Fig.2 shows the dependence of the critical central electron density on the neon concentration at the axis, calculated for the conditions of discharges in TEXTOR heated by one hydrogen neutral beam and bounded by a W test-limiter: $T(0) \approx 1.6keV$, $D_\perp \approx 0.1 m^2 s^{-1}$, $C_I \approx 3\cdot 10^{-4}$ [4]. Curve 1 has been obtained taking into account the reduction of the "temperature screening" only, 2 - the temperature dependence of D_{neo}^{PS} only and 3 - both effects. It is clear seen that the latter one is significantly more important and leads to a noticeable decrease of $n_{cr}(0)$ with seeding of neon. In agreement with measurements for a typical C_{Ne} of 1% the critical central density is of $4\text{-}5\cdot 10^{13} cm^{-3}$.

Plasma states after accumulation seem to be uninteresting from the point of view of reactor applications, but study of them is a useful tool for a better understanding of processes in Tokamak plasmas, in particular, of impurity transport. To describes the plasma evolution during and after an accumulation equation (5) has been replaced by the heat balance equations

written separately for electrons and ions to take into account that T_e is important for radiation and T_i - for the neoclassical transport :

$$\frac{3}{2}n_e\frac{\partial T_e}{\partial t}+\frac{1}{r}\frac{\partial}{\partial r}\left(-r\kappa^{e}{}_{\perp}\frac{\partial T_e}{\partial r}\right)=\frac{j^2}{\sigma}+Q_{au}{}^{e}-Q_{rad}-Q_{ei} \tag{7}$$

$$\frac{3}{2}\frac{\partial n_i T_i}{\partial t}+\frac{1}{r}\frac{\partial}{\partial r}\left(-r\kappa^{i}{}_{\perp}\frac{\partial T_i}{\partial r}\right)=Q_{au}{}^{i}+Q_{ei} \tag{8}$$

Here $\kappa_{\perp}^{e,i}$ and $Q_{au}{}^{e,i}$ are the heat conductivities and densities of the auxiliary heating power in the electron and ion components, respectively; Q_{ei} is the density of the energy exchange between electrons and ions due to coulomb collisions; additionally the time variation of the safety factor q and the current density j is taken into account:

$$\frac{\partial}{\partial t}\left(\frac{1}{q}\right)=\frac{c^2}{4\pi r}\frac{\partial}{\partial r}\left[\frac{1}{r\sigma}\frac{\partial}{\partial r}\left(\frac{r^2}{q}\right)\right],\quad j=\frac{cB_t}{4\pi rR_0}\frac{\partial\left(r^2/q\right)}{\partial r} \tag{9}$$

In additionally heated discharges, where the accumulation of tungsten is triggered by puffing of neon, the plasma can reach a new equilibrium state with a strongly peaked profile of radiation and a flat temperature profile, which exists for a long time of 1-2 *sec*. It was not clear why the instabilities, discussed above, are suppressed in this stage; moreover computations according to equations (1)-(4) and (7)-(9) did not lead to any saturation of the accumulation. To reach this it was necessary to take into account that the sign of the component of the impurity convection velocity proportional to the temperature gradient can be altered during an accumulation.

To show that this can happen, it is instructive to recall that the ion temperature gradient influences the radial transport of impurities through two channels: friction and thermal forces acting between different ion species. These channels give definite contributions to the factor θ in equation (2). In relations (3), obtained in the trace impurity approximation i.e. with $\zeta_Z \equiv Z^2 n_Z/n_i << 1$, these contributions are Z and $-3/2Z$, respectively. Increase of the impurity concentration leads to a reduction of the thermal force acting on the impurity [8] and the corresponding variation of θ can be approximated as follows: $\theta \approx Z\cdot\left(1-1.5/1+2.5\zeta_Z\right)$

At a large enough impurity concentration θ becomes positive. Therefore, any deep minimum on the plasma temperature profile should lead to a flux of impurities toward the edge. This results in a reduction of the impurity density and radiation in the core and to a flattening of the temperature profile. For a flat $T(r)$ only the gradient of n is important for the neo-classical transport of impurities and leads in the final stationary state to $n_I \sim n^Z$. Fig.3 presents the profiles in this state after W accumulation computed with θ depending on ζ_Z.

In the case of xenon one can achieve a quasi-stationary conditions by saturation of the wall after a series of short puffing pulses. This allows to study the effect of Xe concentration C_* outside the core on the plasma evolution after accumulative instability. If C_* does not exceed a critical level of $8\cdot10^{-4}$ the accumulation saturates at $T_0 \approx 550\ eV$, $n_I \approx 1.6\cdot10^{11}\ cm^{-3}$ and $q(0)\approx 2.9$ similarly to the neon case. An increase of C_* by less than 10% to $8.5\cdot10^{-4}$ leads to dramatic changes (see Fig.4): a very fast drop of $T_e(0)$ and an increase of $q(0)$ occur finally. This is due to strong increase of the radiation caused by the temperature dependence of the cooling rate of Xe: L_I increases very sharp with decreasing temperature for T_e smaller 500 *eV*.

III. Radiation of low-Z impurities at plasma edge

The behavior of the cooling rate described above, with $dL_I/dT < 0$, being responsible for the cooling instability, is very typical for conditions at the plasma edge where the line radiation of light impurities is predominant. This is considered often as a cause of states with a

"detached plasma" [9] and "Marfe" [10]. Below we discuss these phenomena in a limiter configuration.

To find the conditions of detachment we apply a simple plane model where the heat balance of the plasma in the peripheral region is described by the equation:

$$\frac{d}{dx}\left(-\kappa_{\perp}\frac{dT}{dx}\right) = -Q_{rad}(T) \qquad (10)$$

Here x is the distance toward the plasma core from the last closed magnetic surface (LCMS) touching the limiter. In $Q_{rad}=nn_I L_I(T)$ the densities of electrons and impurities are taken for simplicity independent of x and a simple "box" approximation for the cooling rate $L_I(T)$: $L_I=L_0\cdot\theta(T_L-T)$. The temperature T_L is close to the ionization potential of the lithium-like ions which make the main contribution to the radiation of light impurities. Thus, $Q_{rad}=Q_L\cdot\theta(T_L-T)$. The boundary conditions to equation (10) prescribe the e-folding length of the temperature at the LCMS: $dT/dx\big|_{x=0} = T/\delta_T\big|_{x=0}$, and the density of the heat flux from the plasma core: $\kappa_{\perp}\, dT/dx\big|_{x\to\infty} = q_c$.

Assume $T(x=0)$ as a parameter. In this case the total energy losses from plasma with heat conduction and radiation, $Q_{loss} = \kappa_{\perp}\, dT/dx\big|_{x=0} + Q_L\cdot x_L$, where $x_L=x(T_L=T)$ is the width of the radiating layer, is given by the expression [11]:

$$Q_{loss} = \frac{\kappa_{\perp}}{\delta_T}\sqrt{T^2(0)+\frac{2Q_L\delta_T^2}{\kappa_{\perp}}\left[T_L - T(0)\right]}\,. \qquad (11)$$

As function of $T(0)$ Q_{loss} has a minimum (see Fig.5): at high temperatures the energy losses are determined by the conduction and vary proportionally to $T(0)$; for small $T(0)$ radiation prevails and grows as the width of the radiation layer becomes larger with decreasing temperature.

Since $Q_L\sim n^2$ the minimum losses, Q_{loss}^{min}, increases with the plasma density. When Q_{loss}^{min} becomes larger than the energy flux from the core q_c any stationary equilibrium does not exist in the present approximation. As a result a poloidally symmetric detachment occurs and a thin toroidal radiating shell arises with a minor radius noticeable less than that of the LCMS. This state is called a "detached plasma" and is stabilized by the increase of the heat flux density from the plasma core with the discharge contraction i.e. decrease of the effective minor radius a_p. Indeed, since the total plasma current I_p is maintained the same, the toroidal electric field E_φ increases inversely proportional to the effective plasma cross-section πa_p^2. Thus, the heat flux density $q_c = I_p\cdot E_\varphi/(2\pi R\cdot 2\pi a_p)$ grows as a_p^{-3}. This simple consideration is confirmed by a one-dimensional transport numerical modelling [12].

Under conditions of additional heating when Shafranov shift of magnetic surfaces is pronounced, q_c varies noticeably with the poloidal angle: $q_c(\vartheta) = \overline{q_c}\cdot\left(1-\beta\cdot\cos\vartheta\right)$. In can occur in this case that Q_{loss}^{min} is less than $q_c(\pi)$ but larger than $q_c(0)$. I.e. the plasma detaches and cools down at the inner board and Marfe arises. This processes is intensified by the increase of the plasma density due to pressure equilibration along magnetic field lines: $n\sim 1/T$. The plasma state in a Marfe is stabilized by the thermal force which pushes impurity to the outer board where the temperature is higher. From the balance between the pressure gradient, electric field and thermal force on the impurity ions we find $n_I\sim T^{\alpha}$ with $\alpha=\xi_I Z^2-0.71Z-1$ and ξ_I being a numerical factor of order unity [11]. In This case the dependence of Q_{loss} on the local temperature at the LCMS, $T(x=0,\vartheta)$, is governed by the formula:

$$Q_{loss} = \frac{\kappa_\perp}{\delta_T}\sqrt{T^2(0,\vartheta) + \frac{2Q_L^{at}\delta_T^2}{\kappa_\perp}\left[T_L - T(0,\vartheta)\right]\left[\frac{T(0,\vartheta)}{T_{at}}\right]^{\alpha-1}}, \qquad (12)$$

where T_{at} and Q_L^{at} are the temperature and radiated power density at the outer board. This dependence is shown in Fig.6. T_{at} can be estimated from the local heat balance $Q_{loss}=q_c(\pi)$ and T_{marfe} - from $Q_{loss}= q_c(0)$. Moreover, equation (12) together with the poloidal dependence of $q_c(\vartheta)$ allow to determine the poloidal extension of the Marfe [11].

IV. Radiative Improve Mode

An appropriate choice of radiating impurities and heating scenario is important for achievement of a high radiation level γ_{rad} (≡ radiation losses/total energy losses) without detachment. This in turn allows to reduce the energy of particles bombarding the walls and their erosion significantly without deterioration of the energy confinement [13]. The maximum γ_{rad} attainable before the plasma detaches can be found from equation (11) [11]:

$$\gamma_{rad}^{max} = 1 - \left(2\kappa_\perp T_L / Q_L \delta_T^2 - 1\right)^{-1/2} \qquad (13)$$

It is seen that γ_{rad}^{max} can be increased if an radiator with a higher T_L is selected or and the plasma heat conductivity is enhanced. This occurs e.g. if we transit from an ohmic discharge stage with intrinsic (mainly carbon) impurities (T_L≈64 *eV*) and Alcator scaling for $\kappa_\perp$≈$2\cdot10^{17}$ $cm^{-1}s^{-1}$ to an additionally heated plasma with a higher level of anomalous transport ($\kappa_\perp$≈$2\cdot10^{18}$ $cm^{-1}s^{-1}$ at the plasma edge) seeded with neon (T_L≈207 *eV*). In agreement with measurements [13] equation (13) predicts an increase of γ_{rad}^{max} from 0.5 to 0.9.

Achievement of such a high level of radiation losses in attached plasmas led by heating with hydrogen beams to any deterioration of the energy confinement in spite of fast energy losses from the radiating zone which radial extension in TEXTOR is of 20% of the minor radius. Predictive transport analysis performed by the 1-D code RITM allowed to interpret these observations [13]. The reduction of the electron temperature at the edge by a factor of 3 due to radiation cooling leads to a more peaked profile of T_e. This results in a more peaked electron density since in TEXTOR profiles are close to the „optimal" ones: $n_e \sim T_e^{1/2}$. In the code RITM this is modeled by the following *Ansatz* for the electron flux:

$$\Gamma_\perp^e = -D_\perp n_e \frac{d\,ln\left(n_e/\sqrt{T_e}\right)}{dr} \qquad (14)$$

The particle diffusivity $D_\perp$ is chosen from the comparison of the measured and calculated particle confinement time. For additionally heated discharges this led to the Bohm coefficient at the plasma periphery i.e. in the region where the recycling neutrals and impurity radiating states are localized. In this case $D_\perp \sim T_e$ which explains the fact that the cooling of the plasma edge by impurity radiation results in the experimentally observed reduction of the particle flux and associated convective energy losses.

When deuterium beams were used for NBI heating instead of hydrogen ones an improvement of the energy confinement with the edge radiation cooling has been found in TEXTOR. This regime was called Radiation Improved Mode (RI-mode) [14]. Measurements by the charge-exchange diagnostics has shown that reduction of energy losses from ions is probably an important prerequisite for RIM [15]. It has been found that both the central ion temperature and toroidal velocity are increased and there is a layer at a half of the plasma minor radius where the gradients of both quantities are much larger than in the L-mode.

To interpret these observations it has been taken into account that the cooling of the edge by radiation should also lead to reduction of the perpendicular plasma viscosity [15]. In the RITM modelling this has been taken proportional to $D_\perp$. The toroidal velocities of different ion species induced by the neutral beam are calculated from the motion equations averaged over magnetic surfaces. Reduced viscosity allows the beam to accelerate the plasma core to a velocity higher than in the L-mode in spite of the ion braking at the edge due to friction with recycling neutrals. These changes in the profile of the toroidal velocity have important consequences for the ion anomalous heat transport due to ITG-turbulence [16]: the toroidal rotation induces radial electric field and the velocity shear of the drift motion due to E_r reduces the growth rate of the ITG-instability [15].

Fig.7 demonstrates the calculated profiles of the electron temperature and density which are in good agreement with measurements. The ion temperature and toroidal velocity are shown in Fig.8. They also reproduce the essential features of changes induced by the edge radiation cooling but a further efforts are necessary to explain the formation of the internal transport barrier observed in experiments.

References

[1] Berry, L.A., et al., in Plasma Physics and Controlled Nuclear Fusion Research 1976 (Proc. 6th Int. Conf. Berchtesgaden, 1976), Vol. 1, IAEA, Vienna (1977) 49

[2] Philipps, V., et al., Nucl. Fusion **34** (1994) 1417

[3] Van Oost, G., et al., in Controlled Fusion and Plasma Physics (Proc. 22nd Eur. Conf. Bournemouth, 1995) Vol.3, European Physical Society, Geneve (1995) 345

[4] Rapp, J., Plasma Phys. Control Fusion **39** (1997) 1615

[5] Hirshman, S.P., Sigmar, D.J., Nucl. Fusion **21** (1981) 1079

[6] Tokar', M.Z., et al., Plasma Phys. Control Fusion **37** (1995) A241

[7] Philipps, V., et al., in Controlled Fusion and Plasma Physics (Proc. 22nd Eur. Conf. Bournemouth, 1995) Vol.2, European Physical Society, Geneve (1995) 321

[8] Chapman, S., Proc. Phys. Soc. **72** (1952) 353

[9] Ohyabu, N., Nucl. Fusion **19** (1979) 1491

[10] Neuhauser, J, et al. Nucl. Fusion **26** (1986) 1879

[11] Lasaar, H., Tokar', M.Z., 6th PET Workshop, Oxford, 1997

[12] Tokar', M.Z., Plasma Phys. Contr. Fusion **36** (1994) 1819

[13] Tokar, M.Z., Phys. Scripta **51** (1995) 665

[14] Messiaen, A.M., et al, Phys. Plasmas **4** (1997) 1690

[15] Tokar,M.Z., et al, 6th PET Workshop, Oxford, 1997

[16] Norman,H., Weiland,J., Nucl. Fusion **29** (1989) 251

Figure captions

Fig.1. Reconstructed (solid lines) and calculated according to neoclassical theory transport coefficients of W during accumulation.

Fig.2. Central plasma density critical for accumulation of W versus neon concentration.

Fig.3. Profiles of electron temperature, radiated power density and safety factor in the steady-state after accumulation of W caused by neon seeding.

Fig.4. Evolution of central parameters after accumulation of Xe.

Fig.5. Total energy losses with conduction and radiation versus plasma temperature at the LCMS.

Fig.6. The same in the case of a poloidal inhomogeneous temperature distribution.

Fig.7. Calculated by RITM profiles of n_e and T_e in the L- (broken lines) and RI-modes (solid lines).

Fig.8. The same for the ion temperature and toroidal velocity.

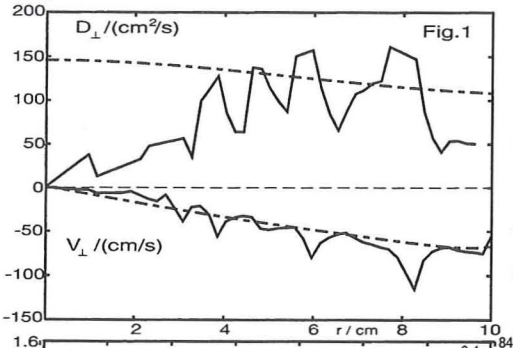
Fig.1
$D_\perp$/(cm²/s)
$V_\perp$ /(cm/s)
r / cm

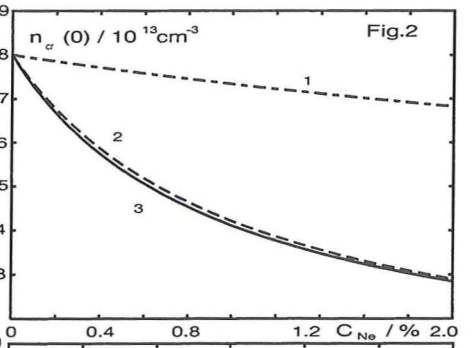
Fig.2
n_α (0) / 10 ¹³cm⁻³
1
2
3
C_{Ne} / %

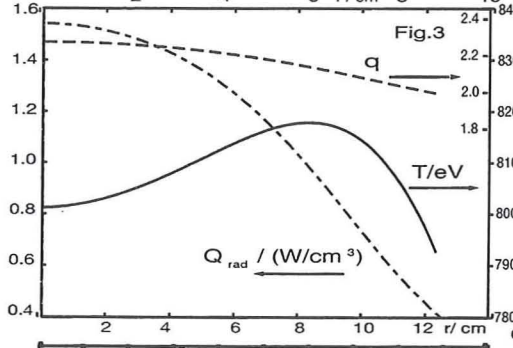
Fig.3
q
T/eV
Q_{rad} / (W/cm ³)
r/ cm

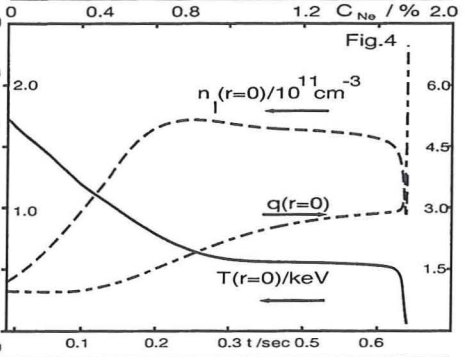
Fig.4
n_i(r=0)/10¹¹ cm⁻³
q(r=0)
T(r=0)/keV
t /sec

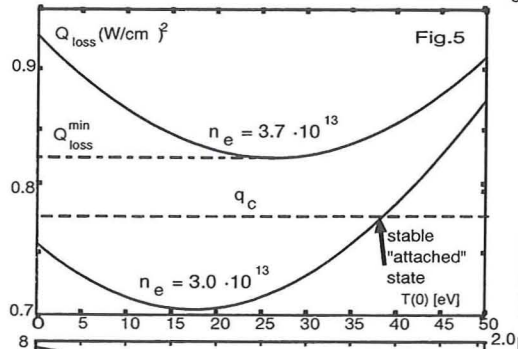
Fig.5
Q_{loss}(W/cm ³)
Q_{loss}^{min}
n_e = 3.7 ·10 ¹³
q_c
n_e = 3.0 ·10 ¹³
stable
"attached"
state
T(0) [eV]

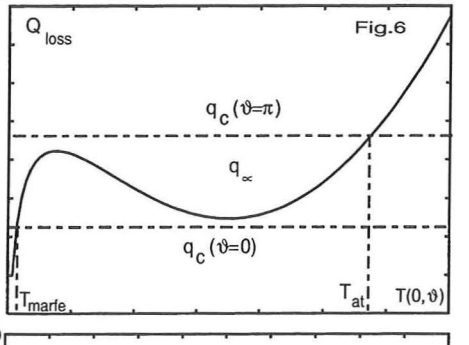
Fig.6
Q_{loss}
$q_c(\vartheta=\pi)$
q_∞
$q_c(\vartheta=0)$
T_{marfe}
T_{at}
T(0,ϑ)

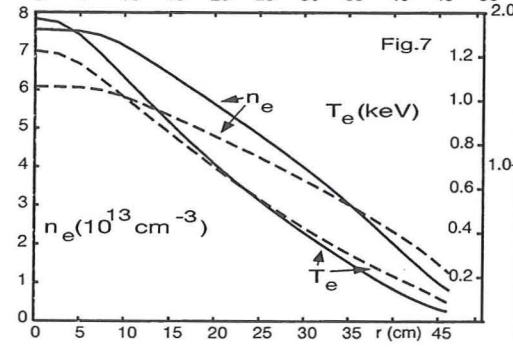
Fig.7
n_e
T_e(keV)
$n_e(10^{13}$cm $^{-3})$
T_e
r (cm)

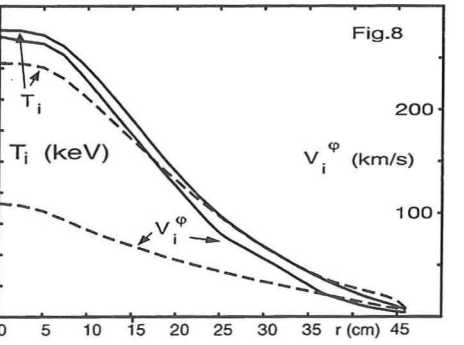
Fig.8
T_i
T_i (keV)
V_i^φ (km/s)
V_i^φ
r (cm)

Finite-β Tearing-Mode Stability for Tokamak Discharges with Current-Profile Control

M. Zabiégo[1], T.A. Gianakon[1], S.E. Kruger[2],
X. Garbet[1], G. Giruzzi[1], E. Joffrin[1], C.C. Hegna[2] and J.D.Callen[2].
[1]DRFC/SPPF, CE Cadarache, F-13108 Saint-Paul-lez-Durance, France
[2]EP/CPTC, Engineering drive, University of Wisconsin, Madison WI 53706-1687, USA

Abstract

In the recent years, significant progress on diagnostics, equilibrium reconstruction and current-drive systems have allowed to achieve some degree of current-profile control in tokamak experiments. This led to promising prospects for attractive reactor concepts based on the so-called *Advanced Scenarios*. Nevertheless, stability analyses for such scenarios have been presently restricted to ballooning, kink and interchange modes. Given the experience of *Conventional Scenarios*, where the long-pulse limit is set by finite-β tearing modes significantly below the *Troyon limit*, it appears interesting to consider this point. This problem is briefly discussed in the present paper, in the context of the Lower-Hybrid-Enhanced discharges of Tore Supra.

I- *Introduction - Motivations*

The observation has recently been made on TFTR, DIII-D, ASDEX-U, COMPASS-D and JT60-U [1-4] that the β-limit of long-pulse tokamak-discharges tends to be set significantly below the ideal β-limit by resistive modes now commonly referred to as *neoclassical-tearing-modes*. In addition, these modes are anticipated [5] to set ITER's β-limit dangerously close to the minimum β required for achieving ignition with a comfortable margin in *conventional* scenarios (as opposed to the so-called *advanced* scenarios).

In the past few years, current-profile control has been somewhat successful in tokamaks, owing to substantial progress on diagnostics, equilibrium reconstruction and current-drive systems. In particular, global current-profile *control* has led to regimes with improved core-confinement [6-9], although the long-pulse MHD stability of such discharges is yet to be documented. However, an urgent need remains for controlling the above mentioned tearing modes. Localised current-drive scenarios are thought to offer interesting prospects [3,4,10].

The aim of this paper is to address the potential effects that current-profile control can have on tearing modes. The discussion is based on a simplified version, as presented in section II, of the *ever-more-complex* finite-β tearing-mode model. Our goal is to identify robust tendencies rather than to attempt such a detailed modelling as required when comparing theory with an extended set of experiments [3,4]. In section III and IV, our analysis aims at exploring a *new* range of parameters (low or negative magnetic shear, low aspect ratio, positive Δ'...), in order to evaluate the prospects for tearing modes in long-pulse *advanced* discharges.

This work was originally motivated by the Tore Supra programme on long-pulse *advanced* scenarios, where current-profile control is achieved with off-axis LHCD [7,11,12]. Although the recent Tore Supra campaigns have been limited to moderate performance, the preliminary indications are that tearing-mode related MHD is a potentially strong limit to *advanced* scenarios. To date, most theoretical studies on the MHD stability of *advanced* scenarios has been devoted to considering ballooning, kink and interchange modes, which subsequently leads to a high β-limit resulting in promising prospects for attractive reactor-concepts [13,14]. This approach seems to be motivated by the observation that the presently achieved transient performance seem primarily limited by such modes. Nevertheless, high-performance long-pulse *advanced* discharges that are yet to be realised might reveal, similarly to what happened for *conventional* scenarios a couple of years ago, that the long-pulse limit is set by tearing modes. An occurrence with detrimental consequences on presently optimistic prospects...

II- *Finite-β tearing-mode model*

The finite-β tearing-mode model has been extensively described in the literature. The island-width (w) evolution can be expressed in terms of the simple Rutherford equation [15]

$$\frac{dw}{dt} \approx 1.22 \frac{\eta_{nc}}{\mu_0} (\Delta' + \Delta'_{boot} + \Delta'_{GGJ} + \Delta'_{pol}), \qquad (1)$$

The first term on the right-hand-side of equation (1), Δ', is the well-known stability index calculated from the asymptotic logarithmic jump of the magnetic perturbation $\tilde{\psi}$ across the resistive layer [15]

$$\Delta' = \Delta'(w) = [\nabla\tilde{\psi}]_{r-w/2}^{r+w/2} / \tilde{\psi}(r). \qquad (2)$$

The dominant finite-β destabilising (for positive magnetic shear) term is Δ'_{boot}, the neoclassical *bootstrap-term* [16,17], including finite-$\chi_\perp/\chi_{//}$ corrections [18]

$$\Delta'_{boot} = \frac{K_b w}{w^2 + w_\chi^2} \qquad \begin{cases} K_b = k_b \, \beta_p \, l_p^{-1} \, \varepsilon^{1/2} \, s^{-1} \\ w_\chi \propto \varepsilon^{1/2} \, |s|^{-1/2} \, \varepsilon_\chi^{1/4} \, R_0 \end{cases}, \qquad (3)$$

with $k_b = O(1)$, R_0 the major radius, $\beta_p = p/(B_p^2/2\mu_0)$, $l_p = -(rdp/pdr)^{-1}$ (assumed positive, so that Δ'_{boot} is stabilising for negative shear), $\varepsilon = r/R_0$, $s = rdq/qdr$ and $\varepsilon_\chi = \chi_\perp/\chi_{//}$, all quantities being evaluated at the resonant surface where the mode develops.

Finite-$\chi_\perp/\chi_{//}$ corrections imply that there exists a range of parameters where tearing modes require a seed-island to be excited [19-21]. The associated threshold condition is

sensitive to current-profile control through a single *control-parameter* [22] which depends on both Δ' and shear.

The third contribution to equation (1), Δ'_{GGJ}, is the so-called *Glasser-term* [23,24], modified for finite-$\chi_\perp/\chi_{//}$ corrections (i.e., non-zero w_G)

$$\Delta'_{GGJ} = -\frac{k_G D_R\, w}{w^2 + w_G^2}, \tag{4}$$

where $k_G = O(1)$, and D_R is the resistive-interchange index [23], that satisfies

$$D_R \approx \varepsilon^2\, \beta_p\, s^{-2}\, l_p^{-1} \left\{(1 - 1/q^2) + s(\beta_p + l_i/2)\right\}, \tag{5}$$

for large-aspect-ratio and circular-cross-section [14]. Here, Δ'_{GGJ} tends to be stabilising (destabilising) for q>1 (q<1). Assuming that w_χ and w_G scale similarly (a theoretical analysis of the latter is yet to be done), Δ'_{boot} and Δ'_{GGJ} are then similarly behaved with respect to the island-width w, as they appear to be, according to equation (6), with respect to l_p and β_p (provided that the contribution of the latter to the curly-bracket is neglected, a condition essentially violated when q≈1 which we do not consider here since tearing modes are not expected to be the dominant instability there). The above circular expression clearly indicates that the *Glasser-effect* is particularly strong for both weak-magnetic-shear and/or low-aspect-ratio; a tendency that persists for shaped equilibria (with a more complex expression for D_R, though [25]).

As analysed in [25] and discussed in section III, the *Glasser-effect* can in principle balance the bootstrap-drive. Nevertheless, such a possibility is restricted to equilibria with weak shear and preferentially low aspect-ratio; for which the tendency to improve stability through the *Glasser-effect* might however be reversed when considering side-effects on Δ' [26].

The fourth contribution to equation (1), which has been strongly argued as important for interpretation of threshold-dynamics on COMPASS-D, ASDEX-U [4] and DIII-D [27], is the *polarisation-current* term (sometimes referred to as the *ω*-effect*) [28,29]

$$\Delta'_{pol} = -\frac{K_p \rho_{p_i}^2}{w^3} H(w - \rho_{p_i}) \qquad \begin{cases} K_p = k_p \beta_p l_p^{-2} s^{-2} \\ \rho_{p_i} = \sqrt{2 m_i T_i / e_i B_p} \end{cases}, \tag{6}$$

where ρ_{p_i} is the ion poloidal-Larmor-radius, and H is the Heaviside step-function. The determination of the parameter k_p, nominally a function of both collisionality (favourable at high $\nu_i/\varepsilon\omega^*$) and mode-propagation-frequency, is still an open problem. The debate, recently opened by Waelbrock and Fitzpatrick [30], is that contributions from viscosity-dependent structures in the flow and polarisation-current profiles at the island separatrix can reverse the

sign of the polarisation-current term. In fact, for w less than the ion-Larmor-radius ρ_i, the ω^*-*effect* is destabilising and inversely proportional to the island-width w [31] (a smooth transition can be assumed for $\rho_i < w < \rho_{p_i}$ [32]).

III- *Stabilisation through the Glasser-effect*

Although it plays a role in determining the mode-onset threshold for marginally-stable conditions [3,4], Δ'_{GGJ} is generally much smaller than Δ'_{boot} in *conventional* scenarios. However, the relative importance of these two terms can be substantially affected --even reversed-- by tailoring the local shear. In a numerical analysis conducted by Kruger et al. [25], which had an emphasis on the role of the plasma-shape on DIII-D and Pegasus (an Extremely-Low-Aspect-Ratio-Tokamak under construction at University of Wisconsin), the authors found that shear-modification through shaping and/or localized current-drive has a potentially strong influence on the balance between Δ'_{boot} and Δ'_{GGJ} when considering equilibria with low-shear --a result very sensitive to the equilibrium profile and mostly significant for low aspect-ratio. These authors demonstrated that for a typical DIII-D-like equilibrium, where Δ'_{GGJ} is much smaller than Δ'_{boot}, shaping and local-shear modification (presumably through localised current-drive) do very little in altering the imbalance between these two terms. On the contrary, an extremely-low-aspect-ratio ($a/R_0 \approx 1.135$) Pegasus equilibrium exhibits a quasi-balance between Δ'_{boot} and Δ'_{GGJ} over some fraction of the plasma radius. The latter is very sensitive to shaping and local-shear modifications. One should also keep in mind that this favorable effect can be counter-balanced by *side-effects* on Δ', which can take large positive values for such equilibria; an issue not addressed in reference [25] but suggested by reference[26]. In such cases when Δ' is positive the polarisation-current seems to be a key ingredient to account for stability in high-β regimes.

IV- *Long-pulse MHD-limit in Tore Supra advanced discharges*

The treatment of the full MHD problem with all the relevant physics of polarisation-current and flow, in realistic geometry is difficult to attempt [33,34]. So, in abeyance of a firmer theoretical footing for this, we use the model equation (7) --where it is assumed that k_p is a positive constant-- which reproduces the essential robust features of the complete model

$$\frac{dw}{dt} = 1.22\,\frac{\eta_{nc}}{\mu_0}\left(\Delta' + \frac{K_b - k_G D_R}{w} - \frac{K_p \rho_{p_i}^2}{w^3}\, f(w/w_p)\right), \qquad (7)$$

where f is a smooth function modelling the transition to $w < \rho_{p_i}$ [32]. Such a model accounts for 1) current-profile effects through Δ', 2) a threshold condition that potentially extends to modes with positive Δ', and 3) competition between stabilising/destabilising finite-β

contributions with a shear-dependence that favours stability for equilibria with low shear. The procedure of [22] is followed, and we assume both s>0 and $\Delta'_{boot}+\Delta'_{GGJ}>0$, so that the *control parameter*

$$C_* = \frac{\Delta' w_*}{K_b - k_G D_R} \propto \frac{\Delta' \beta_p^{-1} l_p^{1/2} s^{1/2}}{\left(1+\Delta'_{GGJ}/\Delta'_{boot}\right)^{3/2}} \tag{8}$$

and the *critical-island-width*

$$w_* = \frac{K_p^{1/2}\rho_{p_i}}{(k_G D_R - K_b)^{1/2}} \propto \frac{l_p^{-1/2}|s|^{-1/2}}{1+\Delta'_{GGJ}/\Delta'_{boot}}, \tag{9}$$

can be introduced,which leads to the stability diagram represented in figure 1c. Note that in figure 1c the transition $\rho_i<w<\rho_{p_i}$ is obtained with an arbitrary model that only reproduces the qualitative features expected from theory. In fact the co-ordinates (C_*^{crit}, w_*^{crit}) of the critical point strongly depend on this model: for instance, when $\Delta'_{boot}+\Delta'_{GGJ}$ approaches zero, w_*^{crit} becomes very big and C_*^{crit} grows like the cubic power of w_*^{crit}, thus actually over-compensating the related increase in C_*.

The model-equation (7) is now used to comment on the present long-pulse MHD-limit of the so-called Lower-Hybrid-Enhanced-Performance Tore Supra *advanced* discharges (LHEP [7]), where current-profile control is achieved with off-axis LHCD (experimental details on these discharges are described in [11,12,35]). The LHEP discharge represented in figure 1 is characterised by q_0 above 1 and a weak --apparently positive-- shear in a core-region that extends up to one third of the plasma. Such safety factor profiles can be modelled by the analytic form $q(r) = q_0 + (q_0 - q_a)(r/a)^\nu$, with ν a function of q_0, q_a and l_i which primarily characterises the flatness of the q-profile in the core: see figure 2.

Discharges associated with such equilibria are essentially limited by the onset of a m/n=2/1 tearing mode with positive Δ' --all the more unstable that Δ' is large. The magnitude of Δ' is essentially controlled by two factors: 1) the proximity of q_0 to a low-order rational number, and 2) the extent of the weak-shear region or the flatness of the safety-factor profile. The benefit of reducing the shear --through increasing the polarisation-current and *Glasser* contributions relative to the bootstrap drive-- can be unfavourably compensated by an increase in the positiveness of Δ'. This tendency has already been suggested by Pletzer [26]. Similarly, Wijnands et al. [12] noticed that in Tore Supra (where the advanced equilibrium is built-up by starting from a *conventional* monotone-safety-factor-profile and progressively replacing the inductive current by off-axis LH-driven current) an operational limit is set by the "difficulty to raise q_0 above a critical value" (see figure 10 in [12]). A careful adjustment of the current profile

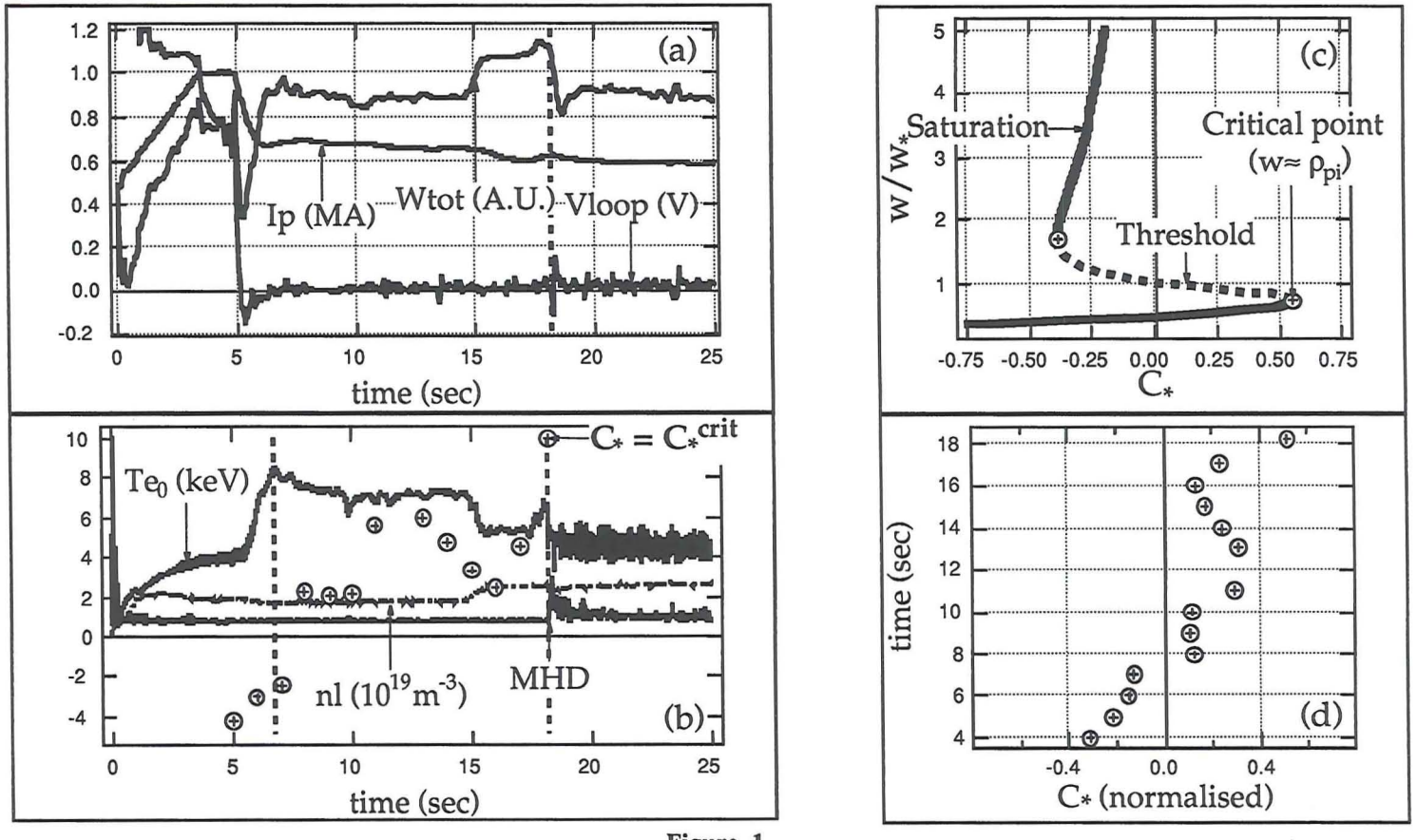

Figure 1

(a-b) A ToreSupra LHEP-discharge exhibits a transition from improved LHEP-regime towards degraded-regime, with MHD-onset at t=18.2 sec.
(c-d) Stability diagram associated with equation (7) and evolution of the *control parameter* (see equation (8)) for the considered discharge.

according to these criteria looks like a critical point to achieve stable *advanced* discharges of this kind. Indeed, an extended weak-shear core with q_0 slightly less than a low-order rational value will require a very high β to enter the *second-stable* domain (i.e. $0 < C_* < C_*^{crit}$) associated with positive-Δ' modes (for which, contrary to negative-Δ' modes, higher β is stabilizing).

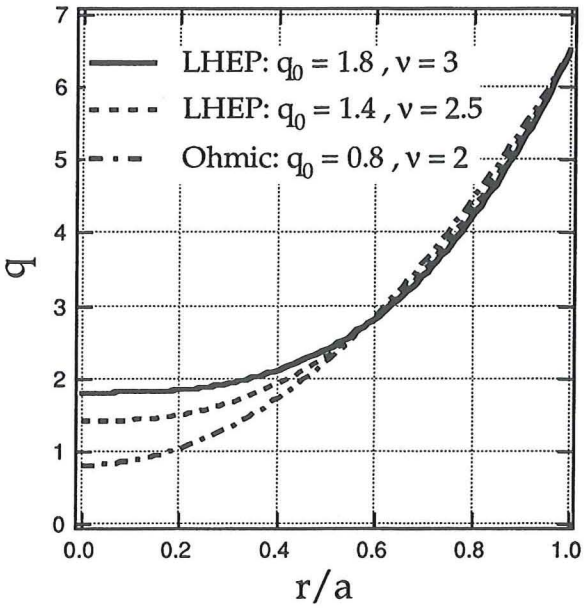

Figure 2

Model q(r)-profiles for Tore Supra ohmic and LHEP discharges.

Owing to a combination of both significant-positiveness-of-Δ' and smallness-of-β for these equilibria, the collapse-termination of the LHEP-phase (leading to a *sawooth-like* degraded regime [35]) results from the relative slow evolution of the pressure and current profiles. This turns out to reduce the stabilising polarisation-current contribution relative to the main drive associated with positive-Δ', thus driving the m/n=2/1 mode (experimentally observed as a postcursor) beyond the critical point where the threshold condition disappears. Figure 1 illustrates the evolution of a typical discharge where such a transition from a LHEP-phase to a degraded phase occurs at t = 18.2 sec. The increase in the positive C_* (arbitrary units) before the fast-transition qualitatively accounts for an evolution of the discharge beyond the critical point. A detailed quantitative analysis of this scenario has yet to be done with improved diagnostics: although this tendency has been observed for several discharges, the interpretation is very sensitive to error-bars on such data as the q-profile.

Acknowledgements

H. Wilson and A. Smolyakov are warmly acknowledged for providing instructive information on the open status of the polarisation-current. Fruitful discussions with H. Zohm are also acknowledged. We are grateful to A. Pletzer and H. Lütjens who provided the PEST-3 and CHEASE codes, as well as assistance in running them for Tore Supra data-analyses. Many thanks are also due to T. Wijnands for helpful comments he made about reference [12].

References

[1] Z. Chang et al., Physical Review Letters **74** (1995) 4463.
[2] H.R. Wilson et al., Plasma Physics and Controlled Fusion 38 (1996) A149.
[3] O. Sauter et al., Physics of Plasmas **4** (1997) 1654.
[4] H. Zohm et al., *Neoclassical MHD in ASDEX-U and COMPASS-D*, (24th EPS Conf., Berschtesgaden, 1997) to appear in Plasma Physics and Controlled Fusion.
[5] J.C. Wesley et al., Physics of Plasmas **4** (1997) 2642.
[6] M. Hugon et al., Nuclear Fusion **32** (1992) 33.
[7] G.T. Hoang et al., Nuclear Fusion **34** (1994) 75.
[8] F.M. Levinton et al., Physical Review Letters **75** (1995) 4417.
[9] E.J. Strait et al., Physical Review Letters **75** (1995) 4421.
[10] C.C. Hegna and J.D. Callen, Physics of Plasmas **4** (1997) 2940.
[11] X. Litaudon et al., Plasma Physics and Controlled Fusion **38** (1996) A251.
[12] T. Wijnands et al., Nuclear Fusion **37** (1997) 777.
[13] E.J. Strait et al., Physics of Plasmas **4** (1997) 1783.
[14] A. Bondeson et al., *MHD β-Limits for Tokamaks with Negative Central Shear*, Chalmers University report CTH-IEFT/PP-1997-10.
[15] P.H. Rutherford, Physics of Fluids **16** (1973) 1903.
[16] W.X. Qu and J.D. Callen, University of Wisconsin report UWPR-85-5 (1985).
[17] R. Carrera et al., Physics of Fluids **29** (1986) 899.
[18] R. Fitzpatrick, Physics of Plasmas **2** (1995) 825.
[19] R. Fitzpatrick, Nuclear Fusion **33** (1993) 1049.
[20] R. Fitzpatrick et al.; Nuclear Fusion **33** (1993) 1533.
[21] R.L. Dewar and M. Persson, Physics of Fluids B **5** (1993) 4273.
[22] M. Zabiégo and J.D. Callen, Nuclear Fusion **37** (1997) 361.
[23] A.H. Glasser et al., Physics of Fluids **18** (1975), 875
[24] M. Kotschenreuther et al., Physics of Fluids **28** (1985) 294.
[25] S.E. Kruger et al., *Geometrical Influence on Neoclassical MHD Tearing Modes*, University of Wisconsin report UW-CPTC 97-10 (1997), submitted to Physics of Plasmas.
[26] A. Pletzer, *Numerical Δ' Studies of the Nonlinear Finite-β Tearing* Mode, Proceedings of the Varenna International Workshop on *Theory of Fusion Plasmas* (Varenna, 1996) p. 259.
[27] R.J. La Haye et al., *Metastable β-limit in DIII-D*, to appear in the Proceedings of the 24th EPS Conference (Berchtesgaden, 1997).
[28] A.I. Smolyakov et al., Physics of Plasmas 2 (1995) 1581.
[29] H.R. Wilson et al., Physics of Plasmas **3** (1996) 248.
[30] F.L. Waelbrock and R. Fitzpatrick, Physical Review Letters **78** (1997) 1703.
[31] A. Samain, Plasma Physics and Controlled Fusion **26** (1984) 731.
[32] M. Zabiégo and X. Garbet, Physics of Plasmas **1** (1994) 1890.
[33] A.I. Smolyakov, Proceedings of the 1997 International Sherwood Fusion Theory Conference (Madison, 1997), p. 1C47; also private communication.
[34] H.R. Wilson, private communication.
[35] S. Turlur et al., Proceedings 22nd EPS Conference (Bornemouth, 1995), Vol. IV, p. 73.

Global Approach to the Spectral Problem of Microinstabilities in Tokamak Plasmas using a Gyrokinetic Model

S.Brunner, M.Fivaz and J.Vaclavik

Centre de Recherches en Physique des Plasmas

Association Euratom - Confédération Suisse

Ecole Polytechnique Fédérale de Lausanne/ PPB – CH-1015 Ecublens/Switzerland

Abstract

A gyrokinetic eigenvalue code has been developed for computing global ion temperature gradient (ITG) -related instabilities in tokamak configurations. Although trapped ion dynamics are not yet considered in this model, it contains full finite Larmor radius and finite orbit width effects of circulating ions. Non-adiabatic trapped electron dynamics are included through a bounce-averaged drift kinetic equation. Differences between the local ballooning approximation and the global approach are presented and discussed. The possible coupling between the trapped electron mode (TEM) and the toroidal-ITG mode is also investigated. Finally, the evolution of the spectrum of these different instabilities is studied for varying central negative magnetic shear configurations.

Introduction: For studying microinstabilities in tokamak-like plasmas, most linear kinetic studies were carried out for high toroidal wave numbers using the ballooning representation[1] which leads to a one-dimensional integral equation along the magnetic field lines. Except for very few cases, these calculations do not include a higher order WKB procedure for determining the radial structure. Thus these results usually stay local to a magnetic surface and there remains some questioning on the actual radial extent of these modes. For low toroidal wave numbers where the ballooning representation breaks down and the full two-dimensional problem cannot be reduced, very little linear computation has been carried out. This limit is of interest as it describes larger wavelength fluctuations which could lead to higher turbulent transport. Until recently the only published results from true global, linear computations came from a spectral code by Marchand, Tang and Rewoldt[2]. This model contains no finite Larmor radius (FLR) effects and is based on a second order expansion with respect to the radial excursion of trapped particles, which leads to spurious modes[3] and thus to a difficult search of physical eigenfrequencies. At the present state full non-linear simulations already exist[4][5], nonetheless there remains a need for global linear studies as they enable to determine more accurately the conditions of marginal stability and in this way, if possible, to find stable configurations. This has prompted us to undertake the development of a new, global, spectral gyrokinetic code. A summary of the present state physical model as well as of first results is given here. More details are found in Ref.[6].

Physical Model for the Spectral Approach

Geometry: At present the geometry of the system is still approximated by a large aspect ratio torus with circular, concentric magnetic surfaces. Therefore finite pressure effects such as the Shafranov shift are not taken into account. The safety factor profile $q_s(\rho)$, the ion and electron temperature profiles $T_{e,i}(\rho)$ as well as the density profile $N(\rho)$ are chosen arbitrarily and in this way are represented by simple polynomial functions of the radial variable ρ. Here (ρ, θ, φ) is the standard set of toroidal coordinates.

Kinetic equations: Although the basic mechanism of ITG instabilities can be described by fluid models, the more detailed behavior of these perturbations also contain specifically kinetic characters, such as wave-particle interaction (e.g. Landau damping) and FLR effects. In order to take them into account - this being essential if one is interested in determining accurately conditions of marginal stability- appropriate kinetic equations for each species must be considered. Assuming a collisionless plasma, these can be derived by reducing the Vlasov equation, linearized for electrostatic perturbations, using different scaling laws. In particular, as microinstabilities have low frequencies i.e. small compared to the cyclotron frequencies $\Omega_{e,i}$, one can for all particles carry out a gyroaveraging procedure.

In the case of **ions** the Larmor radius can be comparable or larger then the wavelengths perpendicular to the magnetic field, giving rise to the above mentioned FLR effects. The appropriate equation of motion is thus given by the gyrokinetic equation (GKE) [7]:

$$\left.\frac{D}{Dt}\right|_{u.t.GC} \tilde{g} = \left[\frac{\partial}{\partial t} + \vec{v}_{GC} \cdot \frac{\partial}{\partial \vec{R}}\right] \tilde{g} = -i\frac{q}{T} F_M(\omega - \omega^*) < \phi >_g,$$

where $D/Dt|_{u.t.GC}$ stands for the total time derivative along the unperturbed trajectories $\vec{R}(t)$ of the guiding centers (GC), including drifts related to the gradient and curvature of the magnetic field. Furthermore, $\tilde{g}$ represents the fluctuating, non-adiabatic part of the particle distribution function written in gyro-center variables, F_M the local Maxwellian distribution of equilibrium, ω^* the diamagnetic frequency related to the temperature and density inhomogeneities and $< \phi >_g$ the gyroaveraged electrostatic potential.

In first approximation the mobile **electrons** have been assumed to respond adiabatically to the low frequency microinstabilities and therefore to follow a Boltzmann distribution. However in the non-trivial tokamak geometry, the trapped electrons in fact have a toroidal precessional drift which can become comparable to the phase velocity of the perturbation. To take into account the resonances which may arise, a more detailed

description has been considered. As electrons have significantly smaller Larmor radii then ions for similar temperatures, FLR effects can usually be neglected (at least when studying ion-driven instabilities), so that the drift kinetic equation (DKE) instead of the GKE is sufficient. Furthermore, due to the high thermal velocity of these particles, this equation can be averaged over the periodic motion in the poloidal plane, giving rise to the so-called bounce-averaged DKE[8]:

$$\left.\frac{D}{Dt}\right|_{u.t.B} \tilde{g}_b = \left[\frac{\partial}{\partial t} + <\dot{\varphi}>_b \frac{\partial}{\partial \varphi}\right] \tilde{g}_b = -i\frac{q}{T} F_M(\omega - \omega^*) < \phi >_b .$$

Here $D/Dt|_{u.t.B}$ stands for the total time derivative along the unperturbed trajectories of the banana (B) orbits, $\tilde{g}_b$ for the fluctuating, non-adiabatic part of the bounce-averaged GC distribution function, $<\dot{\varphi}>_b$ for the average toroidal precessional drift and $< \phi >_b$ for the bounce-averaged potential.

The equations of motion are solved by integrating along the unperturbed trajectories. In the case of ions the modulation of the magnetic field along the trajectory was neglected, so that in particular the dynamics of trapped ions was discarded. In its present state our model therefore still does not enable to describe trapped ion modes (TIM). In this context Fourier representation appears naturally as it enables to integrate explicitly the unknown potential ϕ. For example, when gyroaveraging the potential one obtains

$$< \phi >_g = < \int d\vec{k}\, \hat{\phi}\,(\vec{k},t)\, e^{i\vec{k}\cdot\vec{r}} >_g = \int d\vec{k}\, J_0\left(\frac{k_\perp v_\perp}{\Omega}\right) \hat{\phi}\,(\vec{k},t) e^{i\vec{k}\cdot\vec{R}},$$

where J_0 is the zero order Bessel function containing the full FLR effects and having used the relation $\vec{R}=\vec{r} + \vec{v} \times \vec{e}_\parallel / \Omega$ between the GC and particle position. In fact, instead of a decomposition into plane waves, a Fourier representation in terms of toroidal wave components was chosen as it is more adapted to the geometry of the system:

$$\phi(\rho,\theta,\varphi;t) = \sum_{(\kappa,m)} \hat{\phi}_{(\kappa,m)} \exp i(\kappa\rho + m\theta + n\varphi - \omega t),$$

where κ is a radial, m a poloidal and n the fixed toroidal wave number. Note that a Fourier series decomposition instead of a Fourier transform is considered not only in the periodic direction θ but also along the radial coordinate ρ, this being justified by the finite dimension of the system. The fixed frequency is noted ω.

Eigenvalue equation: The equations of motion are completed with a relation for ϕ. This is provided by the quasineutrality equation (justified when studying low frequency microinstabilities), which leads to the actual eigenvalue equation for (ω, ϕ). It turns out

to be advantageous to solve this eigenvalue problem staying in the discrete Fourier space (κ, m). Indeed, the equation is then naturally discretized and contains no singularity as the one appearing in the kernel of the integral equation when solving in the continuous configuration space (ρ, θ). The eigenvalue problem can formally be written in matrix form:

$$\overleftrightarrow{M}(\omega)\,\vec{\phi} = 0.$$

This is not a standard problem as the matrix $\overleftrightarrow{M}$ has an intricate dependence in the eigenvalue ω. The characteristic equation for ω:

$$D(\omega) = \det \overleftrightarrow{M}(\omega) = 0, \qquad \omega \text{ complex},$$

is solved by taking advantage of the analyticity of $D(\omega)$ and using a practical method proposed by Davies[9]. By sampling $D(\omega)$ along a closed curve in the complex frequency plane, this approach allows not only to find the number of enclosed zeros using the principle of argument (Nyquist), but the value itself of these roots with great accuracy. In this way the full unstable spectrum of a given system can be computed quite effectively.

Results

Benchmarking with time evolution PIC code: The spectral code has been extensively benchmarked against another global, linear gyrokinetic code developed simultaneously at the CRPP, based on a time evolution particle in cell (PIC) method[10][11]. In the regime where trapped ion dynamics (contained in the PIC model) are not important, i.e. for frequencies above the average ion bounce frequency, and for not too short wavelengths (PIC model is only valid to second order in Larmor), comparisons have shown very good agreement. Details of this validation can be found in Ref.[12].

Comparison with local ballooning calculations: Results from the global spectral code have also been compared to those obtained by Dong et al.[13] applying the local ballooning approximation to the same physical model. In this case only the adiabatic response of trapped electrons is taken into account so that the instabilities are essentially toroidal-ITG. To carry out such a comparison, the profiles for the global code must be chosen such that they match the local ballooning parameters on a reference magnetic surface. Here these parameters are given by the safety factor q_s, the temperature ratio $\tau = T_e/T_i$, $\epsilon_n = L_n/R$ =characteristic length of density/ major radius, $\eta_i = L_n/L_{T_i}$ =charac.length of density/ charac.length of ion temperature and the normalized poloidal mode number

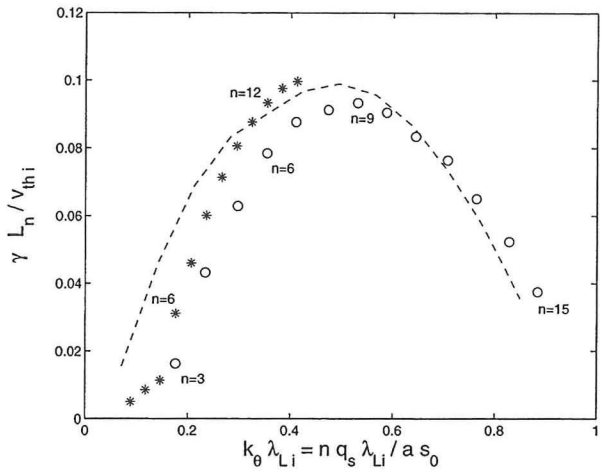

Figure 1: Growth rate γ as a function of $k_\theta \lambda_{Li}$ (only adiabatic response of electrons). Circles and stars represent global results for $a/\lambda_{Li} = 56.5$ and $a/\lambda_{Li} = 113.0$ respectively, a being the minor radius of the plasma. Labels below the circles and above the stars indicate the corresponding toroidal wave number. Ballooning results are reported here with a dashed line.

$\tilde{k_\theta} = n q_s \lambda_{Li}/\rho_0$, where λ_{Li} is the average ion Larmor radius on the reference magnetic surface $\rho = \rho_0$. Note that both, a high temperature plasma with a perturbation having low toroidal mode number n, or a low temperature and high n, can lead to a same value $\tilde{k_\theta}$ and thus be iso-dynamical with respect to the local ballooning calculation. Fig.1 presents the growth rates obtained when carrying out such a comparison along an n-scan. A hot as well as a cold plasma scenario have been considered when running the global code and in both cases the corresponding results indeed join the local ones for sufficiently high toroidal mode numbers, i.e. $n \gtrsim 10$. Ballooning results are from Fig.3 of Ref.[13]. The typical role over of the growth rate around $\tilde{k_\theta} \simeq 0.5$ is the consequence of FLR effects.

Effect of trapped electrons on the toroidal-ITG: The effect of non-adiabatic trapped electron dynamics is essentially twofold. In case of a flat density profile it simply strengthens the growth rate of the toroidal-ITG instability, which thus keeps its dominantly ion driven character. For non-flat density profiles (low values of ϵ_n and η_i) the toroidal-ITG can either couple and convert to, or simply be taken over by a trapped electron mode (TEM). This TEM may remain unstable down to flat ion temperature profiles, thus effectively removing the threshold on η_i predicted for the pure toroidal-ITG when only adiabatic electrons are considered. In this way our global results qualitatively

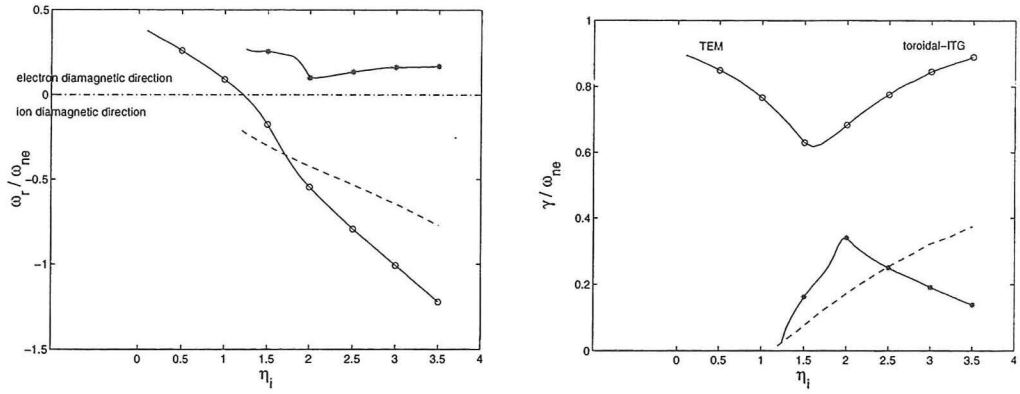

Figure 2: Real frequencies ω_r and growth rates γ of the most unstable eigenmodes as a function of η_i holding in particular $\epsilon_n = 0.2$=const and $\eta_e = 2$ =const, computed with non-adiabatic trapped electrons (full lines). For $\eta_i \lesssim 1$ the toroidal-ITG converts to a predominantly TEM (mode 1) and starts to propagate in the electron instead of the ion diamagnetic direction. A weaker instability propagating essentially in the electron diamagnetic direction (mode 2) is also present. For comparison, results with only adiabatic electrons are reproduced with dashed lines. Note how non-adiabatic trapped electron dynamics have removed the threshold on η_i.

confirm the picture given by Romanelli and Briguglio [14] solving a local dispersion relation. As an illustration, results of an η_i-scan are presented in Fig.2.

Negative shear scan: The global spectral code has been applied for studying the stabilizing effect of negative magnetic shear. Motivation for such studies come from experimental evidence on different tokamaks[15][16][17] of the formation of a transport barrier in regions of shear reversal accompanied by a reduction in core fluctuation amplitudes. Fig.3 presents the results of such a shear scan having fixed $n = 10$ and the profiles such that $\tau = 1$, $\epsilon_n = 0.25$, $\eta_i = \eta_e = 2.5$, $\tilde{k_\theta} = 0.35$, $\alpha_b = 45\%$ (fraction of trapped particles) on the magnetic surface $\rho = \rho_0$ where the modes tend to be centered (steepest gradients). The safety factor profile is varied such that $q_s(\rho_0) = 1.5$ is held fixed while shear varies from $\hat{s}\ (\rho_0) = +1$ to -1. For positive values of shear the spectrum contains eigenmodes propagating in the ion diamagnetic direction, i.e. having a dominantly toroidal-ITG character, as well as instabilities propagating in the electron diamagnetic direction, i.e. having essentially a TEM character. In this case, the TEM's are completely suppressed at negative shear $\hat{s} = -1$, while the toroidal-ITG modes are still present, their growth rate being nonetheless attenuated by a factor ~ 4 with respect

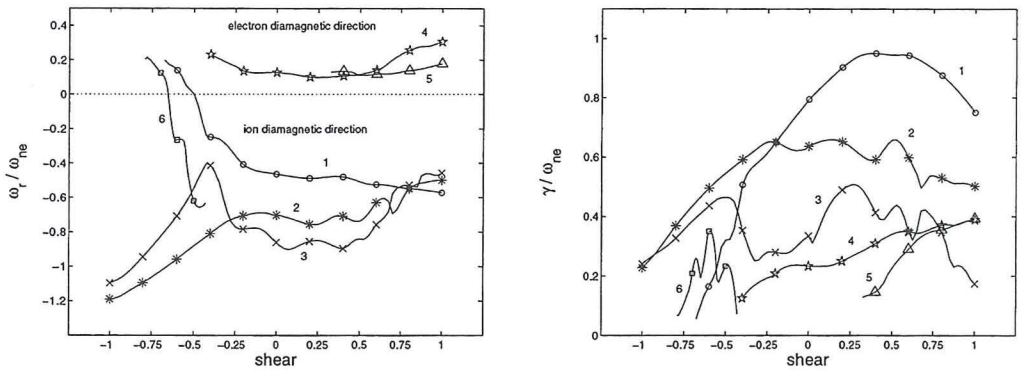

Figure 3: Real frequencies ω_r and growth rates γ as a function of shear $\hat{s}$ for a sampling of unstable eigenmodes, non-adiabatic trapped electron dynamics being taken into account. For $\hat{s}= +1.0$ the unstable spectrum contains simultaneously positive and negative frequencies. At $\hat{s}= -1.0$ only the ITG-type modes remain destabilized, however with a significantly reduced growth rate compared with the highest one around $\hat{s}= +0.5$.

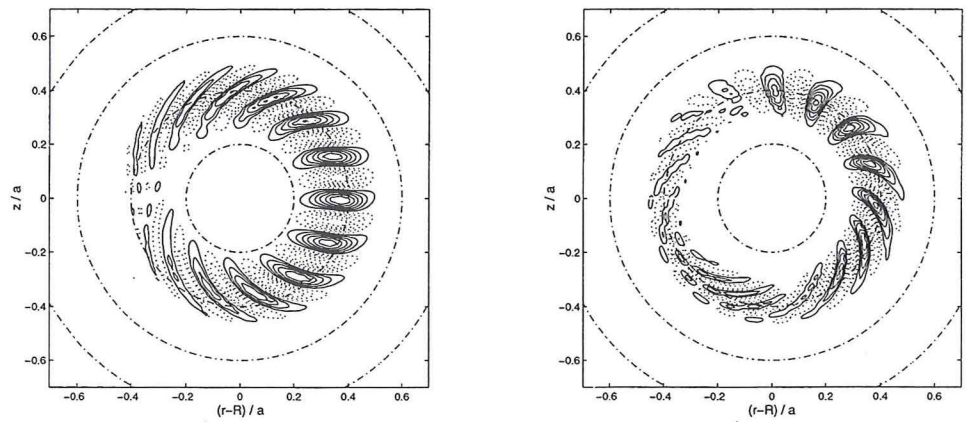

a.) $\hat{s}= +1.$ e.) $\hat{s}= -1.$

Figure 4: Mode structures of most unstable toroidal-ITG-type eigenmodes along shear scan $\hat{s}= +1. \ldots - 1.$

to $\hat{s}$= 0.5. Negative shear stabilizes the toroidal-ITG by twisting the convective cells more rapidly into a vertical position where they are less effectively driven[18]. This appears clearly in the poloidal mode structures of Fig.4 (axis of symmetry on the left). The TEM's are stabilized by reversal of the average toroidal precessional drift of the trapped particles. Thus realistic negative magnetic shear alone does not seem to be sufficient to explain the dramatic improvement of confinement in negative central shear discharges. Experimental results[16] point towards the $\vec{E} \times \vec{B}$ flow shear for being responsible for the full stabilization of microinstabilities[19].

References

[1] J.W.Connor, R.J.Hastie, and J.B.Taylor, Physical Review Letters **40**, 396 (1978).

[2] R.Marchand, W.M.Tang, and G.Rewoldt, Physics of Fluids **23**, 1164 (1980).

[3] W.M.Tang and G.Rewoldt, Physics of Fluids B **5**, 2451 (1993).

[4] S.E.Parker, W.W.Lee, and R.A.Santoro, Physical Review Letters **71**, 2042 (1993).

[5] M.Kotschenreuther, W.Dorland, M.A.Beer, and G.W.Hammett, Physics of Plasmas **2**, 2381 (1995).

[6] S.Brunner, Ph.D. thesis, Ecole Polytechnique Fédérale de Lausanne, 1997.

[7] P.J.Catto, Plasma Physics **20**, 719 (1978).

[8] M.Rosenbluth and M.L.Sloan, Physics of Fluids **14**, 1725 (1971).

[9] B.Davies, Journal of Computational Physics **66**, 36 (1986).

[10] M.Fivaz *et al.*, Physical Review Letters **78**, 3471 (1997).

[11] M.Fivaz, Ph.D. thesis, Ecole Polytechnique Fédérale de Lausanne, 1997.

[12] S.Brunner *et al.*, in *Theory of Fusion Plasmas, Int. Workshop, Varenna, August 1996* (Editrice Compositori, Societa Italiana di Fisica, Bologna, 1997), p. 101.

[13] J.Q.Dong, W.Horton, and J.Y.Kim, Physics of Fluids B **4**, 1867 (1992).

[14] F.Romanelli and S.Briguglio, Physics of Fluids B **2**, 754 (1990).

[15] F.M.Levinton *et al.*, Physical Review Letters **75**, 4417 (1995).

[16] L.L.Lao *et al.*, Physics of Plasmas **3**, 1951 (1996).

[17] Y.Neyatani and the JT-60 Team, Plasma Physics and Controlled Fusion **38**, A181 (1996).

[18] T.M.Antonsen Jr. *et al.*, Physics of Plasmas **3**, 2221 (1996).

[19] T.S.Hahm and K.H.Burrell, Physics of Plasmas **2**, 1648 (1995).

Operational space of Advanced Tokamaks and constraints for steady-state operation

A. Bondeson, M. Benda and M. Persson

Institute for Electromagnetic Field Theory, EURATOM-NFR/Fusion Association, Chalmers University of Technology, Göteborg, Sweden

M. S. Chu

General Atomics, San Diego, California, U. S. A.

1. Introduction

There is considerable interest in Advanced tokamaks with negative central shear (NCS) [1–5]. NCS equilibria can develop internal transport barriers that lead to good central confinement [4,5]. NCS equilibria are good candidates for steady state tokamaks because of good alignment between the bootstrap and parallel equilibrium current. On the other hand, NCS discharges have broad current profiles and often peaked pressure profiles, both of which are destabilizing to low-n MHD modes. Furthermore, the beta limit tends to be low at bootstrap fractions relevant for steady state operation [6,7]. Thus, it is important to study quantitatively the stability limits of NCS equilibria.

2. MHD optimization

Several different types of MHD instability can limit the pressure in NCS discharges. We consider only MHD modes, ignoring the recently observed neoclassical tearing mode, which is believed to limit beta at low collisionality. (Neoclassical tearing modes are stable in regions of negative shear.) We report optimizations of the fusion beta $\beta^* = 2\mu_0\langle p^2\rangle^{1/2}/\langle B^2\rangle$. Another important quantity is the bootstrap fraction $f = I_{bs}/I$, where I_{bs} is the bootstrap contribution to the toroidal plasma current.

The optimizations take into account the following conditions

1. The parallel current density from bootstrap must nowhere be larger than the total parallel current density, so that no negative current drive is needed. The bootstrap current is calculated assuming low collisionality, $T_e = T_i$ and $\eta = d(\log T)/d(\log n) = 1.5$.

2. Stability to ideal ballooning modes with toroidal mode number $n = \infty$.

3. Stability to ideal $n = 1$, 2 and 3 external kink modes without a conducting wall.

The bootstrap condition (1) typically limits the pressure gradient in the outer part of the plasma. In the NCS region, where ballooning does not limit the pressure gradient, the pressure peaking is typically limited by the stability of low-n external kink modes, or if the negative shear is very strong, by resistive interchange.

Ballooning modes are stable in the NCS region and (when the Mercier criterion is satisfied) also for weakly positive shear. In the optimized NCS equilibria, ballooning stability typically limits the pressure gradient in a region extending from slightly outside the shear reversal out to some flux surface where the bootstrap condition becomes more restrictive. In most cases, the region where ballooning is limiting is small or even nonexistent.

We have also imposed the condition that resistive interchanges remain stable. According to MHD theory, resistive interchanges are stable, for a circular cross section and large aspect ratio, when $-s[\beta_p(r) + l_i(r)/2] < 1 - 1/q^2$, where s denotes the shear. Evidently, resistive interchanges can be avoided if the shear does not become too negative and q is sufficiently above unity [8].

Very attractive advanced tokamak equilibria have been found under the assumption of a perfectly conducting closeby wall [1]. In reality, stabilization can be obtained from resistive walls and plasma rotation [9,10]. However, it appears that the required rotation speeds are too high to be of interest for large machines such as JET and ITER, and therefore, we do not take wall stabilization into account here.

The local conditions 1 - 3 are checked on each flux surface by the equilibrium code CHEASE [11]. The stability of low-n modes is checked by the global stability code MARS [12]. The current profile is chosen by specifying the surface averaged toroidal current density $I^*(\psi)$. We have chosen to consider only profiles with zero edge current density $I^*(\psi_a) = 0$ and $dp/d\psi(\psi_a) = 0$. Series of profiles with different internal inductances have been constructed by varying $dI^*/d\psi$ at the edge.

CHEASE is equipped with an algorithm to increase the pressure gradient on every flux surface until it becomes marginal to the most restrictive of the conditions: (a) $\langle \vec{j}_{bs} \cdot \vec{B} \rangle_\psi \leq \langle \vec{j} \cdot \vec{B} \rangle_\psi$ (b) Stability to ideal ballooning (c) $-dp/d\psi < c$. Here c is a ψ-independent parameter used to limit the pressure gradients in the NCS region. Equilibria are computed for different values of c and MARS is then run to find the c for which the low-n external modes are marginal. The optimization has been applied for several plasma

cross sections and $q_{\min}$ has been varied from 1.1 to 2.5 (in some cases, up to 2.9). The current profiles have been varied mainly with respect to the amount of current near the edge.

2.1. *RESULTS*

2.1.1. *JET shaped cross section ($\kappa = 1.6,\ \delta = 0.3$)*

As a first study, we chose four I^* profiles plotted versus the radial variable $s_\psi = (\psi/\psi_a)^{1/2}$ in Fig. 1. In terms of the square root of the enclosed fractional volume, ρ, maximum I^* occurs at $\rho \simeq 0.38$ and minimum q at $\rho \simeq 0.47$. The internal inductances are about 1.05, 0.94, 0.86 and 0.79, respectively. The results for the optimum β^* and bootstrap fraction f are shown in Fig. 2 as functions of the normalized current $I_N = I[\mathrm{MA}]/(a[\mathrm{m}]B_0[\mathrm{T}])$. The optimal pressure profiles are not very peaked, with peaking factors $p_0/\langle p\rangle$ generally between 2.5 and 3. The peaking of the pressure is limited by $n = 1$ stability.

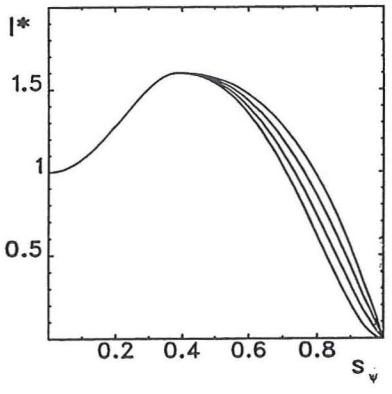

Fig. 1. Current profiles I^* used for optimizations giving $l_i \simeq 1.05$, 0.94, 0.86 and 0.79 in JET geometry.

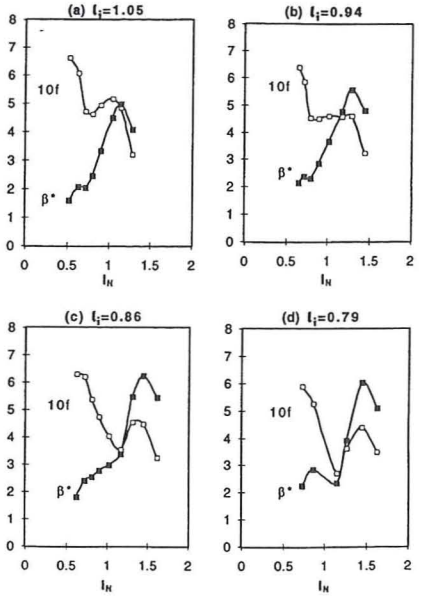

Fig. 2. β^* and bootstrap fraction versus normalized current for the current profiles in Fig. 1 and JET cross section.

In all cases, the maximum β occurs for $q_{\min}$ slightly above unity, typically $q_{\min} \simeq 1.2$.

When $q_{\min}$ approaches unity, the beta limit drops sharply. The main reason for this is destabilization of the $n = 1$ external kink mode. There may be difficulties controlling experimental profiles in such a way as to take advantage of the rather sharply localized maximum in the beta limit as a function of $q_{\min}$.

Figure 2 shows that the maximum beta increases with decreasing inductance. One reason for this is that a broader profile gives more plasma current at fixed $q_{\min}$. Therefore, according to the Troyon scaling $\beta_{\max} \propto I_N$ [13], one may expect a higher maximum beta at low inductance. However, this is not the entire explanation. Also the maximum normalized beta, $\beta_N = \beta[\%]/I_N$ increases when l_i is decreased. However, *at fixed current*, the beta limit does increase with the inductance in accordance with the DIII-D scaling [14], except in regions around the maxima associated with $q_{\min}$ somewhat above 1 or 2. We note that the best case on the low-l_i curve gives $\beta_N \simeq 3.7$ for $l_i = 0.79$, which exceeds the DIII-D scaling $\beta_N \leq 4l_i$.

The main reason for the somewhat unexpected dependence of the beta limit on the inductance is that the broader current profile can support larger pressure gradients at large radius without violating the bootstrap condition (1). Profiles conventionally used for high beta operation have broad pressure profiles and peaked current profiles, consistent with the DIII-D scaling. The beta limit does increase with the internal inductance when the current and pressure profiles are treated as independent.

By comparing the curves for different internal inductances, we can conclude that *at fixed current*, the highest beta limit is obtained for $q_{\min} \approx 1.2$. In fact, the best current profile has as high an inductance as possible without making $q_{\min} < 1.2$. This dependence comes from the stability of external kinks and gives rise to the favorable scaling of beta with inductance at fixed current. For NCS discharges, this explanation is more relevant than one based on ballooning stability. However, there is one strong advantage of low inductance: even β_N improves with the current for these profiles, and low internal inductance allows higher current at fixed $q_{\min}$. Therefore, the maximum β^* and even β_N are obtained at low inductance and maximum current. The broadening is limited by instability of mainly current driven external kinks, causing "ravines" in the beta limit when q_a is just below some rational number m/n, most notable for integers ($n = 1$). The onset of such a ravine can be seen in Figs. 2 for $l_i = 0.79$. The ravine corresponds to q_a just below 3. Considering the risk of causing a disruption at such ravines, the current profile for $l_i \simeq 0.86$ appears to be the best in this set.

Two interesting regions of operation can be identified in Fig. 2 for $l_i = 0.86$. The first is a rather conventional tokamak equilibrium at high current $q_{\min} \simeq 1.2$. In this

region, $\beta^* \simeq 6.2\%$ and $\beta_N \simeq 3.7$ is reached with a bootstrap fraction of about 40%. The other region, relevant for advanced tokamaks, is with $q_{\min}$ slightly above 2. Here, the $l_i = 0.86$ gives a bootstrap fraction of about 65%, $\beta^* \simeq 2.5\%$ and $\beta_N \simeq 2.8$. The β^* value is too low for a reactor but may nevertheless be of interest for the optimization of present experiments. We have checked $n = 2$ and 3 stability for the optimized profile with $l_i = 0.86$. These modes have almost no effect on the beta limit for this cross section.

To study the sensitivity to details of the current profile, we have also carried out optimizations with an I^* profile with deeper shear reversal. The results are very similar to the results for the previous class of profiles with similar inductance. Thus the beta limit is not very sensitive to details of the current distribution other than $q_{\min}$.

2.1.2. *Strong shaping* $\kappa = 2.0$, $\delta = 0.7$

We used the family of current profiles shown in Fig. 1 to compute beta limits for more strongly shaped equilibria with elongation $\kappa = 2.0$ and triangularity $\delta = 0.7$. The results for β^* and f as functions of I_N (including $n = 1$ and ballooning stability) are shown in Fig. 3 for several different inductances.

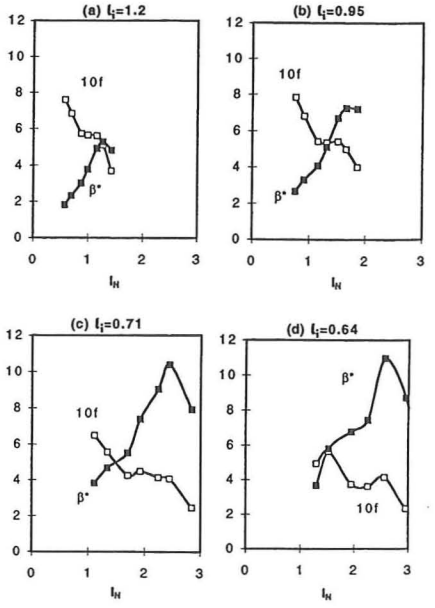

Fig. 3. β^* and bootstrap fraction versus normalized current for the class of current profiles in Fig. 1 and $\kappa = 2$, $\delta = 0.7$.

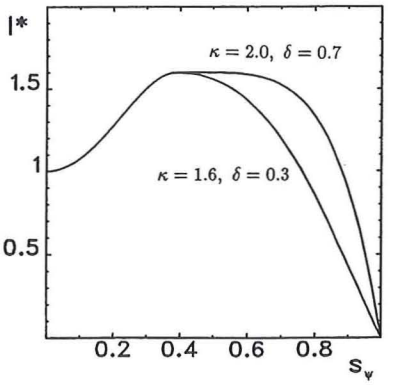

Fig. 4. Optimal current profiles for $\kappa = 1.6$, $\delta = 0.3$ (JET shape) and $\kappa = 2.0$, $\delta = 0.7$.

The dependence on inductance is similar to that in the JET case. For the stronger shaping, much broader current profiles can be used than for the JET-shaped cross section. The I^* profiles producing the highest β^* limit, at $q_{\min} \approx 1.2$ and q_a somewhat above 2, are shown in Fig. 4, both for JET shape and for the strongly shaped case. In the strongly shaped case, the optimized current profile is flat over a large part of the cross section, where the shear is weak. Most remarkable in Fig. 3 is the strong improvement in the maximum β^* achieved by the increased shaping. The maximum β^* is 10.8% with $\beta_N \simeq 4.3$. Consideration of $n = 2$ and 3 stability decreases the maximum β^* to 9.8%. The values of β_N for the broad current profiles in this strongly shaped geometry exceed the DIII-D scaling $\beta_N \leq 4l_i$. When $1.1 \lesssim q_{\min} \lesssim 1.5$, these equilibria give rather similar beta limits for several low-n modes, which is consistent with observations on DIII-D [15].

Concerning the possibilities for a high bootstrap fraction, we note that profile with $l_i = 0.86$ gives $f = 68\%$ with $\beta^* = 3.3\%$, which is considerably better than with the JET shape.

2.1.3. Other shapes

The results in Secs. 2.1.1-2.1.2 show clearly favorable results of increased shaping. To distinguish the effects of elongation from those of triangularity, we have also studied geometries of low elongation and high triangularity ($\kappa = 1.6$, $\delta = 0.7$) as well as high elongation and low triangularity ($\kappa = 2.0$, $\delta = 0.3$). The maximum β^*, stable to ideal $n = 1$, 2, 3, ∞ modes and resistive interchanges are reported in Table 1.

κ	δ	$\beta^*_{\max}[\%]$	$\beta_{\mathrm{N,max}}$	I_N at max β^*	l_i at max β^*
1.6	0.3	6.2	3.7	1.4	0.86
1.6	0.7	7.7	4.0	1.8	0.71
2.0	0.3	6.5	3.3	1.8	0.84
2.0	0.7	9.8	4.3	2.4	0.71

Table 1: Parameters of NCS equilibria with optimized beta for different cross sections

Table 1 shows that it is the combination of high elongation and high triangularity that is favorable. Triangularity itself has a positive effect at low elongation whereas high elongation at low triangularity has little effect on β^* and even decreases β_N. Triangularity is beneficial because it increases both β_N and the possible current.

3. CONCLUSIONS

Beta optimizations for NCS equilibria have been undertaken, imposing stability to ideal low-n modes, without a conducting wall, together with stability to $n = \infty$ ideal ballooning and resistive interchanges. The pressure profile has been constrained so that the bootstrap current nowhere exceeds the equilibrium current to ensure that no negative current drive is needed. The aspect ratio has been held fixed at 3. Under these assumptions, our conclusions on the beta limits for NCS plasmas are [16]:

1. The optimal pressure profiles are never strongly peaked, with optimal peaking factors between 2.5 and 3. Peaking of the pressure destabilizes low-n external modes.

2. At fixed current, the highest beta limit is found when $q_{\min}$ is somewhat above unity ($q_{\min} \approx 1.2$). The beta limit is sensitive to $q_{\min}$ in this region and therefore current profile control is required to reach the theoretical beta limit. The limits both to β^* and β_N decrease when $q_{\min}$ is increased, however, with a local optimum for $q_{\min} \approx 2.1$.

3. The highest β^* and β_N are achieved at high current for broad current profiles. The broadness of the current distribution is limited by the appearance of "ravines" in the beta limit for q_a just below integers. The dependence of the normalized beta on internal inductance *at fixed* $q_{\min}$ is opposite to the semi-empirical DIII-D limit $\beta_N \leq 4l_i$. The semi-empirical limit can be significantly exceeded at low inductance when the shaping is strong.

4. Resistive interchanges can be kept stable by limiting the negative shear and keeping q sufficiently above unity.

5. The beta limits are not very sensitive to details of the current profile other than $q_{\min}$. Weak central shear appears optimal.

6. The beta limit is significantly increased by increasing both the triangularity and elongation. Triangularity has a positive influence also at low elongation, but high elongation is not favorable at low triangularity.

7. If a high bootstrap fraction is required, $\gtrsim 65\%$, the beta limits are rather low, $\beta^* < 2.5\%$, for JET shape. In order to achieve β^* values of at least 3.5% at such bootstrap fractions, significant shaping is required.

REFERENCES

[1] KESSEL, C., et al, Phys. Rev. Lett. **72** (1994) 1212.

[2] TAYLOR, T. S., et al, Plasma Phys. Controlled Fusion **36 B** (1994) 229.

[3] TURNBULL, A. D., et al, Phys. Rev. Lett. **74** (1995) 718.

[4] LEVINTON, F. M., et al, Phys. Rev. Lett. **75** (1995) 4417.

[5] STRAIT, E. J., et al, Phys. Rev. Lett. **75** (1995) 4421.

[6] WEENING, R. H., BONDESON, A., Comments on Plasma Phys. **15** (1992) 77.

[7] BONDESON, A., in *Controlled Fusion and Plasma Physics*, Proc. 20th EPS Conf., Lisboa 1993 (European Physical Society, Geneva 1993), Vol 17C, Part IV, p. 1339.

[8] CHU, M. S., et al, Phys. Rev. Lett. **77** (1996) 2710.

[9] BONDESON, A., WARD, D. J., Phys. Rev. Lett. **72** (1994) 2709.

[10] WARD, D. J., BONDESON, A., Phys. Plasmas **22** (1995) 1570.

[11] LÜTJENS, H., BONDESON, A., SAUTER, O., Computer Phys. Comm. **97** (1996) 219.

[12] BONDESON, A., VLAD, G., LÜTJENS, H., Phys. Fluids **B4** (1992) 1889.

[13] TROYON, F., et al, Plasma Phys. Controlled Fusion **26** (1984) 209.

[14] TAYLOR, T.S., et al, in *Plasma Physics and Controlled Nuclear Fusion Research 1990* (Proc. 13th IAEA Conf., Washington D.C. 1990) IAEA, Vienna (1991), Vol. 1, p. 177.

[15] STRAIT, E. J., et al, Phys. Plasmas **B4** 1783, (1997).

[16] BONDESON, A., et al, Nucl. Fusion **37** (1997) (to appear).

Statistical description of plasma turbulence and anomalous transport

E. Vanden Eijnden
Assoc. EURATOM-Etat Belge
Université Libre de Bruxelles
Physique des Plasmas, CP 231, Campus Plaine
Bvd du Triomphe, 1050 Bruxelles, Belgium

Stochastic modeling of turbulence amounts to inferring the transport properties of a turbulent flow from the statistical behavior of a fluid element, or 'test particle', passively advected. The description is based on the relationship between the statistics of the flow in the laboratory Eulerian reference frame, which is assumed to be known, and the statistics of the flow in the Lagrangian reference frame 'moving' with the flow.

In this lecture, we first review some approximations which have been developed for studying this relationship. We also propose a new approximation scheme -called the modified direct interaction approximation (M-DIA) for the solution this problem. In contrast with other approximations -like the well-known direct interaction approximation- the M-DIA accounts correctly for the short time dynamics of the Lagrangian quantities and for the sweeping effects, that is, the random advection of the small scales by the large scales of the flow.

In the second part of the lecture, we apply these approximations to various situations of interest in magnetized plasmas (electrostatic and magnetic turbulence, turbulent heating,...). We focus on situations leading to non-standard diffusive behaviors, that is, examples in which the test particle displacement has non-Gaussian statistics or in which the mean square displacement of the test particle within the flow does not grow linearly with time.

ROTATION AND ENHANCED CONFINEMENT IN TOKAMAKS

L. García
Universidad Carlos III de Madrid. SPAIN

ABSTRACT

During the last years, several models based on the generation of averaged flows have been developed to explain the transition to enhanced confinement regimes. A simple self-consistent model of the L to H transition has been derived from coupled nonlinear envelope equations for the fluctuation level, and radial electric field shear, E_r'. This model is based on general properties of the coupling between turbulence and averaged sheared flows. The shearing effect on turbulence is a function of the amplitude. There is a threshold in amplitude for shearing effects to drive phase transitions. To illustrate these generic properties we have analyzed the consequences of the interaction between fluctuations and poloidal flow for the case of resistive pressure-gradient-driven turbulence. Here, some of the results obtained are presented with special emphasis on the structure of the Reynolds stress and the existence of limit cycle solutions.

INTRODUCTION

One of the common features that are seen in all devices which achieve enhanced confinement is the formation of a transport barrier in the plasma. The results obtained in many magnetic configurations show that the formation of transport barriers is closely related to increased shear in $E\times B$ velocity.

During the last years, several theoretical models have been developed to explain the transition to enhanced confinement regimes. The models are based on the generation of averaged flows. Linearly, a shear flow in a plasma confined by a sheared magnetic field has generally a strong stabilizing effect. Nonlinearly, the effective turbulence decorrelation time is reduced, leading to a reduction in fluctuation levels and induced transport. For $E\times B$ shear decorrelation of turbulence, the shearing rate must be comparable to the nonlinear decorrelation rate in the absence of $E\times B$ shear [1]. Usually, the maximum linear growth rate of all unstable modes in the plasma is used in the comparison because of the difficulty of the decorrelation rate calculation.

There are several possible sources for the generation of the $E\times B$ velocity shear. From the expression of the radial force balance in steady state

$$\frac{\langle E_r \rangle}{B_\varphi} = -\langle V_{\theta i} \rangle + \langle V_{\varphi i} \rangle \frac{B_\theta}{B_\varphi} + \frac{1}{Z_i \mid e \mid B_\varphi} \frac{1}{\langle n_i \rangle} \frac{\partial \langle P_i \rangle}{\partial r}, \tag{1}$$

we see that an electric field can be generated by a poloidal flow, toroidal flow, and ion pressure gradient. Depending on the confinement regime, one or several of these terms appear to play a role in the formation of transport barriers. Several mechanisms have been suggested to explain the L to H transition: Orbit loss [2, 3], coupling of the pressure gradient to $E\times B$ shear suppression [4, 5], changes in the poloidal flow profile via the Reynolds stress [6]. The last mechanism has been extended to include ion pressure gradient contributions to E_r' [7].

In these models, the turbulent fluctuations modify the mean flow and pressure profiles that simultaneously control the level of fluctuations. Therefore, self-consistent calculations of plasma turbulence in the presence of flows are needed. The more complete models describe the simultaneous evolution of the fluctuation spectrum and the $E\times B$ velocity shear.

The transition from the unimproved confinement regime to the improved confinement regime has the characteristics of a bifurcation. In the velocity shear model, the transition appears as a phase transition [6]. The system is disordered and turbulent in the unimproved confinement regime. For the enhanced confinement regime, the system self-organizes to a higher energy state with reduced turbulence and transport by building up a radial electric field, which induces a global $E\times B$ flow.

The model derived in Ref. 6 is a two-equation model describing the evolution of the fluctuation envelope and the $E\times B$ velocity shear. The model is based on general properties of the coupling between turbulence and averaged sheared flows. To illustrate these generic properties we have been investigated in detail the interaction between fluctuations and poloidal flow for the case of resistive pressure-gradient-driven turbulence.

RESISTIVE PRESSURE-GRADIENT-DRIVEN TURBULENCE EQUATIONS

From the renormalized set of equations [8] and by averaging over the radius, assuming Gaussian dependence for the eigenfunctions, a two-equation system can be derived for the evolution of the fluctuation envelope. To these equation, we must add the poloidal shear flow and averaged pressure evolution equations. The four equations are

$$\frac{\partial \mathrm{E}}{\partial t} = 2\frac{W^2}{W_0^2}P - \left[\frac{W^2}{W_0^2} + 3\bar{\mu} + 1.1\lambda \mathrm{E} + \frac{\Omega_s^2}{2(2\bar{D} + \mathrm{E})}\right]\mathrm{E} \tag{2}$$

$$\frac{\partial P}{\partial t} = \left(1 + \frac{N-1}{\sqrt{2}}\right)\mathrm{E} - (\bar{D} + 0.54\mathrm{E})P \tag{3}$$

$$\frac{\partial \Omega_s}{\partial t} = \left(\frac{1}{16}\frac{W^2}{W_0^2}gN - \frac{1}{6(\bar{\mu} + \lambda E/3)}\right)\Omega_s \mathrm{E}^2 - \frac{\hat{\mu}}{\gamma_0}\Omega_s \tag{4}$$

$$\frac{\partial N}{\partial t} = \overline{Q} - 4\overline{D}N - \frac{1}{2\overline{D} + \mathrm{E}} N\mathrm{E}^2 \tag{5}$$

where, $E = k_\theta \left|\tilde{\Phi}\right| / (\gamma_0 W)$ and $P \equiv \left|\tilde{p}\right| / \left(-W p'_{eq}\right)$ are the normalized velocity stream function and pressure fluctuation envelopes, $\Omega_s \equiv k_\theta \langle V_\theta \rangle' W / \gamma_0$ is the normalized shearing rate [1], and $N \equiv \langle p \rangle' / p'_{eq}$ is the normalized averaged pressure gradient. Here, γ_0 is the linear instability growth rate in the absence of collisional dissipation and sheared flow effects, W and W_0 are the mode width with and without dissipation respectively, k_θ the poloidal component of the wavenumber vector, p'_{eq} is the equilibrium pressure gradient, and $\lambda \equiv k_\theta / \left\{k_\theta^2\right\}^{1/2}$. Here, the curly brackets, $\{\}$, indicate spectral average and the angular brackets, $\langle\ \rangle$, spatial average over the poloidal and toroidal angles. The normalized collisional dissipation coefficients are $\overline{\mu} \equiv \mu_0 / (2\gamma_0 W^2)$ and $\overline{D} \equiv D_0 / (2\gamma_0 W^2)$. In Eq. (4), $\hat{\mu}$ is the flow damping coefficient due to magnetic pumping and the prime indicate radial derivative. The function g is $g \equiv \left[3\overline{\mu} + \overline{D} + 0.5(3\lambda + 1)\mathrm{E}\right] / \left[(\overline{\mu} + \lambda \mathrm{E}/3)^2 (\overline{D} + 0.5\mathrm{E})^2\right]$.

These four equations, Eqs. (2)-(5), are the basic model equations. The phase transition model [6] equations are a simplified version of this model. The fixed points of this system of equations are essentially the same as for the equations in reference 6. In this case, it is not possible to obtain compact analytical expressions. There are two types of stable fixed points, a fixed point with $\Omega_s = 0$, the L-mode type solution, and one with $\Omega_s \neq 0$, the H-mode solution. The first fixed point is independent of $\hat{\mu}$ but the second depends on $\hat{\mu}$. The fluctuation amplitude E is a continuous function of $\hat{\mu}$ with non-continuous derivative at the critical point. This behavior is characteristic of a second order phase transition. The critical point is

$$\hat{\mu}_{crit} = \gamma_0 \left(\frac{1}{16} \frac{W^2}{W_0^2} g(\mathrm{E}_L) N_L - \frac{1}{6(\overline{\mu} + \lambda E_L / 3)} \right) \mathrm{E}_L^2, \tag{6}$$

where the subindex L indicates that the L-mode value for E and N should be used in evaluating Eq. (6).

Numerical calculations using the full system of equations in reference 8 with coupled evolution of the averaged poloidal flow and averaged pressure show same characteristic behavior. In Fig. 1, we show the level of fluctuations E at saturation as a function of $\hat{\mu}$ for the same equilibrium parameters as in Ref. 8, with $\mu_0 = 0.2a^2/\tau_R$, $D_0 = 0.05a^2/\tau_R$, and $\beta_0/2\varepsilon^2 = 0.0075$. The critical transition point is $\hat{\mu}_{crit} = 2.0/\tau_R$.

In deriving Eq. (4), we found that the Reynolds stress has two terms. One is proportional to the poloidal flow velocity and the second one proportional to its second derivative

$$-\frac{1}{r^2}\frac{\partial}{\partial r}\left(r^2\left\langle \tilde{V}_r\tilde{V}_\theta\right\rangle\right)\Big|_{x=0} = \left\langle \tilde{V}_r\tilde{U}\right\rangle\Big|_{x=0} = \alpha\langle V_\theta\rangle + \beta\frac{d^2\langle V_\theta\rangle}{dr^2} \tag{7}$$

Here, α and β are positive coefficients. The α-term leads to a dynamo instability and the generation of flow. The β-term is an effective turbulent viscosity that damps poloidal flow. When an external sheared flow, $V_\theta = x\,V'$, is applied, the second term is zero and sheared flow is generated. However, since the generated flow has no longer the linear x dependence, the β-term becomes increasingly important and it cannot be neglected in the self-consistent flow evolution. For large fluctuations, E >>1, the two terms in Eq. (7) cancel each other and there is no flow generation. In this regime the resistive interchange instability remains always in the L-mode state, as it was found in reference 9. For lower values of E, the cancellation is only partial. In general, the α-term dominates and there is a potential increase in the sheared flow. The balance of the Reynolds stress with the velocity damping term gives the critical transition point. However, since both the α- and β-terms are large and of similar magnitude it is difficult to make an accurate prediction of the critical point based on this approximate model.

In calculating the correlation between the fluctuating radial velocity and the fluctuating vorticity, the α-term comes from the instability drive in the fluctuation evolution equation while the β-term is due to the Kelvin-Helmholtz term. The association of the β-term with the Kelvin-Helmholtz term allows us to test the structure of the Reynolds stress. To do so, we calculate the critical transition point with and without the Kelvin-Helmholtz using the full equations. In the first case, the transition is given by the two terms in Eq. (7) while in the second case is only given by the α-term. The numerical results for α and $\alpha - \beta/W_v^2$ calculated in this way are given in Fig. 2. Here, W_v is the characteristic width of the velocity profile.

LIMIT CYCLE SOLUTIONS

For H-mode type solutions and when $\hat{\mu}$ decreases, one reaches a new regime characterized by the oscillatory behavior of the solutions. This happens for both the full equations solution (Fig. 3), and for the analytical model. By careful analysis of the model, it is possible to identify the oscillatory behavior with the nonlinear modification of the shearing term in the Φ-fluctuation equation. We can understand that by using a further simplified model.

$$\frac{\partial E}{\partial t} = \left[1 - E - \frac{\Omega_s^2}{\delta + E}\right] E \tag{8}$$

$$\frac{\partial \Omega_s}{\partial t} = a\Omega_s E - b\Omega_s \tag{9}$$

This model is a modification of the one given in reference 6 by adding the nonlinear weakening of the shearing effect in Eq. (8). This system of equations has the usual three fixed points: 1) E = Ω_s = 0 the trivial equilibrium solution, 2) Ω_s = 0 and E = 1, the L-mode solution, and 3) $E = b/a$ and $\Omega_s^2 = (\delta + b/a)(1 - b/a)$, the H-mode solutions. The basic properties of the first two fixed points are discussed in reference 6. For the H-mode fixed point, this system of equations verifies the conditions of the Kolmogorov theorem. Therefore, the H-mode solution is either a stable fixed point or a stable limit cycle. Linearizing Eqs. (8) and (9), we test the local stability properties of the H-mode fixed point. For $\delta > 1 - 2b/a$, the H-mode fixed point is locally stable. Therefore, when $\delta < 1 - 2b/a$, the stable solution is a limit cycle. The numerical solution of Eqs. (8) and (9) confirms these results. The numerical calculations clearly show the existence of such solutions and the bifurcation threshold, $\hat{\mu}_{lc}$, from stable fixed point to a limit cycle is compatible with the relationship derived with the two equation model $\hat{\mu}_{lc} = \hat{\mu}_{crit}\left(1 - D_0/\gamma_0 W^2\right)/2$. To reach this threshold, a growth rate (power) more than a factor of two larger than its critical value at the L to H transition is needed. Close to the bifurcation point to a limit cycle, the oscillation frequency can be estimate by a two scale expansion of the Eqs. (8) and (9). This gives:

$$\frac{\omega^2}{\gamma_0^2} = 2b\left(1 - \frac{b}{a}\right) + \frac{b}{a}\frac{1 - \delta - 2b/a}{\delta + b/a}. \tag{10}$$

Near the bifurcation point, $\omega \approx \sqrt{2\gamma_0 \hat{\mu}}$. Since γ_0 increases with power and $\hat{\mu}$ decreases with increasing edge temperature, it is not possible to ascertain the frequency scaling with power without a detailed transport model. The amplitude of the oscillations is such that at most the fluctuation level goes back to L-mode level. Figure 4 shows the comparison between the numerical results for ω and the analytical expression (10) as a function of $\hat{\mu}$. From the numerical solution of Eqs. (8) and (9), it is obtained that the number of cycles depends on the rate of increase of power. This type of behavior is similar to the dithering observed at the L to H transition [10].

CONCLUSIONS

In this paper, we have investigated a self-consisted model of the L to H transition by using primitive equations for the resistive interchange turbulence coupled with averaged shear flow evolution.

For low fluctuation levels, there are second order phase transitions between L-mode and H-mode type solutions. For large fluctuations, there is no flow generation. These results are consistent with the structure of the Reynolds stress.

A dithering behavior of the transition appears for very low viscosity (or high power). This behavior is due to the nonlinear modification of the shearing term in the fluctuation equations.

ACKNOWLEDGMENTS

This research was sponsored in part by Dirección General de Enseñanza Superior of Spain (PB96-0112-C02-01). I would like to thank B.A. Carreras, P.H. Diamond, J.N. Leboeuf, and D. Newman for their contribution to this paper.

REFERENCES

[1] H. Biglari, P. H. Diamond, and P. W. Terry, Phys. Fluids B **2**, 1 (1990).

[2] S.-I. Itoh and K. Itoh, Phys. Rev. Lett. **60**, 2276 (1988).

[3] K. C. Shaing and J. E. C. Crume, Phys. Rev. Lett. **63**, 2369 (1989).

[4] F. L. Hinton, Phys. Fluids B **3**, 696 (1991).

[5] F. L. Hinton and G. M. Staebler, Phys. Fluids B **5**, 1281 (1993).

[6] P. H. Diamond, Y.-M. Liang, B. A. Carreras, and P. W. Terry, Phys. Rev. Lett. **72**, 2565 (1994).

[7] B. A. Carreras, D. Newman, P. H. Diamond, and Y.-M. Liang, Phys. Plasmas **1**, 4014 (1994).

[8] B.A. Carreras, L. Garcia, P.H. Diamond, Phys. Fluids **30**, 1388 (1987).

[9] B.A. Carreras, V.E. Lynch, L. Garcia, P.H. Diamond, Phys. Fluids B **5**, 1491 (1993).

[10] H. Zohm, Phys. Rev. Lett. **72**, 222 (1994).

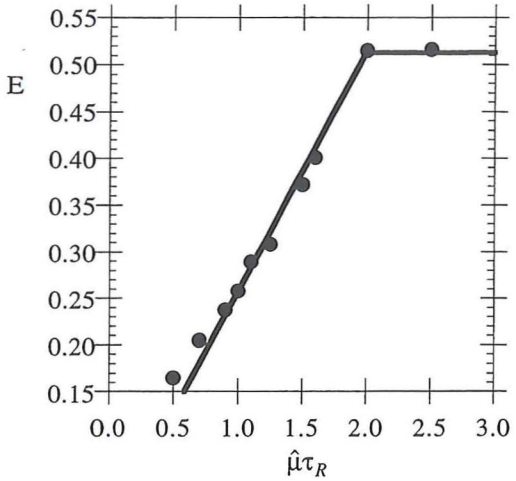

Fig. 1. Level of fluctuations E at saturation versus $\hat{\mu}$ for $\beta_0/2\varepsilon^2 = 0.0075$.

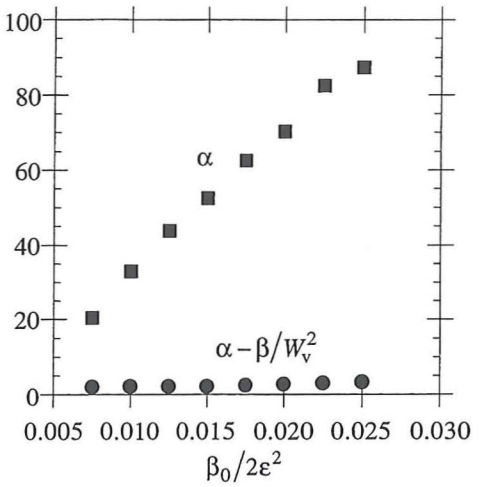

Fig. 2. The α and β-terms of the Reynolds stress versus $\beta_0/2\varepsilon^2$ for the equilibrium parameters of Ref. 8.

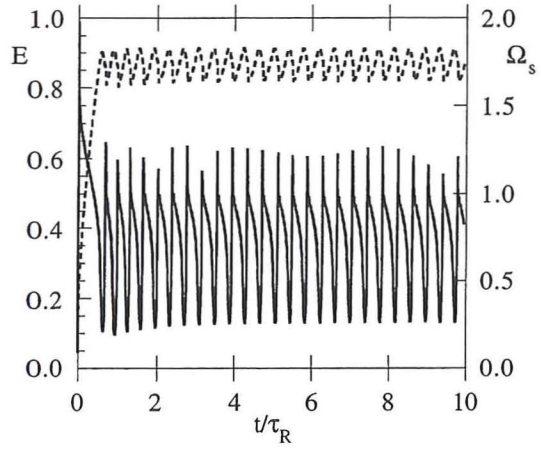

Fig. 3. Time evolution of the level of fluctuations E (solid line) and the normalized shearing rate (broken line) for $\beta_0/2\varepsilon^2 = 0.01$ and $\hat{\mu} = \tau_R^{-1}$.

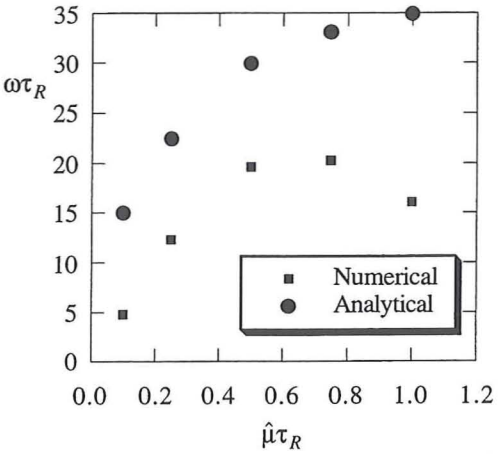

Fig. 4. Frequency of the oscillations versus $\hat{\mu}$ obtained from the numerical calculations and the analytical expression (9).

Contributed Oral Papers

MHD stability analysis of negative central shear plasmas

A.J.C. Beliën[1], B. van der Holst[1], J.P. Goedbloed[1], B.G. Hong[2], S.K. Kim[2]

[1]*FOM-Institute for Plasma Physics 'Rijnhuizen', Association Euratom-FOM, P.O. Box 1207, 3430 BE Nieuwegein, The Netherlands*

[2]*Korean Atomic Energy Research Institute, Taejon, South-Korea*

The good confinement properties of tokamak plasmas with negative central shear have raised great interest in understanding the properties of such plasmas. Such plasmas tend to have large positive shear near the plasma edge and zero shear somewhere in between the center and the edge. Several numerical MHD stability studies have been performed which show that infernal modes and external ballooning-kink modes play an important role in limiting the maximum achievable betas in such plasmas. Most of these studies considered plasmas with ratios $q_1/q_{\min} \approx 4$ and focussed on ideal instabilities.

In this paper we investigate ideal and resistive instabilities in tokamak plasmas with large ratios $q_1/q_{\min}$ (≥ 6). Detailed numerical studies have been performed for $q_{\min} \in [1.0-2.5]$ for the South Korean tokamak KSTAR which is currently being designed. We show that making pressure profiles optimally ballooning stable with respect to the first region of stability automatically leads to small pressure gradients in the low shear region around the minimum in q. Therefore, infernal mode stability does not pose severe limits on the maximum achievable betas for such profiles. However, the maximum achievable betas are strongly limited by external ballooning-kink modes which are localized near the plasma edge in the high positive shear region. Enclosing the plasma with an ideal conducting wall stabilizes these modes only when the conducting wall is brought very near the plasma edge. Resistivity turns out to have a stablizing effect on these modes. Internal resistive modes also occur and have an infernal like character, i.e., their eigenfunction is localized between the two $q = 2$ surfaces that exist in the plasma. Their growth rate, however, is much smaller than the ideal external and internal instabilities.

An Energy principle for stability of ideal magnetohydrodynamic systems in stationary motion

Gerhard Berge

Department of Applied Mathematics,

University of Bergen, N-5007 Bergen, NORWAY

Abstract. Within the framework of ideal magnetohydrodynamics an energy principle for stability of systems in stationary motion is presented.

I Introduction

The stability properties of an ideal magnetohydrodynamic (MHD) -fluid (compressible) in stationary motion is explored based on earlier work [1,2,3].

In Sec. II we discuss the governing equation for the perturbation. in Sec. III we offer a new formulation that results in a necessary and sufficient condition for stability of systems in stationary motion. These systems are subjected to the condition that the normal component of the fluid velocity vanish at the boundary. This can be regarded as an extension of the classic MHD energy principle to systems in stationary motion. A more complete presentation of this result was recently published [4].

II Perturbation, governing equation

We start by considering an ideal MHD-fluid in an arbitrary state of motion. At time $t = 0$ this motion is perturbed and $\boldsymbol{\xi}(\mathbf{r}, t)$ is a measure of deviation from the position the fluid element would have had, if left unperturbed. Let $\mathbf{r}_0$ be the position of a given fluid element at time $t = 0$, and let $\mathbf{r} = \mathbf{r}^0(\mathbf{r}_0, t)$ be the position of the same fluid element at time t. This is the trajectory of the unperturbed motion, with $\mathbf{r}^0(\mathbf{r}_0, 0) = \mathbf{r}_0$. We now perturb this motion by adding a small displacement and velocity at time $t = 0$. The perturbed motion is described by $\mathbf{r} = \mathbf{r}'(\mathbf{r}_0, t)$ and the Lagrangian displacement $\boldsymbol{\xi}(\mathbf{r}^0, t) \stackrel{def}{=} \mathbf{r}'(\mathbf{r}_0, t) - \mathbf{r}^0(\mathbf{r}_0, t)$, where $\boldsymbol{\xi}(\mathbf{r}^0, t)$ will be our measure of stability. Since we are considering only linear stability, the condition that $|\boldsymbol{\xi}(\mathbf{r}^0, t)| < \infty$, i.e., bounded in time is equivalent with a stable system in the meaning of Lyapunov definition of stability.

The governing equation for the displacement vector $\boldsymbol{\xi}$ is given by

$$\rho \frac{\partial^2 \boldsymbol{\xi}}{\partial t^2} + 2\rho \mathbf{v} \cdot \nabla \frac{\partial \boldsymbol{\xi}}{\partial t} + \frac{\partial}{\partial t}(\rho \mathbf{v}) \cdot \nabla \boldsymbol{\xi} = \mathbf{F}_{old}(\boldsymbol{\xi}), \tag{1}$$

$$\mathbf{F}_{old}(\boldsymbol{\xi}) = \frac{1}{\mu_0}(\nabla \times \mathbf{Q}) \times \mathbf{B} + \frac{1}{\mu_0}(\nabla \times \mathbf{B}) \times \mathbf{Q} + \nabla(\gamma p \nabla \cdot \boldsymbol{\xi} + \boldsymbol{\xi} \cdot \nabla p)$$
$$-\nabla \cdot (\rho \mathbf{v}\mathbf{v} \cdot \nabla \boldsymbol{\xi} - \rho \boldsymbol{\xi} \frac{d\mathbf{v}}{dt}) + \nabla \cdot (\rho \boldsymbol{\xi}) \nabla \phi \,, \tag{2}$$

where $\mathbf{Q} \stackrel{def}{=} \nabla \times (\boldsymbol{\xi} \times \mathbf{B})$, $\mathbf{B}$ is the magnetic field, p the pressure, γ the ratio between the specific heats, ρ the density and $\mathbf{v}$ the velocity of the unperturbed motion and ϕ the potential for an external force (the volume-force is $-\rho \nabla \phi$). Notice that all the unperturbed quantities may now have a time dependent (oscillatory) component. Also notice that in the case of a uniform external force the last term in the form given in Eq. (2) is zero and the simple interpretation is that the only term that is formally modified is the external force term that now also includes a force due to an accelerated system, however, all unperturbed quantities like $\mathbf{B}$, p and ρ are now explicit functions of time.

III Hamiltonian formulation

It turns out to be of prime importance to find a Hamiltonian formulation in terms substantial derivatives instead of the partial derivatives with respect to time of the field quantities $\boldsymbol{\xi}$ and $\boldsymbol{\pi}$. This can be achieved by the following formulation. Let

$$\dot{Q} \stackrel{def}{=} \frac{\partial Q}{\partial t} + \mathbf{v} \cdot \nabla Q \stackrel{def}{=} \frac{d}{dt} Q \,. \tag{3}$$

then we may write

$$\rho \ddot{\boldsymbol{\xi}} = \mathbf{F}_{new}(\boldsymbol{\xi}) \,, \tag{4}$$

where now

$$\mathbf{F}_{new}(\boldsymbol{\xi}) \stackrel{def}{=} \frac{1}{\mu_0}(\nabla \times \mathbf{Q}) \times \mathbf{B} + \frac{1}{\mu_0}(\nabla \times \mathbf{B}) \times \mathbf{Q} + \nabla(\gamma p \nabla \cdot \boldsymbol{\xi} + \boldsymbol{\xi} \cdot \nabla p)$$
$$+\nabla \cdot (\rho \boldsymbol{\xi} \frac{d\mathbf{v}}{dt}) + \nabla \cdot (\rho \boldsymbol{\xi}) \nabla \phi \,, \tag{5}$$

and

$$\delta W_{new}(\boldsymbol{\xi}, \boldsymbol{\xi}) \stackrel{def}{=} -\frac{1}{2} \int_V \boldsymbol{\xi} \cdot \mathbf{F}_{new}(\boldsymbol{\xi}) dV \,. \tag{6}$$

Details can be found in Ref. 4. Notice that the difference between $\mathbf{F}_{old}(\boldsymbol{\xi})$ and $\mathbf{F}_{new}(\boldsymbol{\xi})$, where $\mathbf{F}_{old}(\boldsymbol{\xi})$ corresponds to the Frieman Rotenberg formulation for stationary systems, is the term $-\nabla \cdot (\rho \mathbf{v}\mathbf{v} \cdot \nabla \boldsymbol{\xi})$. This term is absent in the expression for $\mathbf{F}_{new}(\boldsymbol{\xi})$. Eqs.(4) and (5) are a more compact way of writing Eq. (1) and (2).

1 Variational principle

Consider the Lagrangian density and functional

$$\mathcal{L} = \frac{1}{2}\rho\dot{\boldsymbol{\xi}}^2 + \frac{1}{2}\boldsymbol{\xi}\cdot\mathbf{F}_{new}(\boldsymbol{\xi}), \quad L = \int_V \mathcal{L}dV, \tag{7}$$

where the volume to be integrated over is the instantaneous fluid volume which may be moving, and therefore dV is to be considered as a material fluid volume element. We find

$$\frac{\delta\mathcal{L}}{\delta\boldsymbol{\xi}} = \mathbf{F}_{new}(\boldsymbol{\xi}), \quad \frac{\delta\mathcal{L}}{\delta\dot{\boldsymbol{\xi}}} = \rho\dot{\boldsymbol{\xi}}, \quad \rho\frac{d}{dt}\left[\frac{1}{\rho}\frac{\partial\mathcal{L}}{\partial\dot{\boldsymbol{\xi}}}\right] - \frac{\delta\mathcal{L}}{\delta\boldsymbol{\xi}} = 0, \tag{8}$$

and the last of these equations readily recover the equation of motion Eq. (4).

2 Hamiltonian formulation

Let the momentum and Hamiltonian densities be defined as

$$\boldsymbol{\pi} \overset{def}{=} \frac{1}{\rho}\frac{\partial\mathcal{L}}{\partial\dot{\boldsymbol{\xi}}} = \dot{\boldsymbol{\xi}}, \quad \mathcal{H} \overset{def}{=} \rho\boldsymbol{\pi}\cdot\dot{\boldsymbol{\xi}} - \mathcal{L} = \frac{1}{2}\rho\boldsymbol{\pi}^2 - \frac{1}{2}\boldsymbol{\xi}\cdot\mathbf{F}_{new}(\boldsymbol{\xi}). \tag{9}$$

Then the Hamiltonian functional is

$$H = \int_V \mathcal{H}dV = \frac{1}{2}\int_V \left\{\rho\boldsymbol{\pi}^2 - \boldsymbol{\xi}\cdot\mathbf{F}_{new}(\boldsymbol{\xi})\right\}dV. \tag{10}$$

It follows that the equations of motion in canonical form are

$$\rho\dot{\boldsymbol{\pi}} = -\frac{\delta\mathcal{H}}{\delta\boldsymbol{\xi}}, \quad \rho\dot{\boldsymbol{\xi}} = \frac{\delta\mathcal{H}}{\delta\boldsymbol{\pi}}, \tag{11}$$

where the functional derivatives, $\frac{\delta\mathcal{H}}{\delta\boldsymbol{\pi}} = \rho\boldsymbol{\pi}$ and $\frac{\delta\mathcal{H}}{\delta\boldsymbol{\xi}} = \mathbf{F}_{new}(\boldsymbol{\xi})$.

The first of Eqs. (11) is a restatement of the definition of $\boldsymbol{\pi}$ and the second gives the equation of motion i.e. Eq. (4).

Then we consider

$$\frac{d}{dt}H = \int_V \left\{\frac{d}{dt}\mathcal{H} + \frac{\delta\mathcal{H}}{\delta\boldsymbol{\xi}}\cdot\dot{\boldsymbol{\xi}} + \frac{\delta\mathcal{H}}{\delta\boldsymbol{\pi}}\cdot\dot{\boldsymbol{\pi}} + \nabla\cdot\mathbf{v}\mathcal{H}\right\}dV. \tag{12}$$

The last term in this expression represents the derivative of the moving fluid element. Since $\nabla\cdot\mathbf{v} = -\frac{1}{\rho}\frac{d\rho}{dt} = \rho\frac{d}{dt}\frac{1}{\rho}$, this can be combined with the first term in Eq. (12) and in addition using $\frac{\delta\mathcal{H}}{\delta\boldsymbol{\xi}}\cdot\dot{\boldsymbol{\xi}} + \frac{\delta\mathcal{H}}{\delta\boldsymbol{\pi}}\cdot\dot{\boldsymbol{\pi}} = 0$, which is readily obtained from the canonical equations of motion, we finally obtain

$$\frac{d}{dt}H = \int_V \frac{d}{dt}\left[\frac{\mathcal{H}}{\rho}\right]\rho dV. \tag{13}$$

This result is general in the sense that it applies to the stability analysis of any ideal MHD-system in an arbitrary state of motion. There are, however, three special cases of prime interest: A static system (gives the familiar MHD Energy Principle), a system with stationary flow and a forced oscillatory system. We shall here only consider a stationary system with flow. For such a system we have $\frac{\partial}{\partial t} = 0$ and $\frac{d}{dt} = \mathbf{v} \cdot \nabla$, thus

$$\frac{d}{dt}H = \int_V \rho \mathbf{v} \cdot \nabla \left[\frac{\mathcal{H}}{\rho}\right] dV = \int_V \nabla \cdot \left[\rho \mathbf{v} \frac{\mathcal{H}}{\rho}\right] dV = \int_S \mathbf{n} \cdot \mathbf{v} \mathcal{H} dS\,, \tag{14}$$

where S is a surface bounding the volume V. This result shows that the rate of change of H in this case is connected to the transport of $\mathcal{H}$ through the bounding surface. Therefore, in cases where the net transport through the bounding surface is zero, H is a constant of motion. From Eqs.(6) and (10) it follows that: $\delta W_{new}(\boldsymbol{\xi}(\mathbf{r}), \boldsymbol{\xi}(\mathbf{r})) > 0 \quad \Rightarrow$ $H > 0$. Thus H is a Lyapunov functional in this case and implies that the system is stable.

By a similar technique to that used by Laval *et al.* [5] it has also been proved that this condition is sufficient [4]. In ref. [4] an analysis based on normal modes also support this conclusion.

Conclusion: $\delta W_{new}(\boldsymbol{\xi}(\mathbf{r}), \boldsymbol{\xi}(\mathbf{r})) > 0$ *is therefore a necessary and sufficient condition for stability of ideal stationary systems.*

This theory should for example have relevance to a tokamak in a state of stationary motion.

Acknowledgment: This work was supported by The Research Council of Norway.

References

[1] E. Frieman, and M. Rotenberg, Rev. Mod Phys. **32** ,833 (1960).

[2] I. Bernstein, E.A. Frieman, M.D. Kruskal, and R.M. Kulsrud, Proc. Roy. Soc. (London) **A244**, 17 (1958).

[3] G. Berge, Dynamic Stabilization of Unstable MHD Equilibria. A General Approach. Culham Laboratory Report CLM-R97, 1969 Abingdon Oxon. OX14 3EA, UK.

[4] Gerhard Berge, Phys. Plasmas **5**, 1201 (1997).

[5] G. Laval, C. Mercier and R. M. Pellat, Nucl. Fusion **5**, 156 (1965).

Equilibrium Analysis of JET Tokamak Discharges

W Zwingmann, D P O'Brien, D Bartlett
JET Joint Undertaking, Abingdon, OX14 3EA, U.K.

Abstract. Equilibrium analysis is one of the essential tools for determining the plasma shape and profiles, in particular the current density and safety factor, as well as global physical quantities. We report on recent developments of the equilibrium code EFIT, which is used for the routine analysis of JET Tokamak discharges. A new method to treat the iron transformer surrounding the JET device is presented. This is one of the prerequisites for the development of a real-time discharge analysis and feedback of physical quantities. A new type of constraint derived from the shape of the ECE temperature profile has been implemented which allows for an enhanced precision of the position of the magnetic axis and the safety factor.

I. Equilibrium analysis

The plasma equilibrium for an axisymmetric device is described by the Grad-Shafranov equation

$$-\frac{\partial^2\Psi}{\partial R^2}+\frac{1}{R}\frac{\partial\Psi}{\partial R}-\frac{\partial^2\Psi}{\partial Z^2}=\mu_0 R^2 P'(\Psi)+FF'(\Psi)+J_{ext}, \qquad (1)$$

where $\psi(R,Z)$ is the poloidal flux function, P the isotropic pressure, and $F=RB_z$. J_{ext} denotes the poloidal field coil currents and the magnetisation currents of an iron transformer. To reconstruct an equilibrium from measured data, an ansatz for the unknown profiles e.g. $P'(\Psi)=\sum_k c_k g_k(\Psi)$ with suitable functions g_k is selected. The Grad-Shafranov equation is then used as a constraint to determine the unknown coefficients c_k by minimising the functional

$$\chi^2=\sum_n \frac{1}{\sigma_n^2}(F_n^{calc}\{\Psi;C\}-F_n^{meas})^2+R(C) \qquad (2)$$

where F_n^{calc} is a functional which generates the value of the measured quantity from ψ and c_k .

σ_n denotes a typical standard deviation of measurement, and R(C) controls higher derivatives in the current profile. The algorithm EFITJ[1] is used routinely to solve the reconstruction problem at JET. The code is based on the original EFIT code by Lao et al [2], modified to model the JET iron core. As input data for automatic analysis between discharges, we use magnetic data from 57 magnetic pick-up coils and 27 flux-loops located at the vacuum vessel of the torus. This intershot equilibrium reconstruction is in routine use for all JET discharges since the pumped divertor installation in 1994.

II. Iron transformer model

The presence of the iron transformer in the JET device complicates the equilibrium calculation, because the response of the iron to external magnetic fields is nonlinear and cannot be easily calculated. In the EFITJ code, the magnetisation currents of sections of the iron structure are added as free variables to the fitting procedure, and determined by the measurements[1]. This method gives good results for the equilibrium reconstruction, but it has a few drawbacks. The large number of parameters leads to long execution times. The algorithm is also unsuitable for predictive calculations. We have devised a model to pre-calculate the iron magnetisation with a permeability model. The field generated by the iron magnetisation **M** is given by

$$\mathbf{B}_{\text{iron}} = \nabla \times \mu_0 \left(-\oint \frac{\mathbf{M}' \times \mathbf{n}'}{|\mathbf{x} - \mathbf{x}'|} da' + \int \frac{\nabla \times \mathbf{M}'}{|\mathbf{x} - \mathbf{x}'|} d^3x' \right). \qquad (3)$$

The total magnetic field is related to **M** via the permeability μ(B) through $\mathbf{B} = \mu\mu_0 / (\mu - 1)\mathbf{M}$, which inserted in (2) gives the nonlinear equation for **M**

$$\nabla \times \mu_0 \left(-\oint \frac{\mathbf{M}' \times \mathbf{n}'}{|\mathbf{x} - \mathbf{x}'|} da' + \int \frac{\nabla \times \mathbf{M}'}{|\mathbf{x} - \mathbf{x}'|} d^3x \right) + \frac{\mu}{\mu - 1} \mu_0 \mathbf{M} = \mathbf{B}_{\text{plasma}} + \mathbf{B}_{\text{PFC}}. \qquad (4)$$

This equation is solved by the integral equation method [e.g. 5]. The region containing iron is subdivided into finite elements, and the magnetisation is assumed to be constant within the elements. A similar method was suggested in [4]. The resulting algebraic equation is solved with a Newton-Raphson method. This gives the iron contribution of the magnetic field in equation (1). As a further simplification to solve equation (4), the 8 JET transformer limbs are modelled with an axisymmetric equivalent geometry [5]. Details are given in figure 1. The method described leads to the first full domain equilibrium reconstruction code for iron core Tokamaks. A comparison with the existing database of JET equilibria however shows negligible differences, which proves that the old model was good enough for its purpose. The number of fitting variables, on the other hand, is reduced to those for the plasma current profiles, giving a reduction from typically 67 parameters to 5. The singular value decomposition as the fitting algorithm now consumes negligible CPU time, so that one obstacle for real-time application is removed. On a Pentium 150MHz PC, the algorithm for the iron model itself takes about 400 ms CPU time per time-slice, the rest of only partially optimised EFIT code about 1 sec, with the aim of cutting it down to 50 ms on a suitable platform. The code is applicable to a wide range of Tokamaks, and allows for equilibrium reconstruction and prediction. It is suitable for future

Tokamak devices, such as ITER, which require continuous processing of diagnostic data for monitoring and control

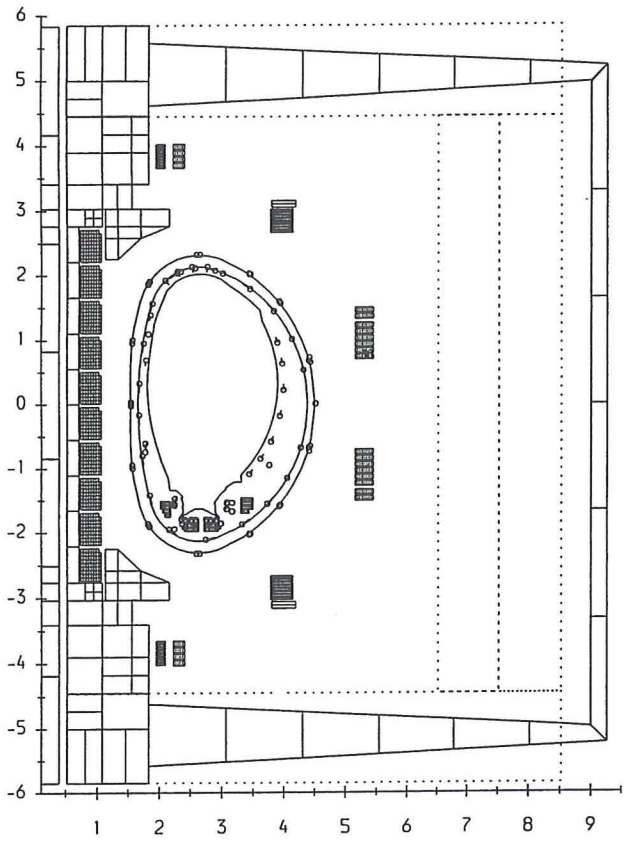

Figure 1.

Cross section of the JET device. It shows the vacuum vessel with magnetic diagnostics marked with circles, the poloidal field coils and the finite elements of the axisymmetric iron model. The dashed lines mark the real shape of the transformer limbs.

III. Improvement of reconstruction with ECE constraint

The equilibrium reconstruction from external magnetic data is a mathematically ill-posed problem of Hadamard type, since flux and derivative (magnetic field) are given as boundary conditions at approximately the same location. Therefore, the reconstructed profiles can become quite inaccurate. One solution is to add additional internal data for the fitting procedure. The EFIT code is presently capable of using Faraday rotation data, pressure profile, q-profile (e.g. from soft X-ray), and motional Stark data. We present a new type of constraint derived from the shape of the temperature profile from the electron cyclotron emission (ECE) measurement, which is potentially available in real time. The measurement gives the electron temperature profile $T_e(B_{total})$ as a function of the total magnetic field, since it is proportional to the electron

cyclotron frequency. We assume that the temperature peak is close to the magnetic axis, such that both radial locations coincide. We then impose as constraint

$$B_z(R_p) = 0 \qquad \text{at } B_{total}(R_p) = B_{ECE} \tag{5}$$

where R_p is the unknown radial position of the peak and B_{ECE} the corresponding field at the peak. The constraint is linearised and introduced into the fitting procedure. We analysed discharge 40554 with this new condition. Figure 2 shows a comparison of two equilibrium reconstructions, with magnetic data only, and with the additional ECE constraint. There is a significant shift of the magnetic axis with the ECE data applied.

Acknowledgement

We gratefully acknowledge discussions with J. Ellis, W. Kerner, B. Tubbing and M. Edward.

References

[1] O'BRIEN, D.P., LAO, L.L., SOLANO, E.R., GARRIBBA, M., TAYLOR, T.S., CORDEY, G. ELLIS, J.J., Nuclear Fusion **32** (1992) 1351

[2] LAO, L.L, FERRON, J.R., GROEBNER, R.J., HOWL, W., St. JOHN, H., STRAIT, E.J., TAYLOR, T.S., Nuclear Fusion **30** (1990) 1035

[3] Trowbridge, C.W., in: Finite Elements in Electrical and Magnetic Field Problems, Chari, M.V.K., Silvester, P.P. (eds.), Wiley, New York, 1980, 191

[4] DU, S., WANG, S., Nuclear Fusion **35** (1995) 359

[5] Khalafallah, K., JET technical note JTN/E(76)68, (1976)

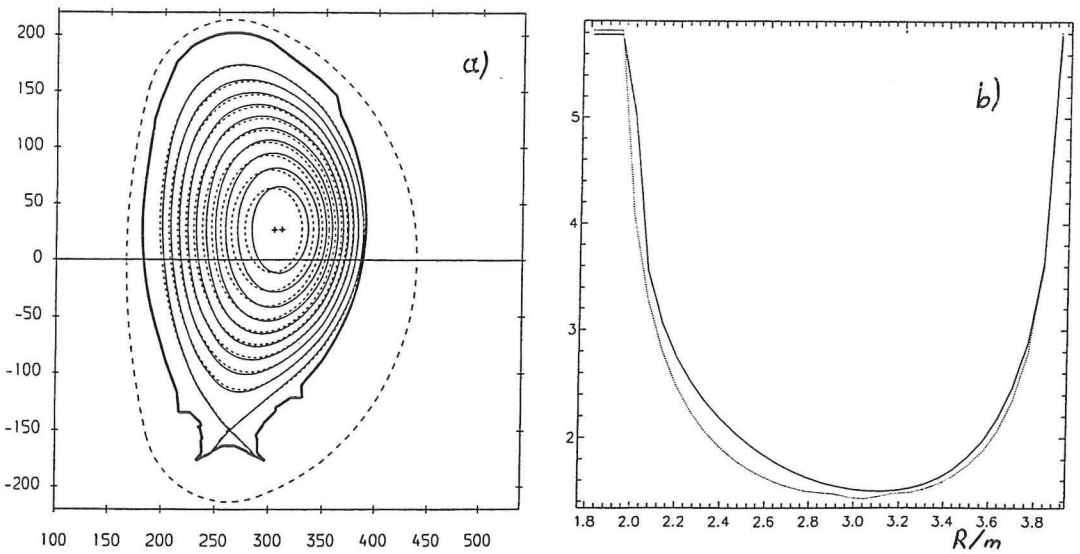

Figure 2. Flux contours(a), and safety factor(b) of discharge 40554, t=46.1 sec. Solid lines are for the reconstruction with the ECE constraint, dashed with only magnetic data.

Structures and Transport in Drift-Wave Turbulence

V. Naulin
Association EURATOM-Risø National Laboratory
Optics and Fluid Dynamics Department
Risø, DK-4000 Roskilde, Denmark

Abstract. Anomalous transport in magnetically confined plasmas is a still not well understood phenomenon. A simple 2D model for driven drift-wave turbulence is considered [1]. Nonlinear structures in the flow trap and de-trap particles. They not only change the fluctuation induced transport, but also add an additional component to it [2], which is due to the nonlinear polarization drift.

I. Introduction

Anomalous transport is observed to be highly intermittent, with large transport events occuring at random intervals. These large transport events are often related to coherent, non-wavelike structures in the plasma. However the turbulent transport is most often evaluated as the radial $E \times B$ flux only[3]. Any other contribution to the particle velocities, especially the non-linear polarization drift is therefore not accounted for.

II. Model

We use a simple 2D-model of drift-wave turbulence to demonstrate the impact of the polarization drift and coherent structures on the transport. In the limit of near adiabaticity $n \approx \phi$ the well known Hasegawa-Wakatani equations can be reduced to

$$d_t(1-\nabla^2)\varphi + \partial_y\varphi = \delta d_t\left(\partial_t + \partial_y\right)\varphi\,, \tag{1}$$

$$\tilde{n} = \varphi - \delta\left(\partial_t + \partial_y\right)\varphi\,. \tag{2}$$

δ is the adiabaticity parameter containing the parallel resistivity. The time derivative is $d_t = \partial_t + \hat{z} \times \nabla\varphi \cdot \nabla$. Only one mode parallel to the homogeneous outer magnetic field $\vec{B} = B_0\hat{z}$ is excited, so that all differential operators work in the (x,y)-plane and usual normalizations are used.

III. Polarization Drift Induced Transport in the HME

For an adiabatic electron response ($\delta = 0$) and with $\mu = 0$ Eq. (1) transforms into the Hasegawa-Mima Equation. We focus on the poloidal averaged radial particle flux

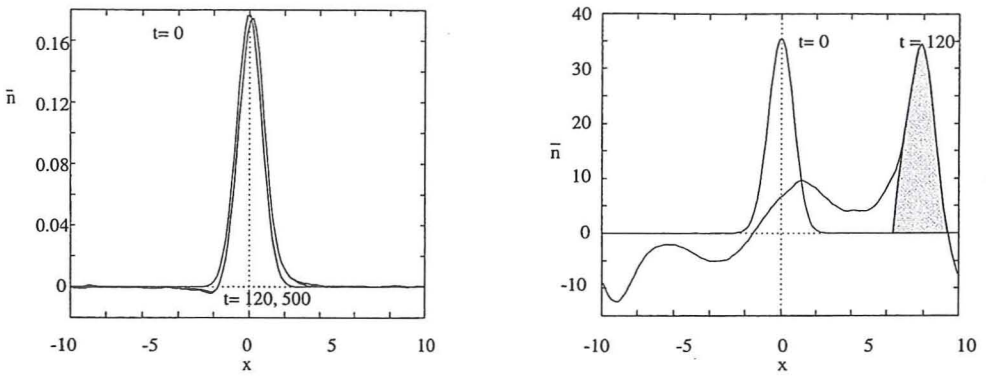

Figure 1: Fluctuation density profiles for the linear (a) and non-linear (b) Gaussian

$< \Gamma_x(x,t) >_y = \frac{1}{L_y} \int n v_x dy$. If $\vec{v}$ is given by the $E \times B$ drift, then $< \Gamma_x >_y$ vanishes in the adiabatic case $\tilde{n} = \varphi$. Nevertheless the HME reveals transport. To demonstrate this we introduce the density-profile $\bar{n}$ which splits up into a background and a fluctuation part $\bar{n}(x,t) =< n(x,y,t) >_y = n_0(x) + < \tilde{n}(x,y,t) >_y$. Only a divergence in the flux can change this profile. We consider the evolution of Gaussian pulses with a width $l \approx 1$. First the amplitude is $\varphi_{max} = 0.1$ thus the pulse is in the linear regime, where the nonlinear time t_{nl} is shorter than the linear dispersion time: $t_{nl} = \frac{1+k^2}{k^4}|\varphi_k| \approx 0.2 < 2 \approx \frac{1+k^2}{k} = t_{disp}$. Consequently the pulse disperses into waves and the fluctuation-profile (shown as Fig. 1(a)), stays constant in accordance with a vanishing flux. For a large amplitude pulse ($\varphi_{max} = 20$), giving $t_{nl}/t_{disp} = 20$, the dynamics is dominated by the nonlinearity. The pulse survives for long times as a coherent structure and moves both in x and y direction. While the structure propagates the density profile changes significantly (Fig. 1(b)). Part of this change is directly connected to the x movement of the coherent structure (shaded in Fig. 1(b)), while the rest is due to large amplitude drift-waves. The origin of this flux (whose PDF is shown in Fig. 2(a)), connected to the movement of coherent structures, is the polarization-drift, the only particle-drift besides the $E \times B$ drift which enters the derivation of the HME [4].

In experiments only the transport due to the $E \times B$ drift is measured, as $\Gamma_x^{E \times B} = -n\partial_y\varphi = \tilde{n}\tilde{E}_{pol}$ [3] is evaluated. Thus, for the adiabatic scenario described above the experimentally observable flux is zero, in contradiction to the observed change in density profile.

The transport induced by the polarization drift includes the transport made by non-linear

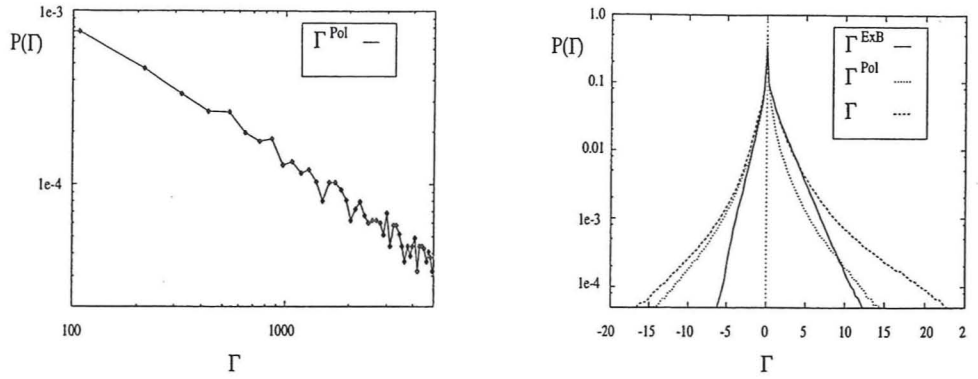

Figure 2: Transport PDFs in the adiabatic limit (a) and with $E \times B$ flow (b)

structures *in toto*, as coherent structures contribute in two ways to transport: On the one hand large fluctuation amplitudes are associated with the nonlinear structures. Thus there is also a large $E \times B$ flux at their slopes. This is measurable experimentally, as it relies on a non-vanishing phase shift between density and potential fluctuations. On the other hand structures contribute to the transport by trapping density and carry it along the background density gradient [2], an effect not observable by measurements of the $E \times B$ flow.

IV. $E \times B$ and Polarization Drift Flow Compared

We now investigate the influence of polarization-drift implied transport on the overall transport in the presence of an $E \times B$ flux. Numerical simulations of Eq. (1) for $\delta = 0.5$ and $\mu = 0.03$ on a 21×21 length units sized square show a saturated turbulence at fluctuation-amplitudes of order one [2]. The dimensionless fluxes averaged in space and time evaluate to $\overline{< \Gamma_x^{E \times B} >} = 0.52$ and $\overline{< \Gamma_x^{pol,\tilde{n}} >} = 0.005$. So even for a moderately low value of non-adiabaticity $\delta = 0.5$ the $E \times B$ flux is responsible for 99 % of the total net-flux.

Fig. 2 (b) shows the PDFs of the different fluxes in this case. Even when the overall impact of the flux induced by the polarization drift is small, it is responsible for most of the transport events larger than $\Gamma = 5$. Moreover, as the polarization-drift is large where the fluctuations are strong, the additional transport occurs more frequently when there is also a strong $E \times B$ flow. That makes the joint PDF for the total flux even larger for strong transport events.

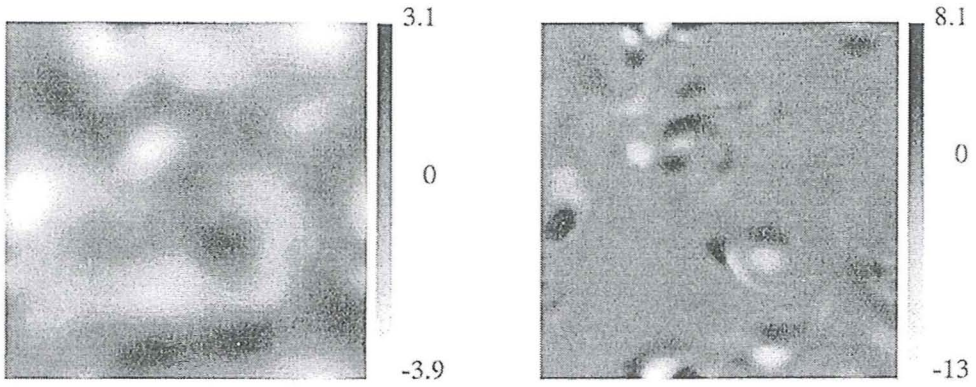

Figure 3: Saturated turbulence after Eq. (1). Potential (left) and vorticity (right).

V. Conclusion

For a realistic estimate of the transport PDF in experiments as well as numerical simulations the polarization drift cannot be ignored. Its contribution to the net-transport is small, when compared to the $E \times B$ induced transport in the presence of a finite phase shift between density and potential fluctuations. Nevertheless the statistical properties of the flux are changed towards a power-law behaviour, as the polarization drift is connected to large fluctuations. Finally, the relation of the polarization drift induced transport to the dynamics of coherent structures clearly calls for further attention.

Acknowledgements Discussions with J.J. Rasmussen, and K.H. Spatschek are greatfully acknowledged. Part of the work was performed under the European Union Marie Curie grant N° 5004-CT96-5023.

References

[1] J. Crotinger und T. H. Dupree, *Trapped structures in drift wave turbulence*, Phys. Fluids B 4 (1992) 2854–2870.

[2] V. Naulin und K. H. Spatschek, *Nonlinear drift-wave structures and their influence on particle transport*, Phys. Rev. E **55** (1997) 5883–5893.

[3] B. A. Carreras, C. Hidalgo, E. Sánchez, M. Pedrosa, R. Balbín, García-Cortés, B. van Milligen, D. E. Newman und V. E. Lynch, *Fluctuation induced Flux at the plasma edge in toroidal devices*, Phys. Plasmas **3** (1996) 2664–2672.

[4] A. Hasegawa und K. Mima, *Pseudo-three-dimensional turbulence in magnetized nonuniform plasma*, Phys. Fluids **21** (1978) 87–92.

Simulations of dimensionless scaling experiments on JET

P. Strand, H. Nordman, J. Weiland
Institute for Electromagnetic Field Theory and EURATOM/NFR Association
Chalmers University of Technology, S-412 96 Göteborg.
J.P. Christiansen
JET Joint Undertaking, Abingdon, Oxon, OX14 3EA, UK

Abstract. Predictive transport code simulations of JET beta scaling and gyro-radius scaling experiments are presented. The simulations are based on a first-principle gyro-Bohm drift wave transport model. The weak beta scaling inferred from the beta similarity scan is well reproduced by the code as well as the difference in transport scalings observed in the L-mode (Bohm) as compared to H-mode (gyro-Bohm) gyro-radius scaling experiments.

I. Introduction

In the design of dimensionally similar tokamak discharges, attempts are made to vary only one dimensionless parameter while keeping the others almost constant. By isolating the dependence of energy confinement on a single dimensionless parameter, several key issues of anomalous transport, such as the scaling of local transport with system size (Bohm vs gyro-Bohm scaling) and beta (electrostatic vs electromagnetic turbulence) can be studied.

The similarity approach is based on the assumption that the thermal diffusivity can be expressed as [1]

$$\chi = \chi_B \rho_*^{\alpha} F(\lambda_1, \lambda_2, ...) \qquad (1)$$

where $\chi_B = T_e/eB$ is the Bohm diffusivity, $\rho_* = \rho_s/a$ is the normalized gyro-radius and F is a function of the other dimensionless parameters characterizing the discharge.

The simulations presented here are based on a fluid model [2-4] for ion-temperature gradient modes, impurity modes and collisionless trapped electron modes. The model is collisionless and electrostatic and the exponent α, which indicates the characteristic wavelength of the turbulence, is unity corresponding to an intrinsic gyro-Bohm scaling of the transport coefficients.

The exponent α has been determined experimentally in both L-mode and H-mode gyro-radius scaling experiments. The local effective diffusivity in the JET L-mode similarity scans [5] was found to satisfy a Bohm-scaling ($\alpha = 0$, $\chi \propto B^{-1/3}$) whereas in the ELMy H-mode similarity scans, a gyro-Bohm scaling ($\alpha = 1$, $\chi \propto B^{-1}$) was inferred from the experiments [6].

The H-mode beta similarity experiments considered here showed that the dependence of confinement on beta was very weak. This result contradicts the global ITERH93-P scaling which has a strong beta scaling, $B\tau_{E,th} \propto \beta^{-1}$.

II. Gyro-radius scaling

This work expands on a previous investigation [7] by introducing an impurity species in the simulations and by considering H-mode as well as L-mode similarity scans. A detailed description of the similarity experiments are given in Refs. [5,6]. In the simulations, the evolution of ion and electron pressure, electron density and impurity density are followed in time with the outer boundary conditions (at r/a=0.8) taken from TRANSP profile databases and with zero derivatives imposed on the axis for each profile (for details, see Ref.7).

The L-mode results are similar to the those obtained in the previous simulations neglecting impurities [7] and are only briefly summarised here. Thus, it is found that the Bohm-scaling obtained in the experiments is reproduced by the simulations as well as the temperature and density profiles. The scalings obtained are caused by imperfections in the dimensionless parameters originating from the edge boundary conditions. The result is a systematic increase in the $\eta_{i,e}$-values over the whole cross-section in the low ρ_*-pulse. This leads to an increase in the function F of Eq.1 (assumed to be held constant) in the low ρ_*-pulse which masks the intrinsic gyro-Bohm scaling in the code. Similar results have been reported in Ref. 8 including edge transport from resistive modes.

The two H-mode discharges studied are taken from the neutral beam heated ELMy H-mode similarity experiments [6]. As in the L-mode scan, the normalized gyro-radius was varied by a factor 1.6 between the high field discharge #35156 (B=2T, I=2MA) and the low field discharge #35171 (B=1T, I=1MA). The deposited power was increased from 4.8MW in the low field discharge to 9.2MW in the high field discharge in order to satisfy the similarity scaling $T \propto B^{-2/3}$.

In Fig. 1, the time evolution of the predicted thermal energies for the H-mode pulses #35156 and # 35171 are compared with experiments. Experimental energies are rather well reproduced, with no systematic deviation between the two discharges. The experimental temperature and density profiles are also well reproduced by the simulations with relative errors <10 - 15% in the good confinement region.

In Fig. 2, the ratios (2T to 1T for H-mode, 1.7T to 3.4T for L-mode) of the ion and electron heat diffusivities obtained in the simulations are shown as functions of normalized minor radius. In contrast to the L-mode similarity scan, where apparent Bohm- to Goldston-like scalings are obtained, the diffusivities in the H-mode scan scale close to gyro-Bohm. The systematic deviations in the similarity conditions, that were found in the simulations of the L-mode scan, are smaller in the predictive simulations of the H-mode similarity experiment. Since

profile effects arise through the edge boundary conditions, the different scalings obtained in the simulations are attributed to differences in edge confinement between L- and H-mode plasmas.

III. Beta scaling

In the beta similarity scaling experiments, the density and temperatures are scaled as $n \propto B^4$ and $T \propto B^2$ in order to keep ρ_* and ν_* constant. This leads to a strong magnetic field scaling of plasma beta and energy, i.e. $\beta \propto B^4$ and $W \propto B^6$. In the ELMy H-mode beta-scan considered here, the magnetic field is varied from 1.5T for pulse #38407 to 1.7T for pulse #38415, corresponding to an increase in beta with a factor 1.6. To achieve the similarity conditions, the neutral beam power was increased from 6 MW for #38407 to 16 MW for #38415.

In Fig. 3, the time evolution of the thermal energies (predicted vs experimental) and RMS-errors (for Ti, Te and Ne) are displayed during 3s of evolution time. The energies are reproduced to within 10% and the RMS-errors are within 10-15% and no systematic trend is observed in the deviations between the two pulses.

At the end of the simulation (t=58s), the predicted profiles are compared with the experimental and the relative errors are computed. The results are presented in Fig. 4. In the confinement zone, the temperature profiles are matched to within 10% whereas the densities are within 15 %. The electrostatic model is able to reproduce the results with well matched profiles, i.e. the function F of Eq.1 remains basically unchanged as beta is varied.

The discharges considered are predominantly ion heated and the η_i-mode dominates the transport. The inclusion of finite beta electromagnetic effects in the model is expected to be slightly stabilizing in this range of beta ($\beta_N \sim$ 1.5-2.2) but are unlikely to substantially modify the results presented here. More work is needed in order to verify this conclusion.

References

[1] Kadomtsev, B., B., Sov. J. Plasma Phys. 1, (1975) 295.

[2] Weiland, J., Jarmén, A., Nordman, H., Nucl. Fusion 29, (1989) 1810.

[3] Jarmén, A , Andersson, P., Weiland, J., Nucl. Fusion 27, (1987) 941.

[4] Nordman, H., Weiland, J., Jarmén, A, Nucl. Fusion 30, (1990) 983.

[5] Christiansen, J.P., et al., Nucl. Fusion 33 (1993) 863.

[6] Cordey. J.G., et al., Plasma Phys. Control. Fus. 38, (1996), A67.

[7] Nordman, H., Strand, P., Weiland, J., Christiansen, J.P., Nucl. Fusion 37, (1997) 413.

[8] Kinsey, J.E., Bateman, G., Phys. Plasmas 3, (1996) 3344.

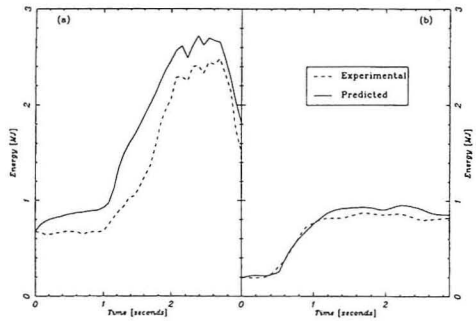

Fig. 1. Comparison between simulated and experimental thermal energy for discharge a) #35156 and b) #35171.

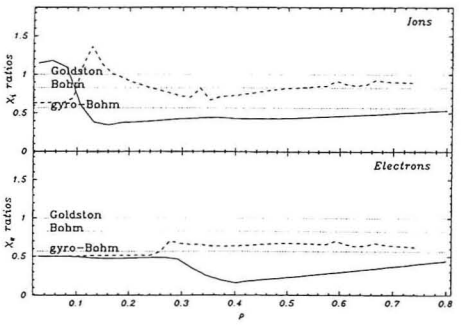

Fig. 2. The high field to low field ratios of ion and electron thermal diffusivities as obtained in simulations of L-mode (dashed) and H-mode (solid) gyro-radius scaling experiments.

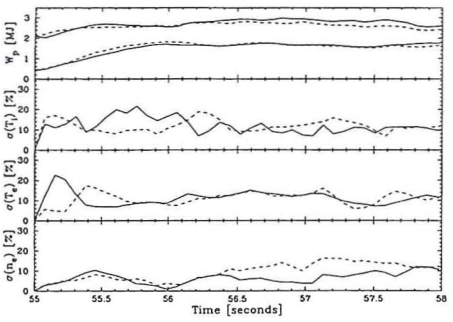

Fig. 3. Thermal energy (simulated and experimental) and RMS-errors for beta similarity pulses #38407 (solid line) and #38415 (dashed line).

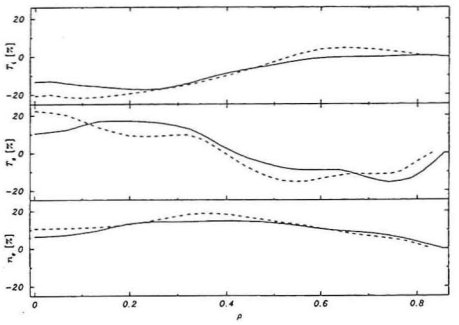

Fig. 4 Relative errors in Ti, Te and Ne as function of ρ for #38407 and #38415 after 3s of simulation.

Overview of improved confinement in impurity seeded discharges in TEXTOR-94, DIII-D and TFTR

J.ONGENA[1*], J.BOEDO[2], G.BONHEURE[1], R.V.BUDNY[3], C.E.BUSH[3], P.DUMORTIER[1], T.EVANS[4], K.HILL[3], A.HYATT[4], G.JACKSON[4], A.M.MESSIAEN[1], D.MUELLER[3], A.RAMSEY[3], G. STAEBLER[4], B.UNTERBERG[5], P.E. VANDENPLAS[1], M.WADE[4], G.VAN WASSENHOVE[1], R.R.WEYNANTS[1], TEXTOR-94, DIII-D and TFTR teams

(1) Laboratoire de Physique des Plasmas-Laboratorium voor Plasmafysica, Association "EURATOM-Belgian State", Ecole Royale Militaire-Koninklijke Militaire School, B-1000 Brussels, Belgium**

(2) Fusion Energy Research Program, Mechanical Engineering Division, University of California at San Diego, La Jolla, USA

(3) Princeton University, P.O. Box 451, Princeton NJ, 08543, USA
supported by US DoE Contract No. DE-AC02-76-CH03073

(4) General Atomics, 3550 General Atomics Court, P.O.Box 85608, San Diego, CA 92186-9784,USA

(5) Institut für Plasmaphysik, Forschungszentrum Jülich, GmbH, Association "EURATOM-KFA", D-52425 Jülich, FRG**.

* Researcher at NFSR, Belgium
**Partner in the Trilateral Euregio Cluster (TEC)

A new confinement regime has been established in 1993 on TEXTOR and confirmed on the upgraded TEXTOR-94, a tokamak with a circular cross-section, equipped with the toroidal pump limiter ALT-II, and with a heating system consisting of 2 tangential neutral beam lines (1 co and 1 counter) and 2 antenna pairs. This new regime is called the Radiative I-Mode or RI-Mode. Originally intended to show the possibility of a radiating zone confined to the edge of the plasma in order to cool the edge of the plasma and thus to reduce the maximum heat flow to the wall components, many additional characteristics of interest to a future fusion reactor have been discovered in these discharges : quasi-stationarity of the plasma parameters, high confinement close to ELM-free H-mode confinement, high plasma density near the Greenwald limit, high normalised β, and the possibility to operate at low edge q. The RI-Mode has been obtained in deuterium discharges heated with NBI-co ($D^\circ \rightarrow D^+$), combined with ICRH and/or NBI-counter heating ($D^\circ \rightarrow D^+$) and with (i) a minimum of $P_{NI\text{-}co}/P_{tot} \geq 20\text{-}25\%$ (ii) at sufficiently large central line-averaged densities $\bar{n}_{eo}$ such that the Greenwald number $\bar{n}_{eo}/\bar{n}_{eo,Gr} \geq 70\%$ (where $\bar{n}_{eo,Gr} = I_p/(\pi a^2)$ with as units $10^{20} m^{-3}$, MA, m [1]) (iii) with impurity seeding such that the radiated power fraction exceeds about 50%. The quasi-stationarity has been obtained with the feedback control of (i) the radiating power and (ii) the plasma energy content by acting on the ICRH power level.

This paper will address questions related to the choice of the impurity which can be used for the edge cooling, to the global confinement of the RI-Mode scaling expressed in engineering and non-dimensional parameters and give a brief overview of recent experiments with impurity seeding on different tokamaks in the world.

1. RI-Mode obtained with Ar seeding in TEXTOR-94

RI-Mode characteristics obtained with Ne cooling have been extensively discussed in previous papers [2-3]. New experiments have been performed with Ar as a radiating impurity and a summary of the effects observed is given in Fig. 1, where a comparison of the time evolution of basic plasma parameters of two discharges, seeded respectively with Ar and Ne are compared, The plasma current in these discharges was I_p = 350 kA and in both discharges (i) NBI-co and ICRH are applied at the same heating level. From t=1.8 onwards Ne resp. Ar impurity seeding is applied and the intensity of the Ne-VIII resp. Ar-VIII line is feedback controlled. Note the striking similarity in many signals of both discharges : (i) increase in the central line-averaged

density $\bar{n}_{eo}$ to values close to the Greenwald limit, (ii) increase in the diamagnetic energy E_{dia} triggered shortly after the start of the Ne resp. Ar seeding (iii) increase of the deuterium particle confinement time visible through the decrease of the D_α-light; (v) similar behaviour as a function of time of different impurity lines; (vi) no degradation of the neutron yield [4] but on the contrary, an increase in the presence of impurity seeding resulting mainly from the density increase at rather constant temperatures and from the (vii) low central dilution [5]. In addition, a decrease of the safety factor on axis is observed, and an increase in the peaking of the electron density profile. Note also the long duration of the high confinement phase which is about 50 confinement times ($\tau_E \cong 42$ ms), which is terminated on purpose at $t \cong 3.8$s, and a fast ramp down of the plasma current is started, which helps to decrease the density and to terminate the discharge without disruption.
The principal difference between Ar and Ne cooled discharges is the extent of the radiating mantle, which is broader in the case of Ar [5]. In addition, from the present experimental data, γ-values close to 90% and densities above the Greenwald limit seem more difficult to obtain than in discharges with Ne seeding.

2.Confinement behaviour in RI-Mode discharges seeded with Ne and Ar in TEXTOR-94

Previous studies [6] have shown that the confinement of RI-Mode discharges seeded with Ne is well approximated by :

$$\tau_{RI} = (\bar{n}_{eo}/\bar{n}_{eo,Gr})\ \tau_{ITERH93\text{-}P} \qquad (1)$$

where $\tau_{ITERH93\text{-}P}$ is the confinement time as given by the ITERH93-P ELM-free H-mode scaling law. The resulting confinement scaling expression is given by :

$$\tau_{RI} = 0.0113\ \bar{n}_{eo}^{1.17} I_p^{0.06} R^{1.9} a^{1.89} B_t^{0.32} P_{tot}^{-0.67} A_i^{0.41} \qquad (2)$$

(where A_i is the atomic mass and where the units used are s, $10^{19}m^{-3}$, MA, m, m, T, MW). Note the linear dependence on the density (as for ohmic discharges) and the near absence of a current dependence. The usual power degradation remains however. Note also that up to now only the dependence on $\bar{n}_{eo}$, I_p and P_{tot} has been checked experimentally.

A similar confinement scaling is found for Ar seeded discharges. This is illustrated in Fig.2, where data points are selected with $f_{H93} \geq 0.8$ for a broad parameter range, obtained from discharges seeded with Ar and Ne.

An interesting question is how the RI-Mode can be expressed as a function of non-dimensional variables. It is well known that the ELM-free H-mode scaling is of the Gyro-Bohm type ($B\tau \propto \rho^{*-2.70}\nu^{*0.28}\beta^{-1.23}$). If one considers ρ^*, β and ν^* as the only significant dimensionless parameters [7], then one would obtain for the RI-Mode $(B\tau)_{RI} \propto \rho^{*-4.23}\nu^{*0.48}\beta^{1.04}a^{0.87}$.
Note (i) that we have retained the dependence on the minor radius a, because the scaling (2) does not fulfil the Kadomtsev constraint, in contrast to ITERH93-P; (ii) the ρ^* dependence which is even stronger than Gyro-Bohm and (iii) the increase of confinement with β, in contrast with the usual L- and H-Mode scalings.
However, this choice of non-dimensional variables overlooks a possible role of atomic processes in confinement [7]. A way to take these into account is to use the Hugill number H_u, as an additional dimensionless parameter, proposed by Kadomtsev [8]. This is easily done in our case, since $\bar{n}_{eo}/\bar{n}_{eo,Gr} = 5/\pi\ H_u$ and we propose : $\tau_{RI} \propto H_u\ \tau_{ITERH93\text{-}P}$.

This scaling retains the gyro-Bohm property of the ELM-free H-Mode and takes into account the influence of atomic processes on transport in the RI-Mode.

3. Experiments with Ne and Ar cooling in TFTR.

In view of the extrapolation to a device of the size of a future fusion power reactor, an important question is whether the RI-Mode can be obtained in devices larger than TEXTOR-94. To this end, experiments have been performed recently in TFTR [9] with both Ne and Ar cooling in deuterium discharges heated with deuterium NBI-co injection.

The maximum plasma density obtained in these discharges corresponded to $\bar{n}_{eo}/\bar{n}_{eo,Gr} \approx 70\%$. It was difficult in the short time available to obtain larger densities. Striking similarities with the RI-Mode in TEXTOR-94 have been observed during Ne puff on TFTR [2,3] :

(i) no decrease of the stored energy E with large values of γ but on the contrary, an increase of E of about 10% corresponding to $\tau_E \approx 1.1 \times \tau_{ITER\text{-}89L}$ (ii) increase in $\tau_{p,D}$ (iii) decrease in the carbon flux, as seen from the intensity of a C-II line (iv) increase in the peaking factor of the density profile $\gamma_n = n_e(0)/\langle n_e(r)\rangle$ (v) increase in the central electron temperature T_{e0} (vi) no decrease in the neutron reactivity (vii) low central Z_{eff} value leading to a low central concentration of the seeded impurity of about 0.7-0.8 %.

Experiments with feedback controlled Ar cooling have also been performed on TFTR and confirm the observations made in the Ar seeded RI-Mode discharges on TEXTOR-94. They also show a similar signature of RI-Mode physics as the discharges obtained with Ne in TFTR. A wall retention of Ar has been observed, also found in TEXTOR-94, making Ar seeded operation more difficult.

4. Experiments with Ne cooling in DIII-D

Experiments with Ne seeding have also been recently undertaken on DIII-D, in limiter and divertor plasmas. All plasmas were heated with NBI-co (5-10 MW), and only Ne seeding was tried up to now. The results obtained can be summarized as follows :

(i) in limiter plasmas the elongation was $\kappa = 1.4\text{-}1.6$; maximum Greenwald number $\bar{n}_{eo}/\bar{n}_{eo,Gr} \approx 90\%$ and and radiation fractions P_{rad}/P_{tot} obtained were about 80% . At the highest densities, ELMing H-Mode was observed (#93520-93522) moderately peaked density profiles were observed, with f_{L89} between 1.5 and 1.6, comparable to ELM-free H-mode scalings. At lower densities ($\bar{n}_{eo}/\bar{n}_{eo,Gr}$ between 0.5 and 0.75), enhanced confinement with an L-Mode edge was observed with signatures similar to those of the RI-Mode on TEXTOR-94.
(ii) in divertor plasmas, H-mode ($f_{H93} = 1$) plasmas could be obtained with Ne seeding, at $\bar{n}_{eo}/\bar{n}_{eo,Gr} \approx 71\%$ and radiation fractions $P_{rad}/P_{tot} \approx 94\%$ and a confinement characterised by $f_{L89} \approx 2.5$, equivalent to $f_{H93} \approx 1.5$ (i.e.better than ELM-free H-Mode confinement) was observed under these conditions (#93520, $t > 3.1$s). In addition a kind of a "Super RI-Mode" or high density "VH-Mode" was observed, in single null plasmas. Confinement improved to values for f_{L89} between 3 and 4 equivalent to f_{H93} between 2 and 3, at densities up to $\bar{n}_{eo}/\bar{n}_{eo,Gr} \approx 60\%$ and radiation fractions $P_{rad}/P_{tot} \approx 50\%$. Flat density profiles with densities up to $7 \times 10^{19} m^{-3}$ and central temperatures up to 4 keV have been observed, and peak values of $\beta_n = 4$ (#93530, t=1.6-1.9s) with $\beta_n \times f_{L89} = 13$ (#93458, t = 3.7s). A value of $\beta_n \times f_{L89} = 6$ has been observed for more than 800ms (#93450).

5. Experiments with impurity seeding in high density discharges on other machines

First experiments with impurity seeding in high density discharges have been carried out on also Tore-Supra and Compass-D. Further experimental investigations are planned on both machines, as in the short time available, it was not possible to explore sufficiently the parameter domain in order to investigate fully the confinement properties of the discharges.

6.Conclusions

Recent experiments with impurity seeding in high density discharges on TEXTOR-94 and different tokamaks around the world show that it is possible to simultaneously obtain high confinement (of at least ELM-free H-mode quality), high radiation (needed to solve the heat exhaust problem) and high density (needed for a reactor grade plasma). The results obtained on DIII-D show, more in particular, that plasmas with these properties can be realized in both limiter and divertor configuration. Although a better understanding of the underlying physical mechanisms is required, it seems to justify hopes that such a regime could be extended to reactor scale machines.

REFERENCES :

[1] M.Greenwald, J.L.Terry, et al., Nucl.Fusion **28**, 2199 (1988).
[2] A.M.Messiaen, J.Ongena, et al., Phys. Rev. Lett. **77**, 2487 (1996).
[3] A.M.Messiaen, J.Ongena, et al., Phys. Plasmas **4**, 1690 (1997).
[4] G.Van Wassenhove, S.Helbing, et al., Contributed Papers of the 24th EPS Conference on Controlled Fusion and Plasma Physics, 9-13 June 1997, Berchtesgaden, Part IV, 1697
[5] B.Unterberg, A.Messiaen, et al., Invited paper to the 24th EPS Conference on Controlled Fusion and Plasma Physics, 9-13 June 1997, Berchtesgaden; to be published in Plasma Physics and Controlled Fusion.
[6] A.M.Messiaen, J.Ongena et al., "*Recovery of a Neo Alcator type scaling with auxiliary heating in radiatively cooled discharges on TEXTOR-94*", Comments Plasma Physics Contr. Fusion, in print.
[7] J.G.Cordey, B.Balet, et al., Plasma Physics Control. Fusion, **38**, A67-A75 (1996).
[8] B.B.Kadomtsev, *"Tokamak Plasma : a complex physical system"*, Plasma Physics Series, IOP Publishing Ltd., Bristol and Philadelphia, 1992, pp 100-101.
[9] J.Ongena, R.Budny, et al., Contributed Papers of the 24th EPS Conference on Controlled Fusion and Plasma Physics, 9-13 June 1997, Berchtesgaden, Part IV, 1693

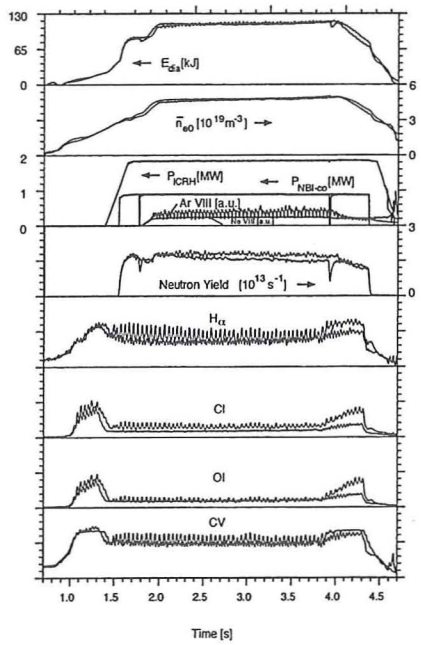

Fig. 1: Comparison of a discharge with Ne (#70686) and (#70667) Ar seeding on TEXTOR-94

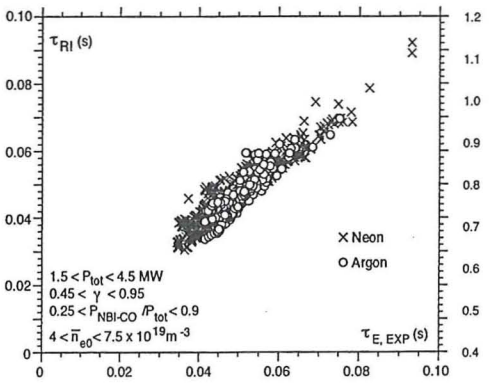

Fig. 2: Confinement as given by the RI-Mode scaling versus experimentally observed confinement time for Ne (crosses) and Ar (circles) cooled discharges in TEXTOR-94. All datapoints satisfy fH93 > 0.8

ENHANCED TRANSPORT VIA KIRCHHOFF RADIATION

Satish Puri

MPI für Plasmaphysik, EURATOM Association, 85748 Garching, Germany

Momentum transfer via Kirchhoff radiation of electrostatic electron and ion-cyclotron-harmonic waves contributes an enhanced collisionality far in excess of that given by the Fokker-Planck term in the existing neoclassical models. The resultant particle and thermal transport resembles the observed anomalous transport in ohmically heated toroidal plasmas.

It is shown that the collisionality occurring via the collective process of radiative momentum exchange far exceeds that due to the Fokker-Planck encounters. The resultant thermal and particle transport parallels the experimentally observed behavior. The collisionality contribution of the Kirchhoff radiation may be expressed as [1],

$$\nu^{rad}_{\sigma\xi} = \frac{T}{\pi^2 n_\sigma} \int_0^{\alpha_D k_D} \int_0^{\alpha_D k_D} \left| \frac{1}{m_\sigma v_{\|\sigma}} \frac{\Im[\omega^\sigma]\,\Im[\omega^\xi]}{\Re[\omega]\,\Im[\omega]} \right| k_\| k_\perp \, dk_\| dk_\perp \ , \qquad (1)$$

where T is the temperature (in energy units), $\Re[\omega] + i\Im[\omega] = \omega(\mathbf{k})$; $\Im[\omega]$ is comprised of contributions $\Im[\omega^\sigma]$ from all the particle species σ such that $\sum_\sigma \Im[\omega^\sigma] = \Im[\omega]$; $v_{\|\sigma}$ is the parallel velocity of particles of σ species defined in Eq.(3); $\alpha_D \sim \mathcal{O}(1)$ defines the small-wavelength limit for the applicability of the Vlasov-Boltzmann equation; and $k_D = 2\pi/\lambda_D$ is the Debye wavenumber corresponding to the Debye length

$$\lambda_D = \left(\sum_\sigma \frac{n_\sigma q_\sigma^2}{T_\sigma} \right)^{-1/2} . \qquad (2)$$

Small-wavelength, large-$|\mathbf{k}|$, electrostatic-cyclotron-harmonic modes are the prime contributors to ν^{rad} in Eq.(1). These highly-damped modes are the large-$k_\|$ extensions of the Bernstein [2] modes. For $k_\| > \omega/v_{te}$ (v_t is the particle thermal velocity), the ionic branch is known as the electrostatic-ion-cyclotron wave [3].

For a given $\mathbf{k}$, $\Im[\omega^\sigma]$ for each of the particle species consists of contributions from all the cyclotron-harmonic numbers n, such that $\Im[\omega^\sigma] = \sum_n \Im[\omega^\sigma]_n$. The corresponding particle parallel velocities in Eq.(1) are given by the relation

$$\omega - n\omega_{c\sigma} - k_\| v_{\|\sigma} = 0 \ . \qquad (3)$$

Equation (1) shows that $\nu^{rad}_{ei}/\nu^{rad}_{ie}$ ratio for a given $\mathbf{k}$ and $T_e = T_i$ scales as $(m_i/m_e)(v_{\|i}/v_{\|e})$. For the ion-cyclotron-harmonic waves the electrons are Landau damped ($n = 0$), whereas the ions undergo cyclotron-harmonic damping ($n \neq 0$), one obtains from Eq.(3), $v_{\|i}/v_{\|e} = (1 - n\omega_{ci}/\omega)$. Thus, $\nu^{rad}_{ei}/\nu^{rad}_{ie} = (m_i/m_e)(1 - n\omega_{ci}/\omega)$ for the nth ion-cyclotron harmonic component in contrast to $\nu^{nc}_{ei}/\nu^{nc}_{ie} \sim m_i/m_e$ for the neoclassical case.

Unless otherwise stated, it is assumed that $T_e = T_i = T$, atomic mass number $A = 1$, and $\alpha_D = 1$ in the following computational results for a two-component, electron-ion plasma in thermodynamic equilibrium.

Figure 1 shows ν^{rad} versus B_0 computed using Eq.(1). ν_{ee}^{rad} increases linearly with B_0, while ν_{ei}^{rad}, ν_{ie}^{rad} and ν_{ii}^{rad} exhibit a quadratic dependence on B_0. The resultant diffusivities (to the lowest order, ignoring off-diagonal terms) scale as $\chi_e \sim B_0^{-1}$, $\chi_i \sim B_0^0$, and $D \sim B_0^0$. With increasing B_0, the smallest permissible perpendicular wavelength $\mathcal{O}(\lambda_D)$ comes nearer in value to the much larger ion gyroradius, causing a more intense interaction of the waves with the ions. The effect is weaker for electrons because their gyroradius is already close to the Debye length. For $B_0 \sim 2\,\mathrm{T}$, $\nu_{ee}^{rad}/\nu_{ii}^{rad} \sim m_i/m_e$, so that electrons and ions become equal participants in thermal conduction. χ_e dominates energy transport below $B_0 \sim 2\,\mathrm{T}$ and χ_i above $B_0 \sim 2\,\mathrm{T}$. ν_{ee}^{rad} is almost forty times larger than the corresponding Fokker-Planck value. This discrepancy becomes still more pronounced at lower plasma densities (up to and over one hundred times the neoclassical value). *The enhancement in χ_e is at the core of the transport riddle; its resolution alone establishes the importance of radiative collisionality.*

An increase in the ion gyroradius for higher atomic mass number A results in a weakened wave-ion interaction and ν_{ii}^{rad}, $\nu_{ie}^{rad} \sim A^{-3/2}$ (Fig.2), leading to a $A^{1/2}$ isotope mass dependence of ion energy containment time [4]. A, however, has no direct influence on electron heat transport; the isotope mass effect on χ would be weak in low-field ($B_0 \lesssim 2T$) tori. Also, the transition from χ_e dominance to χ_i dominance would occur at larger B_0 for larger A. Since the Landau damping remains unaffected by A, ν_{ei}^{rad} decreases only as $A^{-1/2}$. The particle containment time response to A is a mixture of a favorable ν_{ie} scaling and an unfavorable ν_{ei} scaling.

In Eq.(1) $\nu^{rad} \sim k_D^4 v_t \sim T^{-3/2}$, so that radiative collisionality follows the neoclassical $T^{-3/2}$ temperature dependence (Fig.3). Accordingly, thermal as well as particle diffusivities grow rapidly towards the plasma edge [4].

An inspection of Eq.(1) would indicate a linear dependence of ν^{rad} on n_e due to the n_e^2 variation of k_D^4. However, the simultaneous shift of λ_D away from the gyroradius offsets the gain in ν^{rad} due to the density increase. This is most pronounced for ions whose gyroradius is already well in excess of the Debye length. Figure 4 shows that $\nu_{ee}^{rad} \sim n_e^{0.6}$, $\nu_{ei}^{rad} \sim n_e^0$ while $\nu_{ii}^{rad} \sim n_i^{0.1}$. The crossover of ν_{ei}^{rad} and ν_{ei}^{nc} occurs at a density of $n_e \sim 6 \times 10^{19}\,\mathrm{m}^{-3}$. Below these densities, the electron and ion populations are uncoupled [4], so that the Debye length is determined by the colder ion population. The low value of λ_D with a correspondingly larger integration limit in Eq.(1) would lead to larger collisionalities than those appearing in Fig.4. The combined effect of ν_{ei} crossover and the electron-ion thermal coupling may be responsible for the linear (LOC) and saturated (SOC) ohmic confinement regimes [4]. At higher values of B_0, and with the accompanying higher plasma temperatures, the ν_{ei} crossover, the electron-ion thermal coupling and the LOC-SOC transition shift to higher densities, in accord with observations [4]. Conversely, for lower B_0, the LOC-SOC transition occurs at lower densities. Higher isotope mass results in poorer electron-ion coupling, pushing the LOC-SOC transition to higher densities, as observed experimentally [5]. The ν_{ii}^{rad}, ν_{ii}^{nc} crossover occurs at the somewhat higher density of $n_e \sim 10^{20}\,\mathrm{m}^{-3}$. The electron-electron radiative collisionality ν_{ee}^{rad}, on the other hand, continues to dominate over the neoclassical value ($\nu_{ee}^{nc} \approx .5\nu_{ei}^{nc}$) for densities as high as $n_e \sim 10^{22}\,\mathrm{m}^{-3}$.

Figure 5, showing the velocity distributions of the colliding particles, confirms that the bulk of the ν_{ei}^{rad} collisions is contributed by trapped particles. Hence the enhancement in the electron-ion collisionality has no primary effect on parallel resistivity. Also, the enhancement in parallel diffussivity may not be accompanied by a corresponding reduction of the slowing down time.

Figure 6 shows the extreme sensitivity of ν^{rad} to α_D. Thus a fourfold increase in α_D causes ν_{ee}^{rad} to grow by almost two orders of magnitude. A careful comparison of the supraclassical theory with the experimental data would allow an accurate determination of α_D and thereby settle a long-standing uncertainty regarding the low-wavelength limit for the applicability of the Vlasov-Boltzmann equation.

In addition to thermal transport via enhanced collisionality due to radiative momentum exchange, direct transfer of radiative energy also takes place. In the present context, however, such direct transport is insignificant [6].

The total radiated power per unit volume ($n_e = 10^{20}\,\mathrm{m}^{-3}$, $T = 10\,\mathrm{keV}$, $B_0 = 6\,\mathrm{T}$) by the electron and ion components is $\sim 1000\,\mathrm{GWm}^{-3}$ and $\sim 50\,\mathrm{MWm}^{-3}$, respectively. However, reabsorption within picoseconds results in a net energy density $U = T/(2\pi)^3 \int_{\mathbf{k}} d\mathbf{k}$ of only $\sim 130\,\mathrm{mJm}^{-3}$, much too low to be detected experimentally.

The results of this paper are strictly applicable only for plasmas in thermodynamic equilibrium. Significant deviations from Maxwellian velocity distributions in auxiliary heated plasmas require separate treatment. Non-equilibrium plasmas, with free energy sources residing in plasma and magnetic-field inhomogeneities, are subject to a vast array of transport processes including plasma turbulence. The present results define the minimum irreducible limit of toroidal transport in plasmas near thermal equilibrium, such as ohmically heated tokamak plasmas and large, reactor-scale machines like ITER where the energy and particle containment times are much greater than the electron-ion energy exchange time.

In summary, radiative collisionality is able to resolve some of the perplexing dilemmas of toroidal transport; namely, (i) enhanced electron thermal conduction, (ii) magnetic-field dependence, (iii) isotope mass dependence, and perhaps (iv) the cause behind the linear (LOC) and saturated (SOC) ohmic confinement regimes.

The implications of radiative collisionality for perpendicular momentum transfer rate, energy equipartition, auxiliary-heated plasma confinement, impurity effects, alpha-particle transport (ash removal), transient transport, profile resiliency, heat pinch, bootstrap current, and ITER scaling are being studied. Kirchhoff's law has been extended to non-thermal plasmas in Ref.[7], while the Balescu-Lenard equation allows the inclusion of collective interactions in the collision operator [8, 9].

Although this paper is devoted to toroidal plasma confinement objectives, the findings of enhanced transport across inhomogeneous magnetic fields has significance for astrophysical and cosmic plasmas as well.

References

[1] S. Puri, Max-Planck-IPP Report IPP 4/273 (1996); Sherwood Fusion Theory Conference, Madison, Paper 1D35 (1997).

[2] I. B. Bernstein, Phys. Rev. **109**, 10 (1958).

[3] N. D'Angelo and R. W. Motley, Phys. Fluids **5**, 633 (1962).

[4] F. Wagner and U. Stroth, Plasma Phys. Control. Fusion **35**, 1321 (1993).

[5] E. Simmet, private communication.

[6] S. Puri, in *Proc. 17th EPS*, Amsterdam, **14B**, 1770 (1990).

[7] N. Rostoker, Nuclear Fusion **1**, 101 (1961).

[8] R. Balescu, Phys. Fluids **3**, 52 (1960).

[9] A. Lenard, Ann. Phys. **3**, 390 (1960).

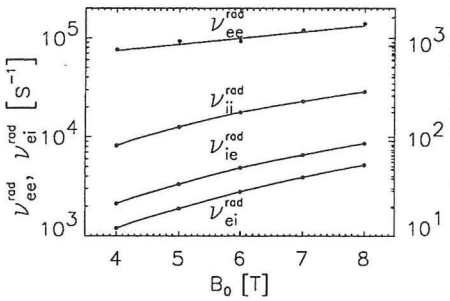

Figure 1: ν^{rad} versus B_0.

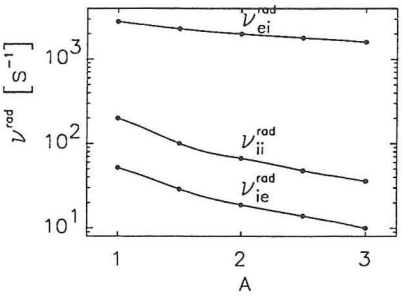

Figure 2: ν^{rad} versus atomic mass A.

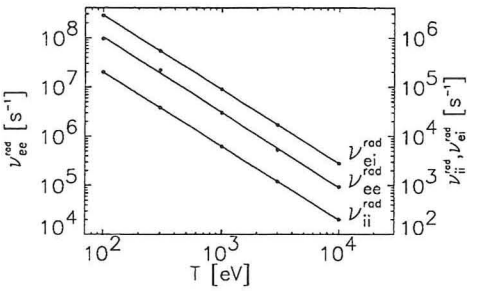

Figure 3: ν^{rad} versus T.

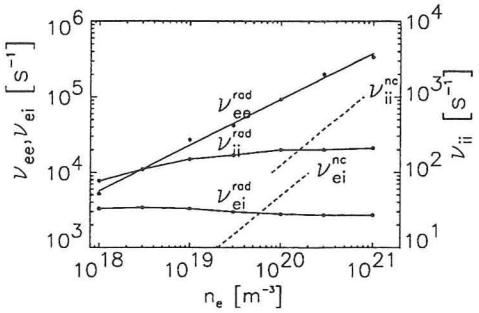

Figure 4: ν^{rad} and ν^{nc} versus n_e.

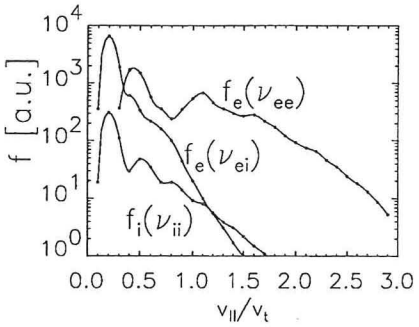

Figure 5: Velocity distribution of colliding particles.

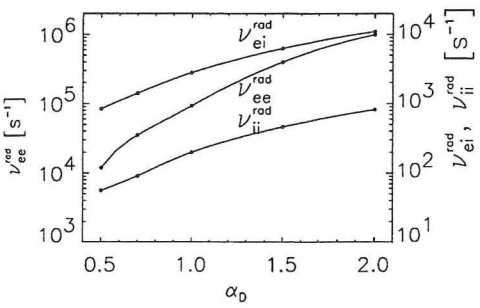

Figure 6: ν^{rad} versus α_D.

Aspects of driven reconnection of low order modes in tokamaks

E.Lazzaro[1], R.Coelho[2], M .F. Nave[2]

[1]Istituto di Fisica del Plasma , Euratom-ENEA-CNR Assoc.- Milan, Italy

[2]Centro de Fusão Nuclear, Instituto Superior Técnico,Euratom Assoc.Lisboa, Portugal

Abstract. In tokamaks an important case of driven reconnection is due to the action of time varying external fields with helical pitch resonant with q=m/n rational magnetic surfaces. Such fields may be created for control purposes or exist as "error fields" due to machine imperfections. To design a control system it is important to know the plasma response to *oscillating fields* in a finite frequency band, and also the role of *nonlinear coupling* of rotating islands.Novel aspects of these two problems are presented.

1. Problems of electrodynamical control of rotating islands.

In the large aspect ratio limit of circular cross section tokamaks a single helical magnetic field perturbation can be expressed through a magnetic flux function $\delta\vec{B}_{mn} = \nabla\times\left(\Psi_{mn}\vec{b}_{mn}\right) = \delta\vec{B}_{mn}(r).e^{i\left(m\theta-\frac{n}{R}z+\zeta_{mn}\right)} + c.c$ ($\vec{b}$ is the magnetic field unit vector). Such a perturbation is associated with a current density perturbation $\mu_0\delta J_{zk} = -\nabla^2_{*k}\psi_k.e^{i\left(m\theta-\frac{n}{R}z+\zeta_k\right)} + c.c.$ On a q=m/n surface the current continuity equation $\nabla\cdot\vec{J}=0$ (quasineutrality condition) has a singularity which indicates the presence of a boundary layer across which the flux function has a discontinuous logarithmic derivative, equivalent to the appearance of a surface current, which *tears* the topology of the nested tokamak equilibrium magnetic surfaces. Due to resistive diffusion in a narrow layer around the q=m/n surface the field lines reconnect and a rotating structure of finite radial size $w = 8\left(\frac{\Psi_{mn}}{nB_\theta q'}\right)^{1/2}$ and periodic in $m\theta - n\phi$ .is formed. As such magnetic island grows it traps plasma increasing its mechanical inertia, and is subject to the electrodynamical and mechanical forces due to external fields and the other islands. As a consequence of torques and of dissipation the magnetic islands rotate and the nonlinear evolution equations for the width w and the angular frequency ω_{mn} derive from the rate of flux reconnection obtained fron Faraday-Ohm law and from momentum balance, in the essential form:

$$\frac{dw_{mn}}{dt} = \frac{\eta}{\mu_0}\mathrm{Re}\,\Delta'_{mn}$$
$$k_0\frac{d\omega_{mn}w_{mn}}{dt} = k_1\,\mathrm{Im}\,\Delta'_{mn} - \mu_\perp\left[\omega_{mn} - \left(\omega_E + \omega_* + g\omega_{*T}\right)\right] \qquad (1)$$

The frequencies ω_E, ω_*, $g\omega_{*T}$ are the electric, and gradient drifts frequencies respectively and k_0, k_1 geometric coefficients and $\mu_\perp$ the (anomalous) perpendicular viscosity. The driving terms are the real and imaginary part of the effective parameter Δ'_{mn} that contains all internal and external sources of instability, including the effect of error fields, control fields and coupling to other islands. In a problem of control of the evolution of w, where the goal is $\mathrm{Re}\,\Delta'_{mn} \le 0$ it is important to "keep track" of the island rotation. In general the applied time dependent control field is partly "reflected" and it is important to know what is its frequency response. To assess this we consider a boundary value problem the *linearized* 'Shear Alfvèn" equations for ψ and ϕ in cylindrical geometry :

$$\begin{aligned} \frac{\partial\psi}{\partial t} - i\frac{m}{r}B_{0\vartheta}(r)\left(1-\frac{n}{m}q(r)\right)\varphi &= \frac{\eta_0}{\mu_0 g(r)}\nabla^2\psi \\ -\frac{\partial\nabla^2\varphi}{\partial t} &= -i\frac{m}{\rho_0\mu_0 r}B_{0\vartheta}(r)\left(1-\frac{n}{m}q(r)\right)\nabla^2\psi + i\frac{m}{\rho_0 r}\frac{\partial J_0}{\partial r}\psi \end{aligned} \qquad (2)$$

where g(r) is the slowly varying normalized profile of resistivity. The boundary conditions matching the external driving fields are $\left.\frac{\partial\psi}{\partial r}\right|_a + h\psi|_a = 0$, with $h = B_\theta^{ext}/B_r^{ext}$.

2. Driven tearing regime and excitation of Alfvèn waves.

For any m>2 eqs. (2) in the limits of $\omega \to 0$ or $S \to \infty$ reduce to the quasineutrality condition $\vec{B}\cdot\nabla\left(\frac{J_{//}}{B}\right) = 0$ describing tearing modes, while for S finite and $|\omega| > 0$ it describes Alfvèn waves with non negligible finite resistivity effects. Assuming mild variations of the profiles eqs(3) can be combined in the single fourth order equation

$$\frac{i\omega}{S}\nabla^2\left(\frac{1}{gG}\nabla^2\psi\right) + \left[\omega^2\nabla^2\left(\frac{\psi}{G}\right) - G\nabla^2\psi\right] - H\psi = 0 \qquad (3)$$

The fourth order term in eq.(3) is weighted by the small parameter S^{-1} and therefore for $\omega \neq 0$ it is a singular perturbation, indicating the appearance of a boundary layer of width $\delta \approx S^{-1/3}$ where the Alfvèn resonance condition $G(x) = \pm\omega$ is met.

3. Structure of driven perturbations and reflected field

The flux Re(ψ) driven the by external m=2, n=1 perturbation, is shown in Figures 1 and 2 over the interval 0<x<1 (plasma), for a plasma with $S=10^8$, for a range of frequencies $10^{-10} \le \omega \le 10^{-3}$ and $6\cdot10^{-3} \le \omega \le 2.4\cdot10^{-2}$. The q=m/n surface shields the plasma interior from the external perturbation; as the ω decreases field penetration increases and field lines reconnect. The slope jump at the rational surface (x~0.66) shows that, in this case, the system is being driven unstable. As the frequency increases reconnection at the q=m/n surface is replaced by two "wavefronts" at the Alfvèn resonances; the reflected field in this situation is affected by the outer Alfvèn wavefront. Consequently the frequency response is essentially flat in the very low frequency region but has a pole near $\omega \le 2.4\cdot10^{-2}$.

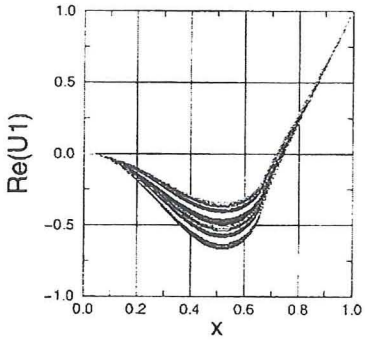

Fig.1- m=2 flux $Re(\Psi_1)$ vs x

$(10^{-10} \le \omega\tau_A \le 10^{-3})$

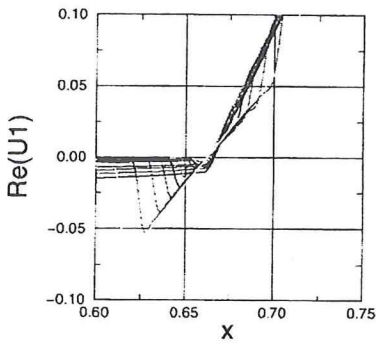

Fig.2- m=2 flux $Re(\Psi_1)$ vs x

$(6\cdot10^{-3} \le \omega\tau_A \le 2.4\cdot10^{-2})$

Another effect is that in a resistive plasma subject to oscillating fields, there is a net force

$$\vec{f}(r) = Re[\delta\vec{J}_{m,n} \times \delta\vec{B}_{m,n}] \cong -\frac{1}{2\mu_0} Im\left(\psi^*_{m,n} \nabla^2_\perp \psi_{m.n}\right)\left[\frac{m}{r}\vec{e}_\theta - \frac{n}{R}\vec{e}_\phi\right] \quad (4)$$

In presence of a rational surface this force, localized around it, it drives island rotation. In general however there is a very small distributed force, which becomes considerable when resistive Alfvèn waves are driven .

4- Electrodynamic interaction of rotating islands

Another problem in the understanding and controlling island growth and rotation is the role of coupling between modes, even in non disruptive regimes. Here we outline an extension of the theory to include the mutual electrodynamic coupling of a triplet of rotating magnetic islands of different helicities arranged to realize a "resonant wavenumber matching". The quasineutrality condition in presence of modes with a triplet of matching numbers is:

$$\vec{B}_0 \cdot \vec{\nabla}\left(\frac{\delta J_{//k}}{B}\right) + \delta\vec{B}_k \cdot \vec{\nabla}\left(\frac{J_{0//}}{B}\right) = -\sum_{k'} \delta\vec{B}_{k'} \cdot \vec{\nabla}\left(\frac{\delta J_{//k-k'}}{B}\right) + \delta\vec{B}_{k-k'} \cdot \vec{\nabla}\left(\frac{\delta J_{//k'}}{B}\right) \quad (5)$$

These coupled mode equations can be written symbolically in operator form and solved iteratively:

$$\begin{cases} \hat{A}_k \psi_k = Q_k(\psi_{k'}, \psi_{k-k'}) \\ \hat{A}_{k'} \psi_{k'} = Q_{k'}(\psi_k, \psi_{k-k'}) \\ \hat{A}_{k-k'} \psi_{k-k'} = Q_{k-k'}(\psi_{k'}, \psi_k) \end{cases} \quad (6)$$

with

$$\hat{A}_k \equiv \left(\frac{\partial}{\partial r} r \frac{\partial}{\partial r} - \frac{m^2}{r}\right) - \frac{k_\perp r \mu_0 q \sigma'}{(m - nq)}, \quad \sigma' \equiv R\left(\frac{J_{0//}}{B}\right)' \quad (7)$$

At first iteration *each equation* can be cast as an integral equation using the Lagrangian method of variation of parameters, using the independent solutions $F_{j\pm}(x)$ of the

homogeneous uncoupled equations and, *in the integrals*, the nonlinear source terms $Q_k(\psi_{k'},\psi_{k-k'}) = H^{(k)}_{k'}\delta(r-r_{k'}) + H^{(k)}_{k-k'}\delta(r-r_{k-k'})$, gives the coupled solutions in a form which shows the effect of the other islands as concentrated "filamentary" currents:

$$\psi_k(r) = C_{+k}F_{+k}(r) + C_{-k}F_{-k}(r)\theta(r-r_k) + \int_0^r \frac{\begin{vmatrix} F_{+k}(t) & F_{-k}(t) \\ F_{+k}(r) & F_{-k}(r) \end{vmatrix}}{W[F_{+k}(t),F_{-k}(t)]} Q_k(\psi_{k'},\psi_{k-k'})d \qquad (8)$$

W being the wronskian of the $F_{j\pm}(x)$. From these explicit solutions the ("outer") complex tearing instability parameters $\hat{\Delta}'_i$ are thus obtained for the coupled modes fullfilling prescribed boundary conditions. The real and imaginary parts of these $\hat{\Delta}'_i$ inserted in the island width and torque balance eqs.(1) complete the formulation of the electrodynamic part of the problem. Figs.3,4,5 show an example of coupled evolution of w and ω of islands (1,1), (2,1),(3,2). The initially stable (2,1) island is destabilized after locking, while the other two stop rotating later .

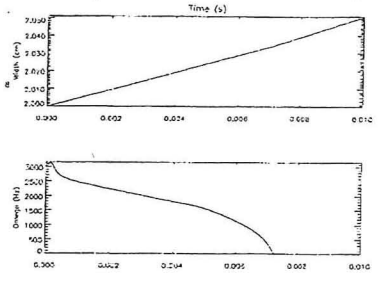

Fig. 3- W(t) (upper and ω(t) (lower) for (1,1)

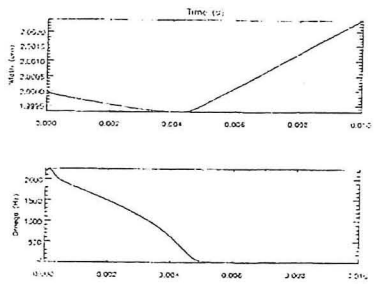

Fig. 4 -W(t) (upper) and ω(t) (lower) for (2,1)

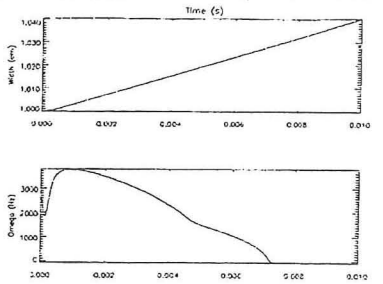

Fig. 5 -W(t) (upper) and ω(t) (lower) for (3,2)

Conclusions

.The linear response of to external helical fields with frequecies as low as $\omega\tau_A \approx 10^{-2}$is influenced by Alfvèn waves and the nonlinear response by $\bar{J}\times\bar{B}$ coupling of islands.

References

[1] Lazzaro E., Gianoli L., Valdettaro L.,"Linear frequency response of reconnecting perturbations" in Proceedings 24th EPS Conference on Controlled Fusion and Plasma Physics Berchtesgaden 1997

[2]Fitzpatrick R., Hastie J. et al.Nuc. Fus. 33 (1993) 1553

Study of second stability for ITG modes

M. Fivaz, O. Sauter, K. Appert, S. Brunner, T. M. Tran, J. Vaclavik

Centre de Recherches en Physique des Plasmas, Association Euratom-Confédération Suisse
EPFL, PPB, 1015 Lausanne, Switzerland

Abstract The second stability regime for ion-temperature-gradient (ITG) modes is studied in details with a global linear gyrokinetic Particle-In-Cell code which takes the full toroidal MHD equilibrium data. The trapped-ion and the toroidal ITG regimes are explored. We perform simultaneous ideal MHD stability computations for both kink ($n = 1$) and ballooning ($n = \infty$) modes. We use the results to find partially optimized configurations that are stable to ideal MHD modes and where the ITG modes are stable or have very low growth rates. Such configurations are expected to have very low level of ITG-induced transport.

Introduction. Unstable ITG modes are now commonly held responsible for anomalous ion heat transport in tokamaks. The ion temperature gradient provides free energy to the instability and the magnetic field gradient provides an efficient destabilizing mechanism on the outer side of the torus. These modes are stable when the ion temperature gradient is below a critical values (first stability regime). At high pressure, the plasma diamagnetism can reduce of even reverse the gradient of the equilibrium magnetic field, which then becomes favorable everywhere in the plasma; the ITG modes can then be completely stabilized [1] in what can be called a second stability regime. This effect is sometimes referred to as "Shafranov-shift stabilization".

Previous calculation [2] [3] [4] are undetailed and were done using the ballooning approximation and (except [2]) with the "$s - \alpha$" approximation to the equilibrium magnetic field, a high aspect ratio, circular shifted magnetic surface approximation. The ballooning approximation, though, breaks down at low n or low magnetic shear, and cannot describe slab-like modes that are not localized on the outer side of the torus, i.e. that do not "balloon". The "s-α" model also breaks down at realistic aspect ratio and in non-circular plasmas.

We study here in detail the conditions that lead to the second stability for ITG modes, using a global approach (no ballooning approximation) and the full MHD equilibrium data. We focus on cases where a low magnetic shear stabilizes the local, short wavelength MHD ballooning modes. We use the code GYGLES (GYrokinetic Global LinEar Solver)[5] [6], which uses a radially global approach in toroidal geometry. The simulation model is based on the linear gyrokinetic equations for the ions in which the full guiding center trajectories are kept. We assume the electrons to respond adiabatically and the equilibrium perturbation to be electrostatic and quasineutral. The gyrokinetic equations are linearized around an equilibrium local Maxwellian distribution function. The code uses a Particle-In-Cell method with finite elements defined in magnetic coordinates. The code can simulate routinely global modes of all (very short to very long) toroidal wavelengths, can treat realistic (MHD) equilibria of any

Global parameters	$R_0 = 3$ m, $a/R_0 = 1/.36$, elong. 1.6, triang. .3, vac. field $B_0(R_0) = 3$ T, $\rho \approx 4.8$ mm (deuterium)
Temperatures	$\frac{T_i}{dT_i/ds} = -\frac{1}{2}\kappa_T \left(1 + \cos\left[\frac{\pi}{2}\frac{s-s_0}{\Delta s}\right]\right)$ for $\lvert s - s_0\rvert < 2\Delta s$, 0 elsewhere
	$\kappa_T = \frac{1}{\Delta s}\log(T_{mul})$, $s_0 = .6$, $\Delta s = 0.1$, $T_i(s_0) = 10$ Kev, $T_e = T_i$
Density profile	$n_i(s) = n_0(1 - s^2)^4$
Norm. current density	$\hat{I}^*(s) = j_0(1 - s^2) + j_a \exp\left[-\frac{(s-s_0)^2}{\Delta s_j^2}\right]$
	$j_a = T_{mul} * (.14 * j_0 + .24)$, $\Delta s_j = 0.15$
Scan parameters	$j_0 \in [.8, 100]$, $T_{mul} \in [1.1, 1.8]$
Parameters at $s = s_0$	$R_0/L_T \equiv \kappa_T R_0/a$, $R_0/L_n = 2.8$, $q = 1.5$, shear $\hat{s} \approx 0.2$

Table 1: *Specification of the equilibria studied.*

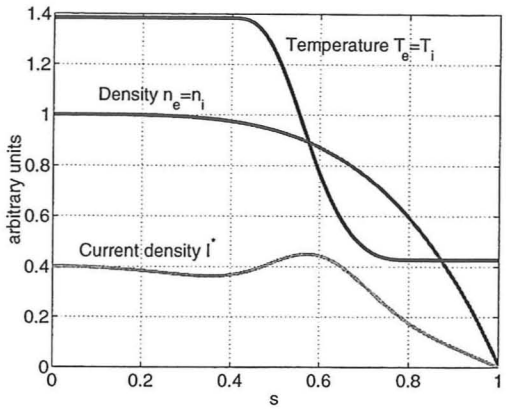

Figure 1: *Profiles from table (1).*

size and runs on a massively parallel computer.
The inclusion of electromagnetic perturbations can affect (usually stabilize further) ITG modes at high β [7] [4] [8] [9]. This effect is not included here; we focus rather on the stabilizing effect of the modification of the equilibrium at high β using realistic (MHD) equilibrium magnetic structure.

Parametric study. We introduce a radial variable $s = \sqrt{\Psi/\Psi_a}$, where Ψ is the equilibrium poloidal magnetic flux and Ψ_a its value at the plasma boundary, the plasma major and minor radii R_0 and a and the normalized temperature gradient $\frac{R_0}{L_T} \equiv \frac{R_0}{a}\frac{\partial T/\partial s}{T}$. Locally on the outer plasma mid-plane, one can derive from the MHD equilibrium condition a criterion for magnetic gradient reversal:

$$\alpha \equiv -\mu_0 \frac{R}{B_t^2}\frac{\partial p}{\partial R} > 1$$

The reversal parameter α is such that $\alpha = 0$ at low pressure and $\alpha > 1$ when the magnetic field gradient is reversed on the outer mid-plane. It is therefore a local parameter characterizing the magnetic field gradient at the most unfavorable point. It differs by a factor q^2 from the usual α parameter from "$s - \alpha$" equilibria and that is important in MHD ballooning computations.
The table (1) defines a set of JET-size equilibria where the profile of R_0/L_T is inspired by a high-confinement JT60-U discharge [10] and peaks at a given magnetic surface at $s = s_0$, thus confining the unstable modes around that surface. In what follows, R_0/L_T and α refer to their values at $s = s_0$. Both α and R_0/L_T can be chosen by varying the parameters j_0 and T_{mul}. In the region where the modes lie, the safety factor does not depend on R_0/L_T and α. The magnetic shear $\hat{s}$ is low, $0 < \hat{s} < 0.2$, where the modes lie. This has the effect that all these equilibria are stable to MHD ballooning modes; in particular, equilibria with high pressure gradients lie in the second stability zone [12].
We use this set to do a generic study of ITG stability as a function of R_0/L_T and α at fixed safety factor profile, in both the regimes of toroidal ITG (high toroidal mode number n, mode frequency $\equiv \omega > \omega_b \equiv$ trapped-ion bounce frequency) and the trapped-ion regimes (low n, $\omega < \omega_b$).
The profiles of the surface-averaged current $I^*(s)$ and of the pressure $p(s) = n_i(s)\,(T_e(s) + T_i(s))$ are first used to solve the Grad-Shafranov equation with the code CHEASE [11], yielding the magnetic field structure that is then used by GYGLES to compute ITG stability.

Results. Figure (2) shows the contours of the growth rates obtained for $n = 12$ and $n = 48$ in the (α,R_0/L_T) plane. The frequency of these modes increases with R_0/L_T and with n, while

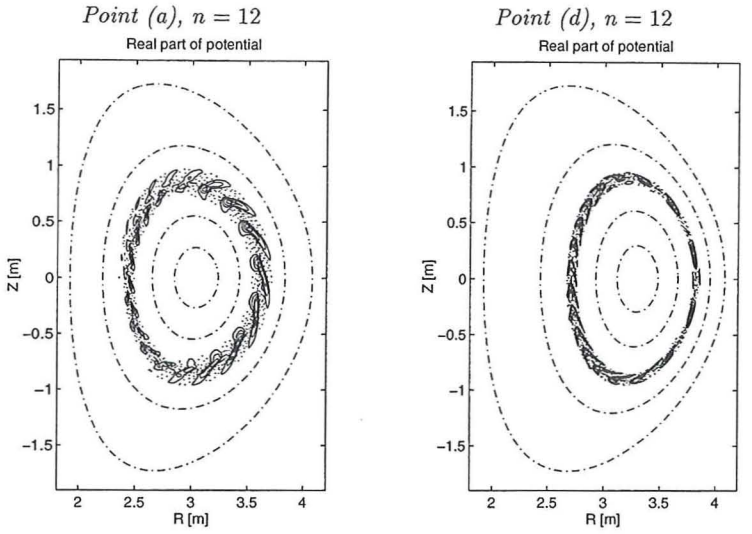

Figure 3: *Eigenmodes corresponding to the points (a) and (d) shown in Fig. (2).*

ballooning modes. The MHD ballooning modes are stabilized by low shear on the surface of interest in all the configurations presented. The stabilization of ITG modes is well described by the local magnetic field gradient reversal parameter α, and any ITG-induced transport should be strongly reduced for $\alpha \approx 1$.

Global kink modes are stable without ideal wall up to relatively high values of α, $\alpha = 1.1$ for $R_0/L_T = 16.3$. When a ideal wall at r_{wall}/a=1.2 is included, one obtains stability at $\alpha = 1.8$ for the same temperature gradient. This equilibrium has therefore good MHD properties and should have sustainable ITG transport ($\chi_\perp \approx 1$ m^2/s, Fig. (2)) while its temperature gradient is three times higher than the critical gradient at low β. By optimizing the plasma shape and profiles, we expect to find in the near future improved optimized high-performance configurations that are stable to all ideal MHD modes and stable or weakly unstable only to global ITG modes.

We finally note that some experimental discharges seem to have accessed $\alpha \approx 1$ [6].

This research work was supported in part by the Swiss National Science Foundation and the Cray-EPFL PATP project. The computations were done on the Cray-T3D parallel supercomputer of the EPFL-PATP.

References

[1] M. Fivaz *et al.*, Phys. Rev. Lett. **78**, 3471 (1997).
[2] G. Rewoldt, W. M. Tang, and M. S. Chance, Phys. Fluids **25**, 480 (1982).
[3] X. Q. Xu and N. M. Rosenbluth, Phys. Fluids B **3**, 627 (1991).
[4] M. Yamagiwa, A. Hirose, and M. Elia, Plasma Phys. Control. Fusion **39**, 531 (1997).
[5] M. Fivaz *et al.*, submitted to Computer Physics Communications **0**, 0 (1997).
[6] M. Fivaz, PhD thesis No. 1692, Ecole polytechnique Fédérale de Lausanne, Switzerland, 1997.
[7] J. Y. Kim, W. Horton, and J. Q. Dong, Phys. Fluids B **5**, 4030 (1993).
[8] R. R. Domingez and R. W. Moore, Nucl. Fusion **26**, 85 (1986).
[9] A. Jarmen, P. Anderson, and J. Weiland, Nucl. Fusion **27**, 941 (1987).
[10] Y. Neyatani and the JT60-Team, Plas. Phys. Control. Fusion **38**, A181 (1996).
[11] H. Lütjens, A. Bondeson, and O. Sauter, Comput. Phys. Commun. **97**, 219 (1996).
[12] D. Lortz and J. Nührenberg, Phys. Lett. **68A**, 49 (1978).
[13] R. Gruber *et al.*, Comput. Phys. Commun. **21**, 323 (1981).

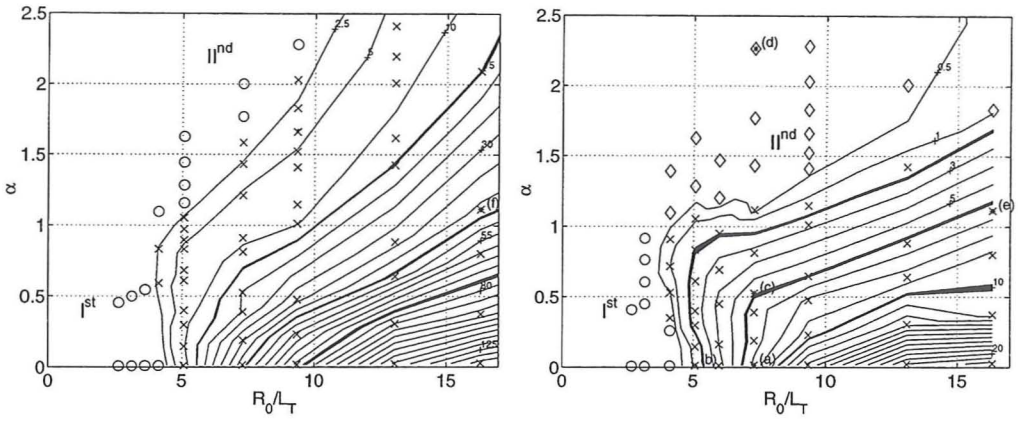

Figure 2: *Contours of the growth rate (in kHz). Left: n=48, Toroidal ITG regime. Right: n=12, Trapped-ion mode regime. The crosses (o), circles (x) and diamond (◇) represent respectively equilibria that were found stable, unstable to toroidal modes, and very weakly unstable to slab-like modes.*

the ion bounce frequency ω_b is fixed. As a results, the $n = 12$ modes are in the trapped-ion regime with $\omega < \omega_b$, except at high R_0/L_T, where they have a small toroidal ITG character. Conversely, the $n = 48$ modes are in the toroidal ITG regime, except at very low values of R_0/L_T.

We call "first stability zone" the stable zone, marked "Ist" on Fig. 2, that lies below a critical temperature gradient. Above this gradient, the mode is stabilized for increasing α as ∇B decreases and is reversed for $\alpha \geq 1$, leading to the "second stability zone" for ITG modes, marked "IInd" on the same figure. In the toroidal ITG regime, these equilibria are fully stable, while in the trapped-ion regime, a weakly unstable slab-like ITG mode remains. The second stability regime is therefore strictly stable to toroidicity-related modes only (at least at low shear), but the slab-like modes are not expected to cause much anomalous transport, as they are radially narrow and very weakly unstable. The structure of the eigenmodes marked (a) (a trapped-ion mode) and (d) (a slab-like ITG mode) on Fig. (2), are shown in Fig. (3). The contours of growth rates corresponding to mixing-length estimates of the heat diffusivity $\chi_\perp = 1$, 3 and 5 m^2/s are shown in bold in Fig. (2). While these values should not be taken as more than rough estimates, they show that the scan covers most of the experimentally relevant range of $0.1 - 10$ m^2/s.

MHD stability calculations. The CHEASE code was used to compute the stability of MHD ballooning modes. All the equilibria presented here are stable to these modes at the surface $s = s_0$; this was achieved by lowering the magnetic shear to a $0 < \hat{s} < 0.2$, so pushing the equilibria with high values of α into the second stability regime for ballooning modes. Kinetic effects on these modes were not considered [4]. This demonstrates the existence of a simultaneous second stability regime for ITG modes and for MHD ballooning modes. The code ERATO [13] was used to compute the stability to kink modes. The points (a), (c) and (e) on Fig. (2), the latter at $\alpha = 1.1$, are stable to the global n=1 kink mode; stability at values of α that are roughly 50% higher is obtained if an ideal wall is added at $r_{wall}/a = 1.2$, assuming sufficient toroidal rotation and wall stabilization effect. In particular, the equilibrium corresponding to the point at $R_0/L_T = 16.3$ and $\alpha = 1.8$ is MHD-stable with an ideal wall and is only weakly unstable to ITG modes; it is the most interesting global case in our scan. The corresponding profiles are those of Fig. (1).

Conclusions. We studied the simultaneous access to second stability for ITG modes and for

THEORY OF ION BERNSTEIN AND LOWER HYBRID WAVES SYNERGY

A. Cardinali, S. Bernabei*, F. Paoletti†, W. Tighe*, S. von Goeler*

Associazione Euratom-ENEA sulla Fusione, Centro di Frascati,
C.P. 65 - 00044 Frascati, Rome (Italy)

INTRODUCTION

The synergistic behavior of a lower hybrid wave (LHW) and an ion Bernstein wave (IBW) on the PBX-M tokamak is theoretically investigated on the basis of a quasilinear model. The analytical approach to this investigation is oriented to solve simultaneously, the 2D ray tracing equation for both waves, to reconstruct the WKBJ electric field and the quasilinear diffusion coefficient. The Fokker-Planck equation for the 2-D distribution function is numerically solved and coupled to the ray tracing in the calculation of the absorption. A numerical code which solves the ray tracing equations and calculates the 2 D ($v_{\|}$,$v_{\perp}$) distribution function has also been run to compare the results with the analytical one. The numerical and analytical results are compared with the experimental observations obtained by a 2-D hard X-ray (HXR) camera[1]. The camera measures the bremsstrahlung emission from fast electrons on the tail of the distribution function. Experimentally, when IBW is injected in a plasma during LHCD, there is a strong increase in the HXR emission with respect to the signal detected with LHW alone[2]. This increase appears to be predominantly localized off-axis. This phenomenology can be correlated with the Landau damping of the LHW power on the tail of the electron distribution function modified by IBW.

THEORY AND CALCULATION RESULTS

In our model (analytical and numerical), we consider the interaction between LHW and IBW, by coupling a 3-D toroidal IBW+LHW ray-tracing algorithm with a 2-D ($v_{\|}$,$v_{\perp}$) relativistic Fokker-Plank code. On each magnetic surface, the quasilinear distribution function is calculated as a result of the presence of both waves. This distribution function is used to calculate the power decrement and the non-inductive current and power density profiles.

In previous studies, an analytical solution of the ray-tracing equations for IBW were obtained[3,4,5]. Following this formalism, we observe that the parallel wave number oscillates along the trajectory with a frequency that increases as the ray approaches the plasma center. From the Poynting theorem we obtain the expression of the field squared amplitude in terms of the antenna power spectrum. Substituting the quantity in the expression which gives the quasilinear diffusion coefficient we obtain the following expression:

---

* Plasma Physics Laboratory, Princeton, NJ, USA

† Columbia University, New York, NY, USA

$$< D(v_{||}, r,) >= \Sigma_{\psi}^{-1} \int_{\Delta\Sigma_{\psi}} d\Sigma_{\psi} \frac{16\pi^2 (e/m_e)^2 P_{cgs}}{\nu^{ee} v_{the}^2 \omega |v_{||}|} \cdot \left[\frac{P_{NOR}(n_{||}) \exp\left(-2 \int_0^t \Gamma dt \right) \delta(\frac{c}{v_{||}} - n_{||})}{(1+\alpha_{pol}^2)(\partial H/\partial n_{\psi}) \Delta\Sigma_{\psi}} \right] \quad (1)$$

$$\Gamma = \frac{\mathbf{k} \cdot \mathbf{e}^A \cdot \mathbf{k}}{|k|^2 (\partial H/\partial \omega)} = \frac{2\pi^2}{\partial H/\partial \omega} \frac{\omega_{pe}^2}{\omega^2} \frac{k_{||}}{|k_{||}|} [k_{||} \omega v_{the} x_{0e}] \int_0^{\infty} v_{\perp} dv_{\perp} \frac{\partial F_{0e}}{\partial v_{||}} \quad (2)$$

which is the damping. In eqs. (1) and (2), $v_{||}$ is the resonant parallel velocity ($v_{||}=c/n_{||}$), $\alpha_{pol}=E_{\perp}/E_{||}$ is the polarization factor which can be deduced from the dispersion relation, $(\partial H/\partial n_{\psi})$ is the time-normalized group velocity $\left((\partial H/\partial n_{\psi})=v_{group}(\partial H/\partial \omega)\right)$, and H is the electrostatic dispersion relation. In eq. (1), P_{cgs} is the total launched power in cgs unit, P_{NOR} is the normalized power spectrum. The IBW quasilinear diffusion coefficient has an oscillating behaviour because it follows the oscillation of the parallel wavenumber. Due to this oscillatory behavior, quasilinear modifications of the distribution function are localized in space. The power damping and the current generation are also regulated by the oscillation of $n_{||}$. Fig. 1 shows the simulated power density profile generated by the presence of both waves (solid line) and the damping of the LHW (dotted) and IBW (dashed) propagating spectra. The peaks in the deposition that we observe in Fig. 1 can be seen as current channels generated by IBW in localized regions of the space. Due to the limited spatial resolution of the HXR camera (±5 cm), we are able to detect only the first oscillation. It is interesting to note that the LHW damps strongly in correspondence to the first two deposition locations of the IBW. This signifies that the IBW in these zones modifies so strongly the distribution function to allow a consequent deposition of the LHW. In the case of LHW alone the wave deposition was located on the magnetic axis. The plasma parameters of a typical target plasma used in the LHW+IBW experiment on PBX-M are: I_p=120 kA, B_0= 1.89 T, $n_e(0) = 2.5\times10^{13}$ cm^{-3}, $T_e(0)$=1.1 keV, R_{mag}=164 cm, a=32 cm, q(0)=0.8, q(a)=3.0. The features of the IBW system are: n_{IBW}=43 MHz, $n_{||}$(range)=±[2-16], $n_{||}$(peak)=±9, P_{IBW}= 50 kW, Pulse Duration=400-450×10^{-3} s. While, the characteristics of the LH system are: n_{LH}=4.6 GHz, $n_{||}$(range)=[1.9-2.3], $n_{||}$(peak)=2.1, P_{LH}=139 kW, Phase=90°, Pulse Duration=300-600×10^{-3} s. For the specific case of the shown PBX-M plasma discharge, $n_{||}$ reaches its first maximum around x=0.56 which corresponds to a radial location of R=181.9 cm.

EXPERIMENTAL FINDINGS

The HXR diagnostic is a pinhole camera providing a tangential view of the PBX-M plasma[1,2]. Our investigation is based on horizontal profiles obtained operating a cut of the HXR

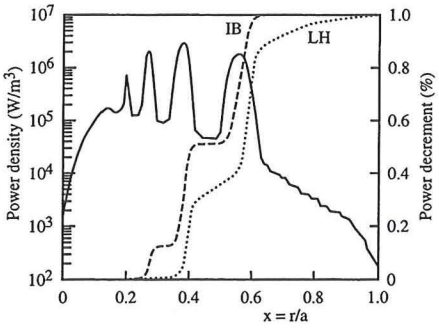

Fig. 1 - Simulated power density profile (solid line) and IBW (dashed)/LHW (dotted) damping generated by IBW and LHW vs. normalized minor radius.

images along the midplane through the plasma center. To assess the impact of IBW injection during LHCD, we refer to the time evolution of the spatial profile of the variable: $\Delta_{HX}(t) \equiv I_{HX}(t_{LH+IBW}) - I_{HX}(t_{LH})$ where: $I_{HX}(t_{LH})$ is the vertical HXR intensity at a time frame just before the onset of IBW (i.e., when only LHW is present) and $I_{HX}(t_{LH+IBW})$ is the vertical HXR intensity at a time when both types of waves are present in the plasma. In this experiment, the data acquisition was programmed to have one HXR image every 5 ms. We refer to each image as a *time frame*.

In Fig. 2a we show traces of $\Delta_{HX}(t)$ at different time frames for a typical circular PBX-M plasma. Since the IBW is triggered at 400 ms with a sharp ramp-up, so we can choose the reference LH-only time frame as: t_{LH}=400 ms. At t= 410 ms (time-frame #24), this centrally-peaked distortion extends up to R=182 cm. At t=415 ms (time-frame #25), a distinct peak begins to emerge around R=180 cm. At t=415 ms (time-frame #26), the peak is very well formed and represents the major part of the distortion in the HXR emission. The synergy between LHW and IBW appears to take place more efficiently in a region located off-axis as if the IBW electric field, interacting with the bulk electrons located in that region of space, moves them at higher energy where they are accelerated by the LHW. Following the evolution of the discharge, as in Fig. 2b, we see the peak in $\Delta_{HX}(t)$ moving further out from its original position while it is growing in amplitude. This effect can be related to two different coexisting causes; first, a radial diffusion of the fast electrons population. This diffusion would help the extension of the suprathermal electron tail in the more peripheral regions enhancing the damping rate of the IBW low $n_{||}$ wave component. Second, a LHW *first-pass* damping on the tail of the distribution which has been extended in space and sustained by IBW. This can be seen as a non-linear loop interaction between LHW and IBW where the latter can help the former to be partially deposited off-axis. After IBW is turned off at t=450 ms (frame #32 in Fig 2b.) the off-axis peak in $\Delta_{HX}(t)$ continues to rise for about 10-15 ms proving the fact that now LH alone is damping off-axis on a tail that is progressively disappearing. At this point, in fact, the profile starts relaxing towards its original shape while the variable $\Delta_{HX}(t)$ goes to zero. Here, LH

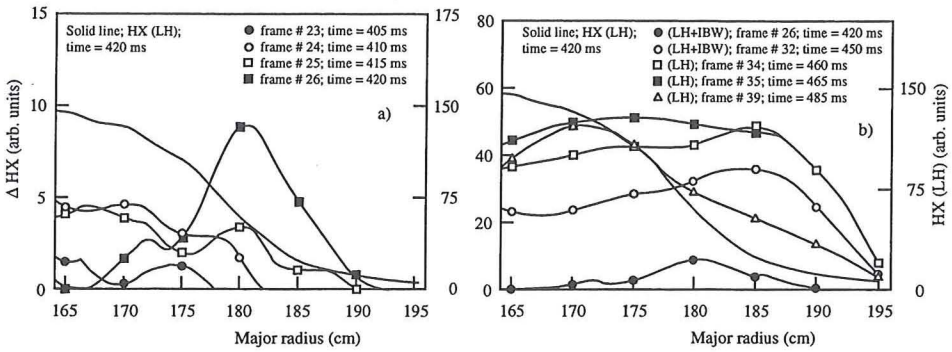

Fig. 2 - Plot of $\Delta_{HX}(t)$ vs. major radius for different time-frames for a PBX-M circular discharge

waves no longer find enough fast electrons in the off-axis regions and they are required to reach the center to deposit their power (frame #34,35,39 in Fig. 2b). We can conclude that the location of the peak we observe from the analysis of the HXR images is consistent with the location of the region of strong interaction around the first maximum of the IBW $n_{||}(x)$ oscillation.

CONCLUSIONS

Our theoretical investigation included the use of a toroidal 3-D LHW+IBW ray-tracing + 2-D Fokker-Planck numerical code as well as the analytical integration of the WKBJ equations for both waves. The results can be summarized as follows: due to the IBW $n_{||}$ oscillatory behavior, the IBW power is deposited in limited regions of space. The distortion of the distribution function owing to IBW deposition induces a consequent deposition of the LHW in localized zones of the plasma. Moreover the IBW power, damped on a preexisting electron tail (generated through LHCD), generates, in turn, localized current channels. We presented too, a strong experimental confirmation of a synergistic interaction between LH and IB waves on PBX-M. We reached the following conclusions: variations of the HXR emission profile, induced by IBW during LHCD, are predominantly observed off-axis. We refer to this result as the experimental proof of the LHW deposition on the tail formed by the successive IBW injection. During central LHCD, a portion of the LH power can be deposited off-axis with a *first pass* damping on the electron tail sustained by IBW.

REFERENCES

1. von Goeler, S., et al., *Rev. Sci. Instrum.* **65**, 1621, (1994).
2. Tighe, W., et al., *Bull. Am. Phys. Soc.* **38**, 2094 (1993).
3. Cardinali, A., and Romanelli, F., *Phys. Fluids B* **4**, 504 (1992).
4. Cardinali, A., *Phys. Fluids B* **5**, 2778 (1993).
5. Cardinali, A., et al., *Phys. Plasmas* **2**, 1510 (1995).

Modeling of quasi-linear RF heating effects in complex magnetic geometries*

S.V. Kasilov

Institute of Plasma Physics, National Science Center "Kharkov Institute of Physics and Technology", ul. Akademicheskaya 1, 310108 Kharkov, Ukraine

1. Introduction. The modeling of quasilinear RF heating effects in toroidal magnetic traps with broken axial symmetry (stellarators, tokamaks with toroidal field ripples) is an important task. Presently, due to the high dimensionality, only the Monte-Carlo (MC) methods can address this problem without simplifying the unperturbed particle motion significantly. However, a full account of nonlocal wave-particle interaction in MC models is still required. At the same time, due to the low computational speed of traditional MC methods based on the direct integration of stochastic particle orbits it is desirable to develop more efficient MC approaches. In the present report, the background for consistent numerical model of quasilinear particle dynamics [1-3] and an efficient new MC method for the solution of drift-kinetic equation in complex magnetic geometries based on the stochastic mapping technique [4] are summarized. The nonlocal quasilinear MC-operators are then presented for the traditional MC method and for the new method.

2. The non-local drift kinetic quasilinear equation. The slow dynamics of the distribution function during RF heating is described by the non-local drift-kinetic quasilinear equation which in covariant form is

$$\frac{\partial f}{\partial t} + V^\alpha \frac{\partial f}{\partial z^\alpha} = \hat{L} f - \nu_0 f + Q, \quad \hat{L} f = \frac{1}{J}\frac{\partial}{\partial z^\alpha} J \left(D^{\alpha\beta} \frac{\partial f}{\partial z^\beta} - F^\alpha f \right). \qquad (1)$$

Here, $\mathbf{z} = (\mathbf{x}, \mathbf{y})$ is a set of 5 guiding center variables where $(x^1, x^2, x^3 \equiv \vartheta)$ are some curvilinear spatial coordinates of the guiding center, $\mathbf{y} = (\mathcal{E}, \mu)$, where $\mathcal{E} = m_0 c^2 \gamma + e\varphi_0$, $\mu = p_\perp^2/(2m_0 B_0)$ are total energy and magnetic moment, $J = m_0^2 \gamma B_0 \sqrt{g(\mathbf{x})}/|p_\parallel|$ is the Jacobian, Q and ν_0 represent generalized particle sources and sinks due to inelastic processes, and V^α is the 5D velocity of the unperturbed motion in the guiding center approximation ($V^4 = V^5 = 0$). The full collision operator $\hat{L}$ has a form $\hat{L} = \hat{L}_C + \hat{L}_{QL}$, where $\hat{L}_C$ and $\hat{L}_{QL}$ are the operators describing Coulomb collisions and quasilinear effects respectively. The coefficients of the quasilinear operator $\hat{L}_{QL}$ have been derived in [3] with the account of the collisional wave-particle decorrelation effect [1,2] which may significantly affect the RF power absorption [5]. With some change in notation the coefficients take the following form,

$$D_{QL}^{ij} = \frac{1}{4}\mathrm{Re} \sum_{m=-\infty}^{\infty} \int_{-\infty}^{0} \mathrm{d}\tau \left[a_m^{i*}(\mathbf{z}) a_m^j \left(\mathbf{Z}(\tau, \mathbf{z})\right) + a_m^{j*}(\mathbf{z}) a_m^i \left(\mathbf{Z}(\tau, \mathbf{z})\right) \right] \exp(\eta_m) \qquad (2)$$

*This work was partly supported by Ukrainian Foundation of Fundamental Research project 2.4/699 and by the Association EURATOM-OEAW under contract number ERB 5004 CT 96 0020

The force in $\hat{L}_{QL}$ is ponderomotive, and is given the non-canonical Poisson brackets defined in Ref.[6] as $F^i_{QL} = \{z^i, K\}$, where the ponderomotive Hamiltonian K is

$$K = \frac{1}{4}\mathrm{Re}\sum_{m=-\infty}^{\infty}\left[im\omega_c\left(\frac{\gamma}{B_0}\frac{\partial}{\partial\mu}+\frac{\partial}{\partial\mathcal{E}}\right)\tilde{H}^*_m\tilde{S}_m+\left\{\tilde{H}^*_m,\tilde{S}_m\right\}\right]+\langle\langle\hat{H}\rangle_t\rangle_\phi. \tag{3}$$

The set of functions $Z^i(\tau,\mathbf{z})$ is the solution to equations of motion in guiding center approximation, $\dot{z}^i = V^i(\mathbf{z})$, with initial condition $Z^i(0,\mathbf{z}) = z^i$,

$$\tilde{S}_m = \int_{-\infty}^{0} d\tau \tilde{H}_m(\mathbf{Z}(\tau,\mathbf{z}))\exp(\eta_m), \quad \eta_m = -i\int_0^{\tau} d\tau' \left[\omega + m\omega_c\left(\mathbf{Z}(\tau',\mathbf{z})\right)\right] + \delta\Phi_m(\tau,\mathbf{z}) \tag{4}$$

$$a^i_m(\mathbf{z}) = \frac{1}{2\pi}\int_{-\pi}^{\pi} d\phi\, \exp(-im\phi)\left\{z^i, \tilde{H}(\mathbf{z},\phi)\right\}, \quad \tilde{H}_m = \frac{1}{2\pi}\int_{-\pi}^{\pi} d\phi \exp(-im\phi)\tilde{H}(\mathbf{z},\phi) \tag{5}$$

$$\tilde{H}(\mathbf{z},\phi) = \frac{ie}{\omega}\mathbf{v}\cdot\mathbf{E}_A(\mathbf{r}), \quad \langle\langle\hat{H}\rangle_t\rangle_\phi = \frac{e^2}{4\omega^2 m_0\gamma}\frac{1}{2\pi}\int_{-\pi}^{\pi} d\phi\left(|\mathbf{E}_A(\mathbf{r})|^2 + \frac{1}{c^2}|\mathbf{v}\cdot\mathbf{E}_A(\mathbf{r})|^2\right), \tag{6}$$

where $\mathbf{E}_A$ is a complex electric field amplitude, $\tilde{\mathbf{E}}(t,\mathbf{r}) = \mathrm{Re}\left(\mathbf{E}_A(\mathbf{r})\exp(-i\omega t)\right)$. Here $\mathbf{v} = \mathbf{v}(\mathbf{z},\phi)$ and $\mathbf{r} = \mathbf{r}(\mathbf{z},\phi)$ are the actual particle velocity and radius-vector, ϕ is the gyrophase, ω and $\omega_c = eB_0(\mathbf{x})/(m_0c\gamma)$ are the wave frequency and the relativistic cyclotron frequency respectively. Note that as usual in non-canonical Hamiltonian formalism [6], the RF electromagnetic field is included here into phase space variables, $\mathbf{p} = \mathbf{p}_k + e\tilde{\mathbf{A}}(t,\mathbf{r})/c$, where $\tilde{\mathbf{E}}(t,\mathbf{r}) = -\partial\tilde{\mathbf{A}}(t,\mathbf{r})/(c\,\partial t)$ and $\mathbf{p}_k$ is the kinematic momentum.

The expression for the collisional decorrelation function $\delta\Phi_m$ is obtained (see [2]) in the spatial coordinates aligned to the magnetic field, $\mathbf{B}_0\nabla x^{1,2} = 0$, so that the coordinate lines of x^3 coincide with magnetic field lines,

$$\delta\Phi_m(\tau,\mathbf{z}) = \int_0^{\tau} d\tau' \alpha_i\left(\tau-\tau',\mathbf{Z}(\tau',\mathbf{z})\right)\alpha_j\left(\tau-\tau',\mathbf{Z}(\tau',\mathbf{z})\right)D^{ij}_C\left(\mathbf{Z}(\tau',\mathbf{z})\right), \tag{7}$$

where

$$\alpha_i(\tau,\mathbf{z}) = \int_0^{\tau} d\tau' \frac{\partial}{\partial y^i}\left[\omega + m\omega_c\left(\mathbf{Z}(\tau',\mathbf{z})\right)\right] - \frac{\partial Z^3(\tau,\mathbf{z})}{\partial y^i}\,\frac{\omega + m\omega_c\left(\mathbf{Z}(\tau,\mathbf{z})\right)}{V^3\left(\mathbf{Z}(\tau,\mathbf{z})\right)} \tag{8}$$

and D^{ij}_C are coefficients of Coulomb diffusion operator $\hat{L}_C$. Note, that the field-aligned spatial coordinates are used only in eqs. (7) and (8) and further in the formalism the spatial coordinates $\mathbf{x}$ as well as the momentum space coordinates $\mathbf{y}$ can be kept general, if the corresponding tensor transform of the coefficients in eq. (1) is used.

The above integral expressions for the nonlocal quasilinear operator $\hat{L}_{QL}$ are strictly converging due to the presence of the collisional decorrelation function $\delta\Phi_m$ which describes the phase memory loss by resonant particles. This operator which is applicable

to collisionless and collisional confinement regimes, takes into account in its integral form the detailed structure of the wave electromagnetic field and the nonlocal nature of the wave-particle interaction. Therefore, it can be directly used for to model numerically the particle dynamics in magnetic traps with general magnetic field geometry. In systems with axial symmetry in the collisionless regimes, the canonical (bounce) averaging procedure can be applied to this operator and it reduces to the known Hamiltonian form of the quasilinear operator (see [7]) if the collisional decorrelation effects do not show up explicitly. Actually, this happens if decorrelation is negligible within the cyclotron resonance zone but nevertheless leads to a complete phase memory loss about the previous passes by particle of the resonance zones.

3. Stochastic mapping technique. In 5D phase space, Poincaré cuts are introduced as 4D hypersurfaces defined by $\vartheta - \vartheta_{(m)}(\mathbf{u}) = 0$, where $\mathbf{z} = (\vartheta, \mathbf{u})$, $\mathbf{u} = (x^1, x^2, y^1, y^2)$. For negligible quasistationary parallel electric field, these are surfaces where the magnetic field is minimum along the magnetic field lines properly extended with respect to 2D momentum space. Subscript m numbers these cuts (not to confuse with gyrophase harmonic subscript in the previous section). The unperturbed particle motion can be described in terms of a particle coordinate map from cut m with starting values $\mathbf{u}_m$ to the next cut the particle hits at $\mathbf{u}_{m'}$ when moving along its unperturbed trajectory. Obviously, just 3 types of transitions are possible characterized by $m' = m_+, m_-$ which label the cuts crossed by "passing" orbits in positive and negative directions with respect to the magnetic field direction, and by $m' = m$ for a "trapped" orbit. A "bounce" time $\tau_b(\mathbf{u}_m)$ is defined as the time required by the particle for a single transition of this kind.

In the case of weak "collisions", such that $\tau_b \ll \tau_c$, where τ_c is the characteristic time of any stochastic "collisional" process described by the right-hand side of (1) this equation can be reduced to a stochastic mapping equation for the particle flux density $\Gamma_m(\mathbf{u}_m) = J_m(\mathbf{u}_m) f(t, \vartheta_{(m)}(\mathbf{u}_m), \mathbf{u}_m)$ per unit area d^4u_m of the Poincaré cut,

$$\Gamma_{m'}(t, \mathbf{u}_{m'}) \frac{\partial(\mathbf{u}_{m'})}{\partial(\mathbf{u}_m)} - \Gamma_m(t, \mathbf{u}_m) = \frac{\partial^2}{\partial u_m^i \partial u_m^j} \bar{D}_m^{ij}(\mathbf{u}_m) \Gamma_m(t, \mathbf{u}_m) - \tag{9}$$

$$- \frac{\partial}{\partial u_m^i} \mathcal{F}_m^i(\mathbf{u}_m) \Gamma_m(t, \mathbf{u}_m) - \tau_b(\mathbf{u}_m) \frac{\partial}{\partial t} \Gamma_m(t, \mathbf{u}_m) - \bar{\nu}_0(\mathbf{u}_m) \Gamma_m(t, \mathbf{u}_m) + J_m(\mathbf{u}_m) \bar{Q}(\mathbf{u}_m),$$

where

$$\mathcal{F}_m^i = \bar{F}_m^i + \frac{1}{J_m} \frac{\partial}{\partial u_m^j} J_m \bar{D}_m^{ij}, \qquad J_m = J V^\alpha \frac{\partial}{\partial z^\alpha} \left(\vartheta - \vartheta_{(m)}(\mathbf{u}) \right) \Big|_{\mathbf{z}=\mathbf{z}_m}, \tag{10}$$

and $\mathbf{z}_m = (\vartheta_{(m)}(\mathbf{u}_m), \mathbf{u}_m)$. The bared quantities in (9) are time integrals of the respective local quantities previously transformed to the Lagrangian coordinates $\mathbf{u}_m$, along the unperturbed trajectory which emanates from cut m and ends at cut m'.

In this way, the problem of dynamic motion has been separated from modeling the stochastic processes described by (9). The solution of the dynamic problem is obtained with usual ODE integration methods for a certain mesh of initial conditions. The resulting mapping functions, $\mathbf{u}_{m'}(\mathbf{u}_m)$, as well as all other quantities in (9) are then reconstructed by interpolation. The stochastic mapping equation (9) is finally solved with a Monte-Carlo algorithm, consisting of the following steps: (1) particles are removed and added to the cuts with event probabilities $\bar{\nu}_0(\mathbf{u}_m)$ and $J_m\bar{Q}(\mathbf{u}_m)$ respectively; (2) particles remaining on the cuts are shifted in u^i_m by δu^i_m restricting the averages of the random shift δu^i_m to satisfy $\langle \delta u^i_m \rangle = \mathcal{F}^i_m(\mathbf{u}_m)$, $\langle \delta u^i_m \delta u^j_m \rangle = 2\bar{D}^{ij}_m(\mathbf{u}_m)$; particles are exchanged between the cuts according to the unperturbed mapping function $\mathbf{u}_{m'} = \mathbf{u}_{m'}(\mathbf{u}_m)$ and $t' = t + \tau_b(\mathbf{u}_m)$. Note that the higher moments of the random shift δu^i_m introduce small errors of order of τ_b/τ_c. Within this approximation one can model separately the collisional and quasilinear diffusion using the independent random numbers for constructing the respective shifts. In particular, if the small direct modification of the orbit in coordinate space by RF interaction is not important, for the case described at the end of previous section the shifts in momentum space over the variables $u^i_m = \mathcal{E}, \mu$ are

$$\delta u^i_m = \beta^i \left(\sqrt{2\bar{D}^{\mathcal{E}\mathcal{E}}_{QL}}\,\xi + \beta^j \frac{\partial}{\partial u^j_m} \bar{D}^{\mathcal{E}\mathcal{E}}_{QL} \right), \quad \beta^{\mathcal{E}} = 1, \quad \beta^{\mu} = \frac{ne}{\omega c m_0}, \tag{11}$$

$$\bar{D}^{\mathcal{E}\mathcal{E}}_{QL} = \frac{\omega^2}{4} \sum_r \left| \int_{-\infty}^{\infty} \tilde{H}_{-n}(\mathbf{Z}(\tau, \mathbf{z}_r)) \exp\left[i \int_0^{\tau} \mathrm{d}\tau' \left(n\omega_c(\mathbf{Z}(\tau', \mathbf{z}_r)) - \omega \right) \right] \right|^2 . \tag{12}$$

Here ξ is a random number satisfying $\langle \xi \rangle = 0$ and $\langle \xi^2 \rangle = 1$, H_{-n} is given by (5), $\mathbf{z}_r$ are the resonance points which particle crosses during the bounce time and the infinite integration limits over τ assume that the cyclotron frequency is to be expanded over τ' up to the linear (quadratic) order. Note that the shift (11) can be used also in conventional Monte-Carlo methods with direct integration of stochastic orbit where the cyclotron interaction is modeled as an instantaneous change in momentum space coordinates immediately after the particle crosses the cyclotron resonance point.

1. Kasilov S.V., Pyatak A.I., Stepanov K.N. Nucl.Fusion **30** (1990) p.2467.
2. Kasilov S.V., Pyatak A.I., Stepanov K.N. Intern. School of Plasma Physics "Theory of Fusion Plasma", Varenna, 1990. p.301.
3. Kasilov S.V., Pyatak A.I., Stepanov K.N. 22-nd EPS Conf. on Contr.Fusion and Plasma Phys., Bournemouth, 1995, Pt.III, p.349.
4. Kasilov S.V., Moiseenko V.E., Heyn M.F. Phys.Plasmas **4** (1997) p.2422.
5. Van Eester D., Lois Y., Lamalle P.U., Koch R. Phys.Lett.A **218** (1996) p.70.
6. Grebogi C., Littlejohn R.G. Phys.Fluids **27** (1984) p.1996.
7. Timofeev A.V., Tokman M.D. Plasma Phys.Reports **20** (1994) p.1994.

Multiple Autoresonance Accelerations Generated from a Chaotic Base

Y. Gell

CET, P.O.B. 39513, Tel-Aviv 61394, Israel

R. Nakach

Département de Recherches sur la Fusion Contrôlée, Association Euratom – Commissariat à l'Energie Atomique, Centre d'Etudes de Cadarache, 13108 St. Paul lez Durance Cedex, France

ABSTRACT

A multiple autoresonance process for accelerating electrons is presented. It is based on the autoresonance mechanism forwarded in a previous publication [Phys. Lett. A 207, 342 (1995)]. The configuration under study consists of two circularly polarized electromagnetic waves propagating in opposite directions along a constant magnetic field and having frequencies in the electron frequency range. Such a configuration admits under appropriate conditions stochastic motion of the particle. It is shown that the stochastic nature of the motion plays an important role for inducing the multiple autoresonance acceleration. The threshold for onset of stochasticity when considering waves with different characteristics and particles with different initial conditions is evaluated and compared with the numerical data. It is shown that for a proper choice of the parameters of the system, the multiple autoresonance process can generate a bulk of particles moving in a preferential direction and having a considerable time averaged velocity paralell to the magnetic field. Practical applications of this result are mentioned.

Multiple Alfven Eigenmodes in Conventional and Spherical Tokamaks

S.E.Sharapov

JET Joint Undertaking, Abingdon, Oxfordshire OX14 3EA, UK

Conditions for multiplicity of weakly-damped Alfven Eigenmodes (AE) and for the AE excitation by energetic ions are shown to be more favourable for spherical tokamaks (ST) than for conventional tokamaks. Main reasons for the greater importance of unstable AEs in spherical tokamaks are the tight aspect ratio, $a / R_0 \leq 1$ and very low magnetic field, $B_0 \cong 0.3 - 0.6\ T$.

The tight aspect ratio is shown to induce in spherical tokamak an enlarged TAE-gap in the Alfven continuum of the order of $\Delta\omega \cong (5/2)(r / R_0) \leq \omega$; it also significantly affects the Ellipticity and Triangularity induced gaps due to non-small ε^2, ε^3 effects. Structure of Low-Shear Multiple TAEs, which exist in ideal MHD at $\varepsilon / S \geq 1$ [1], is compared for ST and for the "shear-optimised" JET discharges. Existence of multiple Low-Shear AEs, associated with ellipticity and triangularity induced gaps is demonstrated .

Due to small magnetic field in ST the bulk ion FLR effects becomes important even at moderate plasma temperatures. Effect of the FLR-induced splitting of Alfven continuum onto multiple Kinetic TAEs is demonstrated and relation between ideal MHD Low-Shear TAEs and Kinetic TAEs is described.

Energetic particle drive for the different AEs is calculated and possibility of anomalous transport of energetic particles in ST is discussed.

[1] J.Candy, B.N.Breizman, J.W.Van Dam and T.Ozeki, Phys. Lett. **A215**, 299 (1996).

Poloidal flows in resistive MHD equilibria

David Montgomery and Jason W. Bates
Dept. of Physics & Astronomy, Dartmouth College
Hanover, New Hampshire 03755-3528, U.S.A.

Abstract

We argue that poloidal velocity fields are a necessary part of any resistive toroidal MHD steady state. They are a consequence of force balance in toroidal geometry, and need involve no instabilities of any kind. If a current density $\mathbf{j}$ results from an axisymmetric toroidal electric field that is curl-free inside the toroid, it leads to a magnetic field $\mathbf{B}$ such that the curl of $\mathbf{j}\times\mathbf{B}$ is non-vanishing; $\mathbf{j}\times\mathbf{B}$ cannot be balanced, therefore, by the gradient of any scalar pressure. In a steady state, velocity fields are required, associated with toroidal vorticity. The effect is purely geometrical, and disappears in the "straight periodic cylinder" approximation. In the limit of low Reynolds numbers, the velocity field may be straightforwardly calculated for stress-free boundary conditions. A recent generalization to no-slip boundary conditions in toroidal coordinates has likewise proved possible. Zero-flow steady states are possible if the conductivity is allowed to be spatially non-uniform; but the non-uniformity is such that the conductivity varies over a flux surface, and is likely unphysical. Our picture of confined steady states in toroidal MHD should necessarily include flows, from the outset.

We open a magnetohydrodynamic question sometimes considered settled: What are the allowed steady states of a toroidal magnetically-confined magnetofluid? We argue that in the presence of finite resistivity and viscosity, there are inevitably flows (velocity fields). Others have concluded the same thing (*e.g.*, Pfirsch and Schlüter [1], Grad and Hogan [2]), but our flows are qualitatively different and are there for different reasons. We believe that in addition to mechanical force balance, Ohm's and Faraday's laws must be taken equally seriously. Externally-supported electric fields must be present and must be curl-free inside the magnetofluid. These demands complicate the mathematics and greatly restrict the allowed steady states. Imposing boundary conditions, including electromagnetic ones, makes the states virtually unique.

One may ask why we reopen MHD questions of this kind, when it is certain that simple one-fluid MHD with scalar transport coefficients is a poor approximation to fusion plasma dynamics. The answer must be that MHD is our only analytical framework for finding global steady states, and while it may need refinement, the simplest version of MHD is where we should start. In the following discussion, we confine ourselves from the outset to axisymmetric boundary conditions and configurations. Space limitations require that we refer to other papers [3-9] for graphic displays of the details of the MHD steady states.

The equations to be satisfied in the steady state are taken to be

$$\rho\mathbf{v}\cdot\nabla\mathbf{v} = \mathbf{j}\times\mathbf{B}/c - \nabla p + \rho\nu\nabla^2\mathbf{v}\,, \tag{1}$$

$$\mathbf{E} + \mathbf{v}\times\mathbf{B}/c = \eta\mathbf{j}\,. \tag{2}$$

along with $\nabla\times\mathbf{E} = 0$. Here, $\mathbf{v}$ is the velocity, $\mathbf{B}$ is the magnetic field, $\mathbf{j}$ is the current density, $\mathbf{E}$ is the electric field, p is the mechanical pressure, and ν and η are the kinematic viscosity and electrical resistivity, respectively. We assume uniform mass density and

incompressible flow, both restrictions it would be desirable to remove. In the "Alfvénic" dimensionless units, Eqs. (1) and (2) are modified by the disappearance of ρ and c, with ν and η replaced, respectively, by the reciprocals of viscous and resistive Lundquist numbers, and with $\nabla\times\mathbf{B} = \mathbf{j}$.

The curl-free electric field may be written as $-\nabla\Phi$, but in toroidal geometry, the scalar potential Φ will not be single valued, and will contain a term proportional to the toroidal angle. To this basic toroidal electric field can be added the gradient of another scalar, which will follow from solving Laplace's or Poisson's equation [obtained from the divergence of Eq. (2)] subject to boundary conditions.

With no flow ($\mathbf{v} = 0$), a current density results from Eq. (2) that, upon solving for the associated $\mathbf{B}$, leads [3-6,8,9] to a non-vanishing value of $\nabla\times(\mathbf{j}\times\mathbf{B})$, no matter what vacuum component of $\mathbf{B}$ may be present. This means that $\mathbf{j}\times\mathbf{B}$ in Eq. (1) can never be balanced by a pressure gradient alone: velocity fields are required for mechanical force balance. The two velocity-dependent terms in Eq. (1) stand in the ratio of the mechanical Reynolds number, and one of them must be what it takes to cancel the part of $\mathbf{j}\times\mathbf{B}$ that has a curl. The regime which we have so far found calculable (maybe not the most important one) is that of low Reynolds number, or slow flow, so that the viscous term in Eq. (1) must be retained while the inertial term is dropped. (We assume spatially uniform transport coefficients; permitting a wholly general spatial variation of them [5] allows only unphysical zero-flow states to exist.)

Low Reynolds number is in a sense a "high viscosity" regime. The viscous stress tensor is a poorly understood or measured plasma quantity, with viscosity coefficients that differ enormously. If the "ion parallel" viscosity is used to estimate ν, for example, it is more than large enough to justify low Reynolds numbers, while the "shear" viscous coefficient is much too small. For present purposes, we assume the viscosities to be large enough to justify the low Reynolds number approximations (in detail, they are justifiable in the limit of low viscous Lundquist number M [6,8,9]).

Keeping only the lowest significant order in M, it can be shown that Eqs. (1) and (2) reduce to (dimensionless units now):

$$\nabla p - \mathbf{j}\times\mathbf{B} = \nu\nabla^2\mathbf{v}\,, \tag{3}$$

$$\mathbf{E} = \eta\mathbf{j}\,. \tag{4}$$

Thus Ohm's law [Eq. (4)] determines the toroidal $\mathbf{j}$ and thus (with boundary conditions) the poloidal $\mathbf{B}$ (see Fig. 1). The force balance equation, Eq. (3), is then used to determine $\mathbf{v}$ necessary for a steady state. This may be done in two steps, first by taking the curl of Eq. (3) and then its divergence. This leads to a vector Poisson equation for the vorticity and a scalar Poisson equation for the pressure. The vorticity may be found by a spectral method, and the velocity then determined from it upon imposing a boundary condition. We have found the most tractable boundary condition on $\mathbf{v}$ to be one that is stress-free, and the most tractable boundary one with straight edges [5, 6, 9], but Bates and Montgomery have recently proved it possible to satisfy no-slip boundary conditions at a circular boundary [7, 8]. The pressure equation can also be solved spectrally.

At lowest order, the velocity field turns out to be purely poloidal, and to have a dipolar character [6]; see Fig. 2. To lowest order, there are no corrections to the (vacuum) toroidal magnetic field, for scalar resistivity. Recently, Kamp *et al.* [9] have gone beyond the lowest significant order in powers of the Lundquist number, and have found toroidal contributions to $\mathbf{v}$, as well, again with a rectangular poloidal boundary shape. This resulting velocity field consists of four distinct vortices, with streamlines that are essentially

helical and which reverse the toroidal velocity direction both across the mid-plane and at the vertical center line of the cross section of the toroid. Their poloidal projections look like Fig. 2.

The seeming ubiquity of velocity fields has implications for virtually all of analytical MHD concerned with confinement theory. Instabilities of various kinds have typically been calculated on zero-flow, ideal MHD equilibria, even when they are resistive in character. It will require time and experience to determine how the presence of flows in the equilibria will modify the catalogue of instabilities. It should be noted that the vocabulary we use now to assess the dynamical behavior of confinement devices largely derives from linear instability analyses of ideal MHD steady states without flow, and our thinking is to a high degree conditioned by such analyses. There is no reason to expect that linear instabilities of resistive steady states with flow will be only minor modifications of the zero-flow instabilities already in the catalogue.

Acknowledgement

This work was supported in part by the U.S. Department of Energy.

References

[1] Pfirsch, D., Schlüter, A., Max-Planck-Institut Report MPI/PA/7/62 (1962)

[2] Grad, H., Hogan, J., Phys. Rev. Lett. **24** (1970) 1337

[3] Montgomery, D., Shan, X., Comm. Plasma Phys. & Contr. Fusion **15** (1994) 315

[4] Bates, J.W., Lewis, H.R., Phys. Plasmas **3** (1996) 2395

[5] Montgomery, D. *et al.*, Phys. Plasmas **4** (1997) 1080

[6] Montgomery, D. *et al.*, Phys. Fluids **9** (1997) 1188

[7] Bates, J.W., J. Math. Phys. **38** (1997) 3679

[8] Bates, J.W., Montgomery, D., in preparation (1997)

[9] Kamp, L. *et al.*, in preparation (1997)

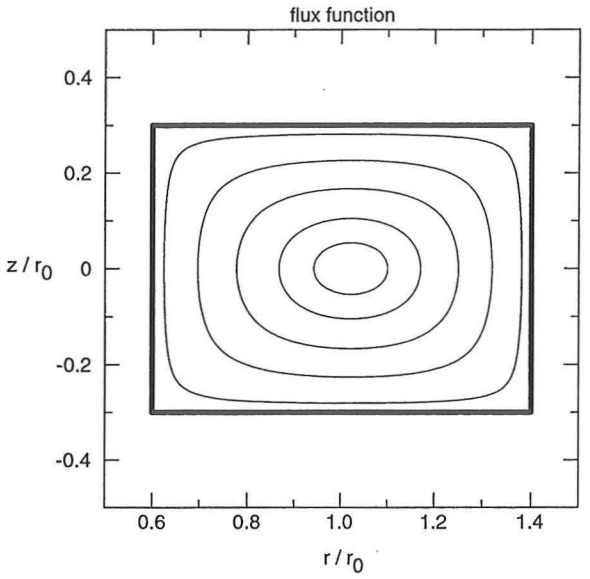

Fig. 1. Contours of the magnetic flux function, which are the projections of the surfaces on which the magnetic field lines lie (from [6]). The parameter r_0 is the major radius of the toroid. The rectangular box shows the location of the toroidal boundary on which the normal component of the magnetic field vanishes.

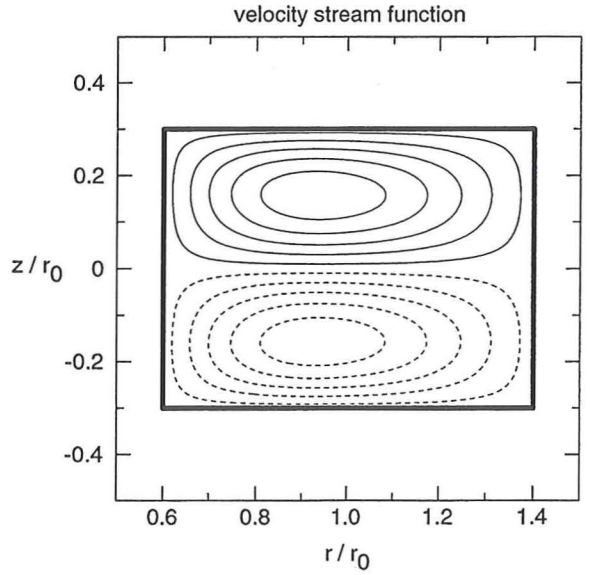

Fig. 2. Contours of the velocity stream function for stress-free boundary conditions (from [6]). Negative contours are denoted by a solid line and positive contours by a dashed line. Thus, above (below) the midplane of the toroid the magnetofluid rotates in a counterclockwise (clockwise) sense, creating a pair of toroidal vortices in a "double smoke ring" configuration.

Critical Isssues in Transonic Magnetohydrodynamic flows

J.P. Goedbloed[1] & **A.E. Lifschitz**[2]

[1]FOM-Institute for Plasma Physics, Association Euratom-FOM,
P.O. Box 1207, 3430 BE Nieuwegein, The Netherlands

[2]University of Illinois at Chicago, Chicago, U.S.A.

1. Introduction

Whereas most of tokamak stability theory is based on the assumption of static equilibrium, neutral beam heating causes the plasma to spin and particle and energy extraction in divertors results in the supersonic flow of a narrow plasma layer on the outside of the tokamak. These kinds of flow present an enormous challenge, both with respect to the construction of stationary flow patterns, with possible transitions to super-Alfvénic flows, and with respect to the investigation of the different oscillations and new types of instabilities. In astrophysics, plasma flows have been investigated for a much longer time since they are prominent in a wide range of important phenomena, like stellar winds, rotating accretion disks, jets from extragalactic nuclei, etc. Therefore, the construction of the different types of plasma flows is a problem of common interest to the fusion and astrophysics communities [1]–[3].

Plasma flows imply a major complication in the field of MHD spectroscopy [4], which demands the construction of stationary equilibrium states and their spectral study. These theories are well developed for static equilibria but for stationary flow they still require an enormous effort. In fusion research, opening up of the magnetic geometry and high speed flows in pumped divertors pose problems of a similar nature as transonic flows in astrophysics. There, an important question is: How does *super* fast/Alfvén *flow* connect onto *sub* Alfvén/slow *flow*? One of the problems encountered is the presence of *limiting line internal singularities* where one set of characteristics in the hyperbolic flow domains starts to develop envelopes. It has been assumed that the other set of characteristics crosses these lines and, thus, facilitates the construction of continuous stellar wind solutions [5]. Our analysis shows this conclusion to be false.

In Secs. 2 and 3 we are concerned with the construction and classification of the different types of MHD flows. Particular attention is paid to the transitions from elliptic to hyperbolic flows, to the existence of limiting lines, and the implications for flow patterns in global magnetic geometries. The limiting line singularities are resolved by means of the explicit construction of symmetric discontinuous solutions.

2. Continuous stationary flows

Stationary ($\partial_t = 0$) symmetric ($\partial_z = 0$) MHD flows are described in terms of a flux function ψ, related to $\mathbf{B}_p$, and a stream function $\chi(\psi)$, related to $\mathbf{v}_p$. The five arbitrary flux functions χ', H, S, I, Ω may be collapsed to three: $\Pi_{1,2,3}(\psi)$. The poloidal Alfvén

Mach number is defined by $M^2 \equiv \rho v_p^2/B_p^2 = \chi'^2/\rho$. The core problem [3] then involves a *nonlinear PDE* for the flux $\psi(x,y)$:

$$\nabla\cdot[(1-M^2)\nabla\psi] + \frac{\Pi_1'}{M^2} - \frac{\Pi_2'}{\gamma M^{2\gamma}} + \frac{\Pi_3'}{1-M^2} = 0\,,$$

end *the Bernoulli equation* for $M^2(x,y)$:

$$\tfrac{1}{2}|\nabla\psi|^2 - \frac{\Pi_1}{M^4} + \frac{\Pi_2}{M^{2(\gamma+1)}} + \frac{\Pi_3}{(1-M^2)^2} = 0\,.$$

Assuming *one master profile* with two constants, A (entropy) and B (longitudinal field), i.e.

$$\Pi_1 = \pi(\psi)\,,\quad \Pi_2 = A\,\pi(\psi)\,,\quad \Pi_3 = B\,\pi(\psi)\,,\qquad \pi = \psi^{2-2/\lambda}\,,$$

and making the Ansatz of *self-similarity*,

$$M^{-2} = X(\theta)\,,\qquad \psi = r^\lambda\, Y(\theta)$$

the problem reduces to two ODE's. Differentiating the Bernoulli equation, $F(X,Y,Z)=0$ with $Z \equiv (1-1/X)Y'$, we obtain a system of ODE's:

$$\frac{dX}{d\theta} = \frac{H(X,Y)}{(1-1/X)\,J(X,Y)}\,Z\,,\qquad \frac{dY}{d\theta} = \frac{1}{1-1/X}\,Z\,,\qquad Z = \pm\frac{\sqrt{F_0(X,Y)}}{1-1/X}\,,$$

where H and J are complicated functions of X and Y. The singularities $J=0$ represent the limiting lines.

In general ($B \neq 0$) seven flow regimes are obtained from the Bernoulli equation, indicated by $\mathcal{H}_{ff}(1^+)$, $\mathcal{H}_f(1^-)$, $\mathcal{E}_f(2)$, [Alfvén gap at $X_A = 1$], $\mathcal{E}_s(3)$, $\mathcal{H}_s(4^-)$, $\mathcal{H}_{ss}(4^+)$, $\mathcal{E}_{ss}(5)$. Here $\mathcal{H}$ and $\mathcal{E}$ indicate the hyperbolic and elliptic domains, and ff, f, s, and ss indicate the super fast, fast, slow, and sub slow speed regimes, respectively.

For $B=0$, the region 2 disappears and the resulting phase plane with the trajectories (solutions $Q(X)$) is shown in Fig. 1. Here, Q is a simple function of Y involving the profile parameter λ. The trajectories appear to cross all the obstacles (fast and slow limit lines and the Alfvén singularity) smoothly, but the corresponding flow patterns shown in Fig. 2 are not smooth at all. In fact, the flow 'reverses' direction at the limit lines (physically impossible), indicating that there are multiple solutions that cannot be connected smoothly. The only way out is to permit discontinuous solutions.

3. Discontinuous stationary flows

The following jump conditions are obtained for the self-similar solutions:

- Y and B continuous: $[\![Y]\!] = 0\,,\quad [\![B]\!] = 0\,,$
- X and A discontinuous:

$$[\![(1-1/X)\,Y']\!] = 0\,,\qquad [\![1/X]\!]\,\lambda^2 Y^{2/\lambda} + \left[X^2 + (1-1/\gamma - X)\,AX^\gamma\right] = 0\,,$$

- Entropy condition: $[\![A]\!] \leq 0\,.$

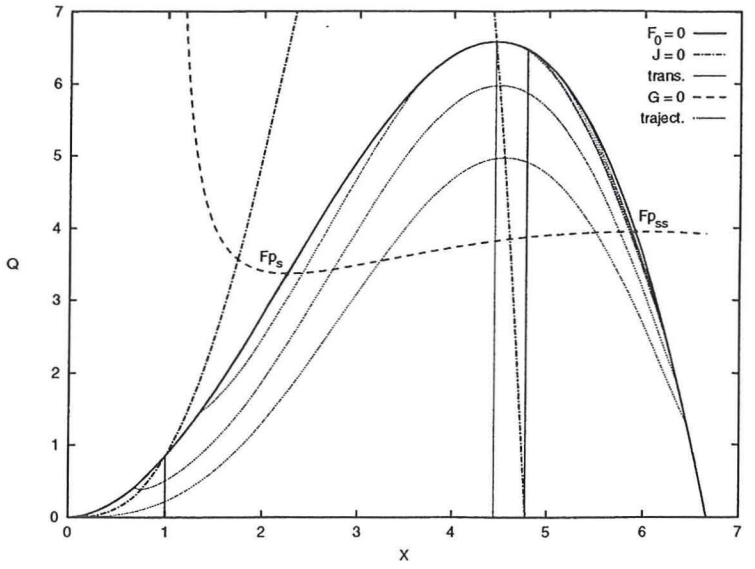

Figure 1. Trajectories in the X–Q phase plane for $A = 0.15$, $B = 0$, $\lambda = 0.5$, $\gamma = 2.0$.

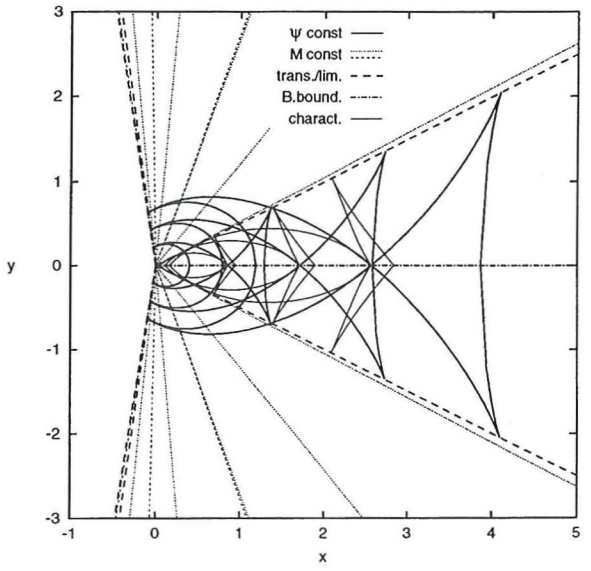

Figure 2. Flow patterns in the physical plane corresponding to the trajectory $X_i = 0.4$ of Fig. 1. Superposed are super-fast 1^+ (outer) & fast-slow $1^-, 3, 4^-$ (inner) & sub slow $4^+, 5$ (innermost) flows.

At the shock positions, the following five variables can be distinguished: $\hat{X}_1 \neq \hat{X}_2$, $\hat{Y} \equiv \hat{Y}_1 = \hat{Y}_2$, $A_1 \neq A_2$. The procedure is then first to eliminate A_2 giving the *distilled jump condition*, $f_1(\hat{Y}, \hat{X}_1, \hat{X}_2, A_1) = 0$, and next to substitute A_2 in the entropy condition giving the *distilled entropy condition*, $f_2(\hat{Y}, \hat{X}_1, \hat{X}_2, A_1) \geq 0$. For given $(\hat{Y}, A_1)$, the possible shocks are then selected by plotting f_1 and f_2 in the $\hat{X}_1$-$\hat{X}_2$ plane. This gives an enormous number of possible shocks, of all categories (fast, intermediate, and slow) [3]. This provides the necessary solutions jumping across the limiting lines and resolving the mentioned paradox in astrophysical flows.

4. Conclusions

- *There are four flow regimes, separated by the limit lines and the Alfvén gap and not connected by continuous flows.*
- *The limiting line signals the expiration of continuous solutions and guarantees the existence of discontinuous solutions jumping across.*
- *Fast shocks jump across the fast limiting line Lf, intermediate shocks jump across the Alfvén gap A, and some also jump across the slow limiting line, slow shocks jump across the slow limiting line Ls.*
- *The three obstacles just create the right conditions to produce the three kinds of strongly discontinuous flow which may be considered as the nonlinear counterpart of the weak discontinuities of linear MHD.*
- *This resolves the paradox in transonic astrophysical MHD flows.*

References

[1] J.P. Goedbloed and A.E. Lifschitz, "Symmetry of magnetohydrodynamic flows", *Astrophys. Lett. and Comm.* **36**, 267 (1996).

[2] A.E. Lifschitz and J.P. Goedbloed, "Transonic magnetohydrodynamic flows", *J. Plasma Phys.*, to appear (1997).

[3] J.P. Goedbloed and A.E. Lifschitz, "Stationary symmetry magnetohydrodynamic flows", *Phys. Plasmas*, to appear (1997).

[4] J.P. Goedbloed, G.T.A. Huysmans, H. Holties, W. Kerner, S. Poedts, "MHD spectroscopy: Free boundary modes (ELM's) and external excitation of TAE modes", *Plasma Physics and Controlled Fusion* **35**, B277–292 (1993).

[5] T. Sakurai, "Magnetohydrodynamic solar/stellar wind models", *Computer Physics Reports* **36**, 247–273 (1990).

Dynamical interpretation of dynamo in the RFP

D.F. Escande and D. Bénisti

Consorzio RFX, Corso Stati Uniti 4, 35127 Padova, Italy

Abstract. The simplest example of a RFP-like equilibrium is introduced. It corresponds to a kinking current-carrying wire inside of a magnetic flux conserving cylinder. It suggests a scenario for dynamo in the RFP, where dynamo is a birth and death process of current filaments carrying them from the center to the edge of the plasma. This scenario and the wire model are consistent with several experimental and numerical results. The existence of reconnection events, expected from the scenario and seen in numerical simulations, is shown to support the two basic assumptions of Taylor theory of relaxation.

I. The wire model for magnetic field self-reversal

We first introduce a simple model, the wire model, which yields the simplest example of a RFP-like equilibrium. The plasma is replaced with a stretchable current-carrying wire initially located on the axis of a cylindrical axial flux conserver (the shell) providing an axial magnetic field (fig. 1). This means an azimuthal current is flowing in the shell to provide the field. The wire is kink-unstable, and takes on a helical shape whose wavenumber k is assumed imposed upon the system. As in a RFP, the axial component I of the current is kept constant during the kinking. The sign of the pitch of the helix is such that the azimuthal component of the current in the wire has the same orientation as that in the shell, which feeds in the instability by the mutual attraction between the two currents. The solenoidal effect of the current increases the magnetic flux inside of the helix, and diminishes it outside due to flux conservation inside of the shell. Therefore sheared magnetic forces are acting inside of the cross-section of the wire. Their resultant is time-decreasing and directed outward. Due to flux conservation, the axial field reverses outside the wire, and the corresponding reversal of the current in the shell makes it a repeller for the wire. The larger the radius of the helix, the larger the reversal of the field. The magnetic force becomes zero, and the wire reaches a stable equilibrium.

Let b be the radius of the shell, and B_T be the initial axial magnetic field. Simple flux calculations yield the following equation for the equilibrium radius r_0 of a tight helix ($k.r_0 >> 1$)

$$b^2/r_0^2 = 2\text{-}4\pi b^2 B_T/k^2\mu_0 I r_0^3. \quad (1)$$

For a RFP-like equilibrium, the second term in the r. h. s. may be neglected, which yields $r_0 = b/2^{1/2}$. In contrast to true RFP's, the equilibrium of tight helices (helical current on a cylinder) has a reversed field opposite to the field inside of the helix, and large with respect to the mean field B_T. For a less tight helix, the azimuthal component of the current is weaker, and the pinch effect due to the axial current increases, which leads to an equilibrium with a less reversed field. If the wire has a mass, the state of equilibrium is reached only if the kinetic energy due to the instability is dissipated by some damping mechanism. This wire model offers an alternate to the non-linear stabilization of the kink instability proposed by Kadomtsev with a wire model where the current vanishes at saturation [1].

II. Scenario for Dynamo

More realistic models of a RFP-like equilibrium with a broader current distribution and a moderate field reversal can be derived by adding to the helix a plasma core with an azimuthally symmetric axial current distribution and an axially invariant poloidal current distribution. However they come across the issue of global current sustainment through a radially uniform axial electric field modelling the effect of the inductive loop voltage in the toroidal case. If the model tries to come close to a Bessel Function Model for the magnetic field with static current carrying elements, the current distribution cannot be sustained with such an electric field. Current will tend to be larger near the axis and smaller when reaching the region of reversal due to the increased length of the circuit. Therefore one is naturally led to consider the RFP equilibrium as a more dynamical one.

This suggests the following scenario. Central currents are bound to be larger than in the BFM, and to become kink unstable. This pushes out the previous current structure, and leaves a hole in the center of the plasma where a current filament appears due to the axial electric field. This filament is also kink unstable, and follows the global radial expansion of the rest of the plasma. As seen in numerical simulations [2,3] with a single helicity, the current filament may take on a bean shape elongating during its radial expansion, and yielding a quasi azimuthally symmetric current distribution. As in these numerical simulations, reconnection events are expected to occur when the two tips of each bean come together. They may also occur because of differential radial velocities between the filaments. These reconnection events create force-free current sheets which help producing a relaxation à la Taylor. Thus the dynamo might be a coherent birth and death process of current filaments carrying them from the center to the edge of the plasma. This image of current filaments keeping their identity is bound to be somewhat artificial due to the magnetic chaos existing in the system. However it might be heuristically useful in the same way as the kinetic beam-plasma instability may be qualitatively understood in terms of simultaneous cold beam- plasma instabilities.

III. Consistency with experiments and numerical simulations

Several results suggest that the wire model captures the basic features of field reversal in RFP's. Numerical simulations with a single helicity display a kinking current-carrying core [2,3]. The original numerical simulation by Sykes and Wesson [4] clearly shows the kinking of a current filament. Field reversal in HBTX-1 was interpreted by considering the plasma as a current-carrying structure [5].

The wire model is consistent with experiments in two different ways. First, when Pulsed Poloidal Current Drive (PPCD) is performed in RFX, the plasma is seen to behave like a vacuum : the average and edge values of the toroidal field vary in the same way [6]. If the helical wire is considered as a perfect conductor, the wire model reproduces this behaviour. Second, when a pellet reaches the center of the discharge in RFX, an increase of the field

reversal is noticed [7]. Such a pellet increases the kinetic pressure in the center of the plasma. Adding such a pressure in the wire model also increases the field reversal, since the equilibrium is shifted toward larger values of r_0.

The scenario for the dynamo is consistent with several experimental facts :

- the existence of an anti-pinch velocity in the RFP [8] (also numerically observed [9]) which might be the consequence of the continuous outward emission of current filaments,
- the increased flow of fast electrons toward the edge during the phases of magnetic field regeneration [10],
- the decrease of the dynamo activity and the increase of temperature and energy confinement during PPCD, as well as the dynamo regeneration events right after [11] ; during PPCD the current in the outer filaments is sustained by a poloidal electric field, which enables a less dynamical equilibrium of the filament structure, and decreases the transport and mixing of different radial domains related to its radial expansion, which yields a higher temperature,
- the clockwise path in the F-Θ plane during Dynamo Regeneration Events [6] ; when the filament is created, Θ increases, but only the kinking provides the decrease of F,
- the fact that operation at constant I is not natural for the RFP : peaks on the loop voltage are seen on RFX and in numerical simulations [9],

Finally it is worth noting that current sheets are seen in 3D MHD simulations [12].

IV. Reconnection events and relaxation à la Taylor

The possible graininess of current filaments and the force-free current sheets due to reconnection events produce localized perturbations of the magnetic field whose combined effect is magnetic chaos. It is interesting to notice that magnetic chaos decreases the constraints due to the conservation of magnetic helicity. Indeed in a chaotic domain, a flux tube cannot close on itself. As a consequence, one cannot define a helicity for any of the flux tubes of a chaotic region. Therefore, no helicity constraint can be imposed in the inside of a chaotic domain. However, helicity can be defined for the flux tube built on the first magnetic surface(s) bounding the chaotic domain. This implies that, as regards a region of magnetic chaos, only one constant of motion exists, the global helicity of the chaotic domain.

This provides a way to justify Taylor's assumption of the conservation of a unique helicity in his theory of relaxation : it would be justified by the existence of a completely chaotic magnetic field. Both experimentally and numerically the Bessel Function Model is found to be wrong in the outer part of the plasma. There magnetic chaos might be negligible either because of the proximity of a conducting shell or because of stabilisation of MHD activity by plasma rotation. Therefore the existence of some kind of magnetic chaos seems to be a condition for a relaxation à la Taylor. However the validity of the BFM in the central part of the plasma does not mean that the magnetic field must be fully chaotic there. Indeed a spatio-temporally intermittent chaos is sufficient to loosen the concept of flux tube and of related magnetic

helicity. Therefore the existence of current sheets in [12] supports the two basic assumptions of Taylor's theory : the dissipation occurs on small scales, and a unique magnetic helicity describes most of the plasma.

Acknowledgements

This work benefited from many discussions with S. Cappello, and from useful suggestions by M. Bagatin, R. Bartiromo, A. Buffa, S.C. Guo, S. Ortolani, R. Paccagnella, and J.B. Taylor.

References

1. B.B. Kadomtsev, Tokamak Plasma : A Complex Physical System (IPP, Bristol, 1992), p. 34.
2. E.J. Caramana, R.A. Nebel, and D.D. Schnack, Phys. Fluids 26 (1983) 1305.
3. K. Kusano and T. Sato, Nucl. Fusion 26 (1986) 1051.
4. A. Sykes and J.A. Wesson, in *Proceedings of the Eighth European Conference on Controlled Fusion and Plasma Physics* (Prague, 1977) p. 80.
5. A.J.L. Verhage, A.S. Furzer, and D.C. Robinson, Nucl. Fusion 18 (1978) 457.
6. S. Martini, private communication.
7. S. Martini,T. Bolzonella, D. Gregoratto, P. Innocente, L. Marelli, A. Murari, P. Martin, R. Pasqualotto, R.Pugno, M. Valisa, to appear in *Proceedings of the 24th European Conference on Controlled Fusion and Plasma Physics* (Berchtesgaden, 1997).
8. T. Bolzonella, S. Martini, P. Innocente, to appear in *Proceedings of the 24th European Conference on Controlled Fusion and Plasma Physics* (Berchtesgaden, 1997).
9. S. Cappello, private communication.
10. V. Antoni, D. Desideri, P. Franz, L. Marrelli, P. Martin, E. Martines, A. Murari, G. Serianni, L. Tramontin, F. Vallone to appear in *Proceedings of the 24th European Conference on Controlled Fusion and Plasma Physics* (Berchtesgaden, 1997).
11. S. Martini, T. Bolzonella, L. Carraro, E. Casarotto, P. Innocente, E. Martines, L. Marelli, A. Murari,R. Pasqualotto, M.E. Puiatti, M. Valisa, to appear in *Proceedings of the 24th European Conference on Controlled Fusion and Plasma Physics* (Berchtesgaden, 1997).
12. S. Cappello and D. Biskamp, Nucl. Fusion 36 (1996) 571.

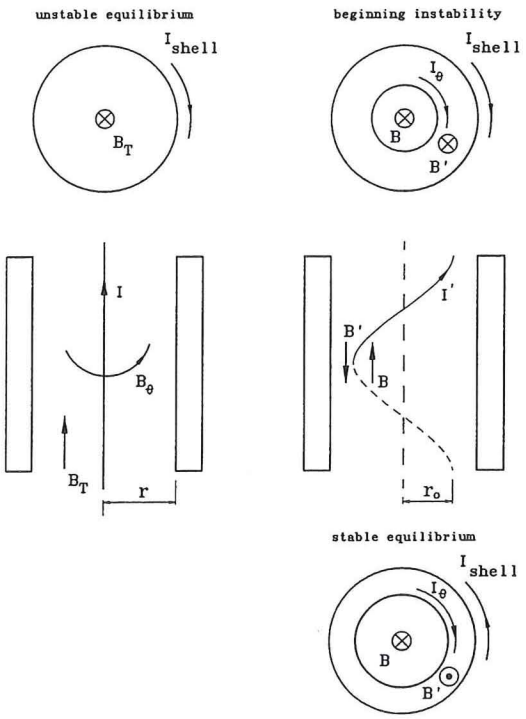

Fig.1 Sketch of the reversal mechanism

A MAP REPRESENTING A STOCHASTIC MAGNETIC FIELD IN A TOKAMAK

R. Balescu

Association Euratom - Etat Belge, Physique Statistique et Plasmas,
CP 231, Université Libre de Bruxelles, Campus Plaine,
Boulevard du Triomphe, 1050 Bruxelles, Belgium

The magnetic field in a toroidally confined plasma (such as a tokamak or a stellarator) has usually a very complex structure characterized by the following elements: a set of magnetic surfaces ("KAM barriers") nested around a magnetic axis, a succession of island chains of various orders (and various widths) sandwiched between magnetic surfaces and surrounded by chaotic regions. Such a structure can, in particular, be enhanced by a "dynamic ergodic divertor". The transport properties of a plasma in presence of such *incompletely chaotic* magnetic fields is very poorly known.

We attempt to study a first aspect of this problem by considering the "diffusion" of the magnetic field lines. Our motivation is to construct a discrete dynamical map (in which the role of time is played by the toroidal coordinate) that could describe the main features of the problem in a much simpler fashion than by solving the differential equations for the field lines. This "TOKAMAP" is Hamiltonian (hence, area-preserving) and retains the basic features of the toroidal geometry (such as the invariance of the magnetic axis). It has some unusual symmetry and scaling properties which will be discussed.

An important feature of the evolution in such stochastic layers is the "sticking property" of the orbits within "basins" surrounding the islands. As a result, the evolution can adequately be described by a continuous time random walk (CTRW). A "particle" sojourns in a given basin for some time, then jumps to another basin, where it remains for some time, etc. The ingredients of such a description are: the *waiting time probability density in basin m,* $\psi_m(t)$, and the *transition probability from basin m to basin n,* f_{nm}. These quantities can be measured from a numerical computation of long orbits. The corresponding CTRW can be solved analytically (in not too complicated situations). It exhibits *strange (subdiffusive) behaviour*, due to the sticking property of the orbits.

Enhanced rotation velocities and electric fields, sub-neoclassical energy transport and density pinch from revisited neoclassical theory

André Rogister
Institut für Plasmaphysik, Forschungszentrum Jülich GmbH, EURATOM Association,
Trilateral Euregio Cluster, D-52425 Jülich, Germany

Abstract. We show that the large negative radial electric fields which are measured in front of the separatrix in H-mode discharges can easily be explained on the basis of the rigorous „revisited" neoclassical theory, including Finite Larmor Radii and Inertia effects that was published earlier (Rogister A 1994 *Phys. Plasmas* **1** 619); the same theory naturally leads to sub-neoclassical energy transport and novel particle pinch terms. The calculation has so far been developed only in the high collisionality regime: step sizes comparable to gradient-scale sizes are therefore not required to explain observed properties! Based on the analysis, we conclude that the radial electric field profile develops a well in front of the separatrix when the plasma is unable to sustain ambipolar flows otherwise. The conditions required for this to occur agree with experimental/empirical knowledge.

I. Outline of the theory and improvement with respect to previous work

The basic theory [1], from which the results presented here are derived, assumed the ordering

$$\Lambda_1 \equiv \left(q^2 R^2 NT_i\right) / \left(reB|L_T|\chi_{\|,i}\right) \sim 1 \qquad (1)$$

according to which

(i) gyro-viscosity ($\propto \eta_{3,i} \partial U_{\|,i} / \partial x$) and collisional-viscosity ($\propto \eta_{0,i} \partial U_{\|,i} / \partial \ell$) are allowed to be of the same order of magnitude if $L_{U_{\|,i}} \sim L_T$ whereas the former is systematically neglected in conventional neoclassical theory ($x = r - r_s < o$ is the radial variable measured from the separatrix; ℓ is the space-variable along field lines; the other notations are from Braginskii [2]);

(ii) energy convection and parallel diffusion rates on magnetic surfaces (respectively $T/reB|L_T|$ and $\chi_{\|,i} / Nq^2 R^2$) are considered on a par, whereas the former is again neglected in conventional neo-classical theory.

The parameter Λ_1 is typically < 0.25 in the edge of L-mode discharges and at the periphery of the transport barrier in H-mode discharges; $\Lambda_1 \geq 1$ within the latter. Note that conventional neoclassical theory is incomplete also when $\Lambda_1 << 1$ as the degeneracy of the ambipolarity constraint is not removed (no equation is provided from which to obtain the radial electric field); in the revisited theory, $\Lambda_1 << 1$ factorizes out of the (higher order) non

degenerate ambipolarity condition. $\hat{\nu}_i \equiv qR\nu_i / \upsilon_{th,i}$ is often larger than 1 in ASDEX-Upgrade and in DIII-D: hence the relevance of the high collisionality regime.

II. Main results concerning energy and particle transport.

Particularizing the results obtained in [1] to circular cross-section tokamaks (and letting the parameter $\Lambda_2 \to o$, where Λ_2 is the ratio of the electron-ion temperature relaxation rate to the parallel ion energy diffusion rate on the magnetic surface), it can be shown that the flux surface average of the radial component of the revisited neoclassical heat flux is

$$q_{i,r} = -\left(1+\frac{1.6q^2}{1+Q^2/S^2}\right)\chi_{\perp,i}\frac{\partial T_i}{\partial x} \qquad (2)$$

where

$$S = 2\left(\chi_{\parallel,i}/rN\right)B_\theta^2/B^2; \qquad Q \equiv 4\left(B_\varphi U_{\theta,i}/B\right) - 5\left(T/eB\right)\partial\ell nNT^{1/2}/\partial x\ ; \qquad (3)$$

$\chi_{\perp i}$ is defined in [2]; q is the safety factor; θ and φ are the poloidal and toroidal angles; we note that Q/S ~ Λ_1 if $U_{\theta,i}$ is of the order of or smaller than the diamagnetic velocity. Thus the neoclassical contribution 1.6 q^2 $\chi_{\perp,i}\partial T_i/\partial x$ to $q_{i,r}$ is reduced by the factor $1 + Q^2/S^2$ leading to the concept of sub-neoclassical energy transport. $q_{i,r}$ is moreover a multivalued function of $\lambda \propto |L_T| \equiv |\partial\ell nT/\partial x|^{-1}$, as shown in Fig. 1 (condition to have three roots is $q > \sqrt{5}$ as may be shown by considering $\partial q_{i,r}/\partial\lambda^{-1}$). Since this property might lead to bifurcation scenarios only if anomalous energy transport were automatically quenched, the transition from L to H confinement will rather be discussed here on the basis of the properties of the edge radial electric field and rotation velocity profiles; the latter may indeed result in tearing the dominant unstable modes apart [3] and hence in quenching anomalous transport.

The revisited ambipolar particle flux will not be given here; worth noting is that it contains a series of new terms generally corresponding to particle pinches.

III. Edge radial electric field and rotation velocity profiles.

The non-trivial ambipolarity constraint and the parallel momentum equation of the revisited theory allow unambiguous determination of the radial electric field and of the parallel velocity profiles or, alternatively, of the polodial and toroidal rotation velocities. Assuming the

temperature and density profiles to be frozen [e.g. proportional to a power (respectively p and p/η) of 1 + kx (k < o)], we find that the general theory [1] leads to a nonlinear first order partial differential equation for either $U_{\|,i}$ or E_r if (i) $\Lambda_1 << 1$ and (ii) the conventional orderings $E_r \sim (T/e)\partial\ell nP/\partial x$, $U_{\|,i} \sim (T/eB_\theta)\,\partial\ell n\, P/\partial x$ and $L_{Er} \sim L_{U_{\|,i}} \sim L_{T,N}$ are postulated. The general solution of this equation may be expressed as the ratio of two linear forms:

$$U_{\|,i} \propto [c_1 - \hat{u}_2 (kx+1)^{p_{\hat{q}_1}} H_1][c_1 - \hat{u}_1 (kx+1)^{p_{\hat{q}_1}} H_1]^{-1} (kx+1)^{p_{\hat{q}_1}} \qquad (4)$$

involving a function H_1 of a specific combination of space and time; H_1 is to be determined from the boundary condition at x = o. This solution diverges if the denominator vanishes at some $x = x_o < o$, which occurs on certain conditions involving [via the constants $\hat{u}_1$, $\hat{u}_2$ and $c_1 = \hat{u}_1 - \hat{u}_2$ (< o)] the density of neutrals, the momentum injection rate per ion, the temperature /density profiles and (via H_1) the boundary condition. The assumed scaling of E_r, $U_{\|,i}$, respectively of L_{E_r}, $L_{U_{\|,i}}$ must then be revised near the „singular" point where enhancement, respectively reduction factors ~ Λ_1^{-2} are required. This now leads to a second order nonlinear equation, of which the solution is well behaved, vary rapidly and reach unusually large values near x_o. Plots of E_r and $U_{\varphi,i} = B_\varphi U_{||,i}/B$ are shown in Fig. 2. It turns out that the large radial electric field is always negative in front on the separatrix, irrespective of the b.c. and as observed. Minimum values of some — 20 kV/m to -40 kV/m have been estimated from DIII-D and ASDEX edge density and temperature profiles [4]. Correspondingly, minimum values of $U_{\varphi,i}$ ranging from -70 km s^{-1} to -150 km s^{-1} are found; note that $U_{\varphi,i}$ is predicted to change sign at the singular point: maximum values ranging from +80 km s^{-1} to +200 km s^{-1} are calculated further inside the plasma. Worth noting is that the minimum toroidal velocity follows a relatively simple scaling law:

$$(U_{\varphi,i})_{min} / c_i = - 0.68\ \hat{\nu}_i^{-1} \qquad (5)$$

(> – 1 in the high collisionality regime!) and that the width of the barrier is ~ $(100/3)\,\Lambda_1^2 L_T \sim 1cm$.

IV Concluding remarks

The question as to which boundary condition should be required at the separatrix is still open. The particular condition

$$U_{\|,i}^{-1}\,\partial U_{\|,i} / \partial x\big|_{x=o} = C \qquad (6)$$

— which may be interpreted as expressing the continuity of the flux of parallel momentum across the separatrix — has been found to lead either to aperiodic or to periodic solutions

depending on a set of parameters already enumerated. Those solutions may correspond respectively to H and dithering H modes. The above b.c. furthermore leads to two realistic transition criteria: one concerns the ratio $N_o/Z_{eff}N_i$; the other involves the logarithmic derivatives of T_i, $\partial T_i/\partial x$ and $U_{\|,i}$ in a way which suggests a minimum temperature requirement. We note further that the obtained profile of $U_{\varphi,i}$ (x) (Fig. 2) is grossly compatible with momentum deposition by a co-injected tangential beam (owing to geometrical effects) but tends to be imcompatible with counter-injection. These conclusions all agree with observations.

The physics underlying the results of this paper is that localized large electric fields and rotation velocities may be necessary to maintain ambipolarity. The resulting enhanced shear will ultimately suppress the turbulence and improve the confinement.

Acknowledgement

I am grateful to M.Z. Tokar for pointing out the bifurcation character of the revisited heat flux.

References

[1] Rogister, A., *Phys. Plasmas* **1,** 619 (1994)
[2] Braginskii, S., Transport Processes in a Plasma, in *Reviews of Plasma Physics* (Consultant Bureau, New York 1965, M.A. Leontovich editor) Vol **1,** 205
[3] Rogister, A., Li, D., *Nucl. Fusion* **33,** 1799 (1993)
Rogister, A., Hasselberg, G., *Nucl. Fusion* **33**, 1817 (1993)
[4] Rogister, A., to be submitted for publication

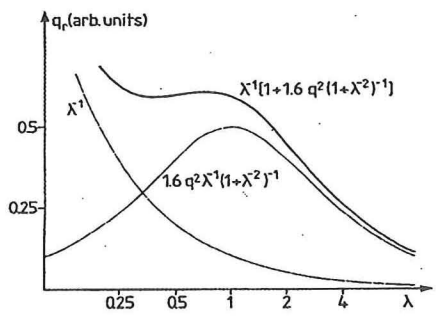

Fig. 1. Revisited heat flux for q=2.5

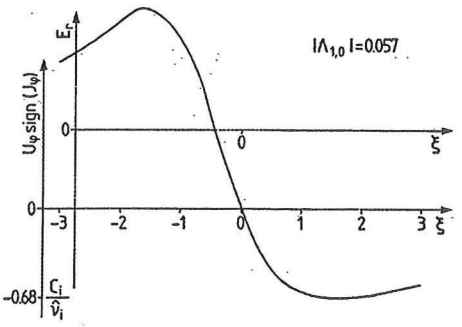

Fig. 2. Sketch of radial electric field near the singular layer at x_o; $\xi \equiv 0.03\,|\Lambda_{1,o}|^{-2}\,(x-x_o)\,|L_{T,o}|^{-1}$.

Poster Contributions

Simulations of Ion-Temperature-Gradient modes in helical symmetry

L. Villard, M. Fivaz, J. Vaclavik
Centre de Recherches en Physique des Plasmas, Association Euratom - Confédération Suisse, Ecole Polytechnique Fédérale de Lausanne

Abstract. We present the first simulations of Ion Temperature Gradient (ITG) modes in straight helical configurations. A linear particle-in-cell gyrokinetic global code initially developed for toroidal axisymmetric geometry [1, 2] has been modified to treat the case of helical symmetry. The model is based on gyrokinetic ions, adiabatic electrons and electrostatic quasineutral perturbations. The code simulates the full plasma cross-section. The potential is represented on a magnetic coordinate system and discretized with finite elements. Analytical extraction of the fast poloidal variation is done on a straight field line coordinate, allowing a speedup of one or two orders of magnitude. A $l = 1$ vacuum field configurations is studied. The very low shear and small ∇B drifts imply that for a wide range of parameters the most unstable ITG modes are "slab-like".

Introduction. Anomalous transport in magnetically confined plasmas is widely believed to be attributed to micro-instabilities of low frequency drift-wave type. Over the past years the efforts in the theoretical analysis have focused on axisymmetric configurations of the tokamak type. In contrast, very little has been done for stellarators: previous works on drift waves [3] - [6] have so far been limited to simple cold ion electrostatic models with local and ballooning approximations. The present work is the first that addresses the question of Ion-Temperature-Gradient (ITG) modes in helical geometry. The specific objective is to get an understanding of ITG modes and to compare with the tokamak results. The longer term goal is to understand whether or not transport in stellarators, if determined by such micro-instabilities, can be different from that in a tokamak.

Helical Geometry. In this paper we shall consider helical symmetry (i.e. straight stellarators). Let r, φ, z be the cylindrical coordinates. Helical symmetry implies that all scalar equilibrium fields can be expressed as functions of two variables: r and $\zeta = \varphi - hz$, where h is the helicity. A toroidal configuration of N_{per} field periods and major radius R_0 is thus modeled by a helicity $h = N_{per}/R_0$. Let us introduce the following coordinates: a helical system (x', y') with $x' = r\cos\zeta$, $y' = r\sin\zeta$, and a magnetic coordinate system (s, θ) with $s = ((\psi - \psi_{min})/(\psi_{max} - \psi_{min}))^{1/2}$, where ψ is the helical flux, $\theta = \arctan(y'/(x' - x'_m))$, where the magnetic axis position is $(x' = x'_m, y' = 0)$. In addition to the "poloidal" coordinate θ, we introduce the straight field line coordinate χ

$$\tilde{q} = \frac{h}{2\pi}\int_0^{2\pi} \frac{\mathbf{B}\cdot\nabla z}{\mathbf{B}\cdot\nabla\theta} d\theta \qquad \chi = \frac{h}{\tilde{q}}\int_0^{\theta} \frac{\mathbf{B}\cdot\nabla z}{\mathbf{B}\cdot\nabla\theta} d\theta \tag{1}$$

where the integrals are on a $\psi = const$ surface. Note that with this definition the rotational transform per helical period length $L = 2\pi/h$ is $\iota = 1/\tilde{q} + 1$.

The equilibrium magnetic field is given by the representation

$$\mathbf{B} = F\mathbf{u} + \nabla\psi \times \mathbf{u} \qquad \mathbf{u} = (hr\mathbf{e}_\varphi + \mathbf{e}_z)/(1 + h^2r^2) \tag{2}$$

with F a function of ψ so that $\mathbf{B}$ satisfies the helical symmetry and $\nabla \cdot \mathbf{B} = 0$. In this

paper we shall restrict ourselves to vacuum fields. They can be expressed as

$$\psi = \frac{1}{2}Fhr^2 - r\sum_l b_l I_l'(lhr)\cos(l\zeta) \tag{3}$$

where F is a constant and I_l is the modified Bessel function of order l.

Gyrokinetic model. The plasma ions are described with a linearized gyrokinetic model with the usual ordering: $\omega/\Omega \sim k_\parallel/k_\perp \sim e\phi/T_e \sim \rho/L_n \sim \rho/L_T \sim \mathcal{O}(\epsilon_g)$, where ρ is the ion Larmor radius, Ω is the ion cyclotron frequency, $L_E^{-1} = |\nabla \ln E|, E = n_0, T$. Another small parameter is $\rho/L_B \sim \mathcal{O}(\epsilon_B)$, with $L_B = B/|\nabla B|$. Consistent with the gyrokinetic ordering, the perturbations of interest have $k_\parallel << k_\perp$. We use this property to extract the poloidal phase variation of the mode

$$f(\mathbf{x},t) = \tilde{f}(s,\theta,t)e^{iS} \quad \phi(\mathbf{x},t) = \tilde{\phi}(s,\theta,t)e^{iS} \quad S(s,\theta,z) = m_0\chi(s_0,\theta) + kz - \omega_0 t \tag{4}$$

where $k = hn/N_{per}$, n is the "helical" mode number, the magnetic surface $s = s_0$ is chosen near the expected maximum mode amplitude, m_0 is an integer close to $-n\tilde{q}_0/N_{per}$, and $\tilde{q}_0 = \tilde{q}(s_0)$. Note that a perturbation having a single Fourier component m in the straight field line poloidal angle χ has

$$k_{\parallel,m} = \frac{B_z}{B}h(\frac{m}{\tilde{q}} + \frac{n}{N_{per}}). \tag{5}$$

The transformed quantities $(\tilde{\phi}, \tilde{f})$ are expected to have a slow poloidal variation, the fast variation having been extracted by the phase factor. This technique will allow us to study high n modes with the same computational performance as low n modes. The quantity ω_0 is not the eigenfrequency but serves to shift the simulated frequencies; this is particularly useful to study modes near the marginal stability with $\gamma << \omega$.

The unperturbed trajectories of the guiding centres (GC) have three constants of motion: the kinetic energy, the magnetic moment and the helical canonical momentum $\Psi_0 = \psi + (m_i/q_i)v_\parallel F/B$. The equilibrium ion distribution function f_0 is assumed isotropic Maxwellian with density and temperature constant on a magnetic surface. The perturbed distribution function is evolved along the unperturbed trajectories. The electrons are assumed to respond adiabatically. The quasi-neutrality condition, in which the polarization density is approximated by a differential expression valid up to $(k_\perp\rho)^2$, close the system of equations:

$$\frac{d\mathbf{R}}{dt} = v_\parallel \mathbf{e}_\parallel + \frac{v_\parallel^2 + v_\perp^2/2}{\Omega}\mathbf{e}_\parallel \times \nabla \ln B, \quad \frac{dv_\parallel}{dt} = \frac{1}{2}v_\perp^2 \nabla \cdot \mathbf{e}_\parallel, \quad \frac{dv_\perp}{dt} = -\frac{1}{2}v_\perp v_\parallel \nabla \cdot \mathbf{e}_\parallel \tag{6}$$

$$\frac{d\tilde{f}}{dt} + i\frac{dS}{dt}\tilde{f} = \frac{-\tilde{\mathbf{E}}}{B}\cdot\left((\mathbf{e}_\parallel \times \nabla\psi)\frac{\partial f_0}{\partial \psi} + \Omega \mathbf{e}_\parallel \frac{\partial f_0}{\partial v_\parallel} + (\mathbf{e}_\parallel \times \nabla \ln B)\left(v_\parallel \frac{\partial f_0}{\partial v_\parallel} + \frac{1}{2}v_\perp \frac{\partial f_0}{\partial v_\perp}\right)\right) \tag{7}$$

$$\tilde{\mathbf{E}}(\mathbf{R}, v_\perp) = -\frac{1}{2\pi}\int \mathcal{G}\tilde{\phi}(\mathbf{x})\delta(\mathbf{x} - \mathbf{R} + \boldsymbol{\rho})e^{i(S(\mathbf{x}) - S(\mathbf{R}))}d\mathbf{x}d\alpha \tag{8}$$

$$\frac{n_0 e}{T_e}\tilde{\phi}(\mathbf{x}) - \mathcal{G}_\perp \cdot \frac{n_0}{B\Omega}\mathcal{G}_\perp \tilde{\phi}(\mathbf{x}) = \int \tilde{f}(\mathbf{R}, v_\parallel, v_\perp)\delta(\mathbf{R} - \mathbf{x} + \boldsymbol{\rho})e^{i(S(\mathbf{R}) - S(\mathbf{x}))}d\mathbf{R}d\mathbf{v} \tag{9}$$

where $\mathcal{G} = (i\nabla S + \nabla)$.

The distribution function $\tilde{f}$ is discretized in a 4-D reduced phase space $(x', y', v_\parallel, v_\perp)$. The potential $\tilde{\phi}$ is discretized with quadratic spline finite elements in (s, θ). The new version of the code has been benchmarked against the axisymmetric version by considering a straight field configuration ($T = B_0 = const, b_l = 0$). We have checked that the results coincide and are independent of the helicity h. Convergence with the timestep, the mesh and the number of particles, and power consistency have been demonstrated.

Results. We consider the following $l = 1$ configuration: $F = 1T$, $b_1 = 0.5T$, $a = 0.5m$, $h = 1m^{-1}$, flat density, $T_e = T_i$, $d\ln T_i/ds$ profile peaking at $s = s_0 = 0.5$ with $L_T/a = 0.1$, $T_i(s_0) = 4keV$. This configuration has a flat $\tilde{q}$ profile: $\tilde{q}_{axis} = -1.0405$, $\tilde{q}_{edge} = -1.0464$, implying that $k_{\parallel,m}(s) \simeq const$. The magnetic gradients are rather small: $L_B/a \sim 8$ (therefore comparable to those of a tokamak of aspect ratio 8).

Simulations have been performed for various helical mode numbers n. The real frequencies ω and the growth rates γ are shown in Fig.1,left. For low n, both ω and γ increase linearly with n. A plot of the mode structure (Fig.1,right) shows a rather pure m poloidal dependence. For $n \geq 2$, $\omega > \omega_b$ and we do not expect to be in the trapped ion regime: this has been checked by artificially suppressing the $v_\parallel$ and $v_\perp$ variation in Eq.(7) and the result is unchanged. Even for $n < 2$ we could not find a trapped ion mode, probably because of the small trapped particle fraction ($\simeq 0.25$). Therefore, for $n \leq 12$ the mode is a slab-ITG. As n is further increased, the mode structure becomes more complicated. In fact, in many cases, several modes are present in the simulation, indicating that two (or more) modes have similar γ but different ω. The interpretation of the PIC simulation results is therefore more difficult. In some cases we were able, by initializing different perturbations and shifting the frequency, to identify two competing modes. Another characteristic of the high n modes is that as n increases the mode amplitude tends to become higher in the unfavourable ∇B region (low field side). An example is shown in Fig.2,left. This behaviour is similar to that of the toroidal ITG in tokamaks. Here we have a "helical-ITG", but the mode structure does not show such a broad m spectrum as in a standard tokamak: even at high n, we do not have overlapping of several m's having resonance surfaces in the gradient region: either the whole plasma is resonant (e.g. for $m = 25, n = 24$) or it is not, because of the flat $\tilde{q}$. Another effect comes into play at high n: finite Larmor radius. For $n = 28$ we have $k_\perp \rho \simeq 1$ at $s = s_0$. The large damping tends to suppress the mode, and this is the reason of the decrease of γ for high n. This FLR effect is also responsible for the change in the mode localization (Fig.2,right): at high n it peaks at $s \simeq 0.6$ where T_i is smaller, whereas at low n it peaks at $s \simeq 0.4$. Thus $k_\theta \rho$ is nearly constant at the maximum radial mode localization, therefore ω is also nearly constant for $n > 22$.

Conclusion. These first simulations of ITG modes in a helical configuration indicate that the modes potentially creating the highest transport are slab-ITGs at relatively low n. The small ∇B and the very low shear are typical for such straight stellarators: these seem to be favourable properties to minimize ITG-based transport.

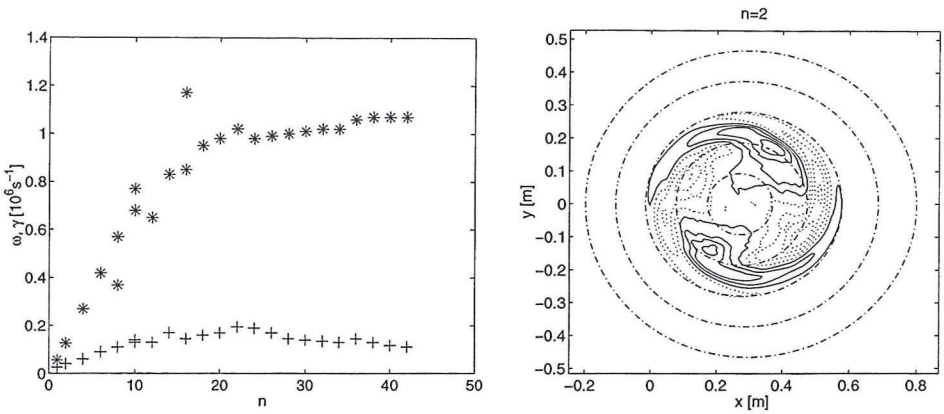

Figure 1: *Left: frequency ω (stars) and growth rate γ (crosses) as function of the helical mode number n. Right: contours of the perturbed potential ϕ for $n = 2$.*

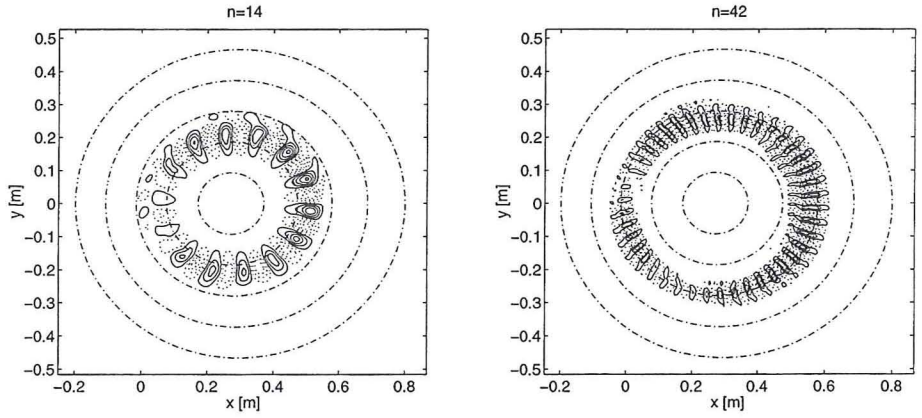

Figure 2: *Contours of the perturbed potential ϕ for $n = 14$ (left) and $n = 42$ (right) .*

Acknowledgements. This work was partly supported by the Swiss National Science Foundation. We thank W.A. Cooper and S. Brunner for helpful discussions.

References

[1] M. Fivaz, *et al.*, Theory of Fusion Plasmas, Int. Workshop, Varenna, August 1996, Editrice Compositori, Societa Italiana di Fisica, Bologna, 1997, p.485.
[2] M. Fivaz, Global ion-temperature-gradient instabilities in finite pressure tokamak plasmas, PhD Thesis no.1692(1997) EPFL, LRP 582/97.
[3] A. Bhattacharjee, *et al.*, Phys. Fluids 26 (1983) 880.
[4] N. Dominguez, *et al.*, (1992) 2894.
[5] R.E. Waltz, A.H. Boozer, Phys. Fluids B 5 (1993) 2201.
[6] M. Persson, J.L.V. Lewandowski, H. Nordman, Phys. Plasmas 3 (1996) 3720.

Ion temperature gradient vortices in shear flow

P.K. Michelsen, J. Juul Rasmussen and N. Chakrabati
Association EURATOM-Risø National Laboratory
Optics and Fluid Dynamics Department
Risø, DK-4000 Roskilde, Denmark

Abstract. The evolution of monopolar and dipolar vortices in an ion temperature gradient model (η_i-model) with velocity shear is investigated theoretically and numerically.

I. Introduction

Recently, numerical simulations and experiments have shown that coherent vortical structures, which may develop spontaneously [1, 2], can have a strong influence on the dynamics of electrostatic plasma turbulence and on the associated transport. Particles may be trapped by vortices and convected over distances much larger than the vortex scale size.

Analytical and numerical investigations have revealed the existence of steadily propagating monopole vortex solutions to the η_i-mode equations [3]. These vortices propagated with velocities outside the phase velocity regime of linear waves. Also dipolar vortical structures for the η_i-modes have been found and expressed analytically for simplified model equations [4, 5].

Recent tokamak experiments have shown improved stability and confinement properties in plasma regions with high velocity shear. A sheared plasma flow caused by an inhomogeneous perpendicular electric field may however have strong influence on the generation and evolution of vortical structures. The shear field may tear the structures apart and result in smaller scales of the coherent structures, thereby limiting their contribution to the transport.

To investigate the influence of velocity shear on coherent structures we have studied the evolution of monopolar and dipolar vortices in an η_i-model. The relevant set of equations was solved numerically in a two-dimensional domain with periodic boundary conditions.

II. The η_i model equations

We have based our analysis on a simplified two-dimensional model of η_i-modes [3, 5, 6]:

$$\partial_t(1-\nabla^2)\phi - [\phi, \nabla^2\phi] + (1 - 2\varepsilon_n + \alpha\nabla^2)\partial_y\phi - 2\varepsilon_n\partial_y p = 0 \quad (1)$$

$$\partial_t p + [\phi, p] + \alpha\partial_y\phi = 0, \quad (2)$$

where $\varepsilon_n = L_n/R$, $\alpha = (1+\eta_i)/\tau$, $\eta_i = L_n/L_T$, $\tau = T_e/T_i$, $L_n^{-1} = \partial_x n/n$, n is the background density, $L_T^{-1} = \partial_x T_i/T_i$, T_e and T_i are electron and ion temperatures, respectively, while R accounts for the curvature of the magnetic field. The time is normalized with c_s/L_n and the spatial coordinates are normalized with $\rho_s(= c_s/\Omega_i)$, where $c_s = (T_e/M_i)^{\frac{1}{2}}$, and Ω_i is the ion cyclotron frequency. The electrostatic potential, ϕ, and the ion pressure perturbation, p, are normalized with $(T_e/e)(\rho_s/L_n)$ and $p_{e0}(\rho_s/L_n)$, respectively. Here p_{e0} is the zero-order electron pressure. Finally, $[f,g]\,(= f_x g_y - f_y g_x)$ denotes the Poisson bracket. Equations 1-2 describe the evolution of the so-called "toroidal η_i–mode" [6]. We have omitted the effects of magnetic shear and thus the parallel ion dynamics. Curvature effects are retained and the instability is reproduced by the equations for a certain critical value of η_i. We have neglected compressional terms in the pressure equation and finite Larmor radius terms, which are both stabilizing [7], and the critical value of η_i for instability is therefore unrealistically low. Including the additional linear terms (due to compressional effects) would change (and complicate) the linear dispersion relation, but it would not change the basic mechanism of vortex propagation. The condition for linear instability for the Eqs. 1–2, i.e. $\mathrm{Im}\omega > 0$, is $\alpha > 0$ (see, e.g., [3]).

III. Numerical Method, introduction of shear and initial conditions

The set of equations 1–2 was solved numerically in a two-dimensional domain with periodic boundary conditions. We employed a fully de-aliased spectral method. To facilitate the numerical solutions Eqs. 1–2 were equipped with dissipative terms: $-D_1\nabla^4\phi$ accounting for cross-field dissipation in Eq. 1 and $D_2\nabla^2 p$ accounting for thermal conduction in Eq. 2.

A velocity shear is introduced by a cosine variation of the potential ϕ_0 in the x-direction. This gives a linear velocity variation near the middle of the x-domain. As seen from the equations this shear field is a stationary solution to the equations and it will therefore not change with time.

To investigate the evolution of vortices in this shear field either monopoles or dipoles are used as initial conditions on top of the shear field. The dipoles used are of the type

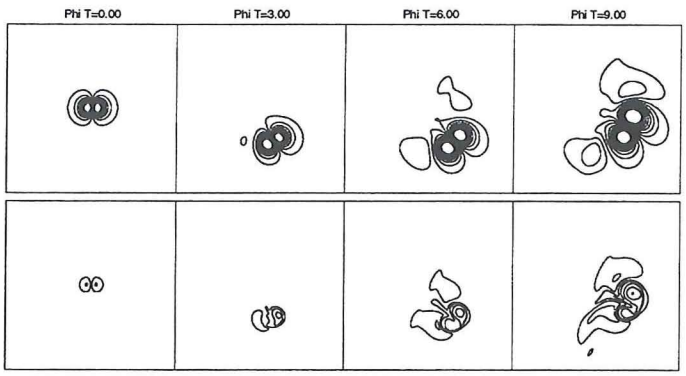

Figure 1: The evolution of a dipole in a shear field. The upper row shows evolution of the potential ϕ, the lower row the pressure p. Full lines indicate positive values and dashed lines negative values.

which are stationary solution to the Eqs. 1–2 without shear (See. Ref. [4, 5]).

We have investigated the vortex propagation for various kinds of initial conditions and for different values of the shear strength. In all cases we have chosen $\varepsilon_n = 0.25, D_1 = 0.005, D_2 = 2D_1$ and we have employed between 64 and 512 modes in the spectral code. In the case of no shear dipoles moving along the y-axis with velocities outside the regime of linear waves were found to be steadily propagating both for $\alpha < 0$ (in the linearly stable regime) and for moderately positive α-values.

IV. Results

The first investigation concerns the evolution of a dipole in the shear field. In Fig. 1 the potential (upper row) and the pressure (lower row) versus time is shown. The dipole is initialized in a strong shear field, but in a region where the mean velocity is zero. By its own vorticity field it starts moving downwards, but it is slowly turning around because of the shear field and it moves into the region where the background velocity is in the y-direction (upwards). Therefore, the dipole eventually moves in the y-direction. Although the dipole itself keeps together new vortices of opposite sign are created where the positive one become the strongest. At this stage the total structure resembles a tripole. Theoretical investigations have indicated that tripoles could be stationary solutions to the equations including velocity shear [8].

Figure 2 shows a case where the initial condition consists of a row of monopoles

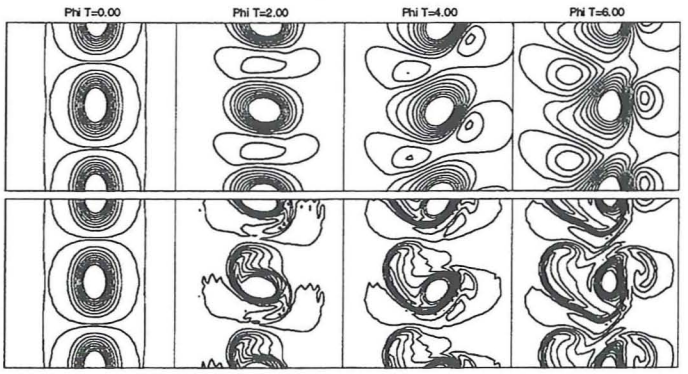

Figure 2: The evolution of a row of monopoles located along a line of maximum shear. The upper row shows evolution of the potential ϕ, the lower row the pressure p. Full lines indicate positive values and dashed lines negative values.

close together in the y-direction. We see here that vortices of opposite sign are created between the monopoles. However, these new vortices are stretched out between the original monopoles by the vorticity field and a row of new monopoles are created on each side. The row of original monopoles located along the line of maximum shear seems to be rather stable for a long time. Investigations of single monopoles, however, have shown that they normally are very unstable in the shear field.

References

[1] M. Ottaviani, F. Romanelli, R. Benzi, M. Briscolini, P. Santangello, and S. Succi, Phys. Fluids B **2**, 67 (1990)

[2] T. Huld, A.H. Nielsen, H.L. Pécseli, and J. Juul Rasmussen, Phys. Fluids B **3**, 1609 (1991); A.H. Nielsen, H.L. Pécseli, and J. Juul Rasmussen, Phys. Plasmas **3**, 1530 (1996)

[3] J. Nycander, J.P. Lynov, and J. Juul Rasmussen, Europhys. Lett. **23** (4) 249 (1993)

[4] P.K. Shukla and J. Weiland, Phys. Lett. A **136**, 59 (1989)

[5] B.-G. Hong, F. Romanelli, and M. Ottaviani, Phys. Fluids B **3**, 615 (1991)

[6] B.-G. Hong and W. Horton, Phys. Fluids B **2**, 978 (1990)

[7] H. Nordman and J. Weiland, Nucl. Fusion **29**, 251 (1989)

[8] N. Chakrabarti and J. Juul Rasmussen (to be published)

Numerical Simulation of Drift and Flute Modes in Cylindrical Geometry

V. Naulin
Association EURATOM-Risø National Laboratory
Optics and Fluid Dynamics Department
Risø, DK-4000 Roskilde, Denmark

Abstract. 2D-Numerical simulations of drift and flute/interchange modes in a cylindrical geometry are presented. Variation of magnetic field strength and background plasma rotation are included in the model. The results induce a strong need for three dimensional simulations which include the interaction of the mentioned modes.

I. Introduction

Electrostatic turbulence of the $E \times B$ velocity is generally believed to be responsible for the anomalous transport observed in the edge regions of magnetically confined plasmas. However most numerical studies on the nonlinear dynamics of drift or flute/interchange modes have been restricted to two dimensions and the use of periodic boundary conditions in slab geometry. First three dimensional simulations [1, 2] show that the interaction of drift-waves with flute modes plays an important role in the development of the turbulence. As a preparational work towards a three dimensional simulation of drift and flute modes in cylindrical geometry, a family of two dimensional solvers on a disk (including $r = 0$) were implemented. First results of these simulations are presented.

II. Model Equations

In the limit of constant electron temperature and cold ions the following equations for density n and electrostatic potential ϕ, and the vorticity $w = \nabla^2\phi$ hold:

$$\partial_t w = \mu\nabla^2 w + \left\{\ln n, B^{-1}\right\} + \{w, \phi\} + \frac{1}{n\eta}\nabla_{\|}^2(\ln n - \phi) \tag{1}$$

$$\partial_t \ln n = \left\{\ln n - \phi, B^{-1}\right\} + \{\ln n, \phi\} + \frac{1}{n\eta}\nabla_{\|}^2(\ln n - \phi) \tag{2}$$

These are equations for the backgound quantities as well, not only for perturbations. While it is assumed that only the strength of the magnetic field varies, so that $\vec{B} = B(r)\hat{z}$, one notices however, that curvature of the magnetic field leads to the same terms in the equations.

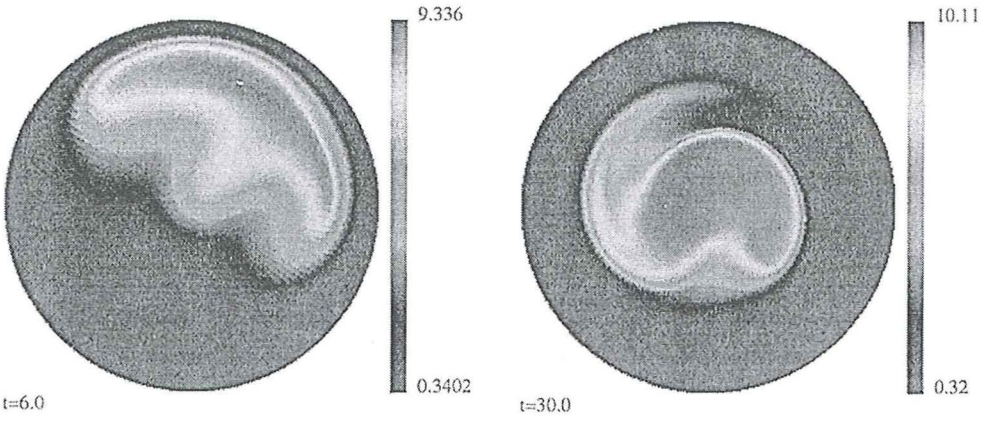

Figure 1: Loss of density (left) with small poloidal rotation and confinement with larger poloidal background flow (right), same initial conditions are used.

III. Boundary Conditions and Numerical Method

The selection of appropriate boundary conditions is very important for the considered problem. While with periodicity in the direction of the background quantities a flow of density through the volume is allowed, in the cylinder case Dirichlet boundaries are used. Then the towards the boundary transported quantities cannot leave the system. This puts a serious constraint on the possible evolution of solutions. In the physical system density constantly leaves the system at the limiter/divertor. Thus we implemented limiter type boundary conditions by damping the density near the boundary towards a fixed value. Sources in the center of the plasma are then used to compensate the density losses at the limiter and to obtain a steady state.

A 2nd order finite difference scheme is used to solve the equation numerically, with an Arakawa implementation of the convective nonlinearities and an implicit treatment of the viscous terms.

IV. Flute Modes

An interesting problem is the observed increased confinement in simple toroidal devices which do not have a poloidal magnetic field component. We use Eqs. (1) and (2) with $k_{||} = 0$ to model these devices. If a finite total circulation is prescribed, the density is trapped in a potential trench. An effect also observed in experiments [3] and described as a *transport dominated equilibrium.*

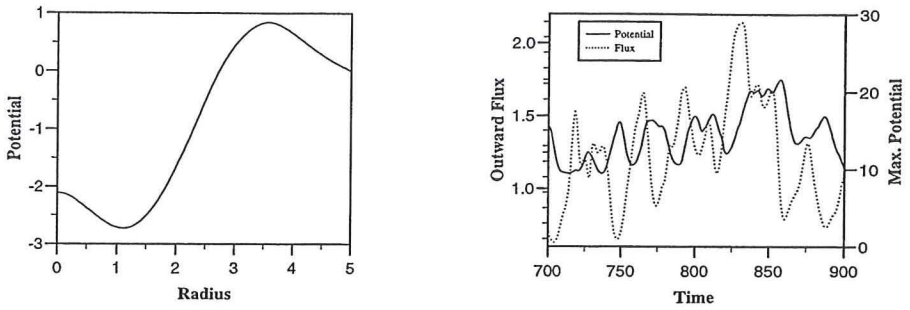

Figure 2: Radial profile of the electrostatic potential (left) and maximum of potential as a measure of shear with particle-flux over time (right)

V. Drift-Waves/Interchange Modes

If we fix background ($k_{||} = 0$) profiles for the potential ϕ_0 and density n_0 and assume that these quantities are constant solutions of the equations we obtain the following set of equations for the perturbations n and ϕ and respectively w

$$\partial_t w = \left\{n, B^{-1}\right\} + \{w_0 + w, \phi\} + \{w, \phi_0\} + \frac{\nabla_{||}^2}{n_0 \eta}(n - \phi) + \mu \nabla^2 w \tag{3}$$

$$\partial_t n = \left\{n - \phi, B^{-1}\right\} + \{\ln n_0, \phi\} + \{n, \phi + \phi_0\} + \frac{\nabla_{||}^2}{n_0 \eta}(n - \phi) + \chi \nabla^2 n \tag{4}$$

This is a system which describes drift-wave perturbations with finite $k_{||}$. The most important feature in these simulations is the buildup of a radial electric field as depicted in in Fig. 2 (left). Oszillations of the shear at the boundary measured by the maximum radial field are anti-correlated with the flux as depicted in Fig. 2 (right).

The pressure driven interchange or ballooning mode might play a role in the transition from L- to H-mode in tokamaks. For the slab geometry Takayama [4] showed the existence of zonal counter-streaming which leads to an oscillatory behaviour in the flux. We use Eqs. (3) and (4) with $k_{||} = 0$ to perform simulations of flute/interchange modes. The coupling between the two equations is then due to the curvature of the magnetic field. In cylindrical geometry we observe the linear ballooning of modes and subsequent in the nonlinear phase oszillations are observed. These are of smaller amplitude then the ones reported for slab geometry.

In both cases the back reaction onto the profiles is not negligible. This back-reaction is only described correctly within a model that allows for modes with and without finite $k_{||}$

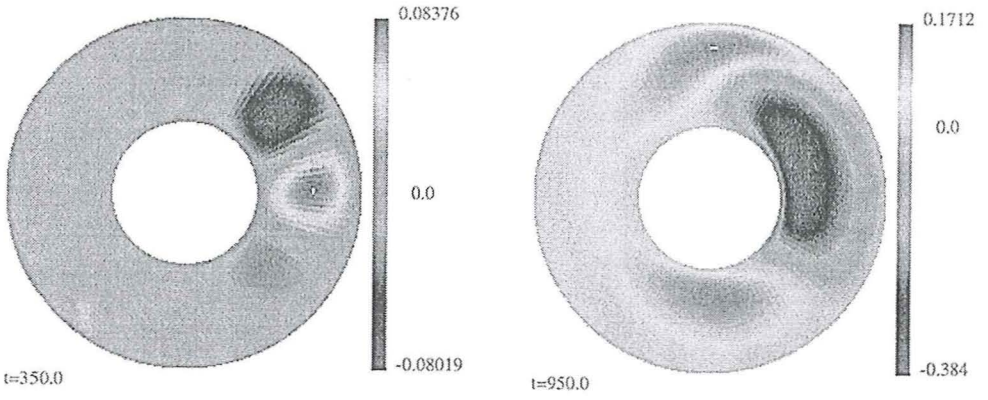

Figure 3: Linear ballooning (left) and non-linear flow phase (right) for the interchange mode.

at the same time.

VI. Conclusion

The simulations show clearly that for an integrated understanding of the plasma behaviour in cylindrical geometry a three dimensional approach is inevitable. Work towards such a solver is on its way and results will be presented in the near future. Nevertheless the two-dimensional simulations give valuable information about the dynamics of the flow at least in some phases of the plasma evolution.

Acknowledgements Discussions with J.J. Rasmussen are greatfully acknowledged. The work was performed under the European Union Marie Curie grant N° 5004-CT96-5023.

References

[1] B. D. Scott, *Three Dimensional Computation of Collisional Drift Wave Turbulence and Transport in Tokamak Geometry*, Plasma Physics and Controlled Fusion 4 (1997).

[2] D. Biskamp und A. Zeiler, *Nonlinear Instability Mechanism in 3D Collisional Drift-Wave Turbulence*, Phys. Rev. Lett. **74** (1995) 706–709.

[3] K. Rypdal, O. E. Garcia und J. V. Paulsen, *Anomalous Cross-Field Current and Fluctuating Equilibrium of Magnetized Plasmas*, Phys. Rev. Letters (1997).

[4] A. Takayama, M. Wakatani und H. Sugama, *Suppression of non-linear interchange mode by zonal couterstreaming flow generation*, Phys. Plasmas **3** (1996) 3–5.

Direct perturbative gyrokinetic approach for non Hamiltonian systems

M. Tessarotto, M. Pozzo, R. Zorat,
Department of Mathematical Sciences, University of Trieste, 34127 Trieste, Italy,

and **R.B. White**
PPPL, Princeton University, Princeton, NJ 08543, USA

Abstract

A fundamental aspect of gyrokinetic theory and particle simulation approaches is the formulation of particle gyrokinetic theory for non-Hamiltonian systems. The most notable example is given by the equations of the characteristics for stochastical partial derivative equations, which describe a collisional magnetoplasma in the presence of perturbations. In this work, a new perturbative approach is developed in order to generalize a non-linear gyrokinetic to non-Hamiltonian systems.

1 Introduction

Regarding stability and transport problems, plasma flows play an essential role on plasma dynamics, particularly in the case of $\mathbf{E} \times \mathbf{B}$-drifts comparable to the thermal speed. Their influence manifests on the linear and nonlinear stability of electromagnetic (e.m.) perturbations present in the magnetoplasma, especially when the perpendicular wavelength is comparable to the ionic Larmor radius. This involves the formulation of nonlinear single-particle gyrokinetics in the presence of flows, able to describe the dynamics of energetic particles as well as the long-time behavior of thermal particles. The most general picture, which aims to describe a magnetoplasma in the presence of binary Coulomb collisions, electromagnetic turbulence or stochastic magnetic fields, requires a perturbative theory for non-Hamiltonian systems, in terms of appropriate expansions parameters characterizing the Larmor radius expansion: $\varepsilon = r_L/L$, λ and δ. Here r_L, L represent, respectively, the particle Larmor radius and a macroscopic scale length, λ the amplitude and δ the perpendicular wavelength of the perturbations of the e.m. fields.

The main goals of the work are therefore: the construction of a direct approach to gyrokinetic theory for collisional magnetoplasmas (i.e., non-Hamiltonian dynamical systems); the construction of a nonlinear gyrokinetic mechanics in the presence of strong

flows and subject to e.m. perturbations with arbitrary perpendicular wavelength, extending the Lagrangian approach developed by Tessarotto *et al.* [1] and Pozzo *et al.* [2]. For this purpose, the Euler-Lagrange equations of motion are represented relatively to a non inertial reference frame locally at rest with respect to the species mass flow velocity ($\mathbf{V}_s$), taking into account of *both equilibrium* and *perturbed* mass flow velocities.

The effects produced both by equilibrium and perturbed flows are analyzed. In particular, the existence of coupling terms between flows and e.m. perturbations, and of diamagnetic contributions and equilibrium gradients is demonstrated.

2 Construction of second-order gyrokinetic theory

For stronly magnetized plasmas, i.e. plasmas immersed in suitably "strong" magnetic fields, it is necessary to introduce the so-called strong $\mathbf{E} \times \mathbf{B}$-drift ordering formulation.[3] This is formally obtained defining the non-canonical particle state $\mathbf{z} \equiv (\mathbf{y} \equiv [\mathbf{r}, u, \mu], \phi)$, (with $\mu = \frac{M_s w^2}{2B}$ the particle magnetic moment, ϕ the gyrophase) and introducing the particle velocity in the form $\mathbf{v} = u\mathbf{b} + \mathbf{w} + \mathbf{V}(\mathbf{r}, t)$, being $\mathbf{V}(\mathbf{r}, t)$ a suitable effective drift velocity assumed to be comparable to the particle velocity

$$\mathbf{V}(\mathbf{r}, t) = \mathbf{v}_E + \mathbf{v}_\chi + U_0(\mathbf{r}, t)\mathbf{b}, \quad | \mathbf{V}(\mathbf{r}, t) | / | \mathbf{v} | \sim O(\varepsilon^0), \tag{1}$$

where $\mathbf{v}_E$ and $\mathbf{v}_\chi$ are respectively the $\mathbf{E} \times \mathbf{B}$-drift velocity $\mathbf{v}_E = \frac{c\mathbf{E}(\mathbf{r},t)\times\mathbf{b}}{B}$ and the effective drift velocity $\mathbf{v}_\chi = \frac{c\nabla\chi\times\mathbf{b}}{B}$ with χ *"a priori"* an arbitrary function.

Guiding center mechanics can be formulated by introducing an appropriate mapping between the (canonical) particle state $\mathbf{x} \equiv (\mathbf{q}, \mathbf{p})$ and a set of generally non-canonical *gyrokinetic* [4] variables $\mathbf{z}' \equiv (\mathbf{y}', \phi')$ which exhibit the properties that their equations of motion are independent of the gyrophase ϕ' (where all primed quantities are evaluated at the guiding center position).

Both for Hamiltonian and non-Hamiltonian system, the gyrokinetic approach is based on a direct construction method of the *gyrokinetic transformation* $\mathbf{r} \to \mathbf{r}'$, to be specified in terms of the *ansatz*

$$\mathbf{r} = \mathbf{r}' + \varepsilon\mathbf{r}'_1 + \varepsilon^2\mathbf{r}'_2, \tag{2}$$

with $\varepsilon\mathbf{r}'_1 = -\varepsilon\frac{\mathbf{w}'\times\mathbf{b}'}{\Omega'_s}$, and the velocity transformation

$$\mathbf{v} = u'\mathbf{b}' + \mathbf{w}' + \mathbf{V}' + \varepsilon\mathbf{v}'_1 + \varepsilon^2\mathbf{v}'_2, \tag{3}$$

i.e., by adopting a perturbative scheme, with $\mathbf{r}'_i$ and $\mathbf{v}'_i$ $(i = 1, 2)$ the unknowns of the problem. For definitess, in the remainder, we present the basic formalism for Hamiltonian

systems. Details and results pertaining specifically to non-Hamiltonian systems will be reported elsewhere.[5] Thus, in particular, for Hamiltonian systems, the Lagrangian

$$\mathcal{L} = \frac{d}{dt}\mathbf{r}\cdot\left[M_s\mathbf{v} + \frac{Z_s e}{c\varepsilon}\mathbf{A}\right] - \mathcal{H}, \tag{4}$$

with $\mathcal{H} = \frac{M_s v^2}{2} + \frac{Z_s e}{\varepsilon}\Phi$, is expanded in power series of ε by introducing the previous gyrokinetic transformations, together with analogous ones for the e.m. potentials. Defining suitable gyrokinetic variables, *i.e.,* for example, $\mathbf{z}' \equiv (\mathbf{r}', u', w', \phi')$, it can be proven that, at arbitrary order n, the gyrokinetic Lagrangian is of the form $\mathcal{L}^{(n)}(\mathbf{z}, \dot{\mathbf{z}}, \mathbf{t}) = \mathcal{L}^{(n)}(\mathbf{r}', \dot{\mathbf{r}}', u', w', \dot{\phi}', t)$ and is manifestly invariant with respect to any *dynamical gauge transformation* $\mathcal{L}^{(n)} \rightarrow \mathcal{L}^{(n)} + \frac{d}{dt}F(\mathbf{r}', u', w', \phi', t)$ being $F(\mathbf{r}', u', w', \phi', t)$ the dynamical gauge function. Furthermore, there follows that since, by construction, in such variables the gyrophase ϕ' is ignorable for $\mathcal{L}^{(n)}$, its conjugate momentum, $p_{\phi'} \equiv \frac{\partial}{\partial \dot{\phi}}\mathcal{L}^{(n)}(\mathbf{r}', \dot{\mathbf{r}}', u', w', \dot{\phi}', t) \equiv -\frac{Z_s e}{M_s c}M'$ [with M' the magnetic moment], is obviously a first integral of gyrokinetic motion at *any order n in* ε.

Furthermore, the gyrokinetic (Euler-Lagrange) equations of motion immediately follow from the *hybrid form of Hamilton variational principle* [6]

$$\delta J(\mathbf{z}') = \delta \int_{t_1}^{t_2} dt \mathcal{L}^{(n)}(\mathbf{z}'(t), \dot{\mathbf{z}}'(t), t) = 0. \tag{5}$$

In particular, the second-order approximation to the gyrokinetic Lagrangian, $\mathcal{L}^{(2)}$, *i.e.,* one order higher than previous gyrokinetic calculations, [3] [7] can be obtained by requiring that the e.m. potentials depend "slowly" on time $\mathbf{A} = \frac{1}{\varepsilon}\mathbf{A}_{-1}(\mathbf{r}, \varepsilon^2 t) + \mathbf{A}_0(\mathbf{r}, t) + \varepsilon\mathbf{A}_1(\mathbf{r}, t) + ..$, $\Phi = \frac{1}{\varepsilon}\Phi_{-1}(\mathbf{r}, \varepsilon^2 t) + \Phi_0(\mathbf{r}, t) + \varepsilon\Phi_1(\mathbf{r}, t) + ..$ and are smooth functions of $\mathbf{r}$ [*i.e.,* at least $C^3(\Re^3)$], which permits to represent them in terms of the Taylor-series expansions.[5] Then, neglecting appropriate gauge-invariant contributions of the form $\frac{d}{dt}F(\mathbf{z}', \dot{\mathbf{z}}' t)$, the Lagrangian $\mathcal{L}^{(2)}$ [$\equiv \mathcal{L} + O(\varepsilon^2)$] correct *through* first order in ε may be cast in the form $\mathcal{L}^{(2)} = \overline{\mathcal{L}}^{(2)} + \tilde{\mathcal{L}}^{(2)}$ where $\overline{\mathcal{L}}^{(2)} \equiv \frac{1}{2\pi}\int_0^{2\pi} d\phi' \mathcal{L}^{(2)}$ and $\tilde{\mathcal{L}}^{(2)}$ can be set equal to zero by properly defining the unknowns of the problem. Correct *through* first order in ε, there follows

$$\mathcal{L}^{(2)} = \overline{\mathcal{L}}^{(2)} \equiv \dot{\mathbf{r}}' \cdot \frac{Z_s e}{c\varepsilon}\mathbf{A}^* - \left(\frac{\dot{\phi}'}{\Omega_s'} + 1\right) M'B' - \frac{M_s}{2}\left(u'\mathbf{b}' + \mathbf{V}'\right)^2 - \frac{Z_s e}{\varepsilon}\Phi^*, \tag{6}$$

where $\mathbf{A}^*, \Phi^*$ are the effective electromagnetic potentials

$$\begin{aligned} \mathbf{A}^* = \mathbf{A}' + \varepsilon\tfrac{M_s c}{Z_s e}\left(u'\mathbf{b}' + \mathbf{V}'\right) + 2\varepsilon^2\tfrac{\mu' c B'}{Z_s e \Omega_s'}\nabla'\mathbf{e}_2 \cdot \mathbf{e}_1 + \\ -\varepsilon^2\tfrac{c\mu'}{2Z_s e\Omega_s'}\left[\left(\nabla'\nabla'\mathbf{A}'\right) : \left(\underline{\underline{1}} - \mathbf{b}'\mathbf{b}'\right) - \left(\underline{\underline{1}} - \mathbf{b}'\mathbf{b}'\right) : \nabla'\nabla'\mathbf{A}'\right], \end{aligned} \tag{7}$$

$$\Phi^* = \Phi - \varepsilon^2 \frac{c\mu'}{Z_s e \Omega'_s} [\nabla' \cdot \mathbf{E}' - \mathbf{b}'\mathbf{b}' : \nabla' \mathbf{E}'] - \varepsilon^2 \frac{2\mu' B'}{Z_s e \Omega'_s} \frac{\partial}{\partial t} \mathbf{e}_2 \cdot \mathbf{e}_1. \quad (8)$$

Furthermore M', the magnetic moment correct through first order reads

$$M' \equiv \mu' \left\{ 1 + \varepsilon \frac{M_s}{B'\mu'} \langle \mathbf{v}'_1 . \mathbf{w}' \rangle_\phi \right\} \equiv \mu' + \varepsilon \mu'^{(1)}, \quad (9)$$

with $\varepsilon \frac{M_s}{B'\mu'} \langle \mathbf{v}'_1 . \mathbf{w}' \rangle_\phi = -\varepsilon \frac{4\pi u'}{c\Omega'_s B'} J'_{||} - \varepsilon \frac{1}{\Omega'_s} \mathbf{b}' \cdot \nabla' \times \mathbf{V}'$. Upon requiring that $\varepsilon \frac{4\pi u'}{c\Omega'_s B'} J'_{||} \sim O(\varepsilon^2)$, Eq.(9) is consistent with the analogous expression obtained by Bernstein and Catto,[3] i.e., $M' \cong \mu' \left\{ 1 - \varepsilon \frac{1}{\Omega'_s} \mathbf{b}' \cdot \nabla' \times \mathbf{V}' \right\} + O(\varepsilon^2)$ implying that, correct to second order in ε, one can replace μ' with M' in Eqs.(7) and (8). The Euler-Lagrange equations of motion for the gyrokinetic variables $\mathbf{z}' \equiv (\mathbf{r}', u', M', \phi')$,[5] result fully consistent with the previous first-order calculations.[3] Analogously, dropping the fluid velocity, the well known first-order gyrokinetic equations [6] are recovered.

3 Conclusions

The present approach extends to strongly magnetized plasmas in the presence of flows the results of nonlinear particle gyrokinetics due to Dubin *et al.*, [8] Hahm *et al.* [9] and Brizard [10] and generalizes the Lagrangian approach due to Tessarotto *et al.* [1] and Pozzo *et al.* [2]. The theory is susceptible of potentially significant applications both to gyrokinetic particle simulations and kinetic theory.

Acknowledgments

This work has been sponsored by the Italian National Research Council, through the "Gruppo Nazionale per la Fisica Matematica"(GNFM, National Group of Mathematical Physics), the Consorzio di Magnetofluidodinamica, Trieste University, Italy and the research program MURST 40% (Italian Ministry of Scientific Research) "Sorgenti di Plasma".

References

[1] M. Tessarotto, L.J. Zheng and G. Favretto, Bull. Am. Phys. Soc. **40**, 1683 (1995).

[2] M. Pozzo, M. Tessarotto and R. Zorat, *Theory of Fusion Plasmas 1996*, ed. by E.Sindoni et al. (Società Italiana di Fisica, Editrice Compositori, Bologna, Italy, 1996), p.295.

[3] I.B. Bernstein and P.J. Catto, Phys. Fluids **28**, 1342 (1985).

[4] P.J. Catto, Plasma Phys. **20**, 719 (1978).

[5] M. Tessarotto, M. Pozzo, R.B. White and R. Zorat, "Non-linear non-Hamiltonian particle gyrokinetic theory in the presence of flows", submitted (1997).

[6] R.G. Littlejohn, J. Plasma Phys. **29**, 111 (1983).

[7] B. Weyssow and R. Balescu, J. Plasma Phys. **35**, 449 (1986).

[8] D.H.E. Dubin, J.A. Krommes, C. Oberman and W.W. Lee, Phys. Fluids **26**, 3524 (1983).

[9] T.S. Hahm, W.W. Lee and A. Brizard, Phys. Fluids **31**, 1940 (1988).

[10] A. Brizard, Phys. Plasmas **2**, 459 (1995).

Improvements on nonlinear gyrokinetic particle simulations based on δf-discretization scheme

R. Zorat and M. Tessarotto
Department of Mathematical Sciences
University of Trieste, I-34127 Trieste, Italy

Abstract

In this work various issues regarding the definition of improved theoretical models appropriate to describe the dynamics of confined magnetoplasmas by particle simulation methods are proposed. These concern in particular an improved non linear δf discretization scheme and the treatment of binary, i.e. Coulomb, and collective interactions.

I - Introduction Particle simulation methods are used to study the dynamics of a mechanical system composed by a very high number of particles, interacting one another, with some approximation. In fact its evolution is determined by evolving a smaller number of so called *test particles*. This approximation introduces an error as higher as fewer are the test particles used. This method is very powerful to study many phenomena regarding magnetoplasmas, but it is necessary to describe with prescribed accuracy the concerned phenomenology. In particular, the motion equations, that advance the test particle gyrokinetic states, must be correct up to prescribed order, when expressed in power series of the parameters which characterize the considered magnetoplasma, to describe the dynamics of energetic test particles in plasmas as well as the long-time behavior of thermal test particles [1], [2]. Another basic aspect of the particle simulation methods concerns the search of advanced weighting schemes with reduced algorithmic complexity. In this regard the δf-weighting schemes [3], [4], [5], [6] are relevant in the study of hot magnetoplasmas by non-linear particle simulations because of its reduced noise.

II - Improved δf discretization scheme In order to obtain the dynamics of the considered magnetoplasma, we must resolve the system of equations, composed, by the Vlasov gyrokinetic equation $\mathcal{L}_s f_s = 0$, the Maxwell equations in the quasi-static approximation $\nabla \cdot \mathbf{E} = 4\pi\rho$, $\nabla \times \mathbf{B} = \frac{4\pi}{c}\mathbf{J}$ and the particle motion equations. Particle simulation methods can be used for a numerical resolution and at this regard in the last years the so called δf weighting schemes [3], [4], [5], [6]had been developed. These reduce the simulation noise, produced mainly by the calculation of the moments from the discretized

form of f_s used in the simulation, as much as f_s remains close to a certain equilibrium function $f_{0,s}$, supposed analytically known. In them, they separate $f_s = f_{0,s} + \delta f_s$, where δf_s is the *perturbation* of $f_{0,s}$. In the calculation of the moments they use the discretized expression of δf_s and the analytically known expression of $f_{0,s}$. The last one doesn't produce simulation noise. Our δf discretization scheme, valid for Hamiltonian particle dynamics (which implies $\mathcal{L}f = \frac{d}{dt}f = 0$), expressed with the non canonical gyrokinetic variables $\mathbf{y}'$ (it is possible to extend the treatment to general non Hamiltonian dynamics [1]) is more general than a previous scheme [6] and can be summarized as follows

$$\delta f^{(D)} = c \sum_{i=1}^{N_T} \delta\left(\mathbf{y}' - \mathbf{y}'_i(t)\right) w_i(t) F\left(\mathbf{y}', t\right) \quad ; \quad w_i(t) = \frac{\delta f(\mathbf{y}',t)}{g(\mathbf{y}',t)} \mid_{\mathbf{y}'=\mathbf{y}'_i(t)} \quad ; \quad \frac{d}{dt} g = \frac{d}{dt} F = 0$$
$$w_i\left(t\right) = \frac{f\left(\mathbf{y}'_i(t_0),t_0\right)}{g\left(\mathbf{y}'_i(t_0),t_0\right)} + \exp\left[\int_{t_0}^{t} dt' S\left(\mathbf{y}'_i\left(t\right),t\right)\right]\left[w_i\left(t_0\right) - \frac{f\left(\mathbf{y}'_i(t_0),t_0\right)}{g\left(\mathbf{y}'_i(t_0),t_0\right)}\right].$$

In fact this scheme permits an arbitrary choice of the initial perturbation $\delta f\left(t_0\right)$ and consequently of the initial values of the weights $w_i\left(t_0\right)$. Moreover, equaling the expression of the δf moments, obtained putting in, respectively, the analytical and the discretized expression of δf, we obtain a more general *normalization condition*

$$\Delta \mathbf{y}'_i\left(t\right) \frac{g\left(\mathbf{y}'_i\left(t\right),t\right)}{F\left(\mathbf{y}'_i\left(t\right),t\right)} = c,$$

where $\Delta \mathbf{y}'_i\left(t\right)$ is the amplitude of the volume element associated to $\mathbf{y}'_i\left(t\right)$. So we have more freedom in the choice of the initial values $\mathbf{y}'_i\left(t_0\right)$ of the test particle variables and we can therefore try to put them prevailing in the gyrokinetic phase space regions where the initial perturbation chosen is localized. So, by using the same number of test particles as before, the noise of the algorithm decreases.

III - Treatment of collective e.m. interactions The e.m. autoconsistent fields produced by the various species of the magnetoplasma can be expressed directly from the gyrokinetic distribution functions f_s. This can be made by expressing the e.m. selfconsistent fields $\mathbf{E}^{(int)}$ and $\mathbf{B}^{(int)}$ in terms of the selfconsistent potentials $\mathbf{A}^{(int)}$ and $\Phi^{(int)}$. In the Coulomb gauge $\left(\nabla \cdot \mathbf{A}^{(int)} = 0\right)$ the e.m. potentials obey the well known equations

$$\nabla^2 \Phi^{(int)} = -4\pi \rho^{(int)}\left(\mathbf{r}, t\right) \quad ; \quad \nabla^2 \mathbf{A}^{(int)} = -\frac{4\pi}{c} \mathbf{J}^{(int)}\left(\mathbf{r}, t\right)$$

whose solution, determined by using the Green functions method, are

$$\Phi^{(int)}\left(\mathbf{r}'^{*},t\right)=\sum_{s=1}^{n_{sp}}Z_s e\left[\int_{V_{pl}}d^3r\int d^3v\,\frac{1}{|\mathbf{r}-\mathbf{r}'^{*}|}f_s\left(\mathbf{r},\mathbf{v},t\right)\right]+\int_{V_{par}}d^3r\,\frac{\rho^{(par)}(\mathbf{r},t)}{|\mathbf{r}-\mathbf{r}'^{*}|}$$

$$\mathbf{A}^{(int)}\left(\mathbf{r}'^{*},t\right)=\sum_{s=1}^{n_{sp}}\frac{Z_s e}{c}\left[\int_{V_{pl}}d^3r\int d^3v\,\frac{\mathbf{v}}{|\mathbf{r}-\mathbf{r}'^{*}|}f_s\left(\mathbf{r},\mathbf{v},t\right)\right]+\frac{1}{c}\int_{V_{par}}d^3r\,\frac{\mathbf{J}^{(par)}(\mathbf{r},t)}{|\mathbf{r}-\mathbf{r}'^{*}|},$$

where the last terms of the two equations include the effects of charges and currents flowing outside the magnetoplasma in the conducting walls of the vessel containing it.

IV - Treatment of binary e.m. interactions We can treat a collisional magnetoplasma too, by using suitable Monte Carlo operators developed by Tessarotto et al. [7]. These operators approximate the linearized Landau-Fokker-Planck operator and satisfy its fundamental conservation laws. The L.-F.-P. equation $\mathcal{L}f_s = C\left(f|f\right)$ is replaced by a suitable *stochastical Liouville equation* $\mathcal{L}\delta f_s = -S_1 f_{0,s}$, where

$$\mathcal{L}\delta f_s=\left[\frac{\partial}{\partial t}\delta f_s+\mathbf{v}\cdot\frac{\partial}{\partial\mathbf{r}}\delta f_s+\frac{Z_s e}{m_s}\left(\mathbf{E}+\frac{\mathbf{v}\times\mathbf{B}}{c}\right)\cdot\frac{\partial}{\partial\mathbf{v}}\delta f_s\right]+\frac{\partial}{\partial\mathbf{v}}\cdot\left[\left(\frac{\langle\Delta\mathbf{v}\rangle}{\Delta t}^{(0)}+\mathbf{a}^{S}\right)\delta f_s\right]$$

$$S_1 f_{0,s}\doteq-\mathcal{L}f_{0,s}+\frac{\partial}{\partial\mathbf{v}}\cdot\left[\frac{\langle\Delta\mathbf{v}\rangle}{\Delta t}^{(1)}f_{0,s}\right]$$

$\frac{\langle\Delta\mathbf{v}\rangle}{\Delta t}^{(0)}$, and $\frac{\langle\Delta\mathbf{v}\rangle}{\Delta t}^{(1)}$ are the components of the friction vector and $\mathbf{a}^S$ is a suitable defined *stochastical force.* Then we express the stochastical Liouville equation in the conservative form by using the gyrokinetic variables $\mathbf{z}' = (\mathbf{r}', \mathcal{H}', M', \phi')$, where now the considered equations of motion expressed as finite difference equations have the form

$$\left(\frac{d}{dt}\mathbf{z}'\right)^{(tot)}\Delta t=\left(\frac{d}{dt}\mathbf{z}'\right)\Delta t+\Delta\mathbf{z}',$$

Δt is the temporal step, $\frac{d}{dt}\mathbf{z}'$ is deduced from suitable deterministic gyrokinetic equations of motion and $\Delta\mathbf{z}'$ is the stochastical effect produced in the time Δt by Coulomb interaction on the test particle gyrokinetic state, which causes the diffusion in the velocity space.

This diffusion can be described with a set of *normal* coordinates, i.e. in terms of which the Coulomb diffusion tensor $\frac{\langle\Delta\mathbf{v}\Delta\mathbf{v}\rangle}{\Delta t}$ is diagonal (for example $T=\frac{m_s v^2}{2}$ and $\lambda=\frac{\mathbf{v}\cdot\mathbf{b}}{v}$) and we can therefore write $\Delta y^i \doteq \frac{\partial y^i}{\partial T}\Delta T+\frac{\partial y^i}{\partial\lambda}\Delta\lambda$. The variations ΔT and $\Delta\lambda$ are determined by using the following Monte Carlo collision operator expressed as finite difference stochastical equations

$$\Delta T\doteq\langle\Delta T\rangle+\alpha_T\sigma_T^{\frac{1}{2}}\ ;\ \Delta\lambda\doteq\langle\Delta\lambda\rangle+\alpha_\lambda\sigma_\lambda^{\frac{1}{2}}$$

$$\langle\Delta T\rangle\doteq\Delta t\frac{\langle\Delta T\rangle}{\Delta t}^{(0)}\ ;\ \langle\Delta\lambda\rangle\doteq\Delta t\frac{\langle\Delta\lambda\rangle}{\Delta t}^{(0)}\ ;\ \sigma_T=\langle\Delta T^2\rangle-\langle\Delta T\rangle^2\ ;\ \sigma_\lambda=\langle\Delta\lambda^2\rangle-\langle\Delta\lambda\rangle^2$$

with $\langle \Delta T^2 \rangle = \Delta t \frac{\langle \Delta T \Delta T \rangle}{\Delta t}$, $\langle \Delta \lambda^2 \rangle = \Delta t \frac{\langle \Delta \lambda \Delta \lambda \rangle}{\Delta t}$. The quantities α_T and α_λ are stochastical numbers, assuming values in the range $[-1, +1]$ and which are different from zero only in a finite set of instants (the *collision instants*) equally spaced. The *stochastical Liouville equation* is always valid, except at the collision instants, where we must impose

$$\left(\delta f_s'\right)_- = \left(\delta f_s'\right)_+ \quad ; \quad (f_{0,s})_- = (f_{0,s})_+$$

as continuity conditions. In the open temporal intervals $]t_k, t_{k+1}[$ the equations of motion for the test particles are deterministic, by contrast the stochastical effects of the collisions for each interval are added at the corresponding collision instant t_k.

V - CONCLUSIONS We have derived an have improved δf discretization scheme for permitting the accurate evaluation of arbitrary velocity moments of δf, which allows an arbitrary choice of the initial perturbation $\delta f(t_0)$ and of the initial states $\mathbf{y}_i'(t_0)$ of the test particles. Finally we have given an accurate description of the e.m. collective interactions making use of the Green functions method taking into account also the effect of boundary conditions on the walls of the vessel and of the binary Coulomb interactions by accurate Monte Carlo operators, which satisfy its fundamental conservation laws.

ACKNOWLEDGMENTS Work sponsored by the Italian National Research Council, through the "Gruppo Nazionale per la Fisica Matematica"(GNFM, National Group of Mathematical Physics) and the Consorzio di Magnetofluidodinamica, Trieste University, Italy.

References

[1] see M.Tessarotto, M.Pozzo, R.B. White and R. Zorat, *"Direct perturbative gyrokinetic approach for non Hamiltonian systems"*, in this Conference
[2] M. Pozzo, M. Tessarotto and R. Zorat, in *Theory of fusion Plasmas*, E.Sindoni *et al.* eds. (Società Italiana di Fisica, Editrice Compositori, Bologna, 1996), p.295
[3] T. Tajima and F. Perkins, 1983 International Sherwood Fusion Theory Conference.
[4] M. Kotschenreuther, Bull.Am.Phys.Soc. **34**, 2107 (1988).
[5] G. DiPeso, E.C. Morse and R.W. Ziolkowski, J.Comput.Phys. **96**, 325 (1991)
[6] S.E. Parker and W.W. Lee, Phys.Fluids **B 5**, 77 (1993)
[7] M. Tessarotto, R. B. White, and L.-J. Zheng, Phys. Plasmas **1**, 951 (1994)
[8] M. Tessarotto and M. Pozzo, Bull. Am. Phys. Soc. **41**, 1493 (1996)

Analysis of collective light scattering in terms of drift wave turbulence models

T. Jessen, P. K. Michelsen, M. Saffman and W. Svendsen

Risø National Laboratory — Association Euratom
Optics and Fluid Dynamics Department
P.O. Box 49, DK-4000 Roskilde, Denmark

Abstract. Drift waves have been proposed as possible mechanisms for particle and energy transport in fusion plasmas, and theoretical drift wave models, such as the Hasegawa-Mima and Hasegawa-Wakatani models, have been derived. Valuable insight into the drift wave dynamics can be gained from numerical studies of these models.

For a number of years, collective light scattering has been used to probe such density fluctuations in fusion plasmas. A recently developed hybrid Doppler and time-of-flight CO_2 laser anemometer has been installed at the Wendelstein 7-AS stellerator. This new configuration enhances spatial resolution by coherent detection of scattering from two neighbouring measurement volumes. Large-scale turbulence structures can be observed by correlating the two scattering signals. Accurate numerical solutions of drift wave model equations, obtained using spectral methods, provide expected signal features and are employed in the data interpretation.

Background. A hybrid Doppler/time-of-flight anemometer is installed at W7-AS. Coherent scattering from elongated measurements volumes, illuminated by a 25 W CO_2 laser, is heterodynely detected and sampled at 20 ns intervals to yield time series of $\tilde{n}(t)$, the electron density fluctuation in the measurement volume. Total density is $n(t) = \tilde{n}(t) + n_0$, where n_0 is time-averaged value. The use of rotating prisms allows the measurement direction to be continuously changed from poloidal to radial. Scattering is currently maximised at fluctuation wave number $k \sim 35$ cm^{-1}, but can be varied by adjusting laser beam width.

The new configuration detects scattering from *two* measurement volumes, of separation ~ 1 cm, and hence allows for correlation analysis. The use of correlation techniques enhances spatial resolution, and large-scale turbulence structures can be probed. The measurement volumes can be aligned poloidally or radially, so transport in both directions can be investigated.

Numerical model. The two-point configuration has prompted several questions regarding correlation techniques and data interpretation. In order to resolve these issues we have recently implemented a numerical turbulence model. The model serves to estimate correlation length and time scales, predict expected signal features and test two-point data analysis procedures by comparison with the full field information available in the numerical simulation.

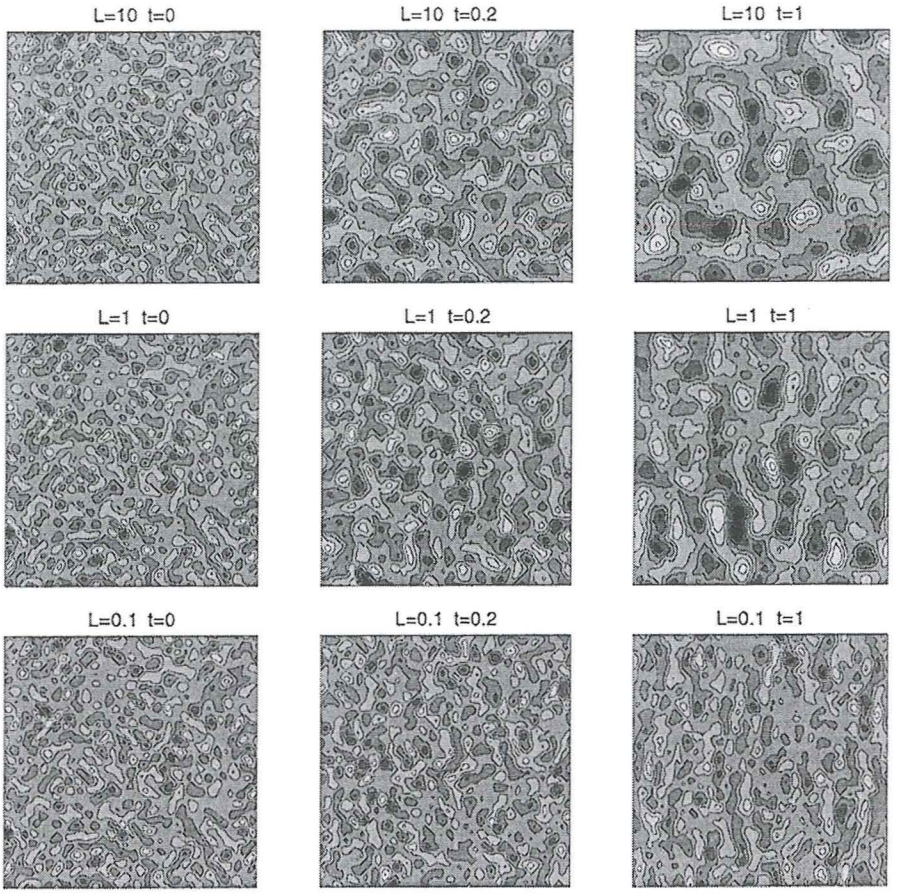

Figure 1. *Evolutions of the ϕ-field from the same initial state, for three values of L. (L given in metres, t in seconds.)*

As a model of drift wave turbulence in the plane perpendicular to the confining magnetic field, we have chosen the well-known Hasegawa-Mima equation[1]

$$\frac{\partial}{\partial t}(\nabla^2\phi - \phi) + \{\phi, \nabla^2\phi\} = \beta\frac{\partial\phi}{\partial y} \tag{1}$$

where $\{\cdot,\cdot\}$ denotes the Poisson-bracket $\{f,g\} = \partial_x f \partial_y g - \partial_y f \partial_x g$, and ϕ is the electrostatic potential. The model parameter $\beta = -1/L$ is defined in terms of density scale length, assuming an exponential background density profile in x-direction $n_0 \propto \exp(x/L)$. The model assumes adiabatic electron response with density fluctuation level $\tilde{n}/n_0 = \phi$.

Equation (1) is given in dimensionless units, by normalising potential by T_e/e, space by C_s/Ω_i and time by $1/\Omega_i$, where $C_s = (T_e/m_i)$ is sound speed and $\Omega_i = eB/m_i$ is ion cyclotron frequency.

The HM equation (1) was solved on a double-periodic rectangular domain for a variety of initial states, using a highly accurate Fourier-Galerkin spectral method with explicit multistep time forwarding. In all simulation we have chosen domain side length 10 cm, magnetic field strength $B = 2$ T and electron temperature $T_e = 1$ keV. The density scale length L was varied, in order to study the transition from weakly to strongly non-linear regimes. $L \to 0$ corresponds to the linear limit without mode coupling, where each mode evolves according to the dispersion relation $w_k = \beta k_y/(1 + k^2)$. $L \to \infty$ corresponds to increasingly non-linear mode coupling.

The effect of varying L is illustrated in figure 1. The same initial state evolves entirely different depending on the choice of L. For small L each mode evolves independently and there is no change of k-spectrum and fluctuation scale. For larger values of L non-linear mode coupling quickly redistributes the spectrum and the 2D inverse energy cascade results in formation of large long-lived vortical structures.

Obviously, non-linear mode-coupling, spectral redistribution and cascade phenomena, must profoundly influence the transport and correlation properties of the system. We have adressed these issues by studying two-point correlations (correlation of time series gathered by sampling the $\tilde{n}/n$-field at two distinct points) and test particle transport (tracking the motion of particles released in the flow and passively advected by it).

Two-point correlation. As a simple model of the scattering experiment we can consider time series of ϕ at fixed points, sampled at regular time intervals. (In the actual experiment scattering originates from a *volume* rather than a point, and hence is predominantly due to fluctuations of a certain scale).

Figure 2 shows time series obtained at two points (x, y) and $(x, y+\Delta y)$, with distance $\Delta y = 0.6$ cm in the y-direction (i.e., the "poloidal" direction), for the simulation in figure 1 (top row). Figure 2 (right) shows the normalised time series correlation. For this particular case, correlation is very good since Δy is well within the correlation length and can reliably be used to estimate the density fluctuation propagation speed.

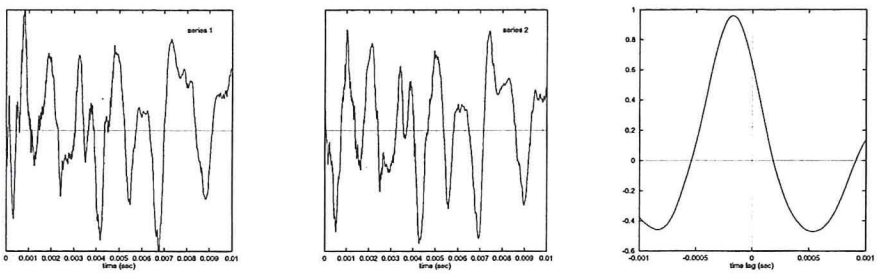

Figure 2. *Left, middle: Time series of $\tilde{n}/n$ at two points of separation Δy. Right: Correlation yields time-of-flight Δt and hence propation speed $\Delta y/\Delta t$.*

Correlation can degrade, however, due to increase in point separation or changes in correlation length due to changes in background density profile. The latter effect is severe. Preliminary results indicate that non-linear coupling markedly increases correlation length and time scales. This is due to the formation of long-lived coherent structures propagating at steady velocity, ensuring long-range correlation.

Particle tracking. Transport patterns are revealed by tracking the motion of particles released in the flow. Figure 3 shows the the final positions (at time $t = 1$ ms) of 500 particles released in the flow for the three simulations in figure 1. Increasing non-linear coupling is seen to lead to increased particle dispersion. In a similar study[2] the opposite effect was reported, i.e., non-linear coupling and coherent structure formation was demonstrated to effectively trap particles in relatively slow moving vortices and hence suppress diffusion. The apparent discrepancy is probably due to the transitional nature of flow. In the strongly non-linear case plasma is violently displaced during the initial formation of large vortex structures, and thereafter diffusion is subdued.

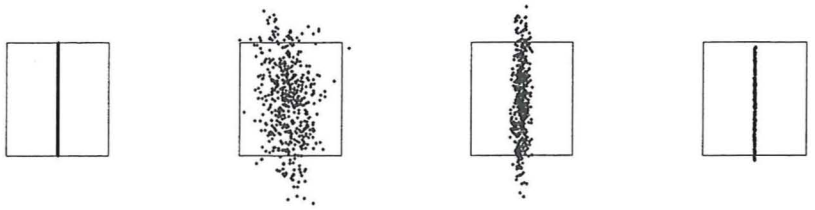

Figure 3. *Left to right: Initial particle positions, positions at time $t = 1$ msec for $L = 10$ m, same for $L = 1$ m, same for $L = 0.1$ m. The box shows the computional domain.*

Summary. A collective scattering diagnostics based on two-point correlations has prompted numerical investigations of drift wave turbulence. A spectral method is employed to obtain high-quality solutions to the Hasegawa-Mima equation. Strongly non-linear mode coupling is found to stimulate formation of coherent structures of long lifetimes that hence covers large distances and promotes long-range correlations. Furthermore, coherent structure formation enhances particle transport. This is probably an effect of the formation phase only and might be suppressed in the fully evolved flow.

Future investigations will aim to solidify these results, broaden the range of initial conditions, enhance model realism and consider the effect of measurement volumes rather than points.

References.

1. A. Hasegawa and K. Mima. *Phys. Fluids* **21**, 87 (1978).
2. G. Manfredi and R. Dendy. *Phys. Plasmas* **4**, 628 (1997).

Analysis of Measured and Simulated Electromagnetic Turbulence in COMPASS-D

W. E. Han, S. Barocio and A. Thyagaraja

UKAEA, Fusion, Culham Science Centre, Abingdon, Oxfordshire, OX14 3DB, UK.
(UKAEA/Euratom Fusion Association)

Abstract

Edge fluctuation data from both COMPASS-D and calculations with the large-eddy simulation code CUTIE have been analysed with a number of techniques. Poloidal asymmetries have been uncovered with an antiballooning character and high frequency standing-wave oscillations have been seen, both between and during ELMs. The latter case is manifested in a strong inverse-chirp feature. These results raise fundamental questions for ELM theory and suggest promising avenues for further exploration.

I Introduction

Edge fluctuations from ELMy H-mode discharges in COMPASS-D have been analysed using Fourier and wavelet transform techniques and singular value decomposition (SVD). Calculations using the large-eddy simulation code CUTIE [1] have also been performed and the results compared with experiment. For the phenomena we have been examining, the benefits of SVD were found to be limited; spatial and temporal Fourier transforms and wavelet transforms are more generally useful. From COMPASS-D we have used magnetic data from a poloidal array of 24 Mirnov coils, during both Ohmic and ECRH shots, and both experiment and simulation used a sampling rate of $1MHz$.

II Wavelet and Fourier Transform Techniques

The wavelet transform has highlighted a number of features which required investigation. Figure 1 shows the wavelet transform of part of the signal from a Mirnov coil during an Ohmic discharge with ELMs on COMPASS-D. The ELMs are distinguished by bursts of activity across the whole observable frequency range $(0 - 500kHz)$. During ELMs it can be seen that there is a strong inverse-chirp feature in the $350 - 450kHz$ range. Figure 2 gives results from a different coil during a time which contains a relatively long period which is free from ELMs. This plot clearly shows activity in three main frequency bands centred at around 60, 120 and $280kHz$ respectively. These three bands of activity are also seen in a shot with $420kW$ of ECRH and twice the toroidal field strength of the Ohmic shots. It is striking that the three features seem independent of these parameters.

We have begun to investigate the structure of the modes which are causing the 3 bands of activity seen in Figure 2. These signals arise from intermittent bursts involving several poloidal harmonics. However, during the times sampled in this investigation, the single most dominant mode corresponded to the harmonics $m = 3$, 7 and 3 for the 60, 120 and $280kHz$ bands respectively. The first two features were rotating, but the $280kHz$ one appeared to be predominantly an $m = 3$ standing wave, suggesting a 'vibrating' locked mode. Figure 3 illustrates this in the phase plot which shows that during the periods of maximum amplitude

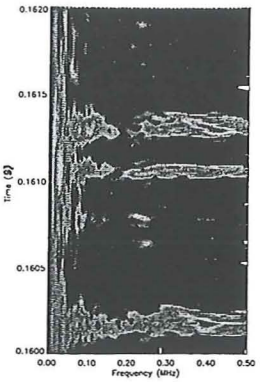

Figure 1. Wavelet transform of a signal from Mirnov coil 14 (toroidal sector 07) on COMPASS-D during an Ohmic shot (#22073) showing ELMs.

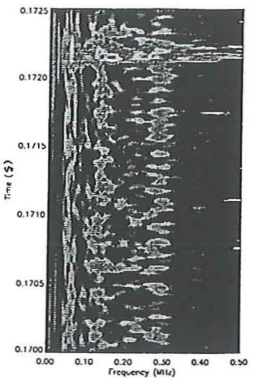

Figure 2. Wavelet transform of a signal from Mirnov coil 4 (toroidal sector 07) on COMPASS-D during an extensive period without ELMing in an Ohmic shot (#22073).

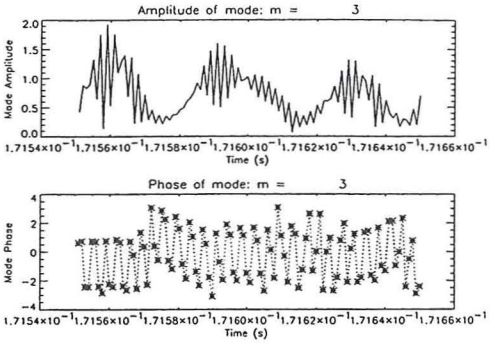

Figure 3. The amplitude and phase of the $m = 3$ (dominant) poloidal harmonic component of the high-frequency (nominally $280kHz$) band during a COMPASS-D Ohmic shot (#22073).

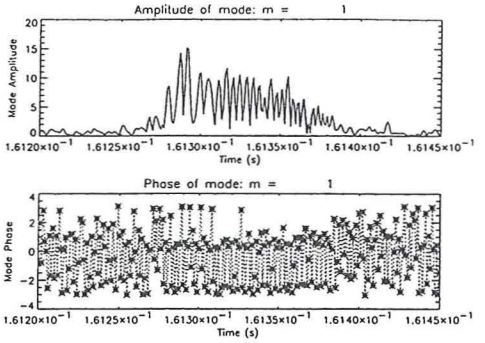

Figure 4. The amplitude and phase of the $m = 1$ (dominant) poloidal harmonic component of the inverse-chirp occurring during an ELM in a COMPASS-D Ohmic shot (#22073).

oscillation the phase of the $m = 3$ harmonic is switching between two values separated by π radians. It is emphasised that this is a 'snapshot' and that the distribution of harmonics will be changing with time.

The inverse-chirp during ELMing has also been looked at and appears to be predominantly an $m = 1$ standing wave (see Figure 4).

Preliminary analyses suggest that, between ELMs, there is a continuous growth of signal energy in the $280kHz$ band, not seen in the other bands. This seems to be accompanied by a gradual increase in the poloidal harmonic content which is initially mainly $m = 1$, cascading to successively higher harmonics. Immediately following an ELM the signal energy and harmonic range are depressed. It is possible that the evolution we see reflects the approach to some threshold conditions which are necessary for the occurrence of an ELM.

III Poloidal Asymmetries

For selected intervals of time we have obtained the temporal Fourier transform of each channel signal and divided the frequency range into three sub-ranges. We have thus defined three

frequency bins, obtaining the fractional signal energy in each bin by integrating over frequencies and normalising. Thus our three bins correspond to: 'low' $(0-100kHz)$, 'medium' $(100-200kHz)$ and 'high' $(200-500kHz)$ respectively. These three ranges were chosen to cleanly capture one of the three bands of strong activity in each bin. We were then able to plot the fractional energy in each bin as a function of channel position. Figures 5 and 6 show plots for a period between ELMs and for the duration of an ELM respectively. The main feature to note about the ELM-free plot is that there are essentially two lobes of significant activity for the high frequencies in relative terms; these lobes are roughly centred near the top and bottom of the poloidal cross-section and are separated from each other by two minima near the inboard and outboard midplane respectively. It can also be seen that the medium frequencies are dominant near the outboard midplane. During an ELM we see that the high frequencies dominate at the lower, inboard quadrant, while the low frequencies dominate on most of the coils above the midplane.

IV Simulation Results

We have also analysed fluctuation data from simulations using CUTIE [1], an electromagnetic, two-fluid, nonlinear code for large-eddy simulations. CUTIE has been applied to COMPASS-D, START, JET and ITER for global transport analysis. As yet, there is no scrape-off-layer or ELM modelling in the code, but we have attempted to simulate a COMPASS-D Ohmic shot with CUTIE and have succeeded in obtaining similar confinement characteristics. Analysis of the CUTIE magnetic fluctuations from a circular array of poloidal locations at one toroidal position reveals low-m modes as in the experiment. We find in CUTIE that, although there are a number of modes, $m = 2$ predominates, with $m = 7$ also significant. Both are rotating poloidally to produce frequencies of around $16kHz$. This calculation was performed without toroidal flow, but including self-consistent radial electric field; it is possible that allowing the modes to rotate toroidally would significantly alter the frequencies generated but this seems unlikely to reproduce the highest frequencies seen.

V Discussion and Conclusions

We have found SVD to have limited usefulness in analysing the time-evolution of coherent structures observed in edge fluctuation data, primarily because there is a tendency for SVD components to blend together several Fourier harmonics, with confusing results. We find

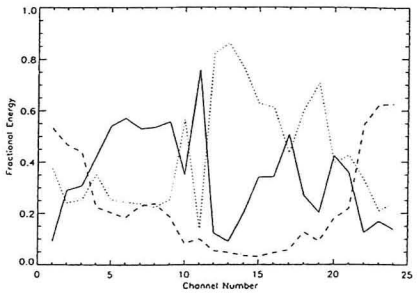

Figure 5. Poloidal distribution of the energy fractions in the low (dotted), medium (dashed) and high (solid) frequency bins during a period without ELMs in a COMPASS-D Ohmic shot (#22073). Channels 1 and 13 are positioned at the outboard and inboard midplane respectively, while channels 2-12 are above and 14-24 below the midplane.

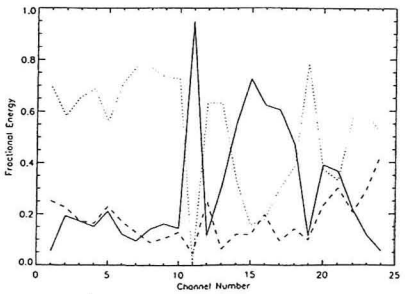

Figure 6. Poloidal distribution of the energy fractions in the low (dotted), medium (dashed) and high (solid) frequency bins during the period of an ELM in a COMPASS-D Ohmic shot (#22073). Channels 1 and 13 are positioned at the outboard and inboard midplane respectively, while channels 2-12 are above and 14-24 below the midplane.

wavelet and Fourier transform techniques to be more generally useful. Features have been revealed having frequencies which seem too high to be caused by drift waves or rotation of magnetic islands, suggesting they are Alfvénic in nature, one possibility being Toroidal Alfvén Eigenmodes (TAEs). Indeed, such a conclusion is consistent with the fact that these features appear to be the result of standing wave oscillations.

Note that the spatial and temporal transform results have to be checked further for possible aliasing, with a combination of experimental and analytical investigations. Thus, bearing in mind that the sampling frequency is $1MHz$ and that there are 24 Mirnov coils in one poloidal array, $400kHz$ features may actually be $600kHz$ or more, and $m = 1$ modes may be $m = 23$ or more. However, this does not alter the fact that the results point to the existence of high-frequency fluctuations with a standing wave character. Similar features have been seen in TFTR [2] where an $m/n = 1/0$ mode has been observed at frequencies as high as $500kHz$.

Asymmetry studies indicate that during ELMs there is a burst of high-frequency dominance which is poloidally situated around the lower inboard quadrant. Such antiballooning characteristics have been seen in high-frequency fluctuations on PBX-M [3], although a ballooning pattern of behaviour has also been recorded [4]. As far as COMPASS-D is concerned, if this ELMing asymmetry reflects that of the ELM trigger, a possible mechanism for this trigger is the pressure-driven external kink instability [5] (also posited for PBX-M [3]) which is destabilised by a finite current density near the edge.

Apart from the need to check for aliasing, already noted, assessing the validity of the speculations covered above requires attention to be focused on a number of fundamental questions: Could the inverse-chirp be created by the slowing of a rotating mode, or does it arise from a nonlinear frequency-amplitude dispersion relation? Perhaps it is dependent on the rapid change in edge density-gradient during the transient loss of confinement. What is the origin of the three frequency bands, and why do they seem independent of the shot conditions? Can the inter-ELM evolution in high-frequency band signal-energy and harmonic content be related to the ELM trigger? How are the important modes toroidally distributed? Continuing efforts are aimed at addressing these issues and investigating reasons for the differences between simulation and experiment.

Acknowledgements

The authors wish to thank S. Fielding, M. Valovic and D. Gates for useful discussions and providing access to the data. This work was funded jointly by the UK Department of Trade and Industry and Euratom.

References

[1] Thyagaraja, A., Journal de Physique IV, C6 **5** (1995) 105

[2] McGuire, K., Arunasalem, V., Barnes, C. W., et al., Phys. Fluids B **2** (1990) 1287

[3] Kaye, S. M., Manickam, J., Asakura, N., et al., Nuclear Fusion, **30** (1990) 2621

[4] Kaye, S. M., Dunlap, J. L., Hahm, T.S., et al., Plasma Phys.Contrl. Fusion **36** (1994) A135-A140

[5] Manickam, J., Phys.Fluids B **4** (1992) 1901

LONG-RANGE PERTURBATIONS PRODUCED BY A PACKET OF ION-ACOUSTIC WAVES IN A PLASMA

Maurizio LONTANO, John D'AVANZO*, Dmitri RYUTOV#

Istituto di Fisica del Plasma "Piero Caldirola", Consiglio Nazionale delle Ricerche
EURATOM-ENEA-CNR Association - Via. R. Cozzi 53, 20125 Milano, Italy
lontano@ifp.mi.cnr.it

1. Introduction

Consider an unmagnetized plasma carrying a well-localized packet of ion acoustic waves. Does the presence of the packet manifest itself at large distance from its location, where the amplitude of the electric field is already zero? Generally speaking, the answer is positive: as the motion of the electrons (which rapidly cross the packet in all directions) is perturbed by the presence of the packet, the electron distribution function (e.d.f.) is also perturbed, even at very large distances from the packet itself.

In this work it is shown that the second order perturbations of the moments of the e.d.f. remains finite even at large distances from the wave-packet, decreasing typically with a power-law. A general technique for finding this long-range part of the packet is developed. It is also argued that the "halo" contains both electric and magnetic perturbations extending far from the packet. Examples of two- and three-dimensional wave-packets are discussed.

2. Second order perturbation of the e.d.f.

Let us consider a wave-packet of the form $\varphi(\mathbf{r},t)=\psi(\mathbf{r},t)\exp(-i\omega t+i\mathbf{k}\cdot\mathbf{r})+c.c.$, where $\varphi(\mathbf{r},t)$ is the perturbation of the electrostatic potential, $\psi(\mathbf{r},t)$ is its complex amplitude slowly varying over the time ω^{-1}, and almost uniform over the scale k^{-1}. Let $\mathbf{k}=\hat{\mathbf{e}}_z k$. The linearized kinetic equation for the first order perturbation of the e.d.f. $f_1(\mathbf{r},\mathbf{v},t)$is integrated along the unperturbed electron trajectories, thus giving

$$f_1(\mathbf{r},\mathbf{v},t)=e^{-i\omega t+ikz}\int_{-\infty}^{t}dt'\,g[\mathbf{r}+\mathbf{v}(t'-t),\mathbf{v},t]e^{i(kv_z-\omega)(t'-t)}+c.c. \qquad (1)$$

where

$$g(\mathbf{r},\mathbf{v},t)=-\frac{\partial f_0}{\partial \mathbf{v}}\cdot\left(ik\psi+\frac{\partial\psi}{\partial \mathbf{r}}\right). \qquad (2)$$

The moments of Eq.(1) take the form

$$M(\mathbf{r},t)=e^{-i\omega t+ikz}\int_{-\infty}^{t}dt'\int d^2v_\perp\int_{-\infty}^{+\infty}dv_z\,P(\mathbf{v})g[\mathbf{r}+\mathbf{v}(t'-t),\mathbf{v},t]e^{i(kv_z-\omega)(t'-t)}+c.c. \qquad (3)$$

where $P(\mathbf{v})$ is a polynomial composed by the products of various velocity components.

When one considers the spatial region well outside the wave-packet, the difference $(t-t')$ can be estimated as $t-t'\cong r/v_\perp$, where $r_\perp > L$ is the distance between the observation point and the packet. Indeed, the function $g(\mathbf{r},\mathbf{v},t)$ is different from zero only if its spatial argument lies within the envelope of the packet. For the electrons with $v_\perp \approx v_{the}=\sqrt{T_e/m}$, the exponential in the integrand of Eq.(3) is a rapidly oscillating function of v_z, with the period

$\approx v_{the}/kr_\perp << v_{the}$. Then the integral over v_z is exponentially small. The v_z-integral is not exponentially small only for very large $v_\perp$ values, i.e. for $v_\perp > v_{the} kr_\perp >> v_{the}$. However for such large $v_\perp$ values, the e.d.f. f_0 that enters Eq.(1) through the function g, becomes itself exponentially small. Then we conclude that the moments of the first order perturbation of the e.d.f. outside the region occupied by the wave packet are negligibly small.

A finite value of the perturbation of the moments of the e.d.f. outside the packet can be found at higher orders. The kinetic equation for the second order perturbation f_2 reads

$$\frac{\partial f_2}{\partial t} + \mathbf{v}\cdot\frac{\partial f_2}{\partial \mathbf{r}} = -\frac{e}{m}\frac{\partial \varphi}{\partial \mathbf{r}}\cdot\frac{\partial f_1}{\partial \mathbf{v}} \equiv H(\mathbf{r},\mathbf{v},t), \tag{4}$$

where a term proportional to $\varphi_2(\mathbf{r},t)$, describing the plasma neutrality, has been neglected.

The solution of Eq.(4) reads

$$f_2(\mathbf{r},\mathbf{v},t) = \int_{-\infty}^{t} dt'\, H\left[\mathbf{r}+\mathbf{v}(t'-t),\mathbf{v},t'\right] \tag{5}$$

The quadratic function $H(\mathbf{r},\mathbf{v},t)$ contains two types of terms: those oscillating at twice the wave frequency ω, and those which are slowly varying. The terms of the first type do not give rise to long range contributions to the moments of the e.d.f. Then, we neglect them and consider the terms of the second type only, which corresponds to averaging Eq.(4) over the short timescale $2\pi/\omega$. The slowly varying part of the e.d.f. $\bar{f}_2(\mathbf{r},\mathbf{v},t)$ can then be put in the form of Eq.(5) where the average function

$$\bar{H}(\mathbf{r},\mathbf{v},t) = -\frac{e}{m}\left(-ik\psi^* + \frac{\partial \psi^*}{\partial \mathbf{r}}\right)\cdot\frac{\partial}{\partial \mathbf{v}}\int_{-\infty}^{0} d\tau\, g(\mathbf{r}+\mathbf{v}\tau,\mathbf{v},t+\tau)e^{i(kv_z-\omega)\tau} + c.c. \tag{6}$$

is defined. Here, "*" indicates the complex conjugate, the new time variable $\tau = t'-t$ has been introduced, and the function g is given by Eq.(2).

In the following we shall demonstrate that, generally speaking, the moments of f_2 are non-exponentially small outside the region occupied by the ion acoustic electrostatic energy.

When the ion acoustic wave damping and the dispersive spreading of their envelope can be neglected, we can assume that the dependence of the field envelope on r and t takes place through their combination $\mathbf{R} \equiv \mathbf{r} - \mathbf{v}_g t$. The function $\psi(\mathbf{R})$ then describes a pure translational motion of the packet, with the group velocity $\mathbf{v}_g$, $\mathbf{R}$ being the spatial coordinate in the packet reference frame. Accordingly, it is worth defining the wave frequency $\Omega \equiv \omega - \mathbf{k}\cdot\mathbf{v}_g$, and the particle velocity $\mathbf{V} \equiv \mathbf{v} - \mathbf{v}_g$. Then, in the moving reference rame, Eqs.(5) reads

$$f_2(\mathbf{R},\mathbf{V}) \cong \frac{e^2}{m^2}\int_{-\infty}^{0} d\tau\, \psi^*(\mathbf{R}+\mathbf{V}\tau)k\cdot\frac{\partial}{\partial \mathbf{V}}\left\{k\cdot\frac{\partial}{\partial \mathbf{V}}\int_{-\infty}^{0} d\tau'\, \psi\left[\mathbf{R}+\mathbf{V}(\tau'+\tau)\right]e^{i(kV_z-\Omega)\tau'}\right\} + c.c. \tag{7}$$

respectively. In the comoving frame, the e.d.f. f_2 is stationary.

3. Evaluation of the density perturbation

First we notice that, when making integrations over V_z, one can expect that the main contribution comes from the electrons which are "in resonance" with the ion acoustic waves. For those electrons $v_z << v_{the}$. Then, since we are interested in the evaluation of the moments at large distances from the wave packet, i.e. for $r >> L$, a characteristic τ-value in Eq.(7) can be estimated as $\tau \approx r/v_\perp$, with possible deviations from this value in the range $\pm L/v_\perp$.

Here, r and L are the distance of the observation point from the packet and the scale-length of the e.s. field distribution, respectively. Let us consider the inner τ'-integral. Due to the localized character of the wave packet non negligible contributions to this integral come from τ'-values satisfying the inequality $|\tau'| \le L/v_{the}$. By integrating Eq.(7) over V_z, we get

$$\int_{-\infty}^{+\infty} dV_z f_2 \cong -\frac{e^2k^2}{m^2v_\perp^2} \int_{-\infty}^{+\infty} dV_z \int_{-\infty}^{0} s\,ds \left[\frac{\partial}{\partial Z}\psi^*\left(\mathbf{r}_\perp + \hat{\mathbf{n}}s, Z + \frac{V_z}{v_\perp}s\right)\right] \times \\ \times \left\{\frac{\partial f_0}{\partial V_z}\int_{-\infty}^{0} ds'\,\psi\left[\mathbf{r}_\perp + \hat{\mathbf{n}}(s'+s), Z + \frac{V_z}{v_\perp}s\right] e^{-iqs'}\right\} + \text{c.c.} \tag{8}$$

where $\hat{\mathbf{n}} \equiv \mathbf{v}_\perp / v_\perp$, $q \equiv (\Omega - kV_z)/v_\perp$, and the new variables $s = v_\perp \tau$ and $s' = v_\perp \tau'$ have been introduced. Notice that the integral over s' can be thought as a single-sided Fourier transform

$$\psi_q = \int_{-\infty}^{0} ds'\,\psi(s') e^{-iqs'}, \tag{9}$$

all other arguments of ψ being independent parameters when integrating over s'. Therefore, we can deduce the limiting behaviours of the function ψ_q for $q = 0$, $\psi_{q=0} \approx \psi(0)L$, and for $q \to +\infty$, $\psi_q \approx i\psi(0)/q + \psi'(0)/q^2 + \ldots$, where $\psi(0) = \psi(s=0)$ and the prime denotes the differentiation with respect to s.

From the above definitions, one sees that, for given values of Ω, k, and $\mathbf{v}_\perp$, the width of the function ψ_q determines the extension of the V_z-interval which contributes to the density perturbation. Two limiting cases can be identified, that of "large" and "small" L.

At large L values, i.e. for $L >> v_{the}/\Omega$, the width of the interval in V_z is small compared to the phase velocity Ω/k. In this case the inner integral in Eq.(8), as a function of V_z,

$$I(V_z) \equiv \int_{-\infty}^{0} ds'\,\psi\left[\mathbf{r}_\perp + \hat{\mathbf{n}}(s'+s), Z + \frac{V_z}{v_\perp}s\right] e^{i\frac{s'}{v_\perp}(kV_z - \Omega)}, \tag{10}$$

is localized around $V_z = \Omega/k$, with a width much smaller than Ω/k. A long non-resonant power-law tail, corresponding to the asymptotic expansion of the function ψ_q, is also present.

In the opposite limit of small scale length, i.e. for $L < v_{the}/\Omega$, the width of the "core" of the integral in Eq.(10) is much larger than Ω/k. That is the V_z-interval over which $I(V_z)$ contributes is $-v_{the}/kL < V_z < +v_{the}/kL$, the Landau resonance being smeared out since the time a thermal electron takes to cross the packet is $L/v_{the} < \Omega^{-1}$. Also in this case a non-resonant power-law tail exists, which is obtained from the asymptotic expansion

$$\psi_q \cong \frac{iv_\perp}{kV_z}\psi(0) + \left(\frac{v_\perp}{kV_z}\right)^2 \psi'(0) + \ldots \tag{11}$$

At large distance from the packet, the integrand in the outer integral in Eq.(8), as a function of V_z, is centered around $V_z \cong -v_\perp \cdot Z/r_\perp$. Moreover, its width can be estimated as $\Delta V_z \cong v_\perp \cdot L/r_\perp$.

In order to get a qualitative description of the density distribution from the complicated general expression obtainable by integrating in $\mathbf{v}_\perp$ Eq.(8), we first assume that ψ is a real function. As a consequence, only the second term of the expansion in Eq.(10) contributes when summing up the explicitly written term in Eq.(1) and its complex conjugate. It means that, asymptotically, $\psi_q \propto q^{-2}$. As a second step we can estimated by the order of magnitude $s\,ds$ as $L r_\perp$ in the outer integral in Eq.(8). We also estimate $\partial\psi/\partial Z$ as ψ/L. With these positions we can right the following approximated expression for the density perturbation

$$\delta n_2(r_\perp,Z) \equiv \int d^2v_\perp \int_{-\infty}^{+\infty} dV_z f_2 \cong \frac{e^2k^2\psi_0^2 L}{m^2} \times$$
$$\times \int_0^\infty \frac{g(v_\perp)dv_\perp}{v_\perp^2} \int_{-\infty}^{+\infty} (v_z - v_g)\cdot Q\left[\frac{v_z-\omega/k}{v_\perp/kL}\right]\cdot\frac{\partial}{\partial z}R\left[\frac{v_z - v_\perp\cdot z/r_\perp}{v_\perp\cdot L/r_\perp}\right]dv_z . \qquad (12)$$

Let us estimate Eq.(12) in the two limiting cases discussed above. First consider the case of "small" L. Neglect v_g and discard ω/k in the argument of the function Q. Introduce the model functions for $Q(x)$,

$$Q(x) = \frac{1}{1+x^2}, \qquad (13)$$

and for the z-derivative appearing in Eq.(12),

$$\frac{dR(x)}{dx} = \delta\left(x-\frac{1}{2}\right) - \delta\left(x+\frac{1}{2}\right), \qquad (14)$$

where $|x|<1$, and $|x|>1$ correspond qualitatively to the resonant particle, and to the adiabatic contributions, respectively. With these representations the density perturbation reads

$$\delta n_2(r_\perp,z) \equiv n_0\left(\frac{e\psi_0}{T_e}\right)^2 k^2L^2\left[\frac{z-L/2}{r_\perp^2+k^2L^2(z-L/2)^2} - \frac{z+L/2}{r_\perp^2+k^2L^2(z+L/2)^2}\right], \qquad (15)$$

which holds far from the wave-packet, i.e. for $r_\perp^2 + z^2 >> L^2$.

In the opposite limit of "large" L, that is of a very broad wave-packet, we can replace v_z in the term $(v_z - v_g)$ with ω/k, and $Q(x)$ with $\pi\delta(x)$. Then we get approximately

$$\delta n_2(r_\perp,z) \cong n_0\left(\frac{e\psi_0}{T_e}\right)^2 \frac{kL^2}{r_\perp}\left(1-\frac{kv_g}{\omega}\right) v_{the}^4\left[v_\perp^{(1)}g(v_\perp^{(1)}) - v_\perp^{(2)}g(v_\perp^{(2)})\right] \qquad (16)$$

where

$$v_\perp^{(1,2)} = \frac{\omega}{k}\frac{r_\perp}{z\pm L/2}. \qquad (17)$$

For $r_\perp < Lkv_{the}/\omega$, the maximum of the density perturbation is strongly localized around the lines $z = \pm L/2$ and is approximately

$$\delta n_2(r_\perp,z) \cong n_0\left(\frac{e\psi_0}{T_e}\right)^2 \frac{kL^2}{r_\perp}\left(1-\frac{kv_g}{\omega}\right). \qquad (18)$$

These ridges are produced by the resonant electrons and their characteristic width is $\Delta z \cong r_\perp \omega/kv_{the}$.

4. Further developments of the theory

Besides the quasi static electric field accompanying the second order density perturbation, steady magnetic fields are also present in the "halo" surrounding an ion acoustic wave packet propagating in an isotropic plasma. The structure of these fields has been also investigated and the relevant results will be reported at the Conference.

* Plasma Physics Division, GSI Darmstadt, Darmstadt, Germany
# Lawrence Livermore National Laboratory, Livermore, U.S.A.

Guiding centre trajectories in perturbed magnetic geometries

B. Weyssow & J.-H. Misguich *

November 21, 1997

Association Euratom-Etat Belge, Université Libre de Bruxelles, Campus Plaine, CP 231, 1050 Bruxelles, Belgium
*Association Euratom-CEA sur la Fusion, DRFC, CE de Cadarache, F-13108 Saint-Paul-Lez-Durance Cedex, France.

Abstract

Stochasticity of Guiding Centre (GC) trajectories in a chain of magnetic islands can be largely enhanced by the drift wave electrostatic turbulence. The conditions for this enhancement are analysed and applied to the Dynamic Ergodic Divertor (DED) configuration.

1 Introduction

The analysis of the GC trajectories in perturbed magnetic fields and a electrostatic turbulence is of great importance in tokamak plasma physics. Indeed, a key method to handle the problems of the protection of the inner wall from overheating and erosion or the limitation of the amount of wall-released imputities in the plasma consists to impose a stochastic barrier at the edge of the plasma. This can be realized by a Ergodic Divertor which generates static magnetic islands as in Tore Supra, but also by a Dynamic Ergodic Divertor as the one planned to be installed on TEXTOR which will induce magnetic islands with phase velocities from 12m/s (50 Hz) to 2400 m/s (10 KHz)). It is to be noticed that it is also at the edge that the Drift Wave turbulence is the most active.

The effect of both types of perturbations, magnetic islands and electrostatic turbulence, on a GC trajectory is not completely elucidated. Here, we adress the question of a possible enhancement of the toroidally induced GC stochasticity of a GC moving around a chain of magnetic islands by a electrostatic wave.

Previous examples of chaotic motion in few regular modes are
- 2 chains of magnetic islands leading to overlapping and magnetic braiding
- gyrating particle in $\mathbf{B}$, plus one oblique electrostatic wave
- particle in $\mathbf{B} = 0$ and two electrostatic waves leading to a Hamiltonian known as the paradigm Hamiltonian.
- GC in three electrostatic waves perpendicular to $\mathbf{B}$

2 GC stochasticity in a sheared slab

The magnetic field of a sheared slab with one magnetic island chain is the following:

$$\mathbf{B} = B_0\,\mathbf{1_z} - x\,B'\,\mathbf{1_y} + B_x\,sin(k_y y)\,\mathbf{1_x}$$

The last term accounts for the magnetic island chain resonant at r_0 where $q_0 = m/n$ (the poloidal wave number is $m = k_y r_0$). The shear parameter, defined here for later reference, is $\sigma = B'/k_y B_0$.

The field line Hamiltonian equations can be reduced to:

$$\frac{dX}{dZ} = \delta\,\sin Y; \quad \frac{dY}{dZ} = -X.$$

The half width of the magnetic island in X is $2\sqrt{\delta}$. Adding an electrostatic wave defined by

$$\mathbf{E} = E_0\,sin(\chi y - \omega t)\,\mathbf{1_y}$$

where $\chi = m_e/r_0 = \Delta m/r_0$. With integer values of Δ, the electrostatic wave is resonant on the same magnetic surface as the magnetic perturbation). We get:

$$\frac{dX}{dt'} = \delta \sin Y + \eta \sin(\Delta Y - \tilde{\omega} t'); \quad \frac{dY}{dt'} = -X; \quad \frac{dZ}{dt'} = 1.$$

where $t' = v_{||} k_y$ and $\tilde{\omega} = \omega / v_{||} k_y$ and the electric field amplitude is $\eta = \sigma c E_0 v_{||} B_0$. The position in X of the electric island is $-v_\phi = -\tilde{\omega}/\Delta$ with half-width $2\sqrt{\eta/\Delta}$. The Hamiltonian is

$$H(X, Y, t') = -\frac{1}{2} X^2 + \delta \cos Y + \frac{\eta}{\Delta} \cos(\Delta Y - \tilde{\omega} t')$$

which has the form of the *paradigm Hamiltonian*. The stochasticity threshold measured by the Chirikov criterium is $K = 2(\sqrt{\delta} + \sqrt{\eta/\Delta})/v_\phi > 1$ or in terms of $u_{||} \equiv v_{||}/V_{Th.\alpha}$: $K = 2(u_{||}\sqrt{\delta} + \sqrt{u_{||}\eta_{Th.\alpha}/\Delta})/v_{\phi Th.\alpha} > 1$. Thus K increases with $u_{||}$ i.e. *fast particles stochastize more easily*. With realistic parameters: $\Delta = 4$, $v_\phi/\sqrt{\delta} = 8$, $k_y = 125\, m^{-1}$, and magnetic island width of 1 cm, $E_0 = 45$. Volts/cm, $\chi = 500 m^{-1}$, $\omega = 1.15\, 10^6\, s^{-1}$ (ω/χ is equal to the electron diamagnetic velocity), $v_{||} = 3\, 10^5 m s^{-1}$, $\delta = 10^{-6}$, $v = 3.6\, 10^7$, $\eta = 4\, 10^{-6}$, $\sigma = 10^{-3}$, we find (1) for a magnetic island of 1cm width (DED = 6cm), one local electrostatic wave is sufficient to produce chaotic GC trajectories and radial diffusion for i) almost all the electron population, ii) all ions with $v_{||} > V_{Th.i}$; (2) each particle has its own stochasticity threshold according to its parallel velocity.

3 GC stochasticity in toroidal geometry

A) In toroidal geometry, the GC equations of motion are obtained by a pseudo-canonical averaging transformation (Weyssow & Balescu)

$$\frac{d\mathbf{Y}}{dt} = U\mathbf{b} + \frac{1}{\Omega}[\frac{W^2}{2B}\mathbf{b} \times \nabla B + U^2 \mathbf{b} \times (\mathbf{b}.\nabla)\mathbf{b} + \frac{e}{m}\mathbf{E} \times \mathbf{b}]$$

Using the standard model for the toroidal magnetic field $\tilde{B} = B_0/h[1_\zeta + G(r)\mathbf{1}_\theta]$ with $h = 1 + (r/R0)cos\theta$ and $G(r) = r/(R_0 q(r,\theta) h$, and simple analytical expression for the security factor (but also for the shear, the temperature a.s.o) (see Weyssow & Misguich))

$$q(r,\theta) = 4\frac{q(0)}{h}\frac{1}{(2-x^2)(x^4-2x^2+2)},$$

we obtain explicit expressions for the three invariants of the motion, the maximum velocity along the GC trajectory $v = \sqrt{(2E/m_\alpha)}$, the reduced magnetic moment $MB_0/E_n = (1 - m_\alpha U^2/(2E_n))(h(r,\theta)/K(r))$ where $K(r) = \sqrt{(1+G^2(r))}$ and the toroidal momentum $L = h(U/K(r)) - (\Omega_0/\epsilon)\int_0^r dr' G(r')$. With these expressions, all the GC trajectories can be classified according to the number of intersection points of two functions (Mercier-Capes-Morera diagram): one function has two maxima, whereas the second one is almost horizontal (see Fig. 1 below).
B) We now add a helical magnetic perturbation to the standard model of magnetic field:

$$B_r = \lambda(B_0/(xh)) \sin(m\theta - n\zeta - \omega_b t)$$

with low frequency ω_b (as in the DED). Here the radial profile is in $1/x$ and $\lambda = B_r/B_0 \approx 10^{-3}$ to 10^{-4}. A different possibility would be to consider a Gaussian B_r centered on the rational surface $q = m/n$ and $B_\theta \neq 0$. The electrostatic perturbation is defined as follows:

$$E_\theta = \frac{m_E}{r}\Phi_0 \sin(m_E\theta - n_E\zeta - \omega_E t)$$

and

$$E_\zeta = -\frac{n_E}{R_0 h}\Phi_0 \sin(m_E\theta - n_E\zeta - \omega_E t)$$

where $\Phi_0 \equiv r E_\theta/m_E$, $E_\theta \approx 50$ Volts/cm thus $\eta = e\Phi_0/2T \approx 7\, 10^{-2}$. Taking into account the two types of perturbations, the equations of motion, with $\tau = \omega_E t/(2\pi)$, become:

$$\frac{dx}{d\tau} = C_T \sin\theta + C_B \sin(m\theta - n\zeta - 2\pi\frac{\omega_b}{\omega_E}\tau) + C_E \sin(\Delta(m\theta - n\zeta) - 2\pi\tau)$$

$$\frac{d\theta}{d\tau} = A\frac{u}{q(x)} + ...; \quad \frac{d\zeta}{d\tau} = Au + ...$$

These equations are similar to the paradigm equations showing that *toroidal trajectories are stochastized* as soon as there is 1 additional perturbation, electrostatic or magnetic. The stochasticity induced by *magnetic* islands can therefore be **enhanced** by an *electrostatic* wave (thus also by a drift wave turbulence) (cf. Fig. 2).

4 Conclusions

We have shown, by reducing the GC equations of motion to paradigm like equations that a drift wave turbulence could enhance the GC toroidicity induced stochasticity for GC moving around a magnetic island chain. We have also shown that for profiles of B_r centered on the rational surface i.e. for magnetic islands at $q(r) = m/n$ the GC is in resonance with the perturbation at $md\theta/dt - nd\zeta/dt - 2\pi\omega_b/\omega_E \approx 0$ or when $1/q(x) \approx n/m + 2\pi\omega_b/(\omega_E Au)$ This resonance condition depends on both the frequencies and the GC parallel velocity. For x too far away from r the function B_r is small or zero and the GC trajectory is regular. The condition for stochasticity is thus $2\pi\omega_b/(\omega_E Au)$ small i.e. large parallel velocity. The resonance condition is satisfied only when the toroidal trajectory crosses its resonant magnetic surface. Crossing domain might be large but for trajectories exhibiting important radial excursions (banana, puffed bananas,a.s.o...) stochasticity could be very localized in the torus (Fig. 3). The GC in the electrostatic wave is resonant at $1/q(x) \approx n_E/m_E + 2\pi/Au$. An enhanced stochasticity is therefore expected when the magnetic and the electrostatic resonances are satisfied almost on the same magnetic surface: $n_E/m_E + 2\pi 1/Au \approx n/m + 2\pi\omega_b/\omega_E Au$. This relation constitutes a further constraint on the parallel velocity. Consequences of this matching condition as well as the effects of phase velocity of the magnetic island chain on the resonance conditions will be further analysed.

5 References

R. Balescu (1988): "Transport Processes in Plasmas", Vol. 2, North Holland, Amsterdam.
D. Escande (1985): Phys. Report **121**,165.
K.H. Finken, Editor (1996): "Dynamic Ergodic Divertor for TEXTOR 94", Julich, KFA report 3285.
R.G. Littlejohn (1983): J. Plasma Phys. **29**,111.
C. Mercier, H. Capes, J.P. Morera (1981): EUR-CEA-FC Report 1127.
J.H. Misguich, B. Weyssow (1989) Note de travail DRFC, Cadarache NTΦ8.
J.H. Misguich, B. Weyssow, R. Balescu (1992) : EUR-CEA-FC Report 1438.
J.H. Misguich, R. Nakach (1991): Phys. Rev. A **44**,3869.
Y. Nishimura, M. Azumi (1997): Phys. of Plasma **4**,2365.
J. Rome , Y. K.M. Peng (1979): Nuclear Fusion **19**,1193.
B. Weyssow, J.H. Misguich, R. Balescu (1991) : J. Plasma Phys.**35**, 449.
G. Zaslavsky, N. Filonenko (1968): Sov. Phys. JETP **27**, 851.

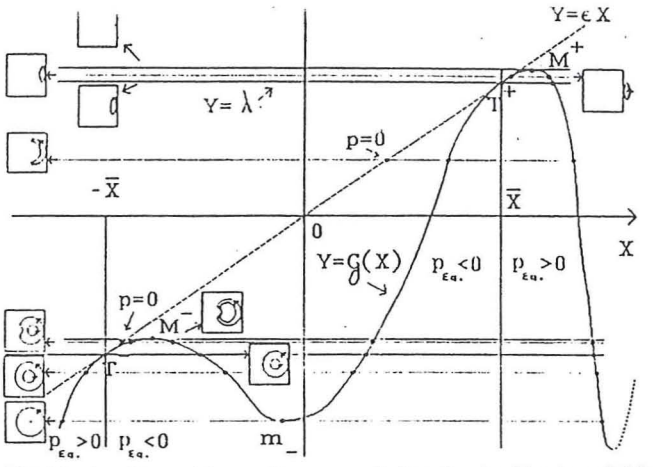

Figure 1: The Mercier. Capes. Morera diagram applied to the classification of GC trajectories in the standard model of magnetic field.

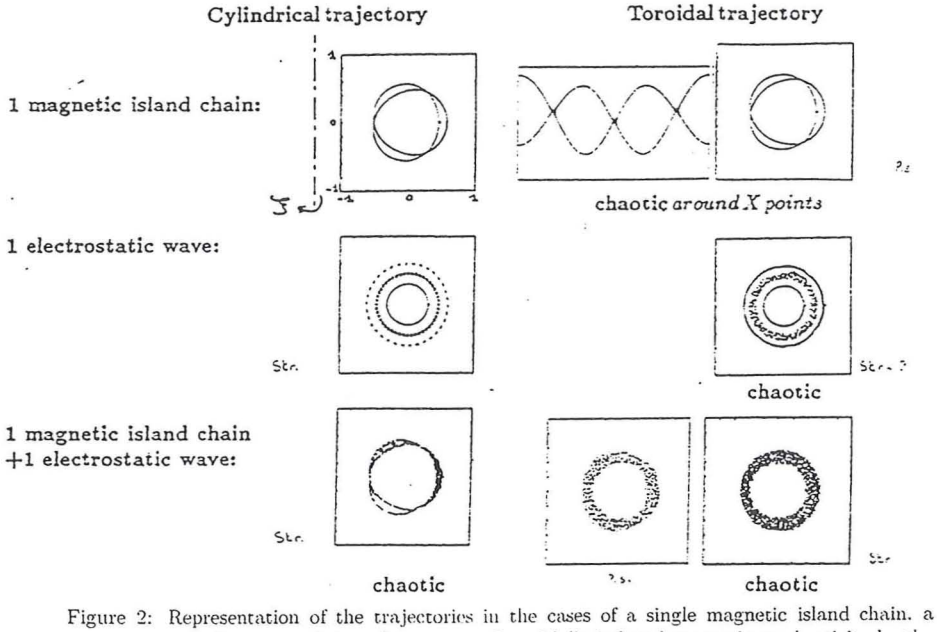

Figure 2: Representation of the trajectories in the cases of a single magnetic island chain, a single electrostatic wave and the enhancement of toroidally induced magnetic stochasticity by the electrostatic wave.

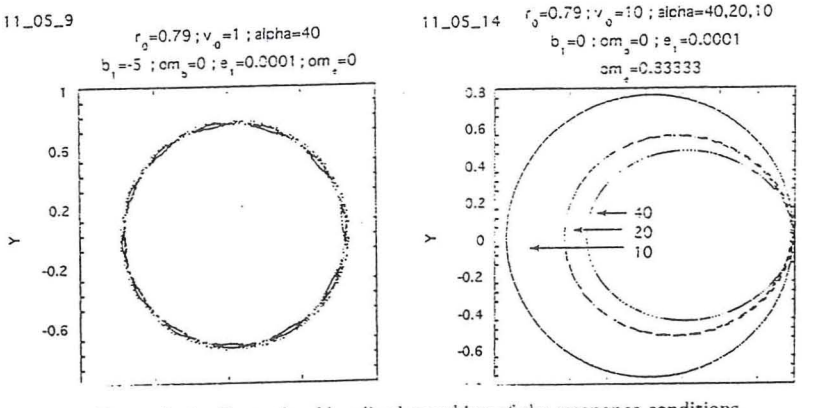

Figure 3: An Example of localized matching of the resonance conditions.

A new renormalization scheme for turbulent transport

E. Vanden Eijnden
Assoc. EURATOM-Etat Belge
Université Libre de Bruxelles
Physique des Plasmas, CP 231, Campus Plaine
Bvd du Triomphe, 1050 Bruxelles, Belgium

The passive advection of a scalar quantity by a random flow is an important problem which arises commonly in the study of turbulent transport phenomena in neutral fluids, in porous media or in plasmas. The equation for the advection-diffusion of a passive scalar is

$$\frac{\partial}{\partial t}T(\mathbf{r},t) + \nabla \cdot (\mathbf{u}(\mathbf{r},t)T(\mathbf{r},t)) = D_0 \Delta T(\mathbf{r},t), \tag{1}$$

where $\mathbf{u}(\mathbf{r},t)$ is a random vector field with specified statistics and D_0 is the molecular diffusion coefficient. The solution of Eq. (1) amounts to determining the statistics of $T(\mathbf{r},t)$ and more specifically the shape of the mean value $\langle T(\mathbf{r},t)\rangle$, where brackets denote averaging over the statistics of $\mathbf{u}(\mathbf{r},t)$. Despite the linear character of Eq. (1), averaging of this equation leads to the non-trivial closure problem of determining the shape of the statistically nonlinear term $\nabla \cdot \langle \mathbf{u}(\mathbf{r},t)T(\mathbf{r},t)\rangle$. One of the most powerful approximation for the solution of this problem is the famous direct interaction approximation (DIA). Yet, the DIA has two main defects which affect the reliability of the predictions of this approximation concerning turbulent transport. First, it does not reproduce correctly the short-time average dynamics of $\langle T(\mathbf{r},t)\rangle$. Second, it misrepresents the sweeping effect, that is, the random advection of the small scales of $T(\mathbf{r},t)$ by the large scales of $\mathbf{u}(\mathbf{r},t)$. We propose a new approximation, called the modified direct interaction approximation (M-DIA), which solves these two defects and provides an efficient new tool for the description of turbulent transport. For instance, the M-DIA reproduces the departure from Gaussianity which are observed in the direct numerical simulations and allows describing the strange diffusive features induced by long-range correlations of $\mathbf{u}(\mathbf{r},t)$.

WIDTH OF ISLANDS IN A TOKAMAK WITH A LOCALIZED HELICAL PERTURBATION FIELD

A. Kaleck, M. Tokar'
Institut für Plasmaphysik, Forschungszentrum Jülich GmbH,
EURATOM Association,
Trilateral Euregio Cluster, D-52425 Jülich, Germany

Abstract To enhance the transport at the edge of a tokamak plasma additional helical coils are used to build ergodic layers [1, 2, 3, 4]. The characteristics of the resulting magnetic field can be described by the island width d and the Chirikov parameter σ_{Chir}. Usually for the calculation of the island width expressions like in [1, 5, 6] are used. Field line tracing calculations for the planned Dynamic Ergodic Divertor (DED) at TEXTOR-94 [2] lead to different results. Here we present an improved expression for the island width in terms of the Fourier components of the perturbation field, which is in agreement with the numerical field line tracing results. The difference to the known expressions depends strongly on the poloidal location of the perturbation field.

Introduction: The perturbation of an axisymmetric tokamak equilibrium by helical fields leads to splitting of resonant surfaces and to stochastization of the magnetic field [6]. The Chirikov parameter σ_{Chir} which is the ratio of the radial island diameter to the distance between adjacent resonant surfaces serves as a measure of the stochastization. $\sigma_{Chir} = 1$ marks the start of overlapping of islands and the onset of enhanced perpendicular transport by field line diffusion. The Dynamic Ergodic Divertor (DED) planned for TEXTOR-94 is based on this idea to influence the transport at the plasma edge.

The island width can be calculated starting with the equations for the magnetic field lines. Under certain simplifying assumptions one can obtain an analytical expression like that reported in [1] which uses the Fourier components of the perturbation field. For the DED project poloidal Poincaré sections from field line tracing calculations were used to evaluate the island width and the Chirikov parameter [2]. The results were significantly different from those obtained on the basis of analytical estimates [7]. Measurements of the island diameters calculated for a series of low level perturbations and an extrapolation to the maximum available perturbation field lead to $\sigma_{Chir} \approx 1$, whereas in [7] $\sigma_{Chir}(q = 3) = 3.3$. Taking into account differences in the configuration and in the definition of the Fourier cofficients [1] the latter has been reduced to $\sigma_{Chir} \approx 1.7$. I.e. a significant discrepancy be-

[1] The $\delta B_{m,n}$ in e.g. [1] are the coefficients of the expansion $\sum_{m=-\infty}^{\infty} \delta B_{m,n} e^{i(m\theta - n\varphi)}$, where the $b_{m,n}$ in [7] are the coefficients of a sin/cos expansion.

tween the standard expression and the reliable field line tracing calculations still remains. It turned out to depend strongly on the location of the perturbation coils.

In the present contribution after an analysis of the standard expression for the island width [1] we derive an improved expression by taking into account the finite aspect ratio when replacing the perturbation vector potential by the measurable magnetic field. The latter expression reflects the effect of the poloidal location of the perturbation coils on the island width. Results of field line tracing calculations by the Gourdon code confirm the improved expression.

Standard formula for island width: In refs. [1, 6] intrinsic coordinates $\Phi_{\rm tor}, \theta^*, \varphi^*$, being the toroidal flux and the poloidal and toroidal coordinates, respectively were introduced. In this reference system with the basis vectors $\nabla\Phi_{\rm tor}, \nabla\theta^*, \nabla\varphi^*$, the field lines are straight. Using the Hamiltonian formalism it can be shown that if a helical perturbation is applied

$$\delta\Phi_{\rm pol}\left(\Phi_{\rm tor}\right) = \sum_{m,n=-\infty}^{\infty} \delta\Phi_{m,n}\left(\Phi_{\rm tor}\right)\, {\rm e}^{{\rm i}(m\theta^*+n\varphi^*)}. \tag{1}$$

a resonant magnetic surface with safety factor $q = m/n$ splits into a chain of islands. The half width of the islands in terms of the toroidal flux is given by the expression ref. [1]:

$$\delta\Phi_{\rm tor} = \left[\frac{8\,\delta\Phi_{m,n}}{-\dfrac{d}{d\Phi_{\rm tor}}\left(\dfrac{1}{q}\right)}\right]^{1/2}, \tag{2}$$

where all variables are surface quantities. In physical units the radial island diameter is

$$d = \frac{2\delta\Phi_{\rm tor}}{|\nabla\Phi_{\rm tor}|} \tag{3}$$

and with $\nabla\Phi_{\rm tor} = q\,\nabla\Phi_{\rm pol}$, $\nabla\Phi_{\rm pol} = RB_{pol}\,\vec{e}_\perp$, we get $|\nabla\Phi_{\rm tor}| = qRB_{\rm pol}$, where $\Phi_{\rm pol}$ is the poloidal flux and $e_\perp$ is the unit vector perpendicular to the unperturbed magnetic surface. The radial diameter of an island depends on its poloidal location $\tilde{\theta}_i$ $(i = 1, \ldots, m)$:

$$d(\tilde{\theta}_i) = w(\tilde{\theta}_i)\,\bar{d}, \quad with \quad \bar{d} = \frac{2\delta\Phi_{\rm tor}}{q\bar{R}\bar{B}_{\rm pol}} \tag{4}$$

and $w(\tilde{\theta}_i) = \frac{\bar{R}\bar{B}_{\rm pol}}{RB_{\rm pol}}$ being proportional to the distance between adjacent flux surfaces. Replacement of the vector potential by the magnetic field component $\delta\Phi_{m,n} = -\frac{rR_0}{m}\delta B_{m,n}$ results in the so called standard formula [1]:

$$\bar{d} = \left[\frac{32qrR_0}{ms}\frac{\delta B_{m,n}}{B_0}\right]^{1/2}, \tag{5}$$

where $B_0 = B_{\rm tor}(R_0)$, R_0 is the major radius of the plasma and s is the shear parameter: $s = r/q\ dq/dr$.

Improved formula for the island width d: The perturbation field can be written as

$$\delta\vec{B} = -\nabla \times (\delta\Phi_{\rm pol}\ \nabla\varphi^*) = -\nabla\delta\Phi_{\rm pol} \times \nabla\varphi^*. \tag{6}$$

Scalar multiplication by $J^{-1}\ \nabla\Phi_{\rm tor}$, with $J = \nabla\Phi_{\rm tor} \cdot (\nabla\theta^* \times \nabla\varphi^*)$ being the Jacobian, and Fourier decomposition leads to

$$[H(\theta^*)\ \delta B_\perp]_{m,n} = \delta\tilde{B}_{m,n} = -\frac{m}{rR_0}\ \delta\Phi_{m,n}, \tag{7}$$

with a poloidal weighting function

$$H(\theta^*) = \frac{1}{r\ R_0}\ J^{-1}\ |\nabla\Phi_{\rm tor}|, \tag{8}$$

which is set equal to 1 in the "standard" expression. Now we get for the mean island diameter

$$\bar{d} = \left[\frac{32qrR_0}{ms}\frac{\delta\tilde{B}_{m,n}}{B_0}\right]^{1/2}, \tag{9}$$

where $\delta\tilde{B}_{m,n}$ are the Fourier components of the weighted function $H(\theta^*)\ \delta B_\perp$, which is correct to all orders in the aspect ratio.

The θ^* - dependence of the weighting function $H(\theta^*)$ is determined by the intrinsic coordinates which were chosen to evaluate the Fourier components $\delta\Phi_{m,n}$:

$$H(\theta^*) = \left(\frac{R}{\bar{R}}\right)^{\alpha}\ \left(\frac{B_{\rm pol}}{\bar{B}_{\rm pol}}\right), \tag{10}$$

with α depending on the choice of the coordinate system ($\alpha = 2$ if $\frac{d\varphi^*}{dz} = \frac{J}{\bar{B}} = 1/\bar{R}$ and $\alpha = 3$ if $\varphi^* = \varphi$). For circular cross sections to first order in the inverse aspect ratio $\varepsilon = r/\bar{R}$ one has $B_{\rm pol} = \bar{B}_{\rm pol}\ (1 + \Lambda\varepsilon\cos\theta)$, where $\Lambda = \beta_{\rm pol} + l_i/2 - 1$. Thus we get $H(\theta) = (1 + \varepsilon\cos\theta)^{\alpha}\ (1 + \varepsilon\Lambda\cos\theta)$. The effect of the coil position now becomes evident. Positioning the coils outboard ($\theta = 0$, $H(\theta) \approx (1+\varepsilon)^{\alpha}\,(1+\varepsilon\Lambda) > 1$) is more efficient than inboard ($\theta = \pi$, $H(\theta) \approx (1-\varepsilon)^{\alpha}\,(1-\varepsilon\Lambda) < 1$).

Comparison with the Numerical Results: The standard and improved expressions (5) and (9) have been checked by carrying out field line tracing calculations with the Gourdon code and evaluating the island diameters from Poincaré plots. The calculations were done for TEXTOR equilibria whith a large radius R_0 of $175cm$, an inverse aspect

ratio ε for the resonant surface of 0.244 and a shear parameter s at the plasma edge of 2.2. To demonstrate the effect of the poloidal position we have analysed three kinds of the coil arrangement: a) The TEXTOR DED how it is planned [4] with 16 helical coils at the inboard side, at a radius of $a_c = 53cm$ exciting an m = 12, n = 4 mode. b) The coils are located at the outboard side. c) The coil set is splitted into 8 coils at the top and bottom. For the calculation of the Fourier components we used the intrinsic coordinates with $\varphi^* = \varphi$. The coil sets have different pitch angles and therefore different components $\delta B_{m,n}$ for the the same current. We choose the currents to create islands of comparable size. The data in the table show that the island diameters, calculated by the standard formula (5) are by a factor of 1.7 larger for the inboard coils than those from field line tracing and by a factor of 0.74 smaller for the outboard coils ($\beta_{pol} = 1$). As expected the results are identical for the top/bottom configuration. The diameters evaluated by the improved formula (9) agree well with the field line tracing results.

config	β_{pol}	$\frac{\delta B_{m,n}}{B_{\mathrm{tor}}}\ 10^{-5}$	$\frac{\delta \tilde{B}_{m,n}}{B_{\mathrm{tor}}}\ 10^{-5}$	$\frac{\bar{d}_{standard}}{cm}$	$\frac{\bar{d}_{Poinc}}{cm}$	$\frac{\bar{d}_{improved}}{cm}$
a	0.5	1.53	0.76	0.65	0.44	0.45
a	1.0	2.04	0.84	0.74	0.48	0.47
a	1.5	1.76	0.58	0.64	0.38	0.37
b	1.0	0.78	1.31	0.46	0.62	0.59
c	1.0	0.93	1.07	0.50	0.51	0.53

References

[1] Ph. Ghendrih, H. Capes, F. Nguyen, A. Samain
Contrib. Plasma Phys. **32** (1992) 3/4, 179–191

[2] A. Kaleck, M. Haßler, T.Evans
Fusion Engineering and Design, **37**, 353 (1997)

[3] Ph. Ghendrih, A. Grosman, H. Capes
Plasma Phys. Control. Fusion **38** (1996) 1653–1724.

[4] K.H. Finken, G.H. Wolf
Fusion Engineering and Design, **37**, 337 (1997)

[5] A.B.Rechester and T.H.Stix, Phys. Rev. Lett. **36**, 587 (1976).

[6] R. B. White, Theory of Tokamak Plasmas, North-Holland, 1989

[7] A.Nicolai, K.H. Finken, B. Giesen et al.
1995 Proc. 22nd European Physical Society
Conference on Controlled Fusion and Plasma Physics (Bournemouth)
Europhys. Conf. Abstr. **19C** Part IV 341

MODELING OF TOKAMAK ERGODIC DIVERTOR BY TWIST MAP

S.S. Abdullaev[1], K.H. Finken[1], A. Kaleck[1], K.H. Spatschek[2]
[1]Institut für Plasmaphysik, Forschungszentrum Jülich GmbH, EURATOM Association, Trilateral Euregio Cluster, D-52425 Jülich, Germany
and
[2] Heinrich-Heine-Universitaet Düsseldorf, Düsseldorf, Germany

Abstract. The symplectic twist mapping is proposed to model the magnetic field line dynamics in the ergodic divertor of the tokamak plasma edge. The mapping is specified for the Dynamic Ergodic Divertor for TEXTOR-94. It is applied to formation of the stochastic layer and field line diffusivity at the plasma edge.

The concept of an ergodic divertor was developed to remove exhaust particles from the plasma edge and to prevent the penetration of wall-released impurities into the plasma core. The study of magnetic field line diffusivity in the ergodic divertor is one of the important issues in the particle transport problem. Field line tracing codes are computationally not efficient for this purpose because it requires a long computational times. In this work we propose an efficient method to study field lines in the ergodic divertor tokamak based on the description of perturbed field lines by an flux-preserving twist map instead of magnetic field line equations. We specify the general symplectic twist map for the Dynamic Ergodic Divertor (DED) proposed for TEXTOR-94 [1].

Consider a tokamak with coordinates $\mathbf{x} = (r, \theta, z)$, and related to them coordinates (r, θ, ϕ) on the torus with the major, R_o, and minor, a, radii: $z = R_o\phi$, θ is a poloidal angle, and ϕ is a toroidal angle. Suppose that the magnetic field $\mathbf{B}^{(o)}(r) = (0, B_\theta^{(o)}(r), B_\phi^{(o)}(r) = B_T = \text{ const})$ describes the equilibrium configuration and divergence-free magnetic perturbations $\mathbf{B}^{(1)}(\mathbf{x})$ contain only radial and poloidal components:

$$\mathbf{B}^{(1)}(r,\theta,\phi) = \left(-\mathbf{e}_r \frac{1}{r}\frac{\partial}{\partial\theta} + \mathbf{e}_\theta \frac{\partial}{\partial r}\right) \sum_{m,n} m^{-1} r B_{mn}(r) \cos(m\theta + n\phi + \mu_{mn}). \qquad (1)$$

From the equations for field lines $(r(\phi), \theta(\phi))$ one can obtain the twist map under the some assumptions on the spectrum $B_{mn}(r)$ of the perturbed field (1): Eq.(1) contains only toroidal harmonics of type $n = pk$, where $p = 1, 2, ..., P; k = 0, \pm 1, \pm 2, ...$, with equal weights, i.e. $B_{mn}(r) \equiv B_m(r)$, $\mu_{mn} \equiv \mu_m$. This flux-preserving map has the form

$$I_{k+1} = I_k + \epsilon f(\theta_k, I_{k+1}),$$

$$\theta_{k+1} = \theta_k + 2\pi/pq(r(I_{k+1})) + \epsilon g(\theta_k, I_{k+1}), \qquad \mathrm{mod} 2\pi, \qquad (2)$$

with

$$I_k = \frac{r_k^2}{2R_o^2}, \qquad r_k = r\Big(k\frac{2\pi}{p}\Big), \qquad \theta_k = \theta\Big(k\frac{2\pi}{p}\Big), \qquad q(r) = \frac{r}{R_o}\frac{B_\phi^o(r)}{B_\theta^o(r)}. \tag{3}$$

The perturbation functions $f(\theta, I)$ and $g(\theta, I)$ satisfy the condition: $\partial f/\partial I + \partial g/\partial\theta = 0$, and they are determined by the Fourier spectrum $f_m(I)$ of the function $f(\theta, I)$:

$$f(\theta, I) = \sum_{m=-\infty}^{\infty} f_m(I)\sin(m\theta + \mu_m), \quad \epsilon f_m(I) = \frac{2\pi}{p}\frac{rB_m(r)}{R_o B_T}. \tag{4}$$

The quantity ϵ is a small dimensionless parameter of perturbation defined by the spectrum of magnetic perturbations $B_m(r)$ in (4).

Under sufficiently weak perturbations, $\epsilon \ll 1$, the behavior of the map (2) is described by the theory of KAM-integrability of dynamical systems. The most good magnetic surfaces, for which the safety factors $q(r)$ are not close enough to low rational numbers, survive under small perturbations. All resonant magnetic surfaces $r = r_{m,n}$, determined by the condition $q(r) = m/n$, are destroyed by any small perturbation. At the certain perturbation $\epsilon > \epsilon_c$ the adjacent resonances are overlapping forming the stochastic layer. For typical perturbations the stochastic layer consists of chaotic domains with KAM-stability islands, and chaotic motion is alternating with intervals of regular behavior.

The perturbation function $f(\theta, I)$ in the map (2) is specified by the magnetic field perturbation for the DED for TEXTOR-94 [2]. We have chosen the perturbation function $f(\theta, I)$, localized in the finite interval $\pi - \theta_c < \theta < \pi + \theta_c$, with the spectrum of poloidal harmonics

$$f_m(I) = (-1)^{m_o+m}\frac{m}{m_o M_p}\frac{\sin(m_o - m)\theta_c}{\sinh(\frac{m_o-m}{M_p}\pi)}\frac{a}{R_o}\left(\frac{r}{a}\right)^{M(m)}, \tag{5}$$

and phases $\mu_m = 0$. Here M_p is an adjustable parameter. For $M_p \gg 1$, $M_p < \infty$, the spectrum $f_m(I)$ near the central harmonics $m = m_o$ and the function $f(\theta, I)$ weakly depend on M_p.

The magnetic field perturbation in the DED contains toroidal harmonics $n = 4k$, $(k = 1, 2, \ldots)$, i.e. $p = 4$ in the map. One iteration of the map (1) corresponds to the evolution of field lines upon a quarter toroidal rotation. For the DED the central poloidal harmonics $m_o = 12$, and $\theta_c = 60^o$. The divertor coils radius $a = 53$ cm and $R_o = 175$ cm. The safety factor $q(r)$ is chosen as a quadratic function of r: $q(r) = q_o r^2/r_q^2$, where r_q is a distance where the safety factor equals to $q_o = 3$. The effective exponents $M(m)$ of the poloidal harmonics are chosen as $M(m) = 19(m-1)/11 + 1$.

The stochastic layer at the plasma edge is formed due to interactions of the main resonant magnetic surfaces m : 4, ($11 \leq m \leq 14$). The critical perturbation amplitude ϵ_c of the formation of the stochastic layer significantly depends on the position r_q of the resonant magnetic surface $q = 3$ ($\epsilon_c \approx 0.04$ for $r_q = 42$ cm). The shift r_q to the outer region decreases ϵ_c. Poincaré sections of field lines are shown in Fig. 1 for two values of ϵ at the fixed $r_q = 42$ cm : (a) $\epsilon = 0.08$; (b) $\epsilon = 0.15$. With the increasing of perturbation the width of the stochastic layer grows and field lines start to leave the stochastic layer at the divertor plate $r_d = 49$ cm. It decreases the sizes of KAM-stability islands, but they are not disappeared even for large perturbations. There are regions of stickiness at the lower boundary of the stochastic layer due to trapping of field lines near the KAM-stability islands. At the regions close to the upper boundary of the stochastic layer behavior of field lines becomes more regular with weak chaotic components.

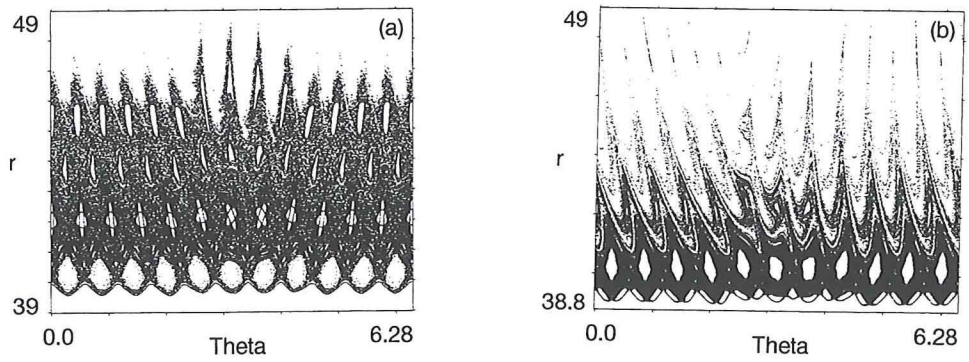

Fig. 1 Poincaré section of field lines

The diffusion of field lines is studied by computing the mean square displacement $\sigma_{r_o}(n) =< (r_n - r_o)^2 >$. When field lines do not leave the stochastic layer, $\sigma_r(n)$ is suppressing after sufficiently large number of iterations n. The diffusion of field lines in this case is subdiffusive (anomalous) with $\sigma_r(n) \sim n^\nu$ ($\nu < 1$) at the starting stage of evolution in n. The exponent $\nu \approx 0.58$ for $\epsilon = 0.05$.

The field lines leave the stochastic layer for the perturbation amplitude $\epsilon \geq \epsilon_l$. For the position r_q= 42 cm of the magnetic surface $q = 3$, $\epsilon_l \approx 0.06$, and $\epsilon_l \approx 0.038$ for r_q= 43 cm. In this case $\sigma_r(n)$ is growing at starting stage $n \leq n_c$ ($n_c \approx 13 - 20$) and rapidly decaying for $n \gg n_c$. The field line diffusion coefficient D_{FL} was estimated by computing $\sigma_r(n)$ at small n and fitting it by a linear function of distance $l = \pi R_o n/2$, i.e. $\sigma_r(n) = 2D_{FL}l$.

Fig. 2 shows the radial profiles of $D_{FL}(r)$ for the different values of perturbation ϵ, and the positions r_q: (a) r_q=42 cm, (b) r_q=43 cm. In Fig. 2a the curve 1 corresponds to ϵ = 0.10; curve 2 corresponds to ϵ = 0.15, and in Fig. 2b: curve 1 corresponds to ϵ = 0.05, curve 2 corresponds to ϵ = 0.1, and curve 3 corresponds to ϵ = 0.15. The corresponding quasilinear diffusion coefficients $D_Q(r)$ are presented by the dashed curves in Fig. 2.

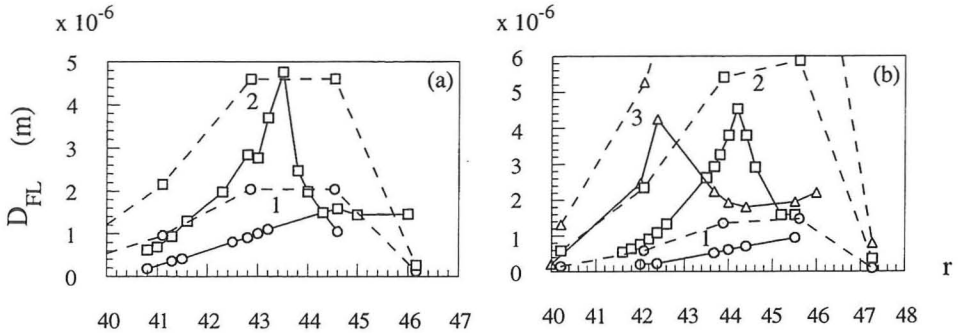

Fig. 2 Field line diffusion coefficients

For the moderate perturbation ϵ the diffusion coefficients, $D_{FL}(r)$, computed by the twist mapping are the same order as the quasilinear ones $D_Q(r)$. They depend on ϵ in the form $D_{FL} \sim \epsilon^2$. The radial profile $D_{FL}(r)$ follows the profile $D_Q(r)$. One can see from Figs. 2a,b that a shift of the position r_q of the resonant magnetic surface $q = 3$ by 1 cm to the plasma edge increases the diffusion of field lines approximately by a factor 2-3.

For the large perturbations the diffusion coefficient at the plasma edge drastically decreases along the minor radius r, and its value are considerably smaller than the one predicted by the quasilinear theory. The reason for such a behavior is that for the large perturbations the convective motion of field lines dominates over their chaotic motion.

For the large n, $\sigma_r(n)$ decays as $n^{-\mu}$, $(\mu > 0)$. It is due to anomalous (not normal) diffusion process at the lower boundary of the stochastic layer because of stickiness of field lines near the KAM-stability islands.

The obtained results show that the twist map sufficiently good describes the main features of the ergodic zone in the ergodic divertor tokamak.

References

1. K.H. Finken, G.H. Wolf, Fusion Technology and Design **37** (1997) 337.
2. A. Kaleck, M. Haβler, and T. Evans, Fusion Technology and Design **37** (1997) 353.

Modeling Efforts for the Helical Near Field Divertor of TEXTOR-94

K.H. Finken, Th. Eich, A. Kaleck

Institut für Plasmaphysik, Forschungszentrum Jülich GmbH, EURATOM Association,
Trilateral Euregio Cluster, D-52425 Jülich, Germany

Abstract: The proposed Dynamic Ergodic Divertor (DED) for TEXTOR-94 will break up the magnetic flux surfaces near the boundary and will establish there an ergodic region and, just in front of the perturbation coils, a helical near field divertor. The near field divertor is the contact zone of the plasma with the divertor target plates. The DED forms eight helical divertor strike lines aligned parallel to the perturbation coils. A first modeling effort is undertaken to treat the DED - divertor zone in a similar way as the classical poloidal one. Similar as there, a scrape-off layer (SOL) is defined for field lines intersecting the target plate after one poloidal rotation. In addition, another characteristic area is introduced which is fed by particles and power from the ergodic sea.

I. Introduction

The highly concentrated heat flux from the plasma to the contact zones of the wall imposes extreme engineering problems to a future fusion reactor. Proposals to reduce the high power flux density are the gas target divertor, plasma sweeping and the radiative mantle concept. In the gas target concept, the surface of the divertor is relatively large and the plasma „flame" transfers its energy via charge exchange and radiation primarily to the side walls. By sweeping the plasma column radially, the arriving heat flux is distributed to an enhanced area such that the averaged flux density is lowered. In the radiative mantle concept, a large fraction of the energy is radiated away by seed impurities, the power is radiated both from the plasma boundary in the main chamber as well as from the plasma in the divertor chamber. In TEXTOR, this mode of operation leads to an enhanced energy confinement[1].

To investigate an alternative way for distributing the power flux to an enlarged area, the concept of the dynamic ergodic divertor[2] is studied at TEXTOR-94. The power flux density is reduced by two means: 1) the number of divertor strike lines is increased from two (poloidal divertor) to eight; 2) by applying a four phase AC-perturbation current, a rotation of the perturbation field is enforced and the foot prints are smeared out over an area of several square meters in TEXTOR. Since the perturbation current is „optimized" for the magnetic field configuration, the required perturbation current for creating a divertor is minimum for a helical divertor aligned parallel to outer magnetic field lines such as foreseen for the DED-setup[3].

In the following we discuss a technique for modeling the plasma and power flux to the wall from the ergodic zone to the divertor strike zone. It will be shown that the power flux is by far not chaotic as it may be expected for an ergodized boundary but well organized. This finding agrees well with the description of the „laminar zone" in TORE SUPRA[4] which, however, uses a quite different approach.

II. Experimental Set-up

To generate an ergodic magnetic field in the TEXTOR boundary, a perturbation system with 16 single turn perturbation coils have been proposed for TEXTOR[2]. The coils, located at the high field side, are aligned parallel to the field lines of the q=3 surface (β_{pol} = 1) and each coil is guided helically once around the torus such that the entrance and the exit of the coils have the same toroidal angle. The coils can be supplied either by DC or by AC up to 10 kHz; the phasing between two successive coils is 90° such that in AC operation the currents generate a rotating magnetic field pattern. This current distribution forms an m=12, n=4 mode which is resonant with the magnetic field near the q=3 surface. By changing coil connections or modifying the current input distribution, also the modes 6/2, 3/1 and combinations of 12/4 and 6/2 with arbitrary amplitudes can be achieved. The perturbation current amplitude ($I_{per\text{-}max}$ = 15 kA) is large enough to provide an ergodization level with a Chirikov level of up to four.

To install the coils (r_{coil}=0.525 m) inside the vessel and to gain space, the liner will be cut away; in this way the minor plasma radius of a=0.46 m can remain unchanged. Since the pitch of the magnetic field lines is lowest at the high field side - the pitch is decreasing with increasing β_{pol} - the coil separation is lower at the high field side than corresponding to the average value. The effective mode number, determining the radial penetration of the magnetic field according to $b_{r,per} \propto (r/a)^{meff-1}$, is $m_{eff} \approx 20$ instead of 12 which would correspond to the average pitch value. To obtain, nevertheless, a sufficient deep penetration of the perturbation field, a new option of mode mixing of the m/n modes 12/4 and 6/2 have been developed.

III. The Model

The ansatz for modeling the plasma flux to the walls and in particular to the divertor target plate is guided by the code developments of the scrape-off layer (SOL) of the poloidal divertor: Similar as there, one finds a class of magnetic field lines connecting the divertor target plate after one poloidal turn around the plasma; in addition another class of field lines is found connecting the divertor target plate with the „ergodic sea". To visualize those field lines with different properties, two characteristic surfaces are introduced: One surface (I) is the cut

through the equatorial midplane of the tokamak at the low field side and the other one (II) is the wall surface.

The first cut is a plane spanned up by the radial and toroidal unit vectors; from this plane we start a tracing of magnetic field lines clockwise and counterclockwise and mark the starting points according to their different qualities of the „fate" of the field lines (starting plane). During one poloidal turn, the field lines can either hit the liner, the divertor target plate, the front surface of the pump limiter, the pump limiter entrance or no wall element. (for the example given here the pump limiter is retracted). The areas in the starting plane which are connected in this way to the liner are represented as squared area, the one connected to the divertor target plate is black and the one which is not connected directly with the walls is dotted. Fig. 1 shows such an example of clockwise tracing for a condition with full perturbation current and a plasma shifted by 1 cm towards the inner wall (to enhance the ergodization). A similar, nearly mirror symmetric picture is obtained for the counter-clockwise tracing of the field lines (the symmetry is uncomplete because the feeder coils are not quite symmetric).

The intersection points of the magnetic field lines with wall elements in surface (II) are shown in Fig 2; they are plotted with the same symbols as in Fig. 1. It is found that just in front of the perturbation coils a helical strike zone is formed. According to the multipolarity of the perturbation coil system, 8 strike zones totally are formed instead of two in case of the poloidal divertor; four strike zones correspond to the clockwise field tracing and the other four to the ctr-clockwise tracing. The distribution of the intersection points on the liner is nearly un-structurized.

In Fig. 3 an „overlay" of the structures in the starting plane (I) for co- and ctr-clockwise tracing is plotted. The overlay defines essentially three areas: a) the area with field lines intersecting wall elements twice after one poloidal turn (black), b) the area with field lines intersecting wall elements on one side and extending to the „ergodic sea" on the other end (squared) and c) areas with field lines open on both ends after a poloidal path (dotted). Area (a) corresponds topologically to a scrape-off layer (SOL) of a limiter or divertor; area (b) is typical for the ergodized edge magnetic field and area (c) belongs to the ergodic sea (the confinement area is still further inwards). For the modeling, area (a) is treated like a normal SOL with convective parallel and diffusive perpendicular transport; for area (b) we assume the same type of transport but prescribe a density and power flux at the open ends of the field lines resulting from feeding in the ergodic zone. Fig. 4 shows the distribution of the heating pattern resulting from these assumptions.

References

1. A.M. Messiaen, J. Ongena, B. Unterberg et al., Physics Plasmas **4** (1997) 1690
2. Collection of articles of the DED in Fusion Engineering and Design, **37**, No 3 (special issue) 1997
3. K.H. Finken, Nucl. Fusion, **37** (1997) 583
4. F. Ngyen, P. Ghendrih, A. Grosman, Nucl. Fusion, **37** (1997) 743

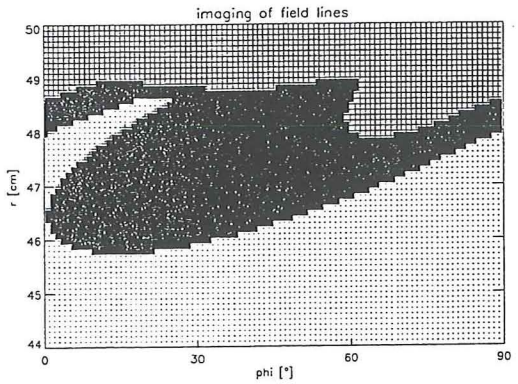

Fig. 1: Characteristic areas in the starting plane; squared: field lines ending on the liner, black: field lines ending on the target plate; dotted: lines ending in the ergodic zone.

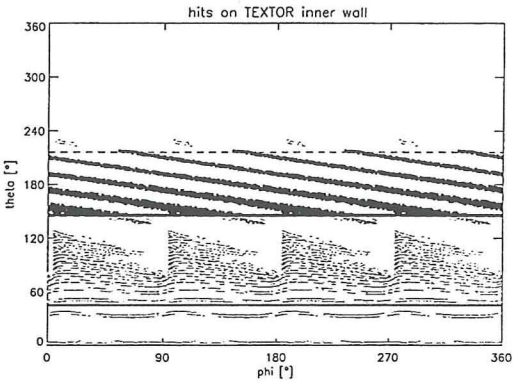

Fig. 2: Intersection points of field lines with the wall

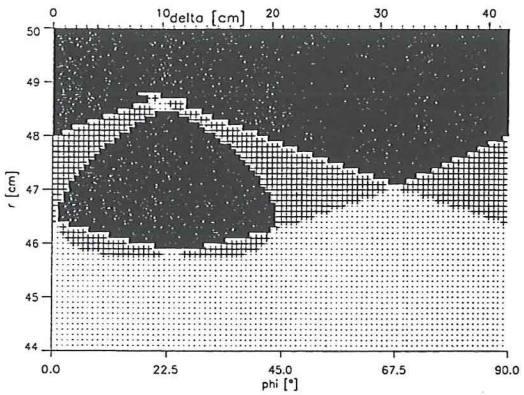

Fig. 3: The overlay of co- and ctr-clockwise tracing

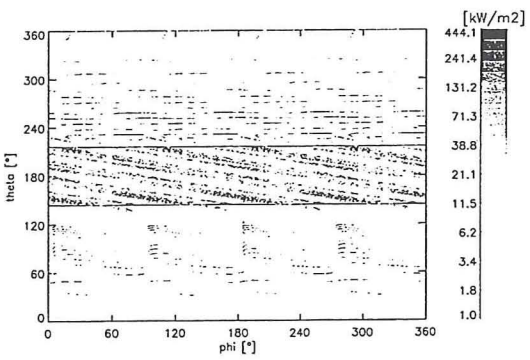

Fig. 4: Power distribution on the walls

Semi–analytical Calculations of Radiation Losses from light Impurities in a non–corona Approximation

H. Lasaar, M.Z. Tokar

Institut für Plasmaphysik, Forschungszentrum Jülich GMBH, EURATOM Association, Trilateral Euregio Cluster, D-52425 Jülich, Germany

I Introduction

A model for the calculation of radiation losses from light impurities is proposed, based on determination of the radial density profiles of radiating particles from balance between transport and ionization processes. The WKB–method is used to take into account the temperature dependence of the ionization coefficient. This allows to describe in particular the effect of the modification of the radial heat conductivity and temperature profile on impurity radiation by Stochastization of the magnetic field.

II Radial Distribution of Impurities

The radial distribution of the particle density of a chosen charged state is described by a continuity equation, taking into account the radial transport as well as ionization processes. The latter couple equations for different ionization stages.
The radiating ion states of light impurities, e.g. carbon, are localized in a thin shell at the plasma edge. Therefore all calculations are performed in plane geometry with the space variable x being the distance to the last closed magnetic surface (LCMS) touching the limiter. For the density n_0 of neutrals, the continuity equation reads

$$\partial_x (v_0 n_0) = -k_0 n_e n_0 \quad , \tag{1}$$

for the ionization stages $i = 1, \ldots, n-1$

$$-\partial_x (D \partial_x n_i) = k_{i-1} n_e n_{i-1} - k_i n_e n_i \tag{2}$$

and for the highest ionization stage $i = n$:

$$-\partial_x (D \partial_x n_n) = k_{n-1} n_e n_{n-1} \quad . \tag{3}$$

Here, the k_i are the ionization coefficients, n_e is the electron density and n_i is the density of the i-th charged state.
The boundary conditions prescribe influx j_0 of impurity neutrals with velocity v_0: $v_0 n_0(0) = j_0$, the vanishing of all charged states at the LCMS: $n_i(0) = 0$ and the absence of particle sources in the plasma core ($x \to \infty$). This means, the fluxes of all charged states reduce here to zero, i.e. $\partial_x n_i|_\infty = 0$ for $i = 1, \ldots n$.
First, we assume, that the plasma parameters, n_e and T_e, are homogeneous, i.e. independent of x. Under this assumption, the solution of eq (1) is

$$n_0(x) = \frac{j_0}{v_0} e^{-x/l_0}$$

with $l_0 = \frac{v_0}{k_0 n_e}$ being the penetration depths of the impurity atoms. The main contributors to the impurity radiation are the low ionized stages. Due to temperature dependence of

the ionization constants, one of them ($i = *$) dominates in the radiation region, i.e. here $n_1 + \ldots + n_* \simeq n_*$. E.g. in the case of carbon the lithium–like ions with $* = 3$ are the main radiator. By adding all continuity equations for the stages with $i \leq *$, this results in the following

$$-\partial_x \left(D \, \partial_x \, n_* \right) \simeq -k_* \, n_e \, n_* + S_0 \, e^{-x/l_0} \tag{4}$$

using $S_0 = (k_0 \, n_e \, j_0)/v_0$. With coefficients independent of x, the solution to this equation is

$$n_*(x) = n_\infty \cdot \frac{e^{-x/l_*} - e^{-x/l_0}}{1 - l_0^2/l_*^2} \tag{5}$$

with $n_\infty = \frac{S_0 \, l_0^2}{D}$ and l_* being the penetration length for the radiating particles $l_* = \sqrt{\frac{D}{k_* \, n_e}}$. Radial integration gives a formula for the total number of these particles

$$N_* = n_\infty \cdot \frac{l_*^2}{l_* + l_0} \quad .$$

The radiated power can be estimated as

$$W_{rad} = 2 \, \pi^2 \, a \, R \, n_e \, L_* \, N_* \quad ,$$

where L_* is the cooling rate of the radiating particles, being a weak function of the electron temperature.
1

III Temperature Dependence

To solve equation (4) analytically, we have assumed, that the coefficients in (4) are x–independent. This assumption is usually violated, because the ionization rate coefficient is a strong temperature function for T less than the ionization potential I_* [1]: $k_* \sim \sqrt{T} \, e^{-I_*/T}$. In the case of carbon, $I_* \simeq 64$ eV, i.e. in the range of typical temperatures at the plasma edge in tokamaks. To avoid the difficulty above, we take into account, that the temperature dependence is of importance only for the term $exp(-x/l_*)$ in (5) (since $l_0 << l_*$, this dependence is not significant for the numerator). If l_* depends on x, we proceed to the WKB–approximation [2] to the solution of (4). This allows to retain the exponential behaviour of the exact constant coefficient solution and to take into account the variation of the coefficient by using a more general ansatz for the exponent: $n_*(x) \sim e^{f(x)}$. In the first approximation, which is called 'eikonal equation', the resulting equation for $f(x)$ reads

$$(\partial_x \, f(x))^2 = \frac{k_*(T(x)) \, n_e}{D}$$

with the solution

$$f(x) = \int_0^x dx' \sqrt{\frac{k_*(T(x')) \, n_e}{D}} \quad ,$$

that directly suggests a redefinition $l_* \to \lambda_*$ of the penetration depth according to

$$\int_0^{\lambda_*} dx \sqrt{\frac{k_*(T(x)) \, n_e}{D}} = 1 \quad .$$

In order to make use of this formula, it is necessary to insert the temperature profile, which is not known. To avoid this difficulty, we first make a substitution to the temperature as a new variable. The link between x and T is made by the equation

$$dx = \frac{\kappa_\perp}{q_\perp} dT \tag{6}$$

with $q_\perp$ being the radial heat flux density. The result is

$$1 = \int_{T_0}^{T_*} dT \frac{\kappa_\perp}{q_\perp} \sqrt{\frac{k_*(T)\, n_e}{D}} \quad . \tag{7}$$

Next, the terms with a radial dependence, n_e and $q_\perp$, are pulled out of the integral as average values, while the remaining terms, k_* and $\kappa_\perp$, naturally depend on temperature:

$$1 \simeq \sqrt{\frac{\bar{n}_e}{D}} \frac{1}{\bar{q}_\perp} \int_{T_0}^{T_*} dT\, \kappa_\perp \sqrt{k_*(T)} \quad .$$

In this way the unknown temperature profile does not enter and is represented by the temperature T_0 at the edge and a characteristic temperature T_* limiting the radiation layer and corresponding to the penetration depth λ_*. In this formula, $\bar{n}_e$ and $\bar{q}_\perp$ are the average values over the radiating layer: $\bar{q}_\perp = (q_{core} + q_0)/2$ with q_{core} the heat flux density coming from the core and q_0 the heat loss to the LCMS, which is proportional to the edge temperature:

$$q_0(T_0) = \kappa_\perp \frac{T_0}{\delta_T}$$

with δ_T the e–folding length of the temperature at the LCMS, typically having a value of $2 - 3\,cm$. Once T_* has been determined by a numerical integration of eq(5), λ_* can be calculated numerical integrating equation (7) from T_0 until T_*. The result of the numerical calculation of λ_* by this formula is inserted instead of l_* into the expression for the radiation losses.

As an example of the applications of the approach described above, we perform a calculation of the sum of energy losses from the edge as a function of the edge temperature, which is an important characteristic in particular for stability analysis:

$$Q_{loss} = q_0 + W_{rad}$$

Fig.1 shows the $Q_{loss}(T)$ dependence calculated for typical parameters in TEXTOR ohmic discharges: $a = 46\,cm$, $R = 175\,cm$, $q_{core} = 1W\,cm^{-2}$, $n_e = 2 \cdot 10^{13}\,cm^{-3}$, $\kappa_\perp = 2 \cdot 10^{17}\,cm^{-1}$, $D = \kappa_\perp/3n$, $\delta_T = 2\,cm$, carbon as the main impurity with $n_\infty = 0.01\,n_e$. Curve (1) has been found with a plasma temperature independent of x, curve (2) with taking into account the temperature variation of k_*. It can be seen, that the latter is of importance especially for low edge temperatures.

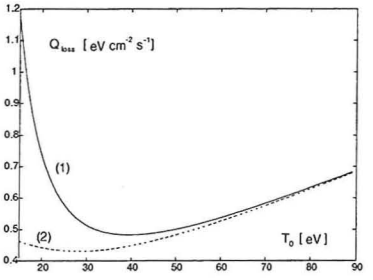

Fig.1: Energy losses with radiation and conduction as a function of the edge temperature at the LCMS; (1) $T(x) = T_0$, (2) T varies with x

IV Stochastization

Destruction of the magnetic surfaces at the plasma edge results in an increase of the radial energy transport and a modification of the behaviour of impurities. The stochastization effect can be included into this model by a modification of the radial heat conductivity $\kappa_\perp$. We apply the Rechester Rosenbluth formula [3], that expresses the effective radial heat conductivity in a stochastic magnetic field as a combination of parallel and perpendicular heat transport:

$$\kappa_{eff} = \kappa_\perp \frac{\sigma_x(T)}{1 + x_0(T) + \ln \sigma_x(T)} \tag{8}$$

with $\sigma_x(T) = \frac{D_{FL}\,\kappa_\parallel(T)}{L_c\,\kappa_\perp}$. Here D_{FL} is the diffusion coefficient for magnetic field lines, L_c the correlation length for magnetic field lines, and $x_0(T)$ takes into account kinetic corrections to the heat flux. Stochastization always increases the radial transport, so in formula (6) κ_{eff} should always be bigger than $\kappa_\perp$. The result of a calculation of the width λ_* of the radiating layer and temperature T_* at its boundary for carbon ($* = 3$) as a function of the 'stochastization level' κ_{eff}/κ is shown in the following picture:

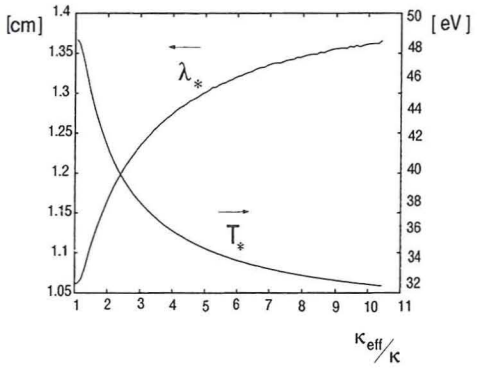

Fig. 2: T_* (1) and λ_* (2) as functions of κ_{eff}/κ for $T_0 = 30\,eV$

With increasing stochastization, the penetration depth λ_* increases. This is, because with increasing radial heat conductivity the temperature profile gets flater making the low ionized radiating stages exist for a longer time before ionization to non radiating stages. Simultaneously, T_* decreases, i.e. radiating ions vanish already at temperatures significantly less than their ionization potential.

References

[1] Tokar M.,Z., Nucl. Fusion 34 (1994) 853

[2] Zwillinger, Handbook of differential equations, Acad. press, 1989

[3] Rechester, A.B., Rosenbluth, M.N., Phys.Rev.Lett. 40 (1978) 38

Kinetic Effects in the Formation of a Radiating Layer

D. Reiser[1], D. Reiter[2], M. Tokar[1]
[1] Institut für Plasmaphysik, Forschungszentrum Jülich GmbH,
EURATOM Association, Trilateral Euregio Cluster, D-52425 Jülich, Germany
[2] Heinrich Heine Universität Düsseldorf, Germany

Abstract. The subject of this paper is the presentation of a refined drift kinetic model test particle model suitable for Monte Carlo simulations of impurity transport in a fluid like background plasma. This model differs from existing approaches in so far that now first order drift effects are included and the approximative treatment of Coulomb scattering of the impurities at the background plasma is removed by the employment of a generalized drift kinetic Coulomb term in Fokker Planck form. This Coulomb term provides an accurate and consistent kinetic description of the scattering at field particles obeying a distorted maxwellian distribution parametrized in the 13 moment expansion. The inclusion of the perturbative part of the background distribution provides the correct treatment of the so called thermal forces due to spatial inhomogenitites in the background temperature. These thermal play a crucial role for the transport of impurities in the scrape off layer of tokamaks and the results of our kinetic approach differ significantly from those of the fluid approximation for low ionized impurities.

I. Basic Equations for Modelling of Impurity Transport

Assuming that the impurities are well described in the framework of the test particle model, a set of linear Fokker Planck equations for the different charge states of the impurities can be separated. The transformation to drift kinetic variables $(\boldsymbol{R}, v_{\|}, v_{\perp})$ yields the following equations

$$\begin{aligned}\frac{\partial \bar{f}^Z}{\partial t} &= -\frac{\partial}{\partial \boldsymbol{R}}\left(\dot{\boldsymbol{R}}\,\bar{f}^Z\right) - \frac{\partial}{\partial v_{\|}}\left(\dot{v_{\|}}\,\bar{f}^Z\right) - \frac{\partial}{\partial v_{\perp}}\left(\dot{v_{\perp}}\,\bar{f}^Z\right) + \bar{C}(\bar{f}) \\ &- S_I^Z\,\bar{f}^Z + S_I^{Z-1}\,\bar{f}^{Z-1} - S_R^Z\,\bar{f}^Z + S_R^{Z+1}\,\bar{f}^{Z+1} \qquad (1) \\ &+ Q_Z^+ - Q_Z^- + \sum_{i,k}\frac{\partial^2}{\partial R_i \partial R_k}\left(\hat{r}_i\hat{r}_k\,D_{\perp}\,\bar{f}^Z\right).\end{aligned}$$

The function $\bar{f}^Z = v_{\perp}\,f^Z$ is the transformed distribution function for the impurities in charge state Z. The coupling of the different charge states results

from the ionization and recombination terms in the second line of equation (1). The coefficients in the first three terms on the right hand side are given by the equations of motion of the drift kinetic variables

$$\begin{aligned} \dot{\boldsymbol{R}} &= v_{\|}\boldsymbol{b} + \frac{\boldsymbol{E}\times\boldsymbol{B}}{B^2} + \frac{1}{2}\frac{v_{\perp}^2}{\Omega}\frac{\boldsymbol{b}\times\boldsymbol{\nabla}B}{B} - \frac{v_{\|}^2}{\Omega}\boldsymbol{b}\times(\boldsymbol{b}\times(\boldsymbol{\nabla}\times\boldsymbol{b})) \\ \dot{v_{\|}} &= \frac{Ze}{m}\boldsymbol{E}\,\boldsymbol{b} + \frac{1}{2}v_{\perp}^2\,\boldsymbol{\nabla}\boldsymbol{b} \quad ; \quad \dot{v_{\perp}} = -\frac{1}{2}v_{\|}v_{\perp}\,\boldsymbol{\nabla}\boldsymbol{b}. \end{aligned} \tag{2}$$

These were obtained by an averaging procedure [1] to eliminate the gyro-angle dependence. The diffusive term in the third line describes an anomalous transport in the radial direction ($\hat{\boldsymbol{r}}$) in real space governed by the diffsuion coefficient $D_{\perp}$. The remaining terms in the third line represent additional sources and sinks. $\bar{C}(\bar{f}^Z)$ is the Coulomb term in the drift velocity variables obtained by direct transformation and assuming $\bar{f}^Z(\boldsymbol{R}, v_{\|}, v_{\perp}, \varphi) = \bar{f}^Z(\boldsymbol{R}, v_{\|}, v_{\perp})$. The drift and diffusion coefficients $K_{\|}$, $K_{\perp}$, $D_{\|\|}$, ..., $D_{\perp\perp}$ can be calculated using Trubnikov potentials which are determined by the distribution function of the background particles [2]. To be consistent with a fluid modelling of the background plasma we have chosen the following form the background distribution function

$$f_b(\boldsymbol{v},t) = (1+\eta(\boldsymbol{v},t))\left(\frac{2\pi T_b}{m_b}\right)^{-3/2}\exp\left(-\frac{1}{2}\frac{m_b}{T_b}(\boldsymbol{v}-\boldsymbol{v}_b)^2\right) \tag{3}$$

This is a shifted Maxwellian distribution with a distortion given by the function $\eta(\boldsymbol{v})$, which is approximated in the 13 moment expansion [3]. It is the inclusion of this perturbation (which is proportional to inhomogenities in the background temperature T_b and the background flow velocity $\boldsymbol{v}_b$) which yields a kinetic model for the thermal forces.

II. Kinetic Thermal Forces

In previous approaches [4], [5] the Coulomb scattering of the impurities at the inhomogenitites in the temperature of the background distribution (here we will discuss only the scattering at the hydrogen ions) has been approximated by

$$\frac{\partial v_{\|}}{\partial t} \approx \frac{\partial <v_{\|}>}{\partial t} = \frac{\beta_Z}{m}\nabla_{\|}T_b \tag{4}$$

where $\partial v_{\|}/\partial t$ is the force acting on a single particle in the kinetic simulation of the impurities and the coefficient of the thermal force is [6]

$$\beta_Z = -3\,\frac{1-\mu-5\sqrt{2}\,Z^2\,(1.1\,\mu^{5/2}-0.35\,\mu^{3/2})}{2.6-2\,\mu+5.4\,\mu^2}, \tag{5}$$

with $\mu = m/(m+m_b)$. This approach implies an inconsistency because the single particle force is approximated by the acceleration of an almost maxwellian ensemble of impurities. But this assumption is not fulfilled for shortlived low ionized impurities. Considering the part of the drift coefficient $K_{\|}$ which depends on the gradient ∇T_b we get the following expression for the coefficient of the thermal force

$$\tilde{\beta}_Z(\boldsymbol{\chi}) \;=\; \left(1+\frac{m_b}{m}\right)\frac{3}{2}\,\frac{Z^2}{Z_b^2}\,\tilde{\kappa}_{\|}\,\left(1-2\,\chi_{\|}^2\right)\,e^{-\chi^2}. \tag{6}$$

with the normalized relative velocity $\boldsymbol{\chi} = \sqrt{\frac{m_b}{2T_b}}(\boldsymbol{v}-\boldsymbol{v}_b)$ between the test particle velocity $\boldsymbol{v}$ and the background flow velocity $\boldsymbol{v}_b$. $\tilde{\kappa}_{\|}$ is the dimensionless heat conductivity for the background ions. Figure 1 shows a comparison of coefficients from fluid theory β_Z (5) and the one from the kinetic approach $\tilde{\beta}_Z$ (6). The coefficient $\tilde{\beta}_Z(\boldsymbol{\chi})$ strongly depends on both the magnitude of the relative velocity $\boldsymbol{\chi}$ and its direction and – most striking – the kinetic thermal force can change sign.

The comparison of the different models for the thermal forces in calculations done with our code DORIS for a typical TEXTOR discharge with neon impurities have demonstrated that the low ionized charge states are much more localized at the limiter than predicted by the fluid model, meaning that the formation of a radiative layer will be less enhanced by thermal forces in the scrape off layer than predicted by fluid models. But for the higher charge states the results of the different approaches do not differ very much, indicating that the fluid assumption is almost valid for these species.

References

[1] Sivukhin, D. V.: in "Reviews of Plasma Physics, Vol. I", ed. by M. A. Leontovich, Consultants Bureau, New York (1965)

[2] Trubnikov, B. A.: in "Reviews of Plasma Physics, Vol. I", ed. by M. A. Leontovich, Consultants Bureau, New York (1965)
[3] Balescu, R.: "Transport Processes in Plasmas Vol. 1", North-Holland, Amsterdam (1988)
[4] Stangeby, P. C. and ELDER, J. D.:
J. Nucl. Mat., Vol. 196/198, p. 258 (1992)
[5] Takizuka, T. und Shimizu, K.: "Impurity Transport Code Based on Monte Carlo Techniques (IMPMC)", ITER Workshop February 21-25, 1994, ITER JCT, Garching Co-Center (1994)
[6] Neuhauser, J., Schneider, W., Wunderlich, R. and Lackner, K.: Nuclear Fusion, Vol. 24, No. 1, p. 39 (1984)

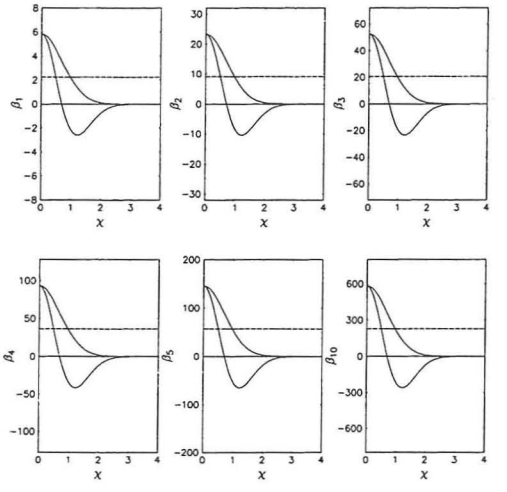

Figure 1: Comparison of the coefficients β_Z and $\tilde{\beta}_Z(\chi)$ of the thermal force in the fluid model (dashed lines) and in the kinetic model (solid lines) respectively, for values $Z = 1, 2, 3, 4, 5, 10$. Z_b is equal 1. $\tilde{\beta}_Z(\chi)$ is shown for the limiting cases $\chi_{||} = \chi$ (lower solid curve) and $\chi_{||} = 0$ (upper solid curve).

THE SCALING OF THE EDGE TEMPERATURE AT THE L-H TRANSITION BASED ON THE ALFVEN DRIFT-WAVE INSTABILITY

W. Kerner and O. Pogutse
JET Joint Undertaking, Abingdon, Oxon., OX14 3EA, UK.

The measurement of the electron edge temperature T_0 and density n_0 on JET and other tokamaks suggest that there is an ideal MHD beta threshold for the onset of Giant ELM's. Furthermore, the data reveal also the existence of a second beta threshold (below the ideal ballooning limit) for the L-H transition and a third threshold for the onset of type III ELMs. These findings suggest that the Alfven drift-wave instability plays an essential role in the edge plasma dynamics. There is strong experimental evidence that the main plasma instabilities change from ion temperature gradient modes in the plasma core to electron drift modes near the plasma edge. The stability theory gives the results that with increasing plasma pressure the Alfven waves mix with electron drift waves and suppress the unstable long wavelength perturbations, which are dominant for transport. The analysis for the Alfven drift type modes leads to a threshold condition for the L-H transition. This condition yields the scaling for the edge temperature.

The main conclusions are: 1) the Alfven drift model predicts that the turbulent transport is suppressed when the condition: $\beta_n > 1 + \nu_n^{2/3}$ is satisfied (where β_n and ν_n denote the normalised beta and the normalised collision frequency) . 2) The transport coefficients change their dependence on plasma parameters from increasing with temperature to decreasing with temperature when this edge beta threshold is exceeded . 3) The Alfven drift model predicts the edge temperature scaling in agreement with the experimental results. Furthermore, the qualitative character of the scaling depends only weakly on the SOL transport.

The Influence of Impurities and Heat Flux Gradients on the Revised Neoclassical Transport in Tokamaks

H.A.Claaßen, H.Gerhauser
Institut für Plasmaphysik, Forschungszentrum Jülich GmbH, EURATOM Association, Trilateral Euregio Cluster, D-52425 Jülich, Germany

1. Introduction

In a number of recent papers [1] the neoclassical theory has been revised by investigating effects due to strong radial gradients of the plasma parameters and the electrostatic potential, which typically arise during the formation of a transport barrier. With the appearance of strong radial gradients finite Larmor radius effects become important, i.e. the diamagnetic time may approach the longitudinal diffusion and heat conduction time and the gyroviscosity may compete with the collisional viscosity for the $\|\vec{B}$ momentum transfer. As a consequence there will be a marked effect on the poloidal variation of the plasma parameters and the electrostatic potential and a corresponding change in the magnetic surface averaged particle and heat fluxes. The radial fluxes are reduced to subneoclassical values, which may even approach the classical ones, going in parallel with a sudden transition from large to small radial gradient lengths and transport coefficients (bifurcation scenario). In the revised neoclassical theory the radial transport coefficients depend on the radial electric field and the longitudinal center-of-mass velocity of the whole plasma, which are related to the radial density and temperature gradients through the ambipolarity constraint and the magnetic surface averaged B weighted parallel momentum equations, both being modified by including the ion gyroviscosity.

So far the neoclassical theory has been revised for a pure plasma in the Pfirsch-Schlüter regime adopting the Navier-Stokes approximation for the parallel momentum flux equation and assuming that the electrons satisfy a Boltzmann equilibrium $\|\vec{B}$, in which case the magnetic surface averaged radial particle fluxes vanish. In the present paper we extend the Pfirsch-Schlüter theory by taking into account the heat flux gradients in the momentum transport relation (Burnett ansatz) [2] and investigate the contribution of a single impurity admixture in charge state z, satisfying $zn_+ \gg n_z$, to the particle and heat fluxes, but still neglect inelastic collisions and deviations from an electron Boltzmann equilibrium $\|\vec{B}$. The results are derived for the standard magnetic field configuration $\vec{B} = [0, -\Theta(r), 1]B_0R_0/R$ with $R = R_0 + r\cos\theta$ and $BR = const.$ for large aspect ratio tokamaks with concentric magnetic flux surfaces.

2. The poloidal plasma distribution

For given radial density and temperature gradients of the ion species the problem under consideration is completely described by the particle and heat balance equations in combination with longitudinal particle and heat transport relations, which yield the poloidal asymmetries of the plasma parameters and allow to evaluate the averaged radial fluxes, the ambipolarity constraint and the averaged B-weighted parallel momentum equations of the ions. Since in a toroidal system the driving forces for the poloidal asymmetries of the various plasma parameters $Q(r,\theta)$ are due to the centrifugal, grad B and electric drifts of the charge carriers, i.e. proportional to the vertical plasma gradients $\nabla_v Q \simeq \sin\theta(\partial Q/\partial r)$ in the standard magnetic field configuration assuming $|r\partial \ln Q/\partial r| \gg 1$, we look for a solution of the particle and heat balance equations in the poloidally periodic form $Q(r,\theta) = Q_0(r) + Q_1^s(r)\sin\theta + Q_1^c(r)\cos\theta$ considering only terms up to first order in r/R_0. For the three component plasma under consideration we get the following solution making use of the definitions $\hat{T}_{+1} \equiv T_{+1}/T_{+0}$, $\hat{n}_{\alpha 1} \equiv n_{\alpha 1}/n_{\alpha 0}$ with $\hat{p}_{\alpha 1} \equiv p_{\alpha 1}/p_{\alpha 0} = \hat{n}_{\alpha 1} + \hat{T}_{+1}$ and $\hat{\Phi}_1 \equiv e\Phi_1/(kT_{+0})$:

$$\hat{T}^s_{+1} = \gamma^*_I \frac{1+\varepsilon_I \gamma^*_{II}}{1+\gamma^{*2}_{II}} \quad , \quad \hat{T}^c_{+1} = \gamma^*_I \frac{\gamma^*_{II} - \varepsilon_I}{1+\gamma^{*2}_{II}}$$

$$\hat{n}^s_{+1} = \alpha^{**}_I - \alpha^*_{III}\hat{T}^s_{+1} + \alpha^*_{II}\hat{T}^c_{+1} \quad , \quad \hat{n}^c_{+1} = \alpha^*_I - \alpha^*_{II}\hat{T}^s_{+1} - \alpha^*_{III}\hat{T}^c_{+1}$$

$$\hat{\Phi}_1 = -\frac{n_{+0}\hat{p}_{+1} + n_{z0}\hat{p}_{z1}}{n_{-0}} \quad , \quad (z+1)\hat{n}_{z1} = -\frac{2n_{+0}}{n_{z0}}\hat{n}_{+1} - \left(1 + \frac{n_{+0}}{n_{z0}}\right)\hat{T}_{+1}$$

where $\gamma^*_I \equiv \dfrac{\alpha^*_I - \beta^*_I}{\alpha^*_{II} - \beta^*_{II}}$, $\gamma^*_{II} \equiv \dfrac{\alpha^*_{III} - \beta^*_{III}}{\alpha^*_{II} - \beta^*_{II}}$, $\varepsilon_I \equiv \dfrac{\alpha^{**}_I - \beta^{**}_I}{\alpha^*_I - \beta^*_I}$

using for both α^*_N and β^*_N the same abbreviations

$$\kappa^*_I \equiv \frac{\kappa_I \kappa_{II}}{\kappa^2_{II} + \kappa^2_{IV}} \quad , \quad \kappa^{**}_I \equiv \frac{\kappa_{IV}}{\kappa_{II}}\kappa^*_I \quad , \quad \kappa^*_{II} \equiv \frac{\kappa_{II}\kappa_V + \kappa_{III}\kappa_{IV}}{\kappa^2_{II} + \kappa^2_{IV}} \quad , \quad \kappa^*_{III} \equiv \frac{\kappa_{IV}\kappa_V - \kappa_{II}\kappa_{III}}{\kappa^2_{II} + \kappa^2_{IV}}$$

We note that the values of $\hat{n}^s_{+1}$ and $\hat{n}^c_{+1}$ are unchanged, if we replace α^{**}_I and α^*_N by the corresponding coefficients β^{**}_I and β^*_N. Indeed, by equating the different formulations of $\hat{n}^s_{+1}$ and $\hat{n}^c_{+1}$ we just arrive at the quoted results for the common ion temperatures $\hat{T}^s_{+1}$ and $\hat{T}^c_{+1}$. Moreover $\hat{T}_{-1} \simeq 0$ due to the high longitudinal electron heat conductivity and $\hat{n}_{-1} = (n_{+1} + zn_{z1})/(n_{+0} + zn_{z0})$ due to quasineutrality. There are three different groups of coefficients α_N and β_N, which determine the poloidal variation of the ion densities and the ion temperature:
1. the coefficients responsible for the up-down asymmetries due to the centrifugal and grad B drifts driven by the magnetic field variation within the magnetic flux surfaces

$$\alpha_I = \frac{5r}{R_0}\frac{kT_{+0}}{eB_0}\frac{\partial \ln T_{+0}}{\partial r} \quad , \quad \beta_I = \frac{2r}{en_{+0}B_0R_0}\left(\frac{\partial p_{+0}}{\partial r} - \frac{n_{+0}}{zn_{z0}}\frac{\partial p_{z0}}{\partial r}\right)$$

2. the coefficients related to the diffusive $\|\vec{B}$ particle and heat fluxes driven by the $\|\vec{B}$ gradients of electrostatic potential, ion pressure and ion temperature

$$\alpha_{IV} = \alpha^T_{++0}\beta_{IV} \quad , \quad \alpha_V = \alpha^0_V + \alpha^T_{++0}\beta_V \quad \text{with} \quad \alpha^0_V = \frac{\Theta^2\lambda_{++0}}{rn_{+0}}$$

$$\beta_{IV} = \frac{\Theta^2 D^*_{+z0}}{r}\left(\frac{Z_{eff0}+1}{z+1}\right) \quad , \quad \beta_V = \frac{\Theta^2 D^*_{+z0}}{r}\left(\frac{Z_{eff0}}{z+1} + \alpha^T_{++0}\right) \quad .$$

$$\lambda_{++0} = \frac{25}{8}\frac{1}{\delta_0(Z_0)}\frac{p_{+0}\tau_{++0}}{m_+} \quad , \quad \alpha^T_{++0} = Z_0\delta_3(Z_0) \quad , \quad D^*_{+z0} = \frac{kT_{+0}}{m_+\nu_{+z0}[1 - \Delta^*_+(Z_0)]}$$

are respectively the longitudinal heat conductivity and the diffusion thermo coefficient of the main ions and the longitunal diffusion coefficient due to Coulomb interactions between main and impurity ions. The $\delta_N(Z_0)$ terms with $Z_0 \equiv z^2 n_{z0}/n_{+0}$ appear in Grad's 21-moment

approximation of the longitudinal transport coefficients [3]. $\Delta_+^*(Z_0)$ passes to $(3/5)\alpha_{++0}^T$ in Grad's 13-moment approximation and extends $\Delta_+(Z_0)$ in [3]. $Z_{eff0} \equiv (n_{+0} + z^2 n_{z0})/n_{-0}$.
3. the coefficients responsible for an additional inboard-outboard asymmetry appearing in the revised neoclassical theory due to the convection terms $U_{\|0}\nabla_\| n_\alpha$ and $U_{\|0}(2.5\, n_\alpha \nabla_\| kT_\alpha - \nabla_\| p_\alpha)$, where $U_{\|0}$ is the $\|\vec{B}$ center-of-mass velocity of the whole plasma assuming $U_{\|0}^2 \ll v_{T+}^2$, and the electric drift terms $\vec{V}_E \bullet \vec{\nabla} n_\alpha$ and $\vec{V}_E \bullet (2.5\, n_\alpha \vec{\nabla} kT_\alpha - \vec{\nabla} p_\alpha)$ in the particle and heat balance equations respectively. They are defined by the relations (valid up to first order in r/R_0)

$$\Theta(u_{+\|1} - u_{z\|1}) - \beta_I \cos\theta \equiv \Theta(u^*_{+\|1} - u^*_{z\|1}) = -\beta_{II}\hat{n}_{+1} + \beta_{III}\hat{T}_{+1}$$

$$\frac{\Theta h_{+\|1}}{p_{+0}} - \alpha_I \cos\theta \equiv \frac{\Theta h^*_{+\|1}}{p_{+0}} = -\alpha_{II}\hat{n}_{+1} + \alpha_{III}\hat{T}_{+1}\ ,$$

$$\text{where}\quad \Theta u^*_{\alpha\|1} \equiv \Big(\frac{\partial \Phi_0}{B_0 \partial r} - \Theta U_{\|0}\Big)\,\hat{n}_{\alpha 1} - \frac{kT_{+0}}{eB_0}\,\frac{\partial \ln n_{\alpha 0}}{\partial r}\,\hat{\Phi}_1 \quad \text{and}$$

$$\frac{\Theta h^*_{\alpha\|1}}{p_{\alpha 0}} \equiv \Big(\frac{\partial \Phi_0}{B_0 \partial r} - \Theta U_{\|0}\Big)\Big(\frac{3}{2}\,\hat{T}_{+1} - \hat{n}_{\alpha 1}\Big) - \frac{kT_{+0}}{eB_0}\Big(\frac{3}{2}\,\frac{\partial \ln T_{+0}}{\partial r} - \frac{\partial \ln n_{\alpha 0}}{\partial r}\Big)\,\hat{\Phi}_1$$

$|\alpha_{II,III}/\alpha_{IV,V}| = O[r/(\Delta\Theta^2\Omega_{+0}\tau_{++0})]$ and $|\beta_{II,III}/\beta_{IV,V}| = O[r/(\Delta\Theta^2\Omega_{+0}\tau_{+z0})]$ with $\tau_{++0} \equiv 2/\nu_{++0} = \tau_{+z0}Z_0\sqrt{2}$ with $\tau_{+z0} \equiv 1/\nu_{+z0}$ are of the order of the ratio between longitudinal diffusion time for $(++)$ respectively $(+z)$ ion interactions and diamagnetic time (Δ being the characteristic radial gradient length scale for the various plasma parameters and the electric potential) and less than 10^{-1} under typical low confinement conditions and therefore taken to be zero in the standard neoclassical theory, with the result

$$\hat{T}^s_{+1} \to \frac{\alpha_I - \alpha^T_{++0}\beta_I}{\alpha^0_V}\quad,\quad \hat{n}^s_{+1} \to \frac{\alpha_V\beta_I - \alpha_I\beta_V}{\alpha^0_V\beta_{IV}}\quad,\quad \hat{T}^c_{+1},\ \hat{n}^c_{+1} \to 0$$

in which case only vertical asymmetries appear. The results of the revised theory of ref.[1] are recovered by passing to the limit $Z_0 \to 0$, $Z_{eff0} \to 1$, $D^*_{+z0} \to \infty$

$$\hat{T}^s_{+1} \to \frac{\alpha_I\alpha^0_V}{\Big(\frac{\alpha_{II}}{2} + \alpha_{III}\Big)^2 + (\alpha^0_V)^2}\quad,\quad \hat{T}^c_{+1} \to \frac{-\,\alpha_I\Big(\frac{\alpha_{II}}{2} + \alpha_{III}\Big)}{\Big(\frac{\alpha_{II}}{2} + \alpha_{III}\Big)^2 + (\alpha^0_V)^2}\quad,\quad \hat{n}^{s,c}_{+1} = -\,\frac{\hat{T}^{s,c}_{+1}}{2} = \hat{\Phi}^{s,c}_1$$

3. The magnetic surface averaged radial particle and heat fluxes

Once the poloidal variations of the plasma parameters are known, we may calculate the neoclassical part of the magnetic surface averaged particle and heat fluxes. In second order drift approximation we have:

$$< \Gamma_{+r} > = -\ < z\Gamma_{zr} > \simeq -\,\frac{p_{+0}}{m_+\Omega_{+0}R_0}\Big[\frac{Z_{eff0}\hat{T}^s_{+1} + (1 + Z_{eff0})\hat{n}^s_{+1}}{z+1} + \frac{R_0}{2r}\,(\hat{n}^c_{+1}\hat{\Phi}^s_1 - \hat{n}^s_{+1}\hat{\Phi}^c_1)\Big]$$

$$< h_{+r} > \simeq -\,\frac{5}{2}\,\frac{p^2_{+0}}{n_{+0}m_+\Omega_{+0}R_0}\Big[\hat{T}^s_{+1} + \frac{R_0}{2r}\,(\hat{n}^c_{+1}\hat{T}^s_{+1} - \hat{n}^s_{+1}\hat{T}^c_{+1})\Big]$$

The formulae have been checked in the limit of the standard nc theory and Grad's 13-moment approximation and exactly agree with those given in ref.[4]. In the above approximation the particle fluxes are automatically ambipolar, although in the revised theory they depend on the radial electric field via the poloidal variation of the plasma parameters. The subneoclassical nature of the radial transport coefficients can be demonstrated most easily for the magnetic surface averaged radial heat flux in a pure plasma [5], where by adding classical and neoclassical contributions

$$< h_{+r} > = -\frac{Q}{S}\left(1 + \frac{8q^2/5}{1+Q^2/S^2}\right)\frac{125}{8n_{+0}r}\left(\frac{\Theta p_{+0}}{m_+\Omega_{+0}}\right)^2 \frac{\partial kT_{+0}}{Q\partial r}$$

using $\delta_0(0) = 4/5$ and the identities $S \equiv 2\alpha_V^0$ and $Q \equiv \alpha_{II} + 2\alpha_{III}$. The above formula exhibits the nonlinear dependence of the ion heat flux in a pure plasma on the dimensionless radial gradient length $S/Q = O[(\Delta/r)\Theta^2\Omega_{+0}\tau_{++0}]$. Note that the radial gradient length scale drops out in the expression $\partial kT_{+0}/(Q\partial r)$.

4. The ambipolarity constraint

Combining classical and neoclassical parts of $< \Gamma_{\alpha r} >$, a genuine ambipolarity constraint $\sum_\alpha e_\alpha < \Gamma_{\alpha r} > = 0$ for the calculation of the electric field appears containing contributions from gyroviscosity (the contributions from elastic collisions vanish identically), inertia and momentum sources by inelastic collisions. Neglecting the latter and omitting the negligibly small electron contribution, we obtain in the present case the following approximate form

$$\sum_{\alpha=+,z}\frac{1}{\Theta B_0\Omega_{\alpha 0}R_0}\left[\frac{\partial}{\partial r}\left(p^s_{\alpha 1}U_{\|0} + e_\alpha n_{\alpha 0}\Phi^s_1\frac{u_{\alpha\perp 0}}{\Theta} + 2p_{\alpha 0}u^{*s}_{\alpha\|1} + \frac{4}{5}h^{*s}_{\alpha\|1}\right) +\right.$$

$$+ e_\alpha U_{\|0}\Theta B_0\left(n_{\alpha 0}u^{*s}_{\alpha\|1} + \frac{1}{2}n^s_{\alpha 1}U_{\|0}\right) + \frac{\partial U_{\|0}}{\partial r}\left(p^s_{\alpha 1} + e_\alpha n_{\alpha 0}\Phi^s_1\right) -$$

$$\left. - \frac{R_0}{2r}e_\alpha U_{\|0}\frac{\partial}{\partial r}\left(n^c_{\alpha 1}\Phi^s_1 - n^s_{\alpha 1}\Phi^c_1\right) + \frac{R_0}{2r}\frac{\partial}{\partial r}\left[\frac{e_\alpha}{\Theta B_0}\frac{\partial\Phi_0}{\partial r}\left(n^c_{\alpha 1}\Phi^s_1 - n^s_{\alpha 1}\Phi^c_1\right)\right]\right] = 0$$

where the contributions from gyroviscosity and inertia have partially compensated and the influence of the heat flux gradients comes about through the term $\sim \partial h^{*s}_{\alpha\|1}/\partial r$. For a pure plasma [1] the last three terms in the ambipolarity constraint vanish. We note that the ratio between second and first term is of order $\Theta\Omega_{\alpha 0}\Delta U_{\|0}/v^2_{T\alpha} \lesssim 1$ for subsonic flows. In combination with the B-weighted parallel momentum equation, which additionally contains the effect of the collisional part of the pressure tensor, and the solution for the poloidal variation of the plasma parameters in terms of their radial gradients we get a system of two coupled nonlinear differential equations in Φ_0 and $U_{\|0}$. This is in contrast to the standard nc theory , where only the dissipative part of the pressure tensor is considered, which leads to algebraic relations between poloidal ion rotation velocity and radial ion temperature gradient (in a simple plasma [6]) as well as radial main and impurity ion pressure gradients (for an additive impurity [7]).

References

[1] A.Rogister, Phys. Plasmas 1(3), 619 (1994); 16th Fusion Energy Conf., Montreal 1996

[2] A.B.Mikhailovskii, V.S.Tsypin, Pl.Phys. 13, 785 (1971); Sov.Phys.JETP 56(1), 75 (1982)

[3,4] H.A.Claaßen, H.Gerhauser et al., KFA-Rep.Jül-2423 (Jan.1991) and Jül-3287 (Sept.1996)

[5] A.Rogister, 24th EPS Conf. on CFPP, Berchtesgaden 1997, see also this conference

[6] R.D.Hazeltine, Physics of Fluids 17(5), 961 (1974)

[7] Y.B.Kim, P.H.Diamond, R.J.Groebner, Physics of Fluids B3(8), 2050 (1991)

Nonlinear Plateau Regime Dynamics of the Poloidal Rotation in Tokamaks

U. Daybelge, C. Yarım and M. Anguelova
Istanbul Technical University, Fac. of Aerospace Sciences
80626 Maslak/Istanbul , Turkey

Abstract. This paper presents a nonlinear evolution equation for the radial electric field in the tokamak plateau regime. It is shown that the solution has bifurcative character, which can decay or increase with time, depending on the initial values and the plasma gradients without any anomalous effects are involved. Substituting in the solutions plasma profiles measured just before and after the L-H Mode transitions, likely scenarios for Mode switch is studied.

I. Introduction

Nearly all models of transport suppression mechanisms utilize the effect of radial electric field shear to reduce the radial transport of particles and energy. In magnetically confined plasmas, radial electric field, E_r is determined by the flux surface averaged ambipolarity condition $\langle j_r \rangle = 0$, where j_r is determined by the perpendicular (to the magnetic field $\vec{B}$) component of the force balance relation within this surface. Starting from the flux-surface-averaged parallel component of the ion momentum equation, Hirshman [1,2] found an evolutionary equation that governs the relaxation of the poloidal flow: $U_p(\psi) = \vec{v} \cdot \vec{B}_p / B_p^2$, i.e.,

$$\rho_i (1+2q^2)\langle B_p^2 \rangle \frac{\partial}{\partial t} U_p(\psi) \approx -\langle \vec{B} \cdot \nabla \cdot \vec{\pi}_i \rangle \qquad (1)$$

The r.h.s. is the surface averaged parallel viscous stress, which damps out the poloidal flow when the driving force has been switched off. The damping term requires the calculation of the gyro averaged ion distrubution function. For the plateau regime a more general evolutionary equation was derived by Rozhansky and Tendler [3] and they discussed the possibility of an increasing poloidal rotation, i.e., "rotational runaway", in neoclassical theory, due both to the nonlinear inertia and the nonlinear viscosity.

II. Outline of The Theory

Novakovskii et al [4] have recently derived a new inertia enhancement, i.e., $1 + q^2 \hat{\nu}^{-1/3} O(1)$ from the time dependent viscosity in the plateau regime and calculated a new relaxation rate as $\nu_{th}/(qR)\,\hat{\nu}^{1/3} O(1)$, where $\hat{\nu} = r\nu_{ii}/(v_{th}\Theta)$ is the plateau collisionality parameter, i.e., $\varepsilon^{3/2} < \hat{\nu} < 1$ and $\Theta = \varepsilon/q = B_p/B_T$. In the following, we shall follow their formalism to derive a nonlinear evolution equation for the radial electric field and the poloidal rotation. We consider an axisymmetric tokamak and consider the drift kinetic equation

$$\frac{\partial f}{\partial t} + \vec{v} \cdot \nabla f + \frac{dv_{\parallel}}{dt} \frac{\partial f}{\partial v_{\parallel}} + \frac{d(v_{\perp}^2/2)}{dt} \frac{\partial f}{\partial (v_{\perp}^2/2)} = C(f) \qquad (2)$$

where $\vec{v} = v_{\parallel}\vec{b} + \vec{v}_E + \vec{v}_D$, with $\vec{v}_E = c\vec{E} \times \vec{B}/B^2$, $\vec{b} = \vec{B}/B$ and

$$\vec{v}_D = \frac{v_{||}^2 + v_\perp^2/2}{\omega_B}\vec{b}\times\nabla \ln B - \frac{1}{\omega_B}\frac{\partial \vec{v}_E}{\partial t}\times\vec{b}, \quad \text{where} \quad \omega_B = eB/mc.$$

Further, $dv_{||}/dt = (-v_\perp^2\cdot\vec{b} + v_{||}\vec{v}_E)\cdot\nabla \ln B$, and $d(v_\perp^2/2)/dt = (v_\perp^2/2)(\vec{v}_E + v_{||}\vec{b})\cdot\nabla \ln B$.

Expanding Eq.(2) in ε, to the lowest orders we find $(\Theta v_{||} + v_E)\partial f_0/r\partial\theta = C(f_0)$. Its solution is a displaced Maxwellian by a small toroidal velocity $U_0(r,t) << \Theta v_{th}$, namely,

$f_0 = n(m/2\pi T)^{3/2}\exp[-(\vec{v} - \vec{U}_0)^2] \approx (1 - mv_{||}U_0/T)f_M$, where $f_M = n(m/2\pi T)^{3/2}\exp[-m(v_\perp^2 + v_{||}^2)]$. In order to find an equation to $O(\varepsilon^2)$, we substitute in (8),

$f = f_0 + \varepsilon(1 - mv_{||}U_0/T)\cos\theta\, f_M + \tilde{f}$. Thus, we obtain

$$\frac{\partial \tilde{f}}{\partial t} + (v_E + v_{||}\Theta)\frac{\partial \tilde{f}}{r\partial\vartheta} = C(\tilde{f}) + \frac{\sin\vartheta}{R}\frac{m(v_{||}^2 + v_\perp^2)}{T}Wf_M \qquad (3)$$

where the ordering $\rho_i/(\Theta L) << 1$ is valid (ρ_i is ion Larmor radius and L is the scale of macroscopic gradients) and

$$W = v_E + V_n + \Theta U_0 + [m(v_{||}^2 + v_\perp^2)/(2T) - 3/2]V_T \qquad (4)$$

with gradients $V_n = cT/(eB)d\ln n/dr$, $V_T = cT/(eB)d\ln T/dr$. The collision operator in the plateau regime is approximated as $C(\tilde{f}) = -\nu_{eff}\tilde{f}$, where $\nu_{eff} = (v_{th}/v_{||})^2\nu_{ii}$. The electric field is assumed to vary slowly, so that $\nu_{eff} \approx v_{th}/(qR)$. The time ordering allows to expand the distribution function as $f \sim f_0 + f_1 + f_2 + \ldots$, and we use Fourier expansion of f_i: $f_i = \sum_\sigma f_{i\sigma}\exp(i\sigma\theta)$, $i = 1, 2, 3, \ldots$; $\sigma = \pm 1$. Thus, from (3) we obtain,

$$f_{i\sigma} = -\frac{\varepsilon\zeta W f_M/2}{v_{||}\Theta + v_E - i\sigma r\nu_{eff}} \qquad \text{where} \quad \zeta = m(v_{||}^2 + v_\perp^2/2)/T \qquad (5)$$

The next equation to be solved is

$$v_{||}\Theta\frac{\partial f_2}{r\partial\theta} + \nu_{eff}f_2 = -\frac{\partial f_1}{\partial t} \qquad (6)$$

Its solution is found as

$$f_{2\sigma} = -i\frac{\varepsilon\sigma r\zeta f_M/2}{(v_{||}\Theta + v_E - i\sigma r\nu_{eff})^2}\left[1 - \frac{W}{v_{||}\Theta + v_E - i\sigma r\nu_{eff}}\right]\frac{\partial v_E}{\partial t} \qquad (7)$$

Using the ordering $v_E << v_{th}\Theta$, we find

$$f_2 = \frac{\varepsilon r\zeta\sin\theta\, f_M x^4}{\Theta^2 v_{th}^2(x^6 + \hat{\nu}^2)^2}\left[\frac{(x^{12} - \hat{\nu}^4) - (W/\Theta v_{th})x^8\left[x + v_E/(\Theta v_{th})\right](x^6 - 3\hat{\nu}^2)}{(x^6 + \hat{\nu}^2)}\right]\frac{\partial v_E}{\partial t} \qquad (8)$$

where $x = v_{||}/v_{th}$ and $\hat{\nu} = r\nu_{ii}/(\Theta v_{th})$. Here, $\hat{\nu}$ can be called the plateau collisionality parameter and is related to the standard neoclassical collisionality parameter ν_{ii} as $\hat{\nu} = \varepsilon^{3/2}\nu_{ii}$. In calculating (8) we have left out the terms proportional to $\cos\theta$, as these are not relevant for the calculations below. f_2 as given in Eq. (8), has a part proportional to W, which is the source of a nonlinear evolution of the radial electric field or the poloidal rotation. Considering $\hat{\nu} << 1$, we can write $\xi = (v_{||}/v_{th})\hat{\nu}^{-1/3}$ and $z = v_\perp/v_{th}$, and find $f_M = (2\pi)^{-3/2}v_{th}^{-3}\exp[-(\xi^2\hat{\nu}^{2/3} + z^2/2)]$ and $f_1 = -\pi q\zeta W f_M\delta(v_{||})\sin\theta$. The average radial fluxes are given by $\langle nV_r\rangle = (2\pi)^{-1}\int_0^{2\pi} h\, v_r\, f\, d^3v\, d\theta$, where

$$v_r = -\frac{v_{\|}^2 + v_{\perp}^2/2}{\omega_B R}\sin\theta + \frac{1}{\omega_B}\frac{\partial v_E}{\partial t} \tag{9}$$

As the radial fluxes are proportional to mass, the condition $\langle j_r \rangle = 0$, can be utilized as a condition on the ion radial flux, i.e., $\langle nV_r \rangle = 0$. Hence,

$$\int\left[f_0\frac{\partial v_E}{\partial t} - f_2\frac{v_{\|}^2 + v_{\perp}^2/2}{R}\sin\theta\right]d^3v\,d\theta = \int f_1\frac{v_{\|}^2 + v_{\perp}^2/2}{R}\sin\theta d^3v\,d\theta \tag{10}$$

With $d^3v = 2\pi\, v_{th}^3\, \hat{\nu}^{1/3} d\xi\, d(z^2/2)$, substitution of f_0, f_1 and f_2 from above yields,

$$\left[1 + q^2\left(\frac{3}{2} + \hat{\nu}^{-1/3} I - Z\right)\right]\frac{\partial v_E}{\partial t} = -\sqrt{\frac{\pi}{2}}\frac{qv_{th}}{R}\left[v_E + V_n + \Theta U_0 + \frac{3}{2}V_T\right] \tag{11}$$

The integral I in the coefficient of the time derivative of v_E was already defined in [4] as

$$I = (2\pi)^{-1/2}\int_{-\infty}^{\infty} d\xi \exp(-\hat{\nu}^{2/3}\xi^2/2)\xi^4(\xi^6 - 1)/(\xi^6 + 1)^2 .$$

It is of zeroth order in $\hat{\nu}$. The new term Z, in (11) is due to the part of f_2, which is proportional to W, as seen in (8).

$$Z \equiv (v_E/(\Theta v_{th}))\left\{\frac{1}{2}(v_E + V_n + \Theta U_0 + V_T)/(\Theta v_{th}) + \right.$$

$$\left. + \left[(v_E + V_n + \Theta U_0 + V_T)/(\Theta v_{th}\hat{\nu}^{1/3})\right]I_1 + \left[(v_E + V_n + \Theta U_0 + \frac{3}{2}V_T)/(\Theta v_{th}\hat{\nu})\right]I_2\right\} \tag{12}$$

Here, we have additional integrals

$$I_1 = (2\pi)^{-1/2}\int_{-\infty}^{\infty} d\xi\, \exp(-\hat{\nu}^{2/3}\xi^2/2)\xi^{10}(\xi^6 - 3)/(\xi^6 + 1)^3, \tag{13}$$

$$I_2 = (2\pi)^{-1/2}\int_{-\infty}^{\infty} d\xi\, \exp(-\hat{\nu}^{2/3}\xi^2/2)\xi^8(\xi^6 - 3)/(\xi^6 + 1)^3 \tag{14}$$

which are also zeroth order in $\hat{\nu}$. From (11) and (12) we note that, when v_E, $(v_E V_n)^{1/2}$, or $(v_E V_T)^{1/2}$ is comparable to or larger than $\hat{\nu}^{1/2}\Theta v_{th}$, then Z is not negligible and is responsible for the nonlinear evolution of v_E. In the plateau regime, this corresponds to v_E, $(v_E V_n)^{1/2}$, or $(v_E V_T)^{1/2}$ being larger than $\varepsilon^{3/4}\Theta v_{th}$. The magnetic pumping frequency, $(\pi/2)^{1/2}(qv_{th}/R)$, i.e., the coefficient of the r.h.s., of the linear equation [4], is now also a nonlinear one. General solution of Eq.(11) has the form

$$C_0 e^t = (v_E + c_1)^{c_2}\exp(c_3 v_E^2 + c_4 v_E) \tag{15}$$

This result, found by neoclassical analysis only, is capable of producing both decaying or increasing radial electrical fields, depending on the initial electric field and the driving temperature or density gradients.

III. Numerical Results

Eq.(11) was treated numerically with gradients substituted from known profiles measured before and after the L-H mode switch in several tokamak experiments, such as JT-60U and DIII-D [5]. Fig.1. shows the radial and temporal variations of $v_E(r,t)$. It indicates that the radial electric field may saturate, decay or runaway. On Fig.2. we note that an increasing L-

Mode branch intercepts an increasing H-Mode branch just before they both saturate at close values. The common saturation level is presumably sufficient to suppress the turbulent plasma transport.

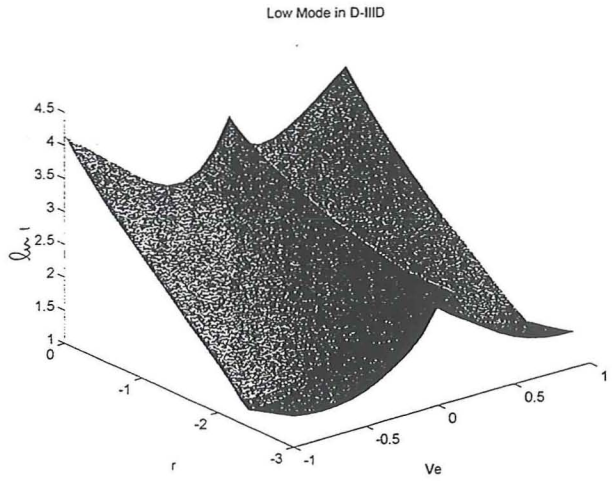

Fig.1. Variation of the radial electric field over time and radius.

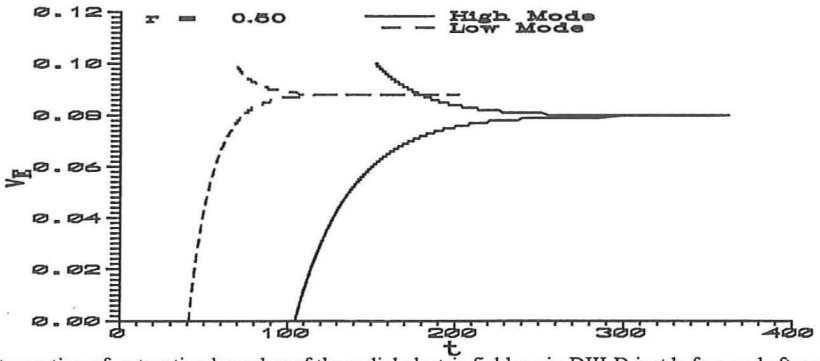

Fig.2. Interception of saturating branches of the radial electric field v_E in DIII-D just before and after mode transition. Radial position is denoted by $r = R_{sep}-R$ (cm). v_E and t are normalized by v_{th} and R/v_{th}, respectively.

References

[1] Hirshmann, S.P., Nucl. Fusion 18 (1978) 917

[2] Lebedev, V.B., Yushmanov, P.N., Diamond, P.H., Novakovskii, S.V., Smolyakov, A.I., Phys. Plasmas 3 (1996) 3023

[3] Rozhanskii, V., Tendler, M., Phys. Fluids B 4 (1992) 1877

[4] Novakovskii, S.V., Galeev, A.A. , Liu, C.S., Sagdeev, R.Z., Hassam, A.B., Phys. Plasmas 2 (1995) 3566

[5] Carlstrom, T.N., Groebner, R.J., Phys. Plasmas 3 (1996) 1867

Fluctuation-Induced Transport and Potential Formation across a Magnetic Field

R. Sugaya

Department of Physics, Faculty of Science
Ehime University, Matsuyama 790, Japan

Abstract. It has been proved theoretically that particle transport along and across a magnetic field and an electric field across a magnetic field can be induced by almost perpendicularly propagating electrostatic waves in a magnetized plasma.

I. INTRODUCTION

Particle transport along and across a magnetic field and an electric field across a magnetic field which are induced by almost perpendicularly propagating electrostatic waves in a magnetized plasma have been investigated theoretically based on quasilinear transport equations derived from Vlasov-Maxwell equations[1-3]. The electrostatic waves accelerate particles and the ratio of parallel and perpendicular drift velocities $v_{s\parallel}/v_d$ can be proved to be proportional to $k_\parallel/k_\perp$. As a result, the strong plasma transport across a magnetic field appears. Simultaneously the intense perpendicular electric field $\mathbb{E}_0=\mathbb{B}_0\times v_d/c$ is generated via the dynamo effect of perpendicular particle drift to satisfy the generalized Ohm's law, that is, the electrostatic waves can produce the perpendicular drift that is identical to $E\times B$ drift. This cross-field transport is able to explain the fluctuation-induced anomalous transport occuring in sawtooth crash[4] or edge plasmas in tokamaks and the perpendicular ion acceleration in tokamaks and space plasmas.

II. TRANSPORT EQUATIONS

We consider the particle transport which arises from quasilinear velocity space diffusion due to electrostatic waves propagating almost perpendicularly to the uniform magnetic field $\mathbb{B}_0=(0,\ 0,\ B_0)$. The transport equations indicating the temporal evolution of energy and momentum densities of magnetized particles of s-species are derived from Vlasov-Maxwell equations by the same manner as described in Refs. 1-3 and are given by

$$\frac{\partial U_s}{\partial t} = -\,2\gamma_k^{(s)} U_k \quad , \tag{1}$$

$$\frac{\partial \mathbb{P}_s}{\partial t} = -\frac{2\gamma_{\mathbb{k}}^{(s)} \mathbb{k}}{\omega_{\mathbb{k}}} U_{\mathbb{k}} \quad , \tag{2}$$

where $U_{\mathbb{k}} = (1/8\pi)\,[\partial(\varepsilon'_{\mathbb{k}}\omega_{\mathbb{k}})/\partial\omega_{\mathbb{k}}]\,|E_{\mathbb{k}}|^2$ is the wave energy density, $\mathbb{k}U_{\mathbb{k}}/\omega_{\mathbb{k}}$ the wave momentum density, $U_s = \int d\boldsymbol{v}\, \frac{1}{2} n_s m_s v^2 g_s$ and $\mathbb{P}_s = \int d\boldsymbol{v} n_s m_s \boldsymbol{v} g_s$ are the energy and momentum densities of particles of s-species, $\gamma_{\mathbb{k}}^{(s)} = -\varepsilon''^{(s)}_{\mathbb{k}}/(\partial\varepsilon'_{\mathbb{k}}/\partial\omega_{\mathbb{k}})$ $(\gamma_{\mathbb{k}} = \Sigma_s \gamma_{\mathbb{k}}^{(s)})$ is the linear damping rate ascribed to particles of s-species, and $\mathbb{P}_s = (P_{\perp s}, 0, P_{\parallel s})$, $\mathbb{k} = (k_\perp, 0, k_\parallel)$, $P_{\perp s} = m_s n_s v_d$, $P_{\parallel s} = m_s n_s v_{\parallel s}$. The dielectric constant $\varepsilon_{\mathbb{k}} = 1 + \Sigma_s \varepsilon_{\mathbb{k}}^{(s)} = \varepsilon'_{\mathbb{k}} + i\varepsilon''_{\mathbb{k}}$ $(\varepsilon_{\mathbb{k}}^{(s)} = \varepsilon'^{(s)}_{\mathbb{k}} + i\varepsilon''^{(s)}_{\mathbb{k}})$ is expressed by

$$\varepsilon_{\mathbb{k}}^{(s)} = -\frac{\omega_{ps}^2}{k^2} \sum_{r=-\infty}^{\infty} \int d\boldsymbol{v} \frac{J_r^2(\mu_{\mathbb{k}}) U_r(\mathbb{k})\, g_{s0}}{k_\parallel v_\parallel + k_\perp v_d - \omega_{\mathbb{k}} + r\omega_{cs}} \quad , \tag{3}$$

$$\begin{aligned} g_s &= \sum_{m=0}^{\infty} \frac{1}{m!} v_x^m \left(-\frac{v_d}{v_\perp}\frac{\partial}{\partial v_\perp}\right)^m g_{s0}(v_\perp, v_\parallel, t) \\ &= g_{s0}((v_\perp^2 - 2v_x v_d)^{1/2}, v_\parallel, t) \quad , \end{aligned} \tag{4}$$

where

$$U_r(\mathbb{k}) = k_\parallel \frac{\partial}{\partial v_\parallel} + \frac{r\omega_{cs}}{v_\perp}\frac{\partial}{\partial v_\perp} \quad , \tag{5}$$

J_r is the Bessel function of rth order, $\mu_{\mathbb{k}} = k_\perp v_\perp/\omega_{cs}$, $\omega_{ps}^2 = 4\pi n_s e_s^2/m_s$, $\omega_{cs} = |e_s|B_0/m_s c$, $v_x = v_\perp \cos\theta$, $\boldsymbol{v} = (v_\perp, \theta, v_\parallel)$ is given by the cylindrical coordinate in velocity space, $v_d = (v_d, 0, 0) = cE_0 \times B_0/B_0^2$ equals $E \times B$ drift velocity, and g_s is the background velocity distribution function containing the fluctuation-induced cross-field drift $v_d = \int d\boldsymbol{v} v_x g_s$. The other notations have the standard meaning. Equation (4) satisfies the unperturbed Vlasov equation

$$(\mathbb{E}_0 + (\boldsymbol{v}/c) \times \mathbb{B}_0) \cdot (\partial g_s/\partial \boldsymbol{v}) = 0 \quad , \tag{6}$$

which leads to the generalized Ohm's law for a collisionless plasma

$$\mathbb{E}_0 + \frac{1}{c} v_d \times \mathbb{B}_0 = 0 \quad , \tag{7}$$

by integration of Eq. (6) multiplied by v in velocity space. This means that $\mathbb{E}_0 = (0, E_0, 0)$ is produced by the dynamo effect of perpendicular particle drift arising from the acceleration due to electrostatic waves. When $v_d = 0$, g_s is reduced to g_{s0} being symmetric with respect to the magnetic field. Transport equations (1) and (2) predict clearly that the electrostatic waves generate anomalous transport or strong particle acceleration along and across the magnetic field. The relation of $P_{\parallel s}/P_{\perp s} = k_\parallel/k_\perp$ ($\mathbb{P}_s /\!/ \mathbb{k}$) found from Eq. (2) with $\mathbb{P}_s(0)=0$ shows that the small parallel and large perpendicular particle transports appear simultaneously. Consequently, it is verified that there exists the strong coupling between the transport along and across the magnetic field and that the parallel transport also becomes anomalous, as was pointed out by Helander *et al.*[5].

In the absence of nonlinear wave-wave and wave-particle interaction the kinetic wave equation is expressed by

$$\frac{\partial U_{\mathbb{k}}}{\partial t} = 2\gamma_{\mathbb{k}} U_{\mathbb{k}} \quad . \tag{8}$$

This equation and the transport equations (1) and (2) yield the conservation laws for total energy and momentum densities of waves and particles and they are represented as

$$\frac{\partial}{\partial t}\left(\sum_{\mathbb{k}} U_{\mathbb{k}} + \sum_s U_s \right) = 0 \quad , \tag{9}$$

$$\frac{\partial}{\partial t}\left(\sum_{\mathbb{k}} \frac{\mathbb{k}}{\omega_{\mathbb{k}}} U_{\mathbb{k}} + \sum_s \mathbb{P}_s \right) = 0 \quad . \tag{10}$$

It can be also proved by adding the nonlinear terms to Eqs. (2) and (3) that these conservation laws hold in the presence of nonlinear wave-wave and wave-particle interaction. Moreover, Eqs. (1), (2) and (6)-(10) can be applicable to the particle transport in the relativistic magnetized plasma by replacing Eqs. (3)-(5) by the corresponding relativistic expressions[2, 3].

III. DISCUSSION AND CONCLUSION

In the experiment reported by the author *et al.*[6] , the Trivelpiece-Gould mode is driven nonlinearly by nonlinear Landau damping occuring in an electron beam-plasma system. This almost perpendicularly propagating electrostatic wave produces the anomalous electron transport and the strong electric field along and across the magnetic field. The typical plasma parameters of this experiment are T_{e0} =5 eV , B_0 =7X10^{-3} Tesla and a =1.5X10^{-3} m (beam radius), then $\omega_{ce}a/v_{te0} \simeq 2$ is given. We set $v_{e\perp max}/v_{te0} \simeq 2$, then $eE_{0max}a/k_B T_{e0} = (\omega_{ce}a/v_{te0})(v_{e\perp max}/v_{te0}) \simeq 4$ is obtained. Thus, the created electric potential and field are inferred to be $V_0 = E_{0max}a \simeq 20$ volt and $E_{0max} \simeq 1.3X10^4$ volt/m , respectively. This estimated value is very close to the experimentally observed potential of $V_{exp} \simeq 10$ volt . Also, the drift velocities are obtained reasonably to be $v_{e\perp max} \simeq 2v_{te0} \simeq 1.9X10^6$ m/s (10 eV) and $v_{e\parallel max} = (k_\parallel/k_\perp)v_{e\perp max} \simeq 0.38X10^6$ m/s (0.4 eV).

In conclusion, it is verified by means of the quasilinear transport equations that the anomalous particle transport along and across the magnetic field and the electric field across the magnetic field can be generated simultaneously by the almost perpendicularly propagating electrostatic waves. The perpendicular electric field is produced by the dynamo effect of cross-field transport to satisfy the generalized Ohm's law. The fluctuation-induced transport can explain successfully anomalous transport and perpendicular ion acceleration in tokamaks, an electron beam-plasma system as well as space plasmas.

The author wishes to thank Dr. M. Sugawa and T. Maehara for useful discussions. This work was supported partially by a Grant-in-Aid for Scientific Research from the Japanase Ministry of Education, Sports and Culture.

References

[1] R. Sugaya, J. Phys. Soc. Jpn. 60, 518 (1991); 60, 3367 (1991); 63, 1775 (1994).

[2] R. Sugaya, J. Plasma Phys. 56, 193 (1996).

[3] R. Sugaya, Phys. Plasmas 1, 2768 (1994); R. Sugaya *et al.*, Phys. Plasmas 3, 3485 (1996).

[4] J. A. Wesson *et al.*, JET-P(97)20 (1997).

[5] P. Helander *et al.*, Phys. Rev. Lett. 77, 2479 (1996).

[6] R. Sugaya *et al.*, J. Phys. Soc. Jpn. 64, 2018 (1995); T. Maehara *et al.*, in *Proceedings of International Conference on Plasma Physics , Nagoya, Japan 1996,* Vol. 1, p. 426.

Particle transport across a circular shear layer with coherent structures

A.H. Nielsen, J.P. Lynov and J. Juul Rasmussen

Association Euratom - Risø National Laboratory,
Optics and Fluids Dynamics Department, DK-4000 Roskilde, Denmark

I. Introduction

In the study of the dynamics of coherent structures, forced circular shear flows offer many desirable features. The inherent quantisation of circular geometries due to the periodic boundary conditions makes it possible to design experiments in which the spatial and temporal complexity of the coherent structures can be accurately controlled. Experiments on circular shear flows demonstrating the formation of coherent structures have been performed in different physical systems, including quasi-neutral plasmas [1], non-neutral plasmas [2] and rotating fluids [3, 4]. In this paper we investigate the evolution of such coherent structures by solving the forced incompressible Navier-Stokes equations numerically using a spectral code. The model is formulated in the context of a rotating fluid but apply equally well to low frequency electrostatic oscillations in a homogeneous magnetized plasma. In order to reveal the Lagrangian properties of the flow and in particular to investigate the transport capacity in the shear layer, passive particles are traced by the velocity field.

II. Model

The physical context for our analysis is the experiments performed with a shallow layer of water in a rotating tank. The shear layer is produced by a secondary rotation of the inner (polar) part, with radius a, of the tank, see [4]. The dynamics is modelled by the forced, two-dimensional, incompressible Navier-Stokes equations

$$\frac{\partial \omega}{\partial t} + (\nabla\psi \times \hat{z}) \cdot \nabla\omega = \nu\nabla^2\omega + \frac{\sqrt{\nu\Omega_0}}{H}(\omega^* - \omega) \quad (1)$$

$$\nabla^2\psi = -\omega, \quad (2)$$

where $\omega = (\nabla \times \vec{v}) \cdot \hat{z}$ is the scalar vorticity, ψ is the stream function, ν is the kinematic viscosity, Ω_o is the background rotation, and H is the depth of the fluid layer. The last term in Eq. (1) is a term forcing the flow to follow the velocity of the tank. The function,

$\omega^* = \nabla \times \vec{v}^*$, is an axisymmetric function which velocity matches the angular velocity of the tank, e.g. Ω_0 in the outer part and Ω_1 in the inner. These two parts are connected by a tanh profile with the width e. We can describe the system by only two parameters; the Reynolds number, $Re = (\Omega_o - \Omega_1)ae/\nu$, and the aspect radius; $\Gamma = a/e$. Equations (1 - 2) also describe low-frequency electrostatic fluctuations generated by a shear flow originating from a radial electric field at the edge of the plasma columns in devices such as the Q-machine, see [1]. In this case the vorticity will corresponds to the charge in Eq. (1 - 2) and the stream function will corresponds to the potential.

Equations (1) and (2) are solved numerically in an annular geometry with inner radius r^- and outer radius r^+, by means of a fully dealiased spectral code using N Fourier modes in the azimuthal direction and M Chebyshev polynomials in the radial direction. Boundary conditions are chosen to be free-slip (stress-free). As initial condition we slightly perturbed the basic flow. Further information of the computer scheme can be found in [5]. Passive particles are convected by evaluating the full spectral expansion of the velocity field.

III. Results

In Fig. 1 we show the saturated vorticity distribution for different values of Re. For Reynolds numbers below a critical number, Re_c, the initial basic flow will be stable, $Re = 24.0$. Above Re_c the basic flow becomes unstable and the most linear unstable modes will grow. When their amplitudes reach a significant size nonlinear forces will take over and by vortex merging the flow finally saturates in a states with fewer vortex than predicted by a linear stability analysis, see [5]. Examples of such saturate states are shown for five different values of Re in Fig. 1. The different states can generally be divided in two groups. For the medium Reynolds number case we find between $5 - N$ stable vortices, where N is a function of Γ. For the high Reynolds number case $2 - 4$ oscillating vortices are found in the shear zone.

To reveal the transport properties of these kind of shear flows we have traced a large number of passive particles in the flow field. In the medium Reynolds number case there is no time evolution of the vortices and particles placed inside the vortices stay trapped and particles placed outside remain in their respective regions. For the oscillating vortices this is not the case. In Fig. 2 we show the time evolution during one oscillation of a mode 3 for the vorticity distribution, Fig. 2a, and the corresponding particle tracing, Fig. 2b. The particles have been initialized in three groups inside each of the three vortices. The oscillating state is here characterized by a mode one modulation perturbing the individual

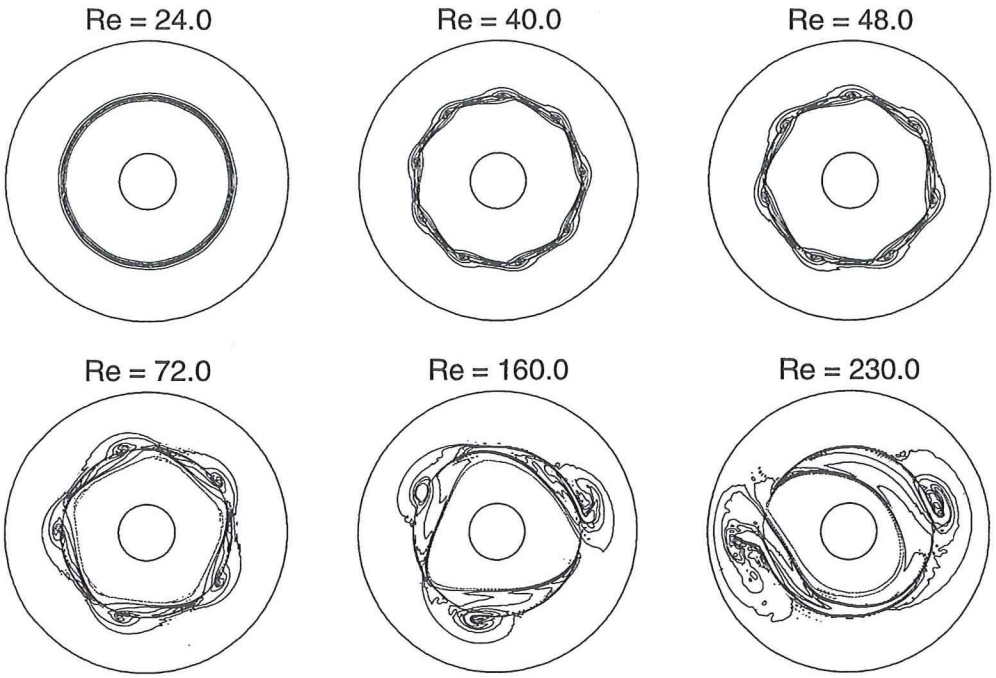

Figure 1: Saturated vorticity distribution for different values of Reynolds number. Parameters: $\Gamma = 50$, $M = N = 256$, $\nu = 0.03535$, $a = 1.5$, $H = 0.15$ and $e = 0.03$.

vortices one by one. We observe that the particles wind up as normally for particles in vortex structures, but when a vortex is perturbed there is a detrapping of particles. Ultimately, particles are mixed in the shear zone, but they do not escape this zone. Thus, the transport across the shear appears to by very weak.

References

[1] Pécseli, H.L. et al, Plasma Phys. Contr. Fusion, **34**, 2065 (1992).

[2] Peurrung, A.J. and Fajans, J., Phus. Fluids, **5**, 493 (1993).

[3] Rabaud, M. and Couder, Y., J. Fluid Mech., **136**, 291 (1983).

[4] Laursen, T.S., Nielsen et al, Experiments in Fluids (1997).

[5] Coutsias, E.A. et al, AIAA **94**, 2407 (1994).

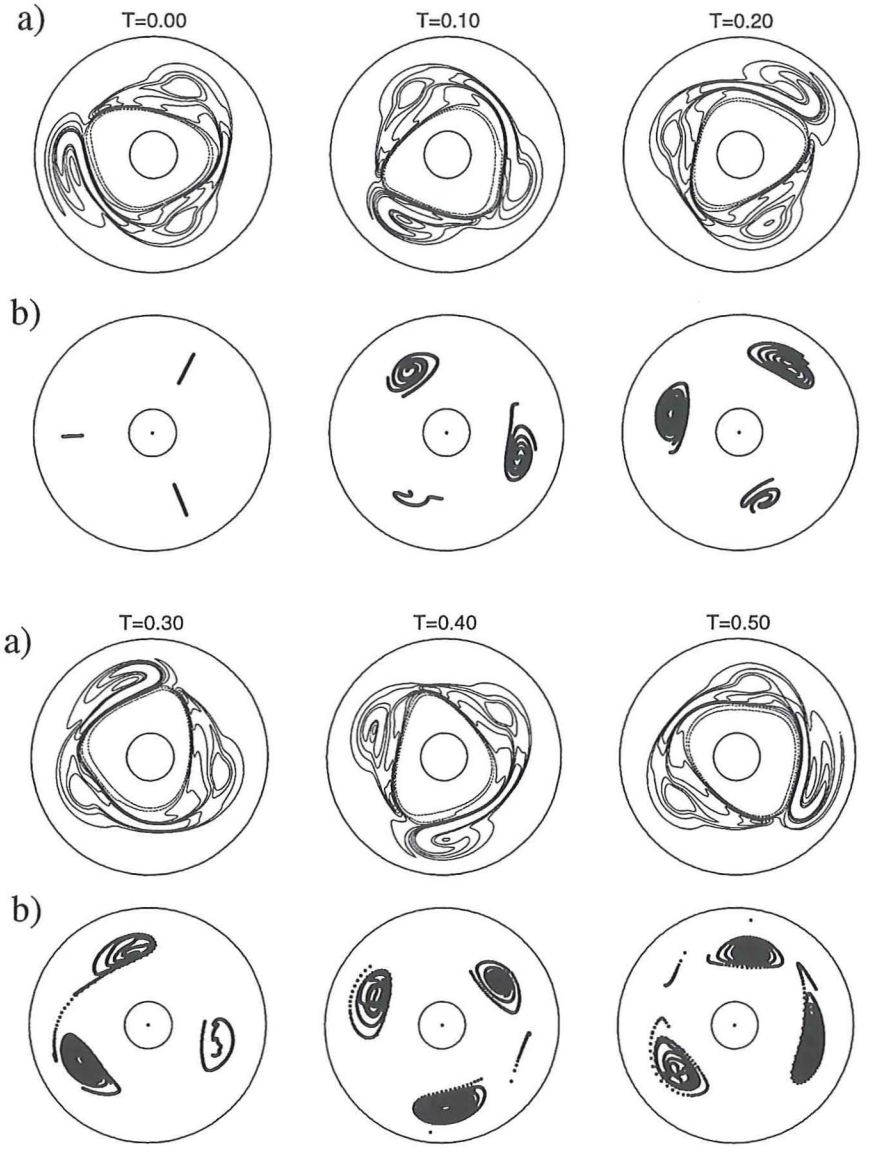

Figure 2: Time evolution of a) the vorticity distribution and b) 6.000 particles divided in three groups and traced in the velocity field from a). Parameters: $Re = 403.3$, $\Gamma = 20$, $M = N = 256$, $\nu = 0.03535$, $a = 1.5$, $H = 0.15$ and $e = 0.075$.

Considerations on the Ignitor performances

G. Cenacchi
ENEA, CRE "E.Clementel", Via Don Fiammelli 2, 40129 Bologna - Italy
and CNR, IFP "P.Caldirola", EURATOM-ENEA-CNR Association

A. Airoldi
CNR, IFP "P.Caldirola", EURATOM-ENEA-CNR Association
Via R.Cozzi 53, 20125 Milano - Italy

Introduction - The Ignitor experiment [1] is designed to explore fusion regimes by exploiting non stationary conditions. The main design parameters are a toroidal field $B_t \leq 13T$, a plasma current $I_p \leq 12MA$ with a high current density, tight aspect ratio and considerable elongation and triangularity (major radius $R_o \cong 1.32m$; minor radii $a \times b \cong 0.47 \times 0.86m^2$, triangularity $\delta \cong 0.4$). The three basic operation scenarios planned in the project have plasma current up to $10,11,12MA$ together with toroidal magnetic field up to $12,13,13T$ and flattop lasting for $6,4,1s$, respectively. The current ramp-up and plasma cross-section expansion in a limiter configuration followed by a condition of constant I_p is here analyzed for the above-mentioned situations.

Simulations

The dynamic nature of the path to ignition requires that simulations based on complex time evolution codes to be used. The updated version [2] of the free-boundary equilibrium-transport code JETTO is here employed. The nominal parameters for the plasma current and the magnetic field are considered in a set of simulations starting at t=0.3 sec, corresponding to $I_p = 1MA$ and $B_t = 7.6T$. Control of plasma current, position and shape is provided by varying the currents in all poloidal field coils. The I_p rise and cross-section expansion are controlled so as to hold $q_\Psi > 3$ and minimum resistive V-s consumption. The avoidance of the disruption boundaries in the (l_i, q_Ψ) diagram is looked for. The chosen (electron/ion) thermal diffusion coefficients are a combination between the Coppi-Mazzucato-Gruber expression and a power depending contribution that accounts for the heating source due to the alpha particles. The working gas is a 50-50 deuterium-tritium mixture. More details about the models are presented in Ref. [2].The line-averaged density, due to the high current density, is always lower than the Greenwald limit, given by:

$$\bar{n}_{Gr} = I_p / (\pi ab) \qquad [10^{20} m^{-3}; MA; m].$$

It results to be $\bar{n}_{Gr} = 9.5; 8.7; 7.9$ respectively for the three scenarios. In all simulations presented here the density profiles are prescribed, with a peaking factor $n(0)/ < n >= 1.8$.
An ignition factor defined by:

$$f_{ign} = \frac{P_\alpha}{P_{th} + P_{rad} + P_{brems} + P_{sync}}$$

marks the achieved goal when it reaches the unity and the Q parameter, expressed as the ratio between the total fusion power produced ($5P_\alpha$) and the ohmic power, is another important indicator of the obtained performances.

Results

a) The most advanced scenario ($12MA - 13T$) is designed to exploit the feature of non-stationary conditions for approaching ignition. The rate of current rise ($3MA/s$) produces a reversed shear region in the plasma centre due to the incomplete current penetration. The off-axis minimum for the safety factor profile is $q_{\min} \approx 0.9$ at the end of simulations. This scenario has been considered and discussed in Ref.[1], where it was found that ohmic ignition could be attained even assuming energy confinement times close to the 'ITER89P' scaling. Fig.1a plots the time evolution of the radial profile of Q along the ramp phase and during the flattop until ignition for a representative case. The results refer to a flattop situation with a volume-averaged density $< n_e >= 5.7 \times 10^{20} m^{-3}$, line-averaged density $\overline{n_e} = 7.1 \times 10^{20} m^{-3}$, $< Z_{eff} >= 1.4$ and ignition attained near the end of flattop.The well known Lawson diagram is shown in Fig.1b together with the values of $n(\rho)\tau_E^*(\rho)$ vs $T_e(\rho)$ at different times (labels 1,2,3,4 refer to t= 4, 4.3, 4.8 and 5s respectively). The local value of the energy confinement time is defined by $\tau_E^* = \Delta W_{tot} / \Delta P_{tot}$, being ΔW_{tot} the total energy content (electrons+ions) in a shell around the flux surface and ΔP_{tot} the power content (alpha+ohmic) in the same region.

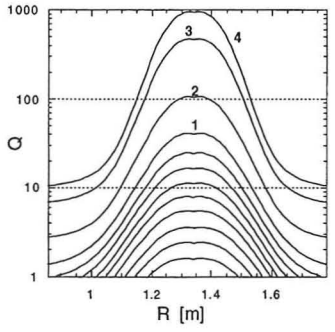

Fig.1a - Evolution of the Q profile

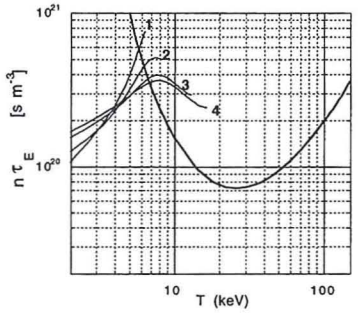

Fig.1b - $n\tau_E^*$ vs. T_e and Lawson plot

The Q evolution shows how the central ignited core diffuses towards the periphery of the plasma column. When ignition is not globally achieved, a central ignited core is anyway present.

b) In the second scenario, where the $11MA$ plasma current is maintained for 4s, the safety factor drops below unity during the flattop, so sawtooth activity cannot be avoided. The model applied here is a Kadomtsev-like reconnection, flattening temperature, density and safety

factor profiles inside the mixing region with preset repetition time ($\Delta t_{rec} = 0.1 \div 0.3s$). The q_{min} value defining the reconnection region spans from 0.8 to unity. The results show that this parameter mainly affects the performance: a large mixing region could prevent the attainment of ignition, so confirming previous analyses [3]. Nevertheless if the involved region does not exceed 25% of the plasma volume, ignition may be attained in transient mode, as shown in Fig.2a. The figure refers to cases with $\Delta t_{rec} = 0.25$ and $q_{min} = 0.8$, but with different final density (see Fig.2b).

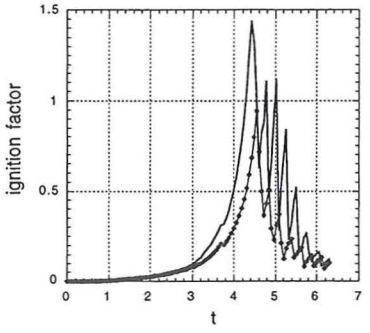

Fig.2a - Ignition factor evolution

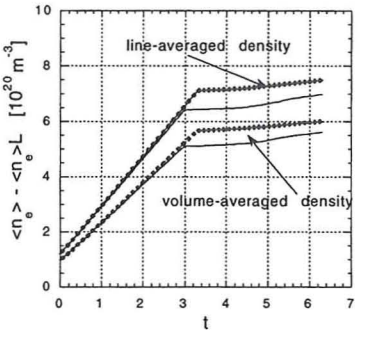

Fig.2b - Density evolution

The transient ignition is also exhibited in the bursts of the alpha power displayed in Fig.3.

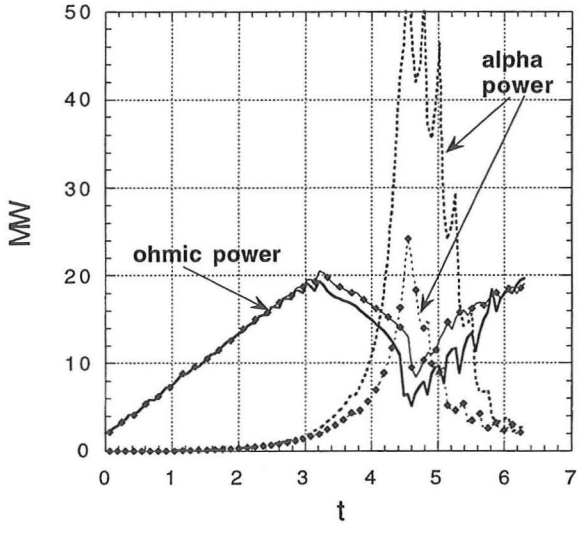

Fig.3 - Time evolution of ohmic and alpha powers relevant to the cases in Figs 2a-2b

The beneficial effects of an appropriate choice of the density, already pointed out in Ref.[2], are stressed also in these simulations.

c)The third scenario is devised to set up the operation of the machine. In principle fusion performance should not be expected. As a matter of fact simulations based on the previous assumptions show modest efficiency in alpha power production. Fig.4 shows the peak electron temperature relevant to cases with $\Delta t_{rec} = 0.25$ and $q_{min} = 0.8 - 0.85$ respectively.

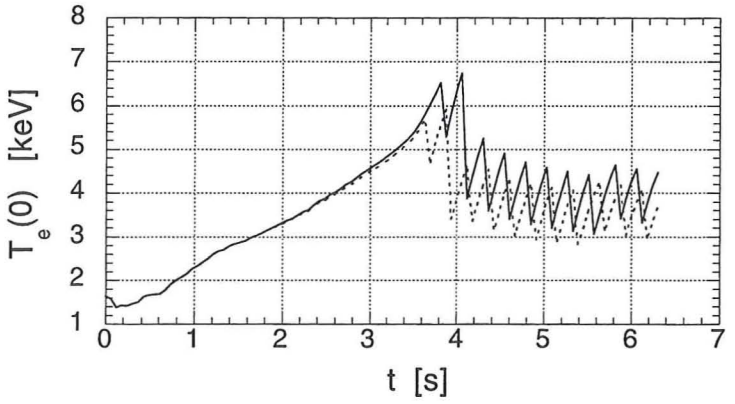

Fig.4 - Peak electron temperature evolution with different mixing regions. Full line marks case with $q_{min} = 0.8$, *dotted line marks case with* $q_{min} = 0.85$

Concluding remarks

The density is the main parameter to control on the path to ignition, but some other items need attention, as plasma shape and dimensions, current density profile and impurity content. When sawtooth oscillations cannot be prevented, the mixing region width is of paramount importance. This analysis points out the specific character of the project: ignition must be reached immediately after the 12 MA current ramp.

References

1 - B. Coppi, A.Airoldi, F. Carpignano, G. Cenacchi, et al., *16th IAEA Fusion Conf*, Montreal, 1996, Paper F1-CN-64/GP-14

2 - A. Airoldi and G. Cenacchi, *Nuclear Fusion* **37**, 1117 (1997)

3 - A. Airoldi and G. Cenacchi, *Plasma Physics and Controlled Fusion* **34**, 1493 (1992)

Numerical Study of the Deformation of the Ion Distribution Function in the Magnetic Presheath

H. Gerhauser, H.A. Claaßen

Institut für Plasmaphysik, Forschungszentrum Jülich GmbH, EURATOM Association, Trilateral Euregio Cluster, D-52425 Jülich, Germany

The deformation of the ion distribution function in the vicinity of a plane completely neutralizing wall intersected by an oblique magnetic field was investigated on the basis of an Eulerian Vlasov code [1]. The present 4D version of this code (with one space- and three velocity coordinates) numerically solves the Vlasov equation consistently with Poisson's equation for a 1D structure of the electric field (perpendicular to the wall) assuming a Boltzmann equilibrium for the electrons and a ($\|\vec{B}$) shifted Maxwellian distribution with a smoothed cut-off for the instreaming ions. The initial profiles are changed during time-relaxation until stationary profiles are obtained. The electric field at the wall is computed selfconsistently by integrating the total electric current to the wall (or the built-up volume space charge in front of the wall) in time. Earlier calculations (by a PIC code [2]) of the electric potential variation across the sheath are nicely reproduced, but with much less numerical noise. The total potential drop is indeed almost independent of the inclination angle α between $\vec{B}$ and the wall, but the part of the potential drop across the magnetic presheath increases with decreasing α.

In agreement with results of analytical studies based on the assumption of a parabolic electric potential variation inside the magnetic presheath region, the numerical results with the selfconsistent electric field show a shift of the ion distribution function in the $\vec{E} \times \vec{B}$ direction exhibiting an asymmetric shape with a maximum near the sound velocity just in front of the wall. Simultaneously the width of the ion distribution function shrinks in the plane perpendicular to $\vec{B}$ on approaching the wall. The latter effect is attributed to the gyro-cooling effect [3] due to the electromagnetic forces in the magnetic presheath, where the thermal energy of the gyro-motion is gradually converted into kinetic energy of the wall-tangential electric drift motion. Since the wall is assumed to be completely neutralizing, the ion distribution function becomes one-sided at the wall surface. A characteristic feature of the sheath is the loss of the drift approximation when approaching the wall: first for the ions inside the magnetic presheath, then for the electrons inside the Debye sheath. As a consequence, the surface-parallel electric current forms a double skin layer with a diamagnetic drift skin related to the ion pressure in the magnetic presheath and an electric drift skin related to the electron pressure near the entrance of the Debye sheath as already depicted in ref.[4].

Since the quantitative results depend on the assumed ion distribution function at the plasma facing boundary of the magnetic presheath, a parametric study of the influence of the velocity shift along the magnetic field and the temperature ratio between electrons and ions was performed. In this context also the question of the formation of a double-humped structure of the ion distribution function inside the magnetic presheath is addressed with respect to the possible triggering of two-stream instabilities, when adding to the thermal ion distribution a small cold ion contribution [5].

[1] G. Manfredi et al., J. Comput. Phys. 121, 298 (1995)
[2] R. Chodura, Phys. Fluids 25(9), 1628 (1982)
[3] H. Gerhauser, H.A. Claaßen, Contrib. Plasma Phys. 36, 381 (1996)
[4] U. Daybelge, B. Bein, Phys. Fluids 24(6), 1190 (1981)
[5] R.H. Cohen, D.D. Ryutov, Rep. UCRL-JC-125077 (1996)

Canonical and magnetic coordinates applied to relativistic guiding centre drifts

W. A. Cooper

Centre de Recherches en Physique des Plasmas, Association Euratom-Confédération Suisse, Ecole Polytechnique Fédérale de Lausanne, CRPP-PPB, CH-1015 Lausanne, Switzerland

Abstract. The formulation of the guiding centre drift orbits is extended to relativistic particles in canonical coordinates with arbitrary time dependent electric and magnetic fields. The transformation to these coordinates from general flux coordinates is cumbersome for practical applications. This transformation is straightforward for Boozer magnetic coordinates which are canonical if the perturbed magnetic field is constrained to the form $\delta \boldsymbol{B} = \nabla \times (\Upsilon \boldsymbol{B})$.

A Hamiltonian formalism in canonical coordinates constitutes the most transparent and compact approach to treat the guiding centre drift orbit problem. In this paper, we extend to relativistic particles the formulation in a canonical coordinate system that is valid for arbitrary three dimensional (3D) time dependent electric and magnetic fields [1,2]. For a 3D equilibrium calculated in a different coordinate system, we demonstrate that the transformation to the canonical coordinates is too complicated for useful applications. For Boozer magnetic coordinates [3], the transformation is simple. However, the perturbed magnetic field structure cannot be arbitrary for this system to retain canonical properties.

To define canonical coordinates in a torus with arbitrary time dependent electric and magnetic fields requires that these coordinates (r, θ, ζ) satisfy the property that the vector potential and the magnetic field be expressed as [1]

$$\boldsymbol{A} = \Phi(r, \theta, \zeta, t) \nabla \theta - \psi(r, \theta, \zeta, t) \nabla \zeta \, , \tag{1}$$

$$\boldsymbol{B} = B_\theta(r, \theta, \zeta, t) \nabla \theta + B_\zeta(r, \theta, \zeta, t) \nabla \zeta \, . \tag{2}$$

where r is the radial variable θ is the poloidal angle and ζ is the toroidal angle. In other words, the coordinates are canonical when the radial components of $\boldsymbol{A}$ and $\boldsymbol{B}$ in the covariant representation vanish. As $\boldsymbol{B} = \nabla \times \boldsymbol{A}$, the magnetic field in the contravariant representation is $\boldsymbol{B} = \nabla\zeta \times \nabla\psi + \nabla\Phi \times \nabla\theta$. The canonical momenta in the drift ap-

proximation are given by $\boldsymbol{P} = p_{\|}\boldsymbol{B}/B + e\boldsymbol{A}$. The corresponding relativistic Hamiltonian is

$$H = H(\boldsymbol{p}, \boldsymbol{x}, t) = \sqrt{p_{\|}^2 c^2 + 2\mu B m_0 c^2 + m_0^2 c^4} + e\chi(\boldsymbol{x}, t) = \gamma m_0 c^2 + e\chi(\boldsymbol{x}, t)\,, \qquad (3)$$

where $\rho_{\|} = p_{\|}/eB$ is the parallel gyroradius, χ is the electrostatic potential, μ is the magnetic moment, e is the particle charge, c is the speed of light, m_0 is the particle rest mass and γ is the relativistic gamma factor. Applying the Hamiltonian formalism, we derive the equations of motion in the drift approximation [2]

$$\begin{aligned}
\dot{r} = {} & \frac{\partial r}{\partial t} - \frac{B_\zeta}{D}\left[\frac{\partial \chi}{\partial \theta}\Big|_{r,\zeta,t} + \frac{1}{\gamma}\left(\frac{\mu}{e} + \frac{eB}{m_0}\rho_{\|}^2\right)\frac{\partial B}{\partial \theta}\Big|_{r,\zeta,t}\right] + \frac{B_\theta}{D}\left[\frac{\partial \chi}{\partial \zeta}\Big|_{r,\theta,t} + \frac{1}{\gamma}\left(\frac{\mu}{e} + \frac{eB}{m_0}\rho_{\|}^2\right)\frac{\partial B}{\partial \zeta}\Big|_{r,\theta,t}\right] \\
& - \frac{eB^2\rho_{\|}}{\gamma m_0 D}\left(\frac{\partial \psi}{\partial \theta}\Big|_{r,\zeta,t} - \rho_{\|}\frac{\partial B_\zeta}{\partial \theta}\Big|_{r,\zeta,t} + \frac{\partial \Phi}{\partial \zeta}\Big|_{r,\theta,t} + \rho_{\|}\frac{\partial B_\theta}{\partial \zeta}\Big|_{r,\theta,t}\right), \qquad (4) \\
\dot{\theta} = {} & \frac{eB^2\rho_{\|}}{\gamma m_0 D}\left(\frac{\partial \psi}{\partial r}\Big|_{\theta,\zeta,t} - \rho_{\|}\frac{\partial B_\zeta}{\partial r}\Big|_{\theta,\zeta,t}\right) + \frac{B_\zeta}{D}\left[\frac{\partial \chi}{\partial r}\Big|_{\theta,\zeta,t} + \frac{1}{\gamma}\left(\frac{\mu}{e} + \frac{eB}{m_0}\rho_{\|}^2\right)\frac{\partial B}{\partial r}\Big|_{\theta,\zeta,t}\right], \qquad (5) \\
\dot{\zeta} = {} & \frac{eB^2\rho_{\|}}{\gamma m_0 D}\left(\frac{\partial \Phi}{\partial r}\Big|_{\theta,\zeta,t} + \rho_{\|}\frac{\partial B_\theta}{\partial r}\Big|_{\theta,\zeta,t}\right) - \frac{B_\theta}{D}\left[\frac{\partial \chi}{\partial r}\Big|_{\theta,\zeta,t} + \frac{1}{\gamma}\left(\frac{\mu}{e} + \frac{eB}{m_0}\rho_{\|}^2\right)\frac{\partial B}{\partial r}\Big|_{\theta,\zeta,t}\right]. \qquad (6) \\
\dot{\rho_{\|}} = {} & \frac{\partial \rho_{\|}}{\partial t} - \frac{1}{D}\left(\frac{\partial \psi}{\partial r}\Big|_{\theta,\zeta,t} - \rho_{\|}\frac{\partial B_\zeta}{\partial r}\Big|_{\theta,\zeta,t}\right)\left[\frac{\partial \chi}{\partial \theta}\Big|_{r,\zeta,t} + \frac{1}{\gamma}\left(\frac{\mu}{e} + \frac{eB}{m_0}\rho_{\|}^2\right)\frac{\partial B}{\partial \theta}\Big|_{r,\zeta,t}\right] \\
& - \frac{1}{D}\left(\frac{\partial \Phi}{\partial r}\Big|_{\theta,\zeta,t} + \rho_{\|}\frac{\partial B_\theta}{\partial r}\Big|_{\theta,\zeta,t}\right)\left[\frac{\partial \chi}{\partial \zeta}\Big|_{r,\theta,t} + \frac{1}{\gamma}\left(\frac{\mu}{e} + \frac{eB}{m_0}\rho_{\|}^2\right)\frac{\partial B}{\partial \zeta}\Big|_{r,\theta,t}\right] \\
& + \frac{1}{D}\left(\frac{\partial \psi}{\partial \theta}\Big|_{r,\zeta,t} - \rho_{\|}\frac{\partial B_\zeta}{\partial \theta}\Big|_{r,\zeta,t}\right)\left[\frac{\partial \chi}{\partial r}\Big|_{\theta,\zeta,t} + \frac{1}{\gamma}\left(\frac{\mu}{e} + \frac{eB}{m_0}\rho_{\|}^2\right)\frac{\partial B}{\partial r}\Big|_{\theta,\zeta,t}\right] \\
& + \frac{1}{D}\left(\frac{\partial \Phi}{\partial \zeta}\Big|_{r,\theta,t} + \rho_{\|}\frac{\partial B_\theta}{\partial \zeta}\Big|_{r,\theta,t}\right)\left[\frac{\partial \chi}{\partial r}\Big|_{\theta,\zeta,t} + \frac{1}{\gamma}\left(\frac{\mu}{e} + \frac{eB}{m_0}\rho_{\|}^2\right)\frac{\partial B}{\partial r}\Big|_{\theta,\zeta,t}\right], \qquad (7)
\end{aligned}$$

where $D = B_\zeta \partial\Phi/\partial r + B_\theta \partial\psi/\partial r + \rho_{\|}\Big(B_\zeta \partial B_\theta/\partial r - B_\theta \partial B_\zeta/\partial r\Big)$.

Now we consider a 3D static equilibrium with nested magnetic flux surfaces. The magnetic field in the contravariant representation is $\boldsymbol{B} = \nabla\alpha \times \nabla\psi$ and in the covariant representation is $\boldsymbol{B} = \nabla\eta + \beta\nabla s$ where $\alpha = \zeta - q(s)[\theta + \lambda(s,\theta,\zeta)]$, $\eta = \mu_0[J(s)\theta - I(s)\zeta + Q(s,\theta,\zeta)]$ and $\beta = \mu_0[I'(s)\zeta - J'(s)\theta - \nu(s,\theta,\zeta)]$, where $q(s)$ is the inverse rotational transform, $2\pi I(s)$ and $2\pi J(s)$ are the poloidal and toroidal current fluxes, respectively. The periodic function λ is determined from the condition $\boldsymbol{j}\cdot\nabla s = 0$. The periodic functions Q and ν are still unspecified. It is usually the case that a 3D equilibrium is known in a different set of coordinates (s,u,v) (calculated for example with the VMEC code) and a transformation procedure to the desired canonical coordinates

(s,θ,ζ) must be prescribed. To do this, we identify $\theta = u + h(s,u,v)$ and $\zeta = v + k(s,u,v)$ where h and k are periodic functions of the known poloidal and toroidal angles u and v, respectively. For straight field lines, $\lambda(s,\theta,\zeta) = 0$. The functions α, η and β, being scalars, are invariant with respect to coordinate transformations. From the relations for α and η, we obtain $h(s,u,v) = Q_v(s,u,v) - Q(s,\theta,\zeta) - q(s)I(s)\lambda(s,u,v)/[J(s) - q(s)I(s)]$ and $k(s,u,v) = q(s)Q_v(s,u,v) - Q(s,\theta,\zeta) - J(s)\lambda(s,u,v)/[J(s) - q(s)I(s)]$ where the function $Q(s,\theta,\zeta) = Q[s,\theta(s,u,v),\zeta(s,u,v)]$ must still be specified. Invoking the expression for β, we obtain that $\nu_c[s,\theta_c(s,u,v),\zeta_c(s,u,v)] = \nu_v(s,u,v) + J'(s)h(s,u,v) - I'(s)k(s,u,v)$ which we combine with the condition that the covariant radial component of $\boldsymbol{B}$ must vanish in the canonical coordinate system to derive the differential equation

$$\left.\frac{\partial Q_c}{\partial s}\right|_{\theta_c,\zeta_c} + \frac{J'(s) - q(s)I'(s)}{J(s) - q(s)I(s)} Q_c = \nu_v(s,u,v) + \frac{J'(s) - q(s)I'(s)}{J(s) - q(s)I(s)} Q_v(s,u,v) + q(s)\frac{I'(s)J(s) - J'(s)I(s)}{J(s) - q(s)I(s)}\lambda(s,u,v)\,. \tag{8}$$

The resolution of this equation for the transformation from an arbitrary coordinates system to canonical coordinates is an extremely cumbersome procedure that makes the applicability of this formulation virtually impractical.

Boozer magnetic coordinates [3] are defined for 3D systems in which the unperturbed magnetic field forms perfect nested magnetic flux surfaces. These coordinates are also canonical if the time dependent portion of the magnetic field is constrained to have the form [4] $\delta\boldsymbol{B} = \boldsymbol{\nabla}\times[\Upsilon(s,\vartheta,\phi,t)\boldsymbol{B}]$. This form is adequate to describe that radial component of any perturbed magnetic field [4]. Furthermore, the Boozer coordinates satisfy $\lambda(s,\vartheta,\phi) = 0$ (straight field lines) and $Q(s,\vartheta,\phi) = 0$ which allows a straightforward determination of the periodic functions h and k and consequently the mapping from VMEC-like coordinates. The vector potential is $\boldsymbol{A} = \Phi(s)\boldsymbol{\nabla}\vartheta - \psi(s)\boldsymbol{\nabla}\phi + \Upsilon(s,\vartheta,\phi,t)\boldsymbol{B}$. The canonical momenta are $P_\vartheta = e[\Phi(s) + \rho_c\mu_0 J(s)]$ and $P_\phi = -e[\psi(s) + \rho_c\mu_0 I(s)]$ where the effective gyroradius is $\rho_c = p_{||}/(eB) + \Upsilon$ [5]. Inverting these relations, we have $s = s(P_\vartheta, P_\phi)$ and $\rho_c = \rho_c(P_\vartheta, P_\phi)$. Applying the Hamiltonian formalism, we obtain the equations of motions

$$\dot{s} = \frac{\mu_0 I(s)}{D_b}\left[\left.\frac{\partial\chi}{\partial\vartheta}\right|_{s,\phi,t} + \frac{1}{\gamma}\left(\frac{\mu}{e} + \frac{eB}{m_0}\rho_{||}^2\right)\left.\frac{\partial B}{\partial\vartheta}\right|_{s,\phi} - \frac{eB^2\rho_{||}}{\gamma m_0}\left.\frac{\partial\Upsilon}{\partial\vartheta}\right|_{s,\phi,t}\right]$$

$$+\frac{\mu_0 J(s)}{D_b}\left[\frac{\partial\chi}{\partial\phi}\Big|_{s,\vartheta,t}+\frac{1}{\gamma}\left(\frac{\mu}{e}+\frac{eB}{m_0}\rho_{\|}^2\right)\frac{\partial B}{\partial\phi}\Big|_{s,\vartheta}-\frac{eB^2\rho_{\|}}{\gamma m_0}\frac{\partial\Upsilon}{\partial\phi}\Big|_{s,\vartheta,t}\right], \tag{9}$$

$$\dot{\vartheta} = -\frac{eB^2\rho_{\|}}{\gamma m_0 D_b}\left[\psi'(s)+(\rho_{\|}+\Upsilon)\mu_0 I'(s)+\mu_0 I(s)\frac{\partial\Upsilon}{\partial s}\Big|_{\vartheta,\phi,t}\right]$$
$$-\frac{\mu_0 I(s)}{D_b}\left[\frac{\partial\chi}{\partial s}\Big|_{\vartheta,\phi,t}+\frac{1}{\gamma}\left(\frac{\mu}{e}+\frac{eB}{m_0}\rho_{\|}^2\right)\frac{\partial B}{\partial s}\Big|_{\vartheta,\phi}\right], \tag{10}$$

$$\dot{\phi} = -\frac{eB^2\rho_{\|}}{\gamma m_0 D_b}\left[\Phi'(s)+(\rho_{\|}+\Upsilon)\mu_0 J'(s)+\mu_0 J(s)\frac{\partial\Upsilon}{\partial s}\Big|_{\vartheta,\phi,t}\right]$$
$$-\frac{\mu_0 J(s)}{D_b}\left[\frac{\partial\chi}{\partial s}\Big|_{\vartheta,\phi,t}+\frac{1}{\gamma}\left(\frac{\mu}{e}+\frac{eB}{m_0}\rho_{\|}^2\right)\frac{\partial B}{\partial s}\Big|_{\vartheta,\phi}\right], \tag{11}$$

$$\dot{\rho}_{\|} = -\frac{1}{D_b}\left[\psi'(s)+(\rho_{\|}+\Upsilon)\mu_0 I'(s)+\mu_0 I(s)\frac{\partial\Upsilon}{\partial s}\Big|_{\vartheta,\phi,t}\right]\left[\frac{\partial\chi}{\partial\vartheta}\Big|_{s,\phi,t}+\frac{1}{\gamma}\left(\frac{\mu}{e}+\frac{eB}{m_0}\rho_{\|}^2\right)\frac{\partial B}{\partial\vartheta}\Big|_{s,\phi}\right]$$
$$-\frac{1}{D_b}\left[\Phi'(s)+(\rho_{\|}+\Upsilon)\mu_0 J'(s)+\mu_0 J(s)\frac{\partial\Upsilon}{\partial s}\Big|_{\vartheta,\phi,t}\right]\left[\frac{\partial\chi}{\partial\phi}\Big|_{s,\vartheta,t}+\frac{1}{\gamma}\left(\frac{\mu}{e}+\frac{eB}{m_0}\rho_{\|}^2\right)\frac{\partial B}{\partial\phi}\Big|_{s,\vartheta}\right]$$
$$-\frac{\mu_0}{D_b}\left[I(s)\frac{\partial\Upsilon}{\partial\vartheta}\Big|_{s,\phi,t}+J(s)\frac{\partial\Upsilon}{\partial\phi}\Big|_{s,\vartheta,t}\right]\left[\frac{\partial\chi}{\partial s}\Big|_{\vartheta,\phi,t}+\frac{1}{\gamma}\left(\frac{\mu}{e}+\frac{eB}{m_0}\rho_{\|}^2\right)\frac{\partial B}{\partial s}\Big|_{\vartheta,\phi}\right]-\frac{\partial\Upsilon}{\partial t}\Big|_{s,\vartheta,\phi}, \tag{12}$$

where

$$D_b = \mu_0[\psi'(s)J(s)-\Phi'(s)I(s)]\Big[1+\mu_0\rho_c[J(s)I'(s)-I(s)J'(s)]/[\psi'(s)J(s)-\Phi'(s)I(s)]\Big].$$

In conclusion, we have extended the formulation of the guiding centre drift orbits in canonical coordinates valid for arbitrary time dependent electric and magnetic fields to relativistic particles. However, the transformation from a general flux coordinate system to these canonical coordinates is too cumbersome for parctical applications. The transformation to Boozer magnetic coordinates, on the other hand, is straightforward and this coordinate system is canonical for perturbed magnetic fields constrined to the form $\delta\boldsymbol{B} = \boldsymbol{\nabla}\times(\Upsilon\boldsymbol{B})$. The relativistic guiding centre drift equations of motion are explicitly derived in this system.

References

[1] Meiss, J.D., Hazeltine, R.D., *Phys. Fluids* **B2** (1990) 2563

[2] Cooper, W.A., *Plasma Phys. Control. Fusion* **39** (1997) 931

[3] Boozer, A.H., *Phys. Fluids* **23** (1980) 904

[4] White, R.B., Chance, M.S., *Phys. Fluids* **27** (1984) 2455

[5] Boozer, A.H., *Phys. Plasmas* **3** (1996) 3297

Plasma dynamics in extended MHD

T.J. Schep, F. Pegoraro[1], V.P. Lakhin*
FOM-Instituut voor Plasmafysica, "Rijnhuizen", Association Euratom-FOM,
P.O.Box 1207, 3430 BE Nieuwegein, The Netherlands
[1] Dept. of Theoretical Physics, University of Turin, Italy

The extension of magnetohydrodynamics (MHD) with features of two-fluid plasma behaviour, leads to the inclusion of a number of interesting dynamical phenomena into the equations. In this paper we will address the incorporation of electron inertia, the Hall term, and of finite electron temperature into the R(educed) MHD model.
The extended system is Hamiltonian in terms of non-canonical Poisson brackets. The role of the associated topological constraints (Casimirs) will be discussed. It will be shown that, in the extended system, the Casimirs generalize in an elegantly symmetrical way different special limits, a.o. the RMHD limit.
Finite electron mass effects originate from two different physical mechanism in the electron momentum balance. A first contribution arises from of the electron inertia term, a second one from the parallel component of the stress tensor. This latter term cancels the pressure gradient contribution to the convective part of the inertia term.

Inertia and finite electron temperature lead to a decoupling of the motion of the electron fluid from that of the magnetic field. Instead of flux conservation, a more subtle conservation law is valid that includes the electron motion along field lines and the electron density. The extended model allows for collisionless reconnection where the magnetic flux can be converted into electron momentum along field lines and into ion vorticity. The creation of current and vorticity layers are a necessary consequence of this Hamiltonian reconnection.

The extended system possesses also solutions that are similar to point-vortices in 2D hydrodynamics. Such solutions are not contained in the MHD system of equations. Three different types of current-vortex filaments exist. Each of these types is frozen into a different "velocity" field. The basic properties of a system of interacting filaments will be presented. The standard omission of the self-energy of these filaments is shown to be related with a canonical transformation involving the quadratic Casimirs of the system.

[1] V.P.Lakhin, T.J. Schep and E. Westerhof, Current-Vortex Filament Model of Nonlinear Alfvén Perturbations in a Finite-Pressure Plasma. This conference.
[2] E. Westerhof, V.P. Lakhin, T.J. Schep, Integrable motion of four current-vortex filaments. This conference.
[3] D. Grasso, E. Cafaro, F. Pegoraro, F. Porcelli, A. Saluzzi, Invariants and geometric structures in nonlinear Hamiltonian magnetic recoonnection. This conference

*Permanent address: Nuclear Fusion Institute, Russian Research Centre "Kurchatov Institute", 123182 Moscow, Russia

MHD cluster spectra of plasmas with flow

B. van der Holst, R.J. Nijboer, J.P. Goedbloed

FOM-Institute for Plasma Physics 'Rijnhuizen', Association Euratom-FOM, P.O. Box 1207, 3430 BE Nieuwegein, The Netherlands

Recently, the interest for MHD instabilities and oscillations of equilibria with flow has grown considerably. In astrophysics, plasma flows play a dominant role, in rotating accretion disks or in collimated jets like the jets emitted from white dwarfs or neutron stars. In fusion research, the problem of rotating plasma equilibria has attracted increasing attention in recent years, owing to the significant toroidal plasma velocity which is induced by 'neutral beam injection' or a 'divertor'.

In order to better understand the effect of flow on MHD instabilities and oscillations, it is preferable to study simple equilibria. In this research, the stationary plane plasma slab with gravitation is investigated. We limit our attention to the stable and unstable cluster spectra. These spectra are like the energy levels of a hydrogen atom clustering to the continuum.

It is found that on the one side by increasing shear flow the plasma will be unstable for smaller density gradient but on the other side the growth rate of the Suydam instability will gradually decrease.

Generalized MHD equilibria in the presence of shear flow

J.L. Johnson[‡], M. Tessarotto[*], R. B. White[‡], and R.Zorat[*]
[‡]Princeton Plasma Physics Laboratory, Princeton University, Princeton, NJ 08543, USA
[*]Department of Mathematical Sciences University of Trieste, I-34127 Trieste, Italy

Abstract

Purpose of the investigation is the kinetic analysis of the conditions of the basic physical properties of suitably generalized toroidal MHD equilibria in the presence of strong flows as well as nonlinear e.m. perturbations. The equilibria here concerned about are defined in terms of a *kinetic equilibrium distribution function*, i.e., a gyrokinetic distribution function, which is appropriately close to a local drifted Maxwellian distribution and is function of the relevant *maximal* adiabatic invariants, to be suitably defined.

I - Introduction An outstanding issue in magnetic confinement is the establishment of MHD equilibria with enhanced flow shear profiles for which turbulence (and transport) may be locally effectively suppressed or at least substantially reduced with respect to standard weak turbulence models. Relevant examples concern flows in tokamak [1, 2, 3, 4] as well as stellarator plasmas [5, 6]. Strong flows develop in the presence of equilibrium $\mathbf{E} \times \mathbf{B}$−drifts produced by a strong radial electric field, as well as due to diamagnetic contributions produced by steep equilibrium radial profiles of number density, temperature and the flow velocity itself. In the framework of a kinetic description, this generally requires the construction of guiding-center variables correct to second order in the relevant expansion parameter. For this purpose, the Lagrangian approach to particle gyrokinetic theory developed recently by Tessarotto et al. [7, 8] is adopted.

To this goal, guiding-center variables and its associated equations of motion are constructed by a suitable perturbative expansion up to second order in the relevant expansion parameters. These are, $\varepsilon = r_L/L$, λ and δ, which characterize, respectively, the Larmor radius and the amplitude and perpendicular wavelength of the perturbations of the e.m. fields. Here, as usual, $r_L = v/\Omega_s$ is the Larmor radius, v a suitable average velocity of the test particle to be identified with the thermal speed $v_{th,s} = (2T_s/M_s)^{1/2}$, $\Omega_s = Z_s eB/M_s c$ the Larmor frequency, and L a suitable equilibrium scale length. Moreover it is assumed true a suitable *strong-drift gyrokinetic ordering*, characterizing the e.m. fields and the basic dynamical variables, in order to allow for the flow velocity $\frac{|\mathbf{V}_s(\mathbf{r},t)|}{v} \lesssim \mathbf{O}(\varepsilon^0)$, being $\mathbf{V_s}(\mathbf{r},t) = \frac{1}{N_s}\int d^3v \mathbf{v} f_s(\mathbf{r},\mathbf{v},t)$, with $\overline{N}_s = \int d^3v f_s(\mathbf{r},\mathbf{v},t)$ the corresponding number

density. The Lagrangian formulation is based, as usual, on the hybrid form of Hamilton variational principle [7]. This permits the construction of the guiding center variables $\mathbf{z}' \equiv (\mathbf{r}', H', M', \phi')$ and of the associated equations of motions in arbitrary non-canonical variables, including in particular, the relevant adiabatic invariants. The gyrokinetic Lagrangian reads

$$\overline{\mathcal{L}}^{(2)} \equiv \frac{Z_s e}{\varepsilon c}\,\dot{\mathbf{r}}' \cdot \mathbf{A}^* - \left(\frac{\dot{\phi}'}{\Omega_s'} + 1\right) M'B' - \frac{m_s}{2}\left(u'\mathbf{b}' + \mathbf{V}_s^* + \mathbf{U}_s^*\right)^2 - \frac{Z_s e}{\varepsilon}\Phi^*,$$

where M' is the magnetic moment and $\mathbf{A}^*$, Φ^*, $\mathbf{V}_s^*$, $\mathbf{U}_s^*$ are suitable effective e.m. potentials and effective drift velocities. One can prove that in the strong drift ordering, besides the magnetic moment two additional adiabatic invariants exist, one is H' to be identified with the guiding center hamiltonian, the other is $P_{Q'}$, the canonical momentum conjugate to the Clebsh potential Q', which reads

$$P_{Q'}' \equiv \frac{Z_s e}{\varepsilon c}\psi_P' + \lambda\frac{Z_s e}{c}\langle A_{\parallel}^{(os)}\rangle_{\phi'}\frac{a'}{B'} + M_s\left\{u'\frac{a'}{B'} + \omega'\frac{a'^2 + g^{11}}{B'^2} + \lambda U_{Q'}^*\right\}. \tag{1}$$

Actually $P_{Q'}$ is an adiabatic invariant of second order in ε and first order in the parameter $\Delta = (\frac{r}{R})^{1/2}$ (with r and R the minor and major radii of the torus) in the sense that

$$\frac{1}{\Omega_s'}\frac{d}{dt}P_{Q'}' \sim O(\varepsilon^2)O(\Delta)P_{Q'}' \tag{2}$$

II - Construction of the equilibria In order to construct MHD equilibria a kinetic approach is adopted, based on the previous formulation of particle gyrokinetic theory of which assumes true the aforementioned strong drift ordering. This permits the treatment of nonlinear electromagnetic perturbations with arbitrary perpendicular wavelength. The conditions of existence of MHD equilibria in such a general framework are investigated. As a basic result, the inclusion of the effect of perturbed flow velocity is found to be essential for the proper formulation of nonlinear gyrokinetic theory. In fact, we prove that *all* relevant guiding-center adiabatic invariants (*i.e.*, besides H' also $P_{Q'}$) become maximal adiabatic invariants when expressed in the reference frame locally at rest with respect to the species fluid.

The kinetic distribution function $f_s(\mathbf{r}, \mathbf{v}, t)$, obeying the Fokker-Planck (F-P) kinetic equation, when expressed in terms of the gyrokinetic variables $\mathbf{z}' = (\mathbf{r}', H', M', \phi')$ be

gyrophase independent, *i.e.*, $(f'_s \equiv) f'_s(\mathbf{r}', H', M', t) \equiv f_s(\mathbf{r}, \mathbf{v}, t)$, thus yielding the *gyrokinetic F-P equation*

$$\frac{\partial}{\partial t} f'_s + \dot{\mathbf{r}}' \cdot \frac{\partial}{\partial \mathbf{r}'} f'_s + \dot{H}' \frac{\partial}{\partial H'} f'_s = \langle C \rangle_{\phi'}. \tag{3}$$

Its solution is seeked in the form [2, 3] $f'_s(\mathbf{r}', H', M', t) = f'_{0s} + \varepsilon h'_s$ where f'_{0s} is assumed to define a *generalized kinetic Fokker-Planck equilibrium*, *i.e.*, both to be an adiabatic invariant and to be suitably close to a local Maxwellian distribution f_{M_s}, namely such that the constraints

$$\frac{1}{\Omega'_s} \frac{d}{dt} f'_{0s} \sim O(\varepsilon^k) f'_{0s}, \;\; ; \;\; \frac{f'_{0s} - f_{M_s}}{f_{M_s}} \sim O(\varepsilon) \tag{4}$$

(with $k \geq 2$) are simultaneously satisfied. Here, f_{M_s} is required to be a drifted local Maxwellian distribution

$$f_{M_s} = \frac{\overline{N}_s}{\{2\pi T_s / M_s\}^{3/2}} \exp\left\{ - \frac{M_s (\mathbf{v} - \mathbf{V}_s)^2}{2 T_s} \right\}, \tag{5}$$

i.e., carrying *both* the equilibrium and perturbed species flow mass velocity $\mathbf{V}_s$, for which the leading-order contribution is assumed to be produced not only by the equilibrium $\mathbf{E} \times \mathbf{B}$ drift velocity but also by a suitable parallel flow velocity, $U_o \mathbf{b}$. It follows that f'_{0s} must be a function of all independent adiabatic invariants.

Detailed calculations prove that the previous constraints can be satisfied both for axisymmetric MHD equilibria (i.e., omitting e.m. perturbations) and for stellarator equilibria *sufficiently* close to quasi-helical ones. Hence, introducing the effective energy in the guiding-center

$$F'_s \equiv H'_s - \omega(\psi'_*) P_{Q'} + \lambda \frac{Z_s e}{c} \frac{u' + (\mathbf{V}^*_s + \lambda \mathbf{U}^*_s) \cdot \mathbf{b}'}{c} \langle A^{(os)}_{\|} \rangle_{\phi'} + \frac{Z_s e}{c} \left[\omega(\psi'_*) \psi'_P - \int_0^{\psi'_*} dx \omega(x) \right], \tag{6}$$

and identifying $\mathbf{V}^{(os)}_s$ and $\mathbf{W}^{(os)}_s$ with

$$\lambda \mathbf{W}^{(os)}_s = \lambda \mathbf{V}^{(os)}_s = - \lambda \frac{Z_s e}{M_s c} A^{(os)}_{\|} \mathbf{b} + O(\varepsilon), \tag{7}$$

it is immediate to prove that F'_s is a *maximal adiabatic invariant.* Similarly, one finds that a further maximal adiabatic invariant can be constructed in terms of the canonical momentum $P_{Q'}$, i.e., by identifying it with the dynamical variable (close to the guiding-center poloidal flux ψ'_P)

$$\psi'_* \equiv \frac{c}{Z_s e} \left\{ P'_{Q'} - \lambda \frac{Z_s e}{JB} \int dt \frac{\partial}{\partial Q'} \left[\langle \Phi^{(os)} \rangle_{\phi'} - \frac{u' + (\mathbf{V}^*_s + \lambda \mathbf{U}^*_s) \cdot \mathbf{b}'}{c} \langle A^{(os)}_{\|} \rangle_{\phi'} \right] \right\}. \tag{8}$$

The invariants F'_s and ψ'_* are maximal only in the reference frame locally at rest with the species fluid. As fundamental consequence, one finds that when expressed in terms of the relevant adiabatic invariants, the equilibrium distribution function reads

$$f'_0(\psi'_*, F'_s) = \frac{N_{0s}(\psi'_*)}{\{2\pi T_s(\psi'_*)/M_s\}^{3/2}} \exp\left\{-\frac{F'_s}{T_s(\psi'_*)}\right\}. \tag{9}$$

Simple algebra yields, to leading orders the number density $\overline{N}_s$. This in turn, permits the evolution of the scalar pressure and of the mass flow velocity. As a basic result one finds that kinetic equilibrium implies that besides a mass flow velocity in the direction of symmetry a finite non-vanishing first order poloidal velocity must exist.

ACKNOWLEDGMENTS Work sponsored by the Italian National Research Council, through the "Gruppo Nazionale per la Fisica Matematica"(GNFM, National Group of Mathematical Physics) , the U.S. Department of Energy through contract #DE-AC02-76-CHO-3073 with Princeton University, New Jersey, USA and the Consorzio di Magnetofluidodinamica, Trieste University, Italy.

References

[1] F.L. Hinton and S.K. Wong, Phys.Fluids **28**, 3082 (1985).
[2] P.J. Catto, I.B. Bernstein and M. Tessarotto, Phys.Fluids **30**, 2784 (1987).
[3] M. Tessarotto and R.B. White, Phys.Fluids B **4**, 859 (1992).
[4] M. Tessarotto and R.B. White, Phys. Fluids B **5**, 3942 (1993).
[5] M. Tessarotto, J.L. Johnson, R.B. White and L.J. Zheng, Phys. Plasmas **3**, 2653 (1996).
[6] M. Tessarotto, J.L. Johnson, R.B. White and L.J. Zheng, in *Theory of fusion Plasmas*, E.Sindoni *et al.* eds. (Società Italiana di Fisica, Editrice Compositori, Bologna, 1996), p.321.
[7] M. Tessarotto, L.J. Zheng and G. Favretto, Bull.Am.Phys.Soc. **40**, 1683 (1995).
[8] M. Pozzo, M. Tessarotto and R. Zorat, in *Theory of fusion Plasmas*, E.Sindoni *et al.* eds. (Società Italiana di Fisica, Editrice Compositori, Bologna, 1996), p.295.

Stability of incompressible hyperbolic MHD flows

R.J. Nijboer[1] J.P. Goedbloed[1] A.E. Lifschitz[2]

(1) FOM-Institute for Plasma Physics Rijnhuizen, P.O. Box 1207, 3430 BE Nieuwegein, The Netherlands

(2) Department of Mathematics, Statistics and Computer Science, University of Illinois, Chicago, Illinois 60607, USA

Abstract We consider incompressible plasma flows with a translational symmetry on an unbounded domain. Equilibria for X-point and O-point geometries are described. Furthermore, the spectrum for X-point geometries is investigated. An essential spectrum is described which corresponds to an instability whenever the poloidal flow dominates over the poloidal magnetic field.

1 Introduction

Linear flow and linear magnetic fields with hyperbolic or elliptic field lines are an approximation of the fields around X-points and O-points, respectively. In tokamak plasmas these stagnation points arise due to a divertor or the presence of magnetic islands. In astrophysical plasmas they occur, for example, in solar flares or in the earth's magnetosphere. Equilibrium flows also occur very naturally in both fusion and astrophysical plasmas. In tokamaks they are due to neutral beam injection, or to divertor action where the plasma flow is used to get impurities out of the plasma.

In this paper we discuss the spectrum of linear, incompressible plasma flows around an X-point geometry. This work is an extension of previous investigations of O-point geometries [1, 2] and pure flow X-point geometries [3]. More details can be found in [4].

2 Equilibrium

We consider a stationary equilibrium for incompressible plasma flows with a translational symmetry. The equilibrium state of these flows is described by the modified Grad-Shafranov equation, which depends on profiles for the poloidal Alfvén Mach number, M, and the Bernoulli function. By choosing a constant profile for the poloidal Alfvén Mach

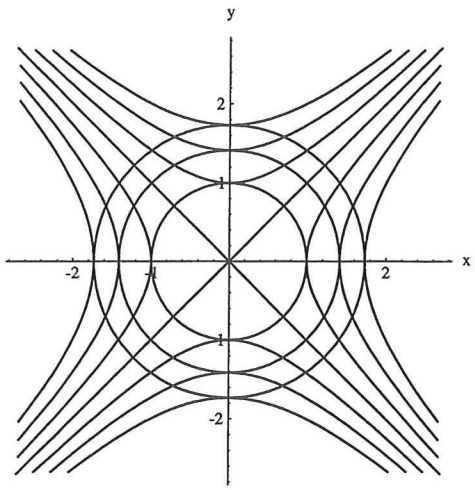

Figure 1: Isobares (circles), flux lines (hyperbolas) and the separatrices for a X-point geometry with $a_1 = a_2$.

number and a linear profile for the Bernoulli function we can describe equilibria with hyperbolic flux surfaces (X-points) and equilibria with elliptic flux surfaces (O-points).

When we take constant profiles for the density and the longitudinal components of the velocity and the magnetic field, V_z resp. B_z, the equilibrium is completely specified (figure 1):

$$\begin{aligned}
\mathbf{V}(x,y) &= \alpha\Omega\left(\frac{a_1}{a_2}y\mathbf{e}_x + \frac{a_2}{a_1}x\mathbf{e}_y\right) + V_z\mathbf{e}_z, \\
\mathbf{B}(x,y) &= \beta\Omega\left(\frac{a_1}{a_2}y\mathbf{e}_x + \frac{a_2}{a_1}x\mathbf{e}_y\right) + B_z\mathbf{e}_z, \\
\Pi(x,y) &= \Pi_0 - \tfrac{1}{2}\frac{a_1a_2}{|a_1a_2|}\left(\alpha^2-\beta^2\right)\Omega^2\left(x^2+y^2\right).
\end{aligned}$$

Here $\mathbf{V}$ denotes the velocity field, $\mathbf{B}$ denotes the magnetic field, Π denotes the total pressure, Ω denotes the strength of the poloidal fields, α and β describe the proportion of the poloidal fields, Π_0 denotes the total pressure 'on axis', and a_1 and a_2 describe the 'shape' of the X-point or O-point.

3 Spectral analysis

Having derived the X-point equilibrium we perturb it and consider the spectral problem. Since these X-point equilibria are two-dimensional, they give rise to a two-dimensional spectral problem in physical space. However, since we consider an unbounded domain we can apply a spatial Fourier transform and consider the spectral problem in Fourier space:

$$f(\mathbf{x},t) = \frac{e^{\sigma t}}{(2\pi)^{3/2}} \int \hat{f}(\mathbf{k}) e^{i\mathbf{k}\cdot\mathbf{x}} d\mathbf{k}.$$

In the Fourier space we can use the divergence-free condition to eliminate the perturbed total pressure. Doing so, we also reduce the spectral problem to a one-dimensional problem, which is an enormous simplification.

The only complication in transforming the spectral problem from partial differential equations in physical space to ordinary differential equations in Fourier space is that these ordinary differential equations necessarily have non-constant coefficients. For azimuthal modes ($k_z = 0$) we find two uncoupled equations. For non-azimuthal modes ($k_z \neq 0$) we have two coupled equations. The domain of the problem is unbounded, since the field lines are open ended. Hence, we may apply 'scattering techniques', like in Quantum Mechanics, to calculate the spectrum.

The spectrum we found belongs to the essential spectrum, by which we mean that it is a dense set of discrete spectral values. This is caused by the fact that the domain is unbounded. If the domain were bounded in physical or Fourier space, this would lead to a discrete spectrum. The possibility of a discrete spectrum on an unbounded domain was not excluded a priori. However, this discrete spectrum will be of a different nature as the discrete spectrum due to finite domains.

For azimuthal modes we calculated the essential spectrum. The spectrum of parallel displacements ($\parallel \mathbf{e}_z$) corresponds to stable perturbations,

$$\sigma = in(\alpha \pm \beta), \qquad n \in \mathbb{R},$$

whereas the perturbations corresponding to the spectrum of perpendicular displacements ($\perp \mathbf{e}_z$) turn unstable whenever $M^2 > 1$, i.e., the poloidal flow dominates over the poloidal magnetic field:

$$\sigma = \alpha n i \pm \sqrt{\alpha^2 - \beta^2 - \beta^2 n^2}, \qquad n \in \mathbb{R}.$$

In the limit of a pure flow our results are in agreement with [3]. It is also found that the essential spectrum does not depend on the geometry or the 'radial' Fourier mode. Finally, whenever we have a 'perfect' hyperbola ($a_1 = a_2$) no discrete spectrum exists on the unbounded domain.

For non-azimuthal modes the spectral problem is very complicated. However, we were able to show that the essential spectrum corresponding to perpendicular displacements of azimuthal modes still exists. Due to the longitudinal magnetic field the complete spectrum is shifted along the imaginary axis with an amount $\alpha k_z B_z/\beta$. Hence, whenever $M^2 > 1$ we again retrieve unstable modes.

Acknowledgement

This work was performed as part of the research programme of FOM with financial support from NWO.

References

[1] Lifschitz, A., *Exact description of the spectrum of elliptical vortices in hydrodynamics and magnetohydrodynamics*, Phys. Fluids A **7** (7), July 1995, 1626-1636.

[2] Lifschitz, A., *A nonlinear spectral problem with periodic coefficients occurring in magnetohydrodynamic stability theory*, in *Proceedings of the 1995 Int. Workshop on Operator Theory and Appl.* (ed. R. Mennicken, and C. Tretter), Birkhoiser 1997, 97-117.

[3] Lifschitz, A., *On the spectrum of hyperbolic flows*, to appear in Phys. Fluids.

[4] Nijboer, R.J., J.P.Goedbloed, A.E. Lifschitz, *The spectrum of MHD flows about X-points*, to be published.

Invariants and Geometric Structures in Nonlinear Hamiltonian Magnetic Reconnection

E. Cafaro[1], D. Grasso[1,2], F. Pegoraro[2,3], F. Porcelli[1], A. Saluzzi[1]

1. Energetics Dept., Politecnico di Torino, Italy 2. Physics Dept., University of Torino, Italy

3. Physics Dept., University of Pisa, Italy

Collisionless magnetic reconnection in a 2D plasma is analyzed, using a two-fluid model where electron mass and pressure effects are important. Numerical simulations show the formation of current and vorticity sheets splitting into two branches crossing at the stagnation point of the plasma flow. These structures are interpreted on the basis of the Hamiltonian Casimirs (conserved fields) of the fluid plasma model.

The problem of magnetic reconnection in collisionless regimes was originally motivated by applications to space plasma processes. Recently it was shown [1,2] that electron inertia may account also for sawtooth crashes in high temperature Tokamak plasmas, which may occur on a time scale short compared to the average electron-ion collision time. In this paper, first we present new numerical simulations in the collisionless regime which confirm that magnetic reconnection remains a fast process in the nonlinear phase. Secondly, we extend this analysis to finite temperature regimes where electron pressure effects are important. We find that in the early nonlinear phase the growth of the magnetic island is even faster than in the *cold* electron limit of Ref. [2].

The 2D model dimensionless equations we consider are [4]:

$$dF/dt = \varrho_s^2[U,\psi] \tag{1}$$

$$dU/dt = [J,\psi] \tag{2}$$

The magnetic field is $\mathbf{B} = B_0\mathrm{e}_z + \nabla\psi \times \mathrm{e}_z$, with B_0 constant and z the ignorable coordinate. The $\mathbf{E}\times\mathbf{B}$ drift on the normal plane is $\mathbf{v}_\perp = \mathrm{e}_z \times \nabla\varphi$, where φ is a stream function, $U = \nabla^2\varphi$, $J = -\nabla^2\psi$ and $F = \psi + d_e^2 J$. The Poisson brackets are defined as $[A,B] = \mathrm{e}_z \cdot \nabla A \times \nabla B$ and $d/dt \equiv \partial/\partial t + [\varphi, \ ]$. This model contains the physics associated with the electron inertial skin depth, $d_e = c/\omega_{pe}$, and with the electron pressure and gyroviscosity, which introduce the scale length $\varrho_s = \sqrt{T_e/m_i}/\omega_{ci}$.

These equations can be written in conservative form for the fields $G_\pm \equiv F \pm d_e\varrho_s U$ as

$$d_\pm G_\pm/dt = 0 \tag{3}$$

where $d_\pm/dt \equiv \partial/\partial t + [\varphi_\pm, \ ]$, with $\varphi_\pm \equiv \varphi - \varrho_s^2 U^2 \mp d_e \varrho_s J$. Since the fields $G_\pm$ are conserved as they are advected by the effective velocity fields $\mathbf{v}_\pm = \mathbf{e}_z \times \nabla\varphi_\pm$, their topology remains frozen during the time evolution of the system. The mathematical model can also be cast in noncanonical Hamiltonian form [3]. We can also define two infinite sets of Casimirs $C_\pm = \int d^2x h_\pm(G\pm)$ with $h_\pm$ arbitrary functions. In the limit of vanishing ϱ_s, upon expanding $h_\pm$ to first order, we find the Casimirs of the cold electron case, $C_1 = \int d^2x h_1(F)$ and $C_2 = \int d^2x U h_2(F)$. In this case, the canonical momentum F is conserved and its topological structure is preserved in time.

Here we present the numerical solution of the nonlinear model defined by Eqs. (1,2) obtained by means of the finite difference method on a nonuniform grid. We adopt a 2D slab geometry with aspect ratio $\epsilon = L_x/L_y$ and double periodic boundary conditions. We assume $\psi_{eq} = \cos x$, $\varphi_{eq} = 0$ and consider initial perturbations of the type $(\varphi, \delta\psi)$ =Re$\left[\varphi(x), \delta\psi(x) e^{\gamma t + iky}\right]$. Our results for the case $\varrho_s \to 0$ were first reported in Ref. [5]. Here we report new numerical simulations for different values of the aspect ratio.

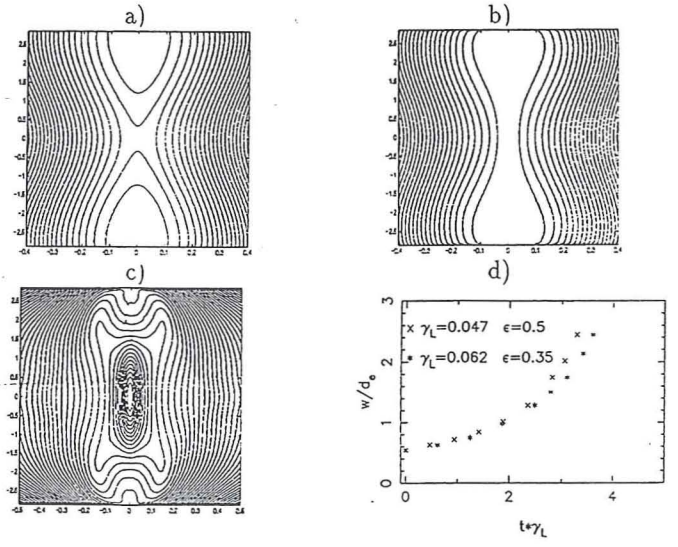

FIG. 1. Contour plots for the case $\varrho_s = 0$, $d_e = 0.08$ and $\epsilon = 0.35$ at t=58: (a) ψ; (b) F; (c) J; (d) behaviour oh the magnetic island width with time for different values of ϵ.

In Fig. 1 are shown numerical solutions for parameters values $\varrho_s = 0$, $\epsilon = 0.35$ and $d_e = 0.08$ at $t = 58$. Fig. 1 (a) shows the formation of magnetic islands in the contour plot

of the magnetic flux ψ; Fig. 1 (b) shows that the topology of F is frozen during the time evolution of the system; from Fig. 1 (c) we see that the spatial distribution of the current density forms a current sheet in the reconnection layer of width $\sim d_e$, with a narrow inner sublayer shrinking with time, in agreement with the analysis of Ref. [2]. In Fig. 1 (d) is shown the growth of the magnetic island width $w(t)$ with time, for two different values of the aspect ratio ϵ and, hence, of the growth rate. We recall that the linear dispersion relation in the cold electron case [6] is $\gamma = -k\pi/\Delta'(Q/4)^{3/2}\frac{\Gamma(\frac{Q-1}{4})}{\Gamma(\frac{Q+5}{4})}$ where $k = m\epsilon$, $Q = \gamma/kd_e$, m is the mode number and Δ' is the instability parameter that measures the logarithmic jump of ψ across the reconnection layer; here, $\Delta' = 2\sigma \tan \sigma\pi/2$ where $\sigma = \sqrt{1-k^2}$. $\Delta' > 0$ is a necessary condition for instability of reconnecting modes. Thus, instability is possible only when $0 \leq k^2 \leq 1$. i.e. $\epsilon < 1$. The maximum mode number which becomes unstable is given by $m_{max} = integer(\epsilon^{-1})$. For $\epsilon = 0.5$ only the mode $m = 1$ is unstable with a growth rate $\gamma_L = 0.05$, while for $\epsilon = 0.35$ also the mode $m = 2$ become unstable with $\gamma_L \sim 0.024$, which is subdominant respect to the growth rate $\gamma_l = 0.06$ of the mode $m = 1$.

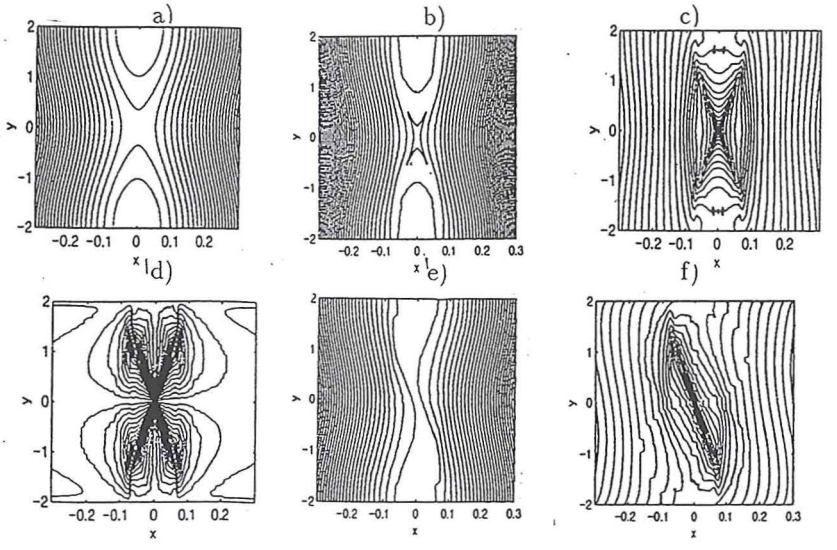

FIG. 2. Contour plots for the case $\varrho_s = 3d_e$, $d_e = 0.08$ and $\epsilon = 0.5$ at t=50: (a) ψ; (b) F; (c) J; (d) U; (e) $G_{\pm}$; (f) $\varphi_{\pm}$.

Numerical solutions for parameter values $\varrho_s = 3d_e$ at aspect ratio $\epsilon = 1/2$ and inertial skin depth $d_e = 0.08$ are shown in Figs. 2. In particular the contour plots of the fields

ψ, F, J, U, G_+ and φ_+ are shown at $t = 50\tau_A$. In the finite ϱ_s regime, the canonical momentum F changes its topology: one O-point forms at the origin and four Y-points form symmetrically around it (Fig. 2b). The initial topology of the $G_\pm$ fields (Fig. 2e), instead, The contour levels of G_- and φ_- are mirror symmetric to those of G_+ and φ_+. A cross-shaped configuration in the current density and plasma vorticity layers is shown in Fig. 2(c,d). This is a distinctly new feature in comparison with the cold electron case, that can be interpreted in terms of the time evolution of the conserved fields $G_\pm$, advected by the effective velocity fields $v_\pm$ [7].

The important difference between Hamiltonian and dissipative reconnection [8] can now be clarified. Both these processes require the localized violation of the topological constraints on the magnetic flux, ψ. In Hamiltonian plasma models, topological constraints continue to be present, but they involve new fields, F or $G_\pm$, which differ from ψ by current density and plasma vorticity terms. Therefore, reconnection of ψ can only proceed unimpeded by the conservation of F or of $G_\pm$ if current and vorticity layers are formed. In the presence of dissipation the topological constraints relax and the current and vorticity layers are limited by diffusion. On the contrary, in Hamiltonian reconnection the presence of the locally conserved fields makes these layers increasingly sharper and leads to the formation of microscales. The long term evolution of these microscales, apart from posing severe numerical problems, cannot be described correctly within the fluid approximation and will require a fully kinetic description. Nevertheless, our analysis is valuable in that it suggests possible links between spatial structures and the conservation of the phase-space volume associated with collisionless kinetic models.

[1] J. Wesson, Nucl. Fusion **30**, 2545 (1990).

[2] M. Ottaviani and F. Porcelli, Phys. Rev. Lett. **71** (23), 3802 (1993).

[3] B.N. Kuvshinov, F. Pegoraro and T.J. Schep, Physics Letters A **191**, 296 (1994).

[4] T.J. Schep, F. Pegoraro and B. Kuvshinov, Phys.Plasmas 1, 2843 (1994).

[5] E. Cafaro *et al.* in *Theory of Fusion Plasmas, 1996*, proc. of the *Joint Varenna-Lausanne International Workshop* (SIF Bologna, 1996) p. 453.

[6] M. Ottaviani and F. Porcelli, Phys. Plasmas **2** (11), 4104 (1995).

[7] E. Cafaro *at al.* submitted to Phys. Rev. Lett. (August 1997).

[8] P.A. Sweet, in *Electromagnetic Phenomena in Cosmic Physics*, edited by B. Lehnert (Cambridge Univ. Press, Cambridge, 1958), p. 123; E.N. Parker, J. Geophys. Res. **62**, 509 (1957).

NUMERICAL STUDY OF THE NONLINEAR SATURATION OF DOUBLE TEARING MODES

E.K. Maschke, M. Berroukeche, B. Saramito*

Association EURATOM-CEA sur la Fusion, D.R.F.C.
Centre d'Etudes de Cadarache
F-13108 Saint-Paul-lez-Durance CEDEX, France

Abstract: A systematic numerical study of the nonlinear saturation of double-tearing modes has revealed the existence of oscillatory solutions which bifurcate from a stationary nonlinear solution.

Recent tokamak experiments have shown evidence of improved confinement in regions of negative magnetic shear [1,2]. However such configurations may give rise to instabilities due to the presence of several rational surfaces having the same value of the safety factor q inside the plasma. In particular, such a situation may result in the appearance of the double-tearing instability, which can lead to sudden loss of confinement or to periodic saw-tooth oscillations. Experimentally, relaxations of the electron temperature have been observed and interpreted in terms of this instability [3].

Here we consider the idealized problem of the nonlinear evolution of the double-tearing instability in cylindrical geometry and with the restriction to a single helicity, thereby excluding the appearance of stochastic magnetic fields. We assume low beta and use the following reduced MHD equations

$$\frac{\partial w}{\partial t} = \nabla.(\mathbf{B}_0 \times \mathbf{V}.\nabla\mathbf{V}) + \rho_0^{-1}\left[R^2\mathbf{B}.\nabla(\mathbf{B}_0.\mathbf{J}) - R^2\mathbf{J}.\nabla(\mathbf{B}_0.\mathbf{B})\right] + \eta\Delta w + S_{mom} \tag{1}$$

$$\frac{\partial \psi}{\partial t} = \frac{\partial \Phi}{\partial \zeta} - R^2\nabla\zeta.\mathbf{V}\times\mathbf{B} + \eta R J_\zeta - RE_0(t) \tag{2}$$

$$w = \Delta\Phi \tag{3}$$

with

$$\mathbf{V} = \frac{\mathbf{B}_0}{B_0^2}\times\nabla\Phi \tag{4}$$

$$\mathbf{B} = \Im(r)\nabla\zeta - \nabla\psi\times\nabla\zeta \tag{5}$$

$$\mathbf{J} = \Delta_p^*\psi\,\nabla\zeta - \frac{1}{R^2}\nabla_p\frac{\partial\psi}{\partial\zeta} + \nabla\Im(r)\times\nabla\zeta \tag{6}$$

---

* Present address : Université Blaise Pascal (Clermont-Ferrand), Dépt. de Mathématiques Appliquées. F-63177 Aubière Cedex, France.

Here ζ is the coordinate along the cylinder axis (normalized with respect to $2\pi L$ with L the periodicity length of the cylinder), B_0 is the equilibrium magnetic field, w and Φ are respectively the vorticity density and the stream function of the perpendicular motion, the function $\Im(r)$ will be chosen constant.

We consider a class of equilibria with hollow current profiles given by [4]

$$J_{eq,\zeta}(r) = J_0(1-r^2)^p(1+kr^2)$$

where J_0 , p, k are constants. In the present work we choose p=3, k=9, with J_0 such that the safety factor in the center is q(0) = 3.8 . Fig.1 shows the corresponding profiles of current density and of q. We assume a time-independant resistivity profile:

$$\eta(r) = \eta_o(J_{eq,\zeta}(0)/J_{eq,\zeta}(r))$$

with η_0 = 1/S = const., and we take $E_o = \eta_o J_{eq,\zeta}(0)$. The viscosity is constant, $\nu = \eta_0$. For the description of perturbed solutions, all physical quantities are represented in the form

$$f(r,\theta,\zeta;t) = f_{0,0}(r,t) + \sum f_{m,n}(r,t)\exp(im\theta - in\zeta)$$

where the sum over m,n contains only terms such that m/n = 3.

We use the DEMA code [5] to investigate the asymptotic states reached by the nonlinear evolution of the instability in the limit $t \to \infty$. In order to investigate such states we proceed as follows. From general theorems of bifurcation theory [6] we know that for sufficiently low values of S the equilibrium is stable, and in fact is the only stable solution of the nonlinear equations. Therefore we start from a very low value of S such that the linear growth rate is zero. Increasing S we reach a critical value $S_c = 2.38 \cdot 10^3$ where the equilibrium becomes unstable and a stable stationary solution bifurcates from the equilibrium solution as shown in Fig.2. It is characterized by two stationary magnetic island chaines situated near the two magnetic surfaces where q =3, similar to the islands shown in Fig.3a. The solution changes slowly as S increases, in such a way that the average current density represented by the (m=0,n=0) component of J_ζ becomes more and more flat in the region between the two q=3 resonant surfaces. The stationary solution exists up to $S = 3.6 \cdot 10^4$, where a new type of asymptotic solution bifurcates. This new solution, which oscillates in time, has been investigated by the technique of Poincaré sections by placing an appropriate hyperplane in the phase space spanned by the mode amplitudes. We find that the phase space trajectory lies on a 2-dimensional torus in this phase space. Thus, the motion is determined by two independant frequencies.

In order to give an idea of the physical processes occurring during the oscillatory evolution of the nonlinear solution, we show in Fig.3 three snap-shots of the island structure. It can be seen that the evolution corresponds to periodic partial reconnection and

recovery of the island structure, with frequency of the order of the linear growth rate of the double-tearing mode.

As the present study was limited to cylindrical geometry and single-helicity perturbations, we have excluded the effects arising from stochastic magnetic fields. Such effects may play a role in the periodic crashes of the electron temperature observed in tokamaks [3].
Therefore, more realistic studies in toroidal geometry are necessary.

Acknowledgements: We thank M.R. De Baar, D.Edery and J.P. Morera for interesting discussions, and M-P. Valentin for assistance in the numerical work.

References

[1] X. Litaudon et al., Plasma Phys. Contr. Fusion 38 (1996) 1603.
[2] E. Mazzucato et al., Phys. Rev. Lett. 77 (1996) 3145.
[3] M.R. De Baar et al. , Phys. Rev. Lett. 78 (1997) 4573.
[4] D. Edery and J.P. Morera, Proceedings Internat. Workshop on Theory of Fusion Plasmas, Varenna 1996, p.369.
[5] R.E. Denton, E.K. Maschke, G. Urquijo, Proceedings Internat. Workshop on Theory of Fusion Plasmas, Varenna 1994, p.289.
[6] B.Saramito and E.K.Maschke in : Proceedings of the Cargese Workshop on "Magnetic Reconnection and Turbulence", M.A.Dubois et al. Eds., Editions de Physique, Orsay1985.

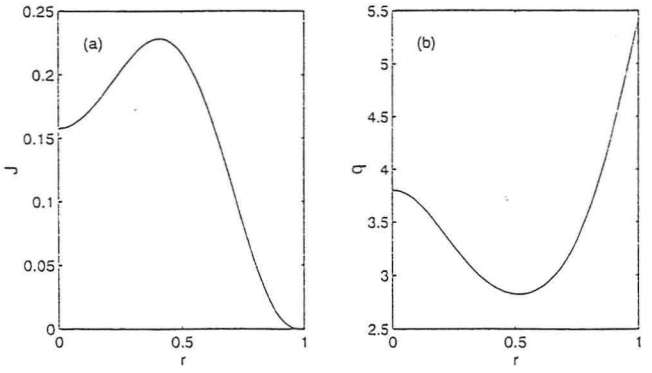

Fig 1. Equilibrium profiles ; (a) current density , (b) safety factor

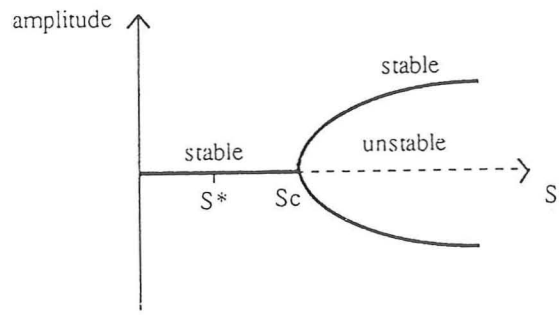

Fig 2. Bifurcation diagram

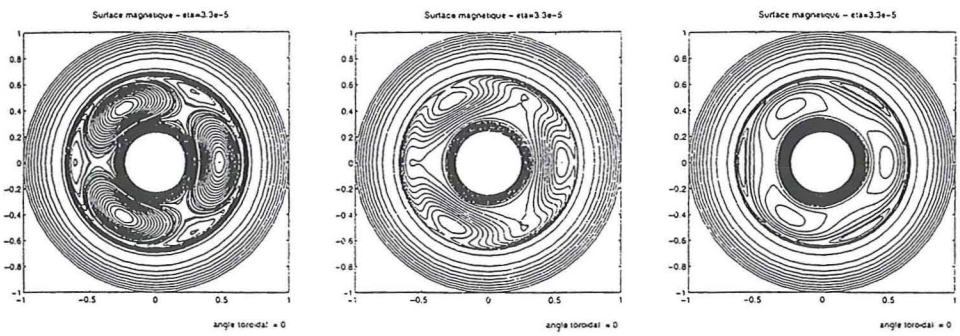

(a) (b) (c)

Fig 3. Periodic partial reconnection and recovery of island structure

Adaptive Mesh Refinement for Singular Current Sheets in Incompressible Magnetohydrodynamic Flows

Rainer Grauer and Christiani Marliani

Institut für Theoretische Physik I
Heinrich-Heine-Universität Düsseldorf
D-40225 Düsseldorf

The formation of current sheets in ideal incompressible magnetohydrodynamic flows in two dimensions is studied numerically using the technique of adaptive mesh refinement. The growth of current density is in agreement with simple scaling assumptions. As expected, adaptive mesh refinement shows to be very efficient for studying singular structures compared to non-adaptive treatments.

RESISTIVE TOROIDAL PLASMA SPECTRA AND POWER ABSORPTION FROM EXTERNAL FIELDS

R. G. STORER

DEPARTMENT OF PHYSICS, FLINDERS UNIVERSITY,
GPO BOX 2100, ADELAIDE 5001, SOUTH AUSTRALIA

Toroidal plasmas respond to external driving fields in a way which is determined by the coupling of these fields to the spectral modes of the plasma. We have extended the toroidal resistive magnetohydrodynamic spectral code, SPECTOR, to include the effects of external fields on tokamak-like plasmas. The code is capable of determining both the stable and unstable modes and also the response to helical applied fields with arbitary mode structure. Resistivity changes the continuous regions of the ideal MHD spectrum into a set of discrete eigenvalues lying along lines in the complex frequency plane with a spacing which is related to the inverse of the square root of the magnetic Reynolds number. The close spacing means that for a particular frequency there are a large number of modes contributing to the plasma response. Results will be presented which relate the spectral distribution to the plasma response and power absorption as a function of frequency and resistivity.

1 Introduction

The spectrum of a cylindrical plasma column for small resistivity is very dense. This applies even more so for a toroidal plasma. Thus, the response to external fields is probably not best calculated as a linear combination of normal modes. Even so, the relation between the spectrum and the plasma response as a function of frequency may give some insights. The physical situation that we consider is that of a plasma being driven by externally imposed fields and we model that situation by using the linearised resistive MHD equations. The inclusion of resistivity will provide a dissipative mechanism which changes the character of the normal mode spectrum from an ideal continuous, real (but singular) spectrum to a discrete spectrum which lies along characteristic lines in the lower half of the complex frequency plane (Ryu and Grimm [1, 2]; Dewar and Davies [3, 4]; Kerner *et al* [5] - [7]; Lortz and Spies [8]; Storer [9]; Schellhase [10]; Storer and Schellhase [11] and Schellhase and Storer [12]). The spacing of the spectral points along the lines is proportional to $\eta^{1/2}$, and η (the normalised resistivity) is small for high temperature plasmas, so at any particular driving frequency we could expect a contribution from a large number of modes. Studies of this type have been carried out for a cylindrical plasma column by Poedts, Kerner and Goosens [13] with particular emphasis on the excitation of Alfvén waves.

The rationale for these studies is twofold. Firstly, the resonant absorption of power from external coils may heat the plasma. This possibility has been studied theoretically and experimentally for some time (REFS). Secondly, measurement of the plasma reponse to external fields may be related directly or indirectly to key aspects of the properties of the plasma and hence act as a diagnostic tool.

2 MHD equations

The toroidal resistive MHD code SPECTOR (Schellhase [10]; Storer and Schellhase [11] and Schellhase and Storer [12]) has been developed to find the complete (stable and unstable) spectrum of a tokamak-like plasma. This code solves the linearised resistive equations for compressible MHD.
The units have been chosen so that the time scale is the toroidal Alfvén transit time,

$$\tau_A = \frac{a\sqrt{\mu_0 \rho}}{B_0},$$

where a, the plasma radius, and B_0, the magnitude of the equilibrium toroidal field at the magnetic axis, are used as length and magnetic field scales.
SPECTOR performs a poloidal Fourier decomposition of the equations and takes all variables to be proportional to $\exp(-in\phi - i\omega t)$ where n is the toroidal mode number. A finite difference analysis of the equations leads to a matrix eigenvalue equation of the form

$$-i\omega \mathcal{R}\tilde{u} = \mathcal{P}\tilde{u},$$

where $\mathcal{R}$ and $\mathcal{P}$ are large block-tridiagonal matrices. This equation involves the (vector) function $\tilde{u}$ which is a combination of the Fourier coefficients of the perturbed magnetic vector potential, the velocity vector and scalar potential and the pressure.
We have modified SPECTOR to model the interaction with external influences (magnetic fields, due to external coils, or pressure perturbations) by resetting the equations to the form

$$(\mathcal{P} + i\omega\mathcal{R})\,\tilde{u} = \tilde{d},$$

where the vector $\tilde{d}$ is a driving term on the boundary of the plasma with a constant real frequency ω. By adjusting the non-zero terms in $\tilde{d}$ one can drive the plasma via e.g. the magnetic field perturbation or the pressure perturbation for various poloidal modes.

3 Results

The spectrum for a cylindrical plasma column with a non-constant current lies along a series of lines in the complex frequency plane (Ryu and Grimm [1, 2]; Dewar and Davies [3, 4]; Kerner *et al* [5] - [7]; Storer and Schellhase [11] and Schellhase and Storer [12]). This shape points towards the end points of the Alfvén continua:

$$\omega_A(\psi) = \frac{\kappa}{nq(\psi)}|m - nq(\psi)|.$$

with ψ being a normalised flux coordinate which takes on the values 0 at the magnetic axis and 1 at the plasma edge, ($\kappa = \frac{na}{R}$.) The ideal continua corresponding to various

poloidal modes may or may not overlap, depending on the values of the safety factor at the magnetic axis and the edge. We would expect that the response of a resistive plasma, as a function of the frequency of the applied field will be dominated by the modes whose spectral values are nearest the real axis but will also have a shape which is influenced by the other modes.

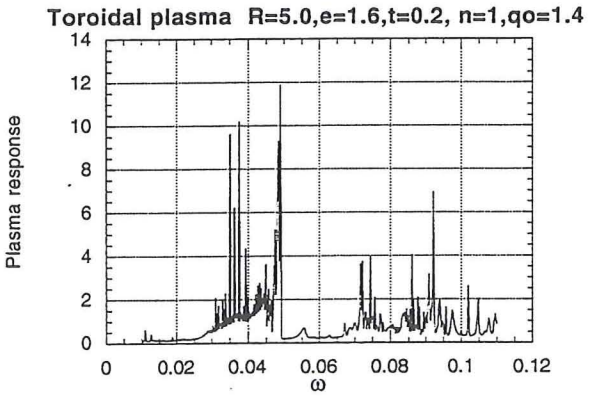

Figure 1

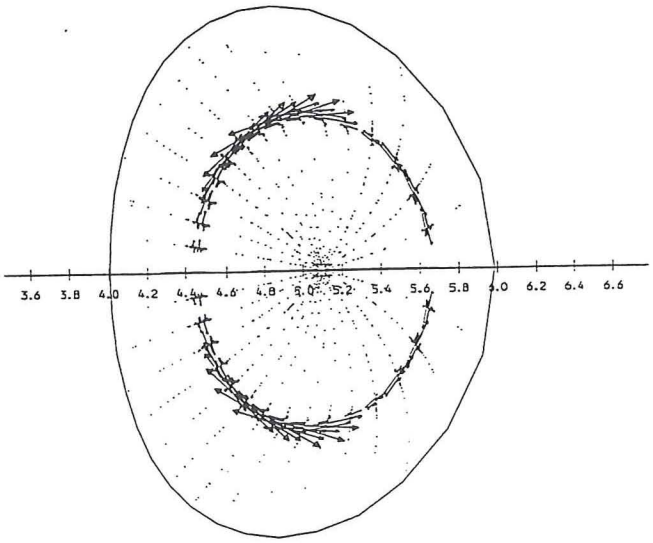

Figure 2

As an example Figure 1 shows the response of a toroidal plasma, with $q_0 \approx 1.4$, $q_s \approx 2.4$ and $\kappa \approx 0.2$ with ellipticity $= 1.6$ and triangularity $= 0.2$. This case has strong poloidal coupling, with substantial $l = 2$ components in the vicinity of $\omega \approx 0.04$. The response magnetic field is strongly peaked about the resonant surface, as is illustrated by Figure 2. Unfortunately, the aim of using these response functions as diagnostic indicators has not been advanced by these calculations, and their complexity seems to be primarily associated with the complexity of the resistive spectrum.

Acknowledgements

The author acknowledges the work of Dr Anthony Schellhase in the development of the code SPECTOR. This work was supported by the Australian Research Grants Scheme, AINSE and the Australian National University Supercomputing Facility.

References

[1] Ryu,C.M. (1983) *Ph.D Dissertation*, Princeton University.

[2] Ryu,C.M. and Grimm,R.C. (1984) *J.Plasma Physics.* **32**, 207

[3] Dewar,R.L., and Davies,B. (1984) *J. Plasma Physics* **32**, 443

[4] Davies,B. (1984) *Phys. Lett.* **100A**, 3

[5] Kerner,W., and Lerbinger,K. (1986). *Phys. Fluids* **29**, 9

[6] Pao,Y.P. and Kerner,W. (1984) *Phys. Fluids* **28**, 287

[7] Kerner,W., Lerbinger,K., Gruber,R., and Tsunematsu, T. (1985) *Com. Phys. Comm.* **36**, 225

[8] Lortz,D., and Spies,G.O. (1984) *Phys. Lett.* **101A**, 7

[9] Storer,R.G. (1983) *Plasma Physics* **25**,1279

[10] Schellhase A.R. (1994) *Ph.D. Dissertation*, The Flinders University of South Australia.

[11] Storer,R.G. and Schellhase,A.R.(1995) *Physica Scripta* **T60**, 57

[12] Schellhase,A.R. and Storer,R.G. (1996) *J. Comp. Phys.* **123**, 15

[13] Poedts,S., Kerner,W. and Goosens,M. (1989) *J. Plasma Phys.* **42**, 27

Ideal MHD stability of plasmas with toroidal, helical and vertical field coils

A. Ardelea, W.A. Cooper
Centre de Recherche en Physique des Plasmas (CRPP/EPFL), Association Euratom-Confederation Suisse, Lausanne, Switzerland

Abstract: A simple configuration consisting in a set of toroidal, helical and vertical field coils is used to calculate free boundary equilibria with nonzero plasma current and approximately helical plasma boundary. The amount of helical boundary deformation is controlled by the ratio of the current in the helical field coils to the current in the toroidal field coils. When this ratio is increased the $(m,n) = (2,1)$ external kink is stabilized at $\beta \simeq 1\%$ for inverse rotational transform profiles in the region $q < 2$.

1. Introduction

In a previous work [1], we investigated the global ideal magnetohydrodynamic (MHD) stability of plasmas with a prescribed (fixed) helical boundary deformation and non vanishing toroidal current with respect to the (m,n) external kink modes $n = 1,2,3$ and $m = n+1$. $L = 2$, 3 single helicity and mixtures (of both) configurations were studied by systematically varying parameters such as the type and amount of helical boundary deformation, the aspect ratio, the number of equilibrium field periods, the toroidal current density and the pressure profiles. Once these parameters were fixed, sequences of equilibria differing in the amount of helical boundary deformation and such that $1 \leq q \leq 2$, were calculated with the fixed boundary version of the VMEC [2] code. The stability analysis was performed with the TERPSICHORE [3] code. It was shown that increasing the helical boundary deformation leads to the stabilization of (m,n) external modes with $n = 1,2,3$, $m = n+1$ at values of $\beta \simeq 1 - 2\%$. These modes are unstable in the circular tokamak at the same value of β. If δ is a measure of the plasma boundary deformation, then windows of stability $[\delta_{min} \quad \delta_{max}]$ may exist and depend strongly on the equilibrium parameters.
We reconsider here the study of the $(2,1)$ mode with equilibria calculated with a free boundary code. The aim is twofold:
1) to test how difficult it is to obtain free boundary equilibria with single helicity bounadry deformation at nonzero plasma current and positive β.
2) to check the results of the fixed boundary calculations in the sense that we search for stability windows when the amount of current in the helical coils is monotonously increased.

2. Equilibrium calculations

The calculations of the free boundary equilibria was performed in several steps. First, a system of coils producing a toroidal (TF), a vertical (VF) and a helical field (HF) is designed; the helical conductors are wound on a torus according to the following winding law

$$v = \frac{1}{N_{per}}(\tilde{u} + \alpha sin(\tilde{u})) - \frac{l}{L}\frac{2\pi}{N_{per}} \qquad \tilde{u} = u + 2\pi\frac{l-1}{L} \tag{1}$$

with u and v the geometrical poloidal and toroidal angles of a particular coil segment, N_{per} the number of field periods, $l = 1,..L$ an index specifying a particular coil and α the pitch modulation coefficient of the helical coils. The magnetic field $\vec{B}$ is determined from the Biot-Savart law and a field line tracing code is used to find the coil geometrical parameters and currents such as to obtain closed helical flux surfaces in vacuum. The field produced by these external currents is given then as input to the free-boundary version of the equilibrium code VMEC [4]. At finite β and nonzero

plasma current, the plasma cross section is distorted; the currents in the coils are adjusted until the plasma cross section recovers an approximate helical shape.
Several types of coils systems (stellarator-, heliotron- and torsatron-like) were considered. We illustrate the results with the example of a L=2 stellarator-like configuration ($N_{per} = 4$) with 16 TF coils two piars of 2 HF coils and one pair of VF coils. Sequences of equilibria were calculated with the following parameters

$$R_0 = 5.0\,[m] \;\; r_t = 1.8\,[m] \;\; r_h = 1.4\,[m] \;\; r_v = 7.0\,[m] \;\; z_v = \pm\, 2.1\,[m] \;\; \alpha = -0.150$$
$$I_t = -1.6 \times 10^5 [A] \quad I_v = 1. \times 10^4 [A] \qquad (2)$$
$$\beta = 1\% \text{ , parabolic pressure profile , } J'(s) \sim (1 - s^{20})^8$$

The subscripts $_t$, $_h$ and $_v$ refer to the TF, HF and VF coils respectively, R_0 is the major radius, r and z are the coils radii and verical positions, I refers to the coils currents and J' is the toroidal plasma current density. The equilibria belonging to one particular sequence differ in the amount of HF coil current I_h. The coil system is illustrated in Fig.1 and plasma cross sections for two values of I_h are shown in Fig.2. In this case the plasma current was $J = 1.27 \cdot 10^5 [A]$. If the conventional (tokamak) definition of normalized beta $\beta_N = \beta / I_N$ with $I_N = J\,[MA]/(a\,[m]\; B_0\,[T])$ where a and B_0 are the averaged minor radius and the magnetic field intensity on the axis respectively, is used we obtain $\beta_N \sim 4 - 6$.

3. Stability calculations

Let $(m_e, N_{per} n_e)$ and (m_l, n_l) represent the Fourier components in Boozer coordinates (TERPSICHORE) of the equilibrium and perturbation quantities respectively. As the equilibrim configurations has several field periods, a partial decoupling of the perturbation components occurs, depending on the values of the toroidal mode numbers. The coupling between two perturabtion components (m_{l1}, n_{l1}) and (m_{l2}, n_{l2}) is nonzero if the following relations hold between the mode numbers: [1]$m_e = m_{l1} \pm m_{l2}$ and $N_{per} n_e = n_{l1} \pm n_{l2}$. This means that the perturbation toroidal mode numbers are distributed in families of non-interacting modes.
If the mode studied is $(m, n) = (2, 1)$ and if $N_{per} = 4$, the contribution of the coupling $(m_e, N_{per} n_e) \times (2, 1) \times (m_l, n_l)$ to the potential energy δW_p is nonzero only if $n_l = 3, 5, 7, 9$, etc. When the numerical study is carried in the parameter region corresponding to $1 \leq q(s) \leq 2$, then a particular attention should be given to those (m_l, n_l) perturbation components which are resonat i.e. $m_l > n_l > n = 1$. Depending on the q profile, these components can be destabilized and could lead a priori to important couplings with $(2, 1)$. The contribution of a particular $(m_{l1}, n_{l1}) \times (m_{l2}, n_{l2})$ coupling to δW_p is determined by the amplitude $A^{eq}_{me,ne}$ of the $(m_e, N_{per} n_e)$ equilibrium coupling term - c.f. [1]. Typical equilibrium quantities appearing in these couplings are $\sqrt{g}_{m_e, n_e}$ (the Jacobian), $|B^2|_{me,ne}$ and in general combinations between the coefficients of the metric tensor [5]. If $N_{per} = 4$ the coupling between $(2, 1)$ and (m_l, n_l) resonant components with $n_l = 3, 5$ requires $(m_e, N_{per} n_e)$ components with $n_e = 1$ and $m_e > 4$; the coupling with resonant (m_l, n_l) having $n_l = 7, 9$ requires $n_e = 2$ and $m_e > 8$.
The systematic study performed in [1] for fixed helical boundary shapes, showed that the $A^{eq}_{me,ne}$ amplitudes of the $(m_e, N_{per} n_e)$ components involved in couplings between $(2, 1)$ and resonant (m_l, n_l) are negligible (compared to the dominant equilibrium components) for any equilibrium quantity ($\sqrt{g}_{m_e, n_e}$, $|B^2|_{me,ne}$, etc) and for any boundary deformation δ. If the free boundary equilibrium has an approximate helical boundary shape, the above mentioned property remains valid - see Fig.3. Thus, the study of a particular mode would not require the inclusion in the calculations of the resonant perturbation components (n and $n_l \in$ the same family). This hypothesis was verified in the sense that the ratio of any of the $(m, n) \times (m_l, n_l)$ coupling contributions ((m_l, n_l) resonant) to δW_p to the dominant contributions to δW_p is very weak i.e. $\leq 10^{-4}$.
At the beginning of the equilibrium sequence presented in Fig.4 i.e for $I_h = 0.6 \times 10^5\,[A]$ the q profile

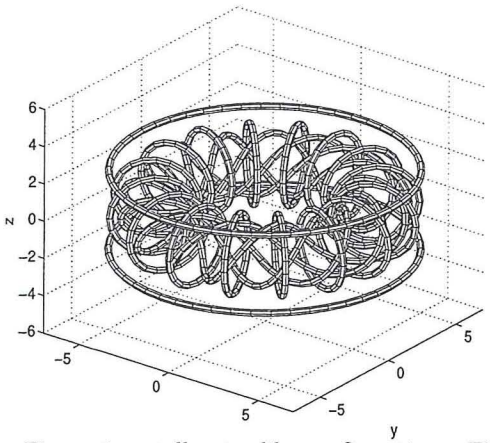

Figure 1 : *stellarator-like configuration with 16 TF coils, two pairs of 2 HF coils and one pair of VF coils*

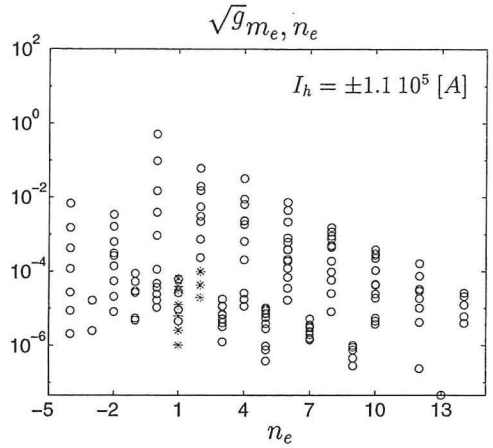

Figure 3 : $\sqrt{g}_{m_e,n_e}$ *amplitudes for the free boundary equilibrium described by Eq.(2) The x-axis corresponds to the* n_e *equilibrium mode number. The points marked with '*' represent the equilibrium components responsible for couplings between the* $(2,1)$ *mode and the* (m_l, n_l) *perturbation components with* $m_l > n_l > 1$ *(only the* $n_e \leq 2$ *i.e.* $n_l \leq 9$ *are shown). All other equilibrium components are marked with 'o'.*

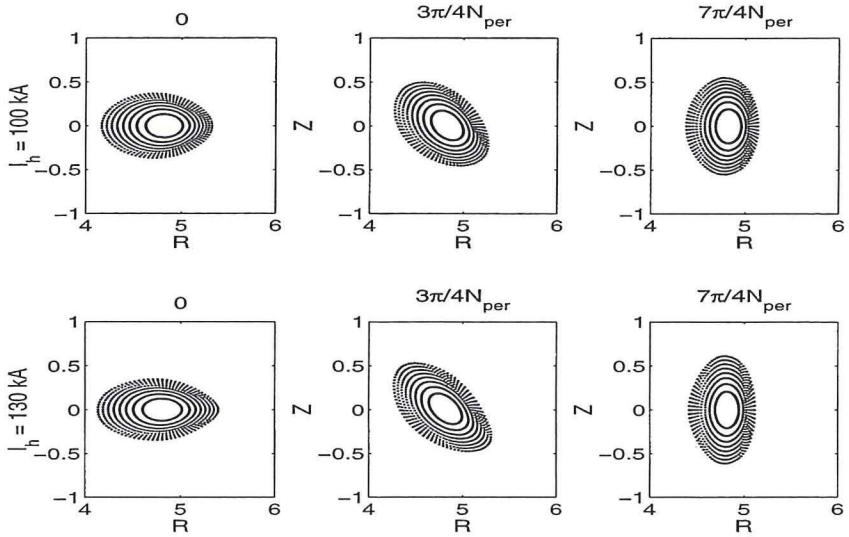

Figure 2 : *Free boundary equilibrium flux surfaces produced with VMEC. Each column represents the cross sections at one toroidal angle and each of the two rows are associated with one value of* I_h. *The coil system is represented in* Figure 1. *The equilibrium parameters are those of Eq.(2); the two equilibria correspond to the points just before and just after the stability window in Fig.4*

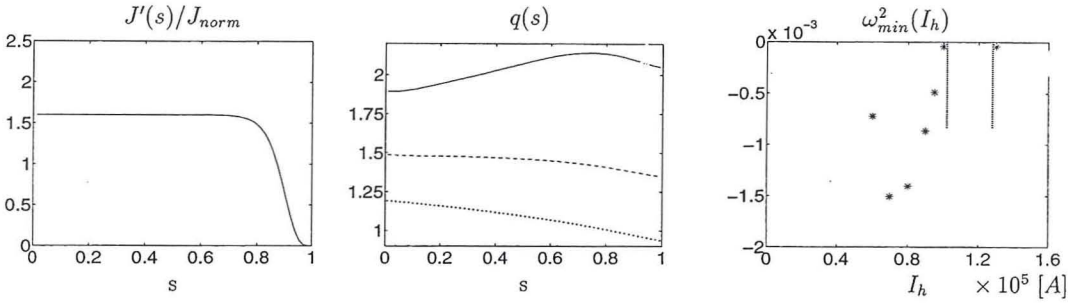

Figure 4 : *Study of the (2,1) mode:* (a) *plasma current density profile,* (b) $q(s)$ *profile,* (c) *sequence of most unstable eigenvalues* $\omega^2_{min}(I_h)$ *when the coil geometry and plasma parameters are given by Eq.(2) and the lines that follow. The aspect ratio is* $1/\epsilon \simeq 10$ *and the toroidal plasma current is* $J = 1.27 \cdot 10^5[A]$. *The inverse rotational transform profile is represented for* $I_h = 0.60 \times 10^5 A$ *(-),* $1.0 \times 10^5[A]$ *(- -) and* $I_h = 1.30 \times 10^5[A]$ *(·). The stability window is delimited by the two vertical lines and is associated with values of* I_h *between* $1 \times 10^5[A]$ *and* $1.3 \times 10^5[A]$

is such that the $(2,1)$ component is already destabilized. The effect of increasing I_h is to lower the inverse rotational transform. The $(2,1)$ component is strongly destabilized and becomes the dominant perturtbation component - we speak then about the $(2,1)$ mode. The most unstable eigenvalue $\omega^2_{min}(I_h)$ decreases until a minimum is attained, after which it starts increasing again; this is the stabilizing effect associated with an increasing (near)helical boundary deformation. Depending on the equilibrium parameters, a stability window $I_{stb} = [I_h^{min}, I_h^{max}]$ may appear in the sense that all $(m,1)$ components with $m > 1$ are stable and the $(1,1)$ component is not yet destabilized. Fig.4 (c) illustrates a stability window bounded by $I_h^{min} \simeq 1.0 \times 10^5[A]$ and $I_h^{max} \simeq 1.3 \times 10^5[A]$.
When the resonant perturbation components i.e. $(m_l,3)$ with $m_l > 3$, $(m_l,5)$ with $m_l > 5$, etc are taken into account and the stability calculations are performed again for those equilibria in the stable window, then several unstable eigenvalues may appear for each $I_h \in I_{stb}$. Each of these eigenvalues is associated to one of the resonant (m_l,n_l) modes (component whith largest amplitude). We systematically checked each of the $(2,1) \times (m_l,n_l)$ and $(1,1) \times (m_l,n_l)$ coupling contribution to δW_P and found that they are indeed negligible i.e. $< 10^{-4}$ compared to the dominant contributions.

4. Aknowledgements

This work was partly supported by the Swiss National Science Foundation.

References

[1] A.Ardelea, W.A.Cooper, "External kinks in plasmas with helical boundary deformation and non zero toroidal current", to appear in Physics of Plasmas, (scheduled for Oct. 1997)

[2] S.P.Hirshman, U.Schwenn, J.Nührenberg, J. Comput. Phys. **87**, 396, (1990)

[3] D.V.Anderson, W.A.Cooper, R.Gruber, S.Merazzi, U.Schwenn, Int. J. Supercomp. Appl. **4**, p.34 (1990)

[4] S.P.Hirshman, W.I.van Rij, P.Merkel, Comp. Phys. Communications, **43**, 143 (1986)

[5] W.A.Cooper, Plasma Physics and Controlled Fusion, **34**, No 6, 1011, (1992)

COMPARISON OF HIGH CURRENT DISRUPTION LIMIT IN ELONGATED PLASMAS IN TCV WITH IDEAL AND RESISTIVE MHD MODELS[†]

O. Sauter, F. Hofmann, H. Reimerdes, I. Furno, R. Behn, M. J. Dutch, Y. Martin, J.-M. Moret, C. Nieswand, Z. A. Pietrzyk, A. Pochelon

Centre de Recherches en Physique des Plasmas
Association EURATOM-Switzerland
PPB - Ecublens, 1015 Lausanne, Switzerland

Abstract

Elongated plasmas up to κ=2.5 have been obtained in the Lausanne Tokamak TCV[1]. For $\kappa < 2.3$, the normalized current limit, I_N=I[MA]/a[m]B[T], increases with elongation and is limited by the standard ideal limit at q_a=2. However for κ>2.3, a disruption occurs at larger values of $q_a(\kappa)$, such that the current limit stays about constant at $I_N \approx 3$[1]. The modes observed at the disruption are typically m/n=2/1 and 3/2 modes. The disruption limit is consistent with the prediction of the n=1 ideal MHD limit presented in Ref.2 for analytical plasma shapes. We have computed the ideal and resistive MHD limit for the actual experimental plasma shapes and profiles. We find that the shots which disrupted are indeed very close to the ideal n=1 external kink β-limit. We also see that, including resistivity, the 4/3, 3/2 and 2/1 modes are unstable even well below this limit, which agrees with the experimental data. For $2.5<\kappa<3$, we have varied the profiles over a wide range and our results confirm the prediction of Refs.2 and 3, which is that only by keeping q_a just above 3 and decreasing the plama inductance, l_i, one can find stable configurations.

Introduction

The upper β-limit, $\beta = 2\langle p \rangle_{vol}/\mu_0 B_0^2$, in an axisymmetric plasma is determined by the ideal MHD limit and is quite well described by the Troyon limit[4]:

$$\beta\ [\%] = c_T\ I_N = c_T\ I\ [MA]\ /\ (a\ [m]\ B\ [T]\ ) \qquad (1)$$

The effective value of the Troyon factor c_T is typically around 2.5 to 4 depending on the pressure and current profiles. The β-limit described by Eq.(1) is not valid for reversed shear profiles, where plasma rotation and wall stabilization effects are necessary to obtain stable high-β plasmas. At very high elongation, which maximizes the plasma current for a given minor radius a, and near the plasma current limit, Eq.(1) is not valid either as has been shown in Ref.2. Therefore, to determine how much we can really increase β when increasing the elongation κ is one of the main objectives of the TCV experiment (Tokamak Configuration Variable)[5]. In the last campaign, highly elongated discharges (κ>2.3) have been obtained, many of which disrupted when approaching a given normalized current $I_N \approx 3.05$[1], close to the prediction of Ref.2. In this work, we compute the ideal and resistive β-limits using the plasma shape and profiles of TCV discharges. As is shown below, we recover the results of Ref.2, and those of Ref.3 for higher κ. Moreover we find that the 4/3, 3/2 and 2/1 modes are the most unstable resistive modes, in agreement with experimental data.

Experimental results and comparison with numerical results

The experimental high elongation discharges are summarized in Figs.1 and 2. For κ=2.3, the current limit, at zero β, is equal to $I_N \approx 2.85$, determined by $q_a \geq 2$.

[†]This Work is supported in part by the Swiss National Science Foundation

However at higher elongation all discharges disrupt for $I_N \geq 3$. This had already been predicted at the time when TCV was designed[2], as shown by the solid lines in Fig.1. In that case, two plasma shapes were analyzed in more detail at κ=2.5, a Racetrack and a D-shaped plasma. We see that the β-limit does follow Eq.(1) at low I_N, however decreases much below the q_a=2 limit. As the discharges in Fig.1 are all in ohmic regime, β is not a free parameter and is typically around 2.5% as seen in Fig.1. Therefore the experimental points are near the D-shape limit, even though the actual shape is closer to a Racetrack, with however a non-negligible triangularity.

We have studied in more detail two shots at $\kappa \approx 2.5$, one which did not disrupt, 12413, and one which did disrupt, 12414. The time traces are shown in Fig.3, where one sees that, in the shot 12414, first a 4/3 mode occured, causing a minor disruption, then a 3/2 and finally a 2/1 mode locked and caused the disruption. This sequence is typical with or without the occurence of the 4/3 mode. In the shot 12413, two 4/3 modes occured, causing two minor disruptions, as seen on the SXR measurement, but as no 2/1 mode appeared the discharge survived. One can see that κ, I_N and β were all slightly lower in the shot 12413. These two discharges are quite typical of high elongation ohmic discharges.

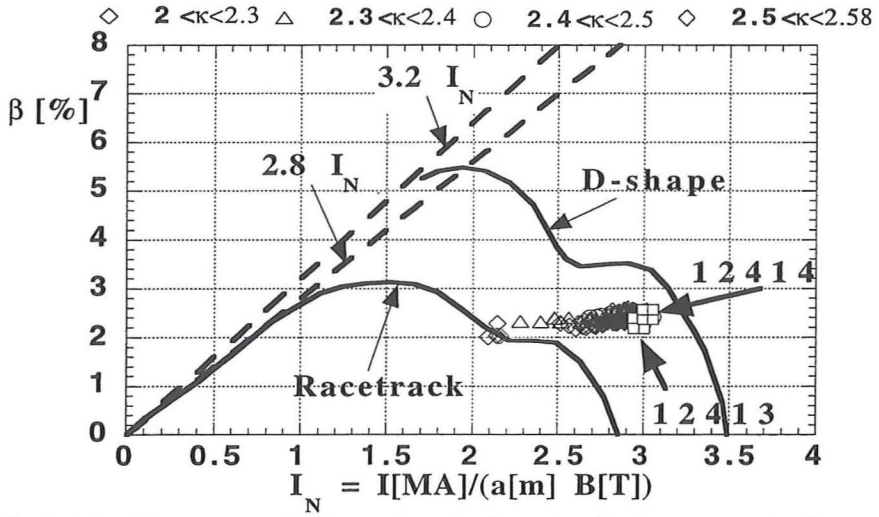

Fig.1: Ideal limit for a D-shaped and a Racetrack plasmas as in Fig.4 of Ref.2. The symbols show TCV results for κ>2.

The equilibria 12413 at t=0.76s and 12414 at t=0.794s have been reconstructed using LIUQE[6] and coupled to CHEASE[7]. Then we have used ERATO[8] and KINX[9] to study the ideal limit, and MARS[10] and a cylindrical Δ' calculation to study the resistive MHD modes. All these codes are coupled to CHEASE. As q_a is relatively low, to have stable n=0 plasmas, the inversion radius is relatively large. Therefore it is difficult to separate the stability limit of the internal 1/1 kink mode from the external kink limit. This is why we have flattened the q profile such as to keep $q \geq 1.05$ everywhere, while keeping l_i equal to the experimental value ($\approx$0.6-0.65). Note that the central q profile is not accurately measured in TCV. Therefore we have varied the current and pressure profiles, around the experimental profiles, to take into account the experimental

uncertainties. For both the 12413 and 12414 discharges we find the same ideal β-limit, shown as a hatched region in Fig.2. The marginal β is not a line as it depends slightly on the profiles. We see that the shot 12414, as well as all the shots with $I_N \geq 3$ which disrupted, are very close to the ideal limit, whereas the shot 12413 is further away, consistent with the experiment. However the modes grow on a resistive time-scale and we have checked that the ballooning and n=2, n=3 kink β-limits are much higher.

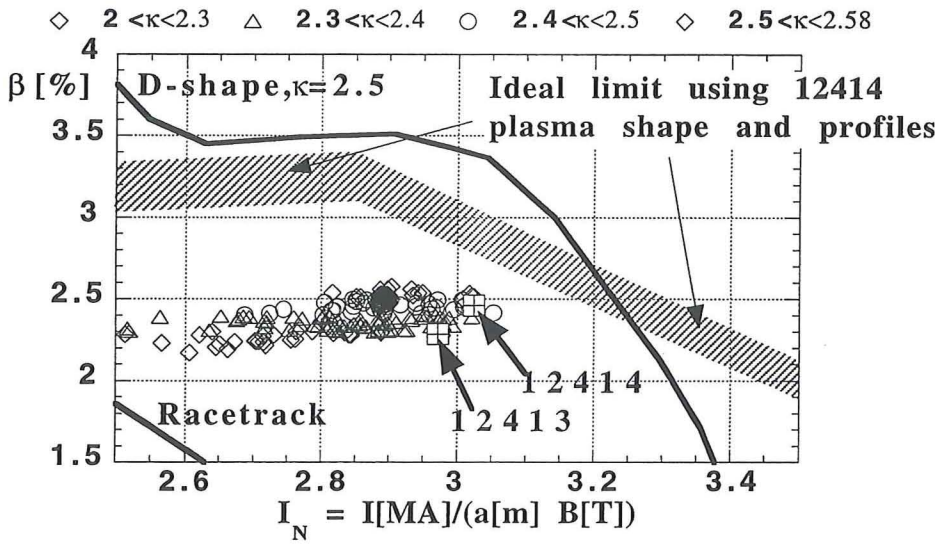

Fig.2: The symbols show TCV results for different elongation. All shots with $I_N \geq 3$ disrupted. The hatched region represents the ideal marginal limit, while the region underneath is unstable to resistive modes.

Therefore we have analyzed these equilibria with the resistive MHD code MARS and found both the 12413 and the 12414 discharges unstable to n=1, 2 and 3, with the largest growth rate for the n=1 mode consistent with the experiment. The resistive unstable region, in Fig.2, is the whole region underneath the ideal limit down to very low β as it depends mainly on the current profile. We have also computed the Δ' values, using the experimental q profiles and a cylindrical approximation. We find the 4/3, 3/2 and 2/1 unstable, whereas the other modes, e.g. 5/4, 5/2, 4/2 and 3/1, are stable. This is consistent with the experiment, as in all the discharges analyzed so far, only 4/3, 3/2 and 2/1 modes have been observed.

In order to increase the operational space, we tried to change the plasma shape and to use different current profiles, reversed shear and low l_i. We find, as first mentioned in Ref.2 and confirmed in Ref.3, that only by keeping $q_a \geq 3$ and reducing I_N as much as possible, one obtains stable configurations for κ up to 3. This reduces l_i and is therefore good for the n=0 stability as well, but reduces the β-limit to a value below 2-3%. The optimal current profiles are very similar to profile (c) in Fig.3a of Ref.2, such that one has finite shear in the center and low shear up to the q=2 surface and l_i is below 0.5. These types of current profiles

will probably require the help of the ECRH system, which is now available on TCV, in order to be able to obtain stable κ=3 discharges.

Conclusion

We have shown that the high elongation, κ>2.3, discharges in TCV which disrupt are at or very close to the ideal MHD limit. We have also shown that the modes occuring just before the disruption or causing minor disruptions are conventional resistive modes, even though the modes with large island width can be further destabilized by the neoclassical perturbed bootstrap current. In order to reach elongations larger than 2.5, while being vertically stable, one will need to control the current profile to decrease l_i below 0.5.

References

1. F. Hofmann et al, in Proc. of the 24th EPS Conference, Berchtesgaden, Germany, June 1997.
2. A. D. Turnbull et al, Nucl. Fus. 28 (1988) 1379.
3. G. Eriksson et al,Plasma Phys. (Proc. 1992 Int. Conf. Innsbruck) 16C, Part I, EPS(1992) 343.
4. F. Troyon et al, Plasma Phys. Controll. Fus. 26 (1984) 209.
5. F. Hofmann et al, Phys. Control. Fusion **36** (1994) 3277.
6. F. Hofmann et al, Nucl. Fus. **28** (1988) 1871.
7. H. Lutjens et al, Comput. Phys. Commun. **97** (1996) 219
8. R. Gruber et al., Comput. Phys. Commun. **21** (1981) 323.
9. L. Degtyarev et al, Comput. Phys. Commun. **103** (1997) 10.
10. A. Bondeson et al, Phys. Fluids B **4** (1992) 1889.

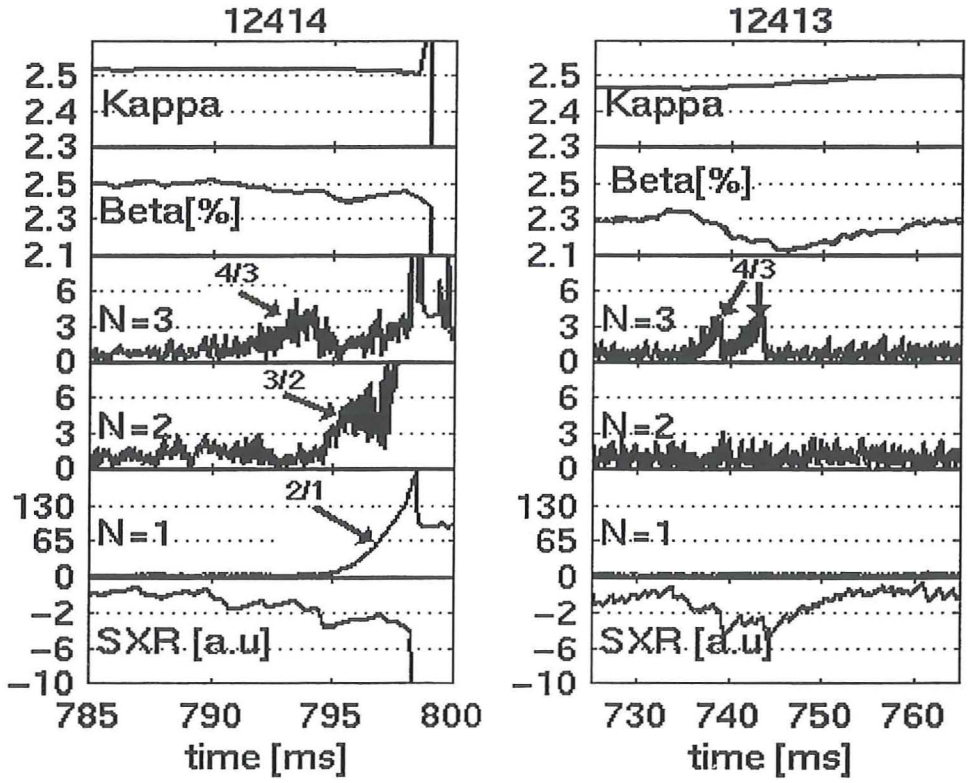

Fig.3: Time traces for shots 12414 and 12413. The 12414 disrupted due to a 2/1 locked mode very near the ideal limit, as shown in Fig.2.

Operational Limits in Tokamaks

André Rogister[1], Ding LI[2]
[1] Institut für Plasmaphysik, Forschungszentrum Jülich GmbH, EURATOM Association
Trilateral Euregio Cluster, D-52425 Jülich, Germany
[2]Institute of Plasma Physics, Chinese Academy of Sciences, Hefei 230031,
The People's Republic of China

Abstract. The operation range of tokamaks is limited at low and high densities by yet unknown mechanisms and at high β by ideal MHD. Experiments suggest that the low density limit is linked to the ratio plasma frequency/gyrofrequency. It is shown that the condition $\omega_{pe}^2 \geq \alpha_L \Omega_e^2$, $\alpha_L \equiv$ constant, would lead, together with the Hugill-Greenwald high density limit, to an *absolute* upper magnetic field limit and an *absolute* upper density limit depending only on the connection length qR and the elongation K; an *absolute* upper current limit depending only on K and a/qR (a being the plasma radius) would also occur. The standard scaling of the β limit would then lead to an *absolute* upper temperature limit. The low density limit might be the consequence of cyclotron radiation becoming a collective emission process when coherent plasma oscillations are excited at the frequencies $\omega = \pm\Omega_e$

It is well known that the operation range of tokamaks is limited at high densities by a law of a heuristic nature, the Hugill-Greenwald limit [1,2], of the form

$$\overline{N}_e \leq K\overline{\overline{J}}_\varphi \qquad (10^{20} m^{-3}; MAm^{-2}) \qquad (1)$$

where K is the plasma elongation; the particle density $\overline{N}_e$ and the toroidal current density $\overline{\overline{J}}_\varphi$ are here expressed in $10^{20} m^{-3}$ and MAm^{-2}, respectively; a bar refers to a line average and two bars to a volume average. Inequality (1) may be rewritten as

$$\overline{\overline{N}}_e \leq 10 K g f^{-1} (B_{\varphi,0} / 2\pi q_\psi R_0) \qquad (10^{20} m^{-3},\ tesla,\ m). \qquad (2)$$

with the help of the toroidal component of Ampere's equation; here $f = \overline{N}_e / \overline{\overline{N}}_e$, the subscript "0" refers to the values on the magnetic axis and

$$g \cong (1+K^2)/2K \qquad (3)$$

for elongated cross–sections [3]; q_ψ is the safety factor on the magnetic surface $\psi(\vec{r}) = const$.

A low density limit also appears in tokamak operation. As it has been observed in all operating devices that the electron plasma frequency $\omega_{pe} = (4\pi N_e e^2 c^2 / m_e)^{1/2}$ is always of the order of the electron cyclotron frequency $\Omega_e = -eB/m_e$, we shall request

$$\overline{\overline{\omega_{pe}^2}} \geq \alpha_L \Omega_{e,0}^2 \qquad (4)$$

where α_L is a numerical coefficient. The conclusions we shall reach of course hold only insofar as the above criterion for the minimum density is valid (and as the profiles assumed later on are verified).

According to Ineqs. (2) and (4), the upper and lower density limits are proportional to B and B^2 respectively. The operation range has consequently the form shown in Fig. 1, being limited by the intersection points ($\overline{\overline{N}}_e = 0$, $B_0 = 0$) on one side and ($\overline{\overline{N}}_e = \overline{\overline{N}}_{e,MM}$, $B_0 = B_{0,MM}$) on the other side; here

$$\overline{\overline{N}}_{e,MM} = 26K^2 g^2 f^{-2} \alpha_L^{-1} (q_\psi R_0)^{-2} \qquad (10^{20} m^{-3},\ m) \qquad (5)$$

and

$$B_{0,MM} = 16.4\, Kgf^{-1} \alpha_L^{-1} (q_\psi R_0)^{-1}. \qquad (tesla,\ m). \qquad (6)$$

$B_{0,MM}$ can easily be transformed into an absolute limit on the plasma current:

$$I_{MM} = 82 f^{-1} \alpha_L^{-1} (aKg / q_\psi R_0)^2, \qquad (\mathrm{MA}) \qquad (7)$$

a being the plasma radius. The upper and lower density limits are estimated in Table I for five tokamaks assuming $N = N_0 [1-(r/a)^2]$ (hence $f = 4/3$), $q_\psi = 3.1$ and $\alpha_L = 0.125$:

	R_0	a	K	g	B_0	$\overline{\overline{N}}_{MAX}$	$\overline{\overline{N}}_{MIN}$	B_{MM}	I_{MM}	$\overline{\overline{N}}_{MM}$	$\overline{\overline{T}}_{MAX}$
TFR	0.98	0.22	1	1	4	1.6	0.19	32.4	2.58	12.7	6.9
TEXTOR	1.75	0.46	1	1	2.5	0.55	0.076	18.1	3.53	4.0	8.1
TFTR	2.5	0.85	1	1	5	0.77	0.30	12.7	5.92	1.9	10.5
JET	3.0	1.25	1.7	1.14	3.5	0.87	0.15	20.5	33.4	5.08	24.9
ITER	7.75	2.80	1.6	1.11	6	0.53	0.44	7.27	21.1	0.64	19.8

Table I Operational Limits for five Tokamaks resulting from criteria (1) and (4)

$\overline{\overline{N}}_{MAX}$ is the Hugill-Greenwald density limit, $\overline{\overline{N}}_{MIN}$ is the low density limit according to Ineq. (4); B_{MM}, I_{MM} and $\overline{\overline{N}}_{MM}$ are the values of the upper magnetic field, plasma current and density beyond which there is no stable operation; Units are m, *tesla*, $10^{20} m^{-3}$, keV.

The following conclusions can be drawn: the upper line average density limit is lower in ITER ($\overline{N}_{MAX} = 4\overline{\overline{N}}_{MAX}/3 = 0.71 \times 10^{20} m^{-3}$) than in JET ($\overline{N}_{MAX} = 1.16 \times 10^{20} m^{-3}$) because the ratio B_0 / R_0 is smaller; the larger magnetic field in ITER however increases the low density limit nonlinearly; as a result, the operation density range decreases dramatically from $[0.15 - 0.87]\, 10^{20} m^{-3}$ in JET to $[0.44 - 0.53]\, 10^{20} \mathrm{m}^{-3}$. The proposed operation field of 6 *tesla* in ITER is actually close to the calculated value $B_{MM} = 7.27$ *tesla*!

We now combine Ineq. (4) with the inequality resulting from the β limit [4]:

$$\overline{\overline{\beta}} \equiv (B_0^2 S / 8\pi)^{-1} \int P dS \leq 0.05 K g \beta_N (a / q_\psi R_0) \tag{8}$$

where $P = N(T_e + T_i)$ is the total pressure. Thus an upper limit for the temperature:

$$(\overline{\overline{T_e + T_i}})_{MM} / m_e c^2 \leq 0.025 K g f^{*-1} \alpha_L^{-1} \beta_N (a / q_\psi R_0) \tag{9}$$

which is independent from the magnetic field strength. Here $m_e c^2$ is the rest energy of the electron and $f^* = \overline{\overline{N(T_e + T_i)}} / \overline{\overline{N}}\ (\overline{\overline{T_e + T_i}})$ another profile factor ($f^* > 1$ for monotonically decreasing profiles). $\overline{\overline{T}}_{MM} \equiv \overline{\overline{T}}_{MAX} = (\overline{\overline{T_e + T_i}})_{MM} / 2$ is also given in Table I under the assumption that $T_e \propto T_i \propto N_e^2 \propto (1 - \rho^2)^2$ (hence $f^* = 3/2$) and $\beta_N = 2.8$ (Troyon factor [4]).

The low density limit in tokamaks has generally been attributed to runaway electrons [5, 6] exciting plasma instabilities [7]. We suggest that cyclotron radiation is emitted *collectively* when the oscillation frequency matches the electron cyclotron frequency; this requires ω_{pe} somewhat below Ω_e, which condition is first met on axis for plasma waves (plasmons) propagating nearly parallel to $\vec{B}$. It can be shown that the cyclotron radiation from an ensemble of N electrons is under those conditions

$$\int_{4\pi} \vec{\mathrm{P}} \cdot d\mathbf{S}_0 \cong \vec{\mathrm{P}} \cdot \hat{n} r_0^2 \delta\Omega$$

$$\cong \frac{3\pi^2}{4} \frac{(2\pi\zeta)^3}{k_z^2 k_\perp \lambda_{D,e}^3} k_\perp^2 \rho_e^2 N \lambda_{D,e}^3 \left(\frac{16\pi}{3} N e_e^2 \Omega_e^2 \frac{c_e^2}{c} \right) \sum_{\pm} \left[\frac{e_e}{T_e} \hat{\Phi}_{\mathbf{k},\omega} \Omega_e \delta(\omega \pm \Omega_e) \right]^2 \tag{10a}$$

where $\wp$ is the Poynting vector, $\rho_e \equiv c_e / |\Omega_e|$ the electron Larmor radius, c_e the electron thermal velocity, $N\lambda_D^3$ the reciprocal of the plasma expansion parameter ($N\lambda_D^3 = 0.4 \times 10^7$ if $N = 1 \times 10^{13} cm^{-3}$ and $T = 1 keV$; $N\lambda_D^3 \propto N^{-1/2} T^{3/2}$) and $\zeta << 1$ a numerical coefficient. The factor in parenthesis represents the power radiated by N incoherent electrons. The Dirac functions $\delta(\omega \pm \Omega_e)$ are manifestations of secular behaviour at the resonances. It is interesting to note that $(e_e \hat{\Phi}_{\mathbf{k},\omega} / T_e)^2 \sim (4\pi N \lambda_{D,e}^3)^{-1}$ in a thermal non magnetized plasma.

In order to estimate the collective cyclotron emission enhancement factor, we assume $T_e = 4 keV$ and $N = 1 \times 10^{13} cm^{-3}$; hence $\omega_{p,e} = 1.8 \times 10^{11} s^{-1}$, $c_e = 2.65 \times 10^9 cm\, s^{-1}$ and $\lambda_{D,e} = 1.50 \times 10^{-2} cm$. $|\Omega_e| = |\omega| \cong 2\omega_{p,e}$ corresponds to B = 2.05 *tesla* and yields $\rho_e^2 = 0.25 \lambda_{D,e}^2$. Both $2\pi\zeta$ and $|k_z| \lambda_{D,e}$ being small numbers, we let $2\pi\zeta / |k_z| \lambda_{D,e} \cong 1$. Assuming furthermore $|k_z|\, k_\perp \lambda_{D,e}^2 \cong 10^{-1}$ and $\Omega_e \delta(\omega \pm \Omega_e) e_e \hat{\Phi}_{\mathbf{k},\omega} / T_e \equiv \int d\omega \varphi_{\mathbf{k},\omega} \sim 10^{-2}$ ($\varphi_{\mathbf{k},\omega}$ being the normalized fluctuation amplitude per frequency unit), Eq. (10a) yields an enhancement factor

$$\left(\int \vec{\mathrm{P}} \cdot d\vec{S}_0 \right)_{collect} / \left(\int \vec{\mathrm{P}} \cdot d\vec{\mathbf{S}}_0 \right)_{incoh} \sim 0.2 \left[2 \left(e_e \hat{\Phi}_{\mathbf{k},\omega} / T_e \right)^2 N \lambda_{D,e}^3 \right] \sim 1.2 \times 10^3 . \tag{10b}$$

Obviously, the estimation of the radiation level (and thus of $e\hat{\Phi}_{k,\omega} / T_e$) must be compatible with machine operation. It is clear however that the latter may be strongly influenced by collective cyclotron radiation.

Acknowledgement

One of the authors (D. Li) was supported by a Fellowship of the Research Center Jülich, Germany and by the National Science Fund for Distinguished Young Scholars of China under Grant No. 19515513.

References

[1] Axon, K. B., et al., in Plasma Physics and Controlled Nuclear Fusion Research 1980 (Proc. 8th Int. Conf., Brussels, 1980; IAEA, Vienna 1981), Vol. 1, p.413.
[2] Greenwald, M., et al., Nucl. Fusion **28** (1988) 2199.
[3] Petrie, T. W., Kellman, A. G., Mahdavi, M. Ali, Nucl. Fusion **33** (1993) 929.
[4] Troyon, F., et al., Plasma Phys. Control. Fusion **26** (1984) 209 (Proc. 11th Europ. Phys. Soc. Conf., Aachen, 1983); Troyon, F., Gruber, R., Phys. Lett. **110A** (1985) 29.
[5] Brossier, P., Nucl. Fusion **18** (1988) 1069.
[6] Knoepfel, H., Spong, D. A., Nucl. Fusion **19** (1979) 785.
[7] Parail, V., Pogutse, O., Fiz. Plazmy **2** (1976) 228 [Sov. J. Plasma Phys. **2** (1976) 125].

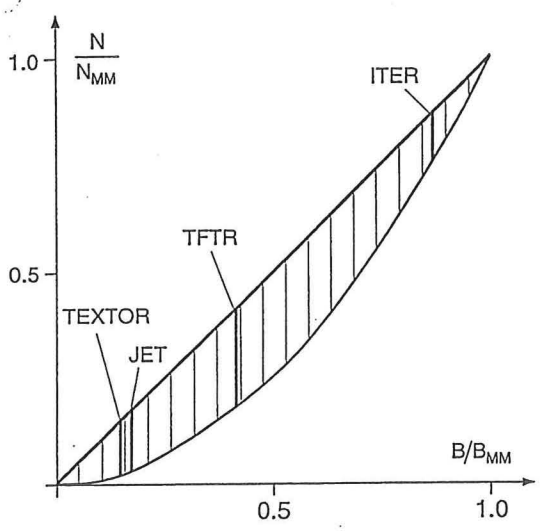

Fig. 1. Assuming Ineqs. (2) and (5), stable tokamak operation (dashed zone) is between the low density limiting curve $N / N_{MM} = B^2 / B_{MM}^2$ and the upper limiting curve $N / N_{MM} = B / B_{MM}$

Stability Properties of the Reversed Field Pinch with realistic boundary conditions

R. Paccagnella

Consorzio RFX
Corso Stati Uniti, 4 - 35127 Padova (Italy)

The magnetohydrodynamic (MHD) stability properties of the Reversed Field Pinch (RFP) have been analyzed in a number of papers [1, 2, 3, 5, 4, 6, 7].
Looking for an optimization of the shell and first wall design in RFP devices, in this paper, a study of current driven instabilities is presented giving detailed informations about spectra and growth rates, when two resistive walls at the plasma boundary are considered.

1 Equilibrium and numerical methods

A zero pressure cylindrical equilibrium is considered and parametrized using two free quantities α and Θ_o which are needed to specify the parallel current profile; in fact:

$$\vec{J} = \mu\vec{B}, \quad \mu = \mu_o \frac{\vec{J}\cdot\vec{B}}{B^2}, \quad \mu = \mu(0)\,(1-(\frac{r}{a})^\alpha) = (\frac{2\Theta_o}{a})\,(1-(\frac{r}{a})^\alpha)$$

where r is the radial position and 'a' is the plasma radius. This model has been already used for example in Ref. [3, 7]. The relevant resistive MHD equations in cylindrical geometry have been linearized about the given equilibrium and the stability of the system has been determined by using a matrix-shooting formulation. The perturbations have been Fourier analyzed chosing m and as the poloidal and toroidal wave numbers respectively As usual in linear theory, a mode, with wave vetor $\vec{k}$, is said to be resonant when: $\vec{k}\cdot\vec{B}_o = 0$ *i.e.* $q(r_s) = \frac{-m}{n}$ where r_s is the resonance radius and q the equilibrium safety factor. Moreover, the following nomenclature is used throughout the paper: a mode is said to be internal or external resonant if $r_s < r_{rev}$ or $r_s > r_{rev}$ respectively, where r_{rev} is the radius at which the toroidal component of the equilibrium magnetic field reverses its sign ($q(r_{rev}) = 0$). Two classes of non-resonant modes can also be defined: when $\frac{-m}{n} > q(0)$ the modes are called internal non-resonant, while if $\frac{-m}{n} < q(a)$ they are said external non-resonant. These are ideal instabilities. Since m=0,1 modes pose the more stringent stability requirements [1, 2, 3, 7], only these poloidal periodicities are considered in this paper.
As regard the boundary conditions: the plasma is in contact with a first resistive wall, which plays the role of the liner, placed at $r = r_l$ and having a vertical field penetration time constant: τ_l, then a vacuum region exists and a second wall, the shell, is placed at $r = r_w$ with a characteristic time constant: τ_w. One, or both of the two walls, can be possibly removed and a simplyfied problem can be studied. To derive the boundary conditions the so-called "thin-shell" approximation [8] has been used. Doing this it is straightforward to show that, the following equation holds for the radial displacement ξ at r_l:

$$\xi(r_l) = \frac{\frac{d(F\xi r)}{dr}\Big|_{r_l^-} \quad f}{(\frac{d(rf)}{dr}\Big|_{r_l^+} - \tau_l\gamma f)F} \qquad (1)$$

where $F = (\vec{k} \cdot \vec{B}_o)$ and:

$$f = \quad (K'_m(k_z r_l) + h \quad I'_m(k_z r_l)), \qquad h = \quad \frac{\tau_w \gamma K'_m(k_z r_w)}{\frac{k_z^2 r_w^2 + m^2}{k_z r_w^2 K'_m(k_z r_w)} - \tau_w \gamma I'_m(k_z r_w)}$$

Finally, it is necessary to remark that all the quantities in this paper are in normalized units: the lengths are normalized to the plasma minor radius, a, and the times to the Alfven time.

2 Numerical results and discussion

A-Ideal wall with vacuum region: The effect of a vacuum region separating the plasma from a perfect conducting wall is generally to increase of the growth rates and also the interval of unstable modes. However the amplitude of these effects depends on the chosen equilibrium configuration and on the mode wavelength. In Fig.1(a,b,c,d) the growth rates versus k_z for different m and different equilibrium parameters are shown. In particular Fig.1(a) shows a case where internal non-resonant m=1 ideal modes are destabilized. These modes are excited at low α's. The configuration is unstable also in the case of a conducting wall in contact with the plasma, but the width of the unstable non resonant modes and the growth rates are enhanced by the vacuum region. Relatively large γ's are found. Case (b) represents instead a medium-α case in which qualitatively the same trend is observed, although now the configuration is stable with $r_w = 1$ and only slightly unstable when r_w is made quite large. These modes are internal tearings. Case (c) gives the spectrum of unstable m=0 modes at a similar value of α. The growth rates of these modes are generally higher than those of internal m=1 at the same α, more sensitive to the vacuum extension, and also the spectrum is peaked at relatively longer wavelength. Finally, case (d) corresponds to unstable external resonant m=1 modes. The behaviour of these modes is similar to that of m=0. It is also seen that m=0 and especially m=1 external resonant are localized near the wall. Only about a $3 \div 4$ % of vacuum extension can destabilize m=0 modes.
A last observation on m=1 ideal, external non-resonant kinks, they are destabilized only at very deep reversal, consistently with Robinson's analysis [1], when $\Phi_T \leq 0$, where Φ_T is the total toroidal flux and/or at relatively high plasma wall distance ($r_w > 1.3$). Therefore these modes are not of practical interest, at least for normal RFP operation ($1.4 \leq \Theta \leq 2, -0.7 \leq F \leq 0$) and moderate vacuum extension.
B-Plasma with Resistive walls and vacuum: It is well known that the marginal stability of a configuration sourrounded by a resistive wall can be studied simply moving the wall at infinity [9]. However looking at the growth rates two cases can happen:
(a) a configuration which is stable with an ideal wall placed at $r = r_w$ (but unstable with the wall at infinity), then the so called "thin shell modes" arise, with growth time of the order of the wall penetration time; (b) a configuration which is unstable with the ideal wall placed at $r = r_w$. In this second circumstance a resistive wall at $r = r_w$ produces generally an increase of the growth rate (by a factor $2 \div 3$), as shown in Fig.2(a,b,c) where the growth rates versus r_w are given for different wall conductivities. Cases with m=1 internal, m=0 and m=1 external modes are presented. The arrows indicate the point (r_w^∞) at which the configurations are marginally stable with an infinite conducting wall, so that for $r < r_w^\infty$ "thin shell modes" arise.
Let us look now to the multiple wall case, i.e. a second resistive wall is positioned at $r = r_l$. This wall plays the role of the liner in real devices, and it is assumed generally to

have a time constant $\tau_l < \tau_w$. First we analyze the effect on the growth rate of different wall positions, r_w, and τ_l, while τ_w is set to infinity. Results are shown in Fig.3(a,b,c) (the modes are the same as before). In Fig.4(a,b,c) the growth rate vs. the time constant of the wall is shown for a case with a single wall at $r = r_w$ and with two walls, putting $\tau_l = \tau_w$. The effect of a secondary shell, for these equilibria, is not very strong, it generally produces a modest decrease of the growth rate (at low values of τ_l), however this effect is stronger for m=0 and especially for m=1 external modes, increasing τ_l.
To summarize: in this paper it has been shown that the so called, "dynamo-modes" are quite insensitive to the wall distance. Even with a big plasma-walll separation the growth of these modes is only weakly affected. Instead m=0 and m=1 modes resonant near the plasma edge are more influenced by the wall position and resistivity.
Although the m=0 and the m=1 external are the most sensitive to plasma wall separation and wall resistivity, it should be however emphasized that, these modes are generally observed in experiments with amplitudes less than those of internal modes. Moreover comparing the experimentally reconstructed equilibrium parameters α, Θ_o, with the marginal curve for stability of internal m=1 modes [10], it is seen that the experimental configurations lie very near to a marginal stable state for these modes, indicating once again that these are, very likely, the modes responsible for the RFP dynamics.
As regard ideal kinks, they appear either at low α (internal non-resonant) or at very deep reversed configurations (external non-resonant). External non-resonant kinks have been also observed in RFPs [11] and lead generally to a strong degradation of confinement and to the plasma termination. As discussed in [7, 8] these ideal modes can only be stabilized by an alfvenic plasma flow.
Hence the results discussed in this paper suggest that the plasma-wall distance and wall resistivity are not really such critical issues in RFPs. In particular if a resistive wall is positioned at $r_w \leq 1.2$, m=0 and m=1 external resonant are the most unstable, both, however, taking advantages from the presence of a thin liner at the plasma edge and being further stabilized by a relatively slow plasma rotation [7], just comparable to those which have been recently measured. Besides, it has been shown that the internal resonant m=1 modes are not very sensitive to the wall position and resistivity, being however, very likely, responsible for the overall RFP dynamics and able to couple with m=0 and m=1 external and nonlinearly stabilize them.

References

[1] D. C. Robinson, Plasma Phys. **13** (1971) 439.
[2] D. C. Robinson, Nucl. Fusion **18** (1978) 939.
[3] V. Antoni, D. Merlin, S. Ortolani, R. Paccagnella, Nucl. Fusion **26** (1986) 1711.
[4] C. Gimblett, T. Hender, R. Paccagnella, in Proc. of Theory of Fusion Plasmas (Chexbres, Lausanne) (1988) 211.
[5] Y.L.Ho,S.C.Prager, Phys. Fluids **31** (1988) 1673.
[6] M.J. Schaffer, Nucl. Fusion **30** (1990) 635.
[7] Z.X. Jiang, A. Bondeson, R. Paccagnella, Phys. Plasmas,**2**, (1995) 442.
[8] C.G. Gimblett, Nucl. Fusion **26** (1986) 617.
[9] D. Pfirsch and H. Tasso, Nucl. Fusion **11** (1971) 259.
[10] T. Bolzonella et al., "Magnetic profile behaviour, dynamo mechanisms and confinement in RFX" to be published in Proc. of 24th EPS Conference, Berchetsgaden (1997).
[11] B. Alper et al., Plasma Phys. and Controlled Fusion **31** (1989) 205.

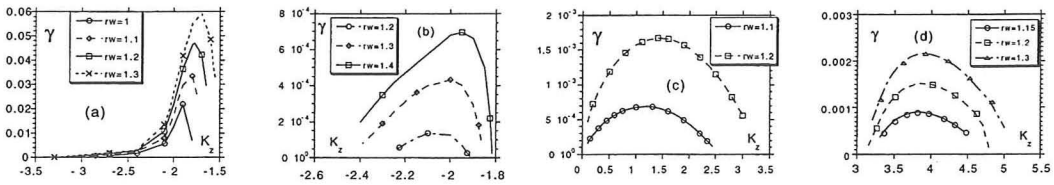

Fig.1

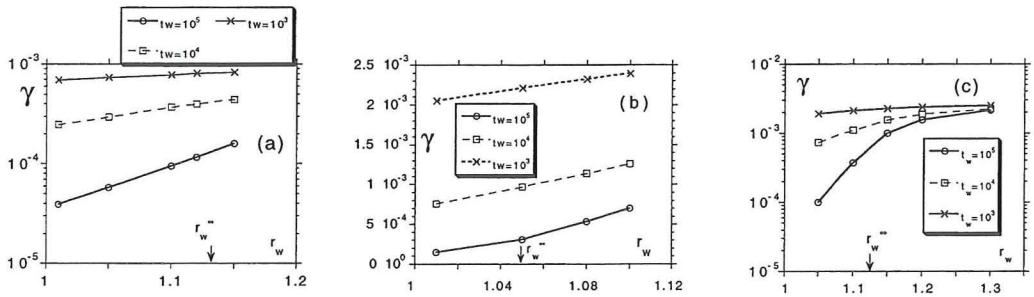

Fig.2

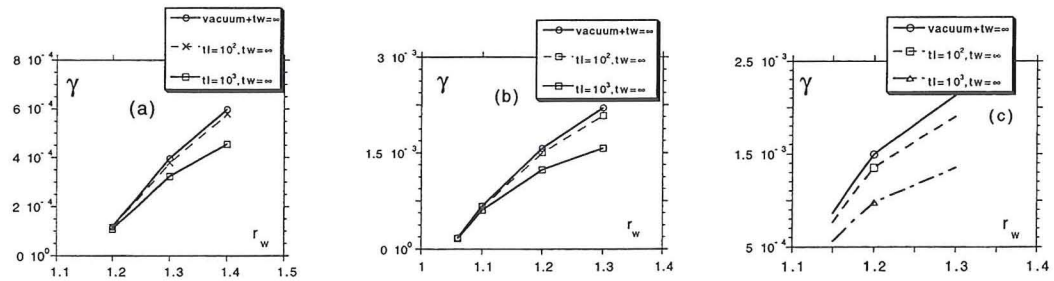

Fig.3

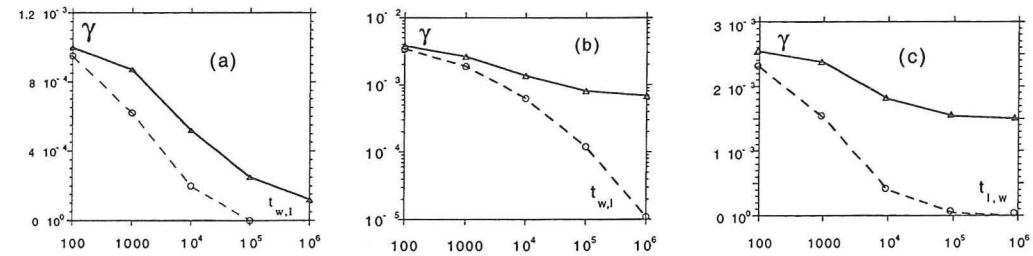

Fig.4

RELAXED STATES OF MAGNETIZED PLASMA WITH MINIMUM DISSIPATION

Brahmananda Dasgupta*,[1], Padmanabha Dasgupta, M. Sita Janaki*, Tomohiko Watanabe*** and Tetsuya Sato***
*Saha Institute of Nuclear Physics
I/AF, Bidhannagar, Calcutta 700 064, India
**Department of Physics, University of Kalyani, Kalyani 741235, India
*** Theory and Computer Simulation Center
National Institute for Fusion Science, Toki, Gifu 509-52, Japan

Abstract. It is proposed that a slightly resistive plasma attains a relaxed state under the constraints of minimum (resistive) dissipation and conserved generalized helicity. The variational principle leads to the following equation:

$$\nabla \times \nabla \times \mathbf{J} = \Lambda \mathbf{B}$$

which includes $\nabla \times \mathbf{B} = \lambda \mathbf{B}$ (Force-free state) as a special case. However, there are other class of solutions of the above equation which are not force free. Existence of such types of solutions is established, and a family of solutions of this equation are explicitly constructed.

Introduction In the well-known theory of Relaxation of magnetoplasma, Taylor[1] proposed that the process of relaxation is governed by the Principle of minimization of total magnetic energy and invariance of total (global) magnetic helicity, K, defined by $K = \int_V \mathbf{A} \cdot \mathbf{B} dV$ where the integration is over the entire volume, is most significant invariant to be considered for investigating the problem of relaxation. Following Taylor's conjecture, the relaxed state of a magnetoplasma is obtained by minimizing the total energy under the constraint of constant total magnetic helicity. A variational technique leads to the following result,

$$\nabla \times \mathbf{B} = \lambda \mathbf{B} \qquad (1)$$

where λ is a constant. The relaxed state is a force-free state.

Taylor's theory, although quite successful in explaining a number of experimental results, including those of RFP, is viewed as inadequate by many workers. Relaxed states as envisaged by Taylor, has only zero pressure gradient. Several efforts [2]have been made to obtain relaxed states which could support finite pressure gradient. Finn and Antonsen studied the turbulent relaxation to equilibrium of compressible plasma. They have shown from the MHD equations with large parallel thermal conductivity, $\int \mathbf{v} \cdot \mathbf{B} dV$ remains

conserved even for compressible plasma, and furthermore, one of the ideal MHD entropy-like functional $S = \int \rho \ ln(p/\rho^{\gamma})dV$ is also conserved. It was found that in presence of parallel flow, equilibria with pressure gradient could be attained. The relaxation process from the two fluid MHD equation and with the constraints of constant entropy and generalized helicity has been worked out. The generalized helicity $\bar{K}$ is defined as $\bar{K} = \int \mathbf{P} \cdot \nabla \times \mathbf{P}dV$ where, $\mathbf{P} = [m\mathbf{v}/q + \mathbf{A}/c]$

Minardi constructed an entropy functional S which is given by, $S = -\int_V j^2 dV + \frac{c}{4\pi\tau}\int_V \mathbf{j}\cdot\mathbf{A}dV$ where τ is a parameter which plays the same formal role of the temperature in the ordinary statistical mechnics, j is the current density and $\mathbf{A}$ is the vector potential. Euler-Lagrange variation $\delta S = 0$ leads to

$$\nabla \times \mathbf{j} = \lambda \mathbf{B} \qquad (2)$$

Relaxation With the Minimum Dissipation The principle of "minimum rate of entropy production", formulated by Prigogine[3] and others, is believed to play a major role in many problems of irreversible thermodynamics. Dissipation, along with nonlinearity, is ubiquitous in systems which evolves towards a self-organized states. The principle of minimum entropy production or equivalently, the principle of minimum dissipation, could play a major role in the process of relaxation and to self-organization.

Montgomery and Phillips[4] investigated the relaxation problem by invoking the principle of minimum dissipation rates in MHD, with the constraints of constant toroidal magnetic flux and constant time-averaged rate of supply of magnetic helicity. The relaxed state, obtained through a variational priciple, can lead to departure from the force-free magnetic profile.

Extensive numerical works by Sato and his collaborators have established[5] the existence of self-organized states with finite pressure, i.e. these states are governed by the magnetohydrodynamic force balance relation, namely, $\mathbf{j} \times \mathbf{B} = \nabla p$, rather than $\mathbf{j} \times \mathbf{B} = 0$.

Recently, it has been demonstrated both by numerical simulation[6] and by experiments[7] that counter-helicity merging of two spheromaks can produce a Field-Reversed Configuration (FRC). FRC has zero toroidal magnetic field and plasma is entirely confined by poloidal magnetic field,has finite pressure with a high β. Remarkable stability of FRC in experiments indicate that FRC is a relaxed state with finite pressure. An FRC-like configuration can be obtained [16] from eqn.(6)

From the point of view of plasma relaxation, the formation of FRC through the counter-helicity merging of two spheromaks is a process where a non-Taylor state emanates from the fusion of two Taylor states. FRC, with its finite pressure gradient and non-zero perpendicular component of current is not a Taylor state. It may be conjectured that there exists a general class

of relaxed states including the states which are not force-free and Taylor's force-free states could be a subclass of these wider class of relaxed states.

In presence of dissipation, a relaxed state with minimum dissipation, under the constraint of conserved generalized helicity, $\bar{K}$, defined earlier, can be obtained. If we consider only Ohmic dissipation, the dissipation rate, R, is given by $R = \int \eta \mathrm{j}^2 dV$ (η being the resistivity). The variational equation is given by

$$\delta \int \left(\eta \mathrm{j}^2 + \lambda \mathbf{P} \cdot \nabla \times \mathbf{P}\right) dV = 0 \qquad (3)$$

which leads to the following equation

$$\nabla \times \nabla \times \mathrm{j} = \Lambda \mathbf{B} \qquad (4)$$

where, Λ is a constant.

We like to emphasize that Eqn.(4) is a general equation which includes Force-free sate as well as the states descibed by eqn.(2) as the special cases.

The main aim of this report is to construct a solution of eqn.(4). It can be shown that general solutions of eqn(4) have the feature for which $\mathrm{j} \times \mathbf{B} \neq 0$. In other words, eqn(4) may lead to a non force-free state.

The construction of a solution of the above equation from the Chandrasekhar-Kendall(CK) eigenfunctions can be done in the following way.

Chandrasekhar and Kendall's [8]solution of eqn.(1) $\nabla \times \mathbf{B} = \lambda\ \mathbf{B}$ can be written (with three parameters μ, m, k in cylindrical co-ord.), as,

$$\mathbf{B} = \mathbf{u}(\mu, m, k) = \lambda \nabla\Phi \times \nabla z + \nabla \times (\nabla\Phi \times \nabla z) \quad (5)$$

where, $\Phi = J_m(\mu r)\ exp[i(m\theta - kz)]$ with $\lambda^2 = \mu^2 + k^2$. In the above expression, J_m is the Bessel Function of order m and μ in the argument is determined from the boundary condition at $r = a$, which is given as $(\hat{\mathbf{n}} \cdot \mathbf{u})_{r=a} = 0$

Analytical continuation of the above solution for complex values of μ (or k) is trivial. However, for the real values of λ (and hence of μ and k) the operator $(\nabla\times)$ has been proved to be self-adjoint. Such analytic continuation will make $(\nabla\times)$ a non-self-adjoint operator.

We now take μ to be complex. We now construct,

$$\mu_n = \left[(\mu^2 + k^2) exp(4n\pi\ i/3) - k^2\right]^{1/2} = \left[\lambda^2 exp(4n\pi\ i/3) - k^2\right]^{1/2} \quad (n = 1, 2)\ (6)$$

with $\mu_n^2 + k^2 = \lambda^2\ exp(4n\pi\ i/3)$. Now we take,

$$\begin{aligned} \mathbf{v} &= \mathbf{u}(\mu, m, k) \\ \mathbf{w_1} &= \mathbf{u}(\mu_1, m, k) = \lambda e^{2i\pi/3} \nabla\Phi_1 \times \nabla z + \nabla \times (\nabla\Phi_1 \times \nabla z) \\ \mathbf{w_2} &= \mathbf{u}(\mu_2, m, k) = \lambda e^{4i\pi/3} \nabla\Phi_2 \times \nabla z + \nabla \times (\nabla\Phi_2 \times \nabla z) \qquad (7) \end{aligned}$$

In the last two expressions above, Φ_1 and Φ_2 are obtained from Φ by replacing μ by μ_1 and μ_2 respectively. It is to be noted that $\mathbf{v}$ is not $\parallel$ $\mathbf{w}_1$, similarly $\mathbf{v}$ is not $\parallel$ $\mathbf{w}_2$, and $\mathbf{w}_1$ is not $\parallel$ $\mathbf{w}_2$.

To construct the solution, we first note that, $\nabla \times \mathbf{v} = \lambda \mathbf{v}$ (whose solution is given in terms of CK eigenfunctions) and further, $\nabla \times \mathbf{w}_1 = \lambda\, e^{2i\pi/3}\, \mathbf{w}_1$, $\nabla \times \mathbf{w}_2 = \lambda\, e^{4i\pi/3}\, \mathbf{w}_2$ A solution of the eqn.(4) can be proposed which is a linear combination of $\mathbf{v}$, $\mathbf{w}_1$, $\mathbf{w}_2$ such that,

$$\mathbf{B} = a\, \mathbf{v} + b_1\, \mathbf{w}_1 + b_2\, \mathbf{w}_2 \qquad (8)$$

where a, b_1, b_2 are constants, with at least two of them are non-zero.

It can be easily demonstrated that the expression for $\mathbf{B}$ given in (8) is a solution of eqn.(4), by taking 'curl' of both sides of eqn.(8) get successively,

$$\begin{aligned} \nabla \times \nabla \times \nabla \times \mathbf{B} &= \lambda^3 (a\, \mathbf{v} + b_1\, \mathbf{w}_1 + b_2\, \mathbf{w}_2) \\ &= \Lambda (a\, \mathbf{v} + b_1\, \mathbf{w}_1 + b_2\, \mathbf{w}_2) = \Lambda \mathbf{B} \end{aligned}$$

Thus, it is shown that the expression (8) is a solution of the eqn.(4).

Acknowledgement [1]One of the authors (BD) wishes to acknowledge the kind hospitality of ICTP, Trieste, Italy, where a part of the work is carried out during his visit as an Associate

References

1. J. B. Taylor, Phys. Rev. Lett., **33**, 139, (1974)

2. E. Hameiri and J. Hammer, Phys. Fluids, **25**, 1855, (1982) J. M. Finn and T. M. Antonsen, Phys. Fluids, **26**, 3540, (1983) K. Avinash, Phys. Fluids B, **b 4**, 3856, (1992) E. Minardi, Plasma Phys. Control. Fusion, **31**, 229, (1989)

3. P. Glansdorff and I. Prigogine, *Thermodynamic Theory of Structure, Stability and Fluctuations*, Wiley Interscience, New York, (1971)

4. D. Montgomery and L. Phillips, Phys. Rev. A. **38**, 2953, (1988)

5. S. P. Zhu, R. Horiuchi, T. Sato, Phys. Rev. E. **51**, 6047, (1995). T. Sato, H. Takamaru, Phys. Plasmas **2**, 3609 (1995). T. Sato and the Complexity Sim. group, Phys. Plasmas **3**, 2135 (1996).

6. B. Dasgupta, T. Sato, T. Hayashi, K. Watanabe and T. Watanabe, Trans. Fusion Tech. **27**, 374, (1995).

7. Y. Ono *et al* Phys. Fluids, **B 5**, 3691, (1993)

8. S. Chandrasekhar and P. C. Kendall, Astro. Phys. J., **126**, 457, (1957)

A Kinetic Energy Principle for a Tokamak Allowing for Bounce and Transit Resonances

B. N. Kuvshinov[1], A. B. Mikhailovskii[2]

FOM-Instituut voor Plasmafysica "Rijnhuizen", Association EURATOM-FOM,
Postbus 1207, 3430 Nieuwegein, The Netherlands

1. Introduction. Most of kinetic energy principles used in the theory of MHD instabilities in tokamaks are based on the assumption that the ratio of the wave frequency ω to the characteristic particle circulation frequency along the torus ω_c is either small $\omega/\omega_c \to 0$ [1,2] or large $\omega/\omega_c \to \infty$ [3]. In a number of problems the above ratio is finite, so it is necessary to have a kinetic energy principle which is valid for arbitrary ω/ω_c [4]. Derivation and analysis of such an energy principle is the object of the present paper.

2. Kinetic energy principle. The kinetic energy principle can be written as

$$W \equiv W^F + W^K - I_\perp = 0, \tag{1}$$

where W^F is the standard fluid (incompressible) part of the perturbation energy [5], $I_\perp = (i\omega/2)\int \rho\xi^* \mathbf{V}_\perp \mathrm{d}\mathbf{r}$ characterizes the perpendicular plasma inertia, where $\mathbf{V}_\perp = \mathbf{V}_E + (c/en)[\mathbf{B}\times\nabla\tilde{p}]$ is the perturbed plasma velocity across the equilibrium magnetic field $\mathbf{B}$, $\tilde{p}$ is the perturbed plasma pressure, and $\mathbf{V}_E = [\mathbf{E}\times\mathbf{B}]/\mathbf{B}^2$. The kinetic (compressible) part of the perturbation energy W^K is

$$W^K = \frac{1}{2}\sum_\alpha \int\int g H^* \mathrm{d}v\mathrm{d}r, \tag{2}$$

where the index α denotes particles species, $H = (M/2)(v^2 + v_\parallel^2)\boldsymbol{\xi}\cdot\boldsymbol{\kappa}$, H^* is the complex conjugate, v is the absolute value of a particle velocity, $v_\parallel$ is the component along the magnetic field, $\boldsymbol{\xi} = (i/\omega)\mathbf{V}_E$, $\boldsymbol{\kappa}$ is the magnetic field curvature, and the function g is determined by the drift-kinetic equation

$$-i\omega g + \frac{v_\parallel}{qR}\left(\frac{\partial}{\partial\theta} - inq\right) g = i\frac{\partial F}{\partial\mathcal{E}}(\omega - \hat{\omega}_*) H. \tag{3}$$

Here F is the equilibrium distribution function, $\mathcal{E} = Mv^2/2$ is the particle energy, $\hat{\omega}_*$ is the drift frequency operator which acts on $\boldsymbol{\xi}$ and is determined by the relation $\hat{\omega}_* = (i/M\omega_{Bs})(\partial F/\partial\mathcal{E})^{-1}[\mathrm{b}\times\nabla F]\cdot\nabla$, $\omega_{Bs} = eB_s/Mc$, B_s is the magnetic field on the plasma axis, n is the toroidal wave number (the dependency of the perturbations on toroidal angle ϕ is taken in the form $\exp(-in\phi)$), θ is the poloidal angle, q is the safety factor, and R is the large radius of the torus. Note that H characterizes the work done by the electric field on a particle when it is displaced due to the magnetic drift, so that $\mathrm{d}H/\mathrm{d}t + e\mathbf{v}_d\cdot\mathbf{E} = 0$,

[1]Permanent address: Nuclear Fusion Institute, Russian Research Centre "Kurchatov Institute", 123182 Moscow, Russia

[2]Nuclear Fusion Institute, Russian Research Centre "Kurchatov Institute", 123182 Moscow, Russia

$\mathbf{v}_d = (v^2 + v_\parallel^2)[\kappa \times \mathbf{b}]/2\omega_B$. It is convenient to introduce the variable τ meaning the normalized time along a particle trajectory, $\tau = \omega_c \int_0^\theta \mathrm{d}l/v_\parallel - \pi$ for circulating particles and $\tau = \omega_b \int_{\theta_{min}}^\theta \mathrm{d}l/v_\parallel - \pi/2$ for trapped particles. Here $\mathrm{d}l = qR\mathrm{d}\theta$ is an element along the trajectory, θ_{min} is the angle corresponding to the trapped particle reflection point, ω_c, ω_b are the transit frequency of a circulating particle along the torus and the trapped particle bounce frequency. Expanding g in a Fourier series in τ, solving (3) and substituting the result into (2) on has $W^K = W_c + W_t$, where W_c, W_t are the parts of W^K resulting from circulating and trapped particles correspondingly, and given by the relations

$$W_c = -\frac{\pi}{2} \sum_\alpha \int \frac{\mathrm{d}r}{qR} \int v^3 \mathrm{d}v \frac{\partial F}{\partial \mathcal{E}} \int_0^{\lambda_{min}} \frac{\mathrm{d}\lambda}{|\omega_c|} \sum_\sigma \sum_j H_j^{c*} \frac{\omega - \hat{\omega}_*}{\omega - (nq+j)\omega_c} H_j^c,$$

$$W_t = -\frac{\pi}{2} \sum_\alpha \int \frac{\mathrm{d}r}{qR} \int v^3 \mathrm{d}v \frac{\partial F}{\partial \mathcal{E}} \int_{\lambda_{min}}^{\lambda_{max}} \frac{\mathrm{d}\lambda}{\omega_b} \sum_j H_j^{t*} \frac{\omega - \hat{\omega}_*}{\omega - j\omega_b} H_j^t. \qquad (4)$$

Here σ is the sign of $v_\parallel$, $H_j^{c,t}$ are the Fourier harmonics of H,

$$H_j^c = \frac{1}{2\pi} \int_0^{2\pi} H \exp\{-i[nq(\theta - \tau) + j\tau]\}\, \mathrm{d}\tau, \quad H_j^t = \frac{1}{2\pi} \int_0^{2\pi} H \exp[-i(nq\theta + j\tau)]\mathrm{d}\tau, \quad (5)$$

$\lambda = v_\perp^2 B_s/v^2 B$ is the pitch angle, $\lambda_{min} = B_s/B_{max}$, $\lambda_{max} = B_s/B_{min}$. Neglecting the drift effects, $\hat{\omega}_* \to 0$, Eqs. (4) reduce to ones obtained in [4]. In the limits $\omega/\omega_{c,b} \to 0$ and $\omega/\omega_{c,b} \to \infty$ they reproduce kinetic energy principles of [1,2] and [3].

3. Compressible part of energy near the singular point. The kinetic effects considered are most important near singular points of the perturbation with the radial coordinate $a = a_m$, where $m - nq(a_m) = 0$ and the perturbation has one dominant poloidal harmonic, $\xi \propto \exp(im\theta)$. The function H is then simplified to

$$H \simeq H_m = i\frac{M}{2m}\left(v^2 + \bar{v}_\parallel^2\right) \frac{\partial \ln B}{\partial \theta} \frac{\partial X_m}{\partial a} \exp(im\theta), \qquad (6)$$

where $X_m = (\xi \cdot \nabla a)_m$ is the m-th poloidal harmonic of the radial plasma displacement. We substituted $v_\parallel$ by $\bar{v}_\parallel$, where in the case of circulating particles $\bar{v}_\parallel = \omega_c qR$, and in the case of trapped particles $\bar{v}_\parallel = 0$. This replacement is justified because for trapped and barely circulating particles $v \gg v_\parallel$, and for strongly circulating particles $\bar{v}_\parallel = v_\parallel$. The equilibrium magnetic field is approximated by $B = B_s(1 + \epsilon\cos\theta)$, $\epsilon = a/R$ is the inverse aspect ratio. Then $H \propto \sin\theta$ and one should expand $\sin\theta$ in Fourier series of τ to calculate $H_j^{c,t}$ (5). The result of this expansion is

$$\sin\theta = -\frac{4\pi^2}{k^2 K^2(k)} \sum_{s=1}^{\infty} s\Lambda_s(k) \sin s\tau, \quad k < 1,$$

$$\sin\theta = -\frac{4\pi^2}{K^2(\kappa)} \sum_{s=0}^{\infty} (s + \frac{1}{2})\Lambda_{s+1/2}(\kappa) \sin\left[(2s+1)\tau\right], \quad \kappa < 1, \qquad (7)$$

$k^2 = 2\epsilon\lambda/[1 - (1-\epsilon)\lambda]$, $\kappa = 1/k$, $\Lambda_s(\rho) = \hat{q}^s/(1 + \hat{q}^{2s})$, $\hat{q} = \exp\left[-\pi K(\sqrt{1-\rho^2})/K(\rho)\right]$, K is the elliptic integral. Using (6), (7) one shows that the kinetic part of perturbation energy W^K in Eq. (1) combines with $I_\perp$ to give

$$\hat{I}_\perp \equiv I_\perp - W^K = \frac{\omega^2 n_0 M_i}{2m^2} \int a^2 |X_m'|^2 \left(K_\perp + 2q^2 K_\parallel\right) \mathrm{d}r, \qquad (8)$$

where $K_\perp = 1 - \omega_{pi}^*/\omega$, $\omega_{pi}^* = mcp_0'/eB_s n_0 a$ is the ion drift frequency with respect to the pressure gradient, $K_\parallel = K_{\parallel c} + K_{\parallel t}$,

$$K_{\parallel c} = A\sum_{\alpha,\sigma} M^2 \int_0^\infty \mathrm{d}v\, v^3 \frac{\partial F}{\partial \mathcal{E}} \left(1 - \frac{\hat\omega_*}{\omega}\right) \int_0^{\lambda_{min}} \frac{\mathrm{d}\lambda}{|\omega_c|} \left(v^2 + \bar v_\parallel^2\right)^2 \left[\frac{1}{kK(k)}\right]^4 \sum_{j=-\infty}^{\infty} \frac{j^2 \Lambda_{|j|}^2(k)}{\omega - j\omega_c},$$

$$K_{\parallel t} = A\sum_{\alpha} M^2 \int_0^\infty \mathrm{d}v\, v^7 \frac{\partial F}{\partial \mathcal{E}} \left(1 - \frac{\hat\omega_*}{\omega}\right) \int_{\lambda_{min}}^{\lambda_{max}} \frac{\mathrm{d}\lambda}{\omega_b} \left[\frac{1}{K(\kappa)}\right]^4 \sum_{j=-\infty}^{\infty} \frac{(j+1/2)^2 \Lambda_{|j+1/2|}^2(\kappa)}{\omega - (2j+1)\omega_b}. \tag{9}$$

Here $A = \pi^3/2\omega n_0 M_i q^3 R^3$ and the operator $\hat\omega_*$ acting on the m-th harmonic converts to a number $\hat\omega_* = -mcF'/eB_s \partial F/\partial \mathcal{E}$. Equations (8), (9) characterize the inertia renormalization for arbitrary particle energy distribution function.

4. Inertia renormalization and Landau damping in Maxwellian plasmas. For a Maxwellian particle velocity distribution function one should take in (8), (9) $F = n_0 \pi^{-3/2} v_T^{-3} \exp(-\mathcal{E}/T)$, $\hat\omega_* = \omega_{n*}[1 + \eta(\mathcal{E}/T - 3/2)]$, where $v_T = (2T/M)^{1/2}$ is the particle thermal velocity, $\omega_{n*} = (mcT/eB_s a) n_0'/n_0$, $\eta = \mathrm{d}\ln T/\mathrm{d}\ln n_0$. Below we consider the frequency range $\omega/\bar\omega_b < \epsilon^{-1/2}$, where $\bar\omega_b = \epsilon^{1/2} v_{Ti}/2qR$ is the characteristic ion bounce frequency. Integrating over velocities one finds that the main contribution into $K_\parallel$ is due to trapped and barely passing ions ($\lambda \simeq 1$), and that $K_\parallel$ has the form $\epsilon^{1/2} K_\parallel = \hat K_\parallel \equiv \hat K_{\parallel c} + \hat K_{\parallel t}$,

$$\hat K_{\parallel c} = \sum_{j=1}^{\infty} \int_0^1 \frac{\mathrm{d}k}{k^4} \frac{\Lambda_j^2(k)}{K(k)} \left\{1 + \frac{\epsilon}{2}\left[\frac{\pi}{kK(k)}\right]^2\right\}^2 G(y_{cj}), \quad \hat K_{\parallel t} = \sum_{j=0}^{\infty} \int_0^1 \kappa \mathrm{d}\kappa\, \frac{\Lambda_{j+1/2}^2(\kappa)}{K(\kappa)} G(y_{tj}), \tag{10}$$

where the variables y_{cj}, y_{tj} are determined by the relations $y_{cj} = (1/j)(\omega/\bar\omega_b)(kK(k)/\pi\sqrt{2})$, $y_{tj} = (j+1/2)^{-1}(\omega/\bar\omega_b)(K(\kappa)/\pi\sqrt{2})$,

$$G(y) = 12\sqrt{2}\pi \left\{\left[1 - \frac{\omega_{n*}}{\omega}\left(1 - \frac{3}{2}\eta\right)\right] G_1(y) - \eta \frac{\omega_{n*}}{\omega} G_2(y)\right\},$$

$$G_1(y) = 1 + \frac{2y^2}{3} + \frac{4y^4}{3} - \frac{8y^5}{3} F(y) + \frac{4i}{3}\sqrt{\pi} y^5 \exp(-y^2), \quad G_2 = \frac{5}{2} + y^2 G_1(y), \tag{11}$$

$F(y)$ is the Dawson integral $F(y) = \exp(-y^2)\int_0^y \exp(t^2)\mathrm{d}t$. Real part of $\hat K_\parallel$ characterizes the inertia renormalization and its imaginary part – the Landau damping. Analytical results can be obtained for small and large frequencies limits. For $\omega/\bar\omega_b < 1$ one has

$$\hat K_\parallel = 0.82\left\{1 - \frac{\omega_p^*}{\omega} + 3.3i\left(\frac{\omega}{\bar\omega_b}\right)^5 \left[1 - \frac{\omega_{n*}}{\omega}\left(1 - \frac{3}{2}\eta\right)\right]\right\}. \tag{12}$$

In the frequency range $1 < \omega/\bar\omega_b < \epsilon^{-1/2}$ Eqs. (10), (11) give

$$\hat K_{\parallel t} = -\frac{4\sqrt{2}}{\pi}\left(\frac{\bar\omega_b}{\omega}\right)^2 \left[1 - \frac{\omega_{n*}}{\omega}(1 + 2\eta)\right],$$

$$\hat K_{\parallel c} = \frac{15\sqrt{2}}{8}\left(\frac{\bar\omega_b}{\omega}\right)^2 \left[1 - \frac{\omega_{n*}}{\omega}(1 + 2\eta)\right] + \frac{\sqrt{\epsilon}}{4}\left(1 - \frac{\omega_p^*}{\omega}\right) + i\frac{\sqrt{\pi}}{2}\frac{\bar\omega_b}{\omega}\left[1 - \frac{\omega_{n*}}{\omega}\left(1 + \frac{3}{2}\eta\right)\right]. \tag{13}$$

For arbitrary $\omega/\bar{\omega}_b$ the function $\hat{K}_{||}$ can be calculated numerically. Results of such calculations are given in the figures. For clarity we neglected the drift effects. The figures show the real and imaginary parts of $\hat{K}_{||}$ versus $\omega/\bar{\omega}_b$: $\hat{K}_{||}^{(0)} = \mathrm{Re}\hat{K}_{||}$, $\hat{K}_{||}^{(1)} = \mathrm{Im}\hat{K}_{||}$. Solid lines marked by 1, 2, 3 represent the circulating particle, trapped particle and the total contribution to $\hat{K}_{||}^{(0,1)}$. Dashed lines represent the analytical expressions (12) and (13).

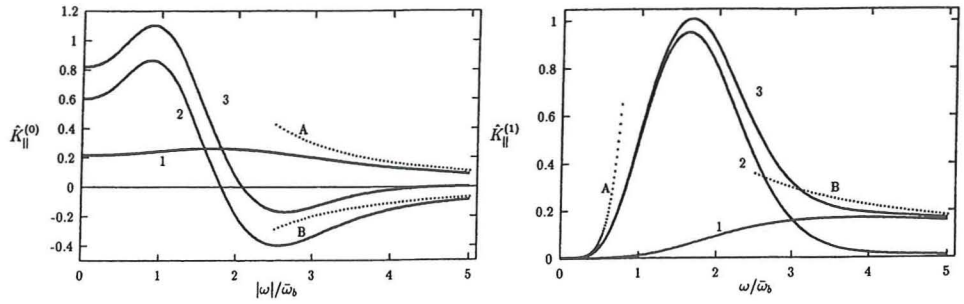

5. Discussion. We derived expressions (8), (9) for the contributions from the passing and trapped particles to the compressible part of the perturbation energy W^K and investigated these expressions both analytically and numerically for Maxwellian plasmas. It can be shown that for $\omega/\bar{\omega}_b \to 0$ the contribution of the trapped particles to the Landau damping is two orders of magnitude higher than that of the passing particles. Note that $\mathrm{Im}\hat{K}_{||}$ given by (12) is four orders of magnitude larger than our previous estimation given in [6]. This discrepancy is explained by having disregarded in [6] the trapped particles contribution and by the fact that the approximation $v_{||} = \mathrm{const}$ used in [6] is too rough for small $\omega/\bar{\omega}_b$. The results obtained in this paper can be used to investigate the resistive-wall external kink modes stabilization by toroidal rotation, the drift-Alfven modes at $\omega_* \approx \bar{\omega}_b$, and high-energy particles induced instabilities, related to the bounce and circulating particle resonances.

Acknowledgements. The research, described in this publication, was made possible in part by Grant # 95-02-03988-a from the Russian Fundamental Research Foundation and Grant # 94-3802 from the INTAS.

References

[1] M.D. Kruskal, C.R. Oberman, Phys. Fluids, **1**, 275 (1958).
[2] M.N. Rosenbluth, N. Rostoker, Phys. Fluids, **2**, 23 (1959).
[3] G.F. Chew, L.G. Goldberger, F.E. Low, Proc. R. Soc. London, **A 236**, 112 (1956).
[4] A. Bondeson, M.S. Chu, Phys. Plasmas, **3**, 3013 (1996).
[5] I.B. Bernstein et al., Proc. R. Soc. London, **A244**, 74 (1958).
[6] A.B. Mikhailovskii, B.N. Kuvshinov, Plasma Phys. Rep., **21**, 802 (1995).

Integrable Motion of Four Current-Vortex Filaments

E. Westerhof, V.P. Lakhin, and T.J. Schep

FOM-Instituut voor Plasmafysica 'Rijnhuizen', Association Euratom-FOM
Postbus 1207, 3430 BE Nieuwegein, Nederland

Introduction

For perturbations propagating with identical velocities along the uniform equilibrium magnetic field, the equations governing three-dimensional drift-Alfvén perturbations in homogeneous low β plasma can be reduced to a set of three coupled 2D equations in Lagrangian form [1]: i.e. they represent three scalar fields, G_α with $\alpha = +, -, 3$, defined below which are convected by different flows as given by three streamfunctions, Φ_α. The fields are defined by (in normalized units [1])

$$G_\pm \equiv \frac{\pm 1}{2\lambda_e}\left(\lambda\Phi - A + (\pm\lambda_e - \lambda)(\ln \tilde{n}/n_0 \pm \lambda_e \nabla_\perp^2 A)\right) \tag{1}$$

$$G_3 \equiv \nabla_\perp^2 \Phi - \ln \tilde{n}/n_0,$$

i.e. combinations of the electrostatic Φ and electro-magnetic A potentials and the density perturbation $\ln \tilde{n}/n_0$, with $\lambda = c_A/u_z$ the inverse of the parallel velocity normalized to the Alfvén speed and $\lambda_e = d_e/\rho_s$ the ratio of the electron skin depth over the ion Larmor radius. The corresponding streamfunctions are given by

$$\Phi_\pm \equiv \frac{1}{\pm\lambda_e - \lambda}(\pm\lambda_e\Phi - A), \qquad \Phi_3 \equiv \Phi. \tag{2}$$

Like the 2D Euler equation for the vorticity, this set of equations has point vortex solutions and additionally two classes of current filament solutions. These are obtained by assuming that the convected scalar fields are distributed as a finite number of singular δ-functions:

$$G_\alpha = \sum_{i=1}^{N_\alpha} \kappa_{\alpha,i}\delta(\mathbf{r} - \mathbf{r}_{\alpha,i}) \qquad \alpha = +, -, 3. \tag{3}$$

Like the 2D Euler case, this system of current-vorticity filaments can be described as a Hamiltonian dynamical system. The Hamiltonian H is obtained directly from the Hamiltonian of the original fluid equations [1], $H = -\frac{1}{2}\int_{\mathcal{D}} \sum_\alpha G_\alpha \Phi_\alpha$, and can be regarded as the sum of the 'interaction potentials' $V_{\alpha,i;\beta,j}$ of the individual filaments excluding self-interactions: i.e.,

$$H = -\tfrac{1}{2}\sum_{\alpha,i} \kappa_{\alpha,i}\Phi_\alpha(\mathbf{r}_{\alpha,i}) = \sum_{\alpha,i}\sum_{\beta,j\neq\alpha,i} V_{\alpha,i;\beta,j} \tag{4}$$

with

$$V_{\alpha,i;\beta,j} = \frac{-\kappa_{\alpha,i}\kappa_{\beta,j}}{4\pi(1-\lambda^2)}\left(\ln r_{\alpha,i;\beta,j} + C_\alpha C_\beta K_0(\gamma r_{\alpha,i;\beta,j})\right),$$

where the coefficients C_α for the different 'types' of the interacting filaments are $C_\pm = (1\mp\lambda\lambda_e)/(\pm\lambda_e-\lambda)$ and $C_3 = -\lambda$. The canonical coordinates and momenta are $\sqrt{\kappa_{\alpha,i}}x_{\alpha,i}$ and $\sqrt{\kappa_{\alpha,i}}y_{\alpha,i}$, respectively.

Note, that the only difference with respect to 2D singular Euler vortices is the presence in the interaction potential of additional terms proportional to $C_\alpha C_\beta K_0(\gamma r_{\alpha,i;\beta,j})$. As a consequence, the short range interaction between two types of filaments changes from attractive to repulsive (or vice versa) when $C_\alpha C_\beta > 1$. On the other hand, the current-vortex filament dynamics is qualitatively identical to that of singular 2D Euler vortices, when all $C_\alpha C_\beta < 1$.

Conditions for integrable motion

Our Hamiltonian systems possesses, apart from the Hamiltonian H, a number of invariants. These are the linear momenta in x, $P_x \equiv \sum_{\alpha,i}\kappa_{\alpha,i}y_{\alpha,i}$, and y, $P_y \equiv \sum_{\alpha,i}\kappa_{\alpha,i}x_{\alpha,i}$, and the rotational momentum, $P_\phi = \frac{1}{2}\sum_{\alpha,i}\kappa_{\alpha,i}(x_{\alpha,i}^2+y_{\alpha,i}^2)$. The Poisson brackets (defined w.r.t. the canonical variables) of these invariants are

$$\{P_x,P_y\} = -\sum_{\alpha,i}\kappa_{\alpha,i}, \qquad \{P_x,P_\phi\} = -P_y, \qquad \{P_y,P_\phi\} = +P_x, \tag{5}$$

while

$$\{P_x^2+P_y^2,P_\phi\} = 0. \tag{6}$$

The system thus is found to possess always three invariants in involution, such that the motion of three filaments is always integrable. In the special case of vanishing total vorticity ($\sum_{\alpha,i}\kappa_{\alpha,i} = 0$) and of vanishing momenta ($P_x = P_y = 0$) the three independent integrals P_x, P_y, and P_ϕ are in involution, and the four-filament problem becomes integrable. In particular, the problem of two pairs of filaments with vanishing total momenta is integrable. The latter case is analyzed in detail below.

Phase space topology and bounded dynamics of filaments

An integrable problem thus results in case of two balanced pairs of filaments with vorticities $\kappa_1 = -\kappa_2 = k_1$ for the first, $\kappa_3 = -\kappa_4 = k_2$ for the second pair, and vanishing momenta $P_x = P_y = 0$. The number of degrees of freedom in the Hamiltonian can than be reduced to one with coordinate ρ and conjugate momentum p_ρ. Possible dynamical solutions are now mapped out by contours of constant H on 2D phase space (ρ, p_ρ). In fact, this reduction can be performed identically to the corresponding one in case of 2D Euler vortices (see Eckhardt & Aref [2]). The relations between (ρ, p_ρ) and the original interparticle distances are:

$$\begin{aligned} r_{12}^2 &= \rho^2/\mu^2\Gamma, & r_{34}^2 &= \mu^2\rho^2/\Gamma, \\ r_{13}^2 &= \Gamma^{-1}\left(p_\rho^2+(\delta_+\rho+P_\phi/\rho)^2\right), & r_{14}^2 &= \Gamma^{-1}\left(p_\rho^2+(\delta_-\rho+P_\phi/\rho)^2\right), \\ r_{23}^2 &= \Gamma^{-1}\left(p_\rho^2+(\delta_-\rho-P_\phi/\rho)^2\right), & r_{24}^2 &= \Gamma^{-1}\left(p_\rho^2+(\delta_+\rho-P_\phi/\rho)^2\right), \end{aligned} \tag{7}$$

where $\Gamma = \sqrt{k_1k_2}$, $\mu = \sqrt{k_1/k_2}$, and $\delta_\pm = (\mu^{-1}\pm\mu)/2$.

Again, when for all interacting types $C_\alpha C_\beta < 1$, is the topology of the contours of constant H identical to that of the corresponding 2D Euler case (see [2]). In particular, there are three fixed points (two stable fixed points on the ρ axis at $\rho = \sqrt{|P_\phi|/|\delta_\pm|}$ and one unstable hyperbolic point close to $(\rho^2, p_\rho^2) \approx |P_\phi|(\sqrt{2}, \frac{1}{2}\sqrt{2})$. Thus, there are two regions of bounded or trapped dynamics of the vortices: one around the stable fixed point $\rho = \sqrt{|P_\phi|/\delta_+}$ describing the trapping of two like signed vortices orbiting each other by two vortices of the opposite sign counter-rotating in a slightly larger orbit; and one around the stable fixed point $\rho = \sqrt{|P_\phi|/|\delta_-|}$ describing two pairs of counter-rotating unbalanced dipoles. Note, that in case of two identical vortex pairs $\delta_- = 0$, such that the second elliptical point is moved to infinity $\rho \to \infty$: the contours on the right hand side below the separatrix then describe a direct scattering, while the contours above the separatrix describe an exchange scattering.

When at least for one set of filements $C_\alpha C_\beta > 1$, the topology of phase space is changed drastically. Depending on the detailed parameters, the hyperbolic fixed point may disappear and/or new hyperbolic and elliptic fixed points appear. In particular, when for all interacting filaments $C_\alpha C_\beta > 1$, while the scale length γ remains of order unity, a new elliptic fixed point is found for relatively large values of ρ and p_ρ. An example of the latter is given in Fig. 1. The new fixed point describes a stable trapezoidal configuration of the four filaments that rotates slowly over a larger circle. As one moves away from this new stable fixed point, the filaments start to exhibit a small, but fast near circular oscillation around their average position in addition to the common rotation. The period and radius of the latter increase slightly. Further away from the fixed point, the fast oscillation becomes strongly deformed as illustrated in Fig. 2 which shows the orbits in the "laboratory frame" and in a frame moving with the common slow rotation.

Summary

We have studied the integrable dynamics of four singular drift-Alfvén vortex-current filaments. In particular, a new type of stable bounded motion of four filaments has been identified. In future studies this work will be extended to more general configurations including, for example, other vorticity types. Furthermore, the relation of the singular filaments with known analytical extended vortex solutions of the original set of equations needs to be clarified.

Acknowledgement This work was performed under the Euratom–FOM Association agreement with financial support from NWO and Euratom.

REFERENCES

[1] T.J. Schep, V.P. Lakhin, E. Westerhof, this conference; B.N. Kuvshinov, V.P. Lakhin, F. Pegoraro, T.J. Schep, to be published in J. Plasma Physics (1998).

[2] B. Eckhardt, and H. Aref, Philos. Trans. R. Soc. London A **326**, 655-696 (1988); B. Eckhardt, Phys. Fluids **31** 2796 (1988).

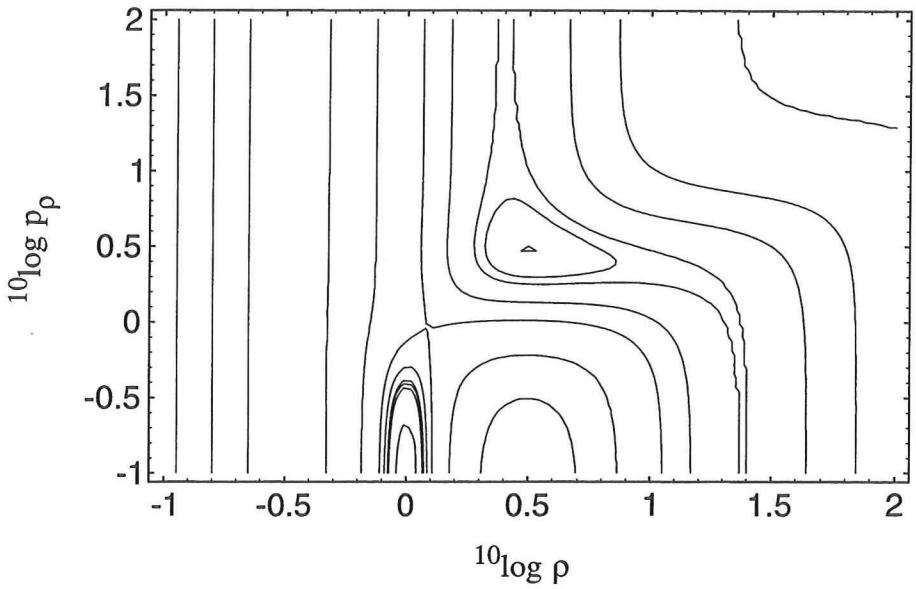

Figure 1. Countour levels of the Hamiltonian (2) for a case with four filaments of type 'κ_-' with strengths $k_1 = 1.1$ and $k_2 = 0.9$. The other parameters are $P_\phi = -1$, $\lambda = 10$ and $\lambda_e = 3$, such that $C_-^2 = 5.96$, and $\gamma = 1.04$. Note the trianlge indicating the additional elliptic fixed point. The closed curve surrounding it represents $H = -.001897$, for which the orbits of the four filaments are given in Fig. 2.

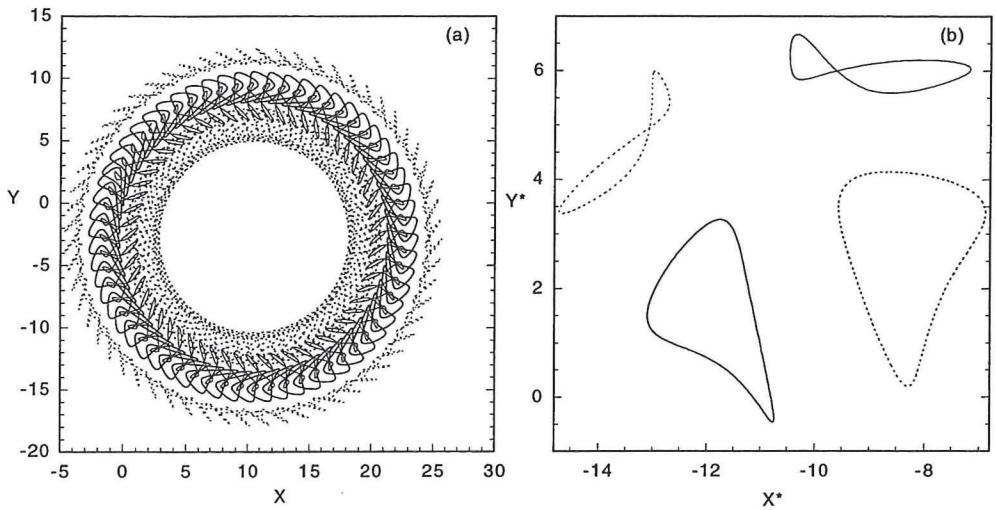

Figure 2. (a) Orbits of four current-vortex filaments of type 'κ_-' parameters are as for Fig. 1, the initial conditions are chosen inside the region with bounded motion around the O-point in Fig. 1 at $(\rho, p_\rho) \approx (3.14, 2.97)$. (b) The orbits in the co-rotating frame. Full curves indicate filaments (1,3) with positive 'vorticity' and the thicker curves indicate the filaments (1,2) with larger strenght.

Future Prospects of Electron Cyclotron Heating and Current Drive in TJ-II Stellarator

V. Tribaldos, J.A. Jiménez, J. Guasp and B.Ph. van Milligen
Asociación EURATOM-CIEMAT para Fusión
Madrid, Spain

Abstract

Electron cyclotron resonance heating (ECRH) has become an attractive issue in today's fusion experiments not only as a heating mechanism but also as a diagnostic tool and as way to induce controllable currents by electron cyclotron current drive (ECCD). In this paper we show, using ray tracing simulations, how one can address all these issues with the ECRH system designed for the TJ-II stellarator. This ECRH set-up consist of two 500 kW gyrotrons at $f = 53.2$ GHz coupled to the plasma through two quasioptical transmission lines, placed at two stellarator symmetric positions, and equipped with an internal steerable mirror. Using 3D Hamiltonian ray tracing techniques, the capabilities of the system to heat different fractions of trapped particles and to gently modify the rotational transform profile in TJ-II, are presented.

Introduction

TJ-II is a mid-size, four period, helical axis stellarator [1] about to start operation in Madrid, Spain. The magnetic field of TJ-II is obtained with the set of coils of Fig. 1. The central conductors, together with the helically positioned toroidal coils, give TJ-II the possibility to access a wide range of magnetic configurations with rotational transforms between 0.9 and 2.5, magnetic shear between -1 and 10% and magnetic well depths between 0 and 6%, almost independently. This flexibility also makes the plasma position shape and size different from configuration to configuration, and makes the design of an ECRH system more complicated than in planar axis devices. The features of the designed ECRH system for both on- and off-axis heating and of inducing currents by ECCD have just been presented in a previous work [2]. The purpose of this study is to show other physic issues that can be addressed with the system. Those issues include the possibility to: *i*) heat at different toroidal angles of the device where the fraction of trapped particles is different; *ii*) modify the rotational transform profile with ECCD.

The ECRH system of TJ-II

The ECRH system consists of two 500 kW gyrotrons at f =53.2 GHz (2^{nd} harmonic of the TJ-II field), and a pulse length of 1 sec. These gyrotrons are coupled to the plasma with two quasioptical transmission lines [3] located at two toroidal stellarator symmetric positions[1] ($\varphi = 25.47°$ and $\varphi = 64.53°$). Both lines are equipped with a steerable mirror, located inside the vacuum vessel, that can rotate $\pm 10°$ with respect to the toroidal injection plane, and from 0° to 35° with respect to the Z axis. Although the mirror movement is small, the parallel refractive index, $N_{\parallel} = (c/w|\mathbf{B}|)\mathbf{k} \cdot \mathbf{B}$, can be considerable, due to the strong dependence of the magnetic field on the toroidal and poloidal angles in TJ-II.

[1] the stellarator symmetry for TJ-II is such that $\psi(R, \pi/4 + \varphi, Z) = \psi(R, \pi/4 - \varphi, -Z)$

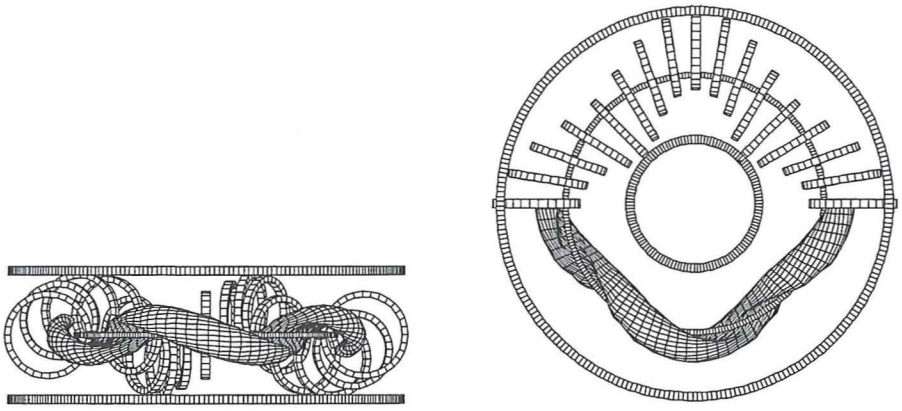

(a) Side View. (b) Top View.

Figure 1: Coil configuration and plasma of TJ-II stellarator.

Trapped Particles

Using the flexibility of the steerable mirror, it is possible to obtain on-axis heating at toroidal angles between $26° < \varphi < 37°$ for the first line, and at $55° < \varphi < 63°$ for the second line. As an example in Fig. 2 (a) the width of the power density profile is plotted versus the toroidal angle at which the maximum absorption takes place; the outer, dotted, curves indicate the bounds within which 90% of the power is deposited, the maximum being at the central, solid, curve. The plasma parameters we have considered for these ray tracing simulations [4] are: $r_{max} = 2$ cm, $w = 1$ cm, electron density and temperature on axis $n_e^o = 1.5 \times 10^{19}$ m^{-3}, $T_e^o = 0.8$ keV, $Z_{eff} = 1$, and $P_{ECRH} = 200$ kW, and giving a single-pass absorption of more than 95%.

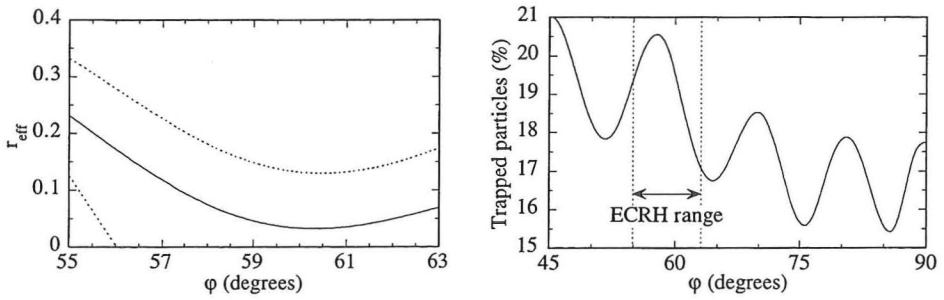

(a) Width of the power deposition profile. (b) Trapped particle fraction, near the axis.

Figure 2: Toroidal angle dependence

Since the fraction of trapped particles in TJ-II depends strongly on the toroidal angle because of the ripple, the possibility of heating at different toroidal angles can be exploited to study the possible influence of trapped particles. To estimate this fraction, a Monte Carlo code [5] that follows the particle orbits in Boozer co-ordinates, using the guiding center approximation and neglecting collisions, has been used. The code was run following 30720 particles, corresponding to 32 toroidal angles (in one machine period), 24 poloidal angles and 40 pitch angles (uniformly distributed in both directions), for each magnetic surface, electric potential, and energy, of a given magnetic configuration. A typical run of the code takes approximately 1 1/2 hours (dedicated time), using 16 processors of a CRAY-T3E. The results of this calculations indicate that the fraction of trapped particles on the toroidal angle, near the magnetic axis, is almost independent of the plasma configuration and is mainly sensitive to the coil structure of TJ-II, see Fig. 1. The fraction of trapped particles near the axis is presented in Fig. 2 (b), for half a period, showing that the maximum change in the trapped fraction ($\approx 5\%$ for the standard configuration) takes place precisely in the available toroidal range of the ECRH system.

Rotational Transform Profile Modification

The flexibility in the launching set-up can also be used to induce rather high currents by ECCD, in both directions for the same effective radius using only one of the lines, due to the strong dependence of the magnetic field on the toroidal angle φ (the dependence of $N_{\|}$ on k being very weak). Moreover since the injection takes place at two stellarator symmetric toroidal angles, it is possible to have on- or off-axis heating without inducing currents by using appropriate settings in both lines, thus making it possible not only to cancel the current but also to add their contributions. We stress that there exists a combination of mirror angles giving zero net current. In Fig. 3 the width of the power deposition profile and the total induced current is plotted versus the tilting of the mirror in the poloidal direction, while keeping $\varphi = 60.4°$ and with the same conditions as in Fig. 2. The localization of the toroidal current density profile is not presented since it is quite similar (the induced current being proportional to the absorbed power).

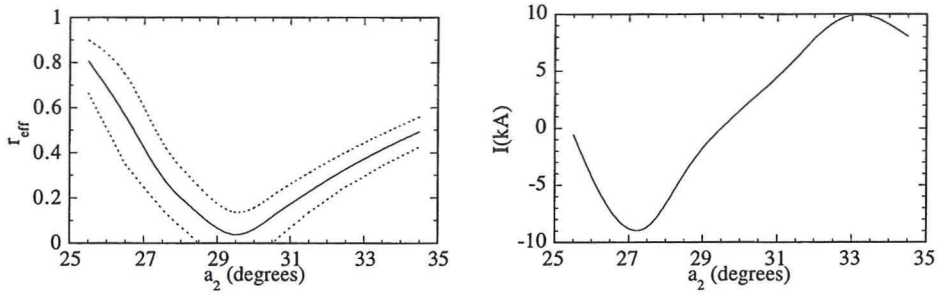

(a) Width of the power deposition profile.

(b) Total induced current by ECCD.

Figure 3: Dependence on the tilting angle

It is possible to use the described flexibility in inducing currents to study the confinement properties of the plasma by modifying the rotational transform profile or the MHD stability properties. To estimate how the equilibrium is affected, the free boundary VMEC 3D

equilibrium code [6] was used, introducing the currents obtained by the ray tracing code for the ECCD. As an example of these calculations the iota profiles for zero current and two launching conditions, both having the maximum current density at $r_{eff} = 0.2$, are presented in Fig. 4. ECCD can also be used to at least partially compensate bootstrap currents. The current density profile of the bootstrap current for TJ-II, derived from neoclassical estimations [7], is centered at approximately half radius i.e.; where the highest induced current is obtained, see Fig. 4. However, the effect of bootstrap currents on the plasma performance of TJ-II is expected to be small since, in the first phase of operation, only ECRH (cut-off density $\simeq 1.75 \times 10^{19} m^{-3}$) will be used for heating.

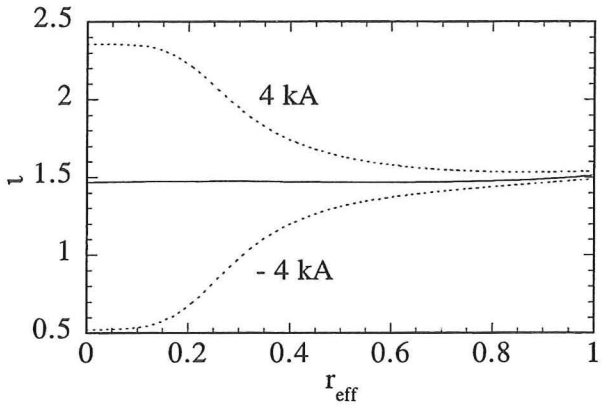

Figure 4: Rotational transform profile for $I = 0$kA (solid) and $I = \pm 4$kA (dashed).

Conclusions

Within the geometric optics approximation it has been shown that the designed ECRH setup allows for heating at positions having different fraction of trapped particles. The system is also capable of inducing and controlling appreciable localized currents in both directions for the same effective radius, thus opening the possibility to use ECCD to locally control plasma currents and the ι profile.

References

[1] C. Alejaldre, et al., Fusion Technol. **13** (1988) 521.

[2] V. Tribaldos, et al., Proc. EC10, Ameland, The Netherlands, (1997).

[3] M. Sorolla, et al., Int. Journal of Infrared and Millimeter Waves **18** (1997) 1161.

[4] V. Tribaldos and B.Ph.van Milligen, Nucl. Fusion **36** (1996) 283.

[5] J. Guasp and M. Liniers, CIEMAT report **824** (1997).

[6] S.P. Hirshman, W.I. van Rij and P. Merkel, Comput. Phys. Commun. **43** (1986) 143.

[7] A. Rodriguez-Yunta, W.I. van Rij and S.P. Hirshman, Proc. 17^{th} EPS **14B** (1990) 505.

Aspects of bounce-averaged Fokker-Planck modeling of radio frequency heating in tokamaks

D. Van Eester, R. Koch

Laboratorium voor Plasmafysica - Laboratoire de Physique des Plasmas
Associatie 'Euratom-Belgische Staat' - Association 'Euratom-Etat Belge'
Koninklijke Militaire School - 1000 Brussels - Ecole Royale Militaire
Trilateral Euregio Cluster, Belgium

Abstract. A selfconsistent description of the RF heating process requires the wave and Fokker-Planck equations to be solved simultaneously. The development of a combined wave equation / Fokker-Planck code with selfconsistent treatment of the RF heating in toroidal geometry is presently being undertaken. The RF model is based on the findings of Lamalle [1]. In the present paper, some details of the bounce-averaged Fokker-Planck model are given.

I. Introduction

In the absence of auxiliary heating and loss mechanisms, the orbit of a charged particle in a tokamak is determined by 3 constants of the motion $\underline{\Lambda}=(\Lambda_1,\Lambda_2,\Lambda_3)$, and 3 angles $\underline{\Phi}=(\Phi_1,\Phi_2,\Phi_3)$ that vary periodically as a function of time and parametrize the gyro-oscillation of the particle around its guiding center (gc), as well as the poloidal bounce and toroidal drift motions of the gc itself. Various processes (e.g. Coulomb relaxation and application of RF electromagnetic fields) destroy the invariance of $\underline{\Lambda}$ and cause a slow diffusion in $\underline{\Lambda}$ space that can be described by a Fokker-Planck equation for the slowly varying distribution function F_o, a function of $\underline{\Lambda}$ only. The RF electric field $\underline{\mathbf{E}}$ and the distribution F_o are closely related. The influence of $\underline{\mathbf{E}}$ on F_o is through the RF diffusion operator. The field $\underline{\mathbf{E}}$ depends on the distribution function via the dependence of the RF currents on F_o. A selfconsistent description of the RF heating process thus requires the wave and Fokker-Planck equations to be solved simultaneously. Lamalle proposed a general formalism to compute $\underline{\mathbf{E}}$ accounting for the actual tokamak geometry and allowing for an arbitrary distribution function F_o [1,2]. The evaluation of the associated RF diffusion operator was discussed by Van Eester [3].

II. The quasilinear diffusion operator

The Fokker-Planck equation is written in terms of $v=|v|$ and $x=\mu B_m/[mv^2/2]$, and is solved on a flux surface ρ (=r for a circular plasma); B_m is the strength of the static magnetic field $\underline{\mathbf{B}}_o$ at the LFS intersection of the gc orbit with the midplane. In absence of auxiliary heating, the first variable v is a true constant of the motion on the rapid time scales on which the bounce, toroidal drift and gyro-motions take place. To leading order in the drift parameter, the magnetic moment $\mu=mv_\perp^2/[2B_o(\mathbf{r}_{gc})]$ is also an invariant.

Similarly, the gc trajectories can roughly be assumed to be confined to magnetic surfaces and the toroidal angular momentum P can be reduced to the poloidal flux function Ψ, which only depends on the flux surface labeling parameter ρ. The replacement of P by Ψ is *not* without consequence, though: since the gc makes *radial* excursions on a poloidal bounce, Ψ is not a true constant of the motion on the rapid time scales over which the Fokker-Planck equation is to be averaged. Consequently, the RF induced radial transport is no longer faithfully described: whereas classical RF induced diffusion due to the gyro-motion can be included by considering the full 3-D Fokker-Planck equation in (v,x,ρ)-space, neoclassical effects are outside the scope of the model. To account for the latter, switching to P instead of ρ is necessary.

The Fokker-Planck equation is solved using a weak Galerkin variational principle. To that end, the Fokker-Planck equation is multiplied by a test function G and integrated by parts. The quasilinear term in the functional is of the form

$$\tilde{\mathcal{Q}}(F_o) = -\int d\Lambda\, J\, \mathcal{L}\, \{\frac{\partial G}{\partial v} + \eta \frac{\partial G}{\partial x}\}\, \{\frac{\partial F_o}{\partial v} + \eta \frac{\partial F_o}{\partial x}\} \qquad (1)$$

where $F_o=F_o(\Lambda,t)$ is the distribution function, $J = \frac{\partial \Psi}{\partial r} \frac{v^3}{4\pi\omega_b B_m}$ is the Jacobian, $\mathcal{L}$ describes the interaction of the rapidly varying electric field $\mathbf{E}=\sum_{mn}\sum \mathbf{E}_{mn}(r)$ $\exp[i\{m\theta+n\varphi-\omega t\}]$ with the orbit characterized by Λ, and $\eta = -\frac{2}{v}(x+m_g\frac{\Omega_m}{\omega})$; ω_b is the poloidal transit frequency and $-m_g$ is the cyclotron harmonic number. The poloidal and toroidal angles are θ and φ, and their respective mode numbers are m and n. Ultimately, $\mathcal{L}$ will be provided by the wave equation solver. When the relative phase of the field and the particle velocity varies rapidly, when the simplest possible decorrelation model is valid and decorrelation is weak ($\omega\rightarrow\omega+i\nu$ with $\nu\rightarrow 0^+$), and for poloidal mode numbers that are not too different, it can be approximated by

$$\mathcal{L} \approx \frac{1}{2}(\frac{q}{mv})^2 \sum_n \sum_{m_1} \sum_{m_2} \mathrm{Re}\{\mathcal{L}_{m_1}(\mathbf{E}_{m_1}(r_{gc}))\, \mathcal{L}_{m_2}(\mathbf{E}_{m_2}^*(r_{gc}))\, \exp[i(m_1-m_2)\theta_{res}]\} \quad (2)$$

in which θ_{res} is the resonant poloidal position associated with the average poloidal mode number and $\mathcal{L}$ is formally identical to the Kennel&Engelmann operator [5], except that $i\mathbf{k}$ is replaced by ∇.

III. The Coulomb collision operator

To remove all short time scale (Φ) dependence from the usual collision operator, only a bounce average is required. When P is approximated by Ψ, and when the background on which the species collisionally relax is supposed in thermodynamical equilibrium,

the result is formally identical to the uniform plasma expression except that the coefficient $\frac{v_{//}^2}{v_\perp^2}$ in the expression for the S_x-flux is now bounce averaged:

$$\tilde{\mathcal{C}}(F_o) = \frac{1}{J}\left[\frac{\partial}{\partial v}\left(J\left\{D_{vv}\frac{\partial F_o}{\partial v} - F_v F_o\right\}\right) + \frac{\partial}{\partial x}\left(J\left\{D_{\Phi\Phi}\left(\frac{2x}{v}\right)^2 < \frac{v_{//}^2}{v_\perp^2} > \frac{\partial F_o}{\partial x}\right\}\right)\right] \quad (3)$$

The expressions for D_{vv}, F_v and $D_{\Phi\Phi}$ (Φ is the pitch angle) can e.g. be found in [6].

IV. Explicit formulae for a plasma with concentric circular magnetic surfaces

In many cases, bounce averaging involves numerical integration. If the plasma has concentric circular magnetic surfaces, however, analytical expressions can be found. The time t needed to reach a poloidal position θ is, for example, $t(\theta) = \frac{2r_{gc}\Pi}{|\sin\tilde{\alpha}|v}\left[\frac{1+\tilde{\varepsilon}}{(1-\tilde{\varepsilon})\xi_m^2}\right]^{1/2}$ for passing and $t(\theta) = \frac{2r_{gc}\Pi}{|\sin\tilde{\alpha}|v}\left[\frac{1+\tilde{\varepsilon}}{2\tilde{\varepsilon}(1-\xi_m^2)}\right]^{1/2}$ for trapped particles [7]. Here, $\tilde{\alpha}$ is the angle between $\underline{e}_{//} = \frac{\underline{B}_o}{B_o}$ and $\underline{e}_\varphi$, $\tilde{\varepsilon} = \frac{r_{gc}}{R_o}$, $\xi_m = \frac{v_{//m}}{v}$, $\Pi(\varphi,\nu,k)$ is the third incomplete elliptic integral, $\nu_{pa} = \frac{2\tilde{\varepsilon}}{\tilde{\varepsilon}-1}$, $\nu_{tr} = \frac{1}{1-\frac{1}{\xi_m^2}}$, $k_{pa}^2 = \frac{1}{k_{tr}^2} = \frac{\nu_{pa}}{\nu_{tr}}$ and, finally, $\varphi_{pa} = \sin^{-1}\left(\left[\frac{(1-\cos\theta)(R_o - r_{gc})}{2(R_o + r_{gc}\cos\theta)}\right]^{1/2}\right)$ while $\varphi_{tr} = \sin^{-1}\left(\left[\frac{(1-\cos\theta)(R_o + r_{gc}\cos\theta_{max})}{(1-\cos\theta_{max})(R_o + r_{gc}\cos\theta)}\right]^{1/2}\right)$.

V. Examples

In this section we provide some results of the newly developed Fokker-Planck code. Figure 1 depicts a D population heated at its second cyclotron harmonic. One toroidal mode (n=20) and 3 poloidal modes (-20<m<-18) were considered only and $|E_+| = |E_-|/3 = 100$ $|E_{//}| = 1$kV/m was assumed for each (n,m). Because second harmonic heating is inefficient at low perpendicular velocities ($\mathcal{L}_m$ in Eq.(2) is zero at $v_\perp = 0$), the bulk of the deuterons are unaffected by the RF field and so F_o is a Maxwellian at $v \approx 0$. At higher velocities, the heating efficiency improves and an energetic tail is formed. The heating is most efficient for the tangent resonance orbits but pitch angle scattering allows particles to diffuse both to lower $v_{//m}$ and into the region corresponding to orbits that are too deeply trapped to feel the influence of the RF field (no cyclotron resonance crossing).

Figure 2 depicts the distribution function for a nearly *tangential* D counterbeam in TEXTOR. The incoming beam has $v_{source} = 2.25\ 10^6$m/s and $x_{source} = 0.25$. Both the collisionally broadened maximum near the source and the thermalized subpopulation can be distinguished. To highlight the location of the source, a somewhat short confinement time (τ_p=15ms) was taken; a τ_p of the order of the slowing down time

τ_{SD}=60ms results in a much larger thermalized part of the distribution and relatively less particles near the source.

Figure 3 shows the synergistic effect of D second cyclotron harmonic and NBI heating for τ_p=60ms. Compared to pure RF heating, a more appreciable fraction of the population, born in the high velocity $v_{//m}<0$ region, is efficiently heated (note the distribution's secondary maxima in that region).

References

[1] Lamalle, P.U. 1993 *Phys. Letters* **175A**, 45
[2] Lamalle, P.U. 1997*Plasma Physics and Controlled Fusion* **39**, 1
[3] Van Eester, D. 1995 *J. Plasma Physics* **54**, 31
[4] Balescu, R. 1988 *'Transport Processes in Plasmas'*, Vol. **I&II**, North-Holland, Amsterdam
[5] Kennel, C.F. and Engelmann, F. 1966 *Phys. Fluids* **9**, 2377
[6] Karney, C.F.F. 1986 *Computer Physics Reports* **4**, 183
[7] Prudnikov, A.P. et al. 1990 *'Integrals and Series'*, Vol **I**, Gordon&Breach Science Publishers, New York

Fig.1: Second cyclotron harmonic heating

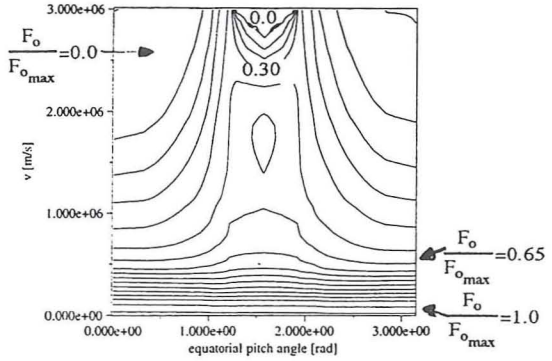

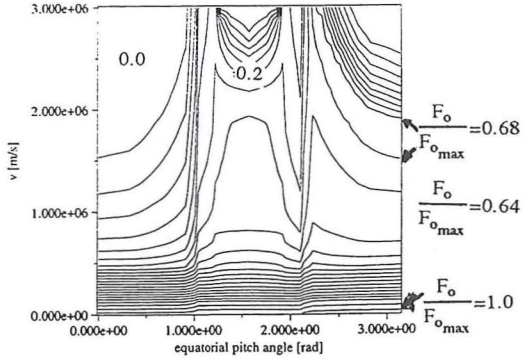

Fig.2: Counter NBI heating

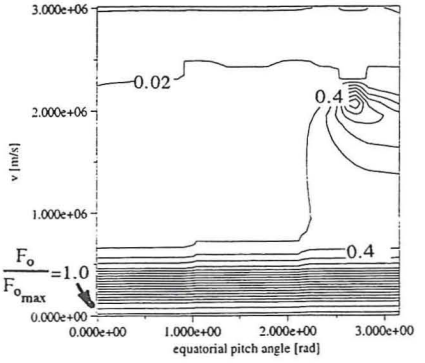

Fig.3: Combined second cyclotron harmonic +NBI heating

A solver for the non-linear Fokker-Planck equation.

Fabrice Louche

Plasma Physics Laboratory - Ecole Royale Militaire/Koninklijke Militaire School,
EURATOM-Belgian State Association, Trilateral Euregio Cluster,
30, Avenue de la Renaissance - 1000 Brussels - Belgium
email : louche@fusion.rma.ac.be

1. Introduction

Ion Cyclotron Resonance Heating (ICRH) is one of the most regularly used auxiliary heating schemes in tokamak experiments. During ICRH, the velocity distribution function f_a of the heated ions becomes highly non-Maxwellian, with a significant part of the energy in the tail. The power is transferred to the background plasma *via* the Coulomb collisions.

A correct description of these effects requires the resolution of the Fokker-Planck (F-P) equation, which describes the evolution of f_a. This equation contains the collision operator, the quasi-linear (Q-L) diffusion operator, describing radio-frequency heating, and a possible source term for describing Neutral Beam Injection (NBI). The latter implies the adding of a loss term that ensures the conservation of the particles.

In the usual minority heating schemes, the self-collisions of the heated particles may be neglected. However, for ITER cases, in which Deuterium and Tritium ions are at about the same concentration, these collisions must be taken into account; consequently the collision operator becomes non-linear.

In this paper, a method for solving the non-linear F-P equation is presented, and some preliminary results are given.

2. The Fokker-Planck equation

The slow evolution of f_a is governed by the F-P equation, that we can write as:

$$\frac{\partial f_a}{\partial t} = \left(\frac{\partial f_a}{\partial t}\right)_{coll} + \left(\frac{\partial f_a}{\partial t}\right)_{Q.-L.} + S - L \qquad (1)$$

S and L are respectively the source and the loss term. The collisional and the QL diffusion are processes that conserve the number of particles. The corresponding operators can then be written as the divergence of a flux **S**:

$$\left.\frac{\partial f_a}{\partial t}\right|_{\substack{coll \\ Q.-L.}} = -\nabla \cdot \overline{S}_{\substack{coll \\ Q.-L.}} \qquad (2)$$

where

$$\overline{S} = -\overline{\overline{D}} \cdot \nabla f_a + \overline{F} f_a \qquad (3)$$

with $\overline{\overline{\mathbf{D}}}$ the diffusion tensor and $\overline{\mathbf{F}}$ the dynamical friction vector.
The expressions of $\overline{\overline{\mathbf{D}}}$ and $\overline{\mathbf{F}}$ for both processes are given in [1].

3. The Legendre representation

Following [1], we have expanded f_a in a series of Legendre polynomials:

$$f_a = \sum_{l=0}^{\infty} f_a^{(l)} P^{(l)}(\mu) \qquad (4)$$

with

$$f_a^{(l)}(v)=\frac{2l+1}{2}\int_{-1}^{1} f(v,\mu)P^{(l)}(\mu)d\mu \quad ; \quad \mu=\cos\theta=\frac{v_{//}}{v} \tag{5}$$

in which θ is the pitch-angle. This representation transforms the 2-D F-P equation into a system of coupled 1D equations for the coefficients $f_a^{(l)}$.

4. The collision operator in Legendre representation

For expressing the collision operator, we have used a representation in terms of Rosenbluth potentials [2], written in the Trubnikov notation [3]:

$$\Phi_b(\bar{v})=-\frac{1}{4\pi}\int\frac{f_b(\bar{v})}{|\bar{v}-\bar{v}'|}d^3\bar{v}' \quad ; \quad \Psi_b(\bar{v})=-\frac{1}{8\pi}\int|\bar{v}-\bar{v}'|f_b(\bar{v}')d^3\bar{v}' \tag{6}$$

where f_b is the velocity distribution function of the background particles or of the particles themselves. The diffusion and friction terms can be written in terms of these potentials.The Rosenbluth potentials can be expanded in a series of Legendre polynomials. The expressions of the coefficients, which are function of the velocity only, can be found in [1].For a Maxwellian background, the 0^{th} component of each potential only is relevant, and the linear equation can be solved. On the other hand, the evaluation of (6) for the self-collisions requires the numerical integration of the unknown function f_a over the velocity space. The partial collision operator can then be expressed in terms of the components of the Rosenbluth potentials by the equation:

$$\left(\frac{\partial f_a^{(q)}}{\partial t}\right)_{coll}=-\frac{4\pi\Gamma^{a/a}}{n_a}\frac{2q+1}{2}\sum_n\left\{f_a^{(n)}A_n^q(v)+\frac{\partial f_a^{(n)}}{\partial v}B_n^q(v)+\frac{\partial^2 f_a^{(n)}}{\partial v^2}C_n^q(v)\right\} \tag{7}$$

with

$$A_n^q(v)=\sum_l[I_2^{nlq}\left(\frac{1}{v^4}\Psi^{(l)}-\frac{1}{v^3}\frac{\partial\Psi^{(l)}}{\partial v}+\frac{1}{v^2}\frac{\partial^2\Psi^{(l)}}{\partial v^2}\right)-\left(\frac{1}{v^4}\Psi^{(l)}I_3^{nql}+\frac{1}{v^3}\frac{\partial\Psi^{(l)}}{\partial v}I_2^{nql}\right)$$

$$-I_1^{lqn}\left(\frac{\partial^2\Phi^{(l)}}{\partial v^2}+\frac{2}{v}\frac{\partial\Phi^{(l)}}{\partial v}\right)+\frac{1}{v^2}\Phi^{(l)}I_2^{lqn}]$$

$$B_n^q(v)=\sum_l\left[I_1^{lqn}\left(\frac{2}{v}\frac{\partial^2\Psi^{(l)}}{\partial v^2}+\frac{\partial^3\Psi^{(l)}}{\partial v^3}-\frac{\partial\Phi^{(l)}}{\partial v}\right)+\left(I_2^{nlq}-I_2^{lqn}\right)\left(\frac{1}{v^2}\frac{\partial\Psi^{(l)}}{\partial v}-\frac{1}{v^3}\Psi^{(l)}\right)\right]$$

$$C_n^q(v)=\sum_l I_1^{lqn}\frac{\partial^2\Psi^{(l)}}{\partial v^2}$$

and

$$I_1^{lqn}=\int_{-1}^{1}P^{(l)}(\mu)P^{(q)}(\mu)P^{(n)}(\mu)d\mu$$

$$I_2^{lqn}=\int_{-1}^{1}\frac{\partial P^{(l)}(\mu)}{\partial\mu}\frac{\partial P^{(q)}(\mu)}{\partial\mu}P^{(n)}(\mu)(1-\mu^2)d\mu$$

$$I_3^{lqn}=-\int_{-1}^{1}\left[(1-\mu^2)\frac{\partial^2P^{(l)}(\mu)}{\partial\mu^2}-\mu\frac{\partial P^{(l)}(\mu)}{\partial\mu}\right]\left[(1-\mu^2)\frac{\partial^2P^{(q)}(\mu)}{\partial\mu^2}-\mu\frac{\partial P^{(q)}(\mu)}{\partial\mu}\right]\frac{\partial P^{(n)}(\mu)}{\partial\mu}\sqrt{1-\mu^2}d\mu$$

These integrals have been computed analytically.

5. The quasi-linear operator in Legendre representation

We have performed the projection (5) for the RF diffusion operator. Due to the resonant interaction between the particles and the RF field, the operator is only non-zero at the resonant velocity. This considerably simplifies its numerical evaluation. The expressions of the two components of the flux vector, projected on the q^{th} Legendre polynomial, are

$$S_v^{(q)} = -\frac{2q+1}{2}\sum_n \frac{\pi}{8}\frac{Z_a^2 e^2}{m_a^2}\frac{1}{|k_{//}|}|\Theta_n|^2\frac{1}{v}$$

$$\sum_l \left\{\left(1-\frac{v_{res}^2}{v^2}\right)P^{(q)}P^{(l)}\frac{\partial f^{(l)}}{\partial v}+\frac{1}{v}\left(\frac{v_{res}}{v}-\frac{v}{v_{ph}}\right)\frac{l(l+1)}{2l+1}P^{(q)}(P^{(l+1)}-P^{(l-1)})f^{(l)}\right\} \tag{8a}$$

$$S_\theta^{(q)} = -\frac{2q+1}{2}\sum_n \frac{\pi}{8}\frac{Z_a^2 e^2}{m_a^2}\frac{1}{|k_{//}|}|\Theta_n|^2\frac{1}{v}\sqrt{1-\frac{v_{res}^2}{v^2}}\left(\frac{v_{res}}{v}-\frac{v}{v_{ph}}\right)$$

$$\sum_l \left\{P^{(q)}P^{(l)}\frac{\partial f^{(l)}}{\partial v}+\frac{1}{v}\left(\frac{v_{res}}{v}-\frac{v}{v_{ph}}\right)\frac{1}{1-\frac{v_{res}^2}{v^2}}\frac{l(l+1)}{2l+1}P^{(q)}(P^{(l+1)}-P^{(l-1)})f^{(l)}\right\} \tag{8b}$$

in which each Legendre polynomial is evaluated at the resonant position:

$$\mu_{res} = \frac{v_{res}}{v} = \frac{\omega - n\Omega}{vk_{//}}$$

The definition of the other terms can be found in [1] and [4].

6. Numerical resolution of the Fokker-Planck equation

The system of equations to which the F-P equation is reduced is solved using a finite-difference scheme. For this purpose, a grid of N points is generated in v [5]. For the computation of the self-collision operator, we have made the approximation:

$$\left(\frac{\partial f_a}{\partial t}\right)_{coll}(t) = \sum_b C(f_a,f_b) = \sum_{b\neq a} C(f_a,f_b) + C(f_a,f_a)$$

$$\approx \sum_{b\neq a} C(f_a(t), f_b^{\max}) + C\left(f_a\left(t+\frac{\Delta t}{2}\right), f_a\left(t-\frac{\Delta t}{2}\right)\right) \tag{9}$$

When the steady-state regime is reached, f_a is independant of time and the second term in (9) is the nonlinear term.

The discretized form of the F-P equation is:

$$\frac{\partial \bar{x}}{\partial t} = \bar{\bar{A}}\cdot\bar{x} - \bar{b} \tag{10}$$

where the vector $\bar{x}$ contains the value of each component of fa on the grid points and $\bar{b}$ is the source term. Using a Cranck-Nicholson method [1] for the time derivative, we obtain:

$$\left(\bar{\bar{1}}-\frac{1}{2}\Delta t\bar{\bar{A}}\right)\cdot\bar{x}\left(t+\frac{\Delta t}{2}\right) = \left(\bar{\bar{1}}+\frac{1}{2}\Delta t\bar{\bar{A}}\right)\cdot\bar{x}\left(t-\frac{\Delta t}{2}\right) - \Delta t\bar{b}(t) \tag{11}$$

7. Preliminary results

For all the examples described here, we have simulated Deuterium plasmas with a minority of Hydrogen. The parameters are typical for TEXTOR [6].

7.1. Convergence of the Legendre expansion

The series (4) must be truncated after a certain number of terms, sufficiently high for correctly describing the anisotropy of the suprathermal tail induced by the quasi-linear diffusion. Our results show that for different heating schemes, the convergence of global properties is good. Figure 1 illustrates the convergence of the expansion by plotting the energy and the RF power density for a simulation of combined NBI + first harmonic heating of H. This behaviour is not very sensitive to the concentration of the species.

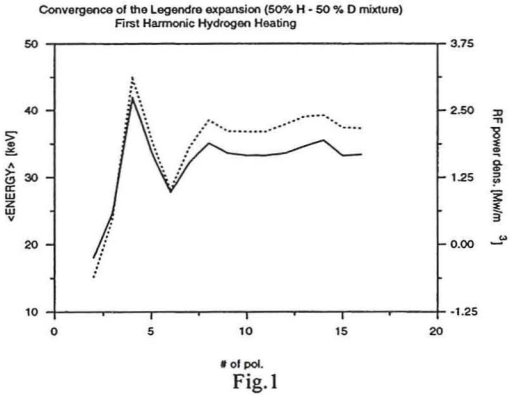

Fig.1

7.2. Effect of the self-collisions

We have solved the non-linear equation for a H-D TEXTOR plasma. The time step in equation (11) is 10 ms. Starting from the linear equation solution, we have investigated the effects of the non-linear contributions by increasing the minority concentration, the other parameters remaining constant. The radio-frequency power density has been plotted on Fig.2. The non-linear contributions become significant when the Hygrogen concentration is about 25 % of the Deuterium concentration.

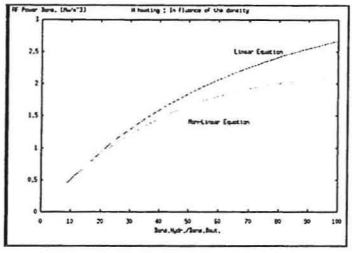

Fig.2

References.

[1] : Karney C.F.F., *Comp.Phys.Rep* 4(1986), p.183
[2] : Rosenbluth M.N., MacDonald W.M. and Judd D.L., *PhysRev.* **107**(1957), p.1
[3] : Trubnikov B.A., in:*Reviews of Plasma Physivs* vol.1, ed.M.A.Leontovitch,(Consultants Bureau, New-York, 1965), p.105
[4] : Kennel C.F. and Engelmann F., *Phys.Fluids* 9(1966), p.2377
[5] : Van Eester D., *Plasma Phys.Control.Fusion* **36**(1994), p.1327
[6] : Messiaen et al., *Plasma Phys.Control.Fusion* **35A** (1993), p.A15

Study of Landau interaction between electrons and r.f. field, incorporating phase decorrelation effects

Y. Louis [1&2], P.U. Lamalle [2]

[1] Service de Physique Générale, Faculté des Sciences Appliquées,
Université Libre de Bruxelles, B-1050 Brussels, Belgium

[2] Laboratoire de Physique des Plasmas / Laboratorium voor Plasmafysica, ERM / KMS,
EURATOM Association, Trilateral Euregio Cluster, B-1000 Brussels, Belgium

1. Introduction

Using the nonlocal model of the plasma r.f. response in tokamak geometry presented in [1,2], we have investigated the contribution of various particle orbits to the electron Landau damping of r.f. wave in the ICRH range of frequencies. Wave-particle phase decorrelation due to Coulomb collisions is included in this description (see section 3). One objective of the present study is to evaluate separately the power absorbed by passing and trapped electrons, in order to check the validity of a common approximation which neglects the contributions of the latter in ICRH scenarios [3]. Our model takes the mutual coupling between r.f. field poloidal modes into account, but we limit the following illustration to a 'diagonal' term corresponding to the single poloidal mode m and the toroidal mode n; ITER geometry with a circular plasma cross section is assumed. The active power W_{nm} is expressed as: $W_{nm} = \int d\rho \int dv \int d\gamma_0 \, w_{nm}$, where ρ is the minor radius of the magnetic surface, v is the particle velocity and γ_0 is the outboard equatorial pitch angle. Each guiding center orbit contribution w_{nm} to the power density in the space of the constants of motion (c.o.m.) is given by a series of bounce time harmonics. Two techniques are used to evaluate this expression, according to the level of inhomogeneity of the Doppler term $k_{//} v_{//}$ induced along the guiding center trajectory by toroidicity and rotational transform [1]. The first method is a direct numerical evaluation of the bounce series. The second, faster method uses an asymptotic expansion well adapted to the situations where $k_{//} v_{//}$ is highly inhomogeneous; it has been shown very accurate for the cyclotron interactions [4]. The following section is devoted to the evaluation of Landau damping by both methods, in order to investigate the validity of the asymptotic expansion for this type of wave-particle interaction.

2. Evaluation of the power density in the c.o.m. space

We study a circular approximation of the ITER tokamak with the following parameters: major radius $R_0 = 7.92$ m, minor radius $a_p = 2.8$ m, magnetic induction on axis $B_a = 6.11$ T, safety factor $q = 1.1$ at the center and $q = 2.5$ at the plasma edge, central electron density $N_{e0} = 1.4\ 10^{20}\ m^{-3}$, electron temperature $T_{e0} = 20$ keV at the center and $T_{eb} = 1$ keV at the plasma edge, and a 50% D-T plasma. We focus on the $\rho = 1.35$ m magnetic surface, choose $f = 20$ MHz as generator frequency in order to avoid cyclotron interactions with D and T ions, study the r.f. field toroidal mode n=16 (which ensures a significant absorption by the electrons for the above parameters), and show the results corresponding to the r.f. field poloidal mode m=0.

We normalize the power density w_{nm} in order to obtain a quantity independent of the equilibrium distribution function and of the r.f. field amplitude, and display on figure 1 the result obtained for a velocity $v = 1.55\ v_{th}$ as a function of the outboard equatorial pitch angle γ_0. The continuous curve is the result of the direct numerical evaluation, and the dotted curve is

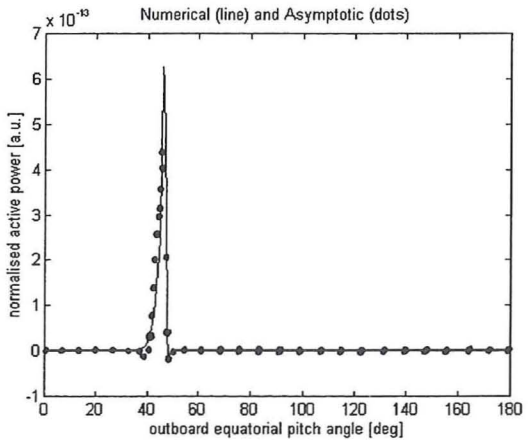

Fig 1

the result of the asymptotic expansion. The results are in good agreement, with significant Landau damping for the co-passing trajectories corresponding to $36° \le \gamma_0 \le 51°$ (the trapped trajectories correspond here to $57° \le \gamma_0 \le 123°$, and the counter-passing ones correspond to $\gamma_0 \ge 123°$). The resonance condition $\omega = k_{//}\, v_{//}$ is equivalent to the following equation:

$$\omega = \left(\frac{n}{R}\cos\Theta + \frac{m}{\rho}\sin\Theta\right)\sigma v\sqrt{1-\frac{(R_0+\rho)}{R}\sin^2\gamma_0} \qquad (1)$$

where R is the distance from the symmetry axis of the tokamak, Θ is the angle between the equilibrium magnetic field and the toroidal direction, and σ is the sign of $v_{//}$. Choosing a Maxwellian distribution function for the electrons and normalizing the results to the r.f. field amplitude $|E_{//nm}| = 1\,V/m$, we display on figure 2 the variations with the velocity v of the quantity $A(\rho,v) = \int_0^{180°} d\gamma_0\, w_{nm}$, that is the total power absorbed from the r.f. field mode n=16,

m=0 by electrons with velocity v located on the magnetic surface with minor radius ρ.

The results given by the asymptotic expansion are in good agreement with the continuous curve given by the direct numerical evaluation. These two curves, integrated over velocity, give evaluations of the power absorbed by the electrons (on this magnetic surface and for the chosen r.f. field mode) differing by less than a percent. This result indicates that the asymptotic expansion may be accurate over a broader range of parameters than the one expected in ref. [1]. Investigation of the situations where the inhomogeneity of $k_{//}$ $v_{//}$ is very weak (small minor radius ρ, r.f. field modes with a small $k_{//}$) is under way in order to reach a final conclusion on this important point.

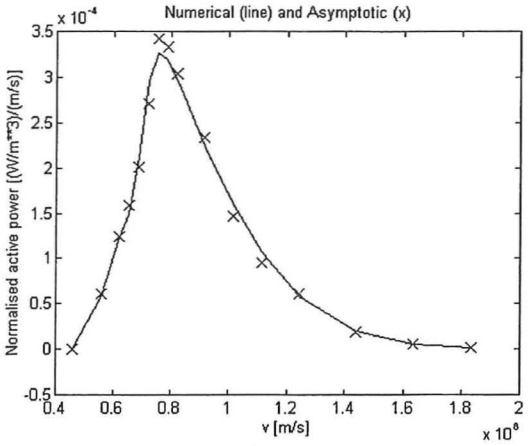

Fig 2

3. Influence of the characteristic decorrelation time

Our model includes a description of the wave-particle phase decorrelation due to collisions [4]. The previous example of an electron with v = 1.55 v_{th} located on the magnetic surface with minor radius ρ =1.35 m gives a characteristic decorrelation time t_L = 5.05 10^{-7} s. Because the resonance condition (1) is satisfied only for a single value of R, encountered twice on a poloidal bounce period for a passing orbit, we expect the power A(ρ,v) to be unchanged for smaller values of t_L. Using the decorrelation time as a free parameter, we check this behavior on figure 3 where this power is displayed as a function of t_L. As t_L increases, we observe a variation of A(ρ,v) when the decorrelation time reaches the order of magnitude of the poloidal bounce period of a well

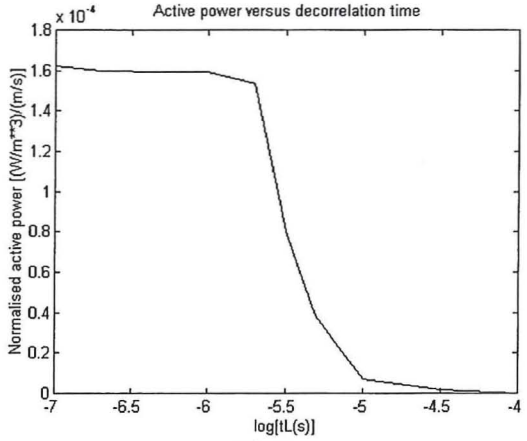

Fig 3

passing trajectory ($\tau_b \approx 10^{-6}$ s in this example). Figure 3 illustrates that the parameter t_L performs a smooth transition to the superadiabatic domain where $A(\rho,v)$ vanishes.

4. Power absorbed by trapped electrons

In order to satisfy the resonance condition (1) with higher values of the outboard equatorial pitch angle γ_0 than the ones obtained on figure 1, higher values of v are needed. As a consequence, only the trapped electrons with high velocities give contributions to the Landau damping. These contributions are weighted by a small factor coming from the Maxwellian distribution function describing the electronic population. Consequently, the Landau damping due to trapped electrons is very small.

We display on figure 4 the variation with ρ of the fraction of r.f. power absorbed by the trapped electrons located on a magnetic surface with minor radius ρ, using the parameters defined previously. The maximum appearing on this curve is due to the fact that the fraction of trapped orbits increases with ρ, but the number of resonant trapped electrons decreases (as ρ increases, resonance is obtained for higher values of v, and also v_{th} decreases).

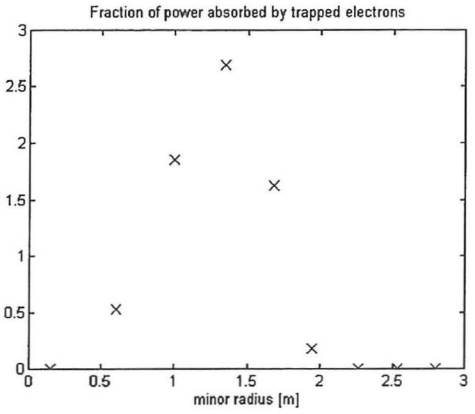

Fig 4

As preliminary conclusions, we have shown that

i) The asymptotic expansion given in [1], generally valid for the cyclotron interaction, also yields accurate results for the Landau interaction.

ii) In the ICRF range of frequencies, the contribution of the trapped electrons to Landau damping appears much smaller than the contribution of the passing electrons. A final answer will be obtained after incorporation of our expressions in a full-wave code, i.e. using a self-consistent set of coupled r.f. field modes.

The authors would like to thank Drs A. Bécoulet and D. Van Eester for fruitful discussions.

[1] Lamalle P.U. (1997) Plasma Phys. Control. Fus. 39 (9) 1409.

[2] Louis Y. (1996) LPP-ERM/KMS Report n°103.

[3] Bécoulet A. *et al.* (1994) Phys.Plasmas 1 (9) 2908.

[4] Louis Y. and Lamalle P.U. (1996) ISPP-17 "Piero Caldirola" Theory of Fusion Plasmas.

Plasma dynamics in box of unshielded fast wave antenna

V.I. Zasenko*, D.W. Faulconer, and R. Koch
Laboratoire de Physique des Plasmas - Laboratorium voor Plasmafysica
Association "Euratom-Etat Belge "- Associatie "Euratom-Belgische Staat"
Trilateral Euregio Cluster
Ecole Royale Militaire-Koninklijke Militaire School
Brussels, Belgium

*on leave from Bogolyubov Institute for Theoretical Physics, Kiev, Ukraine

1. Introduction Since an early date ICRF experiments have been conducted with a Faraday shield (FS) placed between antenna and plasma. Positive effects of the FS are accompanied by adverse ones which include suppression of magnetic flux of the antenna central conductor and sputtering of heavy ion impurities from the shield surface due to radio frequency (RF) sheath effect. After re-evaluation of the role of the Faraday shield [1], successful operation of an unshielded ICRF antenna was demonstrated on the medium-size tokamak TEXTOR [2,3]. This work motivates the present study of plasma dynamics in an unshielded antenna box in the time-asymptotic state, which itself complements an earlier consideration of the transient response [4].

2. Model

2.1 Basic equations Periodic potential ≈20 kV applied to the central conductor produces a strong local electrostatic field which is taken to dominate inductive effects in the near region. The plasma dynamics in the antenna box is then determined by a balance between particle transport in the radial (x) direction across the magnetic lines and particle escape to the walls of the box along the magnetic lines (Fig.1).

The system under consideration is strongly varying in the radial (x) direction but quite uniform along the magnetic lines (//z) due to the difference in transverse and longitudinal box dimensions, whence our introduction of z-averaged quantities, $\overline{(\ )}$.The equations for averaged densities and potential follow from neglect of inertial terms in the species momentum equations:

$$\frac{\partial \bar{n}_\alpha}{\partial t} - \frac{\partial}{\partial x} D_\alpha \left(\frac{\partial \bar{n}_\alpha}{\partial x} + \bar{n}_\alpha \frac{e_\alpha}{T_\alpha} \frac{\partial \bar{\varphi}}{\partial x} - \bar{n}_\alpha \frac{\omega_{c\alpha}}{\nu_{\perp\alpha}} \frac{e_\alpha \bar{E}_y}{T_\alpha} \right) + \frac{2}{L} [nV_z]_\alpha = 0 , \qquad (1)$$

$$\frac{\partial^2 \bar{\varphi}}{\partial x^2} = -\frac{e}{\varepsilon_0} (\bar{n}_i - \bar{n}_e) , \qquad (2)$$

Here, E_x, E_z are components of field characterized by potential φ, E_y - poloidal component of inductive field, $\omega_{c\alpha}$ - cyclotron frequency. The effective collision frequency $\nu_{\perp\alpha}$ describes the change in particle momentum due to collisions with turbulent field and is chosen consistent with $D_\alpha = 4\,m^2/s$. To close the set of Eqns.(1),(2) the fluxes to the walls at $z=\pm L/2$, $[nV_z]_\alpha$, should be written in terms of $\bar{n}_\alpha$ and $\bar{\varphi}$.

2.2 Particle fluxes to the wall Almost all drop of potential along the magnetic lines between plasma and grounded antenna box ($\varphi=0$) occurs at the box walls - in the oscillating sheath. In accordance with probe theory and studies of the RF sheath we assume that in the absence of substantial accelerating field in the bulk or sheath regions particles escape from the plasma with the thermal velocity $v_{Te} = \left[T_e/m_e\right]^{1/2}$ for electrons, and the sound speed $c_s = \left[\left(T_e + \gamma T_i\right)/m_i\right]^{1/2}$ for ions with $\gamma=2$. When the potential difference between the bulk plasma and the wall (i.e. across the sheath) is retarding, the flux is reduced by the Boltzmann factor:

$$[nV_z]_e = \begin{cases} (\bar{n}_e v_{Te}/\sqrt{2\pi})\exp(-e\bar{\varphi}/T_e) & (\bar{\varphi}>0); \\ (\bar{n}_e v_{Te}/\sqrt{2\pi}) & (\bar{\varphi}<0,\ \bar{n}_i>\bar{n}_e); \\ (\bar{n}_e v_{Te}/\sqrt{2\pi}) + \bar{n}_e\sqrt{-2e\bar{\varphi}/m_e}\,\vartheta(1-\bar{n}_e/\bar{n}_i) & (\bar{\varphi}<0,\ \bar{n}_i<\bar{n}_e) \end{cases} \qquad (3)$$

$$[nV_z]_i = [nV_z]_e(\bar{\varphi} \to -\bar{\varphi},\ v_{Te} \to \sqrt{2\pi}\,c_s,\ \text{e index} \leftrightarrow \text{i index}) \qquad (4)$$

The last term in Eqns.(3),(4) models enhanced particle expulsion occurring when a layer at given x has charge of the same sign as the antenna's; $\vartheta\left(1-\left(\bar{n}_\alpha/\bar{n}_\beta\right)\right)$, with properties $\vartheta(0)=0$ (charge of opposite sign) and $\vartheta(1)=1$ (same sign), smoothens the transition between the two cases. The factor $\sqrt{2\pi}$ in $v_{Te} \to \sqrt{2\pi}\,c_s$ in Eqns.(4),(6) was not included in earlier calculations [4], and gives ion flux at the Bohm velocity; it has also been inserted in $\bar{\varphi}_{fl}$ below.

2.3 *Boundary conditions at central conductor and in front of the box* Boundary conditions taken for potential and particle densities at the position of the central conductor, x=d(=3 cm), are: $\bar{\varphi}(d)=\varphi_o \sin(2\pi ft)$ or $\bar{\varphi}_{fl}$ [=floating potential$=(T_e/e)\ln(v_{Te}/c_s\sqrt{2\pi})$] when RF is respectively applied or not, and $n_\alpha(d)=0$. To avoid an arbitrary specification of boundary condition at the mouth of the box, x=0, we also consider the plasma dynamics in front of the box. The same Eqns.(1),(2) are applied over the same region in z as inside the box, but with modified fluxes along the magnetic lines:

$$[nV_z]_e = (\bar{n}_e v_{Te}/\sqrt{2\pi})[-1+\exp(-e(\bar{\varphi}-\bar{\varphi}_{fl})/T_e)] \quad (\bar{\varphi}>\bar{\varphi}_{fl}); \quad (5)$$
$$(\bar{n}_e v_{Te}/\sqrt{2\pi})[1-\exp(e(\bar{\varphi}-\bar{\varphi}_{fl})/T_e)] \quad (\bar{\varphi}<\bar{\varphi}_{fl})$$

$$[nV_z]_i = [nV_z]_e(v_{Te} \rightarrow -\sqrt{2\pi}\, c_s, \text{ e index} \rightarrow \text{ i index}) \quad (6)$$

These fluxes describe the flow of charged particles in front of the box through imaginary surfaces at z=±L/2. The first terms represent free-streaming fluxes out of the region of higher particle potential energy, the second, particle influxes into the same region suitably reduced by the Boltzmann factor where potential is taken as φ_{fl} at large |z| (corresponding to the scrape-off plasma making contact with the grounded (φ=0) tokamak limiter). Particle density and potential profiles are rather insensitive to the boundary conditions imposed at x=-d(=-3 cm): $\partial\bar{\varphi}(-d)/\partial x = k(\bar{\varphi}(-d)-\varphi_{fl})$, $n_\alpha(-d)=n_o$.

3. Particle densities and potential The equations obtained in the previous section have been solved numerically and results are given below. Deuterium plasma parameters taken in the numerical simulations are as follows: $n_e(x=-3cm)\equiv n_o=2\times10^{18}m^{-3}$, $m_i=2m_p$, $T_i=60eV$, $T_e=30eV$, $B_o=3T$, $f=3\times10^7Hz$, $\varphi_o=20kV$, $D=4m^2/s$, $k=12.08m^{-1}$. We neglect E_y in Eqn.(1).

3.1 Evolution in the asymptotic regime Fig.2 shows the strong shielding of oscillating field ($\propto -\partial U/\partial x$) taking place just at the box mouth where there is a corresponding accumulation of charge [4]. The maximum in the stationary potential shown in Fig.3 implies a bidirectional E_x with associated sheared $\mathbf{E}\times\mathbf{B}_o$ y-flow. Fig.4 shows a strong evacuation of density in the antenna box accompanying antenna excitation, as seen in experiment [5]. The slight increase in density just in front of the box could reflect our rough modelling of fluxes in this region (Eqn.(5)). A parasitic loss of energy arises from the averaged product of oscillating current by oscillating sheath potential drop across which the current flows. Integrating this loss over the inner box walls gives values of 11.6, 15.4, 18.3 kW for n_o respectively 2, 10, 20 (10^{18} m^{-3}). The integrated rectified currents accompanying RF, for the same respective densities, are -32, -38, -36 A (negative currents on the order of 100 A have been measured). As density increases the growth in charge carrier density appears to be offset by enhanced shielding of potential.

4. Conclusions The present examination of asymptotic behavior confirms the indications of the transient response [4], notably a strong initial evacuation of plasma from the high potential region immediately in front of the antenna central conductor which should be beneficial to phenomena linked to ion bombardment of the box walls (sputtering; power loss in sheaths). An oscillating charged layer plays the role of a Faraday shield, limiting perturbation of the scrape-off layer for the times examined. Parasitic losses are found in the present study to be modest. These findings support the idea that ICRF antennas can be operated without a Faraday shield.

References

[1] Van Nieuwenhove R., Koch R., Van Oost G. LPP-ERM/KMS Brussels Report nr.93, "Reevaluation of the role of ICRH Faraday Shields", (1990).

[2] Van Nieuwenhove R., Koch R., Van Oost G. *et al.* 1991 *Nucl.Fusion* **31** 1770.

[3] Van Nieuwenhove R., Koch R., Van Oost G. *et al.* 1992 *Nucl.Fusion* **32** 1913.

[4] V.I. Zasenko, D.W. Faulconer, and R. Koch, *24th EPS Conf. on Controlled Fusion and Plasma Physics*, Berchtesgaden, 9-13 June 1997.

[5] Van Nieuwenhove R., Koch R., Van Oost G. 1994 *Controlled Fusion and Plasma Physics (Proc. 21th Eur. Conf. Montpellier , 1994)* , Vol. 18B, part II (Geneva: EPS) p.976.

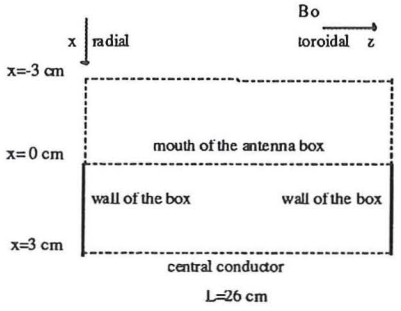

Fig.1 Poloidal view of the antenna box with toroidal extension 26 cm and radial extension 3 cm. The central conductor is modelled as a surface of width L=26 cm at x=3 cm.

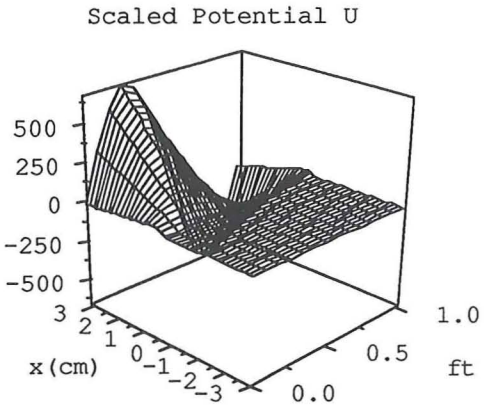

Fig.2 Scaled potential $U=(e\overline{\varphi}/T_e)$ over 1 period, 800 periods after application of excitation (stationary regime). Note shielding over several mm about x=0.

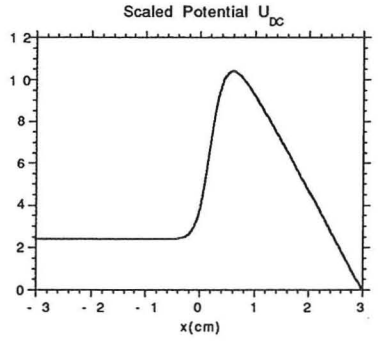

Fig.3 DC component of $U=(e\overline{\varphi}/T_e)$ after 800 periods, showing maximum inside box and descent to floating potential outside.

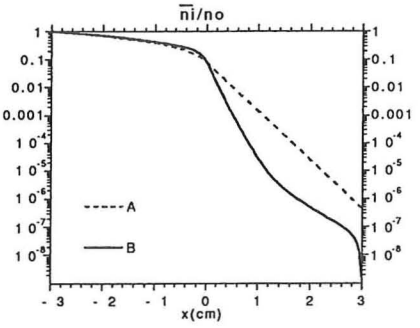

Fig.4 Time-averaged density profile before (curve A), and 800 periods after application (curve B) of RF excitation.

On Resonance Absorption and Continuum Damping

A. Jaun[1,2], K. Appert[1], T. Hellsten[2], J. Vaclavik[1], L. Villard[1]

[1] CRPP-EPFL, CH-1015 Lausanne, Switzerland

[2] Alfvén Laboratory, EURATOM-NFR Association, KTH, SE-100 44 Stockholm, Sweden

ABSTRACT. The absorption of power is studied with fluid and gyrokinetic plasma models, when two Alfvén or ion-ion hybrid resonances provide for a weak damping in a partially standing wavefield. Examples chosen in slab and toroidal geometry show that the the fluid predictions based on resonance absorption are generally very different from the Landau damping of mode-converted slow waves. They in particular suggest that the continuum damping of toroidal Alfvén eigenmodes (TAE) and the power deposition profiles obtained in the ion-cyclotron range of frequencies (ICRF) using fluid plasma models are very misleading.

PACS numbers: 52.35.Bj, 52.35.Py, 52.50.Gj, 52.65.Tt

Ever since Landau's lesson, which leàd to the discovery of the damping associated with the wave-particles resonance, it has been recognized that the integration over time of partial differential equation singularities requires a careful treatment that guarantees in effect that the causality remains preserved. By analogy, when the fluid wave equations are integrated in presence of an Alfvén or ion-ion hybrid resonance, a residual absorption of power appears which may be evaluated either by taking into account an arbitrarily small dissipation of the plasma or by adding artificially an imaginary part to the frequency. Studying the propagation of the fast-magnetosonic wave in the ion-cyclotron range of frequencies (ICRF), Budden [1] for example determined the fraction of the power absorbed, transmitted and reflected by a resonance-cutoff pair using a fluid plasma model, without specifying the mechanism actually responsible for the power dissipation.

If the plasma temperature is sufficiently large, the resonant layers where the fluid equations are singular coincide with the location where the fast wave energy can be converted to slow kinetic waves owing their existence to the finite Larmor radius (FLR) excursion of the ions [2]. The change of polarization accompanied with a rise in the electric field component parallel to the magnetic field is then generally responsible for the power dissipation, with resonant wave-particle interactions that occur as the slow wave propagates away from the conversion layer. Using an FLR expansion [3, 4, 5] and solving the full non-local problem [6], it has been found that the total power converted from a fast wave traveling in a single pass through a resonance depends only weakly on the slow wave parameters; the resonance absorption from fluid plasma models then coincides to a good degree of accuracy with the Landau damping of the slow wave described by the gyrokinetic models.

The aim of this letter is to draw attention to the fact that this is not in general true when two resonances are present in the same global wavefield, this even when the slow wave is damped in the vicinity of the mode conversion surface. In particular, the continuum damping of Alfvén eigenmodes (AE) [7, 8] and the resonance absorption of ICRF driven wavefields calculated with toroidal fluid plasma models [9, 10] are shown to be dramatically different from our gyrokinetic calculations, suggesting that AE mode stability threshold and ICRF power deposition profile predictions are very questionable when using fluid models.

To illustrate the concept first in a simple shearless slab plasma, Fig.1 shows an Alfvén wave heating scenario similar to the TCA tokamak [11] (B_0=1.5 T, $n_{e,0} = 2.3 \times 10^{19}$ m^{-3}, $T_{D,0}$=350 eV, $f_{ant} = 2$ MHz, $k_y = -5$ m^{-1}, $k_z = 2.9$ m^{-1}). An antenna current is imposed in the vacuum region on the right ($x = x_a = +19$ cm) and launches an evanescent fast wave into the plasma ($|x| < x_p = 18$ cm). After reflections, a global wavefield is created oscillating in phase in the entire cavity bounded by perfectly conducting walls ($|x| = x_w = 21$ cm). A parabolic variation of the density $n_e(x) = n_D(x) = n_{e,0}[1 - 0.95(x/x_p)^2]$ generates two Alfvén resonances at $|x| = x_r = 9.2$ cm, which are set to electron temperatures that differ

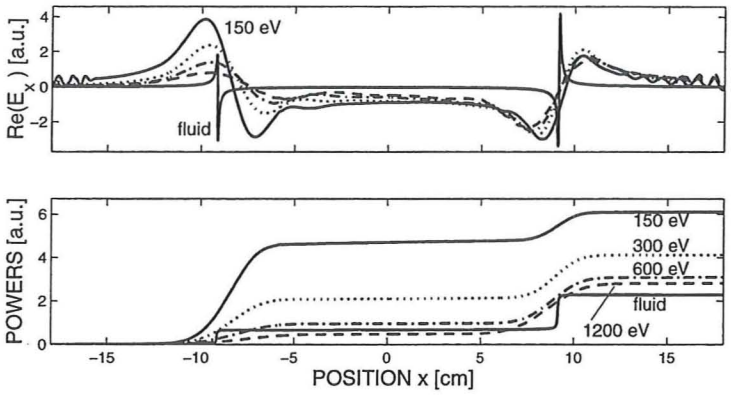

Figure 1: Alfvén wave heating scenario in a TCA-like slab plasma driven with an antenna from the right. The wavefield $Re(E_x)$ (top) and the integrated power $P(x)$ (bottom) calculated using a fluid model are compared with their gyrokinetic counterparts obtained for a rising temperature $T_{e,0}$ = 150, 300, 600, 1200 eV. The conversion layers are set to temperatures that differ by more than a factor two with an asymmetric profile of the form $T_e(x) = T_{e,0}[1 - 0.95(x/18)^2]^2[1 - 0.5(x/18)]^2$.

by more than a factor two $T_e(x) = T_{e,0}[1 - 0.95(x/x_p)^2]^2[1 - 0.5(x/x_p)]^2$, keeping that of the deuterons equal on both sides $T_D(x) = T_{D,0}[1 - 0.95(x/x_p)^2]^2$ eV. Using the full wave code ISMENE [12, 13] to compute the perpendicular wavefield (E_x, E_y) with a cold-fluid plasma model (see Ref.[13], eqs.6.1-6.2), sharp variations appear at the resonances which have been numerically resolved in Fig.1(top) by adding a small imaginary part $\delta = 0.02$ to the antenna frequency $\omega = 2\pi f_{ant}(1 + i\delta)$. Apart from details in the vicinity of the resonant layers, a change of the artificial damping $\delta \in [0.002; 0.02]$ does neither affect the integrated power $P(x) = \int_{-x_p}^{x} Im[\frac{\omega}{8\pi} Im(\mathbf{E}^* \cdot \epsilon \cdot \mathbf{E})]dx'$ in Fig.1(bottom) nor does it modify the relative power fraction absorbed at each resonance (table 1, fluid), suggesting that the power resonantly absorbed does not depend on the manner how the equations are regularized.

This fluid calculation has now to be contrasted with the gyrokinetic results from the same code, when all the wavefield components (E_x, E_y, E_z) are solved in terms of a second order FLR expansion of the plasma dielectric tensor (see Ref.[13], eqs.6.17-6.20). Fig.1(top) shows that a mode-converted kinetic Alfvén wave (KAW) propagates inwards from both sides and gets immediately damped by Landau interactions with the electrons in the neighborhood of the conversion layer. The short wavelength oscillations in the edge region ($|x| > 12$ cm) come from the surface quasi-electrostatic wave (SQEW) which is directly excited at the plasma boundary, but is unimportant for the subsequent analysis. Rising the electron temperature in the center $T_{e,0}$ = 150, 300, 600, 1200 eV while keeping that of the ions fixed, Fig.1(bottom) shows that the integrated power profile $P(x)$ is changing: not only the total power absorption is mod-

$T_{e,0}$ [eV]	$f^{left}_{x=-x_r}$ [%]	$f^{right}_{x=+x_r}$ [%]
150	78	22
300	51	49
600	44	56
1200	17	83
fluid model	30	70

Table 1: Fraction of the power absorbed by each resonance, based on the fluid and gyrokinetic power deposition profiles in Fig.1(bottom)

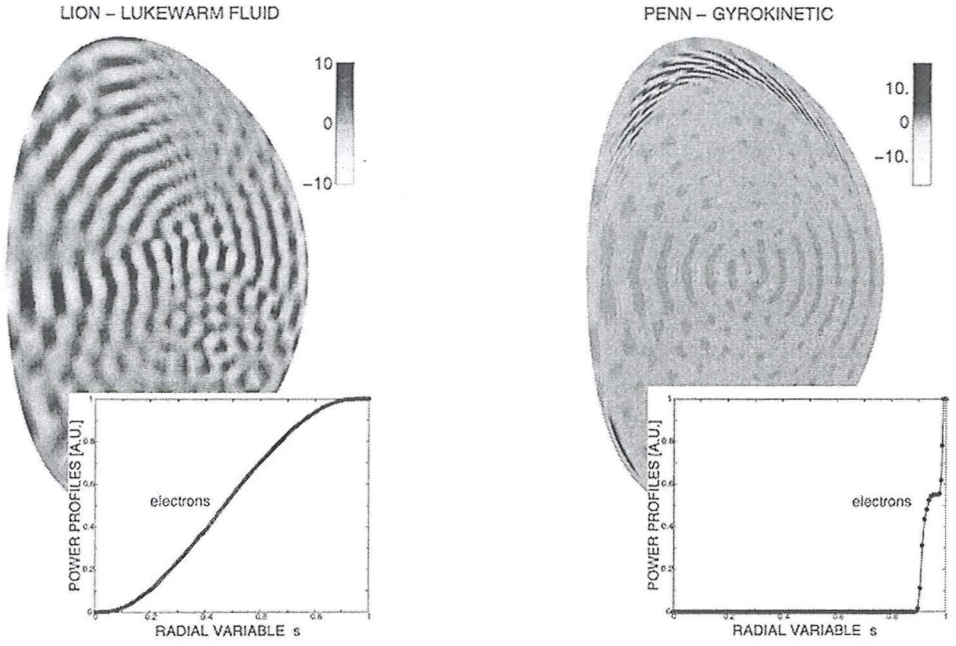

Figure 2: Current drive scenario proposed in Ref.[16] for ITER. The global wavefield $Re(E_n)$ (top) and the integrated power profile $P(s)$ (bottom) both show that the mode-conversion predicted by the gyrokinetic PENN calculation (right) is not reproduced with resonance absorption in the fluid LION code (left), suggesting that fluid predictions can be very misleading.

ified, but also the fraction absorbed by each resonance is dramatically different (table 1). This strong dependence on the temperature is of course not reproduced with the fluid plasma model and is in apparent contradiction with the small dependence on the slow wave parameters which has previously been observed in other comparisons. The paradox is solved by realizing that a small change in the "single pass" mode-conversion efficiency, which is rendered visible because of the temperature asymmetry, is here strongly amplified when the global wavefield carries fast wave energy from one resonance to the other.

This phenomenon, which has for simplicity been illustrated with the simple slab calculation above, becomes particularly important in tokamaks and stellarators where the magnetic curvature and the finite frequency in the ion-cyclotron range couple different poloidal and toroidal harmonics, forming global modes which can interact with resonant surfaces throughout the plasma radius. Alfvén eigenmodes get damped by resonances, but the continuum damping predicted using fluid plasma models [7, 8] sometimes disagrees by an order of magnitude with the gyrokinetic predictions and the experimental measurements [14, 15]. ICRF heating scenarii generally involve a multitude of resonances with large poloidal mode numbers $m > 20$. Global fluid calculations suggest that they are generally not excited because the toroidal coupling, proportional to the inverse aspect ratio power $\epsilon^{|m-m_{ant}|}$, is very weak for low antenna mode numbers $m_{ant} \sim 5$. The gyrokinetic calculations from Ref.[16] however show that large poloidal mode numbers appear because of the toroidicity, when the fast and KAW wavelengths match at a resonance $\vec{k}_{fast} = \vec{k}_{slow}$ where the thermal electron velocity exceeds the parallel wave phase velocity $\omega/(k_\parallel v_{th,e}) < 1$.

The second example illustrates this in Fig.2 with a current-drive scenario proposed in Ref.[17] for the international thermonuclear experimental reactor (ITER) (B_0=6 T, $q_0 = 1.03$, $\beta_{tor} = 2.7\%$, $n_{e,0} = 1.4n_{D,0} = 3.5n_{T,0} = 1.4 \times 10^{20}$ m^{-3}, $T_{e,0} = T_{D,0} = T_{T,0} = 19$ keV, $f_{ant} = 20$ MHz, $n_{tor} = 21$). The lukewarm fluid LION code [9] calculation in Fig.2(left) suggests that the fast wave emmitted by an antenna on the low magnetic field side of the torus, first propagates inwards past the magnetic axis

an antenna on the low magnetic field side of the torus, first propagates inwards past the magnetic axis and forms a partially standing global wavefield that extends throughout the torus. The coupling to high poloidal mode numbers is however sufficiently weak that the resonance absorption remains negligible and the power gets almost homogeneously absorbed by the fast wave electron Landau damping and transit-time magnetic pumping (TTMP). This fluid prediction is dramatically different from the gyrokinetic result obtained from the PENN code [16], which shows that strong mode-conversion takes place where the partially standing fast wavefield meets the KAW scalelength in the neighbourhood of fluid resonances with large poloidal mode numbers $m \simeq 25$. The power is then mainly deposited by the electron Landau damping of the KAW, in the plasma edge region where the resonance absorption computed with fluid plasma models remains negligible. Apart form questioning the validity of fluid plasma models for weak absorption, this mode-conversion at the plasma edge provides for a plausible mechanism explaning the degradation in the heating efficiency which has been observed in the experiments [18].

In summary, both examples chosen above in slab and toroidal geometry show that fluid plasma models cannot be used to correctly predict the power absorption and the continuum damping when two resonances or more are present in a partially standing wavefield. This is in particular true for the prediction of Alfvén eigenmode dampings and the modeling of the power deposition profiles during ICRH, where more sophisticated gyrokinetic descriptions are required - at least.

One of the authors (A.J.) acknowledges useful discussions with F. Zonca. This work was supported in part by the Swiss and the Swedish National Science Foundations and the calculations were performed on the CRAY C-94 super-computer in Linköping.

References

[1] K. Budden, *Radio Waves in the Ionosphere*, Cambridge University Press (1985) 596

[2] A. Hasegawa, L. Chen, Phys. Rev. Lett. **35** (1975) 370

[3] D.G. Swanson, Phys. Fluids **24** (1981) 2035

[4] P. Colestock, R. Kashuba, Nucl. Fusion **23** (1983) 763

[5] J.A. Heikkinen, T. Hellsten, M.J. Alva, Nucl. Fusion **31** (1991) 417

[6] O. Sauter, J. Vaclavik, Comput. Phys. Commun **84** (1994) 226

[7] M. N. Rosenbluth, H.L. Berk, J.W. Van Dam, D.M. Linberg, Phys. Rev. Lett. **68** (1992) 596

[8] F. Zonca, L. Chen, Phys. Rev. Lett. **68** (1992) 592

[9] L. Villard, K.Appert, R.Gruber, J.Vaclavik, Comput.Phys.Reports **4** (1986) 95

[10] D. Gambier, A. Samain, Nucl. Fusion **25** (1985) 283

[11] G.A.Collins, F.Hofmann, B.Joye, Phys. Fluids **29** (1986) 2260

[12] K.Appert, T.Hellsten, J.Vaclavik, L.Villard, Comput. Phys. Commun. **40** (1986) 73

[13] J. Vaclavik, K. Appert, Nucl. Fusion **31** (1991) 1945

[14] A. Jaun, A. Fasoli, W.W. Heidbrink, Phys. Rev. Lett., submitted

[15] A. Fasoli, J. Lister, J.-M. Moret, S. Sharapov, D. Borba, G. Bosia, D. Campbell, J. Dobbing, C. Gormezano, J. Jacquinot, P. Lavanchy, Ph. Marnillod, A. Santagiustina, Phys. Rev. Lett. **75** (1995) 645

[16] A. Jaun, K. Appert, J. Vaclavik, L. Villard, Comput. Phys. Commun. **92** (1995) 153

[17] *Fast Wave Heating and Current Drive in ITER*, Eur. Coord. Comm. on Fast Wave Current Drive and Heating (CCFW), edited by V. Bhatnagar, J. Jacquinot, NET Report EUR-FU/XII/163/94 (1994)

[18] L.-G. Eriksson, T. Hellsten, Nucl. Fusion **29** (1989) 875

List of Participants

Australia	
Dept. of Physics, Flinders University, Adelaide	Storer, A.
Belgium	
Ecole Royale Militaire/Köninklijke Militaire School, Association „Euratom-Belgian State", Trilateral Euregio Cluster, Brussels	Dirickx, M. Faulconer, D. Koch, R. Louche, F. Louis, Y. Vandenplas, P. Van Eester, D. Van Oost, G.
Physique Statistique, Plasmas et Optique Non-Linéaire, Association „Euratom-Etat Belge", Université Libre de Bruxelles	Balescu, R. Grecos, A. Vanden Eijnden, E. Weyssow, B.
Denmark	
Optics and Fluids Dynamics Dept., Risϕ National Laboratory, Euratom Association, Roskilde	Jessen, T. Michelsen, P. Naulin, V. Nielsen, A.H. Rasmussen, J.J.
France	
Dept. de Recherche sur la Fusion Controlée, Centre d'Etudes de Cadarache, Association Euratom-CEA sur la Fusion	Maschke, E. Nakach, R. Zabiego, M.
Université Blaise Pascal, Aubière	Saramito, B.
Germany	
Institut für Plasmaphysik, Forschungszentrum Jülich GmbH, Euratom Association, Trilateral Euregio Cluster, Jülich	Abdullaev, S. Claaßen, H.-A. Finken, K.-H. Gerhauser, H. Kaleck, A. Lasaar, H. Reiser, D. Rogister, A. Tokar, M. Wolf,G.H.
Max-Planck Institut für Plasmaphysik, Euratom Association, Garching	Düchs, D. Puri, S.

	Zeiler, A.
Heinrich-Heine Universität Düsseldorf, Düsseldorf	Grauer, R. Spatschek, K.H.
India	
Saha Institute of Nuclear Physics, Calcutta	Dasgupta, B.
Italy	
Associazione Euratom-ENEA sulla Fusione, Frascati	Cardinali, A.
Centro Ricerche Energia, ENEA, Bologna	Cenacchi, G.
Consorzio RFX, Associazioni Euratom-ENEA-CNR-Universita di Padova, Padova	Escande, D. Paccagnella, R.
Dept. of Mathematical Sciences, Universita di Trieste	Pozzo, M. Zorat, R.
Dept. of Physics, Universita di Pisa	Pegoraro, F.
Dip. di Energetica, Politecnico di Torino	Grasso, D. Porcelli, F.
Istituto di Fisica del Plasma, Associazione Euratom-ENEA-CNR, Milano	Lazzaro, E. Lontano, M.
Japan	
Dept. of Physics, Ehime University, Matsuyama	Sugaya, R.
Norway	
Dept. of Applied Mathematics, University of Bergen	Berge, G.
Portugal	
Centro de Fusào Nuclear, Instituto Superior Técnico Association Euratom-IST	Serra, F.
Spain	
Escuela Politécnico Superior, Univ. Carlos III de Madrid	Garcia, L.
Centro de Investigaciones Energeticas, Association Euratom-CIEMAT, Madrid	Tribaldos, V.
Sweden	
Institute for Electromagnetic Field Theory and Plasma Physics, Chalmers University of Technology, Euratom-NFR Association, Göteborg	Bondeson, A. Nordman, H. Weiland, J. Wilhelmsson, H.

Switzerland

Centre de Recherches en Physique des Plasmas, Association Euratom-Confédération Suisse, Lausanne	Ardella, A. Brunner, S. Cooper, A. Fivaz, M. Jaun, A. Sauer, O. Vaclavik, J. Villard, L.

The Netherlands

FOM Instituut voor Plasmafysica Rijnhuizen, Association Euratom-FOM, Trilateral Euregio Cluster, Nieuwegein	Bellen, S. Gherado, V. Goedbloed, H. Kuvshinov, B. Nijboer, R. Rem, J. Schep, T.J. Van der Holst, B. Westerhof, E.

Turkey

Dept. of Aerospace Sciences, Technical University of Istanbul	Anguelova, M. Daybelge, U. Yarim, C.

United Kingdom

UKAEA Fusion, Culham Laboratory, UKAEA-Euratom Fusion Association, Abingdon	Han, W. O'Brien, M.
JET Joint Undertaking (EC), Abingdon	Kerner, W. Sharapov, S. Zwingmann, W.

Ukraine

National Science Center, Institute of Physics and Technology, Kharkov	Kasilov, S.

United States

Physics and Astronomy Dept., Dartmouth College, Hanover	Montgomery, D.

Fusion Theory

This book contains the manuscripts of the papers presented at the Seventh European Fusion Theory Conference held in Jülich, Germany, from 8 – 10 October 1997.

Forschungszentrum Jülich

Band/Volume 1
ISBN 3-89336-219-3

Energietechnik
Energy Technology